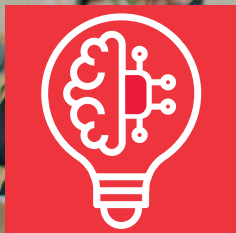**STUDENT EEICT**

BRNO UNIVERSITY OF TECHNOLOGY
FACULTY OF ELECTRICAL ENGINEERING AND COMMUNICATION

PROCEEDINGS I OF THE 31ST STUDENT EEICT 2025
ELECTRICAL ENGINEERING, INFORMATION SCIENCE, AND COMMUNICATION TECHNOLOGIES
GENERAL PAPERS

April 29, 2025
Brno, Czech Republic

BRNO UNIVERSITY OF TECHNOLOGY
FACULTY OF ELECTRICAL ENGINEERING AND COMMUNICATION

STUDENT EEICT

BRNO FACULTY OF ELECTRICAL
UNIVERSITY ENGINEERING
OF TECHNOLOGY AND COMMUNICATION

SPONSORS

Diamond tier

Honeywell

Golden tier

ABB

SKUPINA ČEZ

EATON

e·on

ThermoFisher
SCIENTIFIC

BRNO UNIVERSITY OF TECHNOLOGY
FACULTY OF ELECTRICAL ENGINEERING AND COMMUNICATION

STUDENT EEICT

SPONSORS
Silver tier

ASICentrum — A COMPANY OF THE SWATCH GROUP

Garrett — ADVANCING MOTION

resideo

NXP

Valeo

Honorary tier

SKODA

TECHNICAL SPONSORS & MEDIA PARTNERS

IEEE — IEEE Czechoslovakia Section

VERONI kafestánek

BRNO FACULTY OF ELECTRICAL
UNIVERSITY ENGINEERING
OF TECHNOLOGY AND COMMUNICATION

Contents

Foreword

Bachelor Projects

B1 – Biomedical Engineering

B2 – Communication and Information Systems

B3 – Generation and Transmission of Electrical Energy

B4 – Industrial Automation, Instrumentation and Engineering

B5 – Systems Modeling, Control and Measurement

Master's Projects

M1 – Audio, Image and Biomedical Signal Processing

M2 – Communication and Information Systems, Networks

M3 – Machine Learning and Wireless Communication

M4 – Network Security and Cryptography

M5 – Electrical Energy: Generation, Transmission, Optimization

M6 – Industrial Automation, Control, Machine Vision, UAVs

Ph.D. Projects

D1 – Audio and Biomedical Signal Processing, Bioinformatics

D2 – Communication and Information Systems, Network Security

D3 – Microelectronics and Technology

D4 – Physical Sciences

D5 – Power Electronics, Electric Drives and Machines

D6 – Sensors and Measurement Systems

D7 – Systems Modeling, Control, Machine Vision, UAVs

High School Projects

S1 – General Technical Focus

STUDENT EEICT

OPENING WORD OF THE DEAN

These Proceedings contain papers presented during the 31st annual STUDENT EEICT conference, held at the Faculty of Electrical Engineering and Communication, Brno University of Technology, on April 29, 2025. The fruitful tradition of joining together creative students and seasoned science or research specialists and industry-based experts was not discontinued, providing again a valuable opportunity to exchange information and experience.

The EEICT involves multiple corporate partners, collaborators, and evaluators whose intensive support is highly appreciated. Importantly, the competitive, motivating features of the conference are associated with a practical impact: In addition to encouraging students to further develop their knowledge, interests, and employability potential, the forum directly offers career opportunities through the affiliated PerFEKT JobFair, a yearly job-related workshop and exhibition complementing the actual EEICT sessions. In this context, the organizers acknowledge the long-term assistance from the Ministry of Education, Youth and Sports of the Czech Republic, which has proved essential for refining the scope and impact of the symposium.

In total, 136 peer-reviewed full papers distributed between 19 sessions were submitted and evaluated by examining boards with industry and academic specialists. The presenting authors exhibited a very high standard of knowledge and communication skills, and the best competitors received prize money and/or valuable gifts. Our sincere thanks go to the sponsors, experts, students, and collaborators who participated in, contributed to, and made the conference a continued success.

Considering all the efforts and work invested, I hope that the 31st STUDENT EEICT (2025) has been beneficial for all the participants.

I believe that the inspiration gathered during the event will contribute to the further advancement of open science and research, giving all the attendees a chance to freely discuss their achievements and views.

Prof. Vladimír Aubrecht
Dean of the Faculty of Electrical
Engineering and Communication

BRNO UNIVERSITY OF TECHNOLOGY
FACULTY OF ELECTRICAL ENGINEERING AND COMMUNICATION

Polyvinylidene fluoride doped with hydroxyapatite: cell growth and design of magnetoelectric stimulation

Alena Dudíková

Department of Microelectronics, Faculty of Electrical Engineering and Communication
Brno University of Technology
Technická 2848/8, 61600 Brno, Czech Republic
246993@vutbr.cz

Abstract— **To promote tissue regeneration, functional polymer scaffolds mimicking the human extracellular matrix are in high demand. Piezoelectricity and hydrophilicity are key properties that enhance their performance. Polyvinylidene fluoride (PVDF), known for generating surface charges under mechanical stress, is a promising material for such scaffolds. However, hydrophilicity is crucial for proper cell adhesion and growth. This study produced PVDF nanofibers via electrospinning, seeded them with cells, and analyzed their surface using scanning electron microscopy (SEM). Furthermore, the scaffolds underwent cytocompatibility testing to confirm their suitability for supporting cell growth.**

Keywords— Scaffold, PVDF, HA, fiber, piezoelectricity

I. INTRODUCTION

Piezoelectric polymers, like polyvinylidene fluoride (PVDF), generate electrical voltage when mechanically stressed. PVDF is widely used due to its strong mechanical properties and high piezoelectric response, which can be enhanced by adding dopants like Fe_2O_3 for magnetic properties or hydroxyapatite (HA) for biocompatibility. These composites are promising for advanced tissue scaffolds that support cell growth and regeneration [1].

PVDF is particularly valued for its structural and electromechanical properties, including high melting point, mechanical strength, chemical resistance, and non-toxicity. However, its hydrophobic nature limits cell adhesion, which can be improved through surface treatments like oxygen plasma [2].

Electrospinning is a common method for producing PVDF fibers, allowing control over fiber diameter and crystalline phases. Doping with materials like $BiFeO_3$, TiO_2, or carbon nanotubes (CNTs) enhances piezoelectric and pyroelectric properties. Blending PVDF with CNTs can also improve electrical conductivity and piezoresistive responses under mechanical strain. Single-walled or multi-walled carbon nanotubes are used depending on the desired mechanical and electrical properties [2].

Electrical and magnetic fields influence biological processes. Both AC and DC fields can stimulate cells and promote tissue repair, with new electrode technologies showing positive effects on nerve cell growth. Magnetic fields also affect cell behavior. Weak fields can enhance cell membrane permeability, while stronger fields ($>500\ \mu T$) promote cell growth. [4].

II. MATERIALS AND METHODS

A. Materials and their Parameters

Electrospun polyvinylidene fluoride (PVDF) fibers containing hydroxyapatite (HA) were fabricated using the electrospinning technique. The process employed a single-needle syringe emitter filled with a polymer solution and a cylindrical collector wrapped in aluminum foil. The polymer solution was delivered through the needle at a flow rate of $25\mu l/min$. Simultaneously, the collector rotated at 2000 revolutions per minute, enabling the polymer jet to be drawn onto its surface, forming a thin layer of nanofibers. A voltage of 50 kV was applied between the emitter and the collector.

PVDF was electrospun in its β-phase. The polymer solution consisted of a 20 % PVDF concentration with the addition of either 5 % or 10 % HA particles. The final mixture was stirred and heated at 80 °C for 24 hours at a stirring speed of 200 rpm.

To obtain high-quality scanning electron microscopy images, the PVDF fiber surface was evenly coated due to its dielectric properties. A 16 nm carbon coating layer was applied to prevent surface charging. Without the coating, it would be difficult to focus on the nanofibers and scan them at high magnification.

B. Cultivation of the Cells

For cytotoxicity testing, HT 1080 (human fibrosarcoma) and K2 (rat sarcoma) cell lines were used. HT 1080 is a human fibrosarcoma cell line established in 1964 from a 35-years old male with a fibrosarcoma, a type of malignant soft tissue tumor. The K2 cell line originates from rat sarcoma and is derived from Rattus norvegicus. Cells were passaged twice a week at 80 %

confluency to maintain consistent growth and avoid contamination. They were cultured at 37 °C in a humidified incubator with 5 % CO_2.

After culturing, cells were separated into test tubes. Sterilized PVDF samples (1.5 cm × 1.5 cm) with 5 % and 10 % HA were prepared. In 60 mm Petri dishes, 30,000 cells were seeded with 4 ml of culture medium (MEM with 10 % FBS and antibiotics). The samples were submerged in the medium and incubated at 37 °C. Cell morphology was observed at 24, 48, and 72 hours using a phase-contrast microscope.

C. Methods Used for Assessing Properties of the Samples

1) Scanning Electron Microscopy (SEM): Surface imaging of PVDF fibers was performed using scanning electron microscopy (SEM). A secondary electron detector was selected for the analysis. The working distance between the electron source and the specimen was set to 20 cm, with a beam intensity of 3 keV. The electron beam's emission current was 223.38 µA, and the accelerating voltage was 5 kV. The microscope operated in resolution scan mode.

2) Raman Spectroscopy: Raman spectroscopy was used to identify the phases of PVDF. Analysis of the nanocomposite material, consisting of PVDF nanofibers with 5 % and 10 % HA particles, was conducted using a Nikon CFI S Plan Fluor ELWD objective with 40x magnification and a 380 nm excitation laser. The laser power was 4.9 mW, depending on the sample. The signal was obtained by averaging 50 accumulations, each with an integration time of 10 seconds.

III. RESULT

A. Phase composition

Raman spectroscopy analyzes how light interacts with chemical bonds in a material. By examining peak positions and relative peak intensities, it can reveal the material's chemical structure, crystalline phases, internal stress, contamination, and impurities.

Both samples with 5 % and 10 % HA particles, shown in Figure 1a and 1b and analyzed in the 100–2500 cm^{-1} range, exhibit the presence of the β-phase. Characteristic peaks include 510 cm^{-1} (CF_2, β-phase), 610 cm^{-1} (CF_2, α-phase), 795 cm^{-1} (CH_2 rocking, α-phase), 840 cm^{-1} (CH_2 rocking, β-phase), and 880 cm^{-1} (common to both phases). A peak at 1431 cm^{-1} corresponds to CH_2 bending vibrations [3].

Hydroxyapatite (HA) bonding is identified by phosphate (PO_4^{3-}) vibrations: the bending mode (O-P-O) at 430 cm^{-1}, the symmetric stretching mode (P-O) at 960 cm^{-1}, and the asymmetric stretching mode (P-O) at 1075 cm^{-1}. The (C=C) band appears at 1644 cm^{-1}, indicating structural modifications [5].
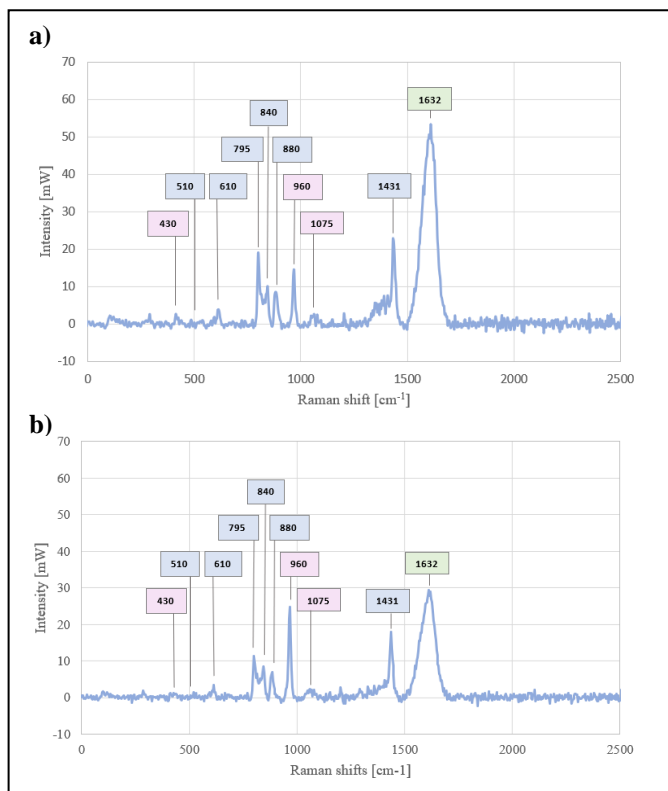
Fig. 1. Raman spectra of PVDF fiber with a) 5 % HA; b) 10 % HA particles

B. Sample morphology

SEM observations provided valuable insight into the complex relationship between the surface morphology of PVDF scaffolds, their physical properties, and the mechanical support they offer to growing osteoblastic cells.

Figure 2 presents SEM images of PVDF samples with 5 % and 10 % HA particles after electrospinning. The fibers appear continuous with few beads. In Figure 2a, a micrograph of fibers with 5 % HA particles is shown, using a backscattered electron detector to highlight the contrast between HA and PVDF fibers. Figure 2b show fibers with 10 % HA particles, demonstrating successful incorporation and good dispersion of HA in the membranes.

The average fiber diameter was measured to be approximately 500 nm. A slight increase in fiber thickness was observed with higher HA content, likely due to increased solution viscosity and the presence of solid particles, which can affect jet elongation during electrospinning.

C. Cytotoxicity test

Cytotoxicity testing of both samples returned a negative result, indicating that the materials were not cytotoxic under the experimental conditions. In all test groups, the cells demonstrated the ability to recover from initial stress (likely caused by handling or sample introduction) and proceeded to proliferate. This proliferation was observed both randomly across the culture dish and around the samples, suggesting that the materials did not hinder cell growth or attachment in any localized area.
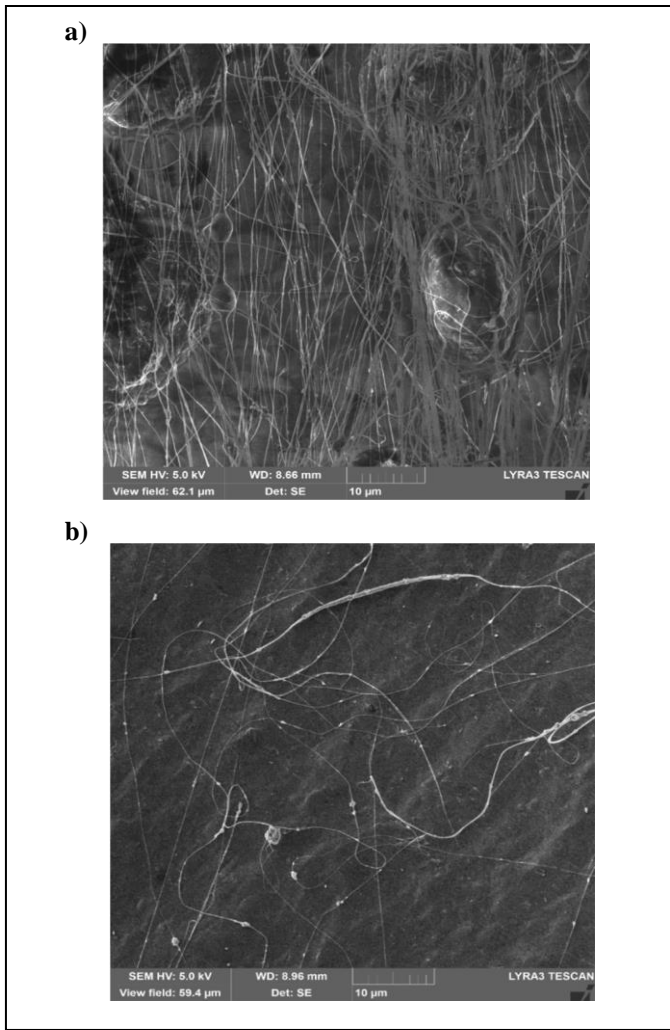
Fig. 2. Representative SEM images of the PVDF composites: a) with HA 5 % particles; b) with HA 10 % particles

Figure 3 presents the third microscopic evaluation after 72 hours, showing 100x magnification images of PVDF samples with 5 % and 10 % HA particles during cell growth.

The visual estimation of cell viability based on the images shows the following results: In Figure 3b, for PVDF + 5 % HA, K2 cells, the cells are well spread, clearly defined, and show no noticeable signs of apoptosis, with a minimal number of dead cells. The estimated viability is approximately 95–98 %. In Figure 3b for PVDF + 5 % HA, HT cells, the cells exhibit a high density and a generally healthy appearance, with slightly more variation in morphology than the K2 cells, but no significant cytotoxicity, resulting in an estimated viability of 90–95 %.

For Figure 3c, for PVDF + 10 % HA, K2 cells, the cells show a small increase in cell growth and proliferation, with larger isolated colonies scattered throughout the dish. The estimated viability is around 88–92 %. Lastly, Figure 3d for PVDF + 10 % HA, HT cells show full recovery, with at least a twofold increase in cell number and normal morphology observed, even near the sample. The estimated viability is 85–90 %.
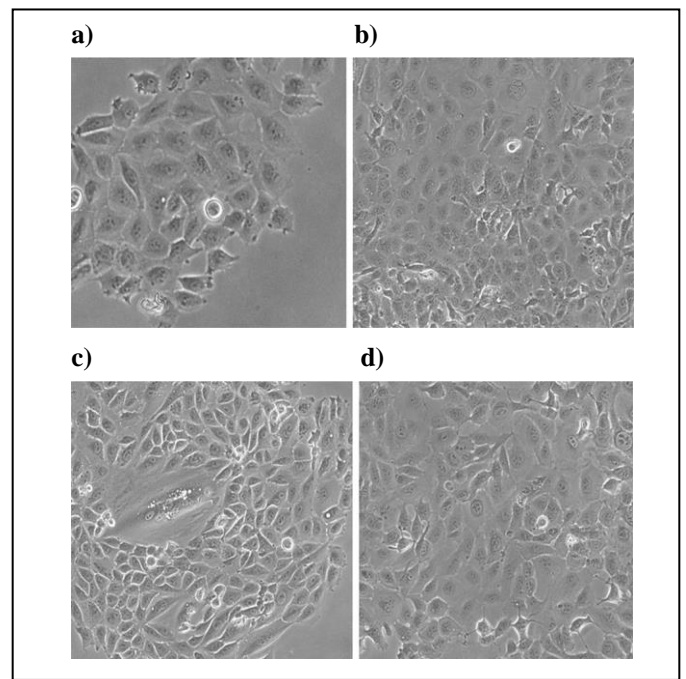
Fig. 3. Third microscopic evaluation: PVDF with HA 5 % particles a) with K2 cells, b) with HT cells; PVDF with HA 10 % particles c) with K2 cells, d) with HT cells.

IV. CONCLUSION

Polymeric electrospun microfiber mats were developed for tissue engineering, regenerative medicine, and drug delivery. PVDF nanofiber scaffolds with 5 % and 10 % HA particles were successfully produced using a single-fluid electrospinning method.

Physical and morphological measurements of the PVDF material were completed, with SEM images requiring a carbon coating to prevent surface charging. HA incorporation was satisfactory, with good particle dispersion throughout the membranes. The average diameter of the fibers was measured to be around 500 nm.

Raman spectroscopy, which analyzes light interactions with chemical bonds, revealed that both the 5 % and 10 % HA particle samples exhibit the β-phase. Characteristic Raman peaks for the α-phase include 610 cm^{-1} and 795 cm^{-1}, while the β-phase is confirmed by peaks at 510 cm^{-1} and 840 cm^{-1}. A common peak for both phases is observed at 880 cm^{-1}.

Cytocompatibility testing with HT 1080 and K2 cells demonstrated high cell viability and healthy morphology, highlighting their suitability for tissue engineering and regenerative medicine.

Future research could examine the interaction between the PVDF scaffold with a magnetic dopant, growing cell tissue, and exposure to an electromagnetic field.

REFERENCES

[1] MISHRA, Soumyaranjan; KUMARAN, K.T.; SIVAKUMARAN, R. et al. Synthesis of PVDF/CNT and their functionalized composites for studying their electrical properties to analyze their applicability in actuation & sensing. Online. *Colloids and surfaces. A, Physicochemical and engineering aspects*. 2016, roč. 509, s. 684-696. ISSN 0927-7757. Dostupné z: https://doi.org/10.1016/j.colsurfa.2016.09.007.

[2] KITSARA, Maria; BLANQUER, Andreu; MURILLO, Gonzalo et al. Permanently hydrophilic, piezoelectric PVDF nanofibrous scaffolds promoting unaided electromechanical stimulation on osteoblasts. Online. *Nanoscale*. 2019. Dostupné z: https://hal.sorbonne-universite.fr/hal-02351810v1

[3] KASPAR, Pavel; SOBOLA, Dinara; ČÁSTKOVÁ, Klára et al. Case study of polyvinylidene fluoride doping by carbon nanotubes. Online. *Materials*. 2021, roč. 14, č. 6, s. 1428. ISSN 1996-1944. Dostupné z: https://doi.org/10.3390/ma14061428.

[4] VAN HUIZEN, Alanna V.; MORTON, Jacob M.; KINSEY, Luke J. et al. Weak magnetic fields alter stem cell–mediated growth. Online. *Science advances*. 2019, roč. 5, č. 1, s. eaau7201-eaau7201. ISSN 2375-2548. Dostupné z: https://doi.org/10.1126/sciadv.aau7201.

[5] KAZANCI, M.; FRATZL, P.; KLAUSHOFER, K. et al. Complementary information on in vitro conversion of amorphous calcium phosphate to hydroxyapatite from raman microspectroscopy and wide-angle X-ray scattering. Online. *Calcified tissue international*. 2006, roč. 79, č. 5, s. 354-359. ISSN 0171-967X. Dostupné z: https://doi.org/10.1007/s00223-006-0011-9.

Tepovka: A Mobile Application for Heart Rate Measurement Using Photoplethysmography

Štěpán Zelníček
Department of Biomedical Engineering
FEEC, Brno University of Technology
Brno, Czech Republic
247326@vutbr.cz

Jakub Kovář
Department of Biomedical Engineering
FEEC, Brno University of Technology
Brno, Czech Republic
247258@vut.cz

David Vavroušek
Department of Biomedical Engineering
FEEC, Brno University of Technology
Brno, Czech Republic
247195@vut.cz

Abstract — This paper presents Tepovka, a mobile application developed to measure heart rate using photoplethysmography (PPG) via smartphone cameras. Leveraging the widespread availability of smartphones, Tepovka offers an accessible, non-invasive tool for monitoring heart rate in real-time. The app employs a custom algorithm to process PPG signals derived from RGB color channels, demonstrating high accuracy when validated against a reference ECG device (Faros). Developed using Flutter for cross-platform compatibility, Tepovka currently performs reliably on iOS devices, with ongoing plans for Android optimization. This work, conducted at the Department of Biomedical Engineering at Brno University of Technology, aims to contribute to the growing field of telemedicine by providing user-friendly, scientifically validated heart rate monitoring solutions.

Keywords — PPG, BPM, Mobile Application, Tepovka

I. Introduction

Mobile applications have become integral to modern healthcare, capitalizing on the ubiquity of smartphones owned by approximately 85% of the global population [1]. Smartwatches and specialized wearable devices are the traditional area of biometric tracking, including heart rate monitoring. While the wearables guarantee continuous monitoring, they are not easily accessible to everyone due to their cost and the need for additional hardware. Thus, most people lack easy accessibility to monitor heart rate outside a medical setting, and this has driven the need for a low-cost, widely available alternative for heart rate monitoring.

Tepovka addresses this need by utilizing smartphone cameras to measure heart rate using photoplethysmography (PPG). Traditionally employed in medical settings, PPG has gained traction in consumer electronics, enabling accurate physiological measurements without the need for specialized hardware. By harnessing smartphone technology, Tepovka provides an affordable and accessible solution, expanding access to biometric monitoring for a broader audience.

Developed at the Faculty of Electrical Engineering and Communication, Brno University of Technology, Tepovka aims to provide a reliable, cost-effective alternative for heart rate monitoring. This paper outlines the app's development, its PPG-based algorithm, testing methodology, and user interface features, with a focus on its potential in telemedicine.

II. Photoplethysmography

Photoplethysmography (PPG) is an optical method that measures changes in blood volume by detecting light intensity variations [2]. In medical environments, PPG is widely used to monitor heart rate and oxygen saturation and was notably used during the COVID-19 pandemic, for assessing lung function [3]. Its simplicity and non-invasiveness make it an ideal candidate for integration into everyday devices such as smartphones.

Tepovka implements PPG using the smartphone's camera and flashlight. When a user places their finger over the camera lens, the flashlight illuminates the skin, and the camera captures subtle changes in light intensity caused by blood flow. These changes are converted into a PPG signal, which the app processes to determine heart rate.

III. Algorithm for Heart Rate Detection

A. Photoplethysmogram Processing

Tepovka extracts PPG data by analyzing video frames from the smartphone camera, isolating red, green, and blue (RGB) color channels. Each channel reflects blood volume changes differently due to differences in light absorption properties. Tests revealed that red and blue channels provide the most reliable data on iPhones, while red and green channels perform better on Android devices—a difference which is likely due to differences in sensor technology.

The app computes the average intensity across selected channels (e.g., green and blue) for each frame, producing a time-series PPG signal. Figure 1. compares different channel combinations, showing that combinations including the red channel produce the most informative signals.
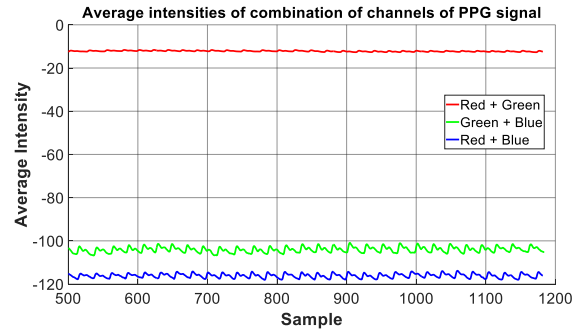
Fig. 1. Comparison of summed RGB channels for PPG signal extraction. The signal is inverted by -1 due to standard nomenclature of the PPG analysis, also due to the initial movement of the finger of the phone which caused artefacts, first hundreds of samples are skipped.

B. Heart Rate Detection

To detect heartbeats, Tepovka applies a derivative to the PPG signal, to mitigate issues such as the dicrotic notch—a secondary wave that can skew peak detection (Fig. 2). Local minima that fall below 60% of the signal's minimum value

are identified as heartbeat endpoints. The inter-beat interval (IBI) is calculated as the time between consecutive peaks, and heart rate (beats per minute, BPM) is derived using the formula:

$$BPM = \frac{60}{Time\ between\ peaks}$$ eq. (1)

To reduce variability, the median IBI from a 150-sample buffer (2–6 seconds, depending on sampling rate) is used. This approach provides a robust heart rate estimate across diverse conditions.
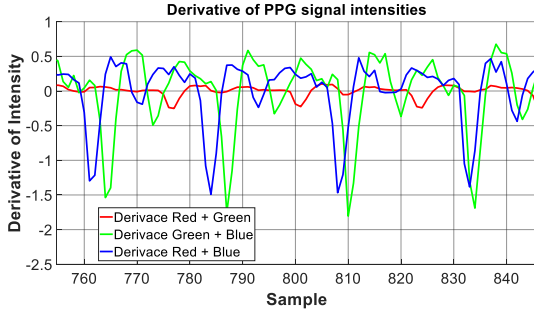
Fig. 2. Derivative of the PPG signal after averaging RGB components.

IV. APPLICATION DEVELOPMENT

A. Flutter Framework

Tepovka was built using Flutter, an open-source framework by Google that enables multi-platform development with a single codebase. Utilizing the Dart programming language, Flutter's widget-based architecture supports modular, reusable components and ensures consistent rendering across devices via its custom engine [4]. The following is a sample function for calculating PPG intensity:

```
double
calculateAverageIntensity(CameraImage
image) {
  double totalIntensity = 0;
  int pixelCount = 0;

  for (var plane in image.planes) {
    final bytes = plane.bytes;
    for (int i = 0; i < bytes.length;
i += 4) {
      final int green = bytes[i + 1];
// Green channel
      final int blue = bytes[i + 2];
// Blue channel
      totalIntensity += (green + blue)
/ 2;
      pixelCount++;
    }
  }

  return pixelCount > 0 ?
totalIntensity / pixelCount : 0.0;
}
```

This code demonstrates the app's signal extraction process by averaging green and blue channels to enhance stability.

V. TESTING AND VALIDATION

A. Testing Protocol

The testing protocol assessed Tepovka's accuracy across varying heart rate conditions:

1. **Resting Phase:** A 30-second baseline measurement.

2. **Hyperventilation:** Brief, intense breathing to elevate heart rate.

3. **Post-Hyperventilation:** A 30-second measurement after hyperventilation.

4. **Exercise (Squats):** 30 squats intended to exceed 100 BPM, followed by a 30-second measurement.

The measurements were compared with the Faros ECG device, a lightweight tool for long-term cardiac monitoring [5]. Motion artifacts were minimized by maintaining stillness during recordings.

B. Tested Devices

Testing focused on iOS devices (iPhone 13, 13 mini, 14) due to compatibility issues with Android devices (Galaxy S24, Xiaomi Redmi Note 11 Pro). The diverse hardware of Android devices, especially the alignment of the camera and flashlight, posed challenges, prompting a focus on iOS optimization.

C. Results

Tepovka accurately detected significant signal peaks, showing close alignment with Faros ECG data (e.g., 112.99 BPM after exercise). Figure 3. compares the app's output with the reference ECG data, confirming its reliability. Future testing will expand the dataset to include 10 comprehensive measurements for more extensive validation.

Figure 4. provides a comparison of the errors between the PPG and EKG signals across all three measurement phases. The highest error is observed in Sample 2 during Phase 1, where our application missed three heartbeats. This anomaly is clearly visible in the chart. Despite this outlier, the results overall are very promising, indicating that our application performs reliably. Missing three beats in a single sample has only a minimal effect on the overall heart rate calculation. With a mean error around 1, the discrepancies between PPG and EKG are minor and acceptable.
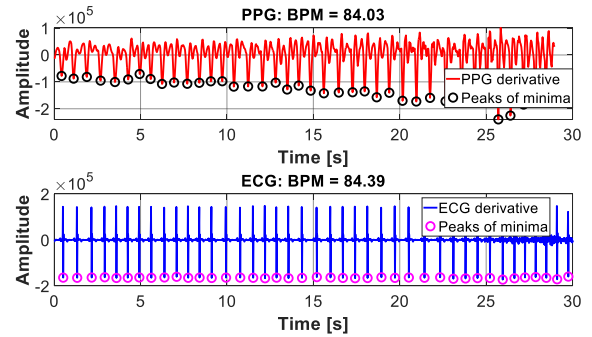
Fig. 3. Comparison of Tepovka (upper) and Faros (lower) data resting phase.
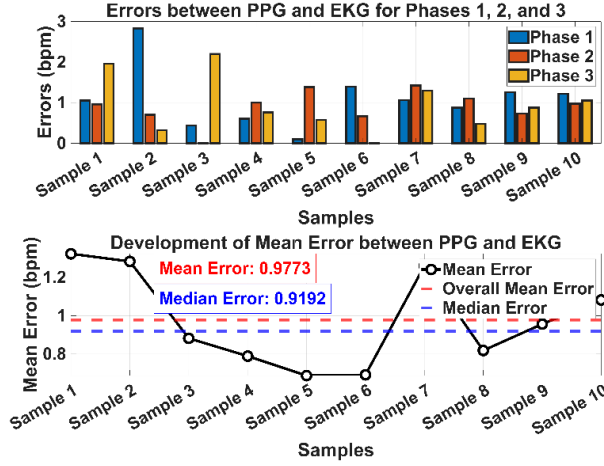
Fig. 4. The errors between PPG and EKG for three phases, with the overall mean error and median error for all samples (n = 10) indicated by dashed lines. The data represents the differences in measurements between the PPG and EKG signals for each phase.

VI. APPLICATION FEATURES

A. Main Menu and Calibration

The intuitive main menu guides users to a calibration phase, where they position their finger over the camera. Real-time camera feedback ensures proper placement, while the flashlight improves signal quality.

B. Heart Rate Measurement

During measurement, raw PPG data is displayed on a live graph, which culminates in a results screen displaying heart rate, safety indicators, and a detailed signal trace. Users can add notes and save data to Apple Health.

C. Record Management and Export

The saved records include 30-second signals and metadata (date, heart rate), which can be viewed as graphs. Exports to PDF include numeric signal values, facilitating analysis in tools like MATLAB.

Fig. 5. Interface progression: Main menu, calibration, measurement, result.

VII. CONCLUSION

Tepovka highlights the potential of smartphone-based PPG for providing accurate heart rate monitoring. Validated against professional ECG equipment, it offers a practical telemedicine tool. Future enhancements will include Android compatibility, additional biometric measurements (e.g., SpO2, HRV), and a larger dataset for improved robustness. Developed at Brno University of Technology, this project highlights the promise of mobile health innovations.

REFERENCES

[1] Canalys, "Chytrým telefonům se daří po celém světě," ChannelWorld, Nov. 2024.

[2] A. J. Allen, "Photoplethysmography and its application in clinical physiological measurement," *Physiol Meas.*, vol. 28, no. 3, pp. R1–R39, Mar. 2007.

[3] Z. Kalvach, "Nečekaný vzestup telemonitoringu během pandemie COVID-19," ProLékaře.cz, 2021.

[4] Flutter, "Architectural Overview," docs.flutter.dev, 2023.

[5] Mindfield Biosystems, "Bittium Faros 180," mindfield.de, 2024.

Detection of Stress using Short-Time Energy Dispersion of Speech Signal

Jan Cícha
Department of Radio Electronics
FEEC, Brno University of Technology
Brno, Czech Republic
256457@vut.cz

Pavel Horský
Department of Radio Electronics
FEEC, Brno University of Technology
Brno, Czech Republic
256484@vut.cz

David Haisman
Department of Radio Electronics
FEEC, Brno University of Technology
Brno, Czech Republic
256476@vut.cz

Abstract—**Our research shows that it is possible to identify stress from a speech signal using energy factors. The proposed method is based on the dispersion of short-time signal energy. The results obtained for full speech and voiced speech are presented. The voiced parts of speech were extracted from continuous speech by means of center clipping algorithm with optimized parameters. The voiced parts provide better results.**

Keywords—speech signal, short-time energy, speech under stress

I. INTRODUCTION

Stress is a body response to stress factor. When an organism is exposed to stress, the adrenal glands produce the hormone cortisol [1], [2]. This hormone is released into blood, where it can be objectively measured. But it is very unpractical to take blood for non-medical research. However, stress also influences human voices [3]. From a practical point of view, it is much more advantageous to investigate the speech signal. This way, stress can be identified even remotely and retrospectively.

Acute stress can be indicated by specific speech features in both time and frequency domains. In the time domain, a well-known effect of stress is an increase in the fundamental frequency of voice [4]. However, other emotions can also induce a similar effect. An increase in the harmonics-to-noise ratio is reported, for example, in [5]. Stress is also reflected in the shape of glottal pulses [6], the waveform of which can be derived directly from the speech signal. A statistical analysis of entire glottal pulses in stressed speech is presented in [7]. Some authors analyzed individual glottal parameters, such as the normalized amplitude quotient describing the glottal closing phase [8] or the ratio of the return to opening phase [9]. In the frequency domain, standard speech features useful for many purposes are mel-frequency cepstral coefficients (MFCC). For automated stress detection, MFCC were used in the model described in [10]. Glottal source features combined with MFCC were applied in [11].

The method based on short-time signal energy we proposed belongs to the time-domain signal processing. In some previous studies, e.g. [12], [13], short-time signal energy was directly used together with other features for stress detection. In this study, we tested the dispersion of short-time signal energy and evaluated it as a separate stress feature.

II. METHOD USED

Speech signals change their parameters dynamically over time and therefore are usually processed using short-time analysis methods. In practice, the signal is first split into short segments, for example into 20 ms long frames, as shown in Fig. 1. Then, signal features are calculated within each frame. In the next step, new higher-level features can be derived from them.
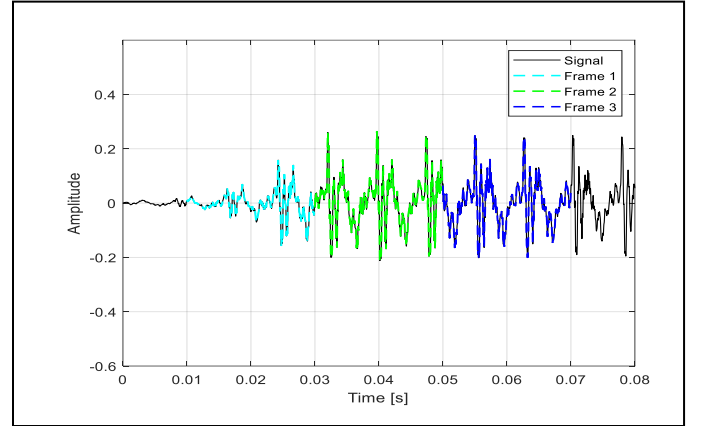
Fig. 1. Speech signal waveform with highlighted 20 ms frames.

A. Energy factor

For each frame, the short-time energy of speech signal $s(n)$ is calculated

$$E_j = \sum_{n=1}^{N} s(n)_j^2 \tag{1}$$

where j denotes frame index and N is the total number of signal samples in the frame. Next, standard deviation and mean are estimated from the short-time energy vector. The ratio of the standard deviation σ to the mean value μ was defined for our purpose as the energy factor

$$EF = \frac{\sigma}{\mu} \tag{2}$$

By normalizing the standard deviation by dividing it by the mean value, the energy factor becomes independent of the intensity of the speech signal.

B. Center-clipping algorithm

In our experiments, we tested full speech and voiced speech. The voiced speech was selected frame by frame. To determine whether a signal frame is voiced or unvoiced, we used the center-clipping (CC) algorithm [14] and optimized it for the reliable selection of voiced frames. For each frame j, the clipping level $\pm CL$ is estimated using the maximum S_{j-1} in the previous frame and maximum S_{j+1} in the following frame. The lower of the two maxima is taken and scaled by a fixed kappa factor (typically $\kappa \approx 0.8$)

$$CL_j = \kappa \cdot \min \{S_{j-1}, S_{j+1}\}. \tag{3}$$

Based on the clipping level, the center clipped speech signal is obtained by a nonlinear operation

$$c(n) = \begin{cases} +1 & \text{for} \quad s(n) \geq CL_j \\ -1 & \text{for} \quad s(n) \leq -CL_j \\ 0 & \text{else} \end{cases} \tag{4}$$

Subsequently, the autocorrelation function $R(k)$ of the normalized center clipped signal $c(n)$ is calculated

$$R(k) = \sum_{n=1}^{N-k} c(n)c(n+k) \tag{5}$$

where N is the total number of signal samples in one frame and k lies in the interval $0 \leq k \leq N-1$. Then, based on the shape of $R(k)$, as shown in Fig. 3, the voicing of the speech signal is detected. The highest peak $R(k_p)$ located at k_p must be found (not searched in the area of the origin) and compared to the value of $R(0)$, which is multiplied by an empirical constant alpha (usually $\alpha \approx 0.3$)

$$R(k_p) \geq \alpha R(0) \quad \approx \quad \text{voiced frame} \tag{6a}$$

$$R(k_p) < \alpha R(0) \quad \approx \quad \text{unvoiced frame} \tag{6b}$$

An example of the relationship between $R(k_p)$ and $R(0)$ leading to a decision on a voiced frame is shown in Fig. 2.
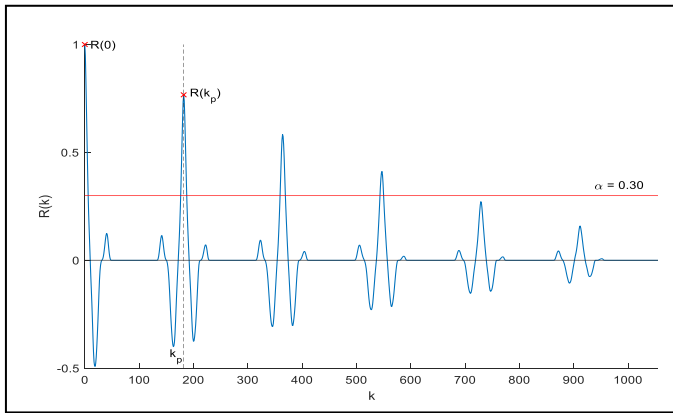
Fig. 2.   Example of autocorrelation function from center clipped signal.

Fig. 3 shows what the speech signal looks like after replacing the unvoiced frames with zero, while voiced frames remain unchanged.
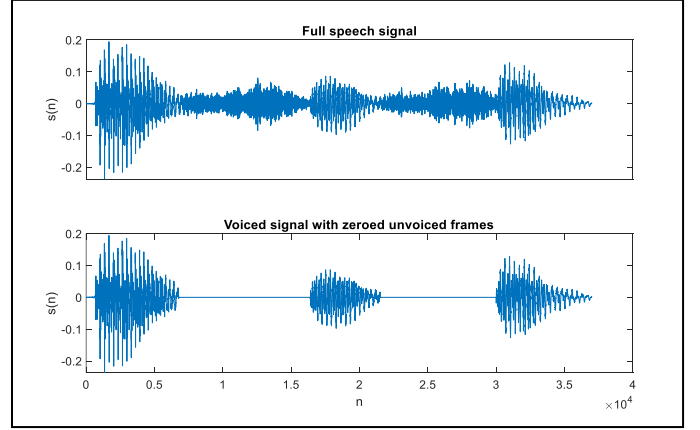
Fig. 3.   Illustration of full speech and corresponding voiced parts of speech.

III. RESULTS

To verify the proposed methods, we used nine pairs of recordings from nine speakers. In each pair, the first recording is under a stress factor (final oral exams at university) and the second one is recorded by the same speaker without stress. The length of the processed recordings is approximately 3 minutes. All speech signals were recorded in mono channel, with 32-bit float precision and sampling frequency of 22 050 Hz. All recordings are in Czech, performed by male speakers, and contain only negligible background noise. The audio samples were scaled within the range ± 1.

Our proposed method was tested in MATLAB separately for full speech and voiced speech. In all tests, we observed difference between stressed and unstressed speech as

$$\Delta EF = EF_S - EF_N \tag{7}$$

where EF_S is the energy factor under stress and EF_N is the energy factor of neutral speech, i.e. without stress. First, we tried to find the optimal values of frame length and, in the case of voiced speech, the alpha and kappa parameters for extracting voiced frames. After several tests, we preferred a frame width of 24 ms. Effect of different combinations of alpha and kappa parameters on ΔEF for one speaker is shown in TABLE I. For comparison, the first row shows the EF values obtained with full speech. The best result according ΔEF is indicated by shading. On average for all speakers, the best results in terms of ΔEF were achieved with the combination $\kappa = 0.75$ and $\alpha = 0.25$ (similarly to the results in TABLE I.). This combination was further used.

An overview of the ΔEF efficiency for all tested speakers is shown in Fig. 4. When comparing full speech to voiced speech, better results were achieved for 8 out of 9 speakers when using voiced speech. Full speech seems to be more suitable for only one speaker (# 1). For two speakers (# 6 and # 7), full speech cannot be used at all. In all cases of both full and voiced speech, the differences ΔEF are positive, which means that the energy factor under stress is higher than without stress, see (7).

EFFECT OF TUNING KAPPA AND ALPHA PARAMETERS FOR
SPEAKER NUMBER 3

		Energy Factor		
		EF_N	EF_S	ΔEF
Full speech signal		1.34390	2.29498	0.95108
$\kappa=0.75$	**$\alpha = 0.25$**	1.46388	2.56349	1.09961
	$\alpha = 0.30$	1.44679	2.53237	1.08558
	$\alpha = 0.35$	1.43118	2.50457	1.07339
$\kappa =0.80$	**$\alpha = 0.25$**	1.47069	2.56012	1.08943
	$\alpha = 0.30$	1.45210	2.53586	1.08375
	$\alpha = 0.35$	1.44132	2.51064	1.06932
$\kappa =0.85$	**$\alpha = 0.25$**	1.47589	2.57221	1.09632
	$\alpha = 0.30$	1.46119	2.55214	1.09095
	$\alpha = 0.35$	1.45131	2.53746	1.08615
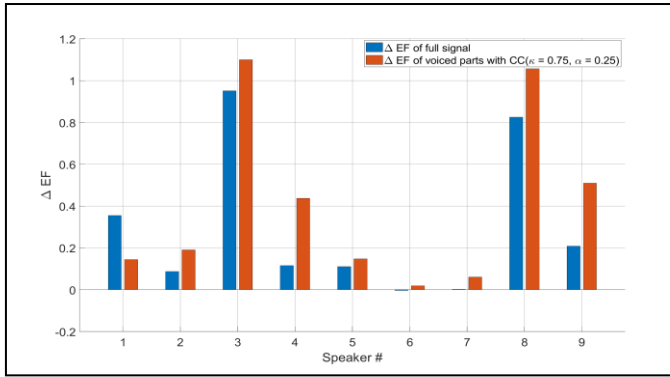
Fig. 4. Comparison of the ΔEF differences obtained for full signal waveform and for only voiced parts of the signal (center clipping, $\kappa = 0.75$ and $\alpha = 0.25$).

In summary, stress was identified by an increase in the energy factor of voiced speech in all the tested speakers. From this point of view, the performance is 100%. However, the indicated value of ΔEF for speaker # 6 is very low and should be considered with respect to statistical inaccuracy. When excluding the result for this speaker, we obtained an overall accuracy of 88.8%. This performance is similar to those reported in other studies; see for example 58% when applying only one type of feature (MFCC) in [15] like our method, or higher accuracies of 97% in [16] and 98% in [17] when approaches using a large number of features are applied.

IV. CONCLUSIONS

Our research shows that it is possible to identify stress by calculating energy factors. The method used is based on the dispersion of short-time signal energy. The initial results obtained from a group of nine individuals in a state of real psychological stress (not simulated stress) are very promising for further development. The method is applicable for individual monitoring of the current occurrence of stress. Our method can handle only normal voice loudness, not extremely low or high ones, which have a significant effect on the energy in voiced frames of the signal. As is known in other areas of speech processing, shouted and whispered speech can significantly affect, for example, the reliability of speech recognition [18] or speaker verification [19].

Recording a greater variety of speakers under stress, including females and individuals with varying voice levels, could be highly beneficial for future research. Our research will continue by identifying stress using more speech features, such as jitter of voice fundamental frequency, which we are planning to do in the very near future. We will also investigate the robustness against noise.

REFERENCES

[1] https://en.wikipedia.org/wiki/Stress_(biology)

[2] https://cs.wikipedia.org/wiki/Kortizol

[3] F. Depestele, "You sound stressed!" The Impact of Psychosocial Stress on Speech Parameters. Doctoral dissertation, Ghent University, 2023.

[4] S. Sondhi, et al. "Acoustic analysis of speech under stress," International Journal of Bioinformatics Research and Applications, 2015, vol. 11, no. 5, pp. 417-432.

[5] M. Kappen, et al. "Acoustic speech features in social comparison: how stress impacts the way you sound," Scientific Reports, 2022, vol. 12, no. 1, art. no. 22022.

[6] K. W. Godin, T. Hasan, and J. H. Hansen, "Glottal waveform analysis of physical task stress speech," In Interspeech, 2012, pp. 1648-1651.

[7] M. Sigmund, A. Prokes, and Z. Brabec, "Statistical analysis of glottal pulses in speech under psychological stress," In 16th European Signal Processing Conference, 2008, Lausanne, pp. 1-5.

[8] X. Yao, et al. "Glottal source related to stressed speech under workload in human-robot interface," In International Conference on Robotics and Automation Engineering, 2017, Shanghai, pp. 141-145.

[9] M. Stanek and M. Sigmund, "Psychological stress detection in speech using return-to-opening phase ratios in glottis," Elektronika ir Elektrotechnika, 2015, vol. 21, no. 5, pp. 59-63.

[10] D. Narzary, U. Sharma, and A. Khanna, "An automated stress detection model based on dual approach of clinical psychologist prediction and machine learning," International Journal of Information Technology, 2025, vol. 17, no. 2, pp. 755-765.

[11] L. Joglar-Ongay and F. Alias-Pujol, "Glottal source features for speech under stress classification, " In International Conference of the Catalan Association for Artificial Intelligence, 2024, Barcelona, pp. 145-148.

[12] A. Sharada, R. Mamatha, K. Meghana, and A. Monika, "Stress detection in women using speech analysis," In Second International Conference on Emerging Trends in Engineering, pp. 797-808, Atlantis Press, 2023.

[13] A. Adeleye, S. Madanian, and O. Adeleye, "Emotion variation detection in discrete english speech: A wavelet transform use case in mental health monitoring," In Australasian Computer Science Week, 2024, pp. 115-119.

[14] L. R. Rabiner and R. W. Schafer, Digital Speech Processing. London, Prentice Hall, 2011.

[15] J. Staš, et al. "Analysis and detection of speech under emotional stress," In 21st International Conference on Emerging eLearning Technologies and Applications, 2023, pp. 493-498.

[16] P. Chyan, A. Achmad, I. Nurtanio, and I. S. Areni, "A deep learning approach for stress detection through speech with audio feature analysis," In 6th International Conference on Information Technology, Information Systems and Electrical Engineering, pp. 1-5, 2022.

[17] A. Kumar, M. A. Shaun, and B. K. Chaurasia, "Identification of psychological stress from speech signal using deep learning algorithm," e-Prime-Advances in Electrical Engineering, Electronics and Energy, 2024, vol. 9, art. no. 100707.

[18] P. Zelinka and M. Sigmund, "Automatic vocal effort detection for reliable speech recognition," In International Workshop on Machine Learning for Signal Processing, 2010, Kittila, pp. 349-354.

[19] S. Prieto, A. Ortega, I. López-Espejo, and E. Lleida, "Shouted and whispered speech compensation for speaker verification systems," Digital Signal Processing, 2022, vol. 127, art. no. 103536.

Stress detection/classification in multimodal data

Nikola Jordánová
Department of Biomedical Engineering
FEEC, Brno University of Technology
Brno, Czech Republic
247247@vutbr.cz

Andrea Němcová
Department of Biomedical Engineering
FEEC, Brno University of Technology
Brno, Czech Republic
nemcovaa@vut.cz

Abstract — **This paper focuses on the detection and classification of stress using multimodal data. Stress monitoring is very beneficial because stress can truly negatively affect the quality of life of an individual. Chronic stress may lead to various health issues, including cardiovascular, autoimmune, and mental diseases, and in severe cases, it can result in premature death.**

The WAUC database, which includes data from mental stress, physical stress, and a combination of both, was used for this work. It contains data from 48 subjects, of which 26 subjects were used. For this study, electrocardiogram, galvanic skin response, respiration, and temperature signals were used.

A variety of machine learning models were trained for several classification tasks. The best model for classifying stress into six groups is the Support Vector Machines (SVM) classifier, with an F1 score of 82.5% for the training dataset and 41.2% for the testing dataset. The SVM classifier shows the best results when stress is classified into three groups representing different levels of physical stress with an F1 score of 73.8% for the testing dataset. The Boosted Trees classifier shows the best results when physical stress is detected with an F1 score of 97.5% for the testing dataset. The best model for stress detection, regardless of whether it is physical or mental, is the SVM with an F1 score of 75.9% for the testing dataset.

Keywords — stress, biological signals, multimodal data, detection, classification, machine learning

I. INTRODUCTION

Stress is an unavoidable part of everyone's life in modern, hectic times. We already know that chronic stress can have a negative impact on our health and that stress can reduce an individual's work performance [1]. In very demanding professions that require total concentration (e.g., pilots, doctors, or firefighters), psychological discomfort can be a significant problem as it could lead to serious accidents or deaths [2]. However, low stress levels are often beneficial because stress increases, for example, the level and effectiveness of communication [1].

Therefore, stress detection/classification is very beneficial. With its help, we can improve an individual's quality of life and prevent possible health problems. The individual is then able to adjust his or her lifestyle before more serious physical or psychological issues become apparent.

This paper deals with stress detection/classification in multimodal data. By multimodal data, we mean biological signals measured by wearable devices, which are time-synchronized and appropriately labelled with the level or type of stress.

II. MATERIALS AND METHODS

A. Database

For this study, the WAUC database (A Multi-Modal Database for Mental Workload Assessment Under Physical Activity) by Albuquerque et al. [2] was used. It is a database that combines mental and physical stress and can be used to develop algorithms for stress monitoring in physically and mentally demanding professions. The database contains data from 48 participants. Three devices were used for measurement during the experiment: the BioHarness 3 chest belt (Zephyr, USA), the E4 wristband (Empatica, USA), and the Enobio 8-channel wireless headset (Neuroelectrics, Spain). The signals measured were electrocardiogram (ECG), skin temperature, electroencephalogram (EEG), galvanic skin response (GSR), photoplethysmogram (PPG), acceleration (ACC), and respiratory signal. The following signals were used for this paper: ECG, with a sampling rate of 250 Hz, GSR (4 Hz), temperature (4 Hz) and respiration (18 Hz). Physical activity was performed on a treadmill and a cycle trainer, while mental stress was induced through the Multi-Attribute Task Battery (MATB-II) test. Participants were also asked to complete the NASA-TLX questionnaire after each experimental session, which is a questionnaire where the subject rates perceived mental demand, physical demand, temporal demand, performance, effort, and frustration using a 21-point scale. Subjects also rated their physical fatigue on the Borg fatigue scale. During the measurement, six possible combinations of mental and physical load were tested:

- No physical and mental load, marked as 0

- No physical load with mental load, marked as 1

- Medium physical load without mental load, marked as 2

- Medium physical load with mental load, marked as 3

- High physical load without mental load, marked as 4

- High physical load with mental load, marked as 5

Before each specific workload segment, two baseline sections were measured. In the first section, the subject sat still for one minute. In the second one, which lasted two minutes, the subject started to move at the desired speed for the following measurement period. Each segment, representing one of the stress combinations, was recorded for 10 minutes. This period was followed by a 5-minute block where subjects completed the NASA-TLX questionnaire and indicated their level of exertion using the Borg scale. The individual segments are labelled with the appropriate markers for each signal.

B. Data preprocessing

The first step of preprocessing was to remove subjects with excess or missing markers, markers that did not coincide with each other in time, or missing data. Eventually, 26 subjects out of 48 were further analysed.

The next step was to synchronize the individual markers. Each signal contains its own set of markers, which, for the remaining subjects, occur at approximately the same time with a maximum deviation of 4 seconds. However, after data, visualization, an issue arose with the respiratory signal. The markers in this signal were shifted by up to 50 seconds compared to markers in other signals.

To solve this problem, graphs were created with the time of selected reference markers displayed on the x-axis. The markers from the ECG signal were used as a reference. The y-axis represented the time deviation between a specific ECG marker and a corresponding marker from the respiratory signal. As can be seen in Fig. 1, this deviation increases linearly. This procedure was performed for five randomly selected subjects. A linear trend line was fitted to each plot including a linear equation. The average was then calculated from the slopes of the lines from all graphs. This value was added to 1, creating a constant of 1.0078829431, which was then used as a multiplier for the time axis, which was corrected using this constant. This approach effectively minimized time variation between markers.
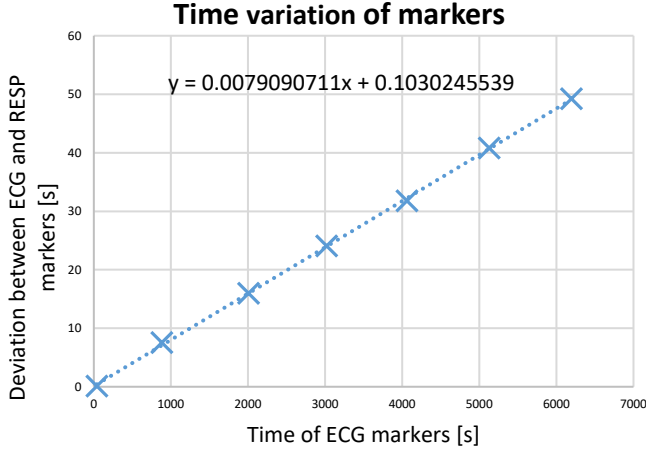
Fig. 1. Example of a marker time variation graph

All signals were then resampled to the same sampling rate of 250 Hz, which is the sampling rate of the ECG signal. All data were divided into individual segments, indicating each stress combination and a baseline was extracted representing when the subject was sitting and was not affected by any of the previous stress marking activities.

The data from the selected database are in raw form and therefore they had to be filtered. The GSR signal was first filtered with a low-pass (LP) filter with a cutoff frequency of 0.05 Hz (2nd order Butterworth filter) to separate the Skin Conductance Level (SCL) component of the signal. Then, the raw GSR signal was again filtered with a band-pass (BP) filter with cutoff frequencies of 0.05 and 0.7 Hz (2nd order Butterworth filter) to separate the Skin Conductance Response

(SCR) component of the signal. The filtering of the GSR signal was developed based on empirical knowledge and using references [3] and [4]. The temperature signal was set to a range between 25 and 40 °C. Data outside this range were set to NaN values to avoid bias by outliers. The ECG signal was filtered with a BP filter with cutoff frequencies of 5 and 25 Hz [2] (4th order Butterworth filter) to highlight QRS complexes for better R wave detection. The detection of QRS complexes was performed using MATLAB's findpeaks function, which is part of the Signal Processing Toolbox. The quality of the ECG signal was estimated using the code developed by Yaghmaie et al. [5]. Signals with quality index lower than 0.25 (1 indicates a very high-quality signal) were excluded so that they would not enter machine learning classifiers later. These excluded signals were then analysed, if the data indicated physical activity as expected. A BP filter with cutoff frequencies of 0.1 and 2 Hz (2nd order Butterworth filter) was applied to the respiratory signal. The filter was designed based on theoretical principles, practical experience, and using [2].

C. Extraction and selection of data

Following data preprocessing, all the stress segments were divided into 60-second non-overlapping windows. Therefore, for most subjects, 10 intervals were extracted from each segment representing a specific stress level. However, for some subjects, the number of segments could vary due to longer or shorter measurement durations.

Then the features were extracted in each window, and also from the baseline. Each window was associated with particular stress label. In total, 52 features were extracted from the various signals: 9 features from the body temperature signal, 14 from the GSR signal, 9 features from the respiratory signal, and 20 from the ECG signal. The specific features will be listed after selection.

Feature selection was performed in two steps. First, boxplots were created for all features, categorized by the six levels of stress previously described. In Fig. 2, an example of the distribution among the groups is illustrated.
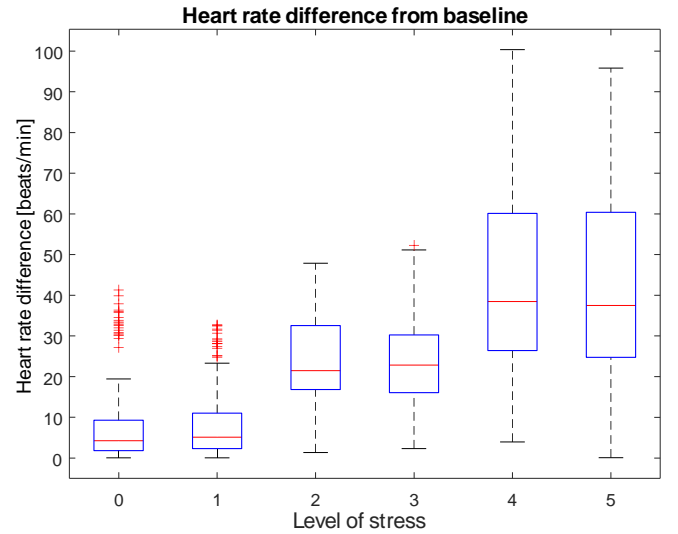
Fig. 2. Boxplot for heart rate difference from baseline

It is noticeable that the groups indicating a combination of mental and physical stress (levels 2 and 3, as well as levels 4 and 5) have some overlap. Particular attention was paid to the features that effectively differentiate mental stress (marked as 1) from the resting state (marked as 0), as the mental stress is not as clearly differentiated as physical stress. After visual analysis of the boxplots, 21 features remained that showed high intergroup variability and are suitable for further analysis.

The second step of selection was to plot the correlation matrix. The matrix was constructed from the 21 features selected in the first step, with each element of the matrix representing the correlation values between these features. Values close to 1 or -1 indicate a strong correlation. Features with correlation values higher than 0.7 or lower than -0.7 were reduced. Out of these correlated pairs, only the feature that performed better in the previous selection step remained. The remaining 12 features are namely: temperature difference from mean temperature, temperature difference from baseline, mean temperature value, SCL difference from the previous value, SCL difference from baseline, SCR standard deviation, respiratory rate, variability of respiratory intervals, heart rate difference from baseline, number of the following NN intervals varying by more than 20 ms divided by the number of NN intervals (pNN20), difference of standard deviation of NN intervals (SDNN) from baseline and difference of pNN20 from baseline.

D. Train-Test split

Out of 26 subjects, five subjects were randomly selected to be used for testing. The remaining subjects were used to train the individual models. The final numbers of 60s segments in the training and testing sets were 1,149 and 263, respectively. Data standardization was performed for the K-Nearest Neighbors (KNN) and the Support Vector Machines (SVM) directly in MATLAB Classification Learner.

E. Classification of stress

Various machine learning models have been used in the MATLAB Classification Learner for several classification tasks. 1) These classifiers were first trained and then tested within the original six groups. 2) However, due to the high confusion between the groups, some groups were merged to create three groups. Specifically, groups labelled no stress (marked as 0) and mental stress (marked as 1) were merged, followed by groups labelled as moderate physical stress without and with mental stress (marked as 2 and 3), and finally, groups labelled as high physical stress without and with mental stress (marked as 4 and 5). 3) Classification into two groups - groups 0 and 1 together (no physical stress; this merged group was extended to avoid imbalance between groups) and groups 2, 3, 4, and 5 together (physical stress) was done. 4) Finally, models were developed to detect stress regardless of whether it was mental or physical. Group 0 was extended 5 times and groups 1, 2, 3, 4, and 5 were merged.

For the classification task, the three best performing models were selected - KNN (k = 11), SVM (kernel = Gaussian), and Boosted Trees (BT) (Ensemble method = AdaBoost). Validation of the training dataset was performed using five-fold cross-validation. And the testing was completed on the five fully independent subjects already mentioned.

As mentioned earlier, some data had to be excluded due to poor ECG signal quality. It was assumed that these data came from segments indicating physical activity. Therefore, an algorithm was developed to detect physical stress using the poor quality signals.

III. RESULTS

Classification success was evaluated using accuracy (Acc) and F1 score. As can be seen in TABLE I. the differences in results of classification into 6 groups between the training and testing datasets are significant. This is due to the large confusion between groups that indicate the same physical activity. The confusion matrix of the test dataset (Fig. 3) for the KNN model was chosen for the demonstration because it displays these confusions most clearly.

TABLE I.   CLASSIFICATION RESULTS FOR 6 GROUPS

Classification	KNN		SVM		BT	
Set	Acc	F1	Acc	F1	Acc	F1
Training set	82.1%	82.2%	82.2%	82.5%	49.4%	47.5%
Testing set	42.2%	39.9%	43.7%	41.2%	39.2%	34.6%

As can be seen in TABLE II. which shows the merging of the groups into three groups, the best model is the SVM classifier. The confusion matrix for BT model can then be seen in Fig. 4, where we can see that confusions mainly occur between groups denoting any physical load.

TABLE II.   CLASSIFICATION RESULTS FOR 3 GROUPS

Classification	KNN		SVM		BT	
Set	Acc	F1	Acc	F1	Acc	F1
Training set	96.4%	96.4%	96.5%	96.5%	91.2%	90.9%
Testing set	71.5%	69.2%	75.7%	73.8%	69.2%	68.1%

TABLE III. displays the results when the groups are fully separated, indicating no physical stress and any physical stress. In this scenario, the results reflect impressive accuracy, with the BT classifier being the best model.

TABLE III.   CLASSIFICATION RESULTS FOR 2 GROUPS

Classification	KNN		SVM		BT	
Set	Acc	F1	Acc	F1	Acc	F1
Training set	99.6%	99.6%	99.2%	99.2%	99.7%	99.7%
Testing set	89.4%	89.1%	93.9%	93.5%	97.7%	97.5%

In TABLE IV. we see the results of the stress detection models. Although the results are quite good with the Acc of the test set up to 86.7%, the results are probably due to the ability of the model to detect physical stress and there is still high confusion between resting state and mental stress.

TABLE IV.   CLASSIFICATION RESULTS FOR STRESS DETECTION

Classification	KNN		SVM		BT	
Set	Acc	F1	Acc	F1	Acc	F1
Training set	95.2%	95.1%	98.5%	98.5%	98.2%	98.2%
Testing set	76.8%	71.2%	86.7%	75.9%	83.7%	72.8%

Confusion matrix for KNN model

	0	1	2	3	4	5
0	31	18	1			
1	18	30				
2		11	11	14	4	1
3	3	6	6	13	8	7
4		1	9	3	19	11
5		1	9	10	11	7

True Class (vertical axis) / Predicted Class (horizontal axis)

Fig. 3. Confusion matrix for KNN model (for 6 groups)

Confusion matrix for Boosted Trees model

	0+1	2+3	4+5
0+1	88	8	2
2+3		38	46
4+5		25	56

True Class (vertical axis) / Predicted Class (horizontal axis)

Fig. 4. Confusion matrix for Boosted Trees model (for 3 groups)

Lastly, the algorithm that tested whether the excluded data due to poor ECG signal quality came from the section indicating physical activity achieved a success rate of 96.6%.

IV. DISCUSSION AND CONCLUSION

This paper deals with stress detection/classification in multimodal data. The WAUC database containing mental stress, physical stress and a combination of both was used. First, the markers of the respiratory signal were adjusted as there was a deviation from the other markers of up to 50 seconds. This error

was solved by creating linear equations from the graphs. Although the exact cause of this error has not been identified, the error could have been caused by, for example, incorrect sampling rate.

Some data had to be excluded due to poor ECG signal quality. These data were further analysed, if these data came from segments indicating physical activity. Therefore, an algorithm was developed to detect physical stress using the poor quality signals. The success rate of this algorithm is 96.6%.

A total of 52 features were extracted from ECG, GSR, temperature, and respiratory signals. Using boxplots and then a correlation matrix, 12 features were selected and then entered into machine learning models.

When separated into the original six groups, the best model achieved an F1 score of only 41.2%. As could be seen in the confusion matrix, there was a lot of confusion between groups that labelled the same physical activity. Therefore, models were developed to classify and detect physical stress. The best model achieved an F1 score of 73.8% when separated into 3 groups and 97.5% when separated into 2 groups. Models detecting stress regardless of whether it is mental or physical, achieved the highest F1 score of 75.9%.

However, the classifiers have difficulty separating mental stress, as the boxplots of the individual features have already indicated this. Each subject may experience mental stress differently, as for some subjects the mental load may not have been stressful and for some, on the other hand, the measurement itself may have been stressful. Thus, a closer analysis and a personalized solution are needed to separate mental stress. Additional biological signals available in the database could be used to improve the accuracy of the separation of mental stress.

REFERENCES

[1] M. Parent, I. Albuquerque, A. Tiwari, R. Cassani, J. -F. Gagnon, D. Lafond, S. Tremblay, and T. H. Falk, "PASS: A Multimodal Database of Physical Activity and Stress for Mobile Passive Body/ Brain-Computer Interface Research", Frontiers in Neuroscience, vol. 14, Dec. 2020.

[2] I. Albuquerque, A. Tiwari, M. Parent, R. Cassani, J. -F. Gagnon, D. Lafond, S. Tremblay, and T. H. Falk, "WAUC: A Multi-Modal Database for Mental Workload Assessment Under Physical Activity", Frontiers in Neuroscience, vol. 14, Dec. 2020.

[3] Galvanic skin response (GSR). Online. Tobii Connect. 2023. Available at: https://connect.tobii.com/s/article/galvanic-skin-response-gsr?language=en_US.

[4] J. J. Braithwaite, D. G. Watson, R. Jones, and M. Rowe, "A Guide for Analysing Electrodermal Activity (EDA) & Skin Conductance Responses (SCRs) for Psychological Experiments", Technical Report, Birmingham, Great Britain, 2013. Available at: https://www.biopac.com/eda-scr-analysis-guide-for-psychological-experiments-updated/.

[5] N. Yaghmaie, M. A. Maddah-Ali, H. F. Jelinek, and F. Mazrbanrad, "Dynamic signal quality index for electrocardiograms", Physiological Measurement, vol. 39, no. 10, Oct. 2018.

Concept drift detection in metabolomics-based predictions under cold-stress conditions in plants

1st Tereza Luskova
Department of Biomedical Engineering
Faculty of Electrical Engineering and
Communication,
Brno University of Technology
Brno, Czech Republic
253298@vut.cz

2nd Wolfram Weckwerth
Molecular Systems Biology (MOSYS),
Department of Functional and Evolutionary
Ecology,
Vienna Metabolomics Center (VIME),
Faculty of Life Sciences,
University of Vienna
Vienna, Austria
wolfram.weckwerth@univie.ac.at

3rd Jana Schwarzerova
Department of Biomedical Engineering
Faculty of Electrical Engineering and
Communication,
Brno University of Technology
Brno, Czech Republic
Molecular Systems Biology (MOSYS),
Department of Functional and Evolutionary
Ecology,
University of Vienna
Vienna, Austria
Institute of Molecular and Clinical Pathology
and Medical Genetics,
Faculty of Medicine, University of Ostrava
Ostrava, Czech Republic
Jana.Schwarzerova@vut.cz

Abstract — **In recent years, there has been a significant surge in the use of prediction models. These models typically assume that input data is stationary; however, much of the data we encounter is dynamic in nature. Among the most dynamic data are metabolomics, which change over time. One common challenge with time-varying data is the occurrence of concept drift. Concept drift can degrade the accuracy and reliability of prediction models, making it a key issue to address. Despite its negative impact, concept drift can also be leveraged to uncover hidden confounding factors in the data. The main goal of this study is to detect concept drift in metabolite concentrations across different ecotypes of *Arabidopsis thaliana* under varying growth conditions. The study is divided into two parts: first, we apply different predictive regressors to metabolomics data, and second, we use these models to detect concept drift. Our focus lies in identifying potential confounding factors that may influence the prediction of relative growth rates in plants.**

Keywords — *Concept drift, Machine learning, Metabolomics, Plant stress, Predictive modeling*

I. INTRODUCTION

Machine learning models assume stationarity of input data, but metabolomics data are dynamic, with values changing unexpectedly due to various factors. The concept of drift in metabolomics data was first introduced in a study by Schwarzerova et al. [1]. In dynamic data, prediction behavior – also known as concept drift – can change unexpectedly. Concept drift often results from shifts in the data distribution, also referred to as data drift [2]. This phenomenon negatively affects new predictions, as once concept drift occurs the machine learning model can no longer correct output values [1]. This issue arises due to the model's inability to adapt to the dynamic evolution of the data in the test set [3].

In machine learning, there are three fundamental approaches to training models: supervised learning, unsupervised learning, and reinforcement learning. Supervised learning is the most commonly used method in both machine learning and systems biology for predictive modeling. Models based on supervised learning are applied to omics data to predict a wide range of clinical, phenotypic, and physiological outcomes [4].

Algorithms for concept drift detection help prevent such mispredictions. Change detection alters us when the model needs to be adjusted. When the data shifts, the detector identifies the change and sends a warning signal. The primary goal of concept drift detection is to enhance the reliability, stability, and accuracy of the prediction models [3].

Metabolomics is part of the panomic sciences, as are genomics, transcriptomics, and proteomics [5], [6], [7], [8]. Metabolomics data are becoming more accessible for the application of predictive models. This integration allows for early detection a more accurate prognoses for various diseases, such as stomach cancer [9]. However, concept drift negatively impacts dynamic metabolic data in predictive models. When detected, the model may over fit, but refining it an ultimately improve prediction accuracy.

Some concept drift detectors, although capable of detecting concept drift, are not well-suited for metabolomics data. This includes detectors based on the sliding window principle, which often lack the necessary sensitivity, potentially leading to poor decisions. Therefore, more traditional methods such as EDDM, are preferable for detecting concept drift [10].

II. MATERIALS

The metabolomics data used in this study are from the study by Weiszmann et al. [11]. The data include metabolite

concentration values and realistic growth rates for 241 *Arabidopsis thaliana* ecotypes. For each metabolite, 37 primary metabolites were measured (see Fig. 1). Measurements were made in 3 to 5 replicates for each ecotype, which were then averaged. Among these, four sugars – maltose, fructose, galactose, and glucose – were selected for further analysis because they play a key role in plant metabolism. These carbohydrates influence energy metabolism and serve as a carbon source for plant growth. Their concentrations change significantly in response to stress conditions, which may enable the detection of concept drift and its impact on plant growth rate [12]. Data were extracted and measured using gas chromatography coupled to mass spectrometry (GC-MS). Only 239 values were used in this study; as 2 values were deemed invalid. The measured data consist of two datasets obtained from *A. thaliana* plants grown under two temperature conditions: under standard growth conditions (16 °C) and under cold stress conditions (6 °C) [11]. The used code is available online at the address: https://github.com/terezaluskova/EEICT2025.

III. METHODS

The methods used in this study are divided into three sections. The first section focuses on data pre-processing, visualization (see Figure 1) and partitioning. The second section addresses different approaches to predictive regression modeling. The final section focuses on the concept drift detection (CDD) using two different methods, followed by a literature-based justification of possible confounding factors. The input data were divided by cross validation into training and test set. Cross split using 10-cross-validation.

The regression prediction models were modeled. Among the regression models, Random Forest Regressor (RF), Support Vector Regression (SVR) and Linear Regression (LR) were used. The regressors were trained and tested in several variations. The first variation involved training and testing the model on a dataset with same temperature-based conditions. In the second variation, the model was trained on a dataset collected under normal temperature conditions (16°C) and tested on a dataset collected under cold-stress conditions (6°C), and vice versa.

In the final section, the concept drift detection was performed using Drift Detection Method DDM and Early Drift Detection Method (EDDM. Both DDM and EDDM detect concept drift in predicted models. Each detector has two thresholds: when the first threshold is crossed (indicating data drift), the detector issues a warning signal. When the second threshold is crossed, concept drift is detected. The concept drift detection methods were chosen based on a technical paper by Lima et al. [13] that describes the fit of each method to regression models.

The first drift detection method is DDM. DDM monitors the error rate in the incoming data and evaluates its changes using statistical thresholds. It tracks the average error rate and is particularly effective for detecting sudden changes. The second method, EDDM, has increased sensitivity compared to DDM. It is better suited for detecting gradual changes by tracking the distance between errors [1]. Both methods were implemented using the Scikit-multiflow package [14] for each regression model used.

IV. RESULTS AND DISCUSSION

The prediction models were created using destination cross-validation and evaluated based on accuracy, calculated as Pearson correlation coefficient (CC). TABLE I. shows the resulting model accuracy parameters for each model. The RF model at 6 °C achieved the highest accuracy, and the RF model trained at 16 °C and tested at 6 °C achieved the same values. In contrast, the SVR model had the lowest accuracy when data from 6 °C and 16 °C were combined. he accuracies may seem
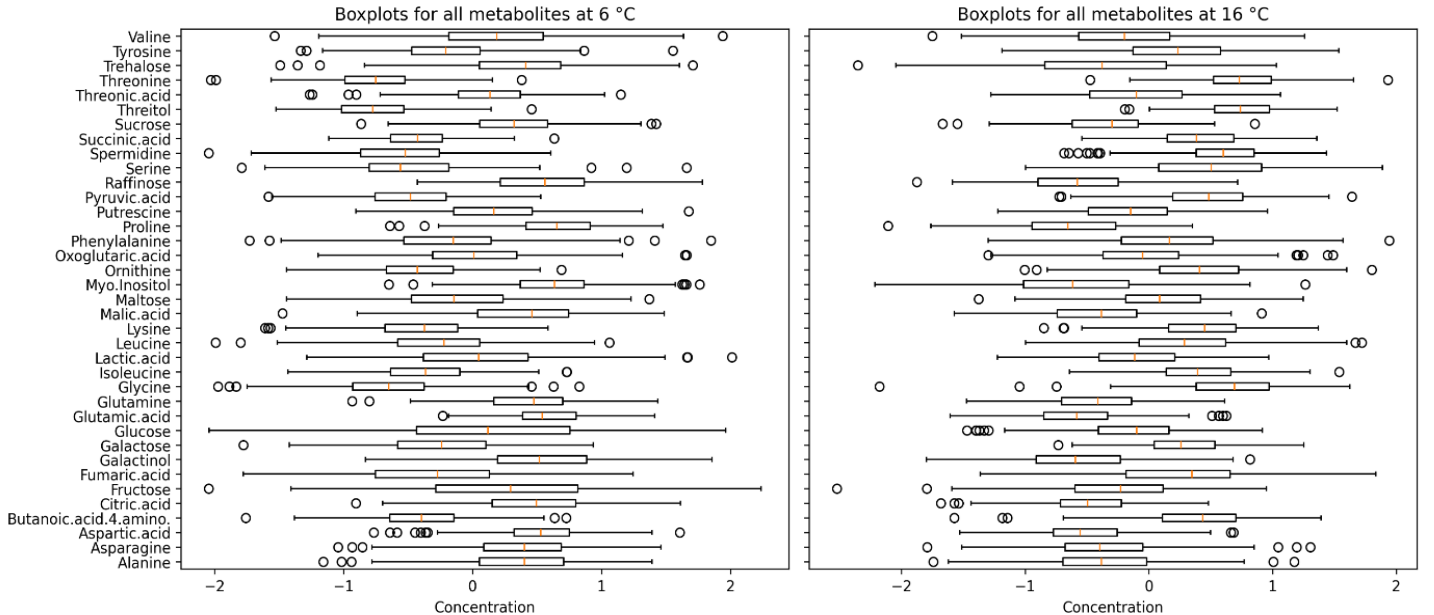
Fig 1: Box plot distribution of concentrations for all 37 individual metabolites.

very low, but even in the study by Weiszmann et al. [11] the accuracies of metabolomics predictions do not exceed 40 %.

TABLE I. MODEL ACCURACY (CC) FOR DIFFERENT TEMPERATURE CONDITIONS

	RF	SVR	LR
6 °C + 16 °C	0.123	0.000	0.067
6 °C	0.138	0.075	0.146
16 °C	0.130	0.075	0.151
6 °C -> 16 °C	0.130	0.075	0.151
16 °C -> 6 °C	0.138	0.075	0.146

Drift detection on our proposed models showed that concept drift is present in two models (RF and SVR) when combining 6 °C and 16 °C. Concept drift was detected only by the DDM detector. TABLE II. and TABLE III. contain the number of warnings levels (W) and detected concept drifts (DC).

TABLE II. COUNT OF WARNING SIGNALS (W) AND CONCEPT DRIFT DETECTION (DC)

	RF	SVR	LR
6 °C + 16 °C	48 W / 1 DC	0 W / 0 DC	50 W / 1 DC
6 °C	0 W / 0 DC	0 W / 0 DC	0 W / 0 DC
16 °C	0 W / 0 DC	0 W / 0 DC	0 W / 0 DC
6 °C -> 16 °C	0 W / 0 DC	0 W / 0 DC	0 W / 0 DC
16 °C -> 6 °C	0 W / 0 DC	0 W / 0 DC	0 W / 0 DC

TABLE III. EDDM : COUNT OF WARNING SIGNALS (W) AND CONCEPT DRIFT DETECTION (DC)

	RF	SVR	LR
6 °C + 16 °C	0 W / 0 DC	0 W / 0 DC	0 W / 0 DC
6 °C	0 W / 0 DC	0 W / 0 DC	0 W / 0 DC
16 °C	0 W / 0 DC	0 W / 0 DC	0 W / 0 DC
6 °C -> 16 °C	0 W / 0 DC	0 W / 0 DC	0 W / 0 DC
16 °C -> 6 °C	0 W / 0 DC	0 W / 0 DC	0 W / 0 DC

The highest number of warning levels was found for LR model using DDM. Warning levels and concept drifts were detected in only two models, RF and LR, at a combined 6 °C and 16 °C. EDDM did not reveal any warning levels or concept drifts. According to the study, the EDDM method should be more sensitive for this type of metabolomics predictive models and thus more suitable to detecting concept drift, as found in previous research [1], [10].

Additionally, the ecotype of *A. thaliana* plants could be considered a confounding factor as different ecotypes may exhibit varying metabolic patterns that influence metabolite concentrations and subsequent plant growth [12]. This factor might help explain why the concept drift has been observed only in certain models and conditions. The examined metabolites - fructose, glucose, galactose, and maltose - can serve as indicators for detecting concept drift. These simple carbohydrates play a key role in plant metabolism, and their metabolite concentrations change under cold stress conditions. The two ecotypes in which conceptus drift was detected at 16 °C, but the data were predicted for a combination of 6 °C and 16 °C, were from Sweden. Which corresponds with the study by

The results of this study showed us that plants in Sweden were much more adapted to temperature fluctuations. This implies that predicting data without treating the concept of drift, will give us erroneous and inaccurate predictions. Future studies could build on these findings by exploring additional metabolites, it may be possible to improve the detection of concept drift in various plant species under different stress conditions. This link between metabolomic concept drift and biological adaptation was mentioned in a study by Schwarzerova et al. [2] and in a study by Weiszmann et al. [11].

We further identified concept drift in predictive modelling, which we attributed to changing metabolite concentrations for 6°C and 16°C *A. thaliana*, see Figure 2. Figure 2 shows the detection of concept drift in the concentrations at 16°C and its corresponding concentrations at 6°C in the metabolites fructose, galactose, glucose and maltose. These changes in metabolite concentrations play a key role in driving the observed drift, highlighting the importance of real-time monitoring of these metabolites to improve prediction accuracy.
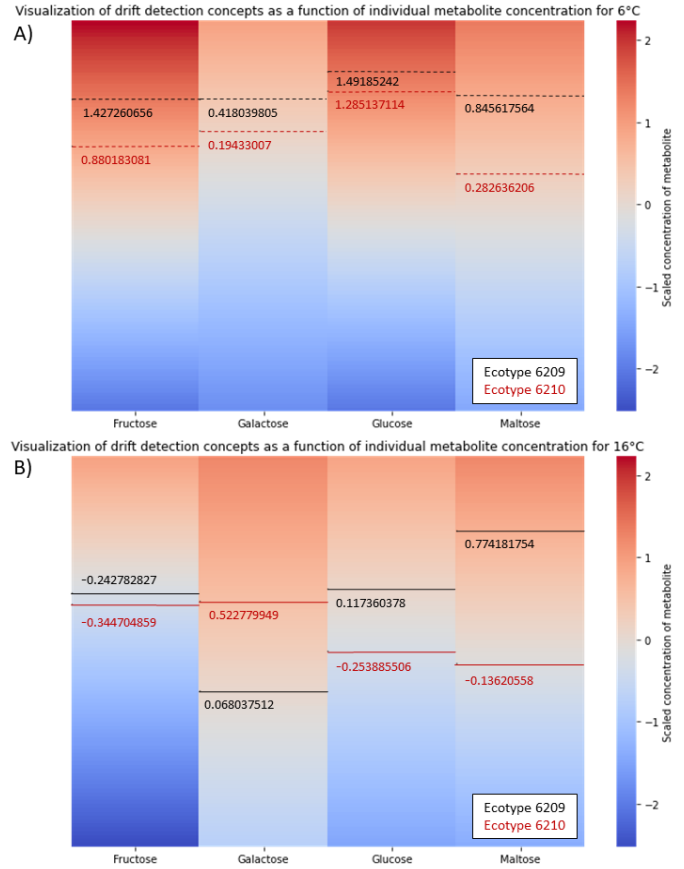
Fig 2: V Visualization of conceptus drift detection based on concentrations of selected metabolites (fructose, galactose, glucose and maltose) at 6 °C (A) and 16 °C (B). The color gradient represents metabolite concentrations, with blue and red indicating low and high concentrations, respectively. The black solid line in Figure B indicates the points at which concept drift was detected at 16 °C. The black dashed line in Figure A indicates the corresponding concentrations for 6 °C.

The presence of concept drift specifically in models combining data from both cold (6 °C) and standard (16 °C) growth conditions, particularly when using data from Swedish ecotypes, suggests that ecological adaptation plays a critical role in shaping metabolite dynamics. The Swedish ecotypes originate from northern regions with naturally colder climates, where they have likely evolved mechanisms for metabolic plasticity and resilience to cold stress. This is supported by the observation that these ecotypes exhibited altered carbohydrate metabolism under cold conditions - consistent with enhanced adaptation. The differential responses in metabolite levels, especially in sugars like the 4 sugars already mentioned, which are known to be involved in osmotic regulation and energy balance under stress, could explain the model prediction instability observed as concept drift. Therefore, the observed concept drift may not be merely a technical artefact, but rather a biologically meaningful signal of ecotype-specific stress responses and evolutionary adaptation.

V. CONCLUSION

Based on metabolite concentrations, metabolomics can predict the relative growth rate or phenotype of plants. Metabolomics data are dynamic in real time and can change and evolve unexpectedly. Prediction models based on these data may experience concept drift. This study presents three prediction models that estimate the relative growth rate in plants based on metabolite concentrations. The main focus of this study is to detect concept drift, which affects model predictions, in metabolomics data.

In the regression models developed, concept drift was detected using DDM and EDDM. The study demonstrated that metabolomics regression prediction models for detecting concept drift are more effectively monitored using DDM. It has also shown that the ecotype of *A. thaliana* plant grown in Sweden are better adapted to the conditions than the ecotype of *A. thaliana* plant in southern regions, suggesting that plants in Sweden are more resistant to cold stress. This finding allows for a better understanding the stress conditions in plants under cold stress e.g. due to changes in climatic conditions. Plant metabolism is closely linked to carbohydrates. This is reflected in the plant's growth rate and photosynthesis.

REFERENCES

[1] SCHWARZEROVÁ, J., BAJGER, A., PIERDOU, I, POPELINSKÝ, L., SEDLAR, K., WECKWERTH, W. An innovative perspective on metabolomics data analysis in biomedical research using concept drift detection. In: 2021 IEEE International Conference on Bioinformatics and Biomedicine (BIBM). Houston, TX, USA, 2021, pp. 3075–3082. DOI: 10.1109/BIBM52615.2021.9669418.

[2] SCHWARZEROVÁ J, et al. Enhanced metabolomic predictions using concept drift analysis: Identification and Correction of confounding factors. Bioinformatics Advances, 2025, vbaf073. DOI: 10.1093/bioadv/vbaf073. Dostupné z: https://doi.org/10.1093/bioadv/vbaf073

[3] BIFET, A. Classifier concept drift detection and the illusion of progress. In: RUTKOWSKI, L., KORYTKOWSKI, M., SCHERER, R., TADEUSIEWICZ, R., ZADEH, L., ZURADA, J., eds. *Artificial Intelligence and Soft Computing. ICAISC 2017*. Lecture Notes in Computer Science, vol. 10246. Cham: Springer, 2017. DOI: 10.1007/978-3-319-59060-8_64.

[4] SIDAK, D., SCHWARZEROVÁ, J., WECKWERTH, W., WALDHERR, S. Interpretable machine learning methods for predictions in systems biology from omics data. *Frontiers in Molecular Biosciences*, 2022, vol. 9. ISSN 2296-889X. DOI: 10.3389/fmolb.2022.926623.

[5] WECKWERTH, W. Metabolomics in systems biology. *Annual Review of Plant Biology*, 2003, vol. 54, pp. 669–689. DOI: 10.1146/annurev.arplant.54.031902.135014.

[6] WECKWERTH, W., GHATAK, A., BELLAIRE, A., CHATURVEDI, P., VARSHNEY, R. K. PANOMICS meets germplasm. *Plant Biotechnology Journal*, 2020, vol. 18, pp. 1507–1525. DOI: 10.1111/pbi.13372.

[7] LIU, X., LOCASALE, J. W. Metabolomics: A primer. *Trends in Biochemical Sciences*, 2017, vol. 42, no. 4, pp. 274–284. DOI: 10.1016/j.tibs.2017.01.004.

[8] HASIN, Y., SELDIN, M., LUSIS, A. Multi-omics approaches to disease. *Genome Biology*, 2017, vol. 18, p. 83. DOI: 10.1186/s13059-017-1215-1.

[9] CHEN, Y., WANG, B., ZHAO, Y., SHAO, X., WANG, M., MA, F., et al. Metabolomic machine learning predictor for diagnosis and prognosis of gastric cancer. *Nature Communications*, 2024, vol. 15, no. 1, p. 1657. DOI: 10.1038/s41467-024-46043-y.

[10] SCHWARZEROVÁ, J., et al. A revealed imperfection in concept drift correction in metabolomics modeling. In: PIETKA, E., BADURA, P., KAWA, J., WIECŁAWEK, W. (eds.) *Information Technology in Biomedicine. ITIB 2022*. Advances in Intelligent Systems and Computing, vol. 1429. Cham: Springer, 2022. DOI: 10.1007/978-3-031-09135-3_42.

[11] WEISZMANN, J., WALTHER, D., CLAUW, P., BACK, G., GUNIS, J., REICHARDT, I., et al. Metabolome plasticity in 241 *Arabidopsis thaliana* accessions reveals evolutionary cold adaptation processes. *Plant Physiology*, 2023, vol. 193, no. 2, pp. 980–1000. DOI: 10.1093/plphys/kiad298.

[12] VEYRÈS, N., DANON, A., AONO, M., GALLIOT, S., KARIBASAPPA, Y. B., DIET, A., et al. The *Arabidopsis* sweetie mutant is affected in carbohydrate metabolism and defective in the control of growth, development, and senescence. *The Plant Journal*, 2008, vol. 55, no. 4, pp. 665–686. DOI: 10.1111/j.1365-313x.2008.03541.x

[13] LIMA M, FILHO TS, FAGUNDES RAA. A Comparative Study on Concept Drift Detectors for Regression. In: BRITTO A, VALDIVIA DELGADO K, eds. Intelligent Systems. BRACIS 2021. Cham: Springer, 2021. Lecture Notes in Computer Science, vol. 13073. Dostupné z: https://doi.org/10.1007/978-3-030-91702-9_26.

[14] MONTIEL, J., READ, J., BIFET, A., ABDESSALEM, T. Scikit-Multiflow: A Multi-output Streaming Framework. *Journal of Machine Learning Research*, 2018, vol. 19, no. 72, pp. 1–5.

[15] SCHWARZEROVÁ, J., et al. From genomic to panomic predictions: An intuitive PANOMICs platform utilizing advanced Machine Learning algorithms. 2024.

Interactive Web Management Interface for the Energy Polygon

1st Dominik Rechtorík
Department of Telecommunications
Brno University of Technology
Brno, Czech Republic
247164@vutbr.cz

2nd Antonín Bohačík
Department of Telecommunications
Brno University of Technology
Brno, Czech Republic
Antonin.Bohacik@vut.cz

Abstract—**This paper presents a modern web management application for an energy polygon that provides control, data processing, and security. The application is designed to manage a simulated energy transmission network, allowing remote control, real-time monitoring, and visualization of substation and power plant data. Facilitates testing and training without interfering with the actual infrastructure. The modern interface provides the best user experience. Implemented security measures, including HTTPS and CSRF protection, ensure the resilience of the system. The result is a user-friendly and efficient platform that optimizes the management of energy polygons and strengthens cybersecurity in critical infrastructure.**

Index Terms—**Energy polygon, Web management application, Django framework, SCADA systems, User interface design, modernization**

I. INTRODUCTION

Modern technologies and digitalization are significantly transforming the energy industry, necessitating robust software solutions for secure and efficient management [1]. Energy polygons serve as vital simulation environments for testing new technologies without affecting real infrastructure [2]. This paper presents my development of a comprehensive web management interface for an energy polygon at Brno University of Technology, which implements new control features, data collection, and visualization functionalities.

My primary contribution through this work was designing and implementing a complete web-based solution that addresses specific challenges in energy polygon management. I created an intuitive and user-friendly interface that simplifies the monitoring and control of complex energy infrastructure simulations. I developed secure SSH-based communication mechanisms between the web server and 47 Raspberry Pi devices representing substations and power plants. The solution implements interactive visualization tools, including an interactive map and statistical dashboards, providing real-time insight into system performance. In addition, I designed a responsive interface that works seamlessly across different devices to facilitate both demonstration and operational use.

The resulting web application, while still under active development, enhances the functionality of the existing energy polygon and serves as an educational tool to demonstrate concepts of energy infrastructure. A crucial aspect of this implementation was the integration with the Supervisory Control and Data Acquisition (SCADA) systems [3].

A. SCADA Systems

Supervisory Control and Data Acquisition (SCADA) systems are essential for monitoring and controlling industrial processes in real time [4]. In the energy sector, SCADA optimizes the power distribution, monitors the state of the grid, and prevents failures by collecting data from remote stations. The key components of SCADA include sensors, remote terminal units (RTUs), programming logic controllers (PLCs), and centralized control systems that process and visualize data [5].

B. Communication Protocols in Energy Systems

The integration of communication protocols is crucial for interoperability in energy management systems [6]. The most widely used protocols include the following.

1) IEC 61850 and IEC 60870-5-104: IEC 61850 is an international standard designed for communication in electrical substations [7]. Provides a data model that enables seamless interoperability between devices. Unlike older protocols, IEC 61850 allows faster and more automated configuration and supports TCP/IP-based communication, making it suitable for modern digital substations.

IEC 60870-5-104 is a crucial protocol for remote monitoring and control of substations over IP networks [8]. Enhances SCADA communications by structuring data transmission and ensuring security through encryption and authentication [9].

II. ENERGY POLYGON OF THE CZECH REPUBLIC

A. Overview and Purpose

An energy polygon is a system designed to simulate the real-world energy infrastructure, allowing the training, testing, and evaluation of new technologies [10]. The energy polygon at the Department of Telecommunications at Brno University of Technology emulates real-time data exchange between stations and a control center. The transmitted data include voltage levels, current measurements, temperature, and protective device statuses.
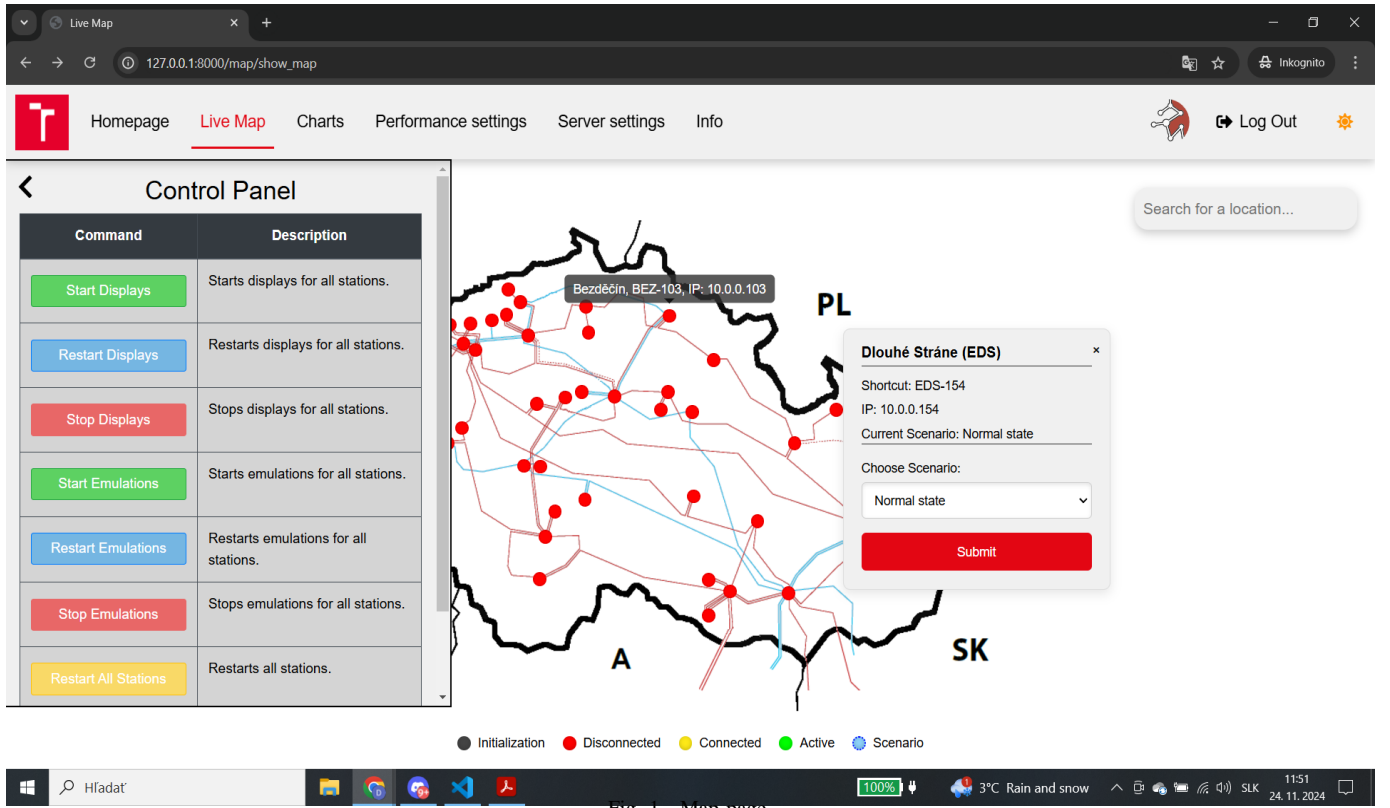
Fig. 1. Map page.

B. Management and Control of the Polygon

The energy polygon is managed through a web application that facilitates communication with remote stations that simulate substations and power plants. The management system follows a client-server architecture, with Secure Shell (SSH) used for secure communication between the Web server and the stations.

The polygon consists of two isolated networks, which ensures that configuration changes or attacks on one network do not impact critical data communication. For example, during a Distributed Denial-of-Service (DDoS) attack simulation, the data network may be overloaded while the service network remains unaffected, preventing total system failure.

The architecture of the web application, responsible for managing the polygon, is illustrated in Figure 2. It depicts the interaction between the client browser, Django-based web server, database, and custom modules that handle remote communication with the Raspberry Pi network. Structured design improves security, scalability, and efficient data processing.

C. Station Emulation

The polygon includes 47 Raspberry Pi devices and four MikroTik hubs. Each Raspberry Pi represents a communication gateway for a simulated power station or substation. The devices interact with the SCADA system through the open source OpenMUC software, which handles data collection and processing.
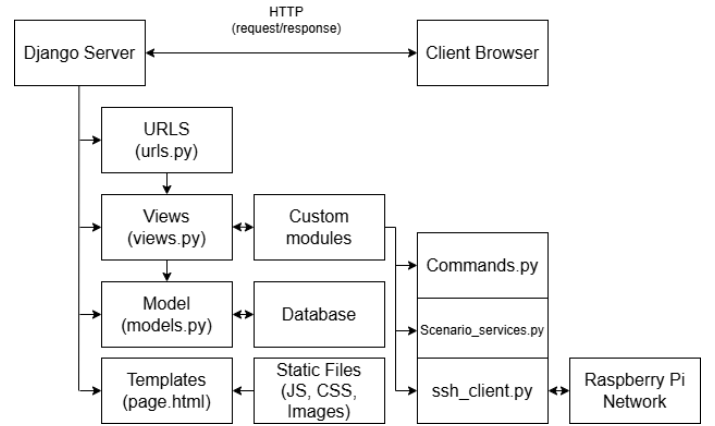
Fig. 2. Web application structure.

Each Raspberry Pi features a dual network configuration that utilizes an additional USB to Ethernet adapter to separate data transmission from maintenance traffic. The devices also include IIC I2C OLED displays for real-time data visualization, providing feedback on system performance and network activity.

D. Response Time Evaluation

Practical response time measurements were conducted to verify the efficiency of communication within the system. Using Wireshark, the latencies between OpenMUC, the man-

agement server, and Raspberry Pi devices were analyzed. The results, shown in Table I, confirm that response times remain within acceptable limits for real-time monitoring and control.

Communication Pair	Response Time (ms)
OpenMUC ↔ Management Server	5–10
Management Server ↔ RPi	15–25
OpenMUC ↔ RPi (indirect)	20–35

TABLE I
MEASURED RESPONSE TIMES BETWEEN SYSTEM COMPONENTS.

Although full-scale testing is still in progress, preliminary results indicate stable performance. Even under network load, response times allow timely data processing and control without disruptions. The achieved performance ensures that operators receive near real-time feedback when executing commands or monitoring system status, making the application suitable for both educational demonstrations and practical simulation exercises.

E. Technologies and Libraries

The web application was developed using a comprehensive technology stack to ensure performance, security, and maintainability:

1) Backend Framework: Django was selected as the primary framework due to its robust security features, scalable architecture, and built-in administration capabilities [11]. The application leverages Django's:

- ORM (Object-Relational Mapping) for database operations
- Authentication system for user management
- Form validation for secure data handling
- CSRF protection middleware to prevent cross-site request forgery attacks

2) Database: SQLite 3 serves as the database backend, chosen for its simplicity, portability, and seamless integration with Django:

- Provides serverless database solution with zero configuration
- Stores station data, status information, and operational parameters
- Maintains user profiles and authentication information
- Manages historical data for statistical analysis and reporting
- Offers excellent performance for the application's concurrent user load

3) SSH Communication: The Paramiko library implements secure SSH communication between the web server and the Raspberry Pi devices:

- Establishes encrypted connections to the stations
- Executes remote commands for scenario deployment
- Handles asynchronous command execution for improved responsiveness

4) Frontend Technologies: The user interface incorporates modern web technologies:

- Bootstrap for responsive layout and UI components

- jQuery for DOM manipulation and AJAX requests
- Chart.js for interactive data visualization on the statistics page
- Font Awesome for iconography

5) Data Processing: JSON is the primary format for data serialization and exchange between components. Django's built-in JSON encoder/decoder handles the conversion between Python objects and JSON strings.

JSON structures are used for:

- Communicating with the Raspberry Pi network
- Storing configuration data for scenarios
- Passing real-time status updates to the frontend
- Formatting API responses

Server responses are formatted as JSON objects to enable asynchronous updates on the client side.

III. MODERN WEB INTERFACE

The Web application was developed to address the need for efficient management and monitoring of the energy polygon, a simulation environment to test power grid technologies. Provides an intuitive graphical interface that allows operators to monitor the status of substations and power plants, send control commands, and analyze system performance. By offering real-time data visualization and interactive controls, the system improves decision making and operational efficiency.

The key functionalities of the web application include the acquisition of real-time data from remote stations, interactive dashboards that display the status of the network, and the ability to execute various operational scenarios for individual stations. This feature enables users to simulate different conditions, test responses to faults, and evaluate system resilience under varying loads. In addition, the system incorporates security measures such as user authentication and role-based access control to ensure data integrity and prevent unauthorized access.

A. Login Page

The authentication system includes a login page, which provides a clean and user-friendly interface to access the system. The login page now includes real-time input validation and error handling, ensuring that users receive immediate feedback on incorrect credentials or missing fields. In addition, the interface is optimized for responsiveness, making it accessible on various devices and screen sizes.

B. Home Page

The home page was designed to provide a seamless and intuitive user experience. It serves as the central hub of the application, offering quick access to essential system functions. A dynamic navigation menu allows users to easily switch between different sections, manage their session by logging out, or customize the application's appearance with mode selection options. The home page can be seen in Fig. 5.

C. Map Page

A dedicated map-based visualization tool was developed to provide a clear and interactive overview of the energy polygon's infrastructure. The map dynamically displays the status of various stations, allowing users to monitor their operation in real time.

Each station is represented by an interactive marker that users can click to access detailed information, including current operational status. In addition, users can select predefined scenarios for each station, enabling controlled testing and simulation of different conditions. The map page also features a sidebar that provides quick access to global commands, allowing efficient management of the entire system. An example of the map page is shown in Fig. 1.

D. Statistics Page

A dedicated statistics page was developed to provide a complete visualization of historical data trends. The page features interactive graphs that dynamically display key system metrics, allowing users to analyze patterns over time. Users can apply filters to refine the displayed data based on specific parameters, improving the clarity and relevance of the insights.

In addition to graphical representations, the page includes summary statistics that highlight critical values, such as peak usage periods or anomaly detections. An example of the statistics page is shown in Fig. 3.
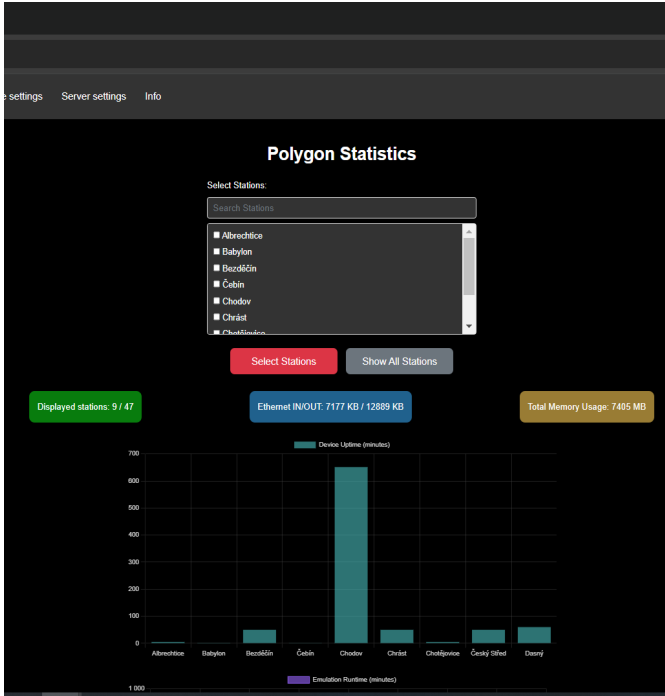
Fig. 3. Statistics page.

E. Server List Page

The server list page provides an overview of all connected servers (stations) within the energy polygon, showing their real-time statuses and key operational parameters. Each server entry includes essential details such as connectivity status and current mode of operation.

Users can interact with individual servers, executing specific commands directly, or utilize global controls to send system-wide instructions to all servers simultaneously. This functionality enhances the efficiency of managing distributed infrastructure, allowing for quick adjustments and troubleshooting. In addition, the page includes filtering and sorting options, enabling users to locate and manage specific servers more easily. This feature significantly improves the monitoring and control capabilities of the system. Provides the same control options as shown in Fig. 1, but also allows access through the PuTTY console, enabling individual station operation. Unlike the main dashboard, this page is designed primarily for back-end control rather than for presentation purposes.

F. Information Page

Provides key information about the web application, including technical and administrative details for users and developers. It also includes contact details and links to the repository and other resources for development and maintenance.

G. Django Administrative Interface

The application includes a Django-based administrative panel to manage users, logs, and system settings. The admin interface provides role-based access control for different user levels. Data are stored in a relational database managed by Django's ORM (Object Relational Mapping); see Fig. 4, which allows seamless interaction with various database backends such as PostgreSQL or MySQL [11]. The ORM simplifies querying, data validation, and migration management, ensuring data integrity and consistency throughout the system.

The database schema is organized around two primary models:

- **Station Model** stores comprehensive information about each Raspberry Pi station, including unique identifiers, network configuration (IP addresses, ports), operational status of stations and their associated transformers, and currently active scenario configurations.
- **Measurement Data Model** captures time-series performance metrics from each Raspberry Pi, including system uptime, process runtime, operational status flags, memory utilization, and network traffic (download/upload throughput).

All database information is dynamically rendered in the web application's interface, providing real-time visibility into system operations.

H. Responsiveness

The modernized interface is fully responsive, ensuring usability across various devices, including desktop, tablet, and smartphone, as shown in Fig. 1. CSS media queries and flexible grid layouts were used to achieve seamless adaptability.

The design also incorporates dynamic scaling of the UI components to maintain readability and usability on different

Change Station

IP: `10.0.0.162`

My dir: `ETU`

Name: `Tušimice`

Traffo amount: `2`

Transformator 0: `401`

☐ Transformator 0 active

Transformator 0 scenario: `Normal state`

Transformator 1: `402`

☐ Transformator 1 active
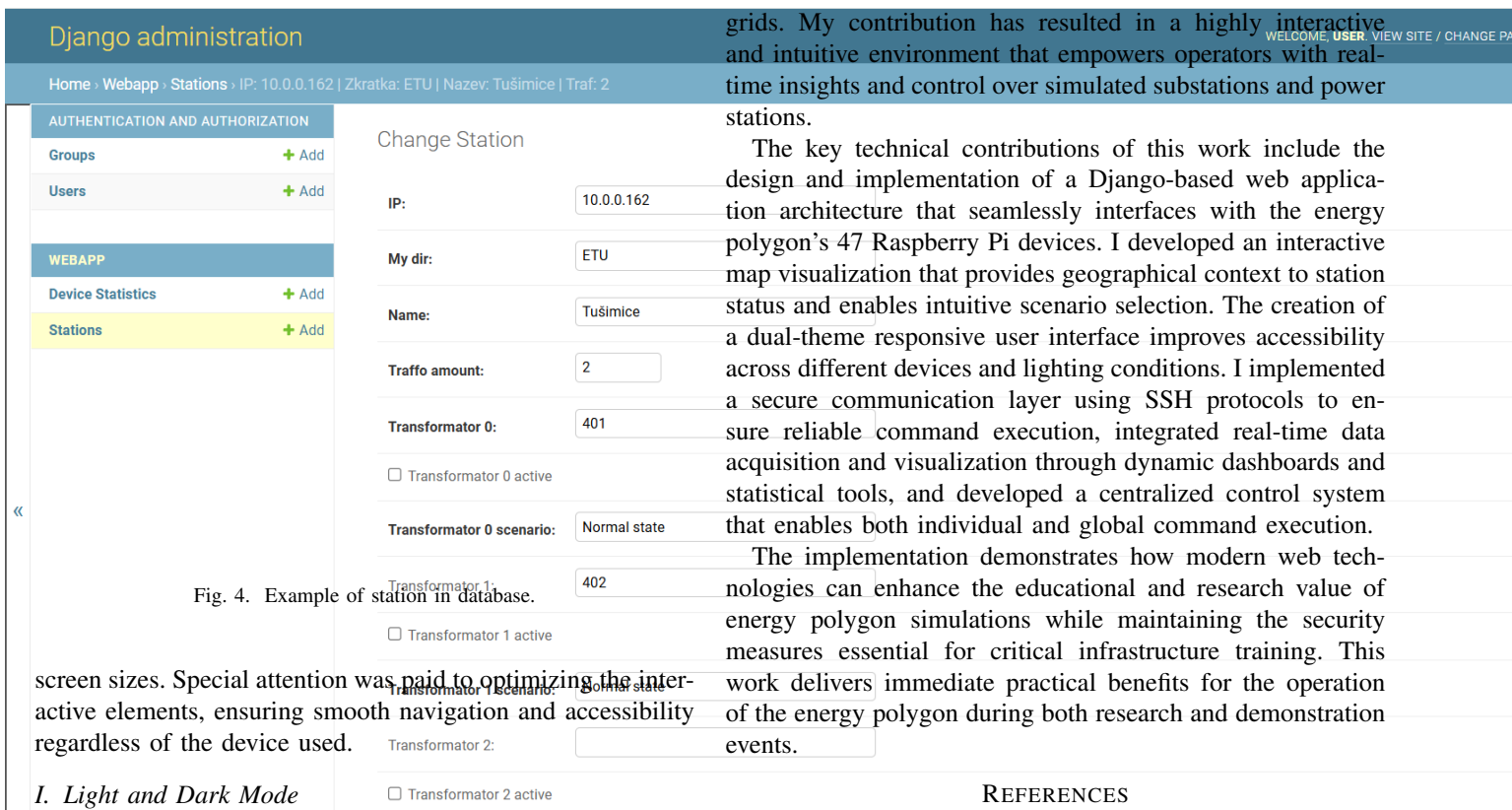
Fig. 4. Example of station in database.

Transformator 1 scenario: `Normal state`

Transformator 2: ` `

☐ Transformator 2 active

grids. My contribution has resulted in a highly interactive and intuitive environment that empowers operators with real-time insights and control over simulated substations and power stations.

The key technical contributions of this work include the design and implementation of a Django-based web application architecture that seamlessly interfaces with the energy polygon's 47 Raspberry Pi devices. I developed an interactive map visualization that provides geographical context to station status and enables intuitive scenario selection. The creation of a dual-theme responsive user interface improves accessibility across different devices and lighting conditions. I implemented a secure communication layer using SSH protocols to ensure reliable command execution, integrated real-time data acquisition and visualization through dynamic dashboards and statistical tools, and developed a centralized control system that enables both individual and global command execution.

The implementation demonstrates how modern web technologies can enhance the educational and research value of energy polygon simulations while maintaining the security measures essential for critical infrastructure training. This work delivers immediate practical benefits for the operation of the energy polygon during both research and demonstration events.

screen sizes. Special attention was paid to optimizing the interactive elements, ensuring smooth navigation and accessibility regardless of the device used.

I. Light and Dark Mode

A theme switcher was integrated into the application, allowing users to switch between light and dark modes (see Fig. 5). This feature improves the user experience, especially in different lighting conditions.

The implementation ensures that all the interface elements, including text, buttons, and graphs, seamlessly adapt to both themes while maintaining readability and visual consistency. User preferences are also stored, allowing the selected mode to persist between sessions for a more personalized experience.

Fig. 5. Light mode and dark mode for web application.

CONCLUSION

This paper presents the development of a modern web interface for the energy polygon at the Brno University of Technology, representing a significant advancement in the monitoring, control and management of simulations of power

REFERENCES

[1] I. Ali and S. M. Suhail Hussain, "Communication design for energy management automation in microgrid," *IEEE Transactions on Smart Grid*, vol. 9, no. 3, pp. 2055–2064, 2018.

[2] A. Sreejith, P. Dhanapala, A. Melagoda, S. A. Enderami, V. Aravinthan, A. Pahwa, and B. Natarajan, "Compsim: A community based smart grid testbed for holistic resilience analysis," in *2023 IEEE International Conference on Communications, Control, and Computing Technologies for Smart Grids (SmartGridComm)*, 2023, pp. 1–6.

[3] D. Pliatsios, P. Sarigiannidis, T. Lagkas, and A. G. Sarigiannidis, "A survey on scada systems: Secure protocols, incidents, threats and tactics," *IEEE Communications Surveys & Tutorials*, vol. 22, no. 3, pp. 1942–1976, 2020.

[4] M. I. Fyodorova, I. I. Zhuravlev, D. S. Kuzenev, A. E. Bannov, and D. P. Khmelyuk, "The scada system digital infrastructure implementation in distribution networks," in *2023 5th International Youth Conference on Radio Electronics, Electrical and Power Engineering (REEPE)*, vol. 5, 2023, pp. 1–6.

[5] M. Aamir and A. Mahmood, "Performance analysis of wide area operation, control and protection using high scale scada system," in *2008 IEEE Canada Electric Power Conference*, 2008, pp. 1–7.

[6] M. Ayello and Y. Lopes, "Interoperability based on iec 61850 standard: Systematic literature review, certification method proposal, and case study," *Electric Power Systems Research*, vol. 220, p. 109355, 2023. [Online]. Available: https://www.sciencedirect.com/science/article/pii/S0378779623002444

[7] R. Mackiewicz, "Overview of iec 61850 and benefits," in *2006 IEEE Power Engineering Society General Meeting*, 2006, pp. 8 pp.–.

[8] P. Musil and P. Mlynek, "Overview of communication scenarios for iec 60870-5-104 substation model," in *2020 21st International Scientific Conference on Electric Power Engineering (EPE)*, 2020, pp. 1–4.

[9] Z. Liguo, L. Yongfu, Y. Peng, and S. Hongyan, "Iec 60870-5-101 protocol based voltage detector data communication," in *2010 International Conference on Measuring Technology and Mechatronics Automation*.

[10] P. Blazek, A. Bohacik, R. Fujdiak, V. Jurak, and M. Ptacek, "Smart grids transmission network testbed: Design, deployment, and beyond," *IEEE Open Journal of the Communications Society*, vol. 6, pp. 51–76, 2025.

[11] P. Thakur and P. Jadon, "Django: Developing web using python," in *2023 3rd International Conference on Advance Computing and Innovative Technologies in Engineering (ICACITE)*, 2023, pp. 303–306.

Measurement of combustion boiler operating parameters

1st Jan Kříž

Faculty of Electrical Engineering and Communications
Brno University of Technology
Brno, Czech Republic
246878@vutbr.cz

Abstract—This paper deals with the testing and analysis of a delivered initial prototype for measuring the operating parameters of combustion boilers. Based on the verification of the characteristics, modifications, and optimizations were made to the code and circuitry for its proper functioning. Subsequently, the schematic and circuit board were designed. In the design, versatility is taken into account due to the possibility of a dual power supply, from an adapter or solar panel. In addition, the comments and shortcomings supplied by the supervisor are elaborated in the design.

Index Terms—ESP32, Environmental sensors, Air quality monitoring, PCB design, IoT, measuring operating parameters, smart home, combustion boiler

I. Introduction

This paper explores a prototype for measuring and monitoring combustion boilers' operating parameters, including flue gas and boiler temperatures, steam pressure, and pollutant emissions. Effective monitoring is essential for safe, efficient, and environmentally friendly operations. It enables remote observation of fuel combustion and storage tank management without constant personal inspections. Monitoring these parameters optimizes boiler performance, reduces fuel consumption, and curbs harmful emissions. Additionally, accurate measurement can prevent breakdowns and prolong equipment life. Exceeding these parameters can lead to increased emissions and higher risks of explosions or fires, underscoring the importance of monitoring equipment, particularly in the context of smart homes and Internet of Things technologies.

II. Technologies in smart homes

Modern households are increasingly adopting IoT (Internet of Things) technology, which consists of a network of smart devices equipped with sensors, software, and connectivity. These devices communicate using various protocols like Wi-Fi, Bluetooth, Zigbee, Z-Wave, and Thread, enabling them to collect and share data autonomously. This data is sent to central servers or cloud platforms for analysis, providing insights, and optimizing processes. IoT enhances automation and remote control, boosting efficiency and convenience. In smart homes, it is applied to manage lighting, thermostats, security systems, and more, all accessible via smartphones or voice assistants. In industrial settings, IoT monitors machinery for predictive maintenance and production optimization, while in transportation, smart traffic systems improve traffic management and parking efficiency, enhancing road safety.

A. Zigbee

ZigBee is a wireless communication protocol for smart devices, operating at lower data rates up to 250 kbps. It is unsuitable for streaming video or audio from security cameras but can transmit small amounts of data with minimal power consumption over short distances (10-100 m). ZigBee is ideal for smart home and IoT applications, emphasizing reliability and low power consumption. It uses mesh networking, allowing devices to communicate directly or through others, enhancing range and stability. Operating on ISM bands (868 MHz or 2.4 GHz), it uses bit rates of 20, 40, or 250 kbps. A ZigBee router (gateway or hub) connects the network to the Internet or a mobile phone.

B. Z-wawe

Z-Wave is a communication protocol similar to ZigBee, with key differences. It offers high bandwidth and strong interoperability, using different frequencies by region (868.42 MHz in Europe) to minimize Wi-Fi interference. Its range is around 30 m, extendable via mesh networking. Z-Wave has a lower data rate (around 100 kbps), unsuitable for streaming video or audio from security cameras, but it consumes even less power than ZigBee. It supports up to 232 devices but is very proprietary, limiting device choices. A Z-Wave router is needed to connect to the internet or a mobile phone.

C. Thread

Thread is a wireless communication protocol for smart homes and IoT, known for low power consumption and reliable, secure mesh networks. Operating at 2.4 GHz, it uses IPv6 for direct internet access and easy integration with other IP devices. Thread employs AES (Advanced Encryption Standard) encryption and DTLS (Datagram Transport Layer Security) for security. It supports broad compatibility and interoperability, especially with the Matter standard, and can connect to other networks like Wi-Fi or Ethernet for internet control.

D. Matter

Matter is a communication standard for smart homes and IoT, ensuring interoperability between devices from different manufacturers. It operates on an Internet Protocol (IP) basis, allowing direct internet communication and integration with other IP devices. Matter supports various network technologies like Ethernet, Wi-Fi, and Thread, offering flexibility. Bluetooth Low Energy is used for commissioning new devices, enabling easy network connection. Matter supports mesh networking and uses strong encryption and authentication (PKI and certificates) for security. It controls lighting, thermostats, security systems, and other devices, unifying smart home technologies and simplifying their use.

III. Monitoring parameters within the boiler room

The work will focus on monitoring equipment in the boiler room for combustion boilers. The boiler room is an essential part of buildings and industrial facilities because it allows to heat buildings in cold weather and to heat water. Measuring these parameters is very important for reasons such as safety, efficiency, air quality, maintenance, or regulatory compliance. Exceeding the recommended values can not only cause equipment failures but can also endanger the surrounding area.

A. Measurement of gases CO, CO_2 and flying dust

Combustion of solid fuels in boilers generates gases like Carbon monoxide (CO), Carbon dioxide (CO_2), and Particulate matter dust (PM). Their formation can be reduced by using better fuels, avoiding wet wood and poor-quality coal, or opting for renewable sources like biomass. CO is a colorless, odorless, and poisonous gas. High concentrations can cause poisoning or death. Measuring CO helps prevent health issues and indicates efficient combustion, leading to better efficiency and less pollution. CO can be measured using methods like non-dispersive infrared, electrochemical, electroacoustic, and semiconductor-based metal oxide sensors. The unit of measurement is parts per million (ppm). CO2 is a colorless, odorless greenhouse gas. At higher concentrations, it can cause headaches, dizziness, convulsions, coma, or even death. CO2 is measured using the same sensors and units (ppm) as carbon monoxide. Fugitive dust consists of small solid or liquid particles that can be pollutants or harmful to health, categorized as PM10, PM2.5, and PM1.0 based on size. PM10 particles stay in the air for hours, while $PM_{1.0}$ can remain for weeks. Laser scattering sensors measure PM by detecting scattered light from dust particles, determining their concentration and size in ppm. Fugitive dust often contains sulfates, carbon, nitrates, or polycyclic aromatic hydrocarbons, which can cause respiratory issues, asthma, and lung cancer.

B. Temperature measurement

In combustion boilers, temperature is measured at key points like the chimney, combustion chamber, and downstream to ensure efficiency and safety. Monitoring flue gas temperature in the chimney prevents condensation, while measuring temperature in the combustion chamber and downstream optimizes the combustion process and ensures proper functioning. Common methods include thermocouples, resistance sensors, and thermistors. Incorrect temperatures can lead to gas leaks, fire risks, condensation, or overheating, reducing boiler efficiency.

C. Humidity measurement

Humidity is measured mainly to prevent mold and corrosion. But proper humidity is also necessary for boiler efficiency and occupant comfort. It is measured using a hygrometer placed in the room.

D. Atmospheric pressure measurement

Atmospheric pressure is measured in the boiler room near the boiler or chimney. Correct pressure is important for boiler combustion efficiency and regulatory compliance. It can be measured using a barometer.

IV. Results of comparison with selected commercial devices for measuring boiler room parameters

The comparison found that the cheapest solution is the ecoNET module, compatible with boilers using ecoMAX controllers. The most expensive is from Bosch, suitable for large buildings due to its high cost. The ACD 03 AGF from Atmos only displays data on its built-in screen and lacks remote access or database storage. VIADRUS uses Siemens' Climatix IC for the A3C boiler, offering cloud-based data storage and display. Compatibility issues may arise with outdated control units or unique communication protocols. OPOP's proprietary solution is only compatible with their boilers, with an optional module for older boilers costing around 14,000 CZK. Another option is creating a custom monitoring system using HomeAssistant and Arduino modules, offering modularity and customization but requiring technical knowledge.

V. Delivered prototype

Prototype of measurement station measures CO_2, CO, fugitive dust concentration, relative humidity, flue gas pressure, and temperature in the chimney and room. Data is sent via Wi-Fi using Message Queuing Telemetry Transport (MQTT) messages and processed in Node-RED. If limits are exceeded, a WhatsApp message is sent. Data is stored in an InfluxDB database and displayed in Grafana. The device runs on a solar cell, recharging the battery and measuring data every 555 seconds to save energy.

A. Demonstration of old prototype

The image shows the device display. The red box indicates the measured temperatures: room, chimney, and outside temperatures, along with the DS18B20 sensor temperature for the heating circuit. Each DS18B20 sensor is installed in a specific position. The time of the last change is displayed below the image. At the bottom, the green rectangle lists the measured values from left to right: carbon dioxide concentration, carbon monoxide concentration, and illuminance. The blue border

Fig. 1. Delivered prototype
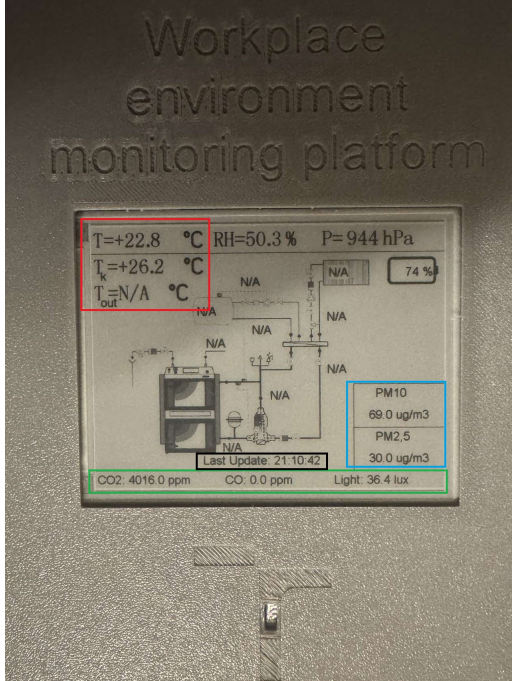
Fig. 2. Display of delivered prototype

shows the concentrations of PM10 and PM2.5 fugitive dust. RH represents the room's relative humidity, and P is the atmospheric pressure. The right corner displays the current battery capacity in percent.

VI. Newly designed prototype

After evaluating the limitations of the original prototype, a newly designed version of the device was developed. The goal was to address power management issues, simplify user interaction, and improve overall system reliability. The following subsections describe the key hardware and software improvements implemented in the new design.

A. Old prototype disadvantages and its adjustments

The newly designed device is designed to run primarily from USB, but the solar panel has been left, but the wiring was modified to make the solar panel disconnectable when not in use, and to remove the biggest disadvantage of the original wiring. This disadvantage was that it allowed the battery to be completely discharged (well below 3 V), which could lead to damage to the Li-ion battery. This happened with insufficient sunlight for a long time and at the same time with inappropriate placement of the solar panel. Another disadvantage was the lack of the ability to recharge the battery within the device, which was also eliminated by this change. An existing module is used, which is based on a TP4056 charger, a DW01A battery disconnector, and a pair of FS8205A MOSFET transistors. This module protects the battery, which is connected in the range of 2.4 V to 4.2 V, from overvoltage and undervoltage. In the case of solar panel power, the battery is connected directly to the CN3791 charger already used in the original circuit. A disconnector has been added, which is made up of MOSFET transistors, which will prevent the power supply from the solar panel when the prototype is connected to USB. Another shortcoming of the prototype was the cumbersome process of resetting Wi-Fi credentials, which required connecting the device to a computer and uploading reset and original codes. To address this, a new AP_RESET button was implemented, connected to a free pin on the ESP, simplifying the process.

B. Code optimization and editing

Today, as software becomes more complex and demanding, it is crucial to ensure that the code is not only functional but also robust, efficient, and easy to maintain. Inadequate error handling and unoptimized code can lead to frequent outages, slow performance, and difficult maintenance, which can have a negative impact on user experience and operational costs. For these reasons, a data structure was created and an array of elements of this data structure was created, where each element corresponds to one sensor. Each element carries the name of the sensor, whether it is detected, the sensor address (only for DS18B20 sensors), its physical quantity, value, correction, and unit. In publishing, we assume that there will be only two-level MQTT topics. The structure is adapted to this. Furthermore, functions have been created to work with this structure. The code has been divided into logical sections such as initialization, publishing measured values, listing to the console, and updating the display. The return value of the object initialization is used to detect the presence of sensors. The change of the measurement frequency depending on the

flue gas temperature measurement in the chimney has been added, i.e. if the flue gas temperature in the chimney is higher than 100 °C, the measurement period will be changed to 255 s. If not, the period will be set to 555 s. The figure 3 shows a flowchart of the new code.
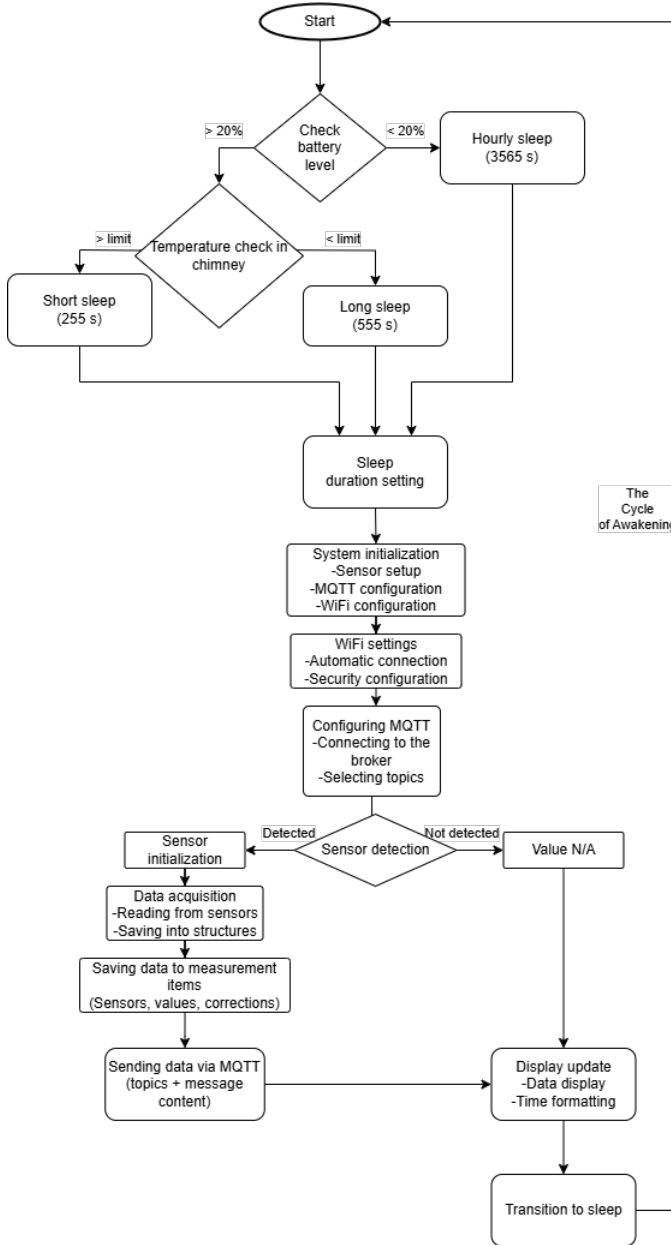
Fig. 3. Flowchart of the new code

C. Printed circuit board design

Due to the addition of a battery protection module, and modification of buttons, connectors, and because of using an OLED display instead of an E-ink display, it was necessary to design a new PCB. KiCad 8.0 software was used to design and draw the schematics. The Printed circuit board (PCB) design was based on the original PCB. Due to the large number of pins of the ESP32 circuit, a four-layer PCB was reused to allow easier distribution of conductive paths from the ESP32 circuit area. The surge protector on the USB port has been changed for easier routing and stretching of the USB bus signal. All three buttons RESET, BOOT_1, and AP_RESET are located in the same area for user accessibility. A two-pin Phoenix connector was chosen for the solar panel connection. All the connectors for sensors and displays have been changed to the same type, only they differ in the number of pins. Onewire connectors can be fitted all together, or if using break-out boxes, only two. Mounting holes have been inserted in the PCB for mechanical anchoring of the sensors. The result is 2 boards, one with the MCU unit and the other with the BME280, SHT45, SCD41, and MiCS5524 sensors. This second board will be placed in the top of the box, in which the airflow will be formed by the SDS011 sensor.

VII. CONCLUSION

The objective of this work was to verify, modify, and enhance a prototype for monitoring the operating parameters of combustion boilers. A thorough analysis led to several hardware and software improvements, including the addition of battery protection, enhanced power supply options, simplified user interaction, and optimized sensor data processing. The newly designed printed circuit board integrates these enhancements and provides a more reliable and user-friendly solution. The implemented system enables effective monitoring of key environmental and safety parameters, such as temperature, humidity, pressure, and concentrations of harmful gases and particles. Data is transmitted wirelessly and visualized using modern tools like Node-RED and Grafana, with alerts sent via WhatsApp when thresholds are exceeded. Compared to commercial solutions, the custom device offers modularity, cost-effectiveness, and flexibility, making it suitable not only for residential boiler rooms but also for broader smart home or industrial monitoring applications.

REFERENCES

[1] "Modul ecoNET 300," *Topeko24.cz*. Dostupné z: https://topeko24.cz/prislusenstvi-kotle/180-modul-econet-300.html, [cit. 2025-04-18].
[2] "Automatický monitoring," *Boiler Planning – Bosch Industrial Heat*. Dostupné z: https://www.boiler-planning.com/cz/ucinnost/zvyseni-ucinnosti-kotle-a-kotloveho-systemu/automaticky-monitoring.html, [cit. 2025-04-18].
[3] "Intoxikaci oxidem uhelnatým je dobré nepodceňovat," *Ministerstvo zdravotnictví ČR*. Dostupné z: https://mzd.gov.cz/intoxikaci-oxidem-uhelnatym-je-dobre-nepodcenovat/, [cit. 2025-04-18].
[4] "Oxid uhličitý: K čemu se používá a kdy je nebezpečný," *Bola.cz*. Dostupné z: https://www.bola.cz/poradna/oxid-uhlicity-k-cemu-se-pouziva-a-kdy-je-nebezpecny, [cit. 2025-04-18].
[5] "Internetový modul CS," *OPOP s.r.o.*. Dostupné z: https://www.opop.cz/internetovy-modul-cs, [cit. 2025-04-18].
[6] "Polétavý prach," *nano4house.cz*. Dostupné z: https://nano4house.cz/pojem/poletavy-prach/, [cit. 2025-04-18].
[7] "Zigbee vs Z-Wave: Comprehensive Comparison of Smart Home Protocols in 2024," *SmartHomePerfected*. Dostupné z: https://www.smarthomeperfected.com/zigbee-vs-z-wave/, [cit. 2025-04-18].
[8] "Internet věcí (IoT): definice, příklady využití, produkty," *Rascasone*. Dostupné z: https://www.rascasone.com/cs/blog/iot-internet-veci-definice-produkty-historie, [cit. 2025-04-18].

TVOJE MYŠLENKY
OBLETÍ SVĚT

PŘÍLEŽITOSTI
PRO STUDENTY
A ABSOLVENTY

V Honeywellu věříme, že budoucnost je taková, jakou ji společnými silami vytvoříme. V Brně se zaměřujeme na oblasti Aerospace a Industrial Automation.

KOHO HLEDÁME?

- Studenty a absolventy všech oborů FEKT VUT
- Zájem o dlouhodobou spolupráci a ochota dále rozvíjet znalosti z oboru
- Stáže: možnost pracovat 16–20 hodin týdně (flexibilní pracovní doba)
- Komunikativní znalost angličtiny

PŘÍKLADY POZIC

- Electrical/Electronics Engineer
- Hardware Engineer
- PLC Controls Engineer
- Systems Engineer
- Prototype/Test Technician
- Technical Support
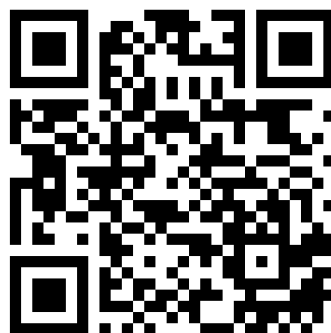
careers.honeywell.com/brno
www.honeywell.com
careers.honeywell.com/EarlyCareersCZ

Water level sensor

1st Matěj Hrdlička
Faculty of Electrical Engineering and Communication
Brno University of Technology
Brno, Czech Republic
247121@vutbr.cz

2nd doc. Ing. Petr Mlýnek, Ph.D.
Faculty of Electrical Engineering and Communication
Brno University of Technology
Brno, Czech Republic
mlynek@vut.cz

Abstract—Monitoring water levels in retention basins is crucial for effective water resource management and the prevention of natural disasters such as floods and droughts. The aim of this work is to design and implement a continuous water level measurement device using Internet of Things (IoT) principles. With the development of IoT technologies, the possibility of using affordable, energy-efficient, and remotely controllable solutions is emerging. The objective of this work is to analyze the available sensors and communication modules, design the overall system architecture, and implement the circuit board. The proposed solution provides an innovative approach to water level monitoring that can be integrated into larger smart infrastructure systems. The work provides a detailed analysis of the technology used and possible future improvements.

Index Terms—Ultrasonic sensors, LPWAN technology, GSM communication, IoT applications, ESP microcontroller, retention tank

I. Introduction

Monitoring water levels in retention basins is a key part of water management. Accurate measurement helps to prevent flooding, optimise water supply and improve the overall sustainability of water resources. This paper focuses on the design of water level measurement equipment in a retention tank. Sensors, microcontrollers and communication technologies will be described in this work. The main objective of this work is component design, architecture design, and circuit board design. To meet these objectives, an analysis of the sensors has been carried out to meet the requirements for proper functionality. The main requirements were accuracy and consistent measurement, lower price range, waterproof, and a minimum measurement distance of 4.5 meters. It was then necessary to select the right microcontroller to communicate with the sensor and control the entire device. Next, a suitable communication module had to be selected that would use GSM network and LPWAN technology for data transmission. Another requirement for the whole device was battery power supply, so it was necessary to select energy-efficient components. After appropriate selection of components, these components were incorporated into the architecture diagram on the basis of which the circuit board will be developed.

II. Sensorics

A sensor is a component or module that is capable of detecting physical quantities and then converting them into some type of desired signal that can be measured and processed to obtain information about the properties of that signal [1].

A. Division of sensors

In electronics, many types of sensors are used for different purposes, which can be, for example, to measure temperature, light intensity, or distance. For this work, a sensor for measuring distance from an obstacle is suitable in this embedding, the obstacle will be the water level in the retention tank. Water level sensors are further divided into contact and non-contact sensors [1].

- Contact sensors have direct contact with the measured variable. It is the simplest type of sensor and is widely used in conventional electronics. The advantages include more accurate measurements because they are in direct contact with the liquid and are not affected by external factors such as air temperature or dust. Disadvantages of contact sensors include the need for maintenance, they may be more prone to fouling or corrosion due to contact with the liquid, and the possibility of limited lifetime with continuous immersion.
- Non-contact sensors do not have direct contact with the measurand. The biggest advantage over contact sensors is that they do not have to have direct contact with the measured quantity, so it does not matter whether the measured quantity is water level or, for example, acid, which would melt the contact sensor. On the other hand, the disadvantage may be less accuracy, for example, when measuring in a tank, which has many folds and the measured signal is reflected there and the resulting value may be distorted [1].

III. Microcontrollers

A microcontroller is an integrated circuit containing a processor, memory, and input/output (I/O) peripherals on a single chip. It is used to control embedded systems, for example, in IoT or industrial automation. The main parts of a microcontroller include:

- **Processor** – executes program instructions
- **Memory** – program (Flash) and operational (RAM)
- **I/O interface** – enables communication with sensors and other devices
- **Communication modules** – UART, I2C, SPI, CAN, USB
- **Timers and power management** – enable economical operation

With their low power consumption and wide interconnect options, microcontrollers are a key component of modern embedded systems [2].

IV. INTERNET OF THINGS

The Internet of Things (IoT) refers to connected devices that contain sensors, software, and other technologies that can transmit and receive data. The purpose is to provide user information or automation of actions. Connectivity is primarily via Wi-Fi, but also includes 5G, LTE, or GSM communications. Huge amounts of data are processed almost anywhere with high speed and reliability [2]. The most commonly used technologies are Wi-Fi, Bluetooth, or NB-IoT.

A. Wi-Fi

Wi-Fi (Wireless Fidelity) translated into English as "wireless fidelity" is a wireless connection of end devices that is used almost everywhere and every day nowadays. For example, it can be in a desktop computer, a smartphone, or IoT devices that have a Wi-Fi module that they use to send data. The basis is a transmitter that sends a signal to the surroundings. The moment there is another device within the signal range, it can connect to the transmitter if it is set up correctly. Wi-Fi is differentiated by the bands in which it operates and uses the IEEE 802.11 standard, which uses the 2.4 GHz and 5 GHz bands [2].

B. Bluetooth

Bluetooth is one of the most widely used wireless communication technologies, which is used for transmission over shorter distances. Here, data is transmitted using radio frequency. Bluetooth is low power consuming and is widely used in mobile phones, desktop computers, car radios, printers, cameras, headphones, watches, and many other electronic devices [3]. The newest version is Bluetooth 5.4. The first version was launched in 2023. It offers the ability to communicate with multiple devices at once, has a better encryption system and improved energy efficiency, so it consumes less power during its operation. It has a choice between 125 kb/s, 500 kb/s, 1 Mb/s and 2 Mb/s, and the lower the baud rate, the higher the range. The range can be up to 240 m outdoors and up to 40 m indoors [4].

C. NB-IoT

NarrowBand IoT is one of the most well-known technologies used in IoT. NB-IoT is designed to be used in GSM (2G), WCDMA (3G) and LTE (4G) networks. The transmission speed is up to 250 Kbps and the bandwidth is 200 KHz [1]. NB-IoT works in 3 modes:

- **Standalone**
  This mode in NB-IoT works in the GSM band by taking one channel instead of the original GSM channel, this is possible due to the fact that they have identical channel width.
- **In-band**
  This mode works by reserving part of the LTE band for NB-IoT.

- **Guard mode**
  This mode operates in a guard zone, which means that it communicates outside the main channels [5].

V. METHODOLOGY

A very important part of this work was to select the right components such as the sensors, the microcontroller that will control the whole device, and the communication module that will send data over the communication networks to the server. In the figure 1 you can see the retention tank where the whole device with the sensor will be placed. The total depth of the retention tank is 4400 mm, of which the shaft is 1500 mm deep, the rest is the depth of the sump itself.

Fig. 1. Retention tank [2]

A. Component design

- **Sensorics**
  When designing the sensors, cost, accuracy, water resistance and measurement method had to be taken into account. It was necessary to take into account the fact that the sensor had to measure consistently in order to know the exact height of the water level, so the float sensor had to be discarded. This sensor only met the price, which was very low, but it only works as a limit switch, so the measurement would not be accurate. A non-contact sensor was chosen as the best option. It did not need to be submerged in water, but it had to be waterproof as there would be extreme humidity in the holding tank. Thus, the JSN-SR-04T ultrasonic sensor was the next suggestion. This sensor is very accurate, the accuracy of this sensor is less than 5mm, easily communicates with microcontrollers (via ECHO and TRIG) and is affordable. Its other advantages include water resistance. Its disadvantages include its limited range (up to 5 meters), thus insufficient for this work.
- **Microcontroller**
  It was necessary to choose a microcontroller that would have low power consumption. Among the requirements

was that the whole device had to communicate primarily via Wi-Fi, so the right microcontroller had to be chosen, preferably one that had a Wi-Fi module built in. The ESP32-S3-wroom-1 microcontroller was selected. This microcontroller meets all the points it should meet and is also quite affordable. In deep-sleep mode it has very low power consumption about 10 µA , so it is ideal for battery power. The Wi-Fi module will be for communication over a Wi-Fi network and if there is no Wi-Fi in range, the microcontroller will switch to the communication module and send data through it.

- **Communication module**
  Next, it was necessary to select the right communication module according to the specification. It was necessary that the communication module should communicate using GSM network and LPWAN technology, with the lowest possible power consumption. The SIMCOM-A7672E was selected as it met all the necessary requirements. This module can communicate via both GSM and LTE CAT 1. Thus, if the whole device is in an area with low coverage and no Wi-Fi range, the module will communicate via GSM and if the device is in a well-covered area, the module will communicate via LTE communication.

VI. IMPLEMENTATION

A printed circuit board was designed that integrates all components into a compact and energy-efficient unit. The proposed device will be implemented using the ESP32-S3-WROOM-1-N16R8 microcontroller, the A7672E communication module, and the JSN-SR-04T ultrasonic sensor. The A7672E communication module will be tested on different LTE network coverages to ensure a stable connection. To increase the measurement accuracy, software filters will be implemented to eliminate noise caused by external influences such as raindrops or surface ripples. The device will also be tested in different temperature conditions to verify its reliability at extremes. The device is designed to measure the water level in the retention tank and then transmit the data via a mobile network.

In the figure 2 you can see the proposed block diagram of this device.

The device consists of several key components:

- **Hardware**:
  The element that takes care of all the operations of this device is the ESP32-S3-WROOM-1-N16R8 microcontroller, which provides control and communication between the individual modules. The ultrasonic sensor JSN-SR04T will be used here to measure the water level. The sensor is connected to the microcontroller, which calculates the current water level based on the distance value according to the formula:

$$s = \frac{t \cdot v}{2} \quad [\text{m}] \tag{1}$$

- **Communication module**:
  The A7672E communication module is used to transfer
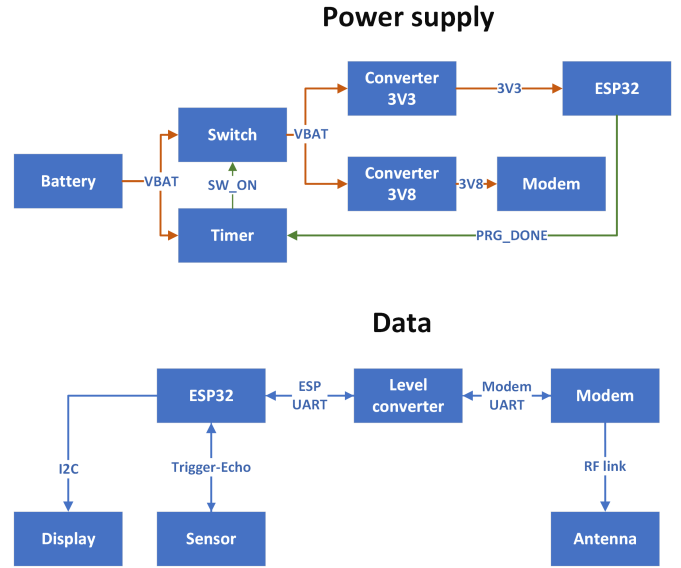
Fig. 2. Block diagram for the whole device [2]

data to the remote database, enabling mobile communication via the LTE Cat-M1 (Long-Term Evolution for Machines) network or GSM network. This module is designed for low power consumption, which is positive for long-term operation on battery power. Since there will be high humidity in the retention tank, it will need to have short-circuit protection. An optocoupler protector is provided for this purpose, which is located between the ESP and the sensor on the TRIG and ECHO signals.

- **Power system**:
  The entire device will be primarily powered by a 3.7V battery. The device is powered by MAX77827DEFD+T regulators, which provide a stable 3.3V to power the microcontroller and other components and 3.8V to power the communication module. A signal is applied to the ESP with the battery voltage value. In case the battery voltage level is low, a USB-C connector is made to recharge the battery. An integrated battery management system (BMS) is used for proper charging and battery protection.

There is a formula for calculating the battery life per charge:

$$T = \frac{C_b}{I_{\text{run}} \cdot t_{\text{run}} + I_{\text{sleep}} \cdot t_{\text{sleep}}} \approx 9414 \, \text{hours} \approx 393 \, \text{days}$$

(2)

Where:

- T is the battery life,
- C_b is the battery capacity after taking into account the safety limit (mAh),
- I_{run} is the current consumption during running (mA),
- t_{run} is the running time (h),
- I_{sleep} is the current draw during sleep (mA),
- t_{sleep} is the sleep period (h),

- **Programming and power management**:
  The device firmware will be developed in the Arduino IDE environment. Programming included the implementation of various power-saving modes. To save power, there will be a timer that will turn on the device itself after a set interval. Once the device measures the water level, converts it to distance, and sends it to the server, the device will turn itself off. In sleep mode, the power requirements are minimized, thus extending the battery life.

- **Data transfer**:
  Water level data is sent to a remote server primarily via Wi-Fi. If there is no Wi-Fi network in range, the device will switch to sending data via LTE CAT 1 or GSM mobile network. The sent values are then processed and visualized on the web platform, allowing the user to monitor the current status of the retention tank in real time. This transmission method ensures that the device can operate even in locations with limited internet access.

The device is therefore designed to provide a reliable and energy-efficient way to measure and monitor water levels in retention tanks with minimal maintenance and maximum battery life. The entire device should last at least one year on a single 10 000 mAh battery.

VII. Conclusion

The proposed device provides an innovative solution for measuring the water level in retention tanks. Using modern 5G-IoT technologies, specifically LTE CAT 1, it ensures reliable data transmission even in areas with poor mobile network coverage. Compared to traditional devices based on older GSM technologies, it offers lower latency, higher energy efficiency, and longer battery life. A key element of the design is the optimization of power consumption, which allows the device to operate for long periods of time without the need for frequent maintenance. This is achieved by using advanced sleep modes of both the microcontroller and the A7672E communication module, such as deep sleep mode or a timer that disconnects the entire device from the power source. These modes are essential for this device. The exact values of device accuracy and consumption are not yet known because the device is only designed and not yet assembled.

VIII. Future work

One possible extension is the integration of automated flow control using additional actuators, such as electric valves. This would allow the outflow to be dynamically controlled based on the current water level in the reservoir and rainfall forecasts. Thus, if the weather forecast indicated a high percentage of rainfall, a valve could be opened that would then release the water to another detention basin with a lower water level or release the water to irrigation systems. The system could also be augmented with a local user interface, such as through a mobile app, which would allow users to monitor and manually control the system in real time.

References

[1] SAMEK, Jakub, "Měření výšky hladiny vody ve studni," *Bakalářská práce*. Brno: Vysoké učení technické v Brně, 2019. Vedoucí práce: Ing. PAVOL KORČEK, Ph.D. Dostupné z: https://www.fit.vut.cz/study/thesis-file/21763/21763.pdf, [cit. 2025-03-14].

[2] HRDLIČKA, Matěj, "Senzor měření výšky hladiny vody," *Online, semestrální práce*. Petr MLÝNEK (vedoucí práce). Brno: Vysoké učení technické v Brně, Fakulta elektrotechniky a komunikačních technologií, 2024. Dostupné z: https://www.vut.cz/studenti/zav-prace/detail/163333, [cit. 2025-03-16].

[3] OMAROV, Adilzhan, "BP Omarov final," *Bakalářská práce*. Praha: České vysoké učení technické v Praze, Fakulta elektrotechnická, 2017. Dostupné z: https://dspace.cvut.cz/bitstream/handle/10467/74437/F6-BP-2017-Omarov-Adilzhan-BP%20Omarov%20final.pdf?sequence=-1&isAllowed=y, [cit. 2025-03-14].

[4] Alza.cz, "Bluetooth – Slovník pojmů," *Online*. Dostupné z: https://www.alza.cz/slovnik/bluetooth-art12370.htm#verze, [cit. 2025-03-14].

[5] ERICSSON, "NB-IoT: A sustainable technology for connecting billions of devices," *Ericsson Technology Review*, 2024. Dostupné z: https://www.ericsson.com/en/reports-and-papers/ericsson-technology-review/articles/nb-iot-a-sustainable-technology-for-connecting-billions-of-devices, [cit. 2025-03-15].

Analysis and suggestion of measure system for measuring quality and consumption of electrical power in campuses CEITEC and FIT BUT

Vojtěch Gabryš
Department of Electrical Power Engineering
Faculty of Electrical Engineering and Communication
Brno University of Technology
Brno, Czech Republic
246814@vut.cz

Daniel Janík
Department of Electrical Power Engineering
Faculty of Electrical Engineering and Communication
Brno University of Technology
Brno, Czech Republic
janikd@vut.cz

Abstract— **Electricity metering and monitoring are becoming an important part of areas with relatively high electricity consumption. It can contribute to the implementation of electricity savings and to a quicker response to a problem. Appropriate tools are required to analyse the measurements in the overall scope. By implementing a suitable measurement system, it is possible to achieve comprehensive coverage of the measurable variables and overall evaluation using appropriate software. Sustainability, power monitoring and savings motivate the Brno University of Technology to implement metering systems at more campuses such as Central European Institute of Technology and Faculty of Information Technology Brno University of Technology.**

Keywords—Measurement, KMB, Software, MTP, Analyser, Switchboard, CEITEC, FIT, Measuring system

I. Introduction

Sub-metering is starting to be introduced in high-consumption areas to get a better overview of the energy load of all parts. It is essential to get acquainted with the topology of the site, which depends entirely on the age of the complex and its subsequent reconstruction. To get a more comprehensive view of the whole analysis, it is necessary to install measurements at least on each floor of the buildings, preferably in all rooms of the whole building. However, such a solution would be very expansive and it would be sufficient to measure only the areas with high electricity consumption or with a high importance for the site. In switchboards, the measurement of only the main supply of the switchboard is usually included to obtain instantaneous values using an electricity meter located on the switchboard door. Measurements are eventually used to record values in the on-site Building Management System (BMS). The installed measurement is mostly outdated and insufficient for a comprehensive analysis. In order to obtain the necessary data, it is essential to equip the selected outputs with four-quadrant meters with the possibility of communication to the superior device, which will further process the information and forward it to the appropriate server with possible energy management software.

A great advantage for campuses can be the monitoring of the 1/4 hour maximum and of any anomalies that may occur during normal operation (blackout, high active/reactive load).

Measurements may help estimating a possible outage or detecting an error that has occurred. In order to achieve complete automation, the metering system must be linked to the energy management software using a suitable communication protocol to create a user-friendly interface in which any changes can be monitored without having to connect to the equipment directly.

Central European Institute of Technology (CEITEC) and the Faculty of Information Technology (FIT) are completely different campuses, especially in terms of construction. CEITEC is a newer building and does not contain any new annexes. On the other hand, the FIT campus consists of an old monastery, a brewery, and new annexes. The topology of the power distribution network of each campus is then crucial to achieving total measurement and data collection coverage. Therefore, a project was created to analyse them and design a measurement system.

II. Current Status in Selected Areas

For the project, it is important to get acquainted with the topology of the power distribution systems of individual sites, which in most cases is quite branched. It is necessary to inspect all premises, buildings, floors and switchboards to determine their condition and possible consumption.

Basic electricity metering occurs at both areas. The electricity meters are insufficient as they communicate via Local Operating Network (LON) and only provide basic consumption information (e.g. active energy consumption). They communicate and collect data for the campus BMS and it is not adequate to interfere with this metering. The BMS would have to be migrated to a new metering system, which would also have to be connected to the server for the BMS and the server for the energy management software. However, if the metering is connected via current transformers, it is advisable to use these transformers and link them to the new and existing metering.

A. Central European Institute of Technology

CEITEC is a campus with high power consumption due to its laboratories. Some of the equipment in the laboratories must be kept in operation continuously, making it difficult to notice any anomalies in the current state. The complex is divided into 4 buildings (A, B, E, S). According to the topology of the power

distribution, there are 123 switchboards, with 44 switchboards equipped with sub-metering, where data are only used for the BMS. It is suggested to add sub-metering to 16 switchboards and communicate their data to a specific server.

B. Faculty of Information Technology

FIT has a high power consumption due to the substantial number of servers. The servers must run 24 hours a day, along with the air conditioning that cools them. The complex consists of two main parts: Božetěchova 1 and Božetěchova 2. Because of the gradual modernization of the site, it is difficult to accurately map the topology of the power distribution. Few sub-meters are installed with the same purpose as in CEITEC campus. The addition concerns 25 switchboards.

III. Measuring system

A. Researched measuring systems

Individual systems from Schneider Electric, Honeywell and KMB were examined for the solution. The individual systems were looked at from the point of view of measuring power quality and not from the economic demands of purchasing the system. The overwhelming requirement was that the systems should be able to communicate and analyse power consumption in a good way.

Schneider Electric offers a wide range of electricity meters and analysers that are capable of high quality electricity analysis. The current and voltage accuracy class of the best available analyser is 0.2 according to IEC 61557-12. They lack the expansion modules to increase the number of current sensing ports. They are the only ones to offer the technology associated with wireless data transfer from the meters to a panel server, which forwards the data for evaluation. [1]

Honeywell tends to focus on creating different sensors and further the integration of them. They are not well equipped for energy management, but could one day contribute to a comprehensive metering system linked to sensors and electricity metering.

KMB focuses on designing equipment directly for power quality measurement and has analysers with the ability to connect multiple modules to maximize the use of measurement. The accuracy class for current and voltage measurement is 0.1 according to IEC 61557-12. [2]

B. Chosen measuring system

Considering the measurement systems offered on the market, the measurement system offered by KMB will be used for the following reasons:
- higher measurement accuracy,
- the possibility of expanding up to 20 three-phase outlets on a single analyser,
- consistency at the expense of the number of outlets to be measured,
- capability of KMB system was experimentally verified and tested as shown in Fig. 2

Fig. 1 shows the overall layout of the measuring system. The measurement begins by connecting the current measuring transformers (MTPs) or Rogowski coil to a single-phase or three-phase output. This counts as one measurement point. Next, the measured values are transmitted via cable to the EMI 12 or EMI 12 FLEX, where the received signal is evaluated via a built-

in, four-quadrant meter located separately for each pin. The data is transmitted to the BCPM 233.012 analyser via the Local Bus. The measured data is concentrated and made accessible to the higher-level system. Using RS-485 and protocol Modbus TCP/IP, the data can then be transferred to the server and stored there or connected to the relevant energy management software for further processing and analysis. In the event of an outage, the analyser includes a 512 MB data and event logging memory.
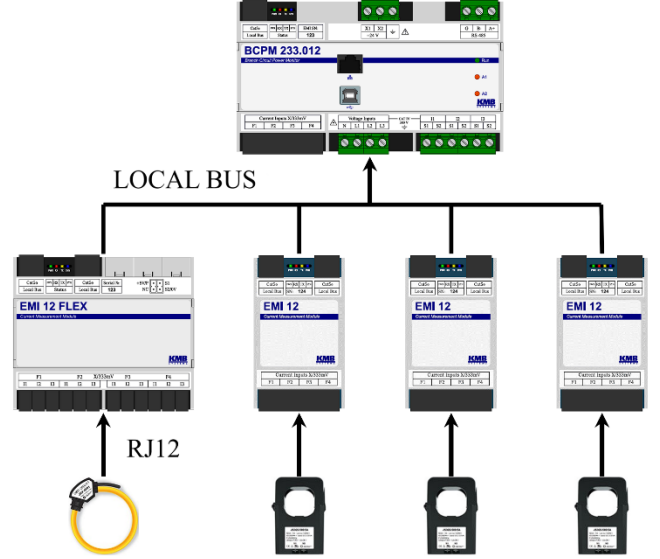
Fig. 1. Hierarchical arrangement of the measuring system, used references [2], [3], [4]
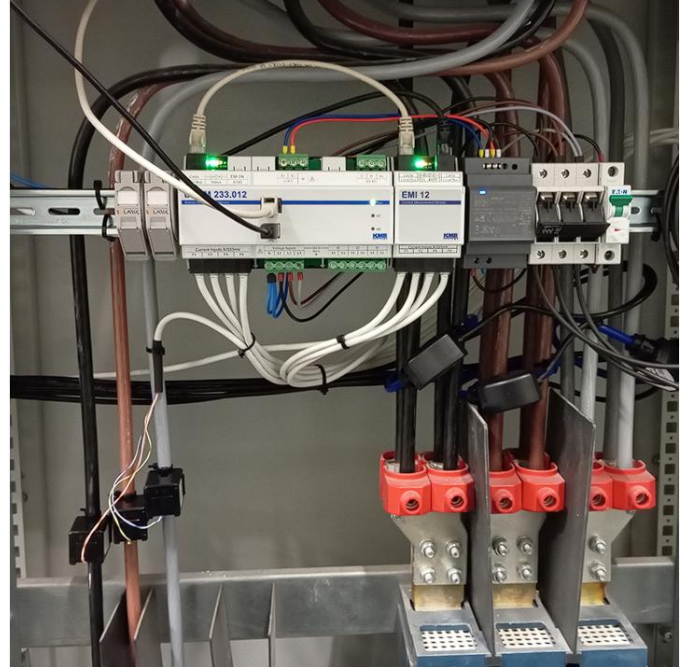
Fig. 2. Installed measuring system, taken over from [5]

C. Current Measuring Transformers

It is commonly known that MTPs are used to convert high currents into smaller more acceptable currents, which can be further sensed and evaluated by various devices (the most

common example is line protection). In our case, a transformer will be used with X/5A conversion for the main switchgear input and X/333 mV for other outputs, which are referred to as current sensors (but are generally referred to as MTPs). Generally, MTPs with a divisible core are used, for simple measurement installation. However, when space is limited, it is necessary to use flexible sensors, namely Rogowski coils, which again have X/333 mV conversion and are more flexible for installation. It is recommended to use an RJ12 cable to connect the MTP to the module.

IV. ENERGY MANAGEMENT SOFTWARE

Measured data must be processed and analysed for further use, which is why energy management software is one of the integral parts. It transforms the data into a clearer and more understandable form. This data can then be sent to the relevant users for further evaluation.

A. Requirements

- detailed visualization and analysis of measurement data,
- alerting when a certain value is exceeded (large peaks),
- control of 1/4 hour peak,
- alarms (exceedance, failure)
  - → preferably in the form of a traffic light within the visualization,
  - → sending information to a defined e-mail,
- reports (preferably automatic reports)
  - → setting of own report with possibility of setting and converting to money (possibility of inserting energy price), comparison of current and previous month's consumption, listing of alarms and exceeding of monitored values (1/4 hour maximum, etc.), report should be used for faculty/university management,
- divided into clear dashboards with hierarchical tree faculty/area, facility and possibly detail on individual measured sections (e.g. 1/2 floor of the building),
- user roles (e.g. secretary, campus administrator, ...)
  - → customize the user interface according to the roles (possibility to set custom visualization),
- a hierarchical structure of the division of buildings and elements
  - → option to select faculty, object, measuring element (from the highest to the last one),
  - → creation of a simple graphical diagram of the element distribution,
- implement the possibility of converting the energy consumed into the carbon footprint of the building.

B. Chosen software

The requirements specify clear criteria for what the software must fulfil. By storing the data on the server, we create the possibility of configuring the Node-RED, which enables data reading via the Modbus TCP/IP protocol. The data are then sent to the InfluxDB database, thanks to which we are able to proceed to their visualization using Grafana.

Grafana is a simple and open-source tool to visualize any measurement data. Histograms, graphs and other various functions are used. An example of visualization can be seen in Fig. 3 It contains many functions that can be adjusted according

to the user's requirements to customize the individual interfaces. The implementation of this software is an opportunity for the university to create own software to work with. However, it is necessary to set up all the device inputs, sort the data and create the visualizations. Also included is the ability to alert when a specific value is exceeded, such as the aftermentioned 1/4 hour maximum. Such graphs and alarms can be forwarded to the users in question and thus improve the running of the faculty/university. Grafana is already in use by Faculty of Electrical Engineering and Communication and will hence also be applied at the CEITEC and FIT campuses.
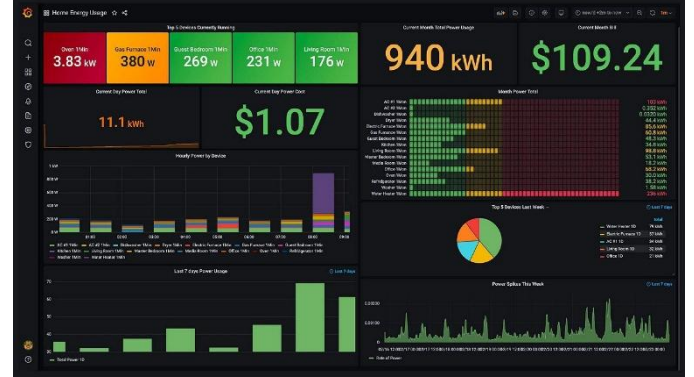
Fig. 3.   Example of data visualization, taken over from [6]

V. RESULTS AND DISCUSSION

The project consists in the creation of a complex system for the analysis and measurement of electrical energy on the premises. Using the measurement system described in chapter III, it is possible to obtain aggregated measurement values at our discretion (200 ms to 24 hours). The values obtained from the measurements are:

- combined voltage (U_{12}, U_{23}, U_{31}),
- phase voltage (U_1, U_2, U_3),
- phase current (I_1, I_2, I_3),
- active energy (E_P),
- reactive energy (E_Q),
- apparent energy (E_S),
- active power (P_1, P_2, P_3),
- reactive power (Q_1, Q_2, Q_3),
- apparent power (S_1, S_2, S_3),
- efficiency ($\cos \phi_1$, $\cos \phi_2$, $\cos \phi_3$),
- frequency (f_1, f_2, f_3),
- voltage harmonic distortion (THD U_1, U_2, U_3),
- current harmonic distortion (THD I_1, I_2, I_3).

This data can be displayed when connected to the IP address of the analyser, as can be seen in Fig. 4, Fig. 5, Fig. 6, Fig. 7, Fig. 8, Fig. 9.

Voltage			
Phase	L1	L2	L3	L4
U [V]	240.5	239.8	241.2	
THD_U [%]	3.05	3.03	2.94	

Fig. 4.   Voltage and THD_U by individual phases from Fig.5
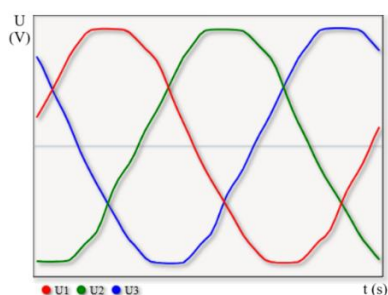
Fig. 5. Phase voltage waveform over time, measured in building T12 FEEC

Current				
Phase	L1	L2	L3	L4
I [A]	530.9	476.4	443.0	
THD_I [%]	14.8	17.7	19.4	

Fig. 6. Current and THD_I by individual phases from Fig. 7
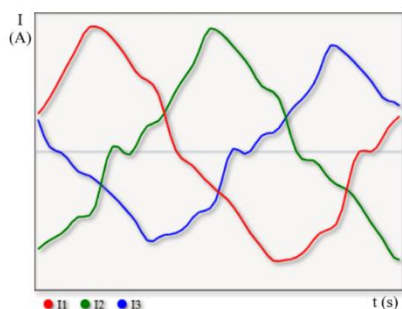
Fig. 7. Phase current waveform over time, measured in building T12 FEEC
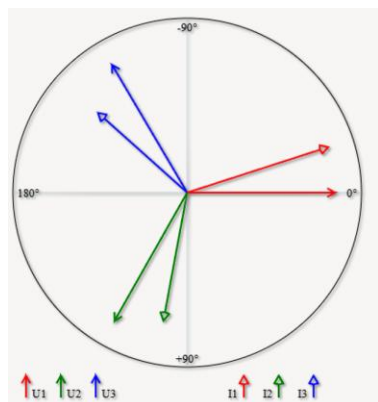
Fig. 8. Phase diagram, measured in building T12 FEEC

Voltage and Current Phases				
Phase	L1	L2	L3	L4
U_{FH} [V]	240.19	239.65	241.03	
φU_{FH} [°]	0.00	119.57	-120.49	
I_{FH} [A]	529.33	465.00	427.39	
φI_{FH} [°]	-17.88	100.53	-138.22	

Fig. 9. Voltage and Current Phases from phase diagram from Fig.8

The data obtained from the measurement system can be used for academic purposes. Research and development of possibilities for further integration of the hardware with a link to the server in automatic readings and production of outputs usable in the implementation of measures. Interfacing with the BMS and creating a unified system that would automatically respond to any anomalies or elevated/lowered readings. Examples could be the automatic switching off and on of air conditioners/radiators or electric water heating according to energy price and actual consumption. For building management, such measures can, for example, lead to the elimination of anomalies exceeding the quarter-hourly maximum. This links analysis with practice, where it is necessary to react to situations in the smallest possible time interval. With the help of alarms sent directly to specific users, it is possible to avoid long outages of a particular sector or as a prevention that some of the measured values may be exceeded.

VI. CONCLUSION

The installation of the measurement system can lead to significant progress in monitoring and measurement at the CEITEC and FIT campuses. Campus leaders will have the opportunity to become familiar with their campus consumption and any deficiencies. For building management, for example, the installation can lead to the elimination of anomalies with 1/4 hour maximum exceedances. This links analysis with practice, where it is necessary to react to situations in the smallest possible time interval. With the help of alarms sent directly to specific users, it is possible to avoid long outages of a particular sector or as a prevention that some of the measured values may be exceeded.

REFERENCES

[1] *Správa energie, fakturační měření a monitorování kvality energie*. Schneider Electric, 2020. Accessed: Oct. 14, 2024. [Online]. Available: https://download.schneider-electric.com/files?p_Doc_Ref=S1663&p_enDocType=Catalog&p_File_Name=S1663.pdf

[2] *Analyzátor sítě a monitor podružných vývodů BCPM 233.012*. KMB Systems, 2021. Accessed: Mar. 09, 2025. [Online]. Available: https://kmb.cz/cs/ke-stazeni/20-dokumenty/24-manualy-pro-merici-pristroje?download=159:bcpm233-012-manual-v3-0-cz

[3] *Systém měření podružných vývodů - jednotka měření proudu EMI 12*. KMB Systems, 2021. Accessed: Mar. 09, 2025. [Online]. Available: https://kmb.cz/cs/ke-stazeni/20-dokumenty/24-manualy-pro-merici-pristroje?download=162:emi12-manual-v3-0-cz

[4] *Systém měření podružných vývodů - jednotka měření proudu EMI 12 FLEX*. KMB Systems, 2021. Accessed: Mar. 09, 2025. [Online]. Available: https://kmb.cz/cs/ke-stazeni/20-dokumenty/24-manualy-pro-merici-pristroje?download=160:emi12-flex-manual-v3-0-cz

[5] R. Dvořák and D. Janík, "Data acquisition, visualisation and data processing of measuring of electrical energy consumption in BUT buildings", *Proceedings I of the 30th STUDENT EEICT 2024: General papers*, vol. 30, no. 1, 2024

[6] "Grafana", Grafana Labs. Accessed: Mar. 19, 2025. [Online]. Available: https://grafana.com/grafana/

Electrification of agricultural operations in the fields

Luboš Franěk
Faculty of Electrical Engineering and Communication
Brno University of Technology
Brno, Czech Republic
247662@vutbr.cz

This article deals with the issue of electrification of agricultural operations in the fields, with emphasis on the analysis of the energy balance in agriculture. The key energy inputs are identified, which are divided into renewable and non-renewable sources, while the possibility of their optimization is explored. The article looks at direct and indirect energy consumption in agriculture and analyses the impact of factors such as weather conditions or technological practices on the overall energy intensity. Furthermore, the possibilities of reducing energy consumption through modern technologies are evaluated, including the use of electrified variants of agricultural machinery. On the basis of the analyses carried out, measures to increase the efficiency and sustainability of agricultural production are proposed.

Keywords— electrification, agricultural technology, energy balance, optimization, efficiency, sustainability

I. Introduction

Energy balances are frequently used tools to evaluate energy efficiency in agriculture. The purpose of energy balances is also to identify key energy inputs to production, which helps to optimize resource use. It should be the goal of every business to analyse the energy consumption for each work operation they perform.

II. Energy consumption

Energy consumption can be greatly influenced by many factors, such as the weather, which can be different each year. Depending on the weather, moulds can form during rainy weather, which will result in higher spraying costs. In dry weather, costs are incurred for watering the plants (pumping water). In winter, costs are incurred by freezing the winter and reseeding during the spring.

Their values can then be compared with a general table where the consumption for the different working operations is averaged for the existing technologies. In agriculture, energy inputs can be divided into four categories:

- Renewable resources

- Non-renewable resources

- Direct resources

- Indirect sources

Renewable resources include human labour, fertilisers or seeds. Non-renewable resources include fuel, machinery, fertilisers and pesticides. Direct energy sources include fuel, agricultural machinery, equipment and agrochemicals, and indirect energy sources include the energy needed to produce fertiliser, machinery or pesticides. Energy consumption can therefore be analysed individually for each of the above forms of energy, or by adding them together. In practice, the direct energy consumption is the key in agriculture, as its reduction leads to an increase in the efficiency of the agricultural products concerned.

III. Reducing of primary energy consumption

The aim of accurately determining the energy balance for a particular crop is to identify the agrotechnical practices and suitable varieties that ensure high energy yields, efficiency and profitability [1]. Although it may not seem so at first sight, agriculture is an energy and transport business. In agriculture, energy is not only produced and transformed but also consumed. The result of the energy balance should not only be an assessment of the energy efficiency but also of the prospectiveness of the enterprise.

Primary energy consumption is an increasingly addressed topic in the agricultural industry, influencing the choice of technological systems and correct farming methods for working both on and off the field. Therefore, the possibility of reducing energy consumption should be of interest to every farmer.

Primary energy consumption can be reduced in many ways:

- By harvesting more efficiently, where optimal harvesting conditions make it possible to increase the efficiency of the process and therefore reduce primary energy consumption. Waiting for suitable conditions is therefore an effective way of reducing the primary energy intensity of harvesting

- Further reductions in primary energy intensity can be achieved by guiding agricultural equipment in the fields using GPS guidance. This achieves finding the most efficient routes around the field. The advantage is the elimination of inaccuracies such as overlaps and omissions during field operations. This results in a reduction in the time required to carry out field operations, resulting in savings in time and fuel costs.

- The correct choice of equipment can also help to reduce primary energy consumption. By selecting the smallest sufficient equipment to do the job, we save fuel that would have been burned unnecessarily by the large equipment selected to do the same work.

- By combining machinery operations, using equipment that allows multiple operations, such as combining ploughing and baling or cultivating and sowing, a reduction in energy consumption of 25-40% can be achieved.

- Optimising tyre size and pressure can achieve reductions in rolling resistance and wheel slip, which will also save energy consumed in the field.

The main objective of all these measures is to reduce energy consumption, specifically energy consumption (e.g. diesel or electricity) per unit of final product. The resulting energy balance depends on the crop yield achieved, but also on minimising losses during harvesting, transport, processing and storage [2].

IV. AGRICULTURAL TECHNOLOGY AND ITS APPLICATIONS

Crop production workflows involve dozens of operations, which are grouped and further subdivided into sub-operations. However, the energy balance is mainly influenced by energy-intensive operations, which include basic tillage, pre-sowing preparation, sowing, fertiliser application and harvesting, including by-product handling [3]. Various agricultural machinery is used for this purpose, among the most common of which are:

- Tractors

- Trucks

- Combine harvesters

Fig.1 Tractor New Holland T4 Electric Power utility [4]

Fig.2 Truck eActros [5]

Fig.3 Harvesting thresher John Deere S7 800 [6]

This can include machinery that is not at first sight considered agricultural, such as dozers, cranes and excavators, which can be used on farms to create access roads to farmland, to pile crops into storage or to move objects from A to B. In order to reduce energy inputs, the conventional internal combustion engine can be replaced by a hybrid or all-electric variant of the engine in agricultural machinery, but not all agricultural machinery currently achieves the performance levels that would allow the replacement of traditional internal combustion engines.

For tractors, diesel engines are commonly used in the fields with outputs ranging from $257 \div 405$ kW. Current technology offers us electric variants with outputs from $33 \div 55$ kW and battery sizes of $50 \div 100$ kWh [4]. These tractors can currently be used to transport crops in orchards or vineyards. They are not currently used for work operations carried out by farms during the cultivation of crops in the fields, such as ploughing.

Trucks can now be fully replaced by electrified variants, where conventional diesel engines have outputs ranging from 298-574 kW, while electric engines are most often found with outputs from $324 \div 471$ kW and batteries from $350 \div 700$ kWh [4], while hybrids have outputs from $110 \div 375$ kW and batteries of $30 \div 90$ kWh.

Combine harvesters are currently most commonly found on the market with internal combustion engines of $126 \div 589$ kW [6].

The performance comparison for the different engine variants of the technique is shown below.

TABLE.1 Comparison of engine performance in agricultural machinery

	Power (kW)	Battery capacity (kWh)
Tractors		
Internal combustion engines	257 ÷ 405	X
Electric motors	33 ÷ 55	50 ÷ 100
Hybrid motors	X	X
Trucks		
Internal combustion engines	298 ÷ 574	X
Electric motors	324 ÷ 471	350 ÷ 700
Hybrid motors	110 ÷ 375	30 ÷ 90
harvester		
Internal combustion engines	126 ÷ 589	X
Electric motors	X	X
Hybrid motors	X	X

V. WORK OPERATIONS

In order to analyse the energy balance of a given crop, it is necessary to analyse the energy consumption of all work operations, from soil preparation to the cutting of the crop. The work operations can be divided into the following phases:

- Soil preparation
- Fertilisation
- Sowing
- Stand care
- Harvesting

Each individual phase involves specific operations to achieve the most efficient crop production. These operations include cultivation, tillage, pre-sowing, fertilisation, sowing, spraying and harvesting [7].

VI. EVALUATION PLAN

For the energy intensity analysis, a specific field will be selected on which an analysis of the consumption of all work operations will be carried out until the crop is grown, which will include the subsequent replacement of the crop grown. The actual analysis of the energy intensity of growing different types of crops will be carried out for the diesel agricultural machinery and then for its electrified variants, after which the efficiency of these variants will be compared and then evaluated.

VII. ENERGY INTENSITY OF WORKING OPERATIONS OF THE SELECTED SEED AREA

In crop farms, it is necessary to carry out work operations that lead to the cultivation of the chosen crop. These work operations include ploughing, sowing, spraying and mowing.
This analysis has been carried out for one year only. During this period, wheat was grown in the field during the analysis. Other more extensive analyses are addressed in the bachelor thesis. This is the basis of the analysis, future analyses will address crop rotation and machine electrification.

VIII. SELECTION OF THE SEED AREA

The seed area selected by the author for the energy analysis is with a plot area 14999 m^2, i.e. 1.5 ha.

Fig.4 Selected seed field

IX. CALCULATING CONSUMPTION WITH INTERNAL COMBUSTION ENGINES

The calculation of the energy consumption for each crop varies by the number of work operations involved leading up to the actual harvesting of the crop. The calculation of the fuel consumption includes the work operations from the preparation of the soil to the harvesting of the crop itself.

TABLE.2 Real fuel consumption of agricultural operations leading to wheat cultivation

Work operations	Consumption in litres
Conditioning	12
Deep ploughing	33
Pre-sowing preparation	9.7
Sowing	12.7
Broadcast spraying	6.6
Harvesting	24
Transporting grain to the granary	1.6
Total consumption	99.7

Table.3 shows the fuel consumption values converted to values corresponding to fuel consumption per 1.5 ha. Grain transport to the granary was chosen to take the grain to the nearest farm which is about 2 km away from the selected field.

To calculate the fuel consumption for transporting crops to the granary, a John Deere 6R 185 tractor was used, which has an average fuel consumption of 19.2 l/h. The selected tractor would take approximately 5 minutes to reach the granary at a speed of 40 km/h. Thus, at the averaged consumption value given in the brochure, the fuel consumption for a grain haul to a granary 2 km away would be 1.6 l [8].

The given values were then converted to kWh. For the conversion, it was assumed that one litre of diesel contains an energy content of 10.7 kWh [9]. The consumption table for the given work operations was then converted into values:

TABLE.3 Real fuel consumption of agricultural work leading to wheat cultivation converted to kWh

Work operations	Consumption in litres	Consumption in kWh
Conditioning	12	128.4
Deep ploughing	33	353.1
Pre-sowing preparation	9.7	104.3
Sowing	12.7	136.4
Broadcast spraying	6.6	70.6
Harvesting	24	256.8
Transporting grain to the granary	1.6	17.1
Total consumption	99.7	1066.8

X. Conclusion

The article explained what the energy balance is used for, how it is distributed, and the possible reduction of direct energy in field operations. Furthermore, the article showed the current variants of farm machinery engines and their currently common outputs. The article presented the working operations that were included in the energy balance calculations of crop cultivation. The article calculated the total energy consumption for the work operations required to grow wheat, where the total energy consumption was 1066.8 kWh. The work operations were performed with internal combustion engines and will be followed by electric motors of agricultural machinery in future analyses.

The energy balance analysis should be carried out in every working farm. The analysis serves not only to obtain information on the energy intensity of the work operations carried out by the enterprise, but also to look for aspects of reduction for the operation, thus increasing the savings and overall efficiency of the enterprise. Therefore, it should be carried out in all enterprises, regardless of their focus, in order to increase their competitiveness and possibly differentiate them in the market from non-innovative enterprises.

References

[1] HNILIČKA, František; HNILIČKOVÁ, Helena; KUKLA, Ján; KEJZLAR, Tomáš and KUKLOVÁ, Margita. "Analýza energetických bilancí pěstování pěti odrůd cukrové řepy" (Analysis of energy balances of cultivation of five sugar beet varieties). Available: http://www.cukr-listy.cz/on_line/2018/PDF/404-409.pdf

[2] Top 10 Ways Field Crop Farms can Save Energy. Online. In: PennState Extension. 2023. Available: https://extension.psu.edu/top-10-ways-field-crop-farms-can-save-energy. [cit. 2024-11-26].

[3] "Zpracování půdy" (Soil processing). Brázda, 1997. ISBN 80-209-0265-1.

[4] Compact tractor T4 with electric drive. Online. In: Eagrotec. 2023. Available: https://www.eagrotec.cz/novinky/new-holland/kompaktny-traktor-t4-s-elektrickym-pohonom. [cit. 2025-03-16].

[5] eActros 300/400 Online. In: mercedes-benz-trucks. 2021. Available: https://www.mercedes-benz-trucks.com/int/en/trucks/eactros-300-400.html /. [cit. 2025-03-16].

[6] JOHN DEERE Harvesting threshers S7 800. Online. In: JOHN DEERE. 2024. Available : https://www.deere.cz/cs/sklizeci-mlaticky/s7-rada/s7-800/. [cit. 2024-12-05].

[7] Soil processing. Online. In. Available: https://www.kws.com/cz/cs/poradenstvi/zakladani-porostu/zpracovani-pudy/. [cit. 2025-03-10].

[8] Tractor 6R 185. Online. In: John Deere. 2022. Available: https://www.deere.cz/cs/traktory/stredni/rada-6r/6r185/. [cited 2025-03-31].

[9] Batteries versus other energy sources not only for vehicle propulsion (part 1). Online. In: Oenergetice. 2021. Available: https://oenergetice.cz/akumulace-energie/baterie-versus-jine-zdroje-energie-nejen-pohon-vozidel-1-cast. [cited 2025-04-01].

Energy balance of a farm using agrovoltaic systems

Vojtěch Paták

Faculty of Electrical Engineering and Communication
Brno University of Technology
Brno, Czech Republic
247701@vutbr.cz

The article is devoted to the introduction to agrovoltaic systems, types of agrovoltaics and relevant legislation in the Czech Republic. It mentions the benefits that farms can achieve if they decide to use their agricultural land for joint crop production and power generation. It explains the issue of energy balance of agricultural holdings and presents important parameters for the analysis of agrovoltaic utilization of agricultural areas, including basic formulas for calculation. The article also includes a comparison of the installed capacity of a conventional PV plant with an agrovoltaic plant.

Keywords— Agrovoltaics, photovoltaics, agriculture, energy balance, energy analysis, legislative

I. Introduction

Part of the sustainable development of our society should be to make efficient use of the space we live on. Agrovoltaics is a modern way of installing photovoltaic modules on agricultural land, but on which the agricultural work necessary for crop production can still take place. The so-called dual use of the land ensures highly efficient use of space and the partial shading provided by the installed agrovoltaics can also improve the conditions for growing crops. This creates a symbiosis between agriculture and energy.

II. A new chapter for photovoltaics

Generating electricity from sunlight is a very familiar process in today's world and photovoltaic plants are easily spotted in many places. Photovoltaics are also extensively discussed in the energy sector as an important part of the energy mix. This is because once installed, it produces clean electricity at minimal cost for self-consumption or for supply to the grid.

The most common way of installing a solar power plant is rooftop photovoltaics. However, larger photovoltaic systems are often installed on a clean surface, which makes it easier to install large numbers of photovoltaic panels. However, such a system occupies 100% of the area on which it is installed.

For the development of the energy sector and our society in general, the pursuit of efficient use of space is inevitable. Agrovoltaics offers us a new way of installing PV modules and will play a key role in the further development of PV systems in the coming years. Farms that choose to install an agrovoltaic system will not only achieve efficient land use, but also other benefits. In fact, if installed correctly, increased crop production or protection from the effects of extreme weather can be achieved. However, in addition to the agronomic benefits, the energy benefits must not be overlooked. An agrovoltaic system can provide the farm with additional profit from the electricity produced or can use this energy to cover part of its own consumption. The overall result of installing agrovoltaics is an improvement in the energy balance of the farm.

Currently, the construction of agrovoltaic systems is complicated by legislation. However, it is undergoing active development, and it is expected that in the coming years the first commercial agrovoltaic projects could start to emerge in the Czech Republic.

III. Types of agrovoltaic systems

The construction of agrovoltaic systems can be divided into two basic types - ground and elevated structures. Agrovoltaic greenhouses are then a special system. These types can then be purely passive or can include an active component. This means, in particular, a swivel joint with one or more axes of rotation. The active system can then adapt to the surrounding environment to provide ideal conditions for both the crops grown under the system and to maximize power generation (if this is a priority). It can also adjust its angle of rotation if farming activity is being carried out underneath - it will rotate so that it does not interfere with the farming equipment at work. The disadvantages of an active system are, of course, its cost, but also its greater failure rate, more complex installation and the need for a control program.

IV. Ground-mounted agrovoltaic systems

Ground-mounted agrovoltaic systems can be installed in several similar ways. The first way may at first glance resemble conventional photovoltaic power plants on a clean surface. This is the simplest agrovoltaic design, and therefore rows of monofacial panels with a tilt typically around 30° depending on the environment. The main difference from a conventional PV plant is the spacing between the panels, which allows free movement of livestock or agricultural machinery. Another difference is in construction design. It is designed to take up as little farmland as possible. If livestock are expected to be present in the vicinity of such a system, the structure is also reinforced for safety reasons.

Other ground installation methods are then derived from this basic system. Adding a swivel joint or replacing monofacial panels with bifacial panels can increase the efficiency of the agrovoltaics installed in this way.

So-called vertical solar farms are one of the most common ways of implementing agrovoltaic systems. This method uses bifacial panels oriented in an east-west style. The modules are installed either fixed in a position perpendicular to the surface or using a uniaxial swivel joint.

The ground-based agrovoltaic systems are mainly installed on permanent grassland for both mowing and grazing. The panels provide shade for livestock present at the installation site to provide relief from direct sunlight. This results in better production and quality of meat and milk. In terms of crops, according to [1], vertical systems are also rarely used in symbiosis with forages, vegetables, root and medicinal plants or cereals. For these crops, the vertical system can again help with shade, which protects the crops from sunburn, for example. Another benefit of shading can be a longer moisture retention in the soil and thus less water consumption.

V. ABOVE-GROUND AGROVOLTAIC SYSTEMS

Elevated above-ground systems are currently the most widespread and, according to [2], also the most desirable variant of the agrovoltaic system in the Czech Republic. Such systems are installed high above the surface using various structures to allow free movement of agricultural equipment. These systems can again, depending on the requirements, be passive or active. As with ground-based systems, the emphasis here is on the structure taking up as little of the agricultural land as possible. The robustness of the support structure is also important. It must be designed to withstand different types of stresses. Aboveground agrovoltaics are suitable for use in combination with fruit cultivation. Most often such systems are installed, for example, over orchards, vineyards or also hop gardens.

VI. LEGISLATIVE

As of 16 March 2025, agrovoltaics in the Czech Republic is defined only by Section 8a, a newly added part of Act No. 334/1992 Coll. on the Protection of Agricultural Land [3], which took effect on 1 July 2024. Until then, the same laws applied to agrovoltaics as to conventional photovoltaics. The problem is that in order to install a conventional photovoltaic power plant on a clean area, this area must be removed from the agricultural land fund. This is often a very complicated permitting process, but more importantly, it deprives the farmer of the possibility of receiving subsidies for this fertile land. This fact has made the construction of agrovoltaic systems significantly more complicated and economically almost impossible. However, Section 8a of Act No 334/1992 Coll. solves this problem and allows, under certain conditions, the construction of agrovoltaics without the need to remove the area from the agricultural land fund.

At a lecture [4], it was stated that the Solar Association is currently working on a decree for agrovoltaics, which better defines the parameters of agrovoltaic plants and thus allows the construction of more types of agrovoltaic systems. The following paragraphs are dedicated to this decree and contain the information communicated at the mentioned lecture.

The forthcoming decree for agrovoltaics should define the permitted agricultural crops for the construction of agrovoltaics. In the first phase of permitting, these crops should include vineyards, hop farms, orchards, container areas, nurseries and truffle areas. However, to maximize the potential of agrovoltaic systems, this list should be extended in the future to include standard arable land, grassland and permanent grassland. Another part of the forthcoming decree is devoted to the technical parameters of the agrovoltaic system.

According to the forthcoming decree, above-ground, or horizontal, agrovoltaic systems must enable the activities necessary to ensure agricultural production to be carried out under the photovoltaic modules. The agricultural area must then be at least 95% of the total area and the structure of the above-ground system must be at least 2.1 m above the surface. In places where the height is lower, this part of the area shall be considered as unusable for agriculture.

For ground-mounted, or vertical, agrovoltaic systems, the spacing between rows of PV modules must allow for the agricultural activities necessary for production. In this case, the area available for farming must be at least 80% of the total area. An area of 0.5 m on either side of the ground system shall be considered as unusable for agriculture. The design of the vertical agrovoltaic system will also have to maintain the spacing between rows of panels as a minimum of three times the height of the modules used.

Another challenge for the Solar Association is to develop a methodology for approving agrovoltaic projects and enabling subsidy support for agrovoltaics.

VII. FARM ENERGY BALANCE

The energy balance of an agricultural holding is given by the difference between the energy produced by the holding through its work and the energy consumed in carrying out that work. This balance is then used as a tool to evaluate the efficiency and sustainability of the farm.

Energy inputs represent consumed energy. They are further divided into direct and indirect inputs. Direct inputs include, according to [5], the consumption of fuel (diesel and petrol for agricultural machinery), electricity (for lighting, cooling, irrigation or driving machinery), water and energy consumed for heating. Indirect inputs include, according to [5], the energy needed to produce direct inputs. In practice, this reflects the energy consumed in the extraction and production of raw materials up to the transport of raw materials to the point of consumption. Source [6] then includes among indirect agricultural inputs, for example, the energy required for the production of seeds, fertilizers and crop protection products.

Energy outputs express produced energy. These include the energy of the crops and livestock products grown, but also the electricity generated on the farm premises, for example by an agrovoltaic system. However, according to [5], only the products that leave the farm gate are considered as energy

outputs. Therefore, the energy produced and subsequently used directly by the farm is not counted as an output.

According to [6], the energy analysis of enterprises uses the conversion of energy inputs and outputs to a comparable unit. One of the units used is the so-called equivalent of a liter of diesel (EQF). The value of 1 EQF is equal to 35.8 MJ or also 1.17 liters of diesel [5]. The deviation from one is due to the inclusion of the energy required to extract, refine and transport one liter of diesel. For electricity, it is also worth mentioning that 1 EQF is equal to about 9.94 kWh. According to [6], the EQF unit was introduced mainly because of its greater telling power compared to calories or joules.

The following table shows the conversion of various energy inputs and outputs into EQF unit, based on data from [5]. These data were verified by the author of the article by his own calculations and by comparing data from various sources.

TABLE I.   Examples of EQF values [5]

INPUTS	Energy in EQF
100 kg of urea	180.57
100 kg of grain seed	22.34
25 kg of feed for calves	30.23
100 l of diesel	117

OUTPUTS	Energy in EQF
100 l of milk	8.54
100 kg of eggs	17.29
100 kg of cereals	44.18
100 kg rapeseed	70.44
100 t of compost	89.38
100 kg live weight of cattle	37.42

To improve the energy balance of the farm, it is advisable to invest in more efficient machinery, but also to work towards energy self-sufficiency. If there is a possibility to utilize, for instance, a by-product of a produced commodity for further production, this option should be preferred to import from other sources in terms of energy balance. The same is true for electricity. Producing electricity on-site results in an improved energy balance.

VIII. ANALYSIS OF AREAS FOR AGROVOLTAIC USE

A typical farm normally caters for several agricultural areas. These need to be identified and grouped according to their parameters. The essential parameters of an agricultural area for agrovoltaic purposes include the size of the area, the orientation and slope of the area, the crop to be grown, the distance of the area from the farm and access to the distribution system.

Size of the area is one of the basic types of information about any surface. In terms of agrovoltaic use, we are particularly interested in this data because of the possible extent of the agrovoltaic system. A larger area allows us to have a larger number of PV modules installed.

The orientation and inclination of the surface is particularly important to maximize the use of the installed PV panels. They must be installed at a certain inclination and oriented either to the south or to the east and west to achieve their highest possible efficiency. The most suitable areas are therefore those that allow rows of PV modules to be installed facing south or east and west in a parallel plane with the boundary of the agricultural area and without having to modify the structure to rotate the modules. This prevents the creation of blind spots for agricultural equipment and locations that complicate work.

The slope tells us how inclined the surface is compared to the horizontal. Too large slopes place increased demands on the structure. It is necessary to ensure that as much light as possible reaches the photovoltaic panels. For example, an east-west oriented array of bifacial panels on a fixed ground structure would not be very suitable for more sloping areas with a westward slope, as there would be significant shading in the morning hours. In such a situation, a south-facing panel system would be more appropriate.

The crop that is grown on a given area plays a major role in the choice of the type of agrovoltaic system. Certain crops benefit from a combination with aboveground agrovoltaics, while others are better served by using ground-mounted agrovoltaics. The choice of the type of design significantly influences the maximum achievable installed capacity in a given area, the economic requirements, but also the complexity of installation and design. Therefore, different numbers of PV modules can be placed on the same size, orientation and slope depending on the crop to be grown, which will vary both the maximum installed capacity and the complexity and cost of the design.

Depending on the purpose of the agrovoltaic system, the distance of the area from the farm or the availability and capacity of the distribution network must also be taken into account.

If the agrovoltaic system is installed to cover own consumption, we will try to use areas that are in the immediate vicinity of the farm. This will allow us to supply electricity to the farm without having to use the distribution network. In this case, the smaller the distance from the farm, the lower the line losses or transmission costs. If we want to use the electricity generated by the agrovoltaic system for our own consumption, but the area on which the system is installed is too far away for direct transmission to the farm, it is possible to use power sharing via the distribution system. However, in this situation the distribution network needs to be used, which adds another party to the system with whom the terms of use need to be agreed, as well as the charges associated with using the distribution network.

If agrovoltaics are installed purely for the purpose of selling electricity to the grid, the distance from the utility is not as important. On the contrary, the presence of the distribution system in the vicinity of the agrovoltaic plant is required. It is also necessary to determine whether the distribution system at the location has the capacity to connect the power of the agrovoltaic system.

IX. BASIC FORMULAS FOR GROUND-MOUNTED AGROVOLTAICS

The design of the agrovoltaic system must be based on legislative requirements. The formulas in this article are created

by the author and are based on the expected wording of the relevant legislation, particularly the forthcoming decree for agrovoltaics.

The known parameters for the design of an agrovoltaic system are the dimensions of the agricultural area and the dimensions of the photovoltaic panels used. The calculation then determines the maximum installed power, the maximum number of rows of panels and the maximum number of panels in a row. The forthcoming decree implies that the spacing between rows must be at least three times the height of the panel. However, the actual spacing is chosen according to the working width of the agricultural machinery that will be working between the rows of panels. Typical values according to [4] are 10 to 12 meters. The minimum spacing is therefore determined by:

$$r_{min} \geq 3 \cdot a \, , \tag{1}$$

where r_{min} (m) is the minimum spacing between rows and a (m) is the height of the panels used.

Consequently, the extent of the agricultural area also varies according to the inclination of the panel from the horizontal plane. The actual range by deflection is calculated by:

$$z = a \cdot \cos \varphi + c \cdot \sin \varphi \, , \tag{2}$$

where a (m) is the panel height, c (m) is the panel thickness and φ (°) is the inclination from the horizontal plane.

For the maximum number of rows of photovoltaic panels that can be placed on an agricultural area, the following relationship applies:

$$N_{max} = \frac{x}{r + (z+1)} \, , \tag{3}$$

where N_{max} (-) is the maximum number of rows of panels, x (m) is the length of the side of the agricultural area perpendicular to the rows of panels, r (m) is the spacing between rows of panels and z (m) is the panel range by deflection increased by the decree specified distance of 0.5 meters on either side of the panel.

The maximum number of panels per row also depends on the type of construction chosen. Therefore, the following formula introduces the dimension x_m (m) to indicate the width of the gap between the panels. The relation for the maximum possible number of panels in one row is therefore:

$$n_{max} = \frac{l}{b + x_m} \, , \tag{4}$$

where n_{max} (-) is the maximum number of panels in a row, l (m) is the row length, b (m) is the width of the PV panel and x_m is the width of the gap between the panels.

The maximum installed power on a given agricultural area is then determined according to the relationship:

$$P_{imax} = P_m \cdot N \cdot n \, , \tag{5}$$

where P_{imax} (Wp) is the maximum installed power of the agrovoltaic plant, P_m (Wp) is the power of one panel, N (-) is the number of rows of panels and n (-) is the number of panels in one row.

X. COMPARISON OF AGROVOLTAICS AND PHOTOVOLTAICS

With the objective of comparing the possible installed capacity of an agrovoltaic and a conventional PV plant on the same area, a random area of 200x400 meters was chosen, with the longer side facing directly south. PV panels with dimensions of 2.3x1.1x0.035 meters were also chosen. The inclination of the panels from the horizontal plane was chosen to be 33°. By calculating the above-mentioned formulas, the installed capacity of a typical agrovoltaic plant (2.7 MWp) and the approximate capacity of a photovoltaic plant on the same area (around 9 MWp) were found. This relatively large difference is due to the requirements of the decree for agrovoltaics, in particular the necessary spacing between rows of panels and the maximum area covered by the agrovoltaic system.

XI. FUTURE RESEARCH

A specific farm has been selected for the analysis of agrovoltaic use and the first data with parameters for the practical application of this theory for the analysis of areas is expected in the near future. Furthermore, data on electricity consumption of either the whole farm or part of it are also expected. Once these data are received, a more specific analysis of the usable areas will be carried out, together with the calculations and design of the agrovoltaic system. Subsequently, the energy balance and electrical self-sufficiency of the farm will also be evaluated.

XII. CONCLUSION

Agrovoltaics has great potential to become an important part of the local energy sector and will play an important role in the future, both in PV systems and in agriculture. With the improvement of legislation, interest in this technology is expected and it is therefore necessary to focus on understanding the design issues of agrovoltaic systems. It is equally important to be able to evaluate the areas for the use of this technology and to determine the energy balance of the farm using agrovoltaics.

REFERENCES

[1] Š. Kubec, "Studium vlastností bifaciálních PV modulů v prostředí agrivoltaiky", (in Czech), Diploma thesis, Prague, 2022.

[2] "Komplexní řešení lokální a regionální energetiky jako součást opatření GreenDealu pro dosažení udržitelného zemědělského a lesnického hospodaření", (in Czech), *VÚKOZ*, 24-Oct.-2023.

[3] "Zákon č. 334/1992 Sb.", *Zákony pro lidi*, 0c2010–2025.

[4] "Agrovoltaika: Součást moderního zemědělství i energetiky – Jiří Bím (ČVUT/Solární Asociace).", (in Czech), 29-Oct.-2024.

[5] J. Špička and L. Jelínek, "Energetická analýza zemědělských podniků – metodický přístup", (in Czech), study, Prague, 2010.

[6] L. Jelínek, "Ekonomický systém hodnocení výkonnosti zemědělských podniků respektující principy trvalé udržitelnosti hospodaření s přírodními zdroji", (in Czech), 2010, p. 95.

Study of the design possibilities of an electrical impedance tomography system

1st Carlos Javier Valles Salas
Department of Electrical and Electronics Engineering
Instituto Tecnológico de Durango
Durango, México
19040877@itdurango.edu.mx

2nd Roman Vaněk
Department of Theoretical and Experimental Electrical Engineering
FEEC, Brno University of Technology
Brno, Czech Republic
240707@vut.cz

3rd Assoc. Prof. Jan Mikulka
Department of Theoretical and Experimental Electrical Engineering
FEEC, Brno University of Technology
Brno, Czech Republic
mikulka@vut.cz

Abstract—**This document shows some general affairs in the design of an electrical impedance tomography system. An introduction to a modular design that facilitates modifications for the system is present. Components selection, and visual verification for voltage levels are the main affairs treated here. Components selection involves 3 tables to compare different voltage converters, specifically for 3.3 V, 12 V, and 48 V, as these are intended to be in the power supply module. Visual verification is implemented to check the output of mentioned converters, and in the corresponding section, basic equations are explained.**

Keywords— EIT, voltage measurement, modular system, power supply, operational amplifier, components comparison.

I. INTRODUCTION

Electrical Impedance Tomography (EIT) is a technique to uncover the interior side of a object of study. Using a variable number of electrodes located around the object to be measured, it is pretended to drive a current through two of them so a voltage differential is developed in the others. Then, measuring the voltages and, as the flow of current is already known, it is easy to calculate the impedance (or at least the real component) of the body being studied. The key, is to create a distribution map of the impedance. A general block diagram is shown in Fig. 1.
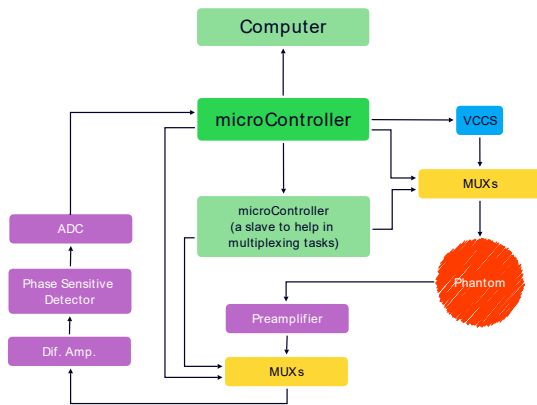
Fig. 1. General diagram of an EIT system

An EIT system is composed by several subsystems/components, and they might vary depending on the self design of it, but the most important are mentioned in table 1.

TABLE 1. PARTS OF AN EIT SYSTEM

Part	Description
μC	A microcontroller is the heart of system, because it has the assignment of managing a big part of it.
VCCS	A Voltage Controlled Current Source is used to generate a current flow (up to 10mA for medical aplications).
MUXs	It is needed to switch the function of each electrode, wheter for current injection or voltage measurement. The multiplexors solve this by simplifying enourmusly the system.
Phantom	This part refers to the container where the object to study is, or where the group of electrodes are.
ADC	An analog-to-digital conversion is needed in order to collect, and analyze the data obtained by the electrodes.

The aplication of this technology envolves many areas, such as medicine, and object structure analysis. In medicine, it is commonly used to examine the condition of the lungs, thus help in diagnosis procedures. In the case of structure analysis, it has been used to analyse internal fractures and distributions.

II. STATE OF THE ART

While not new, EIT has not been sufficiently developed to achieve large-scale commercialization or a crucial application of any kind. The main factor for this could be credited to resolution, which, while not difficult to improve, is closely related to the practicality of the system itself. Thus, most existing systems sacrifice some qualities for others depending on the approach taken to the project. Good examples are the next four.

A. PulmoVista 500

Made by Dräger, a german company, it is a system focused on visualizing the lung ventilation process. It counts with 16

electrodes (plus 1 for referenced measures), deliver up to 50 frames per second, and injects a current with a maximum value of 9 mA in a range from 80 kHz to 130 kHz [1].

B. Villanueva, C.

As a thesis, this design incorporates 16 electrodes, and a Red Pitaya STEMlab 125-10 as the main computer. It has a SNR (Signal to Noise Ratio) of 36.39 dB, and injects a current with a maximum value of 100 µA with a wide bandwidth range (up to 1 MHz) [2].

C. Casas, O.

This is a parallel broadband real-time system with 16 electrodes, a SNR better than 60 dB, and a current with oscilation values from 10 kHz to 250 kHz [3].

D. The Sheffield data collection system

With 16 electrodes, this design is capable of inject a current of 10 mA at 5 kHz. An active shielding is incorporated to reduce the noise due to stray capacitances [4].

III. DESIGN

As learned from the development of other systems (e.g. Analog-digital module for electrical impedance tomography, David Zimniok), it is necessary to have a design with a modular architecture that allows us to improve or correct different parts of it in an easier way, as is needed. So, new advances are being made following Roman Vaněk's ideas (shown in fig. 2) [5].
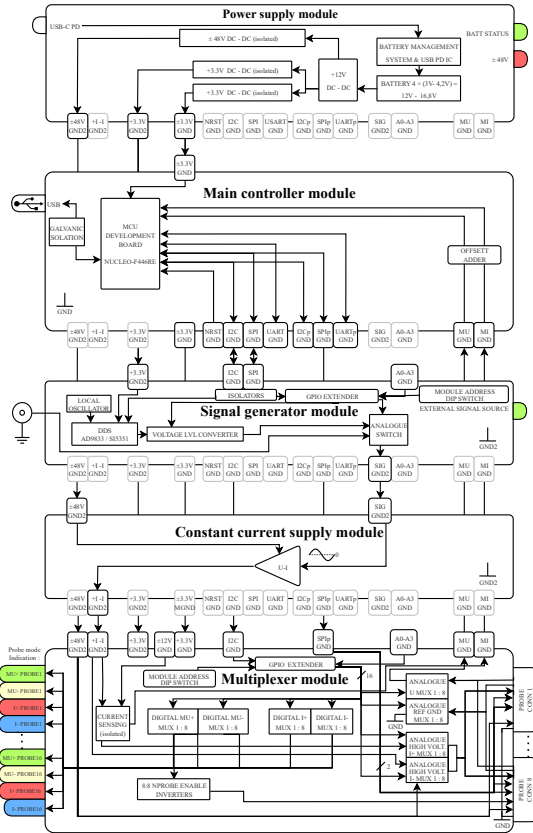
Fig. 2. System block diagram

A. Power Supply Module

Previous problems with the measurement system have taught us that it is necessary to have more than one ground reference: one for the current excitation side and another the measurement one. As actual progress is putting hands-on it, it has been necessary to find out what components are available on the market, compare them with themselves, and then select the most suitable options for our application.

As can be seen in fig. 2, the power supply module is composed of multiple converters. This is because there are different voltage levels required by different parts of the system (e.g. the microcontroller uses 3.3 V, while the constant current supplier needs ±48 V). So, the next tables (2, 3, and 4) serve as comparisons between converters available in the market, specifically distributors Farnell and TME electronic components.

TABLE 2. COMPARISON BETWEEN LOW DROPOUT REGULATORS

MODEL	LINK	COST	INPUT MIN/MAX	OUTPUT MIN/TYP/MAX	CURRENT LIMIT
UA78M33CDCYR	https://www.tme.eu/cz/details/ua7 8m33cdcyr/stabilizatory-napeti-neregulovane/texas-instruments/	12.61 Kč	5.3 V/25 V or 30 V	3.2 V/3.3 V/3.4 V	0.5 A
ADM7150ARDZ-3.3	https://www.tme.eu/cz/details/adm 7150ardz-3.3/stabilizatory-napeti-neregulovane-ldo/analog-devices/	177.03 Kč	4.5 V/16 V	3.282 V/3.3 V/3.305 V	0.8 A
LT1084CT-3.3PBF	https://www.tme.eu/cz/details/lt10 84ct-3.3pbf/stabilizatory-napeti-neregulovane-ldo/analog-	179.84 Kč	2.55 V/30 V	3.27 V/3.3 V/3.33 V	5 A
LT1086CT-3.3	https://www.tme.eu/cz/details/lt10 86ct-3.3/stabilizatory-napeti-neregulovane-ldo/analog-	135.12 Kč	—/30 V	3.267 V/3.3 V/3.333 V	1.5 A
NCV8775CDT33RKG	https://cz.farnell.com/on-semiconductor/ncv8775cdt33rkg/ ldo-fixed-3-3v-0-35a-40-to-	41.84 Kč	4.5 V/40 V	3.234 V/3.3 V/3.366 V	0.35 A

TABLE 3. COMPARISON BETWEEN CONVERTORS WITH 48 VOLTS OUTPUT

MODEL	LINK	COST	INPUT VOLTAGE	OUTPUT VOLTAGE	CURRENT LIMIT	EFFICIENCY
THN 15-2425WI	https://cz.farnell.com/tra copower/thn-15-2425wi/dc-dc-converter-2-o-p-15w/dp/3795641	1,110.998 Kč	9 V to 36 V	up to 48 V	0.315 A	typ 91%
I7C4W008A120V-001-R	https://cz.farnell.com/td k-lambda/i7c4w008a120v-001-r/dc-dc-converter-9-	1,359.74 Kč	9 V to 53 V	9.6 V to 48 V	8 A	near 97%
LM2588S-ADJ/NOPB	https://www.tme.eu/cz/d etails/lm2588s-adj_nopb/stabilizator-napeti-obvody-dc-	300.59 Kč	4 V to 40 V	up to 60 V	5 A	up to 90%
RGC4W300W008A-001.	https://cz.farnell.com/td k-lambda/rgc4w300w008a-001/dc-dc-converter-48v-	2,014.33 Kč	9 V to 53 V	9.6 V to 48 V	8 A	up to 97%
LM2577S-ADJ/NOPB	https://www.tme.eu/cz/d etails/lm2577s-adj_nopb/stabilizator-napeti-obvody-dc-	191.98 Kč	3.5 V to 40 V	up to 65 V	3 A	up to 80%
LM2585T-ADJ/NOPB	https://www.tme.eu/cz/d etails/lm2585t-adj_nopb/stabilizator-napeti-obvody-dc-	230.08 Kč	4 V to 40 V	up to 65 V	3 A	up to 93%

TABLE 4. COMPARISON BETWEEN CONVERTORS WITH 12 VOLTS OUTPUT

MODEL	LINK	COST	INPUT VOLTAGE	OUTPUT VOLTAGE	CURRENT LIMIT	EFFICIENCY
TMR 12-1222WI	https://cz.farnell.com/tra co-power/tmr-12-	886.385	4.5V to 18 V	±12 V	0.5 A	89%
TMR 12-2422WI	https://cz.farnell.com/tra co-power/tmr-12-	908.205	9 V to 36 V	±12 V	0.5 A	89%
THD 12-1222	https://cz.farnell.com/tra copower/thd-12-1222/dc-	1009.088	9 V to 18 V	±12 V	0.5 A	87%
TMR6-7212WIR	https://www.tme.eu/cz/d etails/tmr6-7212wir/dc-	821.06	9 V to 36 V	±12 V	0.25 A	87%
TMR3-7212WIR	https://www.tme.eu/cz/d etails/tmr3-7212wir/dc-	696.39	9 V to 36 V	±12 V	0.125 A	82%
TMR9-1222	https://www.tme.eu/cz/d etails/tmr9-1222/dc-dc-	865.08	9 V to 18 V	±12 V	0.375 A	88%
TMR6-1222	https://www.tme.eu/cz/d etails/tmr6-1222/dc-dc-	537.7	9 V to 18 V	±12 V	0.25 A	83%

The important characteristics to consider when it comes to selecting components are the cost, current limit, and efficiency. For example, for table 4, it can be quickly determined that the best option is the first one, since it has the best efficiency and the highest current limit available, although the relatively high cost. It is also important to double-check the features of the components, e.g. consult the seller's catalog and the fabricator's data sheet. The main reason for doing this is that, sometimes, the main description in the seller's catalog is incorrect or there's a lack of important information.

On the other hand, it was decided that implementing a voltage verifying subsystem would be helpful to maintain the integrity of the entire process. So, a three voltage levels circuit for visual verification was designed (48 V, 24 V, and 3.3 V). There are many ways to approach the design, but the simplest and most direct way to do it is by implementing lower limit comparators, because in this case the important thing is to ensure that the output voltages do not drop. Thus, the circuit in figure 3 shows the proposal (for 24 V, and 3.3 V cases, the circuit is almost the same, as it works under the same principle).
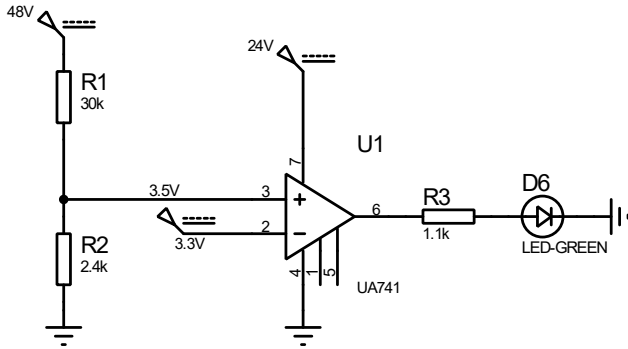

Fig. 3. Comparator for 48 volts verification line

The power supply of each Op. Amp. (Operational Amplifier) depends on the 24 V converter and therefore the resistance for each LED has the same value, this is:

$$R = \frac{V_S - V_L}{I_L} \qquad (1)$$

Where V_S is the supply voltage (24 V), V_L is the voltage drop in a LED (it is supposed to be a 3.2 V drop, as it is the typical value for green LEDs), and I_L is the current flowing trough the LED. As a 20 mA current is chosen, the required resistance value will be:

$$R_3 = \frac{24 - 3.2}{0.02} = 1040 \ \Omega \qquad (1.1)$$

To explain how comparators work, we are taking the 48 V comparison line as an example. The Op. Amp. will output the

positive or negative supply value (24 V or GND) depending on which of the 2 inputs is greater: if the signal from the non-inverting input (+) is greater than that from the inverting input, then the output will be V_{DD} (24 V), and vice versa. A 3.5 V signal is branched from the 48 V signal by means of a voltage divider, where a first resistor with a value of 30 kΩ is preset.

$$R_2 = \frac{V_o R_1}{V_I - V_o} \qquad (2)$$

$$R_2 = \frac{3.5(30000)}{48 - 3.5} = 2360 \ \Omega \qquad (2.1)$$

Where V_O is the desired voltage, V_I the input voltage, R_1 the upper resistor and R_2 the lower resistor that will give us the desired derivation.

The 3.3 V converter signal is selected as reference. So, ideally, the 48 V signal should not go down, that is, in principle we should always have 3.5 V at the output of the voltage divider, which is greater than 3.3 V, therefore, the derivation will go to the non-inverting input and the 3.3 V to the inverting input. In this way we achieve that as soon as the divisor's output is lower than the reference (3.3 V) the LED will turn off. In this case there would be a margin of less than 3 V before the LED would turn off.

In figure 3, the values for the second and third resistors were changed to the nearest commercial values, following the E24 standard.

There is a concern about resistor R_3. Although it allows the desired current flow, the power dissipated by it will be higher than 0.4 Watts. It is important to keep this in mind if a small SMD (Sourface Mounted Device) package is used. The simplest solution is to replace this resistor with three resistors in series: 680 Ω, 680 Ω, and 240 Ω. This way, the power dissipation is distributed among the three new resistors. The current would be approximately 14mA, which would not significantly affect the LED's brightness. In this case, the power dissipated by each resistor would not exceed 0.13 Watts, meaning that a 1206 package can be used, for example.

REFERENCES

[1] Dräger. (2022). PulmoVista 500 SW 1.30: Ventilación y monitorización respiratoria.

[2] Villanueva Ibarra, C. G. (2023). Sistema de Tomografía por Impedancia Eléctrica. Universidad Nacional Autónoma de México, Facultad de Ingeniería.

[3] Casas, O., Rosell, J., Bragós, R., Lozano, A., & Riu, P. J. (1996). A parallel broadband real-time system for electrical impedance tomography. Physiological Measurement, 17(4A), A1-A6.

[4] Brown, B. H., & Seagar, A. D. (1987). The Sheffield data collection system. Clinical Physics and Physiological Measurement, 8(4A), 91-97.

[5] Vaněk, R. (2024). Modular system for electrical impedance tomography. Brno University of Technology, Faculty of Electrical Engineering and Communication, Department of Radio Electronics.

DeltaBot construction for presentation and study of kinematics

Adam Hrežo
Department of Microelectronics
Brno University of Technology
Brno, Czech Republic
247008@vutbr.cz

Abstract— **This article focuses on the potential use of rotary delta-type structures for 3D printing. It also analyzes the DeltaBot construction and describes and designs its main structural components.**

Keywords—FDM, 3D printer, Rotary Delta, kinematics, Klipper, firmware

I. Introduction

DeltaBot or Rotary Delta robots are often used in industry due to their speed and relatively good accuracy. They are designed for the rapid transfer of small, lightweight parts. This work focuses on the design of the main structural components. It also covers the assembly and commissioning of the proposed printer.

The goal of this project is to design and build a fully functional DeltaBot-type FDM 3D printer for public demonstrations and kinematics research.

II. Rotary Delta Robots

Rotary delta printers are a recent innovation and are not yet available on the market. Due to this fact, only a limited amount of information can be found about them.

This chapter therefore focuses mainly on the construction and principle of rotary delta robots, as these robots are commonly used in industry, with the only difference being the type of end effector— in the case of a 3D printer, the hotend. A rotary delta robot is a parallel-type robot with three degrees of freedom.

A. Structural Components of the DeltaBot

Rotary delta robots consist of several key structural components. The base is the part of the robot where arm actuators are mounted. The arms (driving arms) transmit the rotational motion from the actuators to the struts (following arms), which are connected to the arms through joints. Finally, the end platform is attached to the struts via joints [1][2].

B. Principle of the Rotary Delta robot

Now that the main structural components of this type of robot are known, it is possible to describe how this printer works. The rotary delta has an interesting kinematic system. The position of the end platform is determined by the position (rotation) of the three arms.

From the perspective of inverse kinematics, the process works as follows. First, the absolute coordinates of point *V*, which represents the position of the end effector as specified in G-code, are converted into relative coordinates *M1* (1),(2), *M2* (3),(4), and *M3* (5),(6) for each of the three arms individually. This calculation determines the relative coordinates of the connection points between the struts and the end platform (Fig. 1) [3][4].

$$X_{M1} = X_V + d\cos(\alpha_1) = X_V + d \cdot \cos(90) = X_V \quad (1)$$
$$Y_{M1} = Y_V + d\sin(\alpha_1) = Y_V + d \cdot \sin(90) = Y_V + d \quad (2)$$

$$X_{M2} = X_V + d\cos(\alpha_2) = X_V - d \cdot \cos(210) \quad (3)$$
$$Y_{M2} = Y_V + d\sin(\alpha_2) = Y_V - d \cdot \sin(210) \quad (4)$$

$$X_{M3} = X_V + d \cdot \cos(\alpha_3) = X_V + d \cdot \cos(330) \quad (5)$$
$$Y_{M3} = Y_V + d \cdot \sin(\alpha_3) = Y_V - d \cdot \sin(330) \quad (6)$$

where *d* is the radius of an imaginary circle centered at point V, passing through all three points $M1$, $M2$ and $M3$.

The following is the transformation of the coordinates M_1, M_2 and M_3, which are located in the main coordinate system, into the coordinates M_1', M_2' a M_3', where each of these points is located in its own coordinate system (7),(8).

$$X' = M_Y \sin(\beta) + M_X \cos(\beta) \quad (7)$$
$$Y' = M_Y \cos(\beta) - M_X \sin(\beta) \quad (8)$$

where β is the angle between the positive direction of the Y-axis and each of the M points. In this case: $\beta_1 = 0°, \beta_2 = 120°, \beta_3 = 240°$ (Fig. 1).
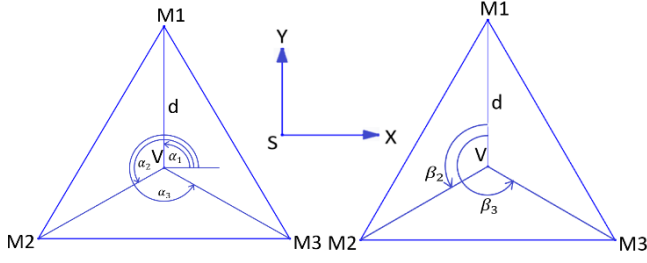

Fig. 1. Graphical representation of key points of the end platform for kinematics calculation.

Next, for each arm, the intersection P is found between a circle formed by the arm k, centered at point Q, and a sphere formed by the strut l, centered at point M (9),(10).

$$(X' - X'_M)^2 + (Y' - Y'_M)^2 + (Z - Z_M)^2 = l^2 \qquad (9)$$
$$\left(X' - X'_Q\right)^2 + \left(Z - Z_Q\right)^2 = k^2 \qquad (10)$$

where X'_M, Y'_M and Z_M are the coordinates of the strut attachment point of length l on the end platform. X'_Q and Z_Q are the coordinates of the arm rotation point of length k (Fig. 2).

After simplifying and solving these two equations, there is a simple formula for calculating the angle theta:

$$\theta = arctan\left(\frac{Z_Q - Z_P}{X'_P - X'_Q}\right) \qquad (11)$$
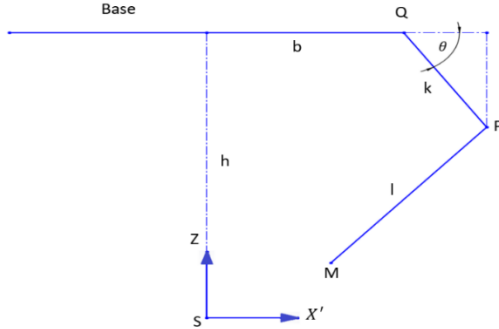
Fig. 2. 2D representation of the connection between the strut of length l and the end platform at point M, and the arm of length k, which is connected to the base at point Q.

III. DESIGN OF STRUCTURAL COMPONENTS OF THE DELTABOT PRINTER

A. Printer Frame

The first step in designing the structural components of the printer frame is determining the required print volume. The size of the working area depends on the maximum achievable height of the printing space. When choosing a cylindrical working volume, it is important to consider that the larger the selected print surface, the smaller the attainable print height. For this printer, a round heated bed on an aluminum substrate with a diameter of 220 mm was selected, with a maximum print height of approximately 150 mm.

Based on this information, the frame's connecting components were designed. The proposed construction of this printer differs from a typical rotary delta (DeltaBot) configuration in that the base is positioned at the bottom near the ground. Consequently, the print bed is located at the top. This arrangement could have several potential advantages. For example, since the actuators for the individual arms, which add weight, are located on the base, the center of gravity of the printer shifts downward. This should have a positive impact on vibration resistance, leading to improved print quality. Additionally, the control electronics would be positioned below the base.

B. Arm Actuation

In DeltaBot actuators, when using standard NEMA17 stepper motors, these motors alone do not provide sufficient torque to move the arms, which support the entire weight of the print head, including the struts, joint connections, and structural components. One option is to use larger and therefore more powerful motors. However, larger motors are more expensive and require higher power consumption. Another alternative is to use mechanical transmission to increase the torque of the actuator.

After consideration, a 5:1 belt drive was chosen, consisting of a NEMA17 stepper motor, a GT2 belt (10 mm wide, 200 mm long), and two pulleys with 16 and 80 teeth. This gear ratio should be sufficient given the structural parameters. The drive is mounted to the printer's base using two PLA-printed brackets.

C. Joints

One of the key structural components of a rotary delta printer is the joint connections, which movably link the end platform to the struts and the struts to the arms. These joints must meet several requirements, such as low weight, minimal backlash, long lifespan, and a large angular range [5]. The larger the angular range of the joint, the greater the working space of the device, in this case, the printer. In DeltaBot-type constructions, ball joints with three degrees of freedom are commonly used. Standard ball joints typically allow an angular range of approximately ±15° to ±18°.

For this printer, commonly available stainless steel spherical joints were used due to their simplicity and low cost. These joints were mounted in 3D-printed holders made from copolyester filament with 20% of carbon fiber, ensuring both strength and low weight (about 25 g) of the entire joint assembly (Fig. 3).

Fig. 3. Assembly consisting of two spherical joints linked by a connector.

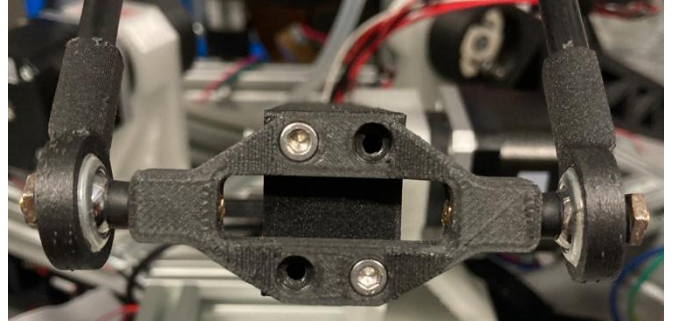## D. Arms and Struts

To achieve the highest possible printing speed, all components of the moving parts must be as lightweight as possible. This applies to both the arms and the struts.

For this reason, a second arm was designed using a composite material. The arm is 3D printed from PA-CF, making it very strong while remaining relatively lightweight. A metal flange coupling was used to attach the arm to its actuator (the output shaft of the gearbox) (Fig. 4). The assembled arm weighs approximately 42 g. The total length of the arm, including the joint connector, is 151.8 mm.

Fig. 4. 3D printed arms.

The struts were designed as carbon fiber tubes with an inner diameter of 4 mm, an outer diameter of 6 mm, and a length of 245 mm. These carbon tubes proved to be an excellent solution, as they provide sufficient strength while keeping the minimal weigh. The total length of a strut including both spherical joints is 300 mm.

E. End platform

Just like the arms, struts, and joints, the end platform is a crucial component of this printer.
It houses several essential parts: a 3010 fan for active cooling of the coldend heatsink, a Bowden extruder, an inductive sensor for print bed calibration, and an aluminum tube that directs airflow to cool the deposited material (Fig. 5). Additionally, the platform contains joint components for connecting the struts to the platform.

As one can see, the platform holds multiple components, and at high accelerations, their weight could cause flexing. To prevent this, the final version of the platform was made from a carbon fiber composite plate, similar to the arms. First, the platform's outline and the extruder mounting hole were cut using a water jet cutter. However, the used water jet was unable to cut holes smaller than 5 mm in diameter, so the M3 screw holes were drilled manually.
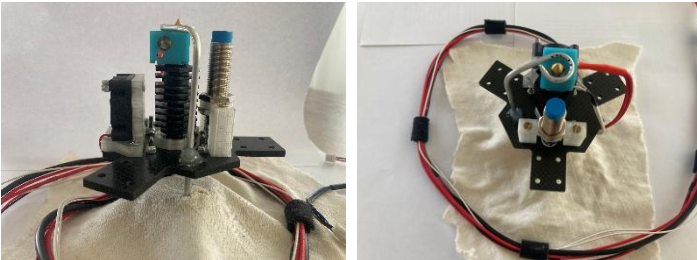
Fig. 5. End platform equipped with an extruder, a fan, and an inductive sensor

F. Extruder

The first part of the extruder consists of a small NEMA17 stepper motor, mounted at the bottom of the printer's base, combined with a 3:1 gearbox (BMG Dual Drive extruder). A standard Bowden tube guides the filament to the second part of the extruder, which is located on the end platform.

The second part of the extruder includes a coupling, which connects the Bowden tube from the stepper motor to a high-temperature Bowden tube. This tube passes through the heatsink and heatbreak all the way to the heatblock, ensuring precise filament retraction during printing. Additionally, the second part of the extruder consists of a 40 W heating element, an NTC 3950 100K thermistor, and a 0.4 mm brass nozzle.

IV. ELECTRONICS

Rotary delta 3D printers are not very widespread. However, when analyzed in detail, they are structurally very similar to linear delta printers. The same applies to their composition in terms of electronic components.

A. Endstop Detection

When analyzing the kinematics of this type of printer, despite the limited amount of literature on the subject, it is evident that a significant challenge lies in determining the endstop position of the arms. There are various methods for detecting end positions in 3D printers, such as mechanical switches, optical sensors, inductive sensors, and others. For accurate operation and coordinate recalculations, it is essential to determine as precisely as possible the angle formed by the printer's arms.

In the design of this printer, microswitches were chosen for endstop detection because they are inexpensive, fairly precise when positioned correctly, and easy to mount.

B. Control Electronics and Power Supply

The next step was selecting and integrating the electronic components of the printer. Due to the relatively simple composition of the components, a 24 V, 350 W power supply was used. This power supply is mounted on the printer's side using a 3D printed mounting bracket.

Also located under the base is a DIN rail with a quick terminal block, which distributes the power supply's output voltage to other components. These components include: a 32-bit BIGTREETECH SKR V1.4 TURBO mainboard equipped with four TMC2209 stepper drivers, a Raspberry Pi (RPi) 4B with active cooling, a 24 V to 5 V buck converter for powering the Raspberry Pi, and a MOSFET module for PWM control of the air pump. Communication between the RPi and the mainboard is handled via a USB-B cable.

Additionally, the printer is equipped with a Mini 12864 RGB LCD display.

Printer is controlled by Klipper firmware using the Rotary_delta kinematics. It is operated via the Mainsail web interface [6].

V. PRINT TESTING

After thorough calibration of the printer, several test prints were conducted. First, a 15x15x15 mm cube with double walls

and 20 % infill was printed using a 0.4 mm nozzle and PLA filament. The print speed was set to 30 mm/s, the extruder temperature to 210 °C, and the bed temperature to 60 °C. Despite being printed upside down, the cube held well to the bed throughout the print.

Due to backlash in the arm and joint mechanisms, significant ghosting occurred on the printed object, and the cube tapered as it moved away from the bed.

Subsequently, several cylinders with a diameter of 15 mm and a height of 50 mm were printed using the same slicer settings as the mentioned cube. The print results for all three cylinders were similar to that of the cube, with slight variation. During printing, the cylinder's diameter alternately shrank and expanded. This could have been caused by the mentioned backlash in the used gearboxes and some faulty joints. The printed objects are shown in Figure 6.

By using a different type of gearing, high-quality spherical joints, and potential input shaping calibration, better results could be achieved.
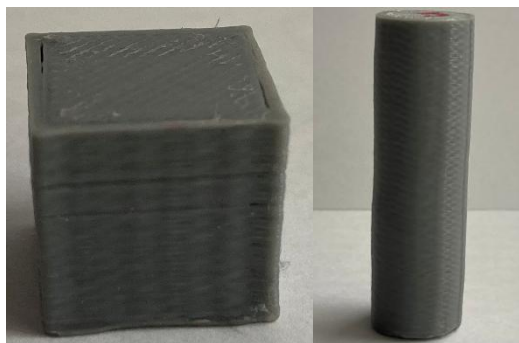
Fig. 6. Example of test prints

VI.   CONCLUSION

The goal of this work was to design, assemble, and commission an FDM printer of the rotary delta type. Ultimately, the following objectives were achieved. All proposed main structural components were designed, manufactured, and assembled. By utilizing composite carbon materials, a low weight of the moving parts was achieved, which should improve both print quality and speed once the printer is fully operational and fine-tuned.

Additionally, thanks to the chosen joint type, an acceptable print area of approximately 220 mm in diameter was achieved. On the other hand, the resulting print volume height is limited to around 150 mm. Theoretically, with a small modification to the frame, it would be possible to increase the print bed diameter to approximately 260 mm at the cost of reducing the print height to around 110 mm.

Due to last-minute changes in the arm drive design, the described printer is currently unable to produce accurate prints. The main issue lies in the spherical joints and planetary gearboxes used to drive the arms, which exhibit excessive backlash in their current configuration. This results in print imperfections, as mentioned in chapter V.

Because of delays in the delivery of components and the ongoing tuning process aimed at minimizing mechanical

imperfections, the printer is still in the final adjustment phase. However, after the installation of the new drive system and overall mechanical fine-tuning, the print quality is expected to improve significantly.

The final assembled design of the printer is shown in Figure 7.
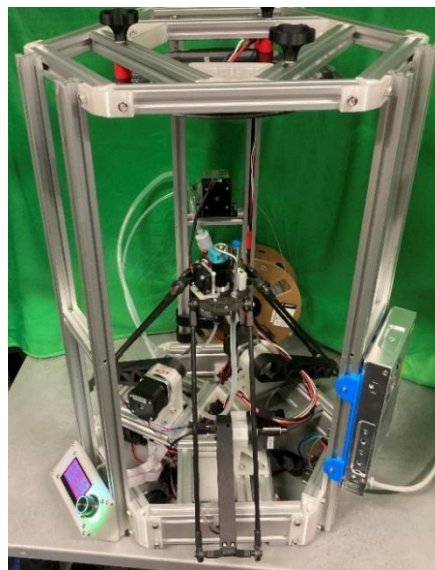
Fig. 7. The assembled printer is a rotary delta type

REFERENCES

[1] Rotary Delta Printer. MyMiniFactory, Egris. Online. February 15, 2021 [cit.2025-02-24]. Available at: https://www.myminifactory.com/object/3d-print-rotary-delta-printer-154247

[2] Design of 3DOF Delta Parallel Capture Robot with High Speed and Light Weight. JUN-LIN, Ma; YING, Liu; YING-KUN, Zhang a CUNMING, Hao. Online. *Journal of Physics: Conference Series*. 2022, roč. 2188, č. 1. ISSN 1742-6588. [cit.2025-02-24] Available at: https://iopscience.iop.org/article/10.1088/1742-6596/2188/1/012008

[3] Workspace Analysis of Delta Robot Based on Forward Kinematics Solution. C. Liu, G. -H. Cao and Y. -Y. Qu. 2019 3rd International Conference on Robotics and Automation Sciences (ICRAS), Wuhan, China, 2019, pp. 1-5, doi: 10.1109/ICRAS.2019.8808987. Online. [cit. 2025-02-25]. Available at: https://ieeexplore.ieee.org/document/8808987

[4] Delta Robot: Working Advantages and Applications. Smlease Design. Online. [cit.2025-02-25]. Available at: https://www.smlease.com/entries/automation/delta-robot-working-advantages-applications/

[5] ŠABART, Adam. Paralelní kinematické struktury průmyslových robotů. Brno: University of Technology, Faculty of Mechanical Engineering, 2015. 52 pages. Bachelor's thesis supervisor doc. Ing. Radek Knoflíček, Dr. [cit.2025-01-03]. Available at: https://www.vut.cz/www_base/zav_prace_soubor_verejne.php?file_id=103516

[6] Klipper documentation. Klipper. Online. [cit.2025-03-09]. Available at: https://www.klipper3d.org/

Visualization tool for industrial production data

Ondřej Michalčík
Department of Control and Instrumentation
FEEC Brno University of Technology
Brno, Czech Republic
247425@vut.cz

Petr Petyovský
Department of Control and Instrumentation
FEEC Brno University of Technology
Brno, Czech Republic
petyovsky@vut.cz

Abstract—This paper deals with the design and implementation of software solutions for the acquisition and visualization of data from industrial production. The first part focuses on data collection. This part is implemented on a machine designed to manufacture automobile stabilizer bars, controlled by the TwinCAT 2 system. The following section describes an application developed using the Python programming language. This application allows the user to upload the collected data to a SQLite database, from where it is then queried for visualization purposes.

Index Terms—PLC, automotive, industrial production data, data visualization, TwinCAT 2, Python, SQLite

I. Introduction

Industrial production is one of the key areas of modern engineering where effective data management and analysis are becoming an essential element for optimizing manufacturing processes. With the development of Industry 4.0, there is an increasing demand for sophisticated systems for the acquisition, storage and interpretation of manufacturing data. These systems not only allow data to be stored for later analysis, but also to be used immediately for decision-making processes, which contributes to production efficiency and stability. In addition, effective data management contributes to reducing production costs, optimizing inventory and increasing overall productivity.

This work focuses on the design and implementation of a software solution for data storing, visualization and management in an industrial production company Mubea s.r.o., which specializes, among other things, in the production of stabilization bars for the automotive industry. Due to the increasing requirements for monitoring production quality and reducing the occurrence of defective products, the development of an efficient data analysis system became necessary. The new solution is designed to ensure not only data collection but also data evaluation, enabling a response to emerging deviations and the prediction of potential problems in production.

The aim of this project was to extend the existing software system with functions enabling long-term storage and analysis of production data. The newly developed tools do not only focus on data collection, but mainly on data visualization in order to optimize decision-making processes within industrial production. At the same time, the system must be flexible and scalable to enable its use in different plants and production processes.

II. New data storage tool

For this project, Mubea selected one of the assembly machines with a lower form of data storage. The previous implementation of data acquisition on this machine used variable storage with data visualization on the machine's touch screen control panel.

This approach had limitations as the data were not stored for long term. Once the product left the assembly line, the associated information was lost. This problem is solved by an add-on for the existing program, which until now has mainly handled automatic and manual machine operation and communication with the user via the HMI touch panel.

The new add-on provides automated acquisition of all assembly data. This means the storage of production (individual piece data) and parametric (set production limits, user interaction, parameter change timestamps) data. Data acquisition is handled by creating two new function blocks storing the mentioned types of data. These blocks handle the actual creation of records and their subsequent saving to CSV files. This file format was chosen mainly because of its high usage in Mubea's production.

As the TwinCAT 2 system runs on an industrial PC (IPC) with a software PLC, it has access to the Windows operating system file system. This allows, using basic file management function blocks, to create a directory structure on the IPC disk in the form C:\Production_data\Year_2025\Month_9\ident_1234.csv, where the file name contains the order number. [1]

File transfer to a regular PC for visualization is currently handled manually using a flash drive or by connecting to the IPC using remote desktop software.

The main elements of the new solution are:

- Structured data archiving in CSV format, which includes both production and parametric data. Thanks to the standardized format, data can be easily exported and shared between different systems.
- Hierarchical directory structure that organizes records by year, month and individual orders. This ensures efficient sorting and easy traceability of required data.

A significant advantage of the new approach is the ability to aggregate and retrospectively analyze historical data, which enables a better understanding of production processes and prediction of potential failure conditions. This approach con-
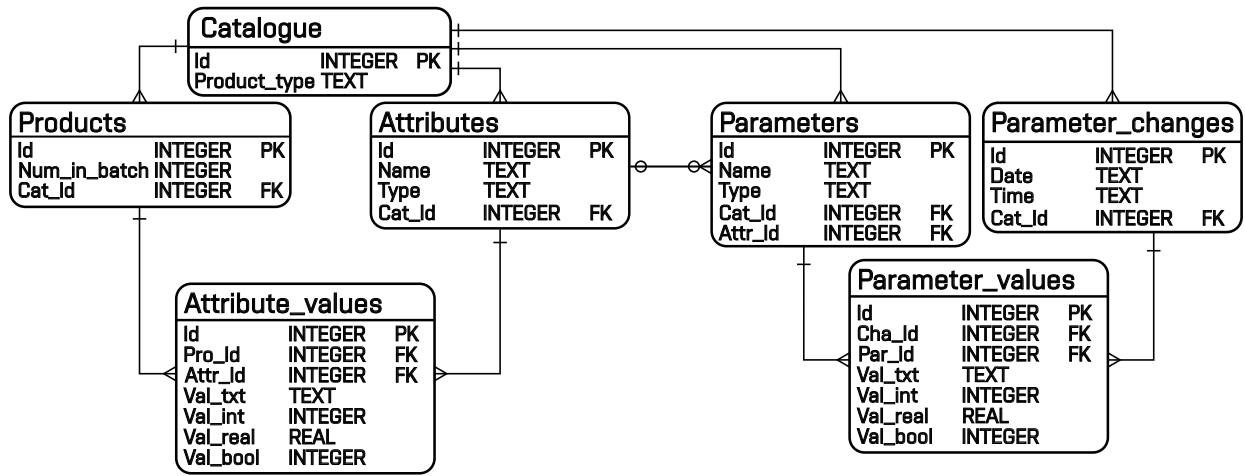
Fig. 1. ER-diagram of the used data model

tributes to the overall strategy of continuous improvement of production, which is key to the competitiveness of manufacturing companies today.

III. DESKTOP APPLICATION FOR DATA VISUALIZATION AND ANALYSIS

To ensure efficient work with the collected data, a desktop application was designed and implemented using Python and its libraries Tkinter, Ttkbootstrap, Matplotlib, Pandas and SQLite3. This application is divided into a data handling part and a user interface. [2] [3] [4] [5] [6]

A. Implementation of data handling

The beginning of the visualization process is the uploading of the data. The actual parsing of the CSV file is done by the read_csv function of the Pandas library. It creates a DataFrame object from the file, which is suitable for representing tabular data. However, using this object to store data from multiple files brings difficulties, mostly if the files are differently formatted. Another difficulty is searching through multiple DataFrame objects at once. [2]

The mentioned problems are solved using SQLite database, whose designed data model is presented in Fig. 1. The read_csv function is used only to facilitate parsing of the CSV files themselves. Data from the created DataFrame object are inserted into the corresponding database tables using the SQLite3 library functions.

The use of SQLite database increases the speed of data retrieval for visualization, this further accelerates the entire process of quality inspection of manufactured products. Another advantage of using a database system to work with data in the background of the application is the creation of a universal data format that the application will work with. It will also simplify working with data from several orders at the same time.

In order to create a uniform format of the data to be uploaded to the database, it is necessary to ensure a certain level of configuration and versatility when loading individual

CSV files. In the current version, configuration in terms of setting the separator type or setting the line on which the file header is located is left to the user. The versatility of loading files of different sizes, either in terms of columns or rows, is implicitly provided by the read_csv function. [7]

The only requirements for the uploaded file are the columns with dates and production times of each product. The date column must be in the format mm/dd/yyyy or yyyy-mm-dd. For the time column, the format hh:mm:ss is required. The padding of the digits indicating months, days, hours, minutes and seconds with zeros from the left-hand side is not required.

B. User interface

The user interface is implemented using the Tkinter, Ttkbootstrap and Matplotlib libraries. This interface gives the user the possibility to upload production data files.

Fig. 2. User interface for uploading files

Its main purpose is to simplify the process of production quality inspection.

For this purpose, two forms of visualization are used:

- Detailed view - Display of individual product data in a dashboard with the possibility of manual annotation. This

view is designed for quick quality checks of individual products and allows visualization of production data values between their limits. All products are displayed in the form of a list.
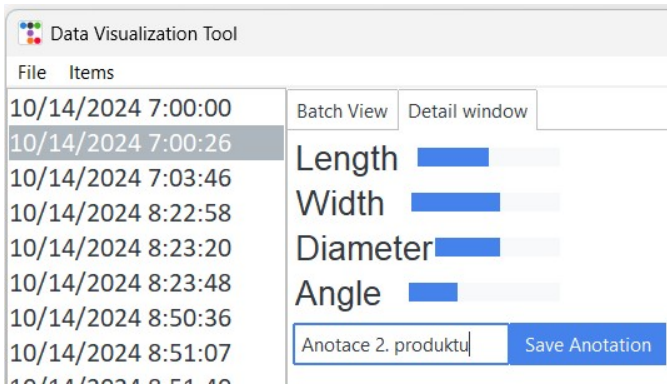
Fig. 3. User interface for detailed view

- Order analysis - Interactive graphs tracking the development of production data within a single order. Users can analyze trends to identify production anomalies.
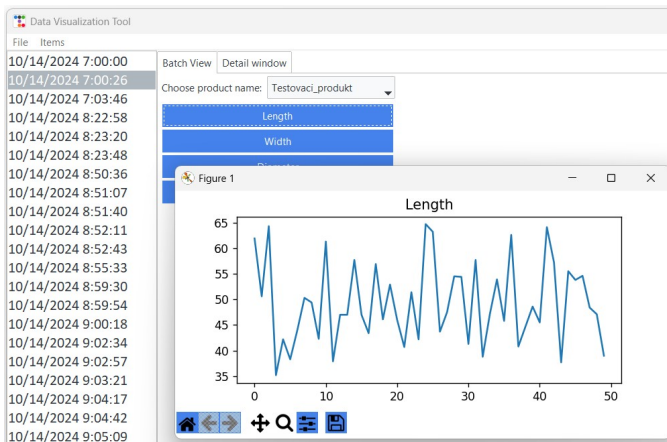
Fig. 4. User interface for order analysis

These two types of data analysis form a presentation layer over the data stored in the database, created in the background of the application when a file is uploaded.

IV. SUMMARY AND FURTHER DEVELOPMENT

The proposed system is a step towards modernizing production data management, providing tools for storage, visualization and analysis. Thanks to the implementation of a database solution, it provides the possibility of working with large volumes of data. In addition, the requirement should arise in the future to convert these data into a new format, the use of a standardized database system always offers the possibility of efficient data migration.

Further development of the system will include:

- Completion of parametric data display implementation.

- Addition of a filtering option to the list for browsing individual pieces.
- Automated generation of reports that can be set to be generated at regular intervals or on demand. Reports include key production quality indicators and summaries of the most common deviations.

REFERENCES

[1] *File Function Blocks*. Online. Beckhoff. 2025. Available: https://infosys.beckhoff.com/english.php?content=.. /content/1033/tcplclibsystem/11827857291.html\&id= 4043060612005427738. [cit. 2025-03-15].

[2] MCKINNEY, Wes. *Python for Data Analysis Data Wrangling with pandas, NumPy & Jupyter*. Third edition. O'Reilly, 2022. ISBN 978-1-098-10403-0.

[3] *tkinter — Python interface to Tcl/Tk*. Online. Python. 2025. Available: https://docs.python.org/3/library/tkinter.html. [cit. 2025-03-15].

[4] *ttkbootstrap*. Online. ttkbootstrap. 2025. Available: https: //ttkbootstrap.readthedocs.io/en/latest/. [cit. 2025-03-15].

[5] *Matplotlib: Visualization with Python*. Online. Matplotlib. 2025. Available: https://matplotlib.org/. [cit. 2025-03-15].

[6] *sqlite3 — DB-API 2.0 interface for SQLite databases*. Online. Python. 2025. Available: https://docs.python.org/3/library/sqlite3.html. [cit. 2025-03-15].

[7] *pandas.read_csv*. Online. Pandas. 2025. Available: https://pandas. pydata.org/docs/reference/api/pandas.read_csv.html. [cit. 2025-03-15].

—

Možná hledáme právě Tebe!

Nabídkový specialista
• Příprava nabídek v oblasti přístrojů nízkého napětí a zpracování cenových kalkulací. Návrh optimálního technického řešení pro zákazníky a aktivní účast na technických a obchodních jednáních.

R&D Simulační inženýr – brigáda
• Podpora designerů na lokálních i mezinárodních projektech vývoje plynem izolovaných rozvaděčů VN. 3D modelování v SolidWorks a SpaceClaim, příprava modelů pro simulace v ANSYS Workbench.

PLC programátor – námořní průmysl
• Vývoj PLC softwaru pro lodní automatizaci, testování a ladění systémů na palubě i v největších přístavech světa – Karibik, Jižní Amerika, Střední východ.

Projektový inženýr elektro – dlouhodobá stáž/brigáda
• Inženýrská činnost v oblasti elektro dodávek na zahraničních projektech. Možnost podílet se na inovativních technologiích, například projektu „Jansz-Io" – těžba zemního plynu s nižší uhlíkovou stopou.

Specialista řízení rozvaděčů
• Konfigurování ovládacích a ochranných terminálů v rozvaděčích VN a odzkoušení jejich správné funkčnosti

Area Sales Manager
• Zodpovědnost za prodej a koordinaci na zahraničních trzích. Péče o zákazníky a vyhledávání nových obchodních příležitostí.

Autonomous precision landing of unmanned aerial vehicles using fiducial optical markers

1st Jakub Prvý
Dept. of Control and Instrumentation
Brno University of Technology
Brno, Czech Republic
247060@vutbr.cz

2nd Jan Klouda
Dept. of Theoretical and Experimental Electrical Engineering
Brno University of Technology
Brno, Czech Republic
xkloud04@vutbr.cz

Abstract— **This paper deals with the design and implementation of a system for autonomous landing of an unmanned aircraft using image recognition technology. The main objective is to use ArUco markers as visual reference points that allow accurate localization and navigation during the landing process. A key part of the work is the integration of the OpenCV library for marker detection and image analysis with the ArduPilot platform, which provides flight control.**

Keywords—landing, ArUco, Python, MAVLink, unmanned aircraft, autonomous

I. INTRODUCTION

Drones are increasingly becoming a normal part of our lives, finding applications in cinematography, transport, logistics, reconnaissance and rescue operations. Unmanned aerial vehicles, also known as drones, play a key role in these fields due to their ability to perform complex tasks with minimal human intervention. Recently, there has been a great emphasis on fully autonomous operation of drones due to the use of large numbers that would be impossible to ensure safe and efficient flight using human pilots alone. For landing, one of the most critical features is landing accuracy and reliability.

The objective of this paper is to design, implement and debug a system for autonomous landing of an unmanned aircraft using image recognition technology. For this purpose, ArUco markers will be used as visual reference points for easy implementation of the recognition software. These markers will be recognized and processed using the OpenCV library for Python. The system will be implemented using the MAVLink communication protocol and the ArduPilot autopilot software suite, allowing fast and efficient communication between the recognition software and the controller.

II. TYPES OF LANDING

Safe landing is important for the operation of unmanned aircraft. It is divided into manual and autonomous landing. For manual landing, the knowledge and experience of the pilot is important and determines how fast or accurately the aircraft will land. Manual landing cannot be replicated due to the effect of human error in control. Autonomous landing, on the other hand, is controlled purely by the autopilot control unit. In this method, parameters such as landing speed, accuracy, etc. can be precisely defined.

A. GNSS based landing

Global Navigation Satellite Systems (GNSS) are systems that can provide coverage of the Earth's surface with navigation signals with a limited number of radio beacons, allowing positioning anywhere on Earth. The main advantage of these systems is that they can determine position in a single coordinate system, anywhere on Earth, regardless of the time of day or weather [1].

1) Standard GNSS: Ground-based receivers, such as the sensors in your phone, pick up signals from satellites orbiting the Earth. The signal carries information about the satellite's position and the time it was sent. Based on the time delay between when a signal is sent from a satellite and when it is received, the receiver can determine its distance from each satellite. It uses a method called trilateration, where the position is calculated as the intersection of spheres around the satellites, each representing the receiver's distance from that satellite. A minimum of three satellites are needed to determine a two-dimensional position (latitude and longitude), four for a three-dimensional position (including altitude) [2]. This method achieves accuracy of a few meters, which is not suitable for precision landing.

2) Differential GNSS (DGNSS): Differential GNSS (DGPS) is a method of improving the accuracy of standard GNSS by using correction signals from a reference station. In conventional GNSS, the receiver calculates its position based on time-delay signals from satellites, but these signals can be affected by various errors such as atmospheric interference, reflections or clock inaccuracies. DGNSS minimizes these errors by using a reference station with an accurately known position [3]. This method is suitable for use in autonomous landing in smaller areas.

3) Real-Time Kinematic (RTK) GNSS: RTK (Real-Time Kinematic) is a high-precision positioning method that uses the differences between signals from GNSS satellites (e.g. GPS) and the phase shift of their carrier wave. Unlike conventional GNSS, which is capable of determining position within meters, RTK can determine position to within centimeters, making it a key technology for applications requiring extreme accuracy, such as autonomous driving, surveying, or agriculture. A reference station, located at a precisely known position, plays a

vital role in the RTK system, receiving signals from satellites, analyzing them, and calculating errors based on known positions and phase shift of the carrier wave. It then transmits this correction information in real time to mobile GNSS receivers in range, which can then determine their position more accurately, even while moving [4].

B. Inertial navigation landing

Inertial navigation landing uses sensors that measure changes in the motion and orientation of the aircraft (or UAV) without the need for external reference points such as GPS or visual markers. The inertial navigation system consists of gyroscopes and accelerometers that continuously sense rotations and accelerations in all axes. Based on this data, the inertial navigation system calculates changes in the aircraft's speed, position and orientation from its starting point.

C. Camera-assisted landing

Camera-assisted landing allows unmanned aerial vehicles (UAVs) and drones to accurately navigate to a landing site using image analysis. The camera scans the environment in front of or below the aircraft, with the software targeting specific visual features or markers (such as ArUco tags or other optical markers) to estimate position and movement relative to the landing pad.

1) Optical marker landing: Optical marker landing is a technique used to land unmanned aerial vehicles (UAVs) accurately and reliably. The principle of this method is the use of special visual markers that are placed on the landing area and serve as a visual reference [5]. The tags, such as ArUco tags, have specific patterns that are easily detectable by camera systems and allow for accurate positioning of the UAV relative to the landing pad.

2) Computer vision and machine learning: Computer vision and machine learning allow the UAV to autonomously identify the landing area and obstacles in real time. Using a camera, the UAV captures an image of the environment and computer vision algorithms analyze the image to identify patterns, shapes or colors that correspond to the landing zone. This is often done by trained machine learning models that learn to recognize the distinctive features of the landing area from the vast amount of image data [6]. As a result, the UAV can accurately identify the location and dimensions of the landing area even in environments with varying background or lighting conditions.

III. MARKER DETECTION

Position estimation is very important in many computer vision applications: robot navigation, augmented reality, etc. This process is based on finding connections between the real environment and the two-dimensional image projection. This step is usually challenging, and therefore the use of artificial optical reference markers is common.

One of the most used techniques is the use of binary square reference markers. Their main advantage is that one marker contains enough points to learn the camera position (4 corners).

Another advantage is the binary encoding of the information inside the marker, this allows error detection and correction.

A. OpenCV

OpenCV is a popular open-source library for image processing and computer vision. It was developed to provide powerful and efficient tools for image analysis, object detection, pattern recognition and machine vision [7].

B. ArUco tags

ArUco tags are special black and white square markers used in computer vision for identification and localization of objects in space.

One of the main advantages is the quick recognition of the marker in the image thanks to the external frame. Inside this frame, the unique identifier and error correction data are encoded in a binary matrix. Due to the square shape, we can determine exactly where the marker is in space from the known marker size and the 4 corners.

The detection itself takes place in the following steps. *Initialization:* The OpenCV library uses dictionaries to distinguish marker types for ArUco marker detection. They can range in size from 4x4 to 7x7 and can contain different sets of unique identifiers. If we choose a dictionary with a larger number of identifiers. *Detection:* ArUco tags can be detected using the detector function. The detector then returns information about the identifier, the corners of the marker, and the incorrectly detected part of the marker [8]. Figure 1 shows detected marker inside green square labeled with ID number of the tag. The red square in the corner of marker is first corner of the tag. With this information we can determine the rotation of the marker.

OpenCV offers a function to calculate a perspective transformation that can determine the exact position of the marker in the image, i.e. relative to the drone. The function needs to know the camera matrix, which stores the outer and inner parameters of the matrix, as well as the distortion coefficients that allow the correction of image distortions caused by light passing through the optical system. The return values of the function are the X,Y and Z coordinates of the marker relative to the camera [9].
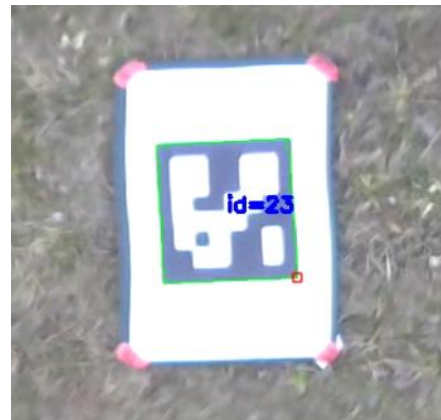

Fig. 1. Detected marker from drone camera

IV. Precision landing

A. MAVLink

MAVLink is a communication protocol used in robotic systems and unmanned aerial vehicles. It is used in these areas because of its low latency, cost-effectiveness and reliability. Compared to standard types of transmissions such as AM/FM signals or PPM, MAVLink provides bi-directional and efficient data exchange.

MAVLink transmits data in the form of short messages that contain information about the drone's status, its telemetry or navigation commands. Each message contains a voice message identifying the message type, a destination ID, and a checksum to ensure data integrity [10].

This protocol includes a message that conveys information about the location of the landing target. The message type is called LANDING_TARGET and carries all the necessary information for accurate landing. The message contains information about the time stamp, target ID, vehicle reference frame type, distance from the ground, landing target type and X,Y and Z coordinates.

B. ArduPilot

ArduPilot is open-source autopilot software that has become one of the most popular systems for controlling drones, robots and other autonomous vehicles. ArduPilot uses the MAVLink protocol for communication, which enables data transfer between the autopilot and the ground station, providing reliable control and monitoring of autonomous operations [11].

For precise landing, it is necessary to set the parameters in the PLND_ group in ArduPilot. After activating the PLND_ENABLE parameter, other parameters for landing are displayed. The most important thing is to set PLND_EST_TYPE to 0, otherwise the landing process is very unstable and unsuccessful. Next, set the PLND_TYPE parameter to 1, i.e. landing using the MAVLink protocol information [12].

Detection and calculation of the landing target position are performed on a computer mounted on the drone body. All processing of the target position information is done in a Python script. The position of the target is transmitted via a MAVLink message to the autopilot in the drone's control unit. The actual guidance and landing process is handled in the control unit. The ArduPilot implementation supports precision landing only when assisted with GPS, for safety reasons. If the target were to be visually lost and GPS was not present the drone could behave erratically.

V. Testing

Testing was carried out on a Holybro X500 V2 drone with Pixhawk flight controller. The computer used was an Intel NUC with a Logitech C290 webcam.

For testing purposes, manually flying over the target is sufficient. Once the algorithm detects it, it starts sending messages about its location. In Mission Planner, a message will appear indicating that the target has been successfully detected. At this point, just switch the drone to LAND mode. Autonomous landing will begin and the drone will begin to descend. If the target is lost from the camera's view, it will fly higher and try to reacquire the target. If it fails to re-find it, it will land vertically at the current location.

Depending on GPS accuracy and properly set parameters, the drone can achieve landing accuracy from 5 to 15 centimeters from the target.

Fig. 2. Landing attempt accuracy

VI. Conclusion

Based on testing, we can say that the system is accurate enough for landing in tight spaces or small landing areas. One potential refinement is to use multiple ArUco tags of different sizes, where the program can switch between them dynamically based on altitude.

The disadvantage of this system is that it only works in good light conditions due to visibility. Usability may be limited even in fog. Future improvements could focus on enhancing robustness by integrating additional sensor inputs or developing more advanced image-processing techniques to mitigate these challenges.

REFERENCES

[1] P. Rapant, "Družicové polohové systémy", Publikace, Institut ekonomiky a systémů řízení, 2002.

[2] P. J. G. Teunissen and O. Montenbruck, *Springer Handbook of Global Navigation Satellite Systems*. Springer, 2017.

[3] A. Delépaut, A. Minetto, and F. Dovis, "Code-Based Differential GNSS Ranging for Lunar Orbiters: Theoretical Review and Application to the NaviMoon Observables", *Remote Sensing*, vol. 16, no. 15, p. 28, 2024.

[4] "Performance Evaluation of the RTK-GNSS Navigating under Different Landscape", p. 5.

[5] Q. Huang, J. DeGol, V. Fragoso, S. Sinha, and J. Leonard, *Optimizing Fiducial Marker Placement for Improved Visual Localization*. 2022/11/02.

[6] B. Ali and R. Sadekov, "A Review of Navigation Algorithms for Unmanned Aerial Vehicles Based on Computer Vision Systems", *Gyroscopy and Navigation*, vol. 30, pp. 87–105, 2023/01/30.

[7] "About", *OpenCV*, 02025.

[8] "Detection of ArUco Markers", *OpenCV*, 02024. .

[9] "Perspective-n-Point (PnP) pose computation", *OpenCV*, 02024..

[10] "Mavlink Basics", *ArduPilot*, 02024..

[11] "ArduPilot Documentation", *ArduPilot*, 02024..

[12] "Precision Landing and Loiter", *ArduPilot*, 02024. .

Implementation of Launch Control on Formula Student monopost

1st Jakub Mahdal

Department of Control and Instrumentation
Brno University of Technology
Brno, Czechia
Jakub.Mahdal1@vutbr.cz

Abstract—This paper deals with the design and implementation of the Launch Control algorithm(Wheel slip control), which is specifically designed for the best possible vehicle acceleration. The algorithm controls the torque applied to each wheel based on the angular velocity of the wheel and the velocity of the vehicle, allowing traction to be optimized for the best acceleration. The algorithm can automatically adapt to changing road conditions and characteristics, ensuring that even in adverse conditions, the best acceleration is achieved. The functionality of the model and design of the algorithm is presented through simulations in the Matlab Simulink environment.

Index Terms—Launch Control, Control system, Formula Student, Vehicle Dynamics, Matlab Simulink, Slip Ratio

I. INTRODUCTION

Formula Student is a motorsport event where teams from universities from all around the world design, build, and race one-seated cars. Each event is divided into different disciplines. One of those disciplines is acceleration. In this discipline, cars accelerate on a straight track of length 75 meters, and the best time wins. In this context, there is a demand for the design of an algorithm for the best acceleration, Launch Control. In the last years, this algorithm was implemented in the car, but with no consideration of load transfer and longitudinal tyre force. The core challenge addressed in this paper is to design a new improved algorithm for Launch Control with consideration of load transfer and longitudinal tyre force.

II. PRINCIPLE OF LAUNCH CONTROL

Launch Control is a term used in motorsport which represents an algorithm for the best acceleration. To achieve the best acceleration by controlling the slip of the tyre. The variable that represents how much your tyre slips is called slip ratio σ_x and it's defined as

$$\sigma_x = 1 - \frac{v}{\omega r_{eff}}. \tag{1}$$

Where:
- v ... Velocity of the vehicle [m/s]
- ω ... Angular velocity of the wheel [rad/s]
- r_{eff} ... Effective radius of the tyre [m]

Usually, slip ratio is represented in %. Next, the important variable is longitudinal tyre force F_x, this force is defined as the friction force from the ground that acts on the tyre [1]. This force is defined as

$$F_x = D_x \sin[C_x \arctan(B_x\sigma_x - E_x(B_x\sigma_x - \arctan(B_x\sigma_x)))] + S_v. \tag{2}$$

Where:
- C_x ... Shape constant for simple slip [-]
- D_x ... Amplitude for simple slip [N]
- E_x ... Curvature constant for simple slip [-]
- S_v ... Sliding in vertical direction for simple sliding [N]

Each of these variables consists of many other variables and they aren't constant, they vary with normal tyre load F_z, camber of the tyre γ, and other parameters [2]. The plot of longitudinal tyre force F_x as a function of slip ratio σ_x and for constant normal tyre load F_z, from equation (2), is in figure 1.
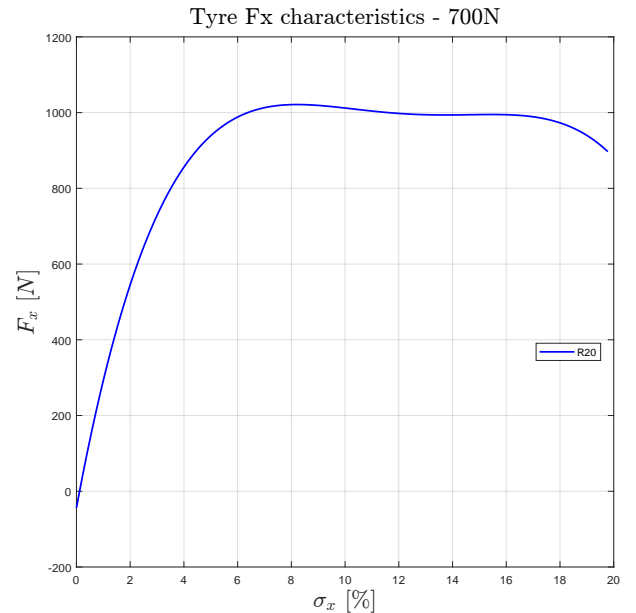
Fig. 1. Graph of $F_x = f(\sigma_x, F_z)$

Hoosier R20, in figure 1, is the name of the tyre and its compound that is being used in Formula Student [3]. The best acceleration is achieved when the highest possible F_x

is transferred to the road. In the figure 1 the highest possible F_x is around 8 - 10%. Our goal for controller design is to achieve a slip ratio σ_x value of around 8 - 10%.

III. MATHEMATICAL MODEL OF THE VEHICLE

Our inputs to the model are torques that drive the rear wheels. Those torques are described as

$$T_{Mi} = G_R \cdot c_\phi \cdot I_{com}, \tag{3}$$

where:

- T_{Mi} ... Torque generated by the motor that drives wheel [Nm]
- c_ϕ ... Motor constant [Nm/A]
- I_{com} ... Current command from vehicle control unit [A]
- G_R ... Gear ratio of transmission [-]

Index i describes: $i = RL, RR$ as for Rear Left and Rear Right wheel. Next are our model states, which are slip ratios σ_{xi} of both rear wheels, angular velocities of both rear wheels ω_i, and the velocity of the vehicle v. Slip ratio σ_{xi} is defined as

$$\dot{\sigma}_{xi} = \frac{(\dot{w}_i \cdot r_{eff} - \dot{v})w_i \cdot r_{eff} - \dot{w}_i \cdot r_{eff}(w_i \cdot r_{eff} - v)}{(\omega_i \cdot r_{eff})^2}, \tag{4}$$

where:

- $\dot{w}_i$ ... angular acceleration [rad/s^2]
- $\dot{v}$ ... acceleration of the vehicle [m/s^2]

Angular velocity for rear wheel ω_i is defined as

$$\dot{\omega}_i = \frac{1}{J_W} \cdot (T_{Mi} - r_{eff} \cdot F_{xi}), \tag{5}$$

where:

- J_W ... Moment of inertia [kg m^2]

For vehicle velocity v the equation is defined as

$$\dot{v} = \frac{1}{m} \cdot \left(\frac{T_{MRL} + T_{MRR}}{r_{eff}} - F_{aero} - F_z \cdot C_R \right), \tag{6}$$

where:

- m ... Mass of the vehicle with driver [kg]
- F_{aero} ... Aerodynamic drag force [N]
- F_z ... Normal tyre load [N]
- C_R ... Rolling resistance coefficient [-]

F_{aero} and F_z are calculated in the model [1].

IV. VALIDATION OF THE MATHEMATICAL MODEL

Validation of the mathematical model ensures that the model accurately represents the real system. The next table describes the values of the mathematical model. Those values were retrieved from the TU Brno Racing team.

TABLE I
VALUES OF PARAMETERS FOR THE MATHEMATICAL MODEL

Variable	Unit
c_ϕ	0.492 Nm/A
J_W	0.126 kgm^2
G_R	12
r_{eff}	0.181 m
m	240 kg
C_R	0.01

The model scheme that was validated is shown in the next figure 2.
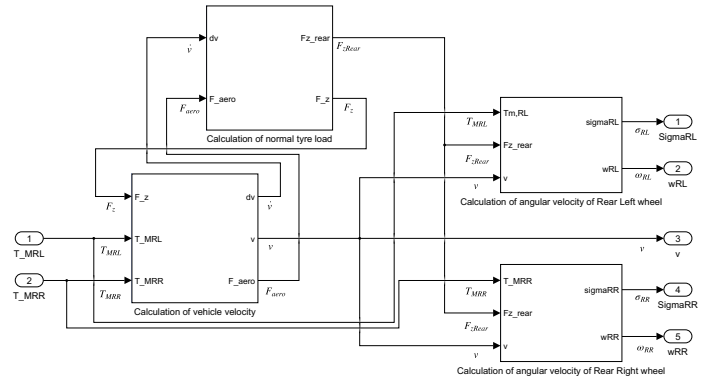
Fig. 2. Validation scheme for model of the vehicle

Next figure 3 shows input torques to the mathematical model. Torques were calculated from equation (3) with measured current I_{com} from the last season's race of the TU Brno racing monopost eD4. These torque values are before multiplication by parameter G_R.
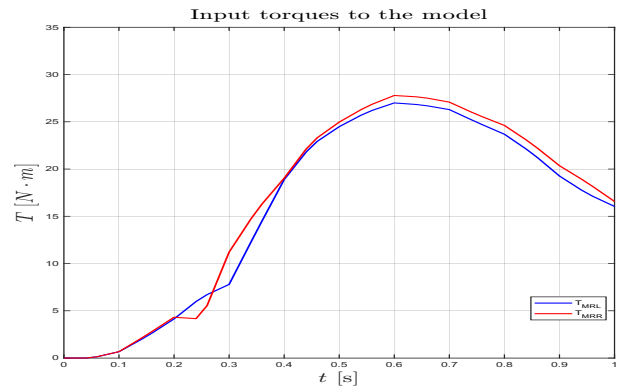
Fig. 3. Input torques to the model

Validation of vehicle velocity is shown in the next figure 4 for data from last season's race of the TU Brno racing

monopost ED4.
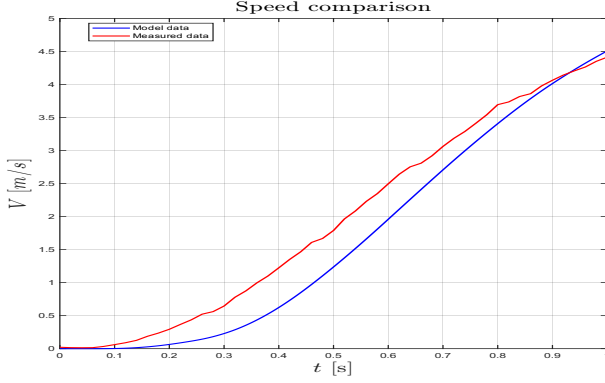
Fig. 4. Validation for vehicle velocity

From figure 4, the model data integrates slower than the measured data. Validation of wheel velocity of the rear left tyre is shown in the next figure 5 for data from last season's race of the TU Brno racing monopost ED4.
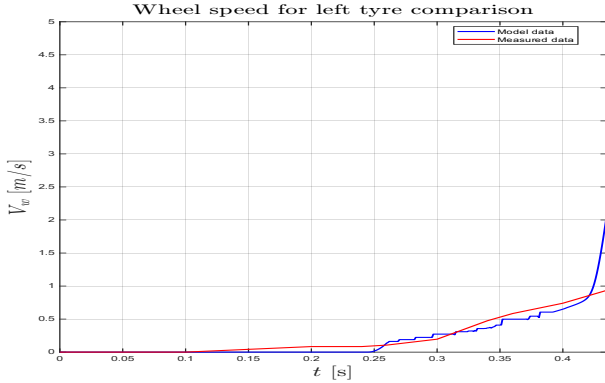
Fig. 5. Validation of wheel velocity of the rear left tyre

Difference in measured and modelled plots from figure 5 is due to the fact that r_{eff} is set as constant, but it changes with normal tyre load by 10-15%. The model also doesn't include longitudinal tyre force for front tyres that don't drive the vehicle. Especially in plot 5, model data copies measured data till 0.43 seconds, when the modelled wheel velocity becomes bigger than measured data.

V. STATE-SPACE MODEL

State-space model is a mathematical representation of a dynamic system that describes how its internal state evolves over time. State-space model of our model, as was said in chapter III, will have 5 states ω_{RL}, ω_{RR}, σ_{xRL}, σ_{xRR} and v. Let the state model of the system be of the form

$$\dot{x} = Ax + Bu \tag{7}$$

$$y = Cx + Du. \tag{8}$$

where x represents states of the model, u represents inputs of the model, and y represents outputs of the model. For our model matrices A, B, C and D are

$$A = \begin{bmatrix} 0 & 0 & A_1 & 0 & A_3 \\ 0 & 0 & 0 & A_2 & A_4 \\ 0 & 0 & 0 & 0 & 0 \\ 0 & 0 & 0 & 0 & 0 \\ 0 & 0 & 0 & 0 & -0.00415v \end{bmatrix} \tag{9}$$

$$B = \begin{bmatrix} \frac{496.8v - 1.35w_{RR}}{w_{RR}^2} & \frac{-1.35}{w_{RL}} \\ \frac{-1.35}{w_{RL}} & \frac{496.8v - 1.35w_{RL}}{w_{RL}^2} \\ 95.5 & 0 \\ 0 & 95.5 \\ 0.26 & 0.26 \end{bmatrix} \tag{10}$$

$$C = \begin{bmatrix} 1 & 0 & 0 & 0 & 0 \\ 0 & 1 & 0 & 0 & 0 \\ 0 & 0 & 1 & 0 & 0 \\ 0 & 0 & 0 & 1 & 0 \\ 0 & 0 & 0 & 0 & 1 \end{bmatrix} \tag{11}$$

$$D = 0. \tag{12}$$

Where
- $A_1 = \frac{15.9vF_{xRR} + 993T_{RR}w_{RR} + 1.35T_{RL}w_{RR} - 0.01v^2w_{RR}}{w_{RR}^3}$
- $A_2 = \frac{15.9vF_{xRL} + 993T_{RL}w_{RL} + 1.35T_{RR}w_{RL} - 0.01v^2w_{RL}}{w_{RL}^3}$
- $A_3 = \frac{496.8T_{RR} - 7.965F_{xRR} + 0.021Vw_{RR}}{w_{RR}^2}$
- $A_4 = \frac{496.8T_{RL} - 7.965F_{xRL} + 0.021Vw_{RL}}{w_{RL}^2}$

Transfer functions are retrieved from the following equation [4]

$$G = C(sI - A)^{-1}B + D. \tag{13}$$

The transfer functions that will be used in controller design are $G[1,1]$ and $G[2,2]$, because $G_{11}(s) = \frac{\sigma_{RR}(s)}{T_{RR}(s)}$ and $G_{22}(s) = \frac{\sigma_{RR}(s)}{T_{RR}(s)}$. For $G_{11}(s)$, the transfer function is defined as

$$G_{sRR}(s) = G_{11}(s) = \frac{s^2 \cdot S_{RR2} + s \cdot S_{RR1} + S_{RR0}}{s^2 \cdot w_{RR}^3 \cdot (s + 0.00415v)}. \tag{14}$$

For $G_{22}(s)$, the transfer function is defined as

$$G_{sRL}(s) = G_{22}(s) = \frac{s^2 \cdot S_{RL2} + s \cdot S_{RL1} + S_{RL0}}{s^2 \cdot w_{RR}^3 \cdot (s + 0.00415v)}. \tag{15}$$

Where:
- $S_{RR0} = -0.2021vw_{RR} + 6.30157F_{xRR}v^2$
- $S_{RR1} = 2.06172v^2w_{RR} + 12.8229T_{RL}w_{RR}$
- $S_{RR2} = 496.800v \cdot w_{RR} - 1.350w_{RR}^2$
- $S_{RL0} = -0.20213vw_{RL} + 6.30157F_{xRL}v^2$
- $S_{RL1} = 2.06172v^2w_{RL} + 12.8229T_{RR}w_{RR}$
- $S_{RL2} = 496.800v \cdot w_{RL} - 1.350w_{RL}^2$

Our system is a 3rd order with a double integrator, and the pole is determined by the velocity of the car. For the calculation of the F_x, the look-up table (LUT) is being used. Velocity of the vehicle v and angular velocities of ω_i will be measured through sensors of the vehicle.

VI. Algorithm structure and compensator design

The limit of the torque of both motors is set to $T_{MAX} = 348$ Nm for each motor. The maximum difference between torques ΔT_M is also set. This limitation is due to the safety of the driver. If the controller sent commands, which were $T_{MRL} >> T_{MRR}$ or $T_{MRR} >> T_{MRL}$, this would result in the car turning right or left on a straight line. The value of this limit is set to ΔT_M = 25 Nm. This value can be changed by small amounts to suit different drivers. To prevent any hazardous states of σ_{xi}, which can happen when $\omega_i = 0$. This can happen in 2 scenarios:

1) $\omega_i = 0$ and $v = 0$, then $\sigma_{xi} = 0$
2) $\omega_i = 0$ and $v > 0$, then $\sigma_{xi} = 1 - \frac{v}{\omega_i r_{eff} + 0.01v}$

Second scenario can happen only during braking, but this case in code is implemented as an edge case.

To regulate slip ratios of both rear wheels, a PI controller is employed for each wheel. The parameters of the PI controller, including the time constant T_i and gain K. T_i is adjusted as functions of v to compensate for the specified pole of transfer functions. The controller design is described by equation(16).

$$G_{Ri}(s) = \frac{K \cdot (T_i s + 1)}{T_i s} \qquad (16)$$

$$T_i = \frac{1}{0.00415v}. \qquad (17)$$

Static gain of the controller is chosen through optimizing the value of the quadratic integral criterion [5]

$$J_K = \int_0^\infty e(t)^2 \, dt. \qquad (18)$$

The flowchart of the design for the algorithm is in the next figure 6
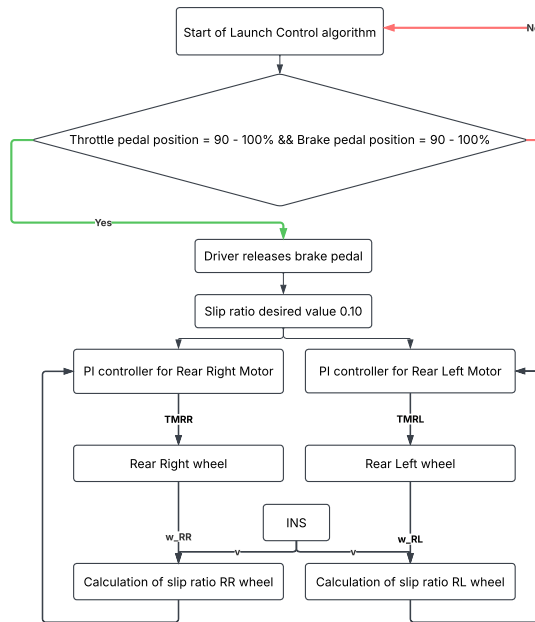
In figure 6 the INS stands for Inertial Navigation System, which measures the velocity of the vehicle v.

VII. Conclusion

Algorithm for Launch Control adeptly utilizes the tyre longitudinal force F_x as LUT due to the challenging calculation of this force. Calculations of each state through the mathematical model are successfully validated through Simulink simulation of the Launch Control and set safety features of the algorithm-designated controller. The next steps are simulation via Simulink with the help of IPG Carmaker software. IPG Carmaker software is used for the development of its own tracks and driver parametrization, with the implemented Formula Student model of the vehicle. The last step is the implementation of this algorithm to the physical car, which is one of the goals for the season 2025 of team TU BRNO Racing.

Further improvements of this algorithm are in implementing full traction control for other disciplines, not for only acceleration.

References

[1] RAJAMANI, Rajesh. Vehicle dynamics and control. Second edition. New York: Springer, [2012]. Mechanical engineering series. ISBN 978-1-4614-1433-9. Dostupné také z: https://ebookcentral.proquest.com/lib/techlib-ebooks/detail.action?docID=884257

[2] PACEJKA, Hans B. Tyre and vehicle dynamics. 2nd ed. Amsterdam: Elsevier/BH, 2006. ISBN 978-0-08-054333-8. Dostupné také z: https://ebookcentral.proquest.com/lib/natl-ebooks/detail.action?docID=311410

[3] Hoosier Racing Tire [online]. 2024 [cit. 2025-02-24]. Dostupné z: https://hoosiertiregp.com/16-0x6-0-10-r20/

[4] ŠOLC, František a VÁCLAVEK, Pavel. Modelování a simulace. Online, Skriptum. Brno, Česká Republika: Vysoké Učení Technické v Brně, 2019. Dostupné z: https://moodle.vut.cz/pluginfile.php/436149/course/section/58330/bmod.pdf. [cit. 2025-02-25].

[5] BLAHA, Petr a VAVŘÍN, Petr. Řízení a regulace I. Online, Skripta. Brno, Česká Republika: Vysoké Učení Technické v Brně. Dostupné z: https://moodle.vut.cz/pluginfile.php/585752/course/section/68732/bpcrr1.pdf. [cit. 2025-03-09].

Fig. 6. The flowchart of the design for the Launch Control algorithm

System for Counting the Number of People in a Room

Josef Sikula
Faculty of Electrical Engineering and Communication
Brno University of Technology
Brno, Czechia
246946@vutbr.cz

Tomas Fryza
Dept. of Radio Electronics
Brno University of Technology
Brno, Czechia
fryza@vut.cz

Abstract—**In this work a system for counting number of people in a room has been designed. It is based on Time of Flight (ToF) infrared sensor VL53L7CX, which measures depth in 64 zones from top of the door. Sensor is controlled by ESP32-C6 and depth data are sent to Flutter application to visualize and process them to count number of people entering or leaving room. Based on that number of people in room is determined. Present number of people is uploaded to Google Sheets via Google Sheets API.**

Index Terms—**People counting, Time of Flight (ToF), Internet of Things (IoT), depth camera, VL53L7CX, Flutter, ESP32-C6, Google Sheets API**

I. Introduction

Knowledge of number of people in time can be used to analyse customer visit patterns in shops, implement IoT for smart buildings such as automation of lights [1], for regulating Heating, ventilation and air-conditioning (HVAC), for fulfilling COVID-19 restrictions [2], for efficient use of reserved rooms, handling crisis situations [3], for optimizing public transportation [4] [5].

Methods for detecting number of people can be divided into two main approaches – device-based and device-free methods. Device-based methods detect people according to device, which people carry with themselves. One method is based on assumption, that vast majority of people has got a smartphone with switched on Wi-Fi, so number of people is detected using counting Wi-Fi devices [3].

Device-free methods do not require any device on a person to be detected. The person is detected due to the dimension and material properties of the human body. Image-based methods process images from the camera often using a neural network [1]. RF-based methods work on the fact that someone attenuates and interacts with electromagnetic waves in radio frequency (RF) [6]. People can be detected using various sensors, for example thermophiles (detects person on the fact that the human body has a higher temperature than a temperature in a room), passive infrared (PIR) sensors (used in security systems, the PIR sensor gives information, whether or not a person is present), ultrasonic sensors (measure distance using ultrasonic waves, which propagate with known velocity, approximately 343 m/s) and IR ToF (infrared Time of Flight) sensors. The following text presents a method using time-of-flight measurement and testing for a single laboratory.

II. Design of System

Sensor VL53L7CX measures data and it is controlled by ESP32-C6 via Inter-integrated Circuit (I^{2}C) and digital pins (reset, interrupt and enable pins). Raw data are backed up on the SD card and are also sent to Flutter application (running on a smartphone or on a PC) via USB UART, where the data are processed to obtain current number of people. The number is uploaded to Google Sheets using HTTPS requests and Google Sheet API as describes in Fig. 1.
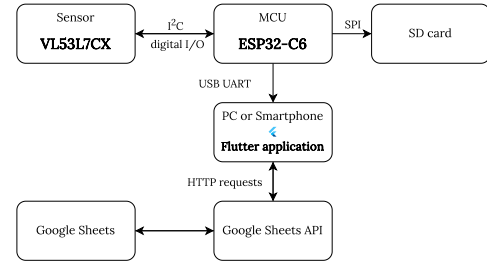
Fig. 1: Block diagram of designed system

A. Selecting sensor

From the described methods, a sensor-based method using the IR ToF sensor has been selected. It is used to detect number of people entering or exiting room via door. The sensor is placed on the top of the door to avoid occlusion problem (a taller person hides a smaller person from a view of the sensor).

The sensor works on the principle that the LASER diode emits an IR wave and is reflected from the target and is detected by the avalanche diode. The depth is counted from measured time of propagation (flight) and speed of light. The type of sensor is suitable for indoor application, because the sun emits IR waves as well and it can affect the measurement. It is simple to subtract background in contrast to image-based methods:

$$\mathbf{Z}(k) = \mathbf{Z}_{dynamic}(k) - \mathbf{Z}_{static} \qquad (1)$$

where matrix $\mathbf{Z}$ contains depth data of kth measurement and $\mathbf{Z}_{static}$ is a measurement of background.

In commercial applications IR ToF sensors have high resolution (76,800 pixels for Irma 6 [5]), so they have to process large amount of data and the sensors are expensive. The minimum resolution is two pixels to detect whether person enters or exits room. The sensor OPT3101 from Texas Instruments measures depth only in three zones, but it can measure in full sunlight 130 klx, it requires external transmitter (LED) and receiver (photodiode). 3D ToF camera based on OPT8241 and controller OPT9221 from Texas Instruments has a resolution of 320x240 pixels, ranging up to 150 Hz, it requires external transmitter (LED). The sensor VL53L7CX from STMicroelectronics with 64 pixels (8x8) resolution has been selected. It has 60°×60° Field of View (FoV), ranging up to 3.5 m and ranging frequency up to 15 Hz.

The distance s, where a person can be detected by sensor can be calculated as follows:

$$s = 2 \cdot h \cdot tg(\frac{\varphi}{2}) \tag{2}$$

where φ denotes field of view of sensor, which is at height h from floor. If a threshold is used in algorithm for detecting person, the height h is reduced by threshold.

B. Microcontroller

For controlling the sensor ESP32-C6 has been selected, because driver for the sensor needs a memory space for firmware (≈ 84 KB), that has to be uploaded to sensor. Wi-Fi connectivity is used for time synchronization and it can be used to upload processed data directly to cloud.

ESP32-C6 is a microcontroller unit (MCU) with 32 bit RISC-V microprocessor, 512 KB SRAM, 320 KB ROM, code is uploaded to 8 MB SPI flash on the devkit ESP32-C6-DevKitC-1.

For controlling VL53L7CX an Ultra Light Driver by STMicroelectronics is used, where library Platform for ESP32-C6 (controlling digital pins and I^{2}C) is implemented. Source available at GitHub public repository [7].

C. Flutter application

Flutter, used for visualisation and algorithm testing, is a cross-platform toolkit. Code is written in Dart language and for Android it is compiled to Java/Kotlin and Android Studio creates the final application. For Windows application, Dart code is compiled to C++ and it uses Visual Studio with Desktop development with C++.

Application connects to microcontroller using Serial Port (USB UART). Methods for controlling Serial port are defined by abstract class SerialPortHandler, which is implemented by classes for Windows and Android platforms (Serial port in Windows is implemented by different library than Serial port in Android).

Data from Serial port are decoded, an algorithm is applied on them and data are visualised as describes Fig. 2.
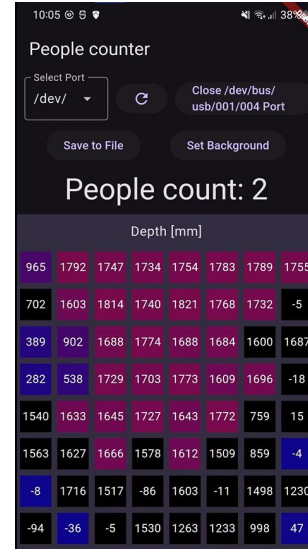
Fig. 2: Data visualiser - Flutter application

D. Algorithm

Algorithm of people counting is based on algorithm presented by C. Perra and others [8], dividing pixels into zones is shown in the Fig. 3. In algorithm four zones are used (nZones = 4), height threshold is set to one meter (heightThreshold = 1000) and 6 pixels have to be above threshold to activate zone (nPixelsToActivateZone = 5).

This algorithm has positive, that is proof against noise caused by detection bad depth in single pixel. The negative is that only one person can be in FoV of sensor to correctly detect person, so there must be distance 2.2 m between persons. Another negative is that when error occurs during detection, error in people count remains till it is manually repaired.

Maximum velocity of moving person to be correctly detected by algorithm:

$$v_{max} = \frac{s}{t_{min}} = s \cdot \frac{f_s}{N_{min}} \tag{3}$$

where s is distance computed by equation (2), t_{min} is minimum time to detect person, which equals time of N_{min} frames, N_{min} is minimum number of frames needed to detect person and f_s is ranging frequency.

In this system sensor is on the top of the door in height 1.9 m and threshold is set to 1 m, so height distance h = 0.9 m, FoV $\varphi = 60°$, ranging frequency $f_s = 10$ Hz and minimum number of frames to detect person by presented algorithm $N_{min} = 4$ frames. Maximum velocity of person to be correctly detected by algorithm is 2.6 m/s, that is 9.3 km/h, so system is able to detect also fast walking people, but not running people. To detect fast-moving individuals it is possible to increase ranging frequency to 15 Hz (which increases amount of processed data) or to change the algorithm to be able to detect direction of moving individual in three or two frames.

Fig. 3: Zones of matrix

(a) single target   (b) multitarget

Fig. 5: Histogram of measured background depth (static) in one zone

III. RESULTS

The designed system has been tested using breadboard put on the top of the door as is shown on Fig. 4. ESP32-C6 was connected via USB to Android smartphone with installed Flutter application. System has been also tested using PC with Windows.
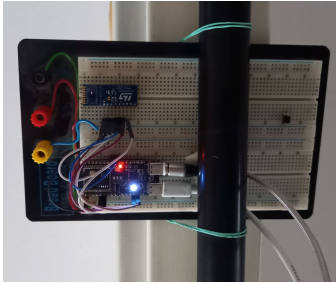
Fig. 4: Experimental realization of sensor VL53L7CX and ESP32-C6 on the top of the door

System reliably works, when single person goes through whole FoV without changing direction, so it works well when normal entering and exiting room. System also correctly detect, when person enters first two zones (half of FoV) and exits back. But when person returns from position further than half of FoV, person is counted with error.

Sensor produces more errors during measurement, when high intensity of sunlight appears in FoV, because in sunlight there are present also waves with 940 nm wavelength and it distorts results. To decrease influence of ambient light it might help to decrease resolution of sensor to 4x4, which can improve signal to noise ratio (SNR).

It has been measured a depth of the background 2800 times. a result of the measurement is shown on Fig. 5a, where is a histogram of a zone with single target with shape of normal distribution and measured depth is better ($\pm$ 3.5%) than the guaranteed deviation (for the best condition $\pm$ 5%, the worst condition $\pm$ 14%). 99.8 % of measured depths the sensor signed as valid by target status.

A result from another zone is shown on Fig. 5b, where two targets were detected - 1400 mm (94.7 %) and 1950 mm (5.3 %). If we take only data signed as valid, 6.1 % of valid measured depths detects the second target.

IV. CONCLUSION

In this work a system of counting people was designed, which is based on measuring data on time of flight sensor VL53L7CX controlled by microcontroller ESP32-C6, raw data are backed up on SD card and they are processed by Flutter application on a device with Android or Windows operating system. The inaccuracy and errors in measured data were handled by setting higher threshold. The results are visualized and they are uploaded to Google Sheets using Google Sheets API.
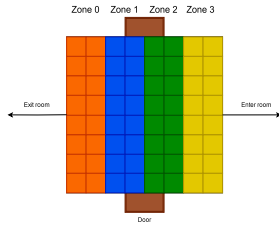
In the future work, algorithm will be processed by ESP32-C6. The changes of people count will be directly uploaded to Google Sheets using Google Sheets API and HTTPS requests with JSON payload via Wi-Fi module on the ESP32-C6 Devkit. The system will be powered by battery, so it will be independent on wire connection. Also more algorithms will be developed and compared to each other. One algorithm will be based on detecting shape of a person, which will reduce the minimum distance between people compared to presented algorithm.

REFERENCES

[1] MYINT, Ei Phyu; SEIN, Myint Myint. People Detecting and Counting System. In: 2021 IEEE 3rd Global Conference on Life Sciences and Technologies (LifeTech). 2021, pp. 289–290. Available from doi: 10.1109/LifeTech52111.2021.9391951.

[2] MATUSKA, Slavomir; MACHAJ, Juraj; HUDEC, Robert; KAMENCAY, Patrik. An Improved IoT-Based System for Detecting the Number of People and Their Distribution in a Classroom. Sensors. 2022, vol. 22, no. 20. issn 1424- 8220. Available from doi: 10.3390/s22207912.

[3] ZELENY, O.; FRYZA, T.; BRAVENEC, Tomas; AZIZI, S.; NAIR, G. Detection of Room Occupancy in Smart Buildings. Radioengineering. 2024, vol. 33, pp. 432–441. Available from doi: 10.13164/re.2024.0432

[4] KOUYOUMDJIEVA, Sylvia T.; DANIELIS, Peter; KARLSSON, Gunnar. Survey of Non-image-Based Approaches for Counting People. IEEE Communications Surveys & Tutorials. 2020, vol. 22, no. 2, pp. 1305–1336. Available from doi: 10.1109/COMST.2019.2902824.

[5] IRIS INTELLIGENT SENSING, Iris-GmbH intelligent sensors. IRMA 6: A new generation of Automatic Passenger Counting — iris intelligent sensing. 2024. Available also from: https://www.iris-sensing.com/products/irma- 6/.

[6] N. Patwari and J. Wilson, "RF sensor networks for device-free localization: Measurements, models, and algorithms," Proceedings of the IEEE, vol. 98, no. 11, pp. 1961–1973, 2010.

[7] ŠIKULA, Josef, 2025. *Detecting number of people*. Online. GitHub. Available at: https://github.com/j-sikula/Detecting-number-of-people. [accessed 2025-03-06].

[8] PERRA, Cristian; KUMAR, Amit; LOSITO, Michele; PIRINO, Paolo; MORADPOUR, Milad; GATTO, Gianluca. Monitoring Indoor People Presence in Buildings Using Low-Cost Infrared Sensor Array in Doorways. Sensors. 2021, vol. 21, no. 12. issn 1424-8220. Available from doi: 10.3390/s21124062.

Efficiency Analysis of an Automatic Production Line

Dominik Bortlík
Department of Control and Instrumentation, FEEC
Brno University of Technology
Brno, Czech Republic
247342@vutbr.cz

doc. Ing. Václav Kaczmarczyk, Ph.D.
Department of Control and Instrumentation, FEEC
Brno University of Technology
Brno, Czech Republic
kaczmarczyk@vut.cz

Abstract— **This paper presents an efficiency analysis of yogurt production line. The goal is to describe a real production line and based on this description, create a digital twin in Tecnomatix Plant Simulation, which will be used to analyze efficiency and identify weak spots. Subsequently, optimizations will be proposed to improve the overall efficiency of the production line.**

Keywords— *Siemens, Siemens Plant Simulation, production line, simulation, efficiency, digital twin*

I. Introduction

Modern manufacturing depends on efficient production processes to minimize waste and maximize productivity. This paper analyzes a yogurt production line using Tecnomatix Plant Simulation, a tool for modeling discrete-event systems. The main objective was to identify inefficiencies and test potential improvements without affecting a run of the real production line.

It is worth noting that this is not a standard production line for small yogurts but rather for large 1 kg yogurts, which are filled into buckets. The mail reason why it was decided to analyze this production line was because it is an older model, so there was a high probability of identifying inefficiencies or issues that could be slowing down overall production.

The yogurt production line (Fig. 1) under examination includes multiple phases: buckets handling, sanitation, filling, sealing, packaging, and storage. Each of these steps presents potential inefficiencies that can accumulate into significant productivity losses. By developing a digital twin of the line, the workflow was analyzed, various failure scenarios were simulated, and practical optimizations were proposed.

Fig. 1. Production line

II. Overview of the Production Line

The production line consists of the following key stages:

A. Buckets Handling

Buckets are manually loaded into the buffer and then automatically placed onto the conveyor belt. The process uses pneumatic grippers and sensors to ensure precise placement. Any defects in the buckets can cause misalignment and production slowdowns.

B. Sanitation Process

Buckets are sanitized using hydrogen peroxide vapor at high temperatures (150 °C). Vapor is injected into the bucket for sterilization, followed by two cycles of hot air blowing to remove any residual peroxide that condensates. The effectiveness of this step is crucial for food safety but also represents a major issue when inconsistent heating occur.

C. Filling

The buckets are filled with yogurt using an automated dispensing system. The amount of dispensed yogurt is precisely controlled by integrated weighing scale to ensure consistency in product weight. The yogurt is supplied from an external storage tank and dispensed into the buckets in a controlled speed to avoid spillage or excess foaming.

D. Sealing

After filling, the buckets are sealed in two stages. First, a thin plastic foil lid is heat-sealed onto the top of the bucket to ensure freshness and prevent contamination. Then, a plastic lid is put on the top and pressed into place to provide additional protection.

E. Labeling and Expiry Date Printing

Before packaging, an inkjet printer marks the expiration date on the bucket. The printing process is fully automated and synchronized with the conveyor belt movement to ensure continuous operation without delays. The inkjet system is designed for high-speed application, but occasional smudging or misalignment can occur, requiring periodic maintenance and calibration.

F. Packaging and Palletizing

And finally, workers pack final products into carton boxes that then stack onto pallet. Once a pallet reaches its full capacity, it is transported by forklifts to the storage area.

G. Workers

This production line is operated by three workers. The first worker is the main operator, who is specially trained to control the line and is also responsible for refilling buckets and lids into buffers. The other two workers handle storage tasks, one puts finished products into cardboard boxes and places them onto pallets, while the other transports full pallets to storage and brings in empty ones.

The digital model incorporated all these stages, as well as potential fail down scenarios, to provide an accurate representation of real-world conditions.

III. PLANT SIMULATION AND DIGITAL MODEL

A. Siemens Tecnomatix Plant Simulation

Tecnomatix Plant Simulation is a powerful software from Siemens for modeling and analyzing production processes. It is use for creation of digital twins, allowing manufacturers to visualize, simulate, and optimize their operations before implementing physical changes. The software supports discrete-event simulation, helping to identify weak spots, test alternative process flows, and assess the impact of various operational strategies [1].

The digital models of production systems are created using a library of predefined objects, such as conveyors, machines, workstations, and buffers. Each object can be configured according to real parameters, such as processing times, capacities, or failure probabilities. Once the model is assembled, the production process simulation is performed, and the results can be visualized using graphs and another tools for analyses [2].

B. Digital Model of the Production Line

The digital model consists of two main parts: the production line (Fig. 2) and the packaging process with product transportation to the warehouse (Fig. 3). Transportation is provided by forklift, that moves full pallets into the warehouse.

The production line was based on the description of the real system and includes all key components, such as buckets handling, sanitation, filling, sealing, labeling and packaging. Each of these sections was created separately and then interconnected to form a complete and functional production system.

In addition to these core components, the model also includes objects that serve as sources of individual products within the system. These include boxes with buckets, lids, and foil, a tank with yogurt, a storage area for pallets, and stacked carboard boxes used for packaging the finished products.

The digital model incorporated various work elements to accurately reflect real production conditions. Workers were simulated for key manual tasks, such as products refilling or packaging. Additional model parameters included machine failure probabilities.

To make model more realistic, custom 3D models and animations were created, for all sections of the production line, such as workstations or conveyors. These custom models allowed for proper visualization and better overall understanding of the production model.
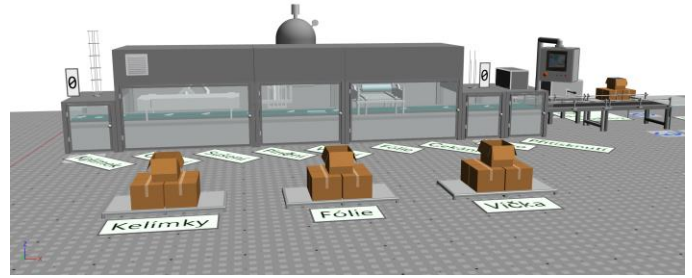
Fig. 2. Digital model – production line
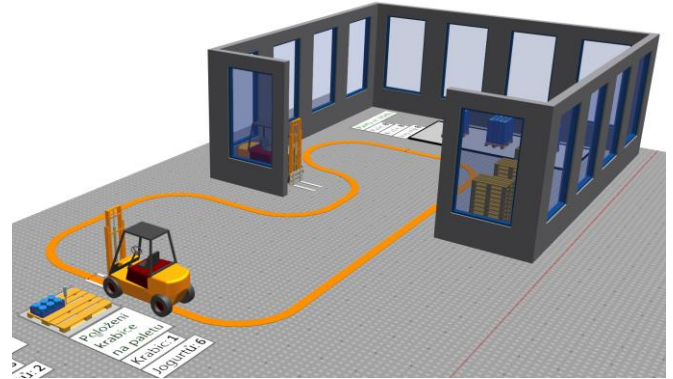
Fig. 3. Digital model – warehouse and transportation

IV. EFFICIENCY ANALYSIS

Data from both real operation of production line and simulation results revealed several recurring problems that led to inefficiencies. The two most significant issues were:

A. Peroxide Heating Error

During the sanitation process, hydrogen peroxide vapor must be heated to an optimal temperature of 150 °C. This heating should occur simultaneously with the operation of the production line. However, due to an error in the line's programming, this did not happen. Instead, whenever the temperature dropped below a certain value, the entire production line stopped and remained stopped until the temperature was restored back to 150 °C. Afterward, the system needed to be manually restarted to resume operation.

This issue occurred approximately every 30 minutes, with each interruption lasting around 30 seconds. As a result, this malfunction led to a 2.7% loss in production efficiency.

B. Buckets and Lids Deformation

The quality of plastic buckets and lids used in the production process was another source of inefficiency. Lower-quality materials led to occasional deformation, causing misalignment on the conveyor belt. This resulted in a 4.76%-time loss due to stoppages and manual corrections by operators.

Additional minor inefficiencies, such as lower pressure in filling pipe or foil jam, were also observed, but their impact was less significant or occurred rarely.
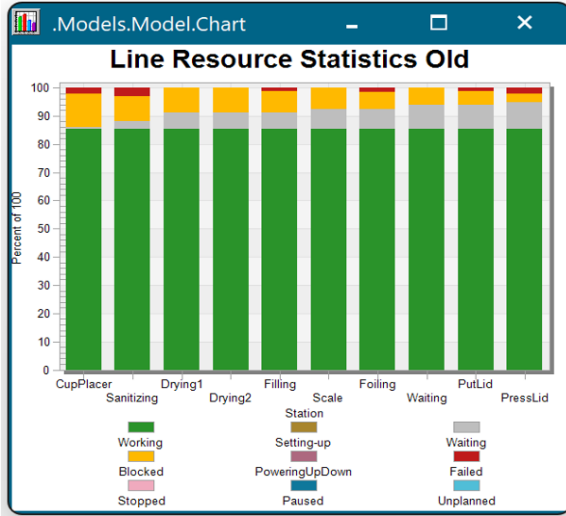
Fig. 4 Statistics of production line individual sections (before optimalizations)

V. OPTIMIZATION AND RESULTS

The overall efficiency of the production line was improved by focusing on solving issues described before.

The overall

A. Fixing the Peroxide Heating Issue

The cause of the peroxide heating issue was identified as a software malfunction in the temperature control system. After reporting this problem to the production manager, he contacted the company that supplied the production line and arranged for the issue to be resolved. As a result, the peroxide heating malfunction has now been fixed, leading to a 2.7% reduction in overall production time.

B. Upgrading Buckets and Lids Quality

After the issue was brought to management's attention, it was explained to me that the lower-quality products were being purchased because they were cheap and more environmentally friendly, because they were made from recyclable materials. However, despite this, management agreed to explore alternative suppliers offering higher-quality products. After some time, the company had successfully found a supplier offering products of the same price and eco-friendly composition but with better quality. Although the issue could not be completely eliminated, this change still resulted in a 0.7% reduction in production time.

C. Increasing Prodiction Line Overall Speed

An effective optimization would be increasing the overall speed of the production line. Analysis revealed that the yogurt filling station is the slowest section, determining the cycle time for the entire production line.

Theoretically, the filling speed could be increased by adjusting the pump pressure. However, this would create a risk of contamination due to potential yogurt splashing outside the bucket. Additionally, even if the filling speed was successfully increased, it could create issues in other sections, such as the bucket handling system. A higher speed might cause the pneumatic gripper to misplace buckets, leading to disruptions in the process.

In conclusion, while increasing the overall speed is technically possible, the current settings are optimized to balance efficiency and reliability. Any modifications to the cycle time could introduce new operational issues, making the current speed the most stable and effective choice.

D. Overall Impact

By resolving these issues, the overall efficiency was improved by 3.4 %. To put this into perspective, producing 5.040 pieces initially took 7 hours and 23 minutes. After optimization, the production time was reduced to 7 hours and 8 minutes, saving 15 minutes per batch. This improvement leads to significant long-term productivity gains, ensuring a more reliable and cost-effective manufacturing process.
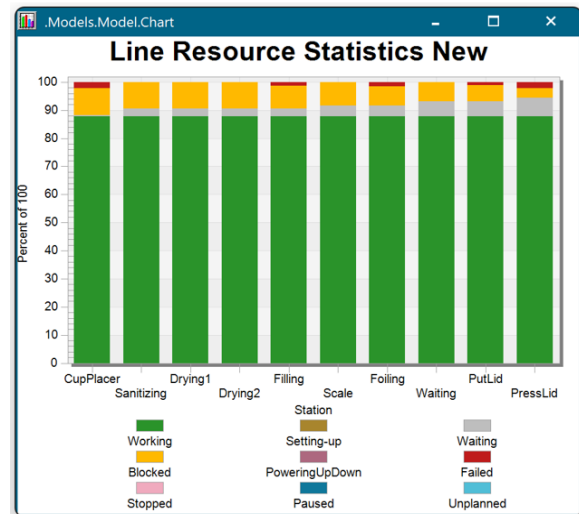
Fig. 5 Statistics of production line individual sections (after optimalizations)

VI. CONCLUSION

This paper demonstrates the effectiveness of using digital twin and simulations for identifying and resolving production inefficiencies. By simulating real-world conditions in Tecnomatix Plant Simulation, manufacturers can detect weak spots, test optimization ideas, and implement solutions with minimal disruption to actual operations. The improvements made in case of this paper, show the potential of such approaches for industrial applications.

REFERENCES

[1] AXIOM TECH. Tecnomatix Plant Simulation. Axiomtech.cz, 2025. Online. Dostupné z: https://www.axiomtech.cz/25357-tecnomatix-plant-simulation. [cit. 2025-03-05].

[2] TPV GROUP. Plant Simulation. TPV Group. Online. Dostupné z: https://www.tpvgroup.cz/plant-simulation/. [cit. 2025-03-05].

Testing conductive layers on flexible and elastic substrates

Vít Kejhar
Faculty of Electronical Engineering and Communication
Brno University of Technology
Brno, Czech Republic
247019@vutbr.cz

Ing. Ladislav Chladil Ph.D.
Faculty of Electronical Engineering and Communication
Brno University of Technology
Brno, Czech Republic
chladil@vut.cz

Abstract—**Flexible and elastic substrates with conductive layers are widely used in modern electronic applications, including wearable sensors and force-sensitive resistors (FSRs). This paper evaluates the electrical and mechanical properties of conductive layers deposited on flexible and elastic substrates. Electrical properties were assessed through resistance measurements, while mechanical durability was tested using elongation and abrasion resistance experiments. Results highlight the impact of substrate elasticity and suggest optimization for sensor technology.**

Index Terms—**Flexible electronics, conductive layers, mechanical durability, electrical properties, flexible substrates.**

I. INTRODUCTION

The rapid development of wearable electronics, smart textiles, and flexible sensors has driven the need for advanced conductive materials compatible with flexible and elastic substrates. These materials play a critical role in applications such as force-sensitive resistors (FSRs), biomedical sensors, and soft robotics. Their ability to maintain stable electrical and mechanical properties under deformation is essential for reliability in real-world applications.

Conductive layers can be manufactured using various deposition and printing techniques, including screen printing, vacuum deposition, and inkjet printing. However, the mechanical durability and electrical stability of these layers strongly depend on the choice of materials and substrate properties. Understanding how these layers respond to mechanical stresses, such as stretching and abrasion, is crucial for optimizing their performance.

This paper focuses on the evaluation of conductive layers on flexible and elastic substrates, analyzing their electrical and mechanical properties. The study investigates the impact of substrate elasticity on layer functionality and examines the response of layers to applied stresses. The results contribute to the development of improved materials for wearable electronics, industrial sensors, and medical applications.

II. OVERVIEW OF CONDUCTIVE LAYERS

The performance of some flexible electronic devices relies heavily on the properties of conductive layers. These layers

must maintain stable electrical characteristics while withstanding mechanical deformation, making material selection and deposition techniques crucial factors in their design. This section provides an overview of materials used for conductive layers and their relevance to force-sensitive resistor (FSR) sensors.

A. Conductive Layers

Conductive layers serve as the primary medium for electrical signal transmission and must exhibit high conductivity while remaining flexible and durable. Various classes of materials are employed to achieve these requirements:

- **Metal-Based Conductors:** Silver, gold, and copper are widely used due to their high electrical conductivity. *Silver* is particularly popular in printed electronics because of its excellent conductivity ($6.2 \times 10^7 S \cdot m$) and processability in nanoparticle-based inks. However, cost and oxidation issues pose challenges for long-term stability [1].
- **Carbon-Based Materials:** Graphene, carbon nanotubes (CNTs), and graphite-based inks provide lightweight, stretchable alternatives to metal conductors. These materials offer high electrical conductivity with superior mechanical flexibility, making them ideal for integration into wearable sensors [2].
- **Conductive Polymers:** Intrinsically conductive polymers, such as *polyaniline (PANI), polypyrrole (PPy), and PEDOT:PSS*, have gained attention due to their tunable conductivity and compatibility with flexible substrates. Their ability to form uniform films on elastic materials makes them valuable for applications requiring high mechanical adaptability [3].

The choice of conductive material depends on the required trade-off between electrical performance, cost, and mechanical resilience. While metals provide superior conductivity, carbon-based materials and polymers offer better durability under repeated deformation.

B. Material Considerations for Flexible Functional Layers

The effectiveness of functional layers on flexible substrates depends on several key material properties:

- **Layer Adhesion and Stability:** Ensuring strong adhesion between the conductive layer and the substrate is critical for long-term performance. Poor adhesion can lead to delamination and inconsistent sensor output, particularly under repeated strain cycles. Surface treatment methods, such as oxygen plasma treatment and silane coupling agents, are often used to enhance adhesion [4].
- **Sensitivity and Durability:** The performance of polymer-based layers depends on the uniform dispersion of conductive fillers within the polymer matrix. Higher filler concentrations generally improve conductivity but may reduce mechanical flexibility. Optimized filler distributions are essential to balance sensitivity and mechanical durability [5].

III. Flexible and Elastic Substrates

Flexible and elastic substrates are essential components in modern electronic devices. These substrates serve as the foundation for conductive layers, ensuring their mechanical integrity under bending, stretching, and compression. The choice of substrate significantly influences the overall performance of the electronic system, affecting factors such as electrical conductivity, strain tolerance, and long-term stability.

A. Impact of Substrate Properties on Functional Layers

The mechanical properties of the substrate directly influence the behavior and stability of *funcional layers*. Several key factors must be considered when selecting a substrate for flexible electronic applications:

- **Mechanical Compliance:** Highly stretchable substrates, such as *elastomers and textiles*, accommodate large deformations. However, excessive stretching can induce cracks in conductive layers, reducing electrical performance [8].
- **Electrical Performance:** Some flexible substrates, such as *graphene-coated textiles and conductive polymer composites*, can inherently contribute to electrical functionality, reducing the need for additional conductive coatings. These hybrid materials show promise in *next-generation flexible circuits and self-powered sensors* [4], [7].

IV. Testing Methodology

To evaluate the performance of conductive layers, a series of *electrical and mechanical tests* were conducted. The testing methodology was designed to assess the materials' behavior under real-world conditions, ensuring reliability for various applications such as *medical devices and pressure sensors*. Additionally, a *3D-printed testing system* was utilized to ensure precise and repeatable measurements.

A. Electrical Characterization

Electrical properties were assessed through *resistance measurements*, focusing on *material conductivity*:

- **Four-Point Probe Measurement:** To obtain *accurate resistivity values*, a four-point probe method was utilized, eliminating *contact resistance errors*. This technique applies a known current through the outer probes while

measuring the voltage drop between the inner probes, allowing for precise *sheet resistance calculations* [9]. Measurements were conducted using a Agilent LCR metr E4980A, applying a controlled alternating voltage of 200mV and 50 Hz frequency, while recording current changes across the material. A specialized measuring fixture was created using a 3D printer to ensure uniform distribution of the current field across the tested layer and achieve accurate results (see fig. 1). The samples were tested under controlled temperature (22 ± 2°C) conditions to minimize external environmental influences on resistance values.
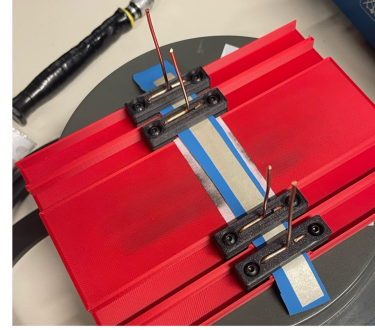
Fig. 1. 3D printer fixture with silver sample.

B. Mechanical Testing

The mechanical robustness of the layers was evaluated through *tensile strength and abrasion resistance* tests:

- The **peel test** (using ASTM D3359 standard) was performed to evaluate the adhesion strength of conductive layers on a flexible substrate. A standardized adhesive tape was applied and swiftly removed at a 90° angle, after which the sample was examined under an **optical microscope** to assess any material detachment.The percentage of removed material was recorded, as poor adhesion may lead to **delamination**, which affects the long-term reliability of flexible electronic devices and makes adhesion a critical parameter for device performance [10].
- **Tensile Testing (Stretchability & Crack Formation):** The samples were subjected to controlled *uniaxial elongation* using a 3D printer setup to ensure uniform stretching. The elongation process increased by 3% every 5 minutes until reaching a total strain of 30%, followed by a stepwise return to the initial state to observe stabilization. Electrical resistance was measured using a Bio-Logic potentiostat with chronoamperometry. The strain limit before failure was recorded, and conductive layers were analyzed under a microscope for *crack formation*, which directly impacts electrical conductivity. The test focused on a single conductive tape with a sandwich structure combining silver and carbon, providing insights into material behavior under mechanical stress [11].
- **Abrasion Resistance:** To assess long-term durability, the layers underwent *repeated mechanical friction cycles*

using a 3D printer-based system with a moving pressure head. The conductive tape was fixed on a specially printed support with clamps, ensuring precise positioning. A program controlled the head movement, applying a calibrated force based on a balance measurement. The layer was subjected to 500 friction cycles at a speed of 8 cm/s, with an applied load of 250 g for initial tests and 500 g for extended testing of promising samples. The resistance change was recorded using a potentiostat with a chronoamperometric technique, monitoring current response at a constant potential of 0.1 V. Poor adhesion and material degradation were evaluated through microscopic inspection and resistance trends, where increasing resistance indicated progressive wear [12]..

C. 3D-Printed Testing System

To ensure *precise, repeatable, and automated testing*, a *custom 3D-printed mechanical testing rig* was developed. The system allowed for:

- **Controlled Application of Pressure and Strain:** Using a *motorized actuator* to apply *uniform pressure and elongation* with high precision.
- **Real-Time Electrical Monitoring:** Integration with a *data acquisition system* consisting of potenciostat Bio-Logic SAS VSP for *continuous resistance tracking* during mechanical testing.

This setup provided a *cost-effective and reliable* alternative to traditional testing systems while maintaining *high accuracy and repeatability*.

V. Results and Discussion

The evaluation of conductive layers focused on their *electrical and mechanical properties*, particularly their *sheet resistance* and durability under mechanical stress. Three types of samples were prepared using *planar printing technology*, each featuring a *flexible polyurethane (PU) substrate* with different conductive coatings.

- **Sample 1**: A *PU substrate* with a *carbon-based conductive layer*.
- **Sample 2**: A *PU substrate* with a *silver-based conductive layer*.
- **Sample 3**: A *PU substrate* with a *sandwich-structured conductive layer* composed of *both carbon and silver*.

A. Electrical Properties

Electrical *sheet resistance* measurements were conducted to assess the *conductivity of each material*. The recorded values confirm the expected trend based on the intrinsic conductivity of carbon and silver:

- **Sample 1 (carbon-based layer)** exhibited the highest resistance of **4.178** $k\Omega$, indicating its lower conductivity compared to silver-based materials.
- **Sample 2 (silver-based layer)** had a significantly lower resistance of **3.379** Ω, demonstrating superior electrical conductivity.

- **Sample 3 (carbon-silver hybrid layer)** achieved the lowest resistance of **1.928** Ω, confirming the benefits of combining both materials to enhance conductivity while maintaining flexibility.

B. Mechanical Properties

1) Peel Test Evaluation: The results indicated significant differences in adhesion between the tested conductive layers.

The **carbon-based layer** exhibited the best adhesion, with only minor particle detachment observed. The **silver-based layer** also demonstrated good surface cohesion, with no visible cracks or significant damage to the conductive coating. However, microscopic analysis of the adhesive tape revealed detached particles from the silver surface, suggesting minor surface degradation.

In contrast, the **sandwich-structured (carbon-silver) layer** showed the weakest adhesion. Large sections of the conductive coating were removed during the peel test (see fig. 2), completely compromising the layer's structural integrity. The delamination of the hybrid structure indicates insufficient bonding between the carbon and silver layers, which may affect its long-term durability in flexible electronic applications.
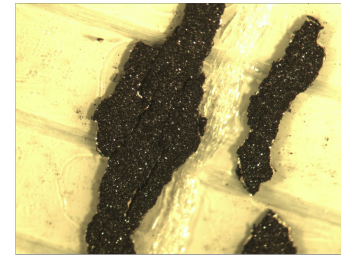
Fig. 2. Detail of the silver-carbon conductive layer adhered to adhesive tape.

2) Abrasion Resistance Evaluation: The abrasion resistance of the conductive layers was tested under repeated mechanical friction cycles. The results revealed contrasting behaviors among the tested samples.

The **silver-based layer** exhibited an *increasing fluctuation in electrical resistance* with each pass of the testing head, indicating *piezoresistive behavior*. However, in this application, such a response is undesirable. Additionally, a *gradual increase in overall resistance* was observed, reaching up to *six times* the initial value after prolonged wear, suggesting progressive degradation of the conductive surface (see fig. 3).

Conversely, the **carbon-based and hybrid (carbon-silver) layers** demonstrated superior *abrasion resistance*. After **500 abrasion cycles**, their electrical resistance increased only *minimally or remained unchanged*. Any minor fluctuations in resistance during individual passes remained within a stable range around the mean value, indicating a robust conductive network resistant to mechanical wear.

These findings suggest that *carbon-based and sandwich-structured conductive coatings* are more durable against mechanical abrasion, making them more suitable for long-term use in *wearable electronics and flexible sensor applications*.
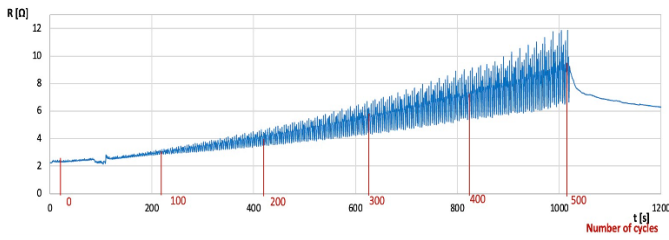
Fig. 3. Detail of the silver-carbon conductive layer adhered to adhesive tape.

3) Tensile Test Evaluation: The tensile test focused on evaluating the *stretchability and electrical stability*. The samples were subjected to a *single elongation cycle* to assess its mechanical integrity and conductivity retention under strain.

The results in sandwich-structured (carbon-silver) conductive layer indicated a **significant drop in conductivity** as soon as the sample was stretched. At the *first stage of elongation*, the electrical conductivity *decreased by 50%*, suggesting early structural disruption within the conductive network. Upon reaching **6% strain**, the *layer's integrity was completely compromised*, causing the conductivity to drop to *near-zero values* (see fig. 4). Simpler structures composed purely of silver and carbon exhibited better performance, with the layer remaining cohesive throughout the entire elongation range

These findings demonstrate that so far the best-performing sample was *insufficient for stretchable applications*, as it failed to maintain a stable conductive path under mechanical deformation. To improve mechanical durability, **alternative conductive layer structures** will be explored in future studies, focusing on *composite materials, flexible conductive networks, or layered reinforcement strategies*.

Fig. 4. Silver-carbon layer before (left) and after (right) 25 % elongation

VI. CONCLUSION

The results demonstrated that while silver-based layers provide excellent conductivity, they suffer from structural degradation under strain. Carbon-based layers exhibited higher mechanical resilience but at the cost of increased resistance. The hybrid carbon-silver structure offered a balance between conductivity and durability, but its adhesion limitations led to a loss of integrity under elongation, highlighting the challenge of maintaining both mechanical flexibility and electrical stability.

These findings are particularly relevant for applications in wearable electronics, pressure sensors, and flexible circuits, where materials must withstand repeated mechanical stress while maintaining electrical performance. One promising direction for practical implementation is the development of *incontinence sensors*, where flexible and durable conductive layers could enable discreet and responsive moisture or pressure detection integrated into textiles. Such sensors would require materials with high sensitivity to mechanical deformation while ensuring long-term wear resistance.

Future research should focus on optimizing adhesion between conductive layers and substrates to prevent delamination, improving stretchability through composite structures, and exploring advanced deposition techniques to enhance conductivity without compromising mechanical robustness. The integration of nanomaterials and hybrid polymer-metal compositions may offer a viable path toward the development of next-generation flexible electronic devices for both medical and industrial applications.

REFERENCES

[1] M. G. Mohammed and R. Kramer, "All-Printed Flexible and Stretchable Electronics," Advanced Materials, vol. 29, no. 19, 2017.
[2] K. S. Novoselov et al., "Electric field effect in atomically thin carbon films," Science, vol. 306, no. 5696, pp. 666-669, 2004.
[3] A. Bráblíková, "Optimization of Printing Organic Electronic Structures for Bioelectronics," Bachelor's Thesis, Brno University of Technology, 2017.
[4] S. Lepak-Kuc et al., "The Influence of the Matrix Selection and the Unification Process on the Key Parameters of the Conductive Graphene Layers on a Flexible Substrate," Materials, vol. 16, no. 3, p. 1238, 2023.
[5] M. Hassan et al., "Significance of Flexible Substrates for Wearable and Implantable Devices: Recent Advances and Perspectives," Advanced Materials Technologies, vol. 7, no. 3, 2022, doi: 10.1002/admt.202100773.
[6] N. D. Sankir, "Flexible electronics: Materials and device fabrication," Doctoral Dissertation, Virginia Tech, 2005. Available: http://scholar.lib.vt.edu/theses/available/etd-12212005-001600/unrestricted/NDSankirDissertation.pdf.
[7] G. B. Tseghai et al., "Integration of Conductive Materials with Textile Structures, an Overview," Sensors, vol. 20, p. 6910, Dec. 2020, doi: 10.3390/s20236910.
[8] A. Pointner et al., "Knitted RESi: A Highly Flexible, Force-Sensitive Knitted Textile Based on Resistive Yarns," ACM SIGGRAPH 2020 Emerging Technologies, 2020, doi: 10.1145/3388534.3407292.
[9] P. P. L. Regtien and E. Dertien, Sensors for Mechatronics, 2nd ed., Elsevier Insights, San Diego: Elsevier, 2012.
[10] J. W. Cookson, "Theory of the piezo-resistive effect," Physical Review, vol. 47, no. 2, p. 194, 1935.
[11] H. Phan et al., "The piezoresistive effect of SiC for MEMS sensors at high temperatures: A review," Journal of Microelectromechanical Systems, vol. 24, no. 6, pp. 1663–1677, 2015.
[12] A. S. Fiorillo, C. D. Critello, and S. A. Pullano, "Theory, technology, and applications of piezoresistive sensors: A review," Sensors and Actuators A: Physical, vol. 281, pp. 156-175, 2018, doi: 10.1016/j.sna.2018.07.006.

Statistical Learning-Based Analysis of Human Driver Model Parameters

1st Kryštof Wojnarowský
Department of Control and Instrumentation
Brno University of Technology
Brno, Czech Republic
krystof.wojnarowsky@vutbr.cz

2nd Ondrej Mihálik
Department of Control and Instrumentation
Brno University of Technology
Brno, Czech Republic
ondrej.mihalik1@vut.cz

Abstract—This paper focuses on the development of functions and scripts capable of analyzing the parameters of a mathematical model of human drivers using the MATLAB environment. The main goal of this work was to confirm or refute the correlation between questionnaire responses and mathematical parameters. For this purpose, a set of scripts and functions was created, utilizing artificial intelligence-based statistical learning methods, such as regression and classification tools.

Index Terms—statistical learning, MATLAB, vehicle simulator, dynamical models, McRuer model, Donges model

I. INTRODUCTION

It is widely recognized that the majority of traffic accidents are caused by human drivers. Therefore, it is crucial to identify the factors that contribute to reduced perception and reaction abilities. One of the most significant factors influencing driving performance is fatigue. Several studies have analyzed drowsiness, identifying it as the second most dangerous condition that can lead to accidents. [1], [2] Furthermore, fatigue may not be the only factor affecting driving performance. Consequently, it is essential to examine the correlations between driving skills and behaviors preceding the drive.

II. METHODOLOGY

Fig. 1. Vehicle simulator [3]

The first objective of the experiment was to choose a human driver model based on the recent literature. For the purposes of our analysis, the 1st order Donges model [4] and the 2nd order McRuer model [5] were utilised. These models were identified using data that had been meticulously measured in this study combined with data from the previous study [6].

The state of the simulator used in the experiments is described in more detail in the papers [7], [8] and [9]. In the experimental work [6], a total of 13 subjects were measured. In the present experiment, additional 10 subjects were included. The total number of subjects analysed was thus 23. The methodology of measurement and data collection has been previously outlined in [6]–[8]. The measurement process was conducted across four distinct scenarios defined in [6]. These were: straight highway driving, straight highway driving with 4th order coloured noise, straight highway driving with 2nd order coloured noise, and straight highway driving with pseudo-random binary sequence (PRBS) noise.
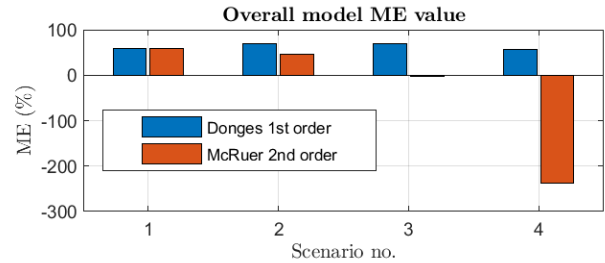
Fig. 2. Human driver models comparison

The more reliable Donges model was then selected through qualitative analysis, as illustrated in Figure 2. This model comprised four parameters, which were subsequently utilised as input parameters for the statistical analysis.

The measurement component entailed the administration of questionnaires to subjects, with the objective of data collection. The questionnaires incorporated a set of ten questions, the purpose of which was to assess drivers' skills, psyche, drowsiness, stimulant ingestion, and frequency of driving. The individual questions are discussed in Section III. The data collected through this method was then utilised as an observed parameter set in the statistical analysis.

In consideration of the qualitative or quantitative nature of the data, it was necessary to divide the entire analysis into two sections. For the purpose of analysis of qualitative

questions, the classification methods were utilised. In the present experiment, the KNN (K-Nearest Neighbours) method was utilised. The questions examined pertained to the impact of stimulant ingestion on driving performance and the discrepancy in driving skills between subjects who possess a driving licence and those who do not.

It is evident that the following questions are characterised by quantitative properties:

2. Psychological well-being measure on a 10-degree scale
3. Measure of subjective fatigue on a 10-point scale
4. Number of hours of sleep
6. Driver's age
8. Duration of driving licence ownership
9. Frequency of driving in number of hours per year
10. Number of km driven

In light of this, regression methods were employed. Given the small number of participants we restricted our analysis to linear methods, in particular linear regression was selected as the most promising approach.

The present study examined the redundancy of certain input features in the context of quantitative inquiries by employing the linear regression model. To this end, the best subset selection (BSS) method [10] was utilised. This approach enabled us to ascertain which parameters do not exert appreciable influence on the magnitude of the validation error, or which have the capacity to reduce it, by combining diverse input parameters.

A. Evaluation metrics

The calculation of model efficiency (ME) is explained in [11]. We used identical scripts to calculate ME for drivers that whose data were collected in this study.

The reliability of the aforementioned methods was validated by means of leave-one-out cross-validation (LOOCV).

The qualitative predictions of the linear regression model were evaluated using root mean square error (RMSE)

$$\text{RMSE} = \sqrt{\frac{1}{N}\sum_{n=1}^{N}[y(n) - y_{\text{m}}(n)]^2} \quad (1)$$

where $y(n)$ is the questionnaire response of the nth driver and

$$y_{\text{m}}(n) = w_0 + w_1 K_Y(n) + w_2 T(n) + w_3 K_\Psi(n) + w_4 \tau(n) \quad (2)$$

is the prediction obtained by the linear regression on the nth validation fold. The features K_Y, T, K_Ψ, and τ are the dynamical parameters of the Donges model [6].

The quantitative predictions of the KNN model were evaluated using the accuracy rate:

$$\text{accuracy rate} = \frac{\text{number of correct predictions}}{\text{number of predictions}} \quad (3)$$

This rate was also computed on validation folds. Furthermore, the holdout validation approach was employed in the KNN model, to compare different validation approaches.

All the aforementioned methods were implemented using scripts and functions within the MATLAB environment.

III. RESULTS

This section presents validation results obtained using methods outlined in theoretical previous section.

A. KNN method
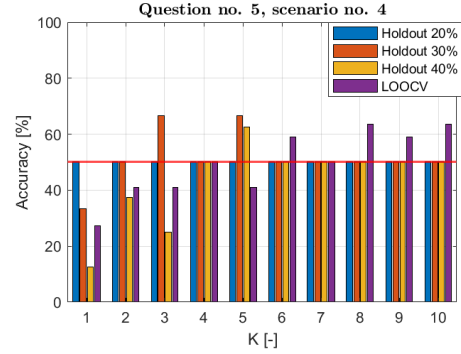
Fig. 3. Validation accuracy rate of KNN for increasing K.

The KNN classification model was utilised to determine the optimal value of K, with the objective of achieving the highest possible accuracy rate on validation data.

Stimulant intake: For this question the model demonstrated optimal performance at $K = 5$, as illustrated in Figure 3. However, the accuracy fluctuates around 50%, which is close to random guessing. Therefore, it appears that there is no relation between the driver's dynamical parameters and the stimulant intake tested within our study.

Driver's licence ownership: The investigation into this question was not possible because all subjects were in possession of a licence. This resulted in a 100% accuracy rate, which is not pertinent to the aforementioned reasons.

B. Linear regression

During the validation process, it was assumed that certain drivers' dynamical parameters might be related to the questionnaire, while others might not. We employed the BSS method to assess the relevance of these parameters. This method evaluates all possible combinations of input features (dynamical parameters) within the linear regression model.
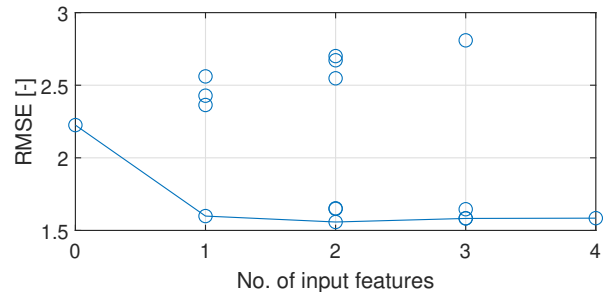
Fig. 4. RMSE for all possible models with varying number of features. Question no. 3 (driver's psyche on ten-point scale), scenario no. 3 (driver's response to lane change signals and random gusts of wind).

The BSS will be illustrated using predictions of drivers' psyche, subjectively rated on a ten-point scale. Figure 4 begins

with the model containing zero input features. It predicts the mean value, w_0, of the training data on the validation data, resulting in a relatively large RMSE of 2.2.

There are four admissible models with one input feature. Figure 4 demonstrates that one parameter is related to the predicted psyche, as its inclusion in the linear regression reduces the validation RMSE to 1.6. The other three parameters alone *increase* the validation RMSE to between 2.4 and 2.6.

The optimal number of input features is two (T and τ) because, with a larger number of inputs, the model overfits and the validation RMSE slightly increases.

This kind of BSS analysis was repeated for the remaining quantitative questions and the optimal models are listed in Table I. The RMSE of these models is plotted in Fig. 5. It was observed that these questions also exhibited a reduced validation RMSE when utilising only some of the four dynamical parameters.

TABLE I
BSS OF LINEAR REGRESSION PARAMETERS

	Best subset selection			
Question no.	1st, scenario	2nd, scenario	3rd, scenario	4th, scenario
2	K_Y, K_Ψ, τ	τ	K_Y	K_Y, τ
3	–	K_Y, T, τ	T, τ	–
4	–	–	–	K_Y, T, K_Ψ
6	–	–	–	–
8	–	–	–	–
9	T, τ	K_Ψ, τ	K_Y, τ	–
10	–	T	τ	τ

Drowsiness: Table I indicates that the subjective level of fatigue (assessed via question no. 2 on a ten-point scale) does not necessitate all four dynamical parameters. The gain K_Y of the lateral feedback loop and the reaction delay τ serve as common elements in three scenarios. The time lag constant T is not linearly related to subjective drowsiness in our dataset.

The second indicator of driver fatigue was the number of hours of sleep prior to driving (question no. 4). Due to its physical nature, we expect this parameter to be more objective compared to those based on subjectively assessed fatigue. BSS suggests that all dynamical parameters are unrelated to hours of sleep, except in the 4th scenario, where the driver is compelled to compensate for the most challenging PRBS disturbances.

Psyche: For the subjective measure of psychological well-being on a ten-point scale (question no. 3), BSS regression analysis revealed that in 2nd and 3rd scenario, the most relevant dynamical parameters are time-related constants T and τ. However, these predictions exhibit higher RMSE compared to driver fatigue predictions mentioned above, see Fig 5.

**Age** and **Years of driver's licence ownership**: The age of the tested subjects (question no. 6) and their years of licence ownership (question no. 8) could not be predicted using

dynamical parameters, as these only increase the RMSE of the linear regression compared to the model with zero inputs that predicts the mean age or duration, w_0, computed from the training data.

Driving skills: The final aspect examined was driving skills, assessed through two questions. One focused on the frequency of driving, where the regression model relies mainly on the reaction delay τ. However, the model has a very high validation RMSE, comparable to the model with zero features.

Predicting the number of kilometres driven per year also relies on the reaction delay τ. The errors are of the order of 10,000 km and do not allow the given model to be considered satisfactory.
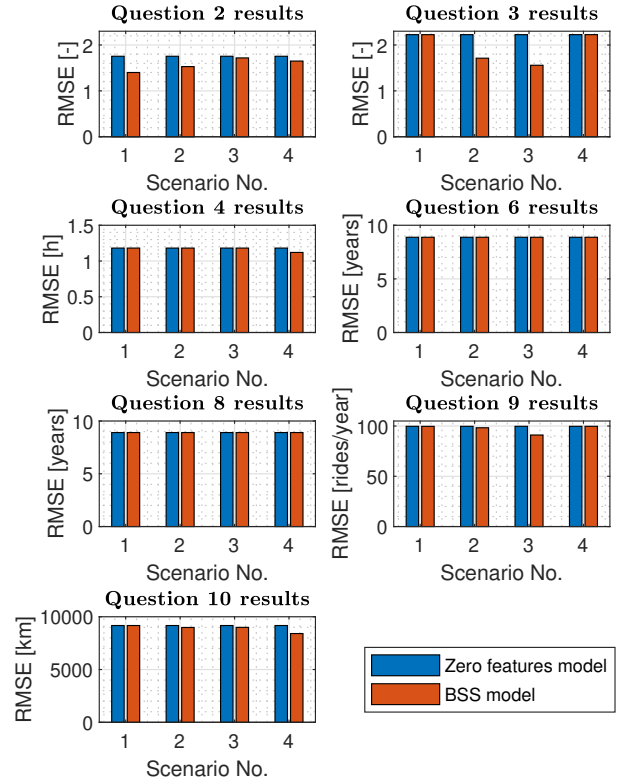
Fig. 5. Validation RMSE obtained using a model that predicts mean of the training data and the optimal model obtained using BSS method.

IV. DISCUSSION

In this paper, we attempted to evaluate the relationship between drivers' personal data obtained using a standardised questionnaire and their dynamical parameters obtained through the identification of a Donges control model.

The study revealed no statistically significant relationship between stimulant intake and driving performance across all four scenarios. No evidence was found to suggest that the amount of stimulant consumed in this study influenced driving skills.

Two questions, which pertain to the level of experienced drowsiness and psyche, can be adequately predicted through the utilisation of a suitable model parameter combination. In

all scenarios, BSS parameter combinations result in an RMSE of 1.5–2 points on the scale. When all the aforementioned facts and the matters examined in previous studies [12], [2] are taken into consideration, it can be concluded that drowsiness exerts a substantial influence on the performance of drivers. Furthermore, the opportunity to predict these parameters based on driver performance using linear regression is significant.

An investigation into the age of drivers or the duration of drivers' licence possession revealed that utilising parameter combinations did not result in an error margin better than the value obtained by predicting the mean value from the training data. However, it is important to note that the subjects of this study were exclusively from the 20–30 age group. The age range of the subjects was limited, with the majority falling within this interval. This restriction may have implications for the generalisability of the results. The relevance of the findings to a more diverse sample of drivers is a subject that merits further discussion.

In evaluating driving ability, the model exhibited significant errors in predicting both annual kilometres driven and driving frequency. Despite employing suitable parameter combinations, it was impossible to reduce the error to an acceptable level; the lowest achievable error remained approximately 1000 trips per year. Although one data point showed exceptionally low error, this anomaly is likely attributable to chance, given the broader context of the dataset. In terms of annual kilometres driven, the validation RMSE can be slightly reduced by considering the drivers' reaction delay τ.

V. Conclusion

In conclusion, it can be stated that the occurrence of drowsiness and insufficient sleep can result in significant changes in drivers' dynamical parameters. Furthermore, it is possible to predict drowsiness based on current driving ability using linear regression.

The examination of age and driving licence ownership duration did not exhibit a linear relation to drivers' dynamical parameters. However, the potential influence of age variability among the study subjects warrants further consideration, particularly with respect to the relevance of these findings.

The correlation between driver skills remains unproven. The predictions based on the reaction delay τ slightly decrease the validation RMSE, but this decrease is negligible. This might also be attributed to the non-linear dependence of the parameters.

Consequently, the examination of non-linear regression methods could prove beneficial. Additionally, the evaluation of mental well-being's impact did not reveal a correlation due to high error rates. Similarly, the examination of stimulant intake failed to establish any correlation. A correlation related to driving licence ownership duration is expected. Therefore, it would be advisable to collect data from non-drivers for comparative analysis with drivers.

In consideration of the limited number of subjects in the experiment, it is imperative to analyse the data methodically. This approach is necessary to avoid the formulation of critical conclusions that may be unwarranted. Nevertheless, the experiment provides a solid foundation for subsequent research in this area. It is recommended that the sample size be increased to ensure the attainment of more accurate and relevant results.

References

[1] FORSMAN M., Pia et al. *Efficient driver drowsiness detection at moderate levels of drowsiness* Online. Accident Analysis & Prevention, 2013. s. 341-350. Dostupné z: https://doi.org/10.1016/j.aap.2012.05.005. [cit. 2024-11-17].

[2] NORDBAKKE, S. a SAGBERG, F. *Sleepy at the wheel: Knowledge, symptoms and behaviour among car drivers* Online. Transportation Research Part F: Traffic Psychology and Behaviour, 2007. s. 1-10. Dostupné z: https://doi.org/10.1016/j.trf.2006.03.003. [cit. 2024-11-17].

[3] JIRGL, M., MIHÁLIK, O. et al. *Experimenting With an Efficient Driver Behavior Dynamical Model Applicable to Simulated Lane Changing Tasks* Online. IEEE Access, vol. 12, 2024. s. 122183-122198. Dostupné z: https://doi.org/10.1109/ACCESS.2024.3451622. [cit. 2024-10-29].

[4] DONGES, E. *A Two-Level Model of Driver Steering Behaviour* Human Factors, 1978, roč. 20, č. 6 s. 691-707.

[5] MCRUER, Duane T. a Ezra S. KRENDEL. *Mathematical models of human pilot behavior* Online. Neuilly sur Seine: North Atlantic Treaty Organization, Advisory Group for Aerospace Research and Development, 1974. Dostupné z: https://www.sto.nato.int/publications/AGARD/. [cit. 2024-09-17].

[6] ČELKO, Jakub. *Rozvětvené dynamické modely řidiče.* Brno: Brno University of Technology, FEEC, Dep. of Control and Instrumentation, 2024, 93 s. Bachelor thesis. Vedoucí práce: Ing. Ondrej Mihálik Dostupné z: https://www.vut.cz/www_base/zav_prace_soubor_verejne.php?file_id=265014. [cit. 2024-09-17].

[7] MICHALIK, D. *Simulátor řízení vozidla.* Online. Diplomová práce, Brno: Vysoké učení technické v Brně, Fakulta elektrotechniky a komunikačních technologií, Ústav automatizace a měřicí techniky, 2019, 81 s. Diplomová práce. Vedoucí práce: Ing. Miroslav Jirgl, Ph.D. Dostupné z: https://www.vut.cz/www_base/zav_prace_soubor_verejne.php?file_id=189346. [cit. 2024-12-23]

[8] MICHALIK, D. et al. *Developing an Unreal Engine 4-Based Vehicle Driving Simulator Applicable in Driver Behavior Analysis—A Technical Perspective.* Online. Safety, 2021. roč. 7, č. 2, s. 1-17. ISSN 2313-576X. Dostupné z: https://doi.org/10.3390/safety7020025. [cit. 2024-12-23].

[9] ČELKO, Jakub. *Modelování systémů člověk-stroj pomocí McRuerových modelů.* Brno: Vysoké učení technické v Brně, Fakulta elektrotechniky a komunikačních technologií, Ústav automatizace a měřicí techniky, 2022, 93 s. Diplomová práce. Vedoucí práce: Ing. Ondrej Mihálik Dostupné z: https://www.vut.cz/www_base/zav_prace_soubor_verejne.php?file_id=238941. [cit. 2024-12-23].

[10] JAMES, G. et al. *An Introduction to Statistical Learning with Applications in R* 1. vydání, Los Angeles: Springer Sciencez + Business Media New York, 2013. ISBN 0-13-656695-2.

[11] CELKO, J., MIHALIK, O. et al. *A Simple State-Space Model of Human Driver Applicable to Windy Conditions.* Online. IFAC-PapersOnLine. 2024, roč. 58, č. 9, s. 229-234. ISSN 2405-8963. Dostupné z: https://doi.org/10.1016/j.ifacol.2024.07.401. [cit. 2025-01-03].

[12] CHAI, M. et al. *Drowsiness monitoring based on steering wheel status* Online. Transportation Research Part D: Transport and Environment, 2019. s. 95-103. Dostupné z: https://doi.org/10.1016/j.trd.2018.07.007. [cit. 2024-11-17].

Predictive maintenance with digital model

1st Matěj Kantor
Dept. of Control and Instrumentation
Brno University of Technology
Brno, Czech Republic
247392@vutbr.cz

2nd Michal Husák
Dept. of Control and Instrumentation
Brno University of Technology
Brno, Czech Republic
xhusak08@vut.cz

Abstract—**This paper addresses the development of a Predictive Maintenance (PdM) detection algorithm applied to a digital model intended for PdM purposes of a heat exchanger station. The detection algorithm has been designed utilising data from a PLC measurement programme in conjunction with a digital model developed using MATLAB Simulink. Machine Learning (ML) techniques, specifically Support Vector Machines (SVM), were employed like two class classificator to identify anomalies. The SVM algorithm classified the measurement points into fault and normal operating states based on modelled temperature values, the Root Mean Square Error (RMSE) of temperatures within the primary circuit. The normal operating states is defined by digital model introduced in [4]. Anomaly state is simulated by serial clogging valve V3 in primary circuit.**

Index Terms—**Digital Model, Heat Exchanger, Machine Learning, Predictive Maintenance, Support Vector Machines**

I. INTRODUCTION

In today's digital age, when we have an overview of probably all the processes being carried out, there may be situations when the monitored equipment breaks down or does not work properly. For this case, predictive maintenance exists, which determines the current state of the equipment based on historical and current data.

The goal of predictive maintenance is to avoid unplanned downtime, reduce maintenance costs, and extend the life of the equipment [1]. It is the most advanced approach to equipment maintenance, based on previous preventive and reactive maintenance models.

Reactive maintenance is performed when the equipment breaks down and needs to be replaced or repaired.

Preventive maintenance, a proactive type of maintenance, is performed most often in specific time cycles that are planned in advance based on statistical data, such as Mean Time To Failure (MTTF) or Mean Time Between Failures (MTBF).

PdM is driven by data collected form process and historical data. Advanced analysis is used to get valuable information in industries where downtime is costly, as it allows maintenance to be planned and financial and operational losses to be minimized [2]. However, there are situations where its use is not effective. For simple and inexpensive machines where repair does not represent a significant cost, reactive maintenance is often chosen - that is, repair only in the event of a breakdown. In some operations where data on

the operating condition of the equipment cannot be reliably collected, preventive maintenance based on regular service cycles or statistical failure models is preferred. These methods are commonly used, for example, in the automotive industry or in manufacturing processes with planned downtime.

Predictive maintenance can be approached in two main ways. The first involves using a digital model that accurately simulates the behaviour of real equipment to support maintenance planning [3]. In this approach, measured data is compared with simulated data, and a Support Vector Machine is used to assess the equipment's functionality. The second approach relies on machine learning algorithms—specifically, a long short-term memory (LSTM) autoencoder and decision trees—to evaluate functionality based on data from healthy equipment. In this paper, we focus on the first method.

In this case, predictive maintenance was performed on a heat exchanger station for which a digital model was created to simulate its behaviour. For predictive maintenance purposes, pipe temperatures were sensed in the primary and secondary circuits near the exchanger, the opening of the valves V1, V2, and V3 which simulated the failure of pipe clogging with rust, limescale, and grease. Furthermore, the switching of the boiler and the differential pressure were detected in the primary circuit upstream and downstream of the circulator.

II. PHYSICAL MODEL DESCRIPTION

The model of the counterflow heat exchanger station is shown in Figure 1. The primary circuit consists of a 2 kW boiler with 10 litres of accumulation, a circulator, three-way valves, PT100 thermometers and thermistors. This primary loop is configured with mixing and forced circulation of the heat transfer medium using standard mains water.

PT100 thermometers and thermistors strategically located close to the upstream connections of the heat exchange are key components of this model. These temperature sensors were crucial to the creation of the digital model. Another important element was the differential pressure sensor, which will subsequently be used for predictive maintenance purposes. For measurement and control purposes, the heat exchanger station model is equipped with two Siemens

S7-1500 industrial Programmable Logic Controllers. These PLCs — one configured as the main controller and the other as an I/O device — were already equipped with the necessary instrumentation for sensor monitoring and actuator control. The main task for instrumentation is collecting data for system identification for the need of the existing digital model and for implementing predictive maintenance.
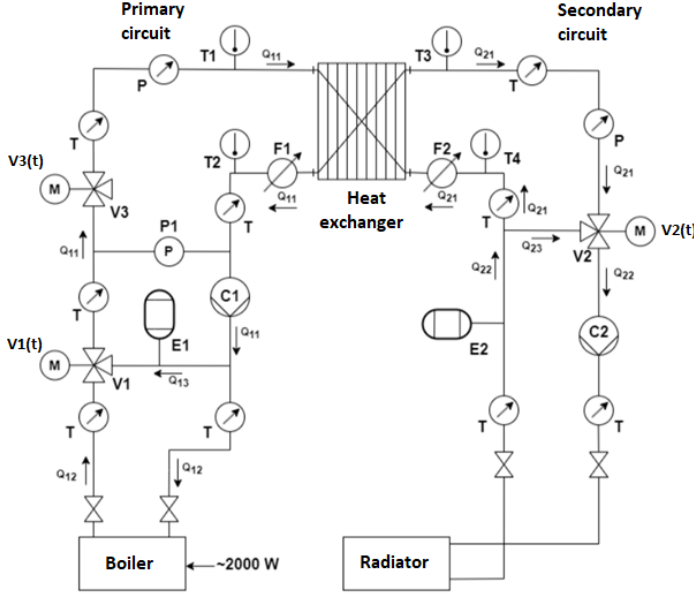
Fig. 1. Heat exchange station model [4]

A. Data acquisition description

The TIA Portal V17 environment from SIEMENS was used to collect data from the physical wiring of the exchanger station using the built-in TRACES function. This function was used to record values in a time series with a five-second sampling rate for 12.5 hours.

This environment recorded the opening values of the three-way valves V1 and V2, which directed water through the large or small circuit of the respective part of the exchanger station; see Figure 1. Then it recorded the opening value of the two-way valve V3 that simulates reduced flow through a pipe in the primary circuit. In addition, the temperatures near the counterflow exchanger, ambient temperature, differential pressure in the primary circuit upstream and downstream of the circulator, and the boiler switching were detected.

At the beginning of the measurement, there is a ten-minute window during which the water in the boiler is heated to the experimentally determined value of 75°C. This is followed by a sequence of opening and closing of valves V1 and V2 in two-hour and one-hour cycles, respectively. Valve V3 is opened at the defined level throughout the measurement.

A total of 10 measurements were taken, during which the opening of valve V3 was changed from 10% to 100%; see Table 1.

TABLE I
TEST SCENARIOS FOR FAILURE SIMULATION USING THE V3 VALVE

State	Time [min]	$V_1(t)$ [%]	$V_2(t)$ [%]	$V_3(t)$ [%]
Start	0	0	100	100
1	10	100	100	10:10:100
2	130	0	100	10:10:100
3	250	100	100	10:10:100
4	370	100	0	10:10:100
5	490	100	100	10:10:100
6	550	0	100	10:10:100
7	610	100	100	10:10:100
8	670	100	0	10:10:100
Stop	730	0	0	0

TABLE II
VALIDATION SCENARIO FOR FAILURE SIMULATION USING THE V3 VALVE

State	Time [min]	$V_1(t)$ [%]	$V_2(t)$ [%]	$V_3(t)$ [%]
Start	0	0	100	100
1	10	65	20	29
2	100	38	30	95
3	190	81	47	41
4	280	53	23	88
5	370	35	85	51
6	460	94	19	18
7	550	22	88	52
8	640	0	0	12
8	730	100	100	70
Stop	750	0	0	0

III. DIGITAL MODEL DESCRIPTION

The digital twin is the result of previous work [4] on the heat exchange station. The individual elements of the exchange station, piping, boiler, heat exchanger, valves, radiator, were created using MATLAB SIMULINK, described by mathematical equations referring to the calorimetric equation and the law of energy conservation. Some elements of the exchanger station were described by linear dynamic models, while other, more complex elements were described using the finite difference method, such as the counterflow exchanger model and the piping model. In contrast to previous work, the ambient temperature was adjusted. In the previous model, the ambient temperature was set constant at 24 °C, whereas now it is being measured with PT100. For more detailed description see [4]

IV. ANOMALY DETECTION

For the purpose of anomaly detection, two methods can be utilized. One is simple to use, employing a simple threshold,

which uses statistical methods to determine whether or not a system is in failure. The other way is based on the use of machine learning algorithms, more specifically SVM, which uses appropriately chosen features to determine whether the system is in failure or not. First, however, let us look at the latter.

A. Preprocessing

In order to detect the anomaly that implements SVM, it was necessary first to filter the data when valve V1 was closed, water flowed through the primary circuit only through the boiler, so the simulated fault with valve V3 did not appear in the system, as you can see in Figure 4. The data were then filtered when the transient occurred by opening the V1. Regarding the evaluation of fault or normal states, it was determined that the opening of valve V3 from 100% to 60 % should be considered normal state, while from 50% to 10% fault state. Thanks to this decision, we have obtained a data set that has normal and fault data of equal size. After the preprocessing section, Feature extraction was then performed.

B. Feature extraction

For feature extraction only the most significant data which were acquainted from measurement and simulation were used. These data were the root mean squared error of individual samples of the simulated and measured temperature near the exchanger but only in the primary circuit and differential pressure also in the primary circuit. RMSE was used as it clearly quantifies the difference between measured and simulated values, highlighting larger errors and aiding in accurate model validation. Secondary circuit temperatures were neglected, as they are also directly affected by the mass flow in the primary circuit, but with a significant time delay and are burdened with digital model error.

$$E = RMSE = \sqrt{\left(T_M - T_S\right)^2} \qquad (1)$$

Where:
- T_M – Measured temperature
- T_S – Simulated temperature

C. Support Vector Machine

With the preprocessed and extracted features, it is possible to construct an SVM that will classify the measured data into normal and fault states. Cross-validation was used to both train and validate the model, where the data were divided into 5 blocks, among which 4 were chosen for training and 1 for validation. This process was repeated for 5 times and then the best network was chosen. After cross-validation training, the SVM had an overall precision of 99,74%.

$$Accuracy = \frac{TN + TP}{TN + TP + FP + FN} \cdot 100 \qquad [\%] \quad (2)$$

Where:
- TP – correctly classified positive cases
- TN – correctly classified negative cases

- FP – negative cases incorrectly classified as positive
- FN – positive cases incorrectly classified as negative

One limitation of this method is that random mixing of data before splitting into folds. Data from different sceneries are mixed in one fold and the algorithm sees the training of data from all conditions and scenarios.
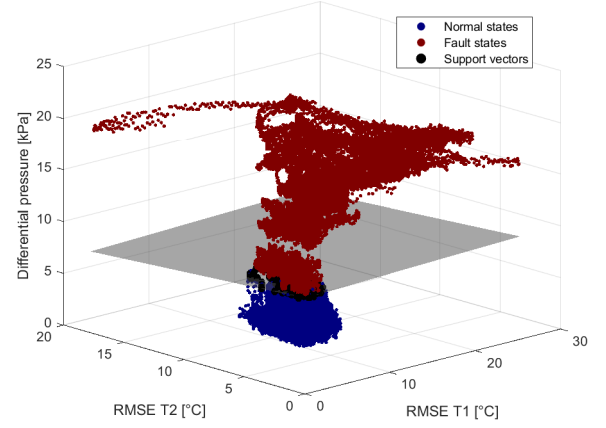
Fig. 2. Training data and decision plane

The model was further tested on an independent dataset presented in Table II, which was not used during the training or validation phases. The aim was to evaluate the model's ability to generalize to new, previously unseen measurements. In this test, the model achieved an overall accuracy of 43.6%, indicating a significant drop in performance compared to the cross-validation results. This indicates that the training dataset may be too limited, while the validation data is more diverse, suggesting a need to expand the training data.
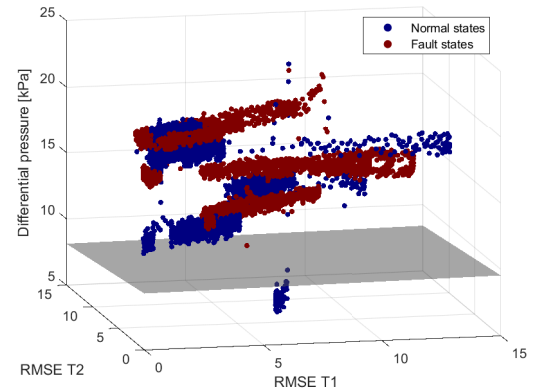
Fig. 3. Validation of SVM on validation data from Table II

V. CONCLUSION AND FUTURE WORK

In this study, we have presented a predictive maintenance algorithm for a heat exchanger station using a digital model and machine learning techniques. The integration of a
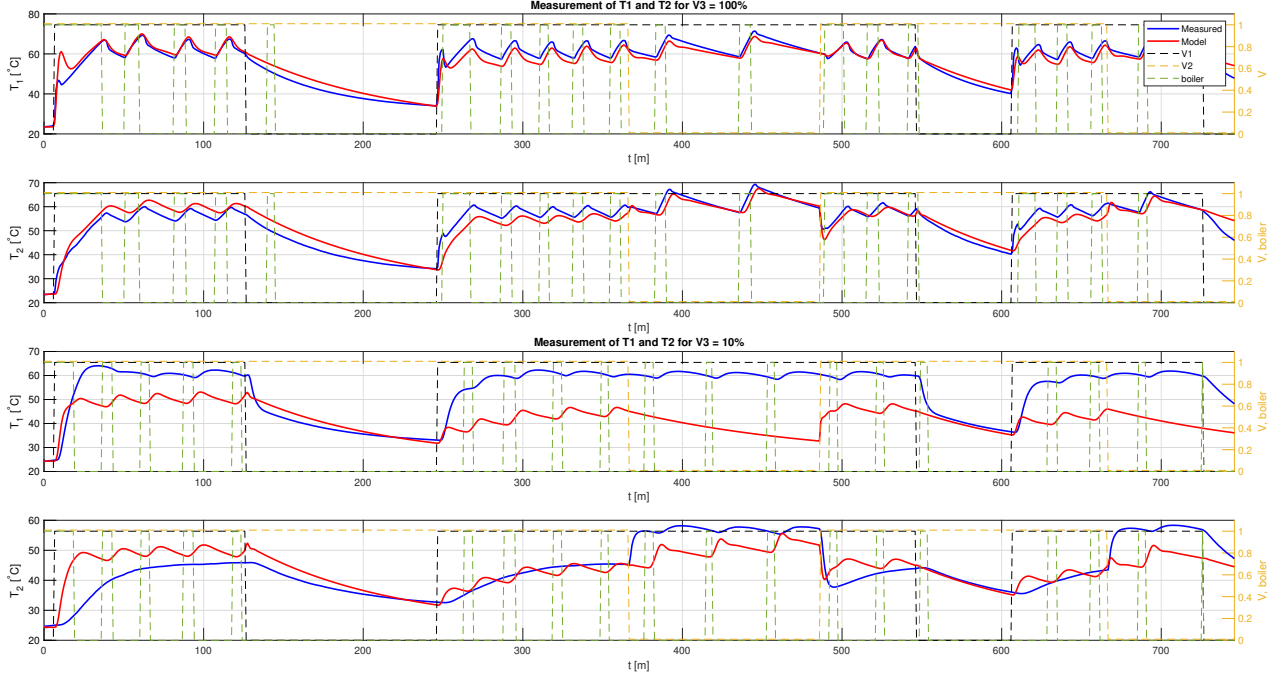
Fig. 4. Temperature Signal Comparison for Normal vs. Clogged Flow Conditions

digital twin with SVM-based anomaly detection has shown promising results in identifying system faults under controlled conditions. However, the validation phase revealed some challenges, particularly in generalizing the model to unseen data, with a drop in performance from training to testing. This suggests that further work is required to enhance the model's robustness, including better generalization strategies,the inclusion of a more diverse training dataset, and possibly the use of more advanced modelling techniques.

Moreover, the limitations of the digital twin, such as simplified thermal models and ignored heat transfer mechanisms, have contributed to inaccuracies in the predictive maintenance system. Future research will need to focus on refining the model's physical accuracy and exploring hybrid methods that combine machine learning with more detailed physical simulations. Despite these challenges, the approach holds significant potential for improving PdM strategies in industrial settings, reducing downtime, and optimizing maintenance costs.

A. Future work

Future research will focus on improving the model's generalization to validation data, aiming to reduce performance drop between training and testing phases. Additionally, a predictive maintenance model based solely on the simulated and measured temperature data from the digital twin will be developed. This approach would leverage only the digital model's outputs, reducing dependency on external sensors while maintaining effective predictive capabilities.

B. Conclusion

In conclusion, while the proposed method shows great promise, addressing its current limitations will be crucial for its successful deployment in real-world industrial systems.

REFERENCES

[1] M. A. Hoffmann and R. Lasch, "Unlocking the Potential of Predictive Maintenance for Intelligent Manufacturing: a Case Study On Potentials, Barriers, and Critical Success Factors", *Schmalenbach Journal of Business Research*, vol. 77, no. 1, 2025, doi: 10.1007/s41471-024-00204-3.

[2] R. D. Frederiksen, G. Bocewicz, G. Radzki, Z. Banaszak, and P. Nielsen, "Cost-Effectiveness of Predictive Maintenance for Offshore Wind Farms: A Case Study", *Energies*, vol. 17, no. 13, 2024, doi: 10.3390/en17133147.

[3] M. Liu, S. Fang, H. Dong, and C. Xu, "Review of digital twin about concepts, technologies, and industrial applications", *Journal of Manufacturing Systems*, vol. 58, pp. 346-361, 2021, doi: 10.1016/j.jmsy.2020.06.017.

[4] T. Benešl, M. Husák, O. Mihálik, R. Vancl, and Z. Bradáč, "Digital twin of heat exchange station", *IFAC-PapersOnLine*, vol. 58, no. 9, pp. 311-316, 2024, doi: 10.1016/j.ifacol.2024.07.415.

[5] M. Achouch, M. Dimitrova, K. Ziane, S. Sattarpanah Karganroudi, R. Dhouib, H. Ibrahim, and M. Adda, "On Predictive Maintenance in Industry 4.0: Overview, Models, and Challenges", *Applied Sciences*, vol. 12, no. 16, 2022, doi: 10.3390/app12168081.

[6] T. Hastie, R. Tibshirani, and J. H. Friedman, *The elements of statistical learning: data mining, inference, and prediction*, 2nd ed. New York: Springer, c2009.

Kde nás najdete

e·on

E.ON Energie, a.s.
F. A. Gerstnera 2151/6
370 01 České Budějovice

eon.cz/kariera

 E.ON Kariéra

eg·d

EG.D, s.r.o.
Lidická 1873/36
602 00 Brno

egd.cz/kariera

Tvořte s námi
energetickou budoucnost

eg·d

e·on

Jsme skupina E.ON, těší nás

Jsme jedním z největších energetických koncernů u nás i ve světě. Centrálu máme v Německu, ale najdete nás už v 15 zemích Evropy včetně České republiky. Zakládáme si na tom, že naše energie můžou šetřit peníze i přírodu a čím dál víc využíváme obnovitelné zdroje.

Kdo patří do naší rodiny

E.ON Energie, a.s.
- Obchoduje s elektřinou a plynem, zajišťuje marketing a komunikaci a stará se i o výrobu energií.
- Pro zákazníky připravuje řešení na míru v oblasti fotovoltaiky, tepelné techniky a elektromobility.

EG.D, s.r.o.
- Distributor elektřiny, který vlastní a provozuje rozvodnou síť zejména na jihu Čech a Moravy.
- Zajišťuje připojení odběrných míst k síti a stará se o dopravu energií k zákazníkům.

E.ON Česká republika, s.r.o.
- Funguje jako podpora výše uvedených společností. Zajišťuje jim služby, jako jsou účetnictví, právo nebo HR, a na starost má i zákaznickou péči.

Na přírodě nám záleží

E.ON Energie je jedničkou ve výkupu zelené elektřiny v České republice.

EG.D pomocí bezpečnostních prvků na sloupech vysokého napětí chrání ptáky před úrazem.

V budovách E.ONu i ve všech dobíječkách elektromobilů využíváme zelenou energii.

Kariéra u nás

Máme téměř 3 500 kolegů, kteří nám pomáhají neustále růst a zlepšovat se.

Všem nabízíme bezpečné zázemí, férové jednání a příjemné prostředí.

Jsme pravidelně oceňováni jako TOP ZAMĚSTNAVATEL.

Koho hledáme

- Místo u nás najdou lidé s praxí i čerství absolventi středních a vysokých škol.
- Potřebujeme techniky, ekonomy i nadšence do IT, marketingu nebo obchodu.
- Kanceláře máme v Českých Budějovicích, Brně a v Praze, ale pracovní místa nabízíme i v jiných městech.

eon.cz/kariera

egd.cz/kariera

Compression Techniques for 4D STEM Data in Electron Microscopy

1st Vít Šimeček
Department of Control and Instrumentation
Brno University of Technology
Brno, Czech Republic
vit.simecek@vut.cz

2nd Ondrej Mihálik
Department of Control and Instrumentation
Brno University of Technology
Brno, Czech Republic
ondrej.mihalik1@vut.cz

Abstract—**This paper explores compression techniques for 4D scanning transmission electron microscopy (STEM) data, aiming to find an optimal, use-case-independent compression approach. Standard image compression methods, including JPEG, PNG, and JPEG2000, are assessed and compared due to their ability to preserve the structural characteristics of the data. Additionally, a method based on Slepian two-dimensional sequences is proposed. It is conceptually similar to JPEG. The methods are evaluated based on compression ratio and data fidelity to identify an optimal format that maximizes data memory demands while minimizing information loss.**

Index Terms—**data compression, diffraction, DPSS, electron microscopy, image compression, Slepian sequences**

I. INTRODUCTION

This paper deals with the topic of data compression in electron microscopy. Nowadays, electron microscopy is an expanding and increasingly significant scientific discipline, essential for advancing research and innovation across multiple fields like semiconductor production, biomedical research and many others [1]. There is an expectation that electron microscopy will play even more important role in the future, caused by the rise of the nanotechnology and semiconductor sciences.

As electron microscopy can produce very large amount of data, in particular cases the compression is necessary. Since there is an abundance of data compression techniques, it is worth studying their suitability for this particular domain. A detailed comparison in terms of compression ration and data fidelity should enable selection of the optimal method.

The paper is organised as follows. Section II provides a brief introduction to scanning transmission electron microscopy followed by description of the acquired data is presented in Section III. Available standard data compression techniques are reviewed in Section IV and a novel method based on Slepian sequences is proposed in Section V. These methods are assessed and compared in Section VI, showing that JPEG2000 seems to be the most suitable method for storing the diffractogram data.

II. ELECTRON MICROSCOPY AND 4D STEM

In general, in the field of electron microscopes, there are two main types. **Scanning electron microscope (SEM)** relies on an electron beam that scans over the sample (in a predefined raster) and various detectors above and around the sample detect and characterize the signal generated during the beam-sample interaction.

Transmission electron microscope (TEM) requires a thin sample, and where the electron passes through the sample (the transmission occurs). Generally, on the detector below the sample, we obtain immediately the whole image of the sample. This, however, depends on the setting of the microscope and its electromagnetic lenses. TEMs provide better resolution, even subatomic, but are as well more sophisticated and expensive in terms of cost and material demands. [2], [3]

STEM microscopes or generally detectors (STEM detector might be used as an extension of a classical SEM microscope) combine the advantage of scanning and detection below the thin sample. This enables detecting diffraction patterns (diffractograms) below a crystal sample [4]. Traditionally STEM detectors have concentric parts and every part detects scattered electrons by a different angle. **4D STEM** enables diffraction maxima positioning thanks to the pixelated design of the detector (more at [5] in the chapter "Timepix"). This has many advantages, for instance crystal orientations might be observable by this method. On the other hand, the data are in form of matrix of matrices - first is classical sample scanning raster (matrix) where every single pixel consists of the diffractogram matrix. This leads to a 4D data matrix, which gave the name to the method, 4D STEM.

III. 4D STEM DATA FORMAT

4D STEM detector provides data of electron hits which can reach values up to 11,810 (14 bits) [5]. The raw data therefore have high memory demands, in range of gigabytes for a dataset of 100×100 pixels. For example for the purpose of data sharing, compression is necessary.

There are many compression possibilities, such as data binning (downsampling the resolution of the diffractogram), quantization or sparse representation of the raw values, storing the peak coordinates and their intensities, etc. This paper covers the area of compressing original diffractograms without any technique mentioned earlier, as those techniques can further improve the compression ratio when applied.

IV. STANDARD DATA COMPRESSION TECHNIQUES

Suitable methods are those used in the computer graphics, as storing the 4D STEM data as diffractogram images respects the character of the 4D data. Both lossy and lossless methods were used. Evaluated were following image formats:

- JPEG - uses image tiling into blocks discrete cosine transform, dynamic quantization dependent on frequency of the component and chromatic information reduction, lossy [6]. In the paper was used the JPEG with quality parameter "Maximum" [7] with quantization table illustrated in the Table I.
- JPEG2000 - wavelet based image compression format, enables lossless and lossy compression. The lossy variant varies from the lossless only by the used data type which introduces quantization noise caused by the rounding. [8]
- PNG - lossless format using DEFLATE [9]

We propose, design and evaluate two additional methods:

- Slepian sequence based JPEG: similar method to JPEG using Slepian sequences, also called Discrete Prolate Spheroidal Sequences (DPSS) [11], instead of the discrete cosine base. Lossy method. Further description below.
- Dynamic data quantization (insitu method) - this method enables on detector compression (bit reduction) using elemetary operations during the coding executable on the FPGAs. Lossy method. Further description in [10]. For the purpose of algorithm evaluation, we expected the format using 7 bits leading to 50 % compression ratio.

V. DPSS BASED IMAGE COMPRESSION

A. Slepian two-dimensional base

Slepian sequences have many signal processing applications, such as signal extrapolation or spectral super-resolution [12], and have generally compressing potential which was demonstrated on a collection of one-dimensional data [13]. Therefore, a JPEG similar image compression was tested on the diffractogram data in purpose to verify whether the method can reach better quality or higher compression ratio than a classical discrete cosine transform. The proposed method was implemented using the SciPy library [14]. As this format has many parameters that can be tested and tuned, in this paper only the basic 8×8 base with the parameter $NW = 2.5$ was used. The basis is derived as a product of one-dimensional sequences (Fig. 1) both in x and y axis, and illustrated in the Fig. 2 for the first 8 sequences (out of 64).

B. Comparison with JPEG

Both compression method were using the same quantization table for the comparison. However, as can be seen in Fig. 3, the Slepian method has larger odd coefficients. However, the odds are only slightly higher (2-6 times), which restricts the space for an improvement by optimizing the quantization table.
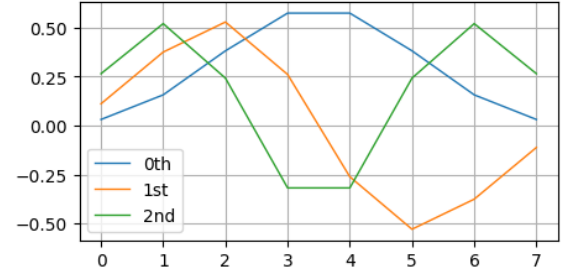
Fig. 1. First three Slepian sequences of the one-dimensional base of the length 8 (similarity with JPEG compression). Note that values are valid only in discrete points as the base is discrete.
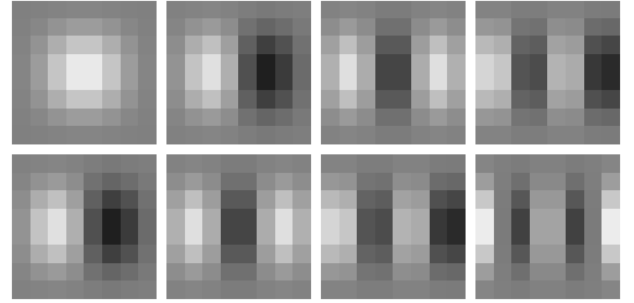
Fig. 2. Slepian base for Slepian based JPEG, first 8 functions as a product of the 0th y axis sequence and all the x-axis sequences. Whole base consists total of 64 functions.
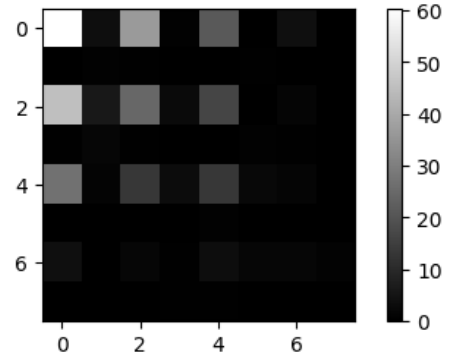
Fig. 3. Average 8×8 tile coefficients

As can be seen in the Fig. 2, Slepian base has no offset function. This was corrected by subtracting and storing the minimal value of the 8×8 tile in a modified algorithm, which uses following improvements:

- subtract minimal value of the 8×8 tile (during decompression is again added)
- use modified quantization table with respect to the average coefficients (see below)
- after the decompression, subtract average decompressed tile from all others - this reduces the noise introduced by the compression

TABLE I
USED JPEG QUANTIZATION TABLE.

	A	B	C	D	E	F	G	H
a	2	2	2	2	3	4	5	6
b	2	2	2	2	3	4	5	6
c	2	2	2	2	4	5	7	9
d	2	2	2	4	5	7	9	12
e	3	3	4	5	8	10	12	12
f	4	4	5	7	10	12	12	12
g	5	5	7	9	12	12	12	12
h	6	6	9	12	12	12	12	12

The modified table is created by swapping the A-D columns to odd positions (A, C, E, G) and E-H to even positions (B, D, F, H). The same applies to rows a-d and e-h. The resulting table respects the average coefficients from the Fig. 3.

TABLE II
MODIFIED QUANTIZATION TABLE FOR SLEPIAN.

	A	B	C	D	E	F	G	H
a	2	3	2	4	2	5	2	6
b	3	8	3	10	4	12	5	12
c	2	3	2	4	2	5	2	6
d	4	10	4	12	5	12	7	12
e	2	4	2	5	2	7	2	9
f	5	12	5	12	7	12	9	12
g	2	5	2	7	2	9	4	12
h	6	12	6	12	9	12	12	12

This modified algorithm is illustrated in the Fig. 4 and used in the following sections. Overall even after the modification, the Slepian method seems to be more noisy than classical JPEG. Since it is a proposed new format with many variables to be tuned, it was not compared in terms of compression ratio, but more evaluated with JPEG in following sections.
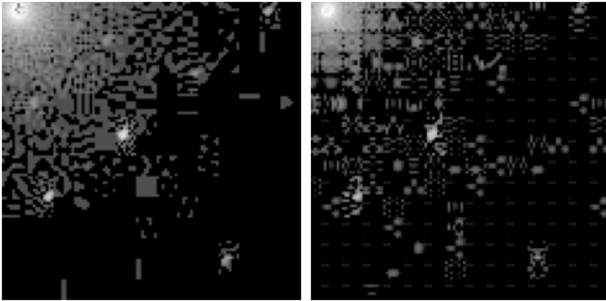
Fig. 4.   JPEG (left) and Slepian compression method (right) used on a diffractogram. Diffractograms are shown in a logarithmic scale.

VI. COMPRESSION EVALUATION

In this study, graphene samples with two crystal orientations (see Fig. 5) were used to collect 4D STEM dataset.

The grid size is 120×160 in real domain, where every single pixel consist of a diffractogram (256×256). This leads to four-dimensional dataset which has $120 \times 160 \times 256 \times 256$ pixels and accounts for 2.34 GB. The dataset was processed using the compression methods listed in Table III.
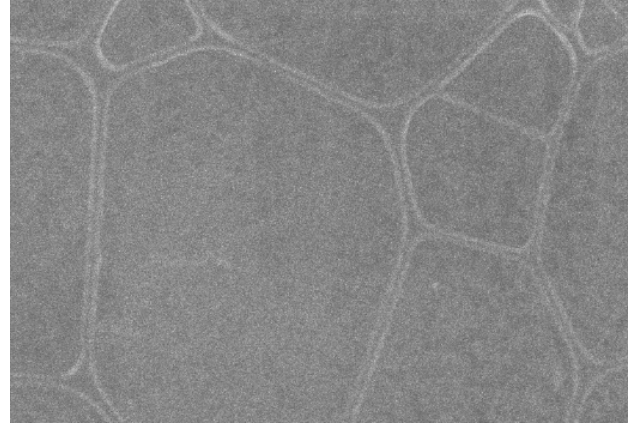
Fig. 5.   Graphene membrane on carbon support net, SEM image.

A. Compression ratios

The compression ratio was calculated using the standard formula:

$$\text{compression ratio} = \frac{\text{compressed size}}{\text{original size}} \tag{1}$$

Obtained results are listed in the Table III.

TABLE III
COMPRESSION MEMORY RESULTS.

Method	Compessed size	Ratio	PSNR raw/sqrt
JPEG	29.8 MB	1,24 %	85/58
JPEG2000 lossy	84.6 MB	3,53 %	91/52
JPEG2000	177 MB	7,39 %	lossless
PNG	239 MB	9,97 %	lossless
(Insitu method)	1.17 GB	50.0 %	93/NA**
Slepian	1.20 GB*	51.3* %	78/45

Explanation:
* Slepian method is JPEG based, but in this paper is not memory-optimized (no further coding algorithm like LZ77 or similar is used, slepian coefficients are stored as a uint8 matrices leading to the value of 1.20 GB).

** Insitu method is considered as an on-detector method using only FPGAs to compress, therefore calculation square-rooted data is not in place.

B. Data loss

Data loss was evaluated for the lossy methods: JPEG, JPEG2000 (lossy) and Slepian. The evaluation metrics was peak signal-to-noise ratio (PSNR) metrics:

$$\text{PSNR} = 10 \log_{10} \left(\frac{I_\text{m}^2}{\text{MSE}} \right) \tag{2}$$

where $I_\text{m} = 11,810$ stands for the highest possible detector output (pixel value) and the mean squared error (MSE) is defined by the following equation:

$$\text{MSE} = \frac{1}{MN} \sum_{i=1}^{N} \sum_{j=1}^{M} [f(i,j) - g(i,j)]^2 \tag{3}$$

Here, $f(i, j)$ is the original image and $g(i, j)$ is the compressed image of dimensions $M \times N$ [15]. PSNRs of individual compression methods are listed in the Table III.

In this particular case, JPEG2000 in the lossy variant decreases the memory demands twice and has satisfying PSNR.

For image formats which brightness levels can not cover the range of detected electrons (like JPEG or Slepian with the maximum brightness level of 255) additional information about the highest value detected was stored, diffractogram was then normalized to the range of the format (in consequence, this introduced an additional quantization noise).

C. Storing squared data

Even if it is not the main topic of this paper, storing the logarithm or square root of the data, rather than the raw values, can be a beneficial approach that offers several advantages, particularly due to the approximately exponential decrease in the detected values from the center of the diffractogram to the edges.

As in the raw image, the higher order maxima disappear in the noise (and can reach only a few brightness levels), for the evaluation, the PSNR was calculated on square root data, where are higher order maxima enhanced.

In Table III, the PSNR column lists values for both the standard approach (raw) and square root approach (sqrt). The latter amplifies not only the higher order maxima, but also the noise in the image, which leads to a lower PSNR. However, with this approach, Slepian reaches similar accuracy as JPEG2000, which makes it a method to consider for further investigation. Surprisingly, the JPEG reaches the best result when storing the square-rooted data, which is caused probably by the noise amplification in compared formats. Therefore, another method might be proposed to evaluate square-rooted data in further research.

VII. Conclusion

In general, based on our evaluation, JPEG2000 is the recommended image format for storing or sharing diffractograms, because it enables lossless compression, and introduces only a slight quantization noise in the lossy variant. In general, lossy formats (JPEG, lossy JPEG2000), exhibit better compression ratio than lossless methods (JPEG2000, PNG), but their use depends on the use case (whether the possible data loss is acceptable or not).

The Slepian-based format seems to be a good option for further investigation, especially because it has PSNR in the same range as JPEG2000 when using the pre-processed data by square rooting. The coding algorithms, such as the LZ77, should be investigated in combination with this method to better quantify its compression capabilities.

Also, there are many other possible compression methods, for instance storing the diffractograms as a video (but disabling approaching single diffractogram in a constant time), or many use case dependent methods. For instance, it may be worth considering storing the maxima coordinates and accumulated electron hits around them (losing information about the background), or other similar options. Electron microscopy is still an emerging scientific discipline; therefore, there is expectation that some use-case-dependent methods will be discovered and advanced in the future.

References

[1] Zhao, J., Zhou, H., Huang, W., et al. (2020). "Cell morphological analysis of SARS-CoV-2 infection by transmission electron microscopy." Journal Of Thoracic Disease, 12(8), 4368-4373. doi:10.21037/jtd-20-1368

[2] J. Goldstein, D. E. Newbury, J. R. Michael, N. W. M. Ritchie, J. H. J. Scott, and D. C. Joy, Scanning electron microscopy and X-ray microanalysis, Fourth edition. New York: Springer, 2018.

[3] R. F. Egerton, Physical Principles of Electron Microscopy: An Introduction to TEM, SEM, and AEM, Second edition. Cham: Springer Nature, 2016.

[4] A. V. Crewe, J. Wall, and L. M. Welter, "A high-resolution scanning transmission electron microscope", Journal of Applied Physics, vol. 39, no. 13, pp. 5861 - 5868, 1968.

[5] "The Timepix Chip", 2025. [online] Available from: https://medipix.web.cern.ch/medipix2 (accessed March 12th 2025)

[6] M. Ghanbari, Standard Codecs: Image Compression to Advanced Video Coding, Second edition. London: The Institution of Electrical Engineers, 2003.

[7] "Pillow (PIL Fork) 11.0.0 documentation: JpegPresets Module", 2024. [online] Available from: https://pillow.readthedocs.io/en/stable/reference/JpegPresets.html (accessed November 11th 2024).

[8] T. Acharya and P. -S. Tsai, JPEG2000 Standard for Image Compression. John Wiley, 2005.

[9] "Portable Network Graphics (PNG) Specification (Third Edition)", 2024. [online] Available from: https://www.w3.org/TR/png/#4Concepts. Encoding (accessed March 10th 2025).

[10] P. Huang, M. Du, M. Hammer, A. Miceli, and C. Jacobsen, "Fast digital lossy compression for X-ray ptychographic data", Journal of Synchrotron Radiation, vol. 28, no. 1, pp. 292-300, 2020.

[11] D. Slepian, "Prolate spheroidal wave functions, Fourier analysis and uncertainty - IV: Extensions to many dimensions; generalized prolate spheroidal functions", Bell System Technical Journal, vol. 43, no. 6, pp. 3009–3057, 1964.

[12] O. Mihálik, D. Michalík, P. Jura and P. Fiedler, "Spectral Super-Resolution and Band-Limited Extrapolation Using Slepian Series". In 16th IFAC Conference on Programmable Devices and Embedded Systems – PDeS 2019. IFAC-PapersOnLine (ELSEVIER). 52. IFAC, 2019. s. 388-393. ISSN: 2405-8963.

[13] V. Šimeček and O. Mihálik, "Compression of Vehicle-Driving Data by Means of Orthogonal Bases", in Proceedings II of the 29st Conference STUDENT EEICT 2023: Selected papers, 2023, pp. 13-16.

[14] "SciPy dpss", 2025. [online] Available from: https://docs.scipy.org/doc/scipy/reference/generated/scipy.signal.windows.dpss.html (accessed March 10th 2025).

[15] A. Horé and D. Ziou, "Image Quality Metrics: PSNR vs. SSIM," 2010 20th International Conference on Pattern Recognition, Istanbul, Turkey, 2010, pp. 2366-2369, doi: 10.1109/ICPR.2010.579.

Application of Neural Networks in Cardiovascular Load Analysis

1st Oliver Jaroš

Department of Biomedical Engineering
Brno University of Technology, FEEC
Brno, Czech Republic
226391@vutbr.cz

2nd Oto Janoušek

Department of Biomedical Engineering
Brno University of Technology, FEEC
Brno, Czech Republic
janouseko@vut.cz

Abstract—**This study investigates deep learning models for estimating aerobic (AeT) and anaerobic (AnT) thresholds using heart rate variability (HRV) analysis. Two CNN-LSTM architectures were developed: one predicting AeT and AnT values directly and another using signal delineation for enhanced threshold identification. The models were trained on HRV data from 119 subjects performing treadmill or cycle ergometer tests, with DFA alpha 1 used for threshold estimation. Performance evaluation showed an MAE of 4.67 bpm for AeT and 4.70 bpm for AnT in the first model, while the second model achieved 6.47 bpm for AeT and 3.15 bpm for AnT. Both models outperformed traditional DFA a1-based methods, with the second model demonstrating greater consistency in AnT detection. These results highlight the potential of deep learning for non-invasive endurance training optimization and cardiovascular monitoring.**

Index Terms—**Heart rate variability, Detrended Fluctuation Analysis, Aerobic, Anaerobic, Neural networks**

I. INTRODUCTION

Cardiovascular load is a key factor in determining athletic performance and physical fitness. The identification of physiological thresholds is crucial for sports diagnostics and performance training. The classical three-zone training model defines the aerobic threshold (AeT) as the transition from the first to the second training zone, while the anaerobic threshold (AnT) marks the transition from the second to the third [1]. Accurate determination of these thresholds allows for optimized training strategies, enhancing performance and reducing the risk of overtraining. Traditional methods include lactate (LT1, LT2) and ventilatory threshold (VT1, VT2) assessments, which require invasive procedures and specialized laboratory equipment [2].

Recently, heart rate variability (HRV) analysis has emerged as a non-invasive tool for assessing cardiovascular autonomic regulation. One promising method is *Detrended Fluctuation Analysis* (DFA), which evaluates heart rate complexity and fluctuations, supported by studies from T. Gronwald and B. Rogers [2]. The DFA α_1 parameter is calculated as the slope of the log-log regression of fluctuation amplitude versus window length. As exercise intensity increases, α_1 decreases—from 0.75 to 1.0 in the aerobic zone to below 0.5 in the anaerobic zone [1]. Research confirms a strong correlation between DFA α_1 reduction and AeT and AnT values, with Pearson's correlation coefficients of $r = 0.87, p < 0.001$ for AeT and $r = 0.90, p < 0.001$ for AnT [3].

HRV artifacts significantly impact DFA α_1 accuracy, with an artifact level of 3 % causing minor deviations and artifact level of 6 % increasing error rates by up to 19 %, depending on the correction method applied [4]. However, deviations in AeT and AnT detection remain within ± 5 bpm, highlighting the robustness of this approach. Techniques such as linear or cubic interpolation can substantially improve precision in AeT and AnT estimation [2]. These findings emphasize the importance of proper data processing in enhancing DFA α_1 reliability for practical applications.

This non-invasive method is applicable in real time, which is valuable for training. However, individual variability remains a challenge, requiring further methodological improvements [3]. This paper focuses on training neural networks to refine physiological threshold detection using the DFA α_1 method. To the best of our knowledge, this is the first study to apply CNN-LSTM neural network architectures specifically trained on DFA α_1 fluctuations for the estimation of both aerobic and anaerobic thresholds from HRV data.

II. MATERIALS AND METHODS

A. Data Collection

The data used in this study were collected during incremental lactate threshold tests at the accredited sports diagnostics center 'Rehordiagnostics'. All subjects participated in the study, undergoing treadmill or cycle ergometer stress tests while recording heart rate variability (HRV), oxygen consumption (VO2), and lactate concentration, from which annotations of aerobic and anaerobic thresholds were determined. Each subject underwent one or two test sessions. A total of 119 subjects (70.6% male, avg. age 25.3 years) completed one or two test sessions. The participants underwent different testing modalities, with 57.1% performing the exercise test on a cycle ergometer and 42.9% on a treadmill. During the incremental lactate threshold tests, heart rate variability (HRV) was recorded using the Polar H10 chest strap by Polar Electro Oy (Kempele, Finland). The study protocol was approved by the institutional ethics committee at the Rehordiagnostics center. All participants provided written informed consent prior to participation.

B. Testing protocol

Each subject underwent a stepwise incremental exercise test designed to assess the cardiovascular response to increasing workload. The test consisted of:

1) **Warm-up phase:** 5 minutes of low-intensity activity to establish baseline HRV values.
2) **Incremental load phase:** The subject performed 6-minute workload intervals, with 1-minute breaks for capillary blood sampling from the earlobe to measure lactate concentration at the midpoint and end of each interval. The intensity was increased at predefined intervals until voluntary exhaustion or reaching predefined physiological markers (e.g., respiratory exchange ratio > 1.1, maximal perceived exertion).
3) **Cool-down phase:** Gradual decrease in intensity over 3–5 minutes to stabilize cardiovascular function.

C. Dataset pre-processing

As shown in Fig. 1, the preprocessing workflow involved multiple steps to ensure a reliable analysis of DFA α_1. Since the measurements followed a stepwise protocol, heart rate did not increase continuously due to workload reductions for lactate sampling. This caused fluctuations in DFA α_1 values, which could interfere with accurate threshold determination.

To address this, RR interval segments recorded during lactate sampling and the following minute were removed using ergometer power and treadmill speed data. This ensured that heart rate progressed smoothly, improving DFA α_1 calculation accuracy and threshold detection reliability.
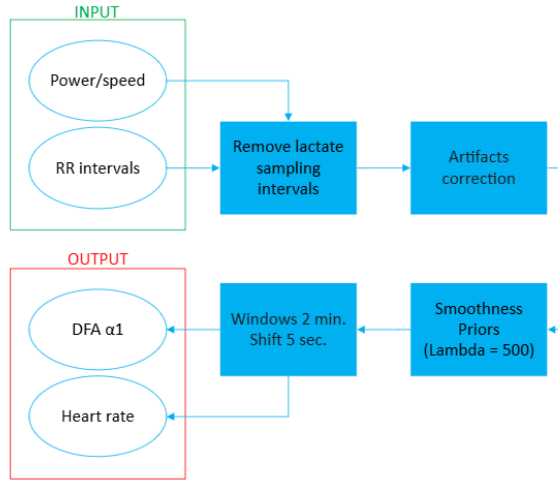

Fig. 1. Block diagram of RR interval preprocessing.

D. Artifact Correction

Artifacts in HRV data, such as ectopic beats, missing R-wave detections, and irregular RR intervals, can significantly impact DFA α_1 calculations. To minimize these distortions, an artifact correction method inspired by Kubios [5] was applied.

Artifact detection relied on two key parameters: the difference between consecutive RR intervals (dRRs) and deviations from the local median (mRRs):

$$dRRs_i = RR_{i+1} - RR_i \tag{1}$$

$$mRRs_i = RR_i - \text{median}(RR_{i-5}, \dots, RR_{i+5}) \tag{2}$$

Thresholds were determined based on statistical distributions of dRRs and mRRs, allowing the identification of abnormal beats. The detected artifacts were classified as ectopic beats, missing beats, or irregular RR intervals, and corrections were applied accordingly:

- Short and long RR intervals were interpolated using neighboring RR values to maintain physiological plausibility.
- Extra detected beats were removed by merging consecutive RR intervals.
- Missing beats were corrected by estimating an interpolated RR interval from adjacent values.

E. DFA α_1 calculation

To minimize the influence of slow non-stationary trends, a detrending process was applied to all RR interval time series using the *Smoothness Priors* method with a regularization parameter ($\lambda = 500$). This value was selected empirically to balance the suppression of low-frequency trends with the preservation of short-term HRV fluctuations essential for DFA α_1 estimation.

DFA α_1 was calculated using 2-minute overlapping time windows, updated every 5 seconds. This configuration was chosen based on previous studies [1], which demonstrated that 2-minute windows provide a reliable compromise between frequency resolution and temporal sensitivity, while 5-second updates maintain responsiveness to intensity changes during incremental testing. Each DFA α_1 value was paired with the corresponding heart rate, calculated as the average heart rate within ± 30 seconds from the window center.

III. MODEL IMPLEMENTATION

In this study, two neural network architectures were designed to enhance the detection of heart rate variability thresholds. Both models integrate convolutional neural networks (CNN) and long short-term memory (LSTM) networks, leveraging their combined ability to extract spatial and temporal features from DFA α_1 signals. The architectures of both models, as illustrated in Fig. 2, outline their respective configurations, input-output relationships, and layer progression.

A. Model 1: CNN-LSTM for AeT, AnT Prediction

The first model integrates convolutional neural networks (CNN) with long short-term memory (LSTM) networks, optimizing time-series processing for HRV analysis. Training was conducted over 110 epochs using the Adam optimizer and mean squared error (MSE) loss function, with a batch size of 16 and 10% validation data allocation. The batch size was selected to ensure a balance between training stability and
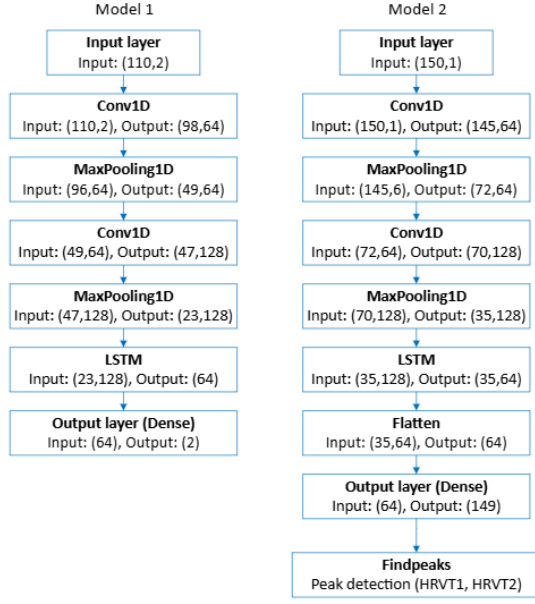
Fig. 2. Architecture diagram of 2 convolutional LSTM neural networks.

GPU memory efficiency. The number of epochs was determined based on preliminary convergence patterns, ensuring sufficient learning without overfitting.

B. Model 2: CNN-LSTM for Signal Delineation

The second model was designed to refine threshold identification by delineating the DFA α_1 signal. Unlike the first model, input data preprocessing involved sorting HR values in ascending order and averaging duplicate DFA α_1 values for the same HR to reduce variability. The input sequence was standardized to 150 samples, spanning HR values from 60 to 210 bpm, with missing values linearly interpolated to ensure signal continuity.

The output layer consists of 149 neurons with a sigmoid activation function, representing threshold probabilities across HR values. The Gaussian-smoothed target labels enhance prediction accuracy by reducing noise in threshold detection.
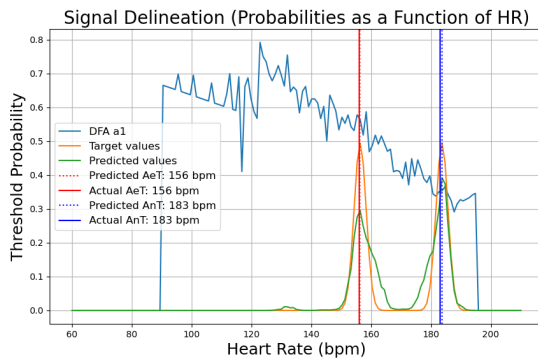
Fig. 3. Visualization of threshold detection from neural network output using delineations.

The model was trained over 200 epochs (batch size 16) using the Adam optimizer and binary cross-entropy loss. Binary cross-entropy was selected to reflect the probabilistic nature of the segmentation task, where the model learns to identify threshold locations across the HR axis. The extended training duration compared to Model 1 was necessary to allow the model to learn the more complex task of delineating threshold regions. Thresholds were identified using peak detection algorithms applied to the output probability distribution (Fig. 3).

IV. RESULTS AND DISCUSSION

After training, the models were tested on a test dataset (21 samples). Both models achieved relatively good results in threshold prediction, although in some signals, the predicted values deviated from the reference annotations.

Fig. 4 presents a comparison of annotated and predicted threshold values for both CNN-LSTM models. The plot includes predicted AeT and AnT values across all test samples, visualized alongside their annotated counterparts.
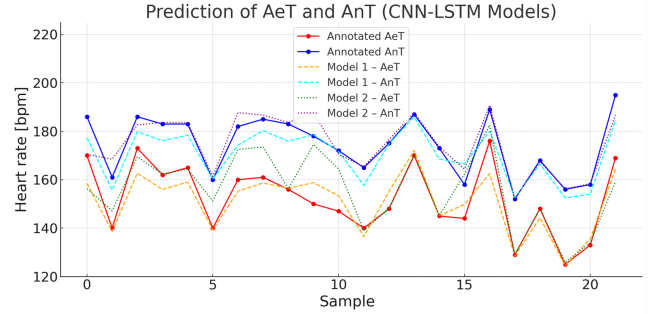
Fig. 4. Prediction of AeT and AnT thresholds for both CNN-LSTM models compared to annotated values.

The boxplot in Fig. 5 illustrates the absolute prediction errors for AeT and AnT for both models, highlighting the differences in accuracy and variability.
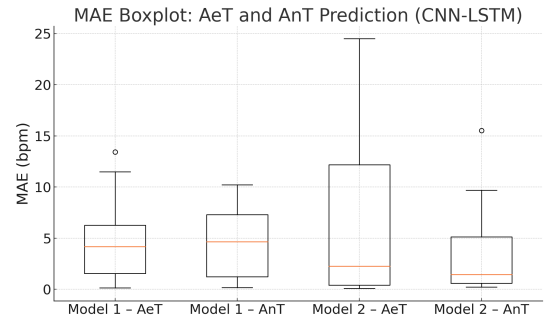
Fig. 5. MAE Boxplot: AeT and AnT Prediction (CNN-LSTM Models).

Tab. I summarizes the calculated metrics for both models, including mean absolute error (MAE) and median error for AeT and AnT predictions.

Both models demonstrated significant predictive capabilities in determining AeT and AnT thresholds. The analysis of

Metric [bpm]	Model 1		Model 2	
	AeT	*AnT*	*AeT*	*AnT*
MAE	4.67	4.70	6.47	3.15
Median Error	4.12	4.64	2.23	1.42

the first model revealed higher accuracy in AeT prediction; however, it exhibited greater variability compared to AnT. In certain cases, notable outliers were observed, likely due to the complexity of the input DFA α_1 signals or the lack of representative samples in the training dataset.

A Bland-Altman difference analysis indicated that the first model had a tendency to systematically underestimate AeT predictions by an average of -1.63 bpm and AnT by -3.76 bpm. In contrast, the second model, which incorporated signal segmentation and peak detection, demonstrated superior generalization and robustness. By smoothing the predicted probability distributions, this model mitigated abrupt fluctuations in DFA α_1 values, enabling more stable threshold identification. The Bland-Altman analysis further revealed that this model systematically underestimated only AeT, while maintaining greater accuracy in AnT detection.

Both models demonstrated improved performance compared to traditional DFA α_1 thresholding methods as reported in the literature [2]. Since our comparison is based solely on published results and not on direct application of DFA threshold cutoffs (e.g., 0.75 and 0.50) to our dataset, the signal conditions and preprocessing may differ. Therefore, this comparison serves primarily as a general performance reference and should be interpreted with caution. The integration of CNN layers facilitated the extraction of spatial features from DFA α_1 data, while LSTM components preserved sequential dependencies, effectively capturing the transitions between aerobic and anaerobic zones.

To validate the contribution of the LSTM layer, we trained reduced versions of both models using only CNN layers. In Model 1, removing the LSTM layer resulted in an increased MAE from 4.67 to 4.84 bpm for AeT and from 4.70 to 5.53 bpm for AnT. The effect was more pronounced in Model 2, where MAE increased from 6.47 to 10.84 bpm for AeT and from 3.15 to 9.22 bpm for AnT. These results confirm that the inclusion of LSTM layers substantially improved performance, particularly in the signal delineation model, by enabling better capture of temporal dependencies in the DFA α_1 signal.

The achieved MAE values ranging from 3.15 to 6.47 bpm are considered acceptable in practical endurance training applications. For example, heart rate zone boundaries typically span 10–15 bpm, and zone drift of ±5 bpm is often tolerated without negatively impacting training outcomes. Therefore, prediction errors in the 3–6 bpm range can be regarded as low and within the precision commonly accepted in applied sports diagnostics [6]. This level of accuracy supports the feasibility of implementing such neural network models in real-time threshold monitoring or training guidance systems.

V. CONCLUSION

This study investigated the use of deep learning models to estimate aerobic (AeT) and anaerobic (AnT) thresholds from heart rate variability (HRV) data. Two CNN-LSTM architectures were developed: one directly predicting AeT and AnT values and the other utilizing signal delineation to refine threshold identification.

The results demonstrated that both models effectively estimated physiological thresholds, with the second model showing greater consistency in AnT detection. The combination of CNN and LSTM layers improved feature extraction from DFA α_1 signals and captured temporal dependencies, leading to more robust threshold estimation. Compared to traditional DFA α_1 thresholding methods, the neural network models reduced prediction variability and enhanced accuracy.

Despite these advancements, some limitations remain, including inter-individual HRV variability and reliance on peak detection methods. Future work should focus on incorporating additional physiological parameters, such as VO2 and metabolic markers, to improve generalizability. Expanding the dataset with diverse athletic profiles and training intensities could further enhance model performance.

Overall, this study highlights the potential of machine learning for non-invasive sports diagnostics. With further refinement, deep learning models could provide a reliable tool for personalized training optimization and cardiovascular performance monitoring.

ACKNOWLEDGMENT

REFERENCES

[1] B. Rogers, D. Giles, N. Draper, O. Hoos, and T. Gronwald, "A new detection method defining the aerobic threshold for endurance exercise and training prescription based on fractal correlation properties of heart rate variability," Front. Physiol., vol. 11, 2021, doi: 10.3389/fphys.2020.596567.

[2] B. Rogers, D. Giles, N. Draper, L. Mourot, and T. Gronwald, "Influence of artefact correction and recording device type on the practical application of a non-linear heart rate variability biomarker for aerobic threshold determination," Sensors, vol. 21, no. 3, 2021, doi: 10.3390/s21030821.

[3] T. Gronwald and B. Rogers, "Fractal correlation properties of heart rate variability: a promising approach to quantify training-induced autonomic adaptations in endurance athletes?," Front. Physiol., vol. 11, 2020, doi: 10.3389/fphys.2020.567874.

[4] L. Mourot, "HRV analysis in sport: methodological considerations and practical applications," J. Sports Sci., vol. 39, no. 4, pp. 517–528, 2021, doi: 10.1080/02640414.2020.1859913.

[5] M. P. Tarvainen, P. O. Ranta-aho, and P. A. Karjalainen, "An advanced detrending method with application to HRV analysis," in Proc. 2002 IEEE EMBS Int. Conf. Biomed. Eng. Sci., 2002, pp. 177–180.

[6] T. Meyer, A. Lucia, C. P. Earnest, and W. Kindermann, "Power output during the Conconi test: what is Conconi's anaerobic threshold?," Int. J. Sports Med., vol. 26, no. 2, pp. 128–132, 2005, doi: 10.1055/s-2004-817862.

System for Measuring Directional Responses of Sound Sources

Benjamin Nimmerrichter
Dept. of Telecommunications, FEEC
Brno University of Technology
Brno, Czech Republic
xnimme00@vutbr.cz

Abstract—**This paper presents a MATLAB-based application for measuring the directional responses of sound sources and performing subsequent analysis. The system incorporates digital signal processing, microphone array calibration, and graphical representation of results. Additionally, an automatic calibration method utilizing an acoustic calibrator is introduced. The paper concludes with the presentation and discussion of measurement results obtained using the developed application.**

Index Terms—**acoustic measurements, directional response, frequency response, sound source analysis, digital signal processing, automatic acoustic calibration, microphone array calibration, spherical plot, fractional octave analysis, anechoic chamber.**

I. INTRODUCTION

Acoustic measurements are very important to today's society. They are used in modern electronic and automotive research and development. At Brno University of Technology, an anechoic chamber is employed for such measurements. To ensure optimal performance, the anechoic chamber must be isolated from the control room. Conducting measurements of sound sources using commercially available software has become increasingly impractical. Many applications support only single-microphone measurements, while others require manual calibration, where an acoustic calibrator is placed on the microphone in the anechoic chamber, and the user must return to the control room to initiate the calibration process. This process becomes time-consuming when a large number of microphones is used, reducing the efficiency of the measurement process. The application described in this paper supports an array of up to 64 microphones, this makes manual calibration time consuming, so it is necessary to introduce an automated calibration procedure. The application described is a dedicated application designed to address these challenges. It has the same name as the master's thesis associated with it. The application is called System for Measuring Directional Responses of Sound Sources (SMDRSS) for brevity and pronunciation purposes, the abbreviation is intended to be read as the name Smithers. The current implementation of the application is tailored for measuring loudspeakers as sound sources and is compatible with audio interfaces supporting a large number of input channels, such as MADI, AVB, and DANTE. It is designed for measurement with a single microphone or with microphone arrays. Future development aims to extend its capabilities to include the measurement of musical instruments, incorporating automated onset detection.

Acoustic measurements are inherently prone to errors. For instance, the addition of a measurement microphone into the anechoic chamber requires a mounting solution, such as an arm which can introduce acoustic reflections into the microphone, thereby skewing the results. Additionally, the measurement system exhibits various non-linearities. The non-linearities can stem from analog-to-digital and digital-to-analog converters, air transmission, and the movement of speaker and microphone membranes. These non-linearities must be considered because many conventional signal processing techniques assume a linear system [1].

The application described in this paper enables the measurement of two-dimensional (2D) and three-dimensional (3D) directional responses, as well as the frequency response of the system at each measurement point. The primary measurement signal used is a one-second exponential sweep. However, the software is flexible and allows for the use of any measurement signal, supplied as a linear pulse code modulation (LPCM) wave file.

II. DEFINING USED ALGORITHMS

A. Sound Pressure Level Calculation

The sound pressure level (SPL) is calculated using the root-mean-square (RMS) value of the signal captured by the microphone. The RMS value is computed in the discrete time domain using samples of the measured signal. The sound pressure level in dB(SPL) is then determined using the ratio of the RMS value obtained with an acoustic calibrator to the RMS value of the measured signal. The acoustic calibrator used in this study generates a 1000 Hz tone at 94 dB(SPL). The reference pressure for dB(SPL) is 20 μPa, which corresponds to the threshold of human hearing for a 1 kHz sinusoidal tone [1].

B. Automated Calibration Using Autocorrelation

The automated calibration process is a key feature that significantly reduces calibration time. Most software implementations require the user to place an acoustic calibrator on each microphone and manually initiate calibration each time in the software. In contrast, the proposed approach automatically detects the frequency and level of the calibration tone. The level detection is achieved by calculating the RMS value of each buffer. If the level exceeds -40 dB(FS), the

autocorrelation algorithm is used to detect the frequency. If the level does not exceed -40 dB(FS) the signal is ignored. This reduces the risk of false frequency detection, which could trigger calibration. In addition the calibration tone using any calibration tool will always be the dominating one, especially in the anechoic chamber, this improves the accuracy of the used frequency detection algorithm. A test recording was measured to prove the viability of the process (see Fig. 1)
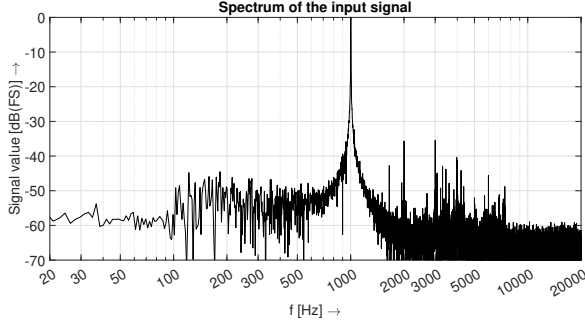

Fig. 1. Spectrum of the recorded test signal

The frequency detection is performed using the autocorrelation algorithm. First, the autocorrelation formula (1) is applied to the signal [2]:

$$R_{\mathrm{XX}}[n] = \sum_{\mathrm{m}=0}^{N-1} x[m] \cdot x[(m+n)_{\mathrm{mod}(N)}], \qquad (1)$$

where $x[m]$ is the input signal, n is the lag, and N is the signal length. The number of samples in the autocorrelation function is quite high, only several peaks are required to detect the frequency of the signal. To reduce computational requirements, the number of samples in the autocorrelation function is trimmed to include only the dominant peaks. The number of samples required to capture a specific number of peaks is given by:

$$N_{\mathrm{S}} = N_{\mathrm{P}} \cdot \frac{f_{\mathrm{S}}}{f_{\mathrm{E}}}, \qquad (2)$$

where N_{P} is the number of peaks, f_{S} is the sampling frequency, and f_{E} is the expected frequency of the calibration tone.

After trimming, the signal is normalized (see Fig. 2) and rectified by setting all samples with a value below zero to zero (see Fig. 3). The final step involves identifying local maxima and their positions, calculating the mean distance between peaks, and determining the frequency using:

$$f = \frac{f_{\mathrm{S}}}{\Delta N_{\mathrm{avg}}}, \qquad (3)$$

where f_{S} is the sampling rate and ΔN_{avg} is the average distance between peaks in samples.

The application reports ΔN_{avg} as 48 samples. Given a sampling rate f_{S} of 48 kHz (used for recording the test signal, as depicted in Fig. 1), the detected frequency f is 1000 Hz, as calculated using (3).

A circular buffer records the signal until calibration is complete. If the detected frequency f calculated using (3) matches the calibration frequency for a sufficient number of buffers (approximately 0.5 seconds), the RMS value of the recorded signal is used as the calibration constant. The 0.5-second recording duration ensures sufficient precision in the RMS calculation. This approach allows the user to remain in the anechoic chamber, calibrating each microphone sequentially or multiple microphones simultaneously using multiple calibrators.

Potential improvements include the use of a bandpass filter tuned to the calibration tone frequency before autocorrelation, which could enhance reliability in noisy environments. To clarify the filtered signal would not be used for the RMS calculation, it would be used for the frequency detection and the unprocessed signal would be used to calculate the RMS for the calibration constant.
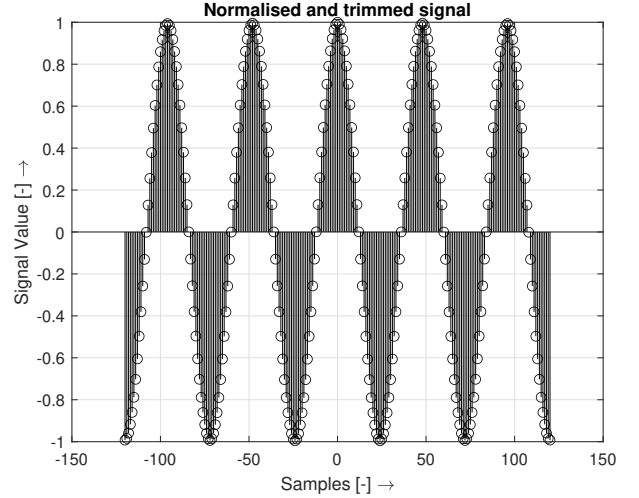
Fig. 2. Trimmed and normalised autocorrelation function of the recorded signal

C. Transfer Function Calculation

The transfer function is calculated using [2]:

$$H(\omega) = \frac{Y(\omega)}{X(\omega)}, \qquad (4)$$

where $X(\omega)$ represents the spectrum of the input signal (flowing into the system under analysis) and $Y(\omega)$ represents the spectrum of the output signal (flowing out of the analysed system). While this equation is precise for a linear system, using it for a non-linear systems introduces inaccuracies. The inaccuracies introduced in non-linear systems are minimal for this application, though they should still be considered.

III. Defining Measurements

A. Single Point Analysis

This measurement type is used to calculate and analyse the frequency response of the measured system using (4). The
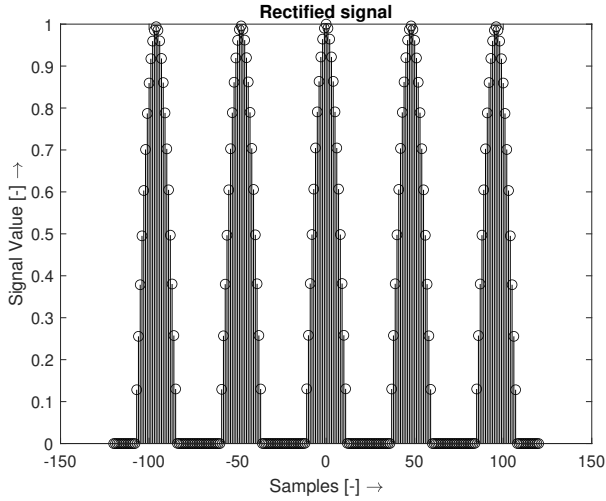
Fig. 3. Rectified autocorrelation function of the recorded signal

frequency response coefficients are subsequently utilized for fractional octave analysis. Fractional octave analysis subdivides the transfer function into octave bands, which can be used for further analysis. The most common fractional octave analysis is 1/3-octave analysis. The RMS value of the sound pressure level within each fractional octave band is computed using:

$$X_{\mathrm{RMS}} = \sqrt{\frac{4}{N} \sum_{k=0}^{N-1} X_k^2},$$ (5)

where X_k is the spectral coefficient and N is the signal length. The number four in the mean calculation needs to be added, because the value of the spectral coefficient X_k is one half of the signal amplitude, this means that the RMS value needs to be multiplied by two, and this two is moved into the square function to make it readable. For brevity, the fractional octave analysis is not demonstrated in this paper. However, (5) is employed to calculate the sound pressure levels for specific third-octave bands, which are used to generate the 2D and 3D directional responses of the measured system.

B. Directional Response

This measurement determines the sound pressure level as a function of the angle relative to the reference axis, using multiple measurement points. It can display 2D directional characteristics in either the horizontal or vertical plane using a polar plot, or 3D directional characteristics using a spherical plot. The directional characteristic is computed for a specific third-octave frequency band, following the guidelines outlined in [3]. In this measurement, 0 degrees of elevation and 0 degrees of azimuth correspond to the direction of the acoustic axis [4]. The directional response is modelled using the solution to the wave equation for a circular piston membrane [1], given by:

$$\eta(\varphi) = \left| \frac{2J_1(kR\sin(\varphi))}{kR\sin(\varphi)} \right|,$$ (6)

where φ is the azimuth angle, J_1 is the first-order Bessel function, k is the wavenumber, and R is the radius of the circular piston membrane. The wave number is calculated using:

$$k = \frac{2\pi f}{c_0},$$ (7)

where f is the frequency of vibration, and c_0 is the speed of sound in air.

IV. RESULTS

This section presents the measurement results obtained using the described measurement system. The equipment used includes:

- Measurement microphone
- Brüel & Kjær 9640 microphone turntable
- Brüel & Kjær NEXUS Conditioning Amplifier
- Computer running the SMDRSS application
- RME Digiface Dante and RME Micstacy audio interfaces
- EVENT Electronics ALP5 active speaker (see Fig. 4)

The measurement was conducted in six passes using a single microphone, rotated in 5-degree azimuth increments, resulting in 73 measurements per pass. The 73rd measurement was included to connect the first and last points of the polar plot. Alternatively, the first measurement can be duplicated as the 73rd point to enclose the plot. The choice between these approaches is left to user preference. These passes were performed at elevations of 0°, 5°, 10°, 20°, 30°, and 40°, with the microphone positioned 1 meter from the speaker's acoustic center [4]. This setup resulted in a total of 438 measurement points, ensuring sufficient spatial coverage for accurate directional response analysis.

Fig. 4. The EVENT Electronics ALP5 active speaker used as the sound source

A. Single Point Frequency Responses

Figures 7, and 8 show the frequency response of the measured system at different azimuths at 0-degree and 40-degree elevations. Higher frequencies exhibit greater directionality,

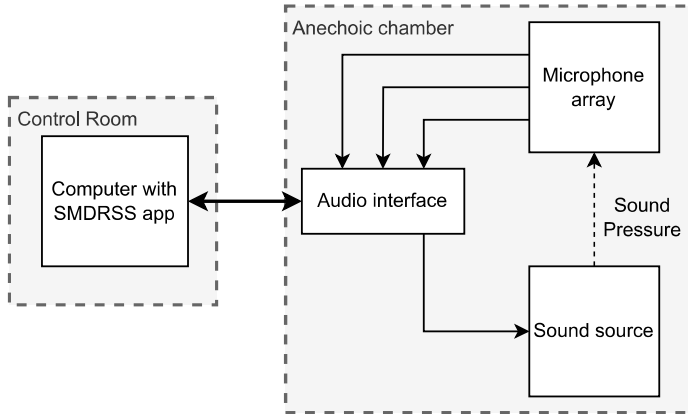Fig. 5. The measurement setup used to gather data for this paper

Fig. 6. Schematic of the signal flow and connections between devices during measurement

leading to a decrease in level as the angle from the acoustic axis increases.

B. Directional Responses in 2D

Figures 9, 10, and 11 present the measured directional responses, compared to a mathematical model, at an elevation of 0 degrees. The theoretical curves are based on the circular piston membrane model, as given by (6), where the radius corresponds to the respective speaker cone radii (in meters) for both the woofer and the tweeter. The plots also include the normalized RMS values of the measured sound pressure.

Figure 9 shows a measurement at a low frequency, where the speaker's crossover causes most of the sound to originate from the woofer, which has a cone diameter of 5 inches. The model does not account for the bass reflex port if the speaker enclosure, which introduces distortion in the shape of the response curve. Figure 10 represents a transitional frequency, where both the woofer and tweeter contribute to the output, resulting in a directional pattern that lies between their respective modelled responses. At higher frequencies, as shown in Figure 11, only the tweeter, with a cone diameter of 1.2 inches, is active.

Figures 12 and 13 show the directional response at 0-degree elevation, while Figure 14 depicts the response at a 40-degree elevation. The mentioned figures demonstrate the same directional effects observed in the frequency response measurements.

C. Directional Responses in 3D

This measurement utilizes all 438 recorded points to generate the 3D directional response. The 3D directional response is represented as a spherical plot, requiring azimuth, elevation, and sound pressure level as inputs. Figures 15 and 16 show the response at 15.85 kHz. In the mentioned figures, the coordinate center—which coincides with the acoustic center of the speaker—is marked with an 'X' and the acoustic axis is indicated by a dashed line in the top view.

V. CONCLUSION

This paper introduced the challenges associated with acoustic measurements, particularly those related to calibration in an anechoic chamber. The issues encountered during calibration were identified, and corresponding solutions were presented. Fundamental problems inherent to acoustic measurements were also discussed, alongside the introduction of a dedicated application designed to address these challenges.

Key algorithms for acoustic measurements, including sound pressure level calculation and transfer function computation, were defined. Manual calibration of a microphone array typically takes 10 to 15 seconds per microphone. In contrast, the automated method proposed in this paper reduces the calibration time to approximately 2 seconds per microphone. Moreover, the operator no longer needs to exit the chamber after calibrating each microphone; instead, the entire array can be calibrated before leaving. These improvements significantly reduce both the time and effort required for the calibration process.

The measurement types employed in this study—single-point analysis, 2D directional response, and 3D directional response—were outlined, demonstrating the versatility of the proposed system. The results of these measurements were presented and analysed, highlighting the system's effectiveness in capturing detailed acoustic characteristics.

The proposed system streamlines the calibration process, enabling researchers to focus on measurement procedures rather than manual calibration tasks. By supporting a wide range of equipment and adaptable measurement scenarios, this application has the potential to accelerate advancements in acoustic research.
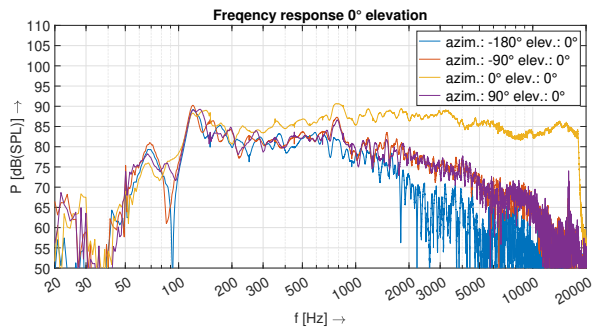
Fig. 7. Frequency response at different azimuths and an elevation of 0 degrees
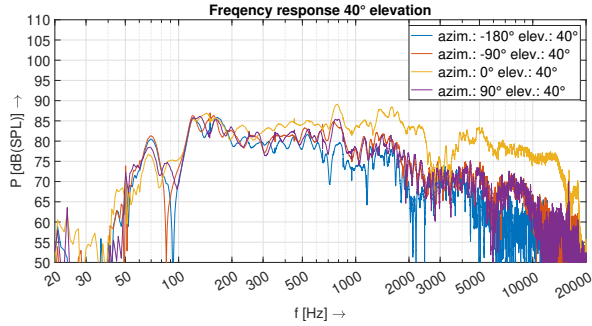
Fig. 8. Frequency response at different azimuths and an elevation of 40 degrees
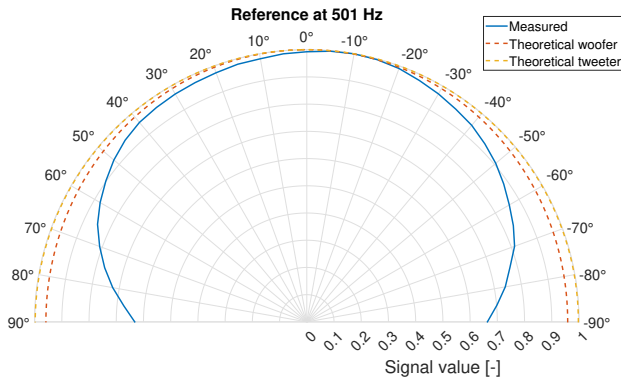
Fig. 9. Comparison of the theoretical and measured directional responses at 500 Hz
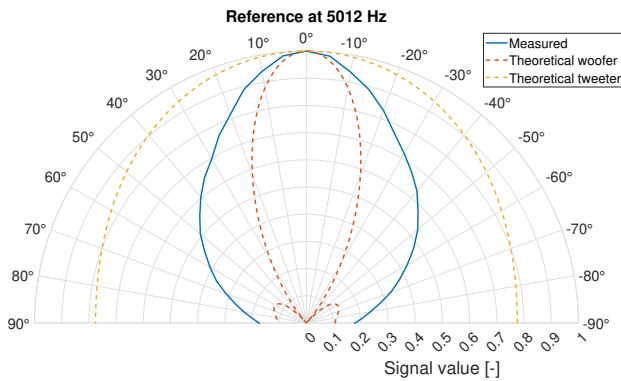
Fig. 10. Comparison of the theoretical and measured directional responses at 5000 Hz
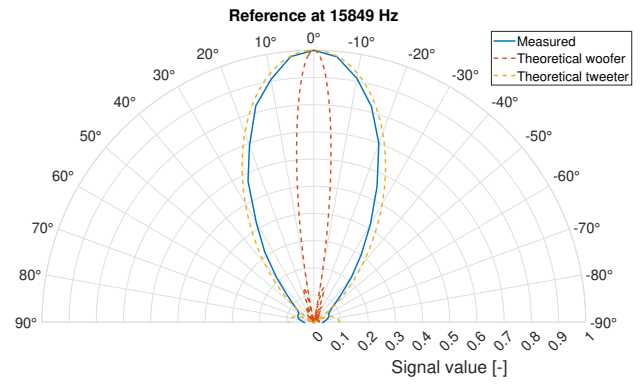
Fig. 11. Comparison of the theoretical and measured directional responses at 15000 Hz
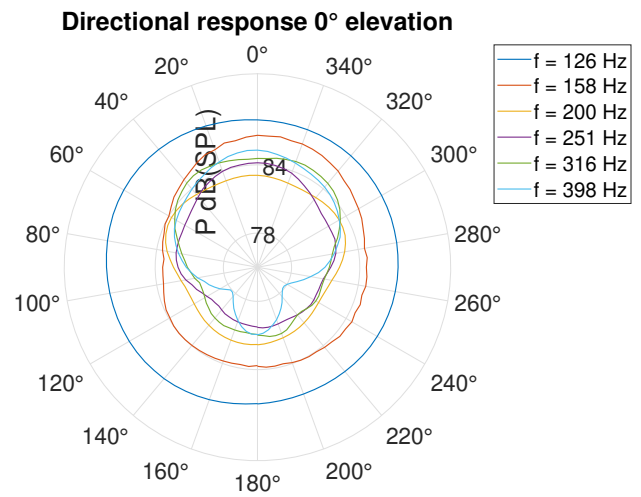
Fig. 12. Directional response of the measured system at low frequencies for a 0-degree elevation
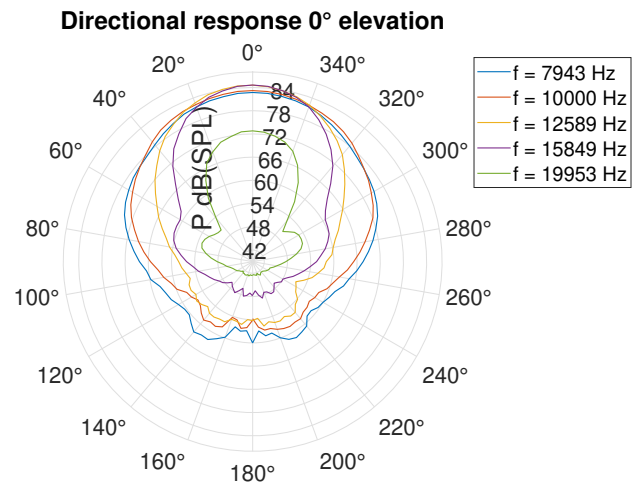
Fig. 13. Directional response of the measured system at high frequencies for a 0-degree elevation
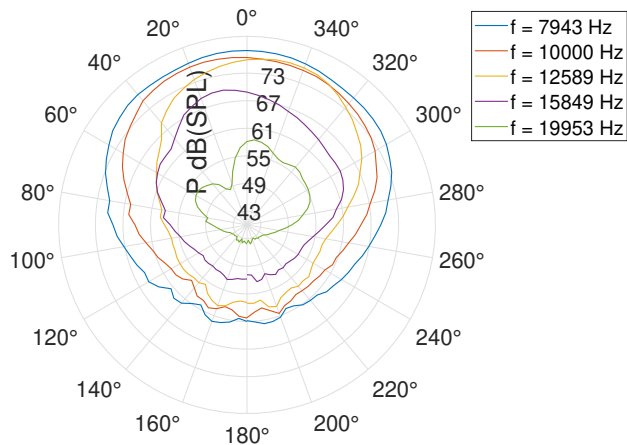
Fig. 14. Directional response of the measured system at high frequencies for a 40-degree elevation

REFERENCES

[1] KINSLER, Lawrence E., Austin R. FREY, Alan B. COPPENS, and James V. SANDERS. *Fundamentals of Acoustics.* 4th ed. New York: Wiley, 2000. ISBN 978-0-471-84789-2.

[2] MITRA, Sanjit Kumar and KAISER, James F. *Handbook for digital signal processing.* New York: John Wiley, 1993. ISBN 0-471-61995-7.

[3] "AES56-2008 (r2024): *AES standard on acoustics* - Sound source modeling - Loudspeaker polar radiation measurements"

[4] BRIXEN, Eddy Bøgh. *Audio metering: measurements, standards and practice.* Second edition. Audio engineering society presents. New York: Focal Press, Taylor & Francis Group, 2014. ISBN 978-0-240-81467-4.
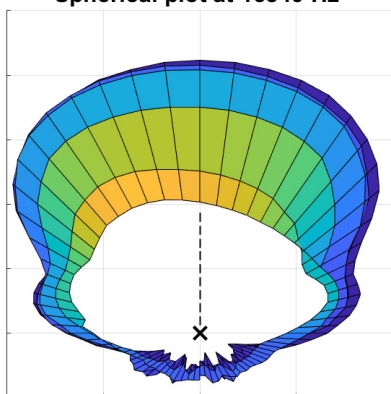
Fig. 15. Top view of the directional response of the measured system at 15849 Hz
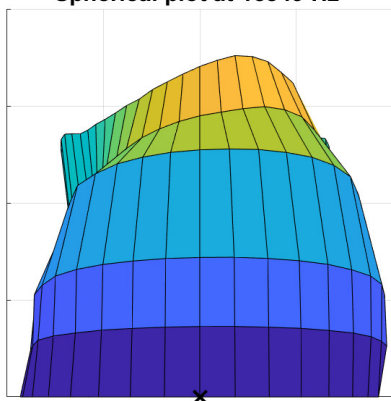
Fig. 16. Front view of the directional response of the measured system at 15849 Hz

Comparative Analysis of Pitch Detection Algorithms for Machine Learning Supported Parkinson's Disease Diagnosis

1st Richard Ladislav
Department of Telecomunications
Faculty of Electrical Engineering and Communication
Brno University of Technology, Brno, Czech Republic
230106@vut.cz

2nd Zoltán Galáž
Department of Telecomunications
Faculty of Electrical Engineering and Communication
Brno University of Technology, Brno, Czech Republic
galaz@vut.cz

Abstract—**Parkinson's disease (PD) is a progressive neurodegenerative disorder characterized by motor and non-motor symptoms, including hypokinetic dysarthria (HD), a speech disorder affecting prosody. Early detection of PD through speech analysis offers a promising, non-invasive diagnostic approach. This study evaluates five pitch detection algorithms—PRAAT, YIN, PYIN, RAPT, and SWIPE'—to extract fundamental frequency-based features from the PARCZ speech database. The extracted features, including relative F_0, standard deviation and various jitter measures, are used to train and evaluate three binary classifiers: Logistic Regression (LR), Support Vector Machine (SVM), and Random Forest (RF). The classifiers are optimized using a stratified cross-validation approach, with balanced accuracy as the primary metric. Results indicate that while pitch-based features alone are insufficient for clinically accurate PD diagnosis, certain classifiers and pitch detection methods show potential in aiding early detection. Future work should incorporate a broader set of speech parameters to enhance diagnostic precision.**

Index Terms—**Parkinson's disease, hypokinetic dysarthria, pitch tracking, fundamental frequency, jitter, machine learning, binary classification, speech analysis, PRAAT, YIN, PYIN, RAPT, SWIPE', logistic regression, support vector machine, random forest.**

I. Introduction

Parkinson's disease (PD) is one of the most widespread progressive neurodegenerative disorders in the world today. It is characterized by the rapid degeneration and loss of dopaminergic neurons in the *basal ganglia* [1], [2]. The symptomatology of Parkinson's disease consists of various primary motor symptoms, such as resting tremor, progressive bradykinesia, postural instability, and muscular rigidity, as well as non-motor symptoms, including gait freezing, dysphagia, and dysarthria, which is the primary focus of this study [3].

Conventional methods for diagnosing Parkinson's disease rely on evaluating developed motor symptoms; however, these symptoms typically appear in the third clinical stage of neurodegeneration, by which point up to 60 – 70% of dopaminergic neurons may already be damaged [4]. Promising supporting tools in PD assessment are novel paraclinical approaches that evaluate non-motor symptoms, which emerge in the early stages of PD. One of the most useful non-invasive methods involves digital signal processing to quantify speech pathologies associated with PD.

Hypokinetic dysarthria (HD) affects all subsystems of human speech production, including faciokinesis, phonation, articulation, speech fluency, prosody, and respiration [5], [6]. Among these subsystems, a wide variety of features can be extracted from voice recordings of patients to assess dysarthric speech. However, this study specifically focuses on evaluating prosodic features related to monopitch occurrence in PD patients.

In the task of estimating the fundamental frequency (F_0) of speech, various algorithms, collectively referred to as Pitch Detection Algorithms (PDAs), have been developed. When evaluating their performance, objectivity is typically ensured through one of two approaches. The first and more common method involves using artificially generated speech signals with a predefined F_0. The second, less frequently employed approach, relies on a ground-truth speech database in which the fundamental frequency is objectively determined via direct measurement of vocal fold vibrations using a laryngograph [17].

However, when assessing the performance of PDAs in patients with hypokinetic dysarthria, neither of these approaches can be reliably applied. Consequently, in this study, we adopt an alternative methodology in which the PARCZ speech database is directly analyzed by individual PDAs to extract input features for training binary classifiers.

II. Methodology

A. PARCZ Database

The *Czech Parkinsonian Speech Database* (PARCZ) is a speech corpus based on a speech acquisition protocol developed in collaboration with doc. Ing. Jiří Mekyska, Ph.D., and PhDr. Mgr. Milena Košťálová. The recordings were conducted at the First Department of Neurology at Faculty of Medicine at Masaryk University and St. Anne's Faculty Hospital. The database consists of recordings from 3F test

voice exercises performed by 100 patients at various stages of PD and 52 healthy control subjects of comparable age.

Before the recordings, all subjects underwent neurological, neuropsychological, and speech-language (logopedic) examinations. The speech sample files are labeled using an alphanumeric code. The format of the code is as follows: `NSxxx`, where `N` indicates the presence of Parkinson's disease (`P` for PD patients, `K` for control speakers), `S` denotes gender (1 - female, 2 - male), and `xxx` represents the sequence number. The demographics of the speech corpus speakers (Table I) and the technical/acoustic conditions of the recordings (Table II) are specified below [7].

All feature extractions performed by the evaluated algorithms in this paper were conducted using the PARCZ database.

TABLE I
DEMOGRAPHIC STATISTICS OF SPEAKERS

Subject	Count		Average age		Age range		STD of age	
	Men	Women	Men	Women	Men	Women	Men	Women
Control	26	26	65.58	61.81	49–83	45–87	8.90	9.05
Parkinson	60	40	66.28	69.98	46–87	49–86	8.63	7.74

TABLE II
TECHNICAL AND ACOUSTIC CONDITIONS OF VOICE RECORDINGS IN THE PARCZ DATABASE

Noise level in the room	less than 30 dB[a]
Acoustic treatment of the room	Flexi Wall panels by Viscoustic
Microphone	condenser microphone M-AUDIO NOVA
Distance of speaker from the microphone	approx. 20 cm
Sound card	M-AUDIO Fast Track
Sampling frequency	48 kHz

[a]Measured using the NTI Acoustilyzer AL1 acoustic analyzer.

B. Pitch Detection Algorithms

1) PRAAT: Parselmouth is a Python library that provides access to a wide variety of speech processing and phonetics tools from the PRAAT software via a Pythonic interface [8]. The original PRAAT software was developed by Paul Boersma [9] at the University of Amsterdam. It utilizes the autocorrelation of a signal divided into frames by a windowing function. Normalization of the autocorrelation is then performed by dividing it by the autocorrelation of the window function [10].

2) YIN: Pitch detection algorithm (PDA) developed by Alain de Cheveigné and Hideki Kawahara [12]. The name YIN comes from "yin and yang" as it combines autocorrelation and cancellation approaches. The core of the algorithm relies on the autocorrelation function, as defined in the equation below (1), and aims to overcome its tendency to bias towards multiples of the fundamental frequency F_0.

$$\sum_{j=t+1}^{t+W} (x_j - x_{j+T})^2 = 0 \tag{1}$$

The signal is modeled as a periodic function $d(\tau)$ of period T, enabling the use of cumulative mean normalization, absolute

thresholding, and parabolic interpolation as error-reduction steps. The best local estimation is then determined through medial smoothing of dynamic programming, with the selection process prioritizing quality rather than mere continuity.

3) PYIN: PDA proposed by Mathias Mauch and Simon Dixon [13] as a modification of the YIN algorithm. Its primary goal is to address the limitations of YIN, which estimates exactly one pitch candidate per frame, thereby disregarding alternative interpretations of the signal. PYIN overcomes this limitation by outputting multiple pitch candidates per frame, along with their associated probabilities derived from YIN's thresholding value. The final pitch track is then refined using a hidden Markov model.

4) RAPT: A Robust Algorithm for Pitch Tracking (RAPT) is a PDA proposed by David Talkin at the Entropic Research Laboratory [11]. It is based on the normalized cross-correlation function (NFCC), which can be described by the following equation (2).

$$\phi_{i,k} = \frac{\sum_{j=m}^{m+n-1} s[j]s[j+k]}{\sqrt{e_m e_{m+k}}}, \tag{2}$$

$$k = 0, \ldots, K-1; \quad m = iz; \quad i = 0, \ldots, M-1,$$

where

$$e_j = \sum_{i=j}^{j+n-1} s^2[j], \tag{3}$$

s is the signal of the audio sample, while *K* is the length of the cross-correlation at analysis frame *i* and lag *k*. $\phi_{i,k}$ tends to be close to 1 for integer multiples of the glottal cycle frequency, so pitch candidates are searched based on this property (first in subsampled, then in the original signal). The final pitch candidate is selected using dynamic programming [10].

5) SWIPE': It is an enhanced version of the Saw Wave Pitch Estimator algorithm, originally proposed by Arturo Camacho and John Gregory Harris [14]. The fundamental idea behind the SWIPE'[1] algorithm is to maximize the normalized inner product between the warped spectrum of the input signal and a predefined *kernel*. This *kernel* is constructed from the fundamental and prime harmonics of a sawtooth waveform. To reduce influence of subharmonics and improve pitch estimation accuracy, a weighting strategy is applied to the *kernel* harmonics.

C. Features

1) relF0SD: This speech feature is defined as the standard deviation of the fundamental frequency relative to its mean, representing variations in the frequency of vocal fold vibrations.

[1]Pronounced as SWIPE prime.

2) Jitter (RAP): This speech feature is defined as the average absolute difference between a period and its two closest neighbors, divided by the average period duration.

$$jitt(rap) = \frac{\frac{1}{N-1}\sum_{i=1}^{N-1}\left|T_i - \left(\frac{1}{3}\sum_{n=i-1}^{i+1}T_n\right)\right|}{\frac{1}{N}\sum_{i=1}^{N}T_i} \times 100, \quad (4)$$

where N is the total number of periods and T is the duration of a period in seconds [15], [16].

3) Jitter (PPQ5): The five-point Period Perturbation Quotient (PPQ5) is a speech feature defined as the average absolute difference between a period and its five closest neighbors, divided by the average period duration [15], [16].

$$jitt(ppq5) = \frac{\frac{1}{N-1}\sum_{i=2}^{N-2}\left|T_i - \left(\frac{1}{5}\sum_{n=i-2}^{i+2}T_n\right)\right|}{\frac{1}{N}\sum_{i=1}^{N}T_i} \times 100 \quad (5)$$

4) Jitter (PPQ11): The eleven-point Period Perturbation Quotient (PPQ11) is a speech feature defined as the average absolute difference between a period and its eleven closest neighbors, divided by the average period duration [15], [16].

$$jitt(ppq11) = \frac{\frac{1}{N-1}\sum_{i=6}^{N-6}\left|T_i - \left(\frac{1}{11}\sum_{n=i-5}^{i+5}T_n\right)\right|}{\frac{1}{N}\sum_{i=1}^{N}T_i} \times 100 \quad (6)$$

D. Description of Experiment

The experiment is carried out in two steps, explained in detail in the following subsections.

1) Feature Extraction and Dataset Creation: In the first phase of the experiment, speech features are extracted from the PARCZ speech corpus, and a labeled DataFrame is generated for training binary classifiers. For each PDA under evaluation, the extracred features (relF0SD, RAP, PPQ5, and PPQ11) are computed separately, resulting in distinct DataFrames (as shown in table Table III). This structure enables a comparative analysis of the performance of each PDA.

To facilitate this process, a dedicated Python script was developed. For PRAAT-based feature extraction, the `.to_Dist_sound()` function from the Parselmouth library [8] was used. For YIN and PYIN, the `.yin` and `.pyin` functions from the Librosa library were utilized. The pitch candidate search range was standardized between 75 Hz and 300 Hz for all PDAs, except for PRAAT, where this setting is not available in Parselmouth. For SWIPE', a threshold value of 0.3 was used, with signal normalization and a hop size of 0.005 times the sampling frequency, as recommended in the documentation. RAPT's voice bias parameter was set to 0, and its normalization and hop size settings were identical to those used for SWIPE'. Both algorithms used functions implemented in the PyTSPSK Python library. Binary labeling of patients in the dataset was dericws from the alphanumeric code in the filenames of the speech samples.

relF0SD	Jitter (RAP)	Jitter (PPQ5)	Jitter (PPQ11)	Label
⋮	⋮	⋮	⋮	⋮

2) Training and evaluation of binary classifer models: In the second phase of the experiment, three widely used binary classifiers were trained using the previously generated DataFrames. The selected classifiers include Logistic Regression (LR), Support Vector Machines (SVM) with a Radial Basis Function (RBF) kernel, and Random Forests (RF). Hyperparameter optimization for each classifier was conducted using a Grid Search algorithm to maximize classification performance.

Before training, all datasets were preprocessed to remove any potentially corrupted data. To ensure robust evaluation, Stratified K-Fold cross-validation was employed for partitioning the data into training and test sets, a necessary step given the relatively small dataset size. Cross-validation was selected to enhance generalization and mitigate overfitting.

All classifiers were trained with the objective of maximizing balanced accuracy to compensate for dataset imbalances and prevent bias toward the majority class. A dedicated Python script was developed for the training and evaluation process, with all machine learning components implemented using the Scikit-learn library. The results of this experiment are presented in the following section.

III. RESULTS

The numerical outcomes of the experiment are presented as a normalized confusion matrix (see Tab. VII–IX), Receiver Operating Characteristic (ROC) curves with their respective Area Under the Curve (AUC) values (see Fig. 1–5), accuracy, and feature importance[2] for classifier-PDA combination (Tab. IV).

For the RAPT PDA, the RF classifier demonstrates a marginal improvement in accuracy compared to the other models. However, all three binary classifiers tend to falsely label subjects as Parkinsonian, as indicated by the high sensitivity and low specificity values.

When evaluating the RAPT PDA, the RF classifier marginally outperforms the others in terms of accuracy. However, the issue of false-positive subject labeling is significantly more prevalent.

In terms of accuracy, binary classifiers trained on features extracted via the YIN PDA exhibit slightly lower accuracy overall. However, among all tested PDAs, YIN-based models achieve the most balanced sensitivity and specificity, suggesting improved classification stability.

Unexpectedly, classifiers trained on features obtained via the PYIN PDA underperform relative to those trained on YIN-derived features, despite PYIN being an extension of the YIN algorithm. This suggests that the modifications introduced in

[2]Feature importance is not listed for SVM, as the RBF kernel is used.

PYIN do not necessarily translate into enhanced classification performance in this context.

Finally, results obtained using the SWIPE' PDA closely resemble those of the RAPT and PRAAT algorithms, exhibiting a heavily imbalanced normalized confusion matrix. This further highlights the persistent challenge of false-positive misclassifications across multiple PDAs.

TABLE IV
ACCURACY AND FEATURE IMPORTANCE

	RAPT			PRAAT			YIN			PYIN			SWIPE'		
	LR	RF	SVM	LR	RF	SVM	LR	RF	SVM	LR	RF	SVM	LR	RF	SVM
Accuracy	0.5872	0.6140	0.617	0.623	0.621	0.617	0.5888	0.5892	0.5704	0.5760	0.5891	0.5689	0.5822	0.6001	0.5905
relF0SD	-0.027	0.260	-	0.225	0.300	-	0.320	0.269	-	0.205	0.268	-	-0.072	0.261	-
Jitt(RAP)	0.146	0.247	-	-0.470	0.217	-	-0.136	0.230	-	0.164	0.254	-	-0.374	0.239	-
Jitt(PPQ5)	0.246	0.241	-	0.376	0.233	-	-0.347	0.240	-	-0.308	0.245	-	0.984	0.246	-
Jitt(PPQ11)	-0.556	0.251	-	-0.261	0.250	-	-0.134	0.261	-	-0.143	0.232	-	-0.822	0.254	-
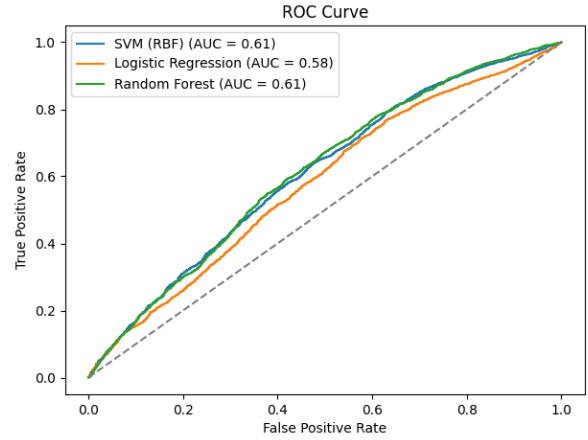
Fig. 1. PRAAT ROC curve.

TABLE V
PRAAT CONFUSSION MATRICES

	Predicted C	Predicted P
Actual C	0.36	0.64
Actual P	0.22	0.78

Logistic Regression

	Predicted C	Predicted P
Actual C	0.43	0.57
Actual P	0.26	0.74

Random Forest

	Predicted C	Predicted P
Actual C	0.41	0.59
Actual P	0.26	0.74

SVM

TABLE VI
RAPT CONFUSION MATRICES

	Predicted C	Predicted P
Actual C	0.46	0.54
Actual P	0.34	0.66

Logistic Regression

	Predicted C	Predicted P
Actual C	0.25	0.75
Actual P	0.18	0.82

Random Forest

	Predicted C	Predicted P
Actual C	0.38	0.62
Actual P	0.27	0.73

SVM

Fig. 2. RAPT ROC curve.

TABLE VII
YIN CONFUSION MATRICES

	Predicted C	Predicted P
Actual C	0.52	0.48
Actual P	0.38	0.62

Logistic Regression

	Predicted C	Predicted P
Actual C	0.53	0.47
Actual P	0.39	0.61

Random Forest

	Predicted C	Predicted P
Actual C	0.61	0.39
Actual P	0.45	0.55

SVM

TABLE VIII
PYIN CONFUSION MATRICES

	Predicted C	Predicted P
Actual C	0.48	0.52
Actual P	0.36	0.64

Logistic Regression

	Predicted C	Predicted P
Actual C	0.47	0.53
Actual P	0.34	0.66

Random Forest

	Predicted C	Predicted P
Actual C	0.56	0.44
Actual P	0.41	0.59

SVM

Fig. 3. YIN ROC curve.

TABLE IX
SWIPE' CONFUSION MATRICES

		Predicted C	Predicted P
Actual	C	0.48	0.52
	P	0.35	0.65

Logistic Regression

		Predicted C	Predicted P
Actual	C	0.28	0.72
	P	0.21	0.79

Random Forest

		Predicted C	Predicted P
Actual	C	0.37	0.63
	P	0.29	0.71

SVM

Fig. 4. PYIN ROC curve.

Fig. 5. SWIPE' ROC curve.

IV. CONCLUSION

Evaluating the symptomatology of hypokinetic dysarthria in patients affected by Parkinson's disease is a challenging task in contemporary medicine and telemedicine. As it has been shown, speech parameters can play a significant role in this diagnostic process. However, it cannot be expected that by using speech parameters describing the purely fundamental frequency F_0, we can predict with clinical accuracy the early stages of Parkinson's disease.

The symptomatology of HD is very complex and it is thus necessary to use a series of parameters describing all subsystems of human speech production. Despite using a dataset with a limited set of one-dimensional parameters, this study achieved a modest level of precision and balance. To improve diagnostic accuracy, it is essential to employ a more robust parameter set that comprehensively captures the full range of HD symptomatology.

Such a set should include dozens of diverse speech features. While the optimal combination of parameters is still the subject of ongoing research. [18] proposed a promising set of features. In addition to those used in this work, their set includes: the standard deviation of the squared energy operator (SEOSD), standard deviation of the Teager–Kaiser energy operator (TEOSD), harmonic-to-noise ratio (HNR), glottal-to-noise excitation ratio (GNE), and various speech rate disturbance metrics such as total pause time (TPT), total speech rate (TSR), and percent pause time (PPT). Other important features include the speech index of rhythmicity (SPIR), the first three formants along with their bandwidths and relative standard deviations (relF1SD, relF2SD), vowel space area (VSA), and vowel articulation index (VAI).

The primary objective of future research is to automate the extraction of such an extensive set of parameters and to develop efficient methods for their subsequent classification.

REFERENCES

[1] F. N. Emamzadeh and A. Surguchov, "Parkinson's disease: biomarkers, treatment, and risk factors," *Frontiers in Neuroscience*, vol. 12, p. 612, 2018.

[2] F. Cauteruccio, P. Lo Giudice, G. Terracina, D. Ursino, and N. Mammone *et al.*, "A new network-based approach to investigating neurological disorders," *Int. J. Data Mining, Modelling and Management*, vol. 11, no. 4, pp. 315–349, 2019.

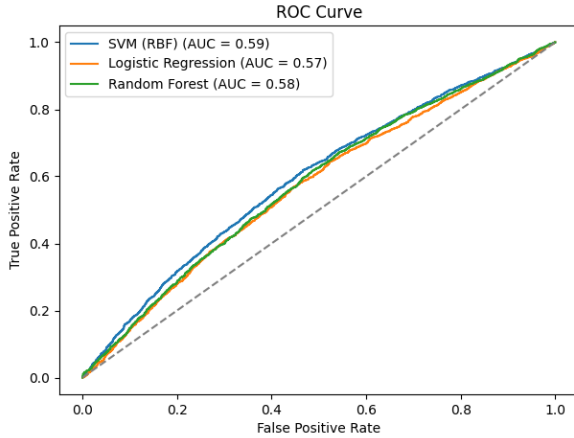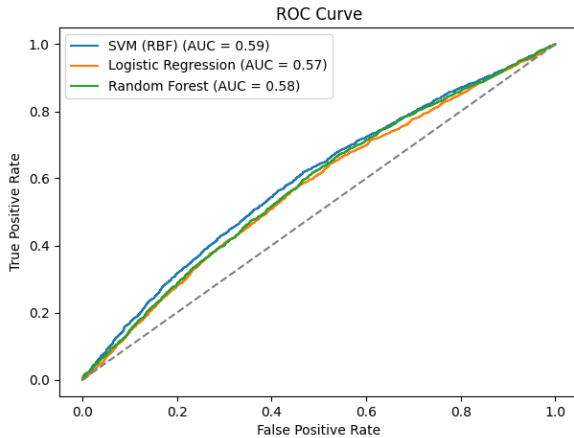[3] Z. Galáž, *Assessment of Parkinson's Disease Based on Acoustic Analysis of Hypokinetic Dysarthria*, Ph.D. dissertation, Brno University of Technology, Brno, 2018.

[4] H. Bernheimer, W. Birkmayer, O. Hornykiewicz, K. Jellinger, and F. Seitelberger, "Brain dopamine and the syndromes of Parkinson and Huntington: Clinical, morphological and neurochemical correlations," *J. Neurol. Sci.*, vol. 20, no. 4, pp. 415–455, 1973.

[5] L. Brabenec, J. Mekyska, Z. Galáž, and I. Rektorova, "Speech disorders in Parkinson's disease: Early diagnostics and effects of medication and brain stimulation," *J. Neural Transm.*, vol. 124, no. 3, pp. 303–334, 2017.

[6] F. L. Darley, A. E. Aronson, and J. R. Brown, "Differential diagnostic patterns of dysarthria," *J. Speech Hear. Res.*, vol. 12, no. 2, pp. 246–269, 1969.

[7] J. Mekyska, *Analysis of Speech Signals for the Purpose of Neurological Disorders Diagnosis*, Ph.D. dissertation, Brno University of Technology, Brno, 2014.

[8] Y. Jadoul, B. Thompson, and B. de Boer, "Introducing Parselmouth: A Python interface to Praat," *J. Phonetics*, vol. 71, pp. 1–15, 2018. [Online]. Available: https://doi.org/10.1016/j.wocn.2018.07.001

[9] P. Boersma, "Praat, a system for doing phonetics by computer," *Glot Int.*, vol. 5, pp. 341–345, 2002.

[10] V. Illner, P. Sovka, and J. Rusz, "Validation of freely-available pitch detection algorithms across various noise levels in assessing speech captured by smartphone in Parkinson's disease," *Biomed. Signal Process. Control*, vol. 58, p. 101831, 2020. [Online]. Available: https://doi.org/10.1016/j.bspc.2019.101831

[11] D. Talkin, "A robust algorithm for pitch tracking (RAPT)," in *Speech Coding and Synthesis*, W. B. Kleijn and K. K. Paliwal, Eds. Elsevier Science B.V., 1995, pp. 497–518.

[12] A. de Cheveigné and H. Kawahara, "YIN, a fundamental frequency estimator for speech and music," *J. Acoust. Soc. Am.*, vol. 111, no. 4, pp. 1917–1930, Apr. 2002.

[13] M. Mauch and S. Dixon, "pYIN: A fundamental frequency estimator using probabilistic threshold distributions," in *Proc. IEEE Int. Conf. Acoust., Speech, Signal Process. (ICASSP)*, Florence, Italy, 2014, pp. 659–663. [Online]. Available: https://doi.org/10.1109/ICASSP.2014.6853678

[14] A. Camacho and J. Harris, "A sawtooth waveform inspired pitch estimator for speech and music," *J. Acoust. Soc. Am.*, vol. 124, pp. 1638–1652, 2008. [Online]. Available: https://doi.org/10.1121/1.2951592

[15] J. Teixeira, C. Oliveira, and C. Lopes, "Vocal acoustic analysis—Jitter, shimmer and HNR parameters," *Procedia Technol.*, vol. 9, pp. 1112–1122, 2013. [Online]. Available: https://doi.org/10.1016/j.protcy.2013.12.124

[16] M. Farrús, J. Hernando, and P. Ejarque, "Jitter and shimmer measurements for speaker recognition," in *Proc. Interspeech*, 2007, pp. 778–781. [Online]. Available: https://doi.org/10.21437/Interspeech.2007-147

[17] F. Plante, G. Meyer, and W. Ainsworth, "A pitch extraction reference database," in *Proc. Eurospeech*, 1995. [Online]. Available: https://doi.org/10.21437/Eurospeech.1995-191

[18] L. Brabenec, J. Mekyska, Z. Galaz, and I. Rektorova, "Speech disorders in Parkinson's disease: early diagnostics and effects of medication and brain stimulation," *J. Neural Transm.*, vol. 124, no. 3, pp. 303–334, 2017.

Predicting Mortality in Patients with Chronic Heart Failure

1st Jan Hýl
Institute of Scientific Instruments of the CAS
Brno, Czech republic
240507@vutbr.cz

2nd Aneta Pchálková
Institute of Scientific Instruments of the CAS
Brno, Czech republic
240546@vutbr.cz

Abstract—**Chronic heart failure affects many people worldwide. A random forest model was created in this study to help predict if the patients die or survive. The model was based on the data from MUSIC database and on data extracted from high-resolution ECG records in the database. In total, 40 features were used for the training. The model achieved 0.50 F1 score, 0.73 AUROC and 0.60 AUPRC on test set.**

The most significant features were "Pro BNP (ng/L)" and "Urea (mg/dL)".

Index Terms—**Chronic Heart Failure, random forest, prediction, data processing, univariate analysis, performance, feature importance**

I. INTRODUCTION

Chronic heart failure (CHF) is a complex clinical syndrome characterized as an inability of the heart to pump enough blood to sustain metabolic needs of an organism. A crucial problem in CHF patients is a sudden cardiac death.

Predicting mortality in patients with CHF would therefore help determine patient's outcome and prevent it by appropriate counter-measures. This study aims to do that by data analysis on the MUSIC database [1], [2] and by construction of a random forest model for the prediction [3].

II. METHODS

A. Database

For this analysis, the MUSIC database [1], [2] was used. It contains 992 patients with CHF and has 102 features. Patients also underwent a 24-hour, 3-lead Holter ECG recording and a 20 minute high-resolution resting ECG recording. All the data were collected at the enrollment of a patient to the MUSIC study. Follow-up lasted 4 years or till the patient's death. We focused on analysis of the high-resolution ECG, which was recorded for a sub-cohort of 691 patients, and the relevant clinical data in the database.

Out of this group of 691 patients, we excluded patients that were lost to follow-up or had cardiac transplantation. This left us with 661 patients, out of them 203 were non-survivors and 458 survivors.

B. Data processing

Data analysis was performed by programming language Python using Pandas [4] and Scikit–Learn [5] packages. For visualization were used Matplotlib [6] and Seaborn [7] packages.

1) Data Preprocessing: Preprocessing was done by finding missing values and incorrectly entered values and replacing them either by forward fill method for continuous values or by mode for binary and categorical values. Features with very high correlation were searched through and taken out in such manner that one feature of correlated feature was kept and the other were taken out, so that the feature importance would not be distorted. Features that were considered target (similar to outcome) features were also left out. One hot encoding was done for categorical features. Features extracted from the 20 minute high-resolution resting ECG recordings were added, for more information see Section II-B3. After preprocessing there were 178 features left.

2) Univariate analysis: The initial approach was to create simple yet informative visualizations in the form of boxplots, histograms and receiver operating characteristic (ROC) curves with area under the curve (AUC) for each feature in the dataset. Mutual information between binary features and the "Exit of the study" was calculated for identifying important features.

The ROC curve depicts how well a feature separates patients according to whether the patient died or survived. Histograms and boxplots show the overall distribution of the feature as well as its distribution of the feature separated by "Exit of the study". Example of the analysis can be seen in Fig. 1, 2 and 3. The p-value of Mann-Whitney test along with importance for these features can be found in the Table II.

3) QRS and arrhythmias detection: QRS complexes and arrhythmias were detected in high-resolution ECG records using the JOSEPH software [8]. The ECG had 3 leads: X, Y and Z. For detection, only the X lead was used. The software detected QRS complexes and arrhythmias present in the records, including their duration and the count of pathological QRS complexes. New features, such as "SR_duration(s)", were extracted from the software output and were added into the

main dataset from the database. Univariate analysis was also done for these features.

4) Feature selection for Random Forest model: Feature selection was based mainly on the permutation feature selection, which was calculated on the random forest model. Additionally, univariate analysis supported the feature selection. This step was taken to reduce the complexity of the model with a goal to find the most prominent features and minimize the risk of overfitting. The permutation feature selection was done with 10-fold cross validation and each feature was permutated 20 times. Features were then sorted by the biggest averaged F1 score loss. We selected 40 features because they accounted for 90 % of the cumulative F1 score loss. Feature permutation importance for the 40 features is depicted in Fig. 7.

5) Random Forest model for prediction: Random forest model was used to predict the mortality outcome based on selected patient features. This type of model was used mainly because of its high performance and simplicity for this kind of data. The model was trained on the selected features and its parameters were optimized by GridSearchCV function from the package Scikit-Learn. All optimized parameters with search space values can be seen in Table I. Final and optimal parameters for the model are highlighted. Random forest therefore had 50 decision trees. Due to imbalance in dataset, SMOTE [9] oversampling technique was used on the training dataset before training the model. Learning curve for the model can be seen in Fig. 6.

TABLE I
SEARCH SPACE FOR OPTIMALIZATION OF MODEL

Hyperparameters	Values
n_estimators	**50**, 100, 200
max_depth	**3**, 5, 10, 20
min_samples_split	**3**, 5, 10, 15, 20
min_samples_leaf	**2**, 4, 8, 12
criterion	**entropy**, gini

III. RESULTS AND DISCUSSION

A. Univariate analysis

Univariate analysis was used as a preliminary analysis of all available features in the data set. The most promising features ended up in the random forest model. Examples of results of this analysis can be seen in Fig. 1, 2, 3 for the top three features according to their importance in the model. Top ten features with related statistical features (p-value is for Mann-Whitney test) are listed in the Tab. II.

B. Random Forest Performance

The Radom Forest model achieved F1 score of 0.50 on the test set and F1 score of 0.77 +- 0.04 on the train set with cross validation. The model scored Precision 0.47 and Recall 0.54 on the test set and Precision 0.75 +- 0.04 and Recall 0.80 +- 0.07 on the train set with cross validation. Model was trained on 40 selected features.

Further performance evaluation was done by calculating the receiver operating characteristics (ROC) curve and the

Fig. 1. (A) Distribution of Pro-BNP (ng/L) levels in the dataset. (B) Receiver operating characteristic (ROC) curve with the area under the curve (AUC), illustrating the ability of Pro-BNP (ng/L) feature to differentiate deceased and surviving patients. (C, D) Distribution of Pro-BNP (ng/L) levels in the dataset distinguishing deceased and surviving patients. (0 – non-survivors, 1 – survivors)

Fig. 2. (A) Distribution of Urea (mg/dL) levels in the dataset. (B) Receiver operating characteristic (ROC) curve with the area under the curve (AUC), illustrating the ability of Urea (mg/dL) feature to differentiate deceased and surviving patients. (C, D) Distribution of Urea (mg/dL) levels in the dataset distinguishing deceased and surviving patients. (0 – non-survivors, 1 – survivors)

area under this curve (AUC), as well as calculating the precision–recall curve (PRC) and its area under the curve (AUPRC). The ROC curve can be seen in Fig. 4 with an AUC equal to 0.84 on train set with cross validation and 0.73 on test set. The AUPRC was 0.84 and the chance level of 0.50 for train set and for test set it was 0.60 and the chance level of 0.31. The AUPRC value is high above the base line chance value. The PRC can be seen in Fig. 5.

Overall, the best results come from the ROC curve, which suggests that the model is effective at making true positive predictions. This helps identify patients who could face more serious conditions in the future.
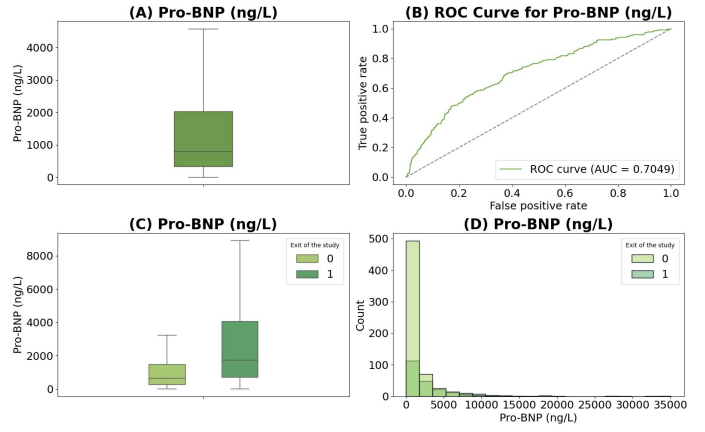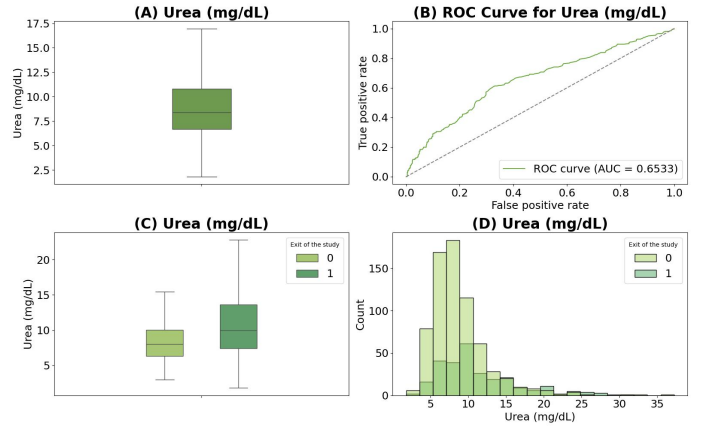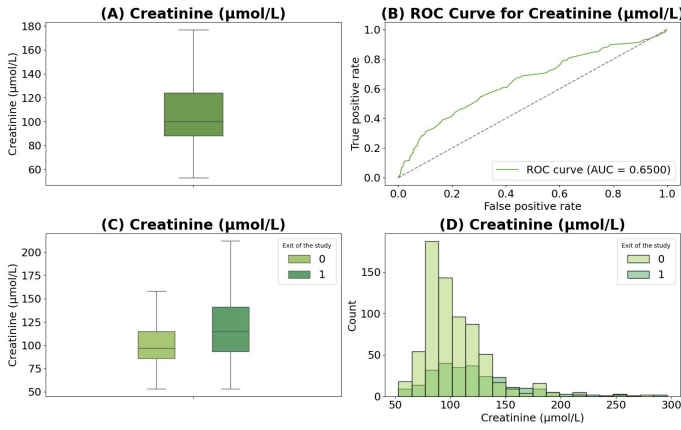
Fig. 3. (A) Distribution of Creatinine (µmol/L) levels in the dataset. (B) Receiver operating characteristic (ROC) curve with the area under the curve (AUC), illustrating the ability of Creatinine (µmol/L) feature to differentiate deceased and surviving patients. (C, D) Distribution of Creatinine (µmol/L) levels in the dataset distinguishing deceased and surviving patients. (0 – non-survivors, 1 – survivors)
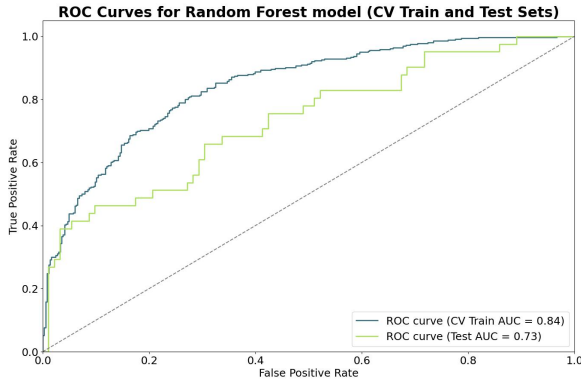
Fig. 4. Receiver operating characteristic (ROC) curve with area under the curve (AUC) calculated as a measurement of reliability of the model for predicting if patient survived or died.
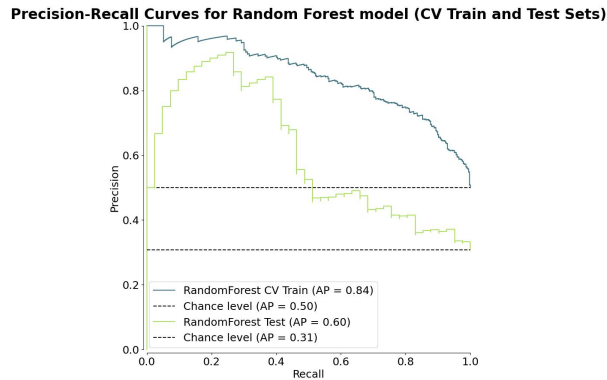
Fig. 5. Area under the Precision Recall curve (AUPRC) calculated as a measurement of reliability of the model for predicting if patient survived or died. Chance level is a AUPRC value of the model randomly guessing and it represents base line for this measurement.
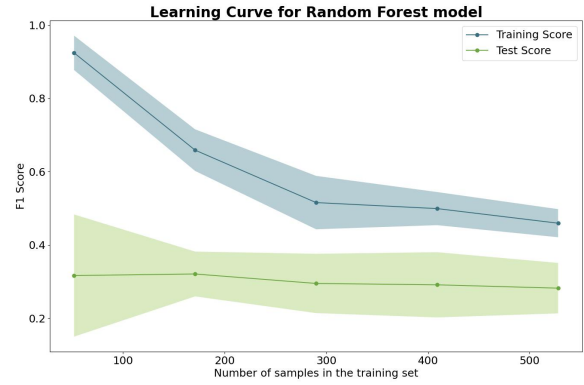
Fig. 6. Learning curve of Random Forest model, which represents F1 score based on increase of samples in learning process.

C. Feature Importance

The most important features were determined by the permutation importance on the train set. An overview of the ten most important features can be found in the Tab. II and in Fig. 7 can be seen the full 40 features, which were used to train the model. The key features include various markers, ranging from laboratory-acquired variables and demographic data to statistics derived from high-resolution ECG. The best of them are Pro-BNP (ng/L) with Urea (mg/dL) and Creatinine (µmol/L). This suggests that laboratory markers should not be neglected and should be obtained whenever possible. Pro-BNP (ng/L) marker is widely recognized and used for diagnosing heart failure and its prognosis. It was therefore expected for it to be one of the best markers [10].

D. Comparison with Existing Study

The MUSIC database was already explored in terms of mortality prediction [11]. In the study they predicted sudden cardiac death (SCD) and pump failure death (PFD) separately for ECG and clinical markers. AUROC for SCD on ECG and clinical markers combined was 0.77 and for PDF it was 0.65. This shows that our model has better results for overall death cause, but could score worse if we wanted to be more specific about the cause of death.

IV. CONCLUSION

This study presented a random forest model for predicting mortality in patients with CHF and shown promising results. Results indicated that "Pro BNP (ng/L)" and "Urea (mg/dL)" laboratory markers are the most important for mortality prediction. However, our study also highlighted importance of features derived from automated ECG analysis.

TABLE II
TEN MOST IMPORTANT FEATURES IN THE MODEL

			Univariate analysis	
Order	Feature	Importance	p-value	AUC
1	Pro-BNP (ng/L)	0.1184	0.000	0.705
2	Urea (mg/dL)	0.0744	0.000	0.653
3	Creatinine (μmol/L)	0.0496	0.000	0.650
4	PVC(%)	0.0425	0.000	0.619
5	Age	0.0374	0.000	0.632
6	NYHA class	0.0352	-	-
7	Left atrial size (mm)	0.0335	0.000	0.648
8	Gamma-glutamil transpeptidase (IU/L)	0.0280	0.000	0.575
9	Body Mass Index (Kg/m2)	0.0227	0.000	0.412
10	Normalized Troponin	0.0207	0.000	0.637
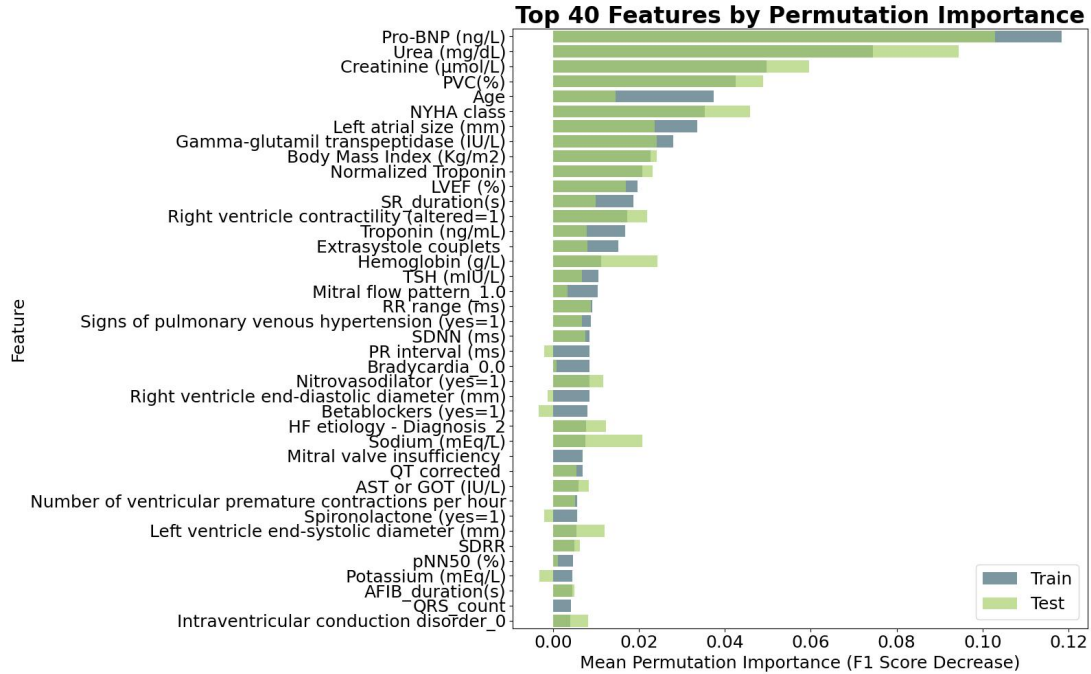
Fig. 7. Permutation feature importance calculated on whole dataset using cross validation. It shows how much the performance of the model decreases if we remove given feature. The feature with the highest decrease is the most valuable. Top 40 features were selected because they represent 90 % of cumulative score decrease. Model was trained on these features.

REFERENCES

[1] A. Martin-Yebra, J. P. Martínez, and P. Laguna, "Music (sudden cardiac death in chronic heart failure) (version 1.0.1)." PhysioNet, 2025.

[2] A. Martin, A. B. de Luna, R. Vazquez, P. Caminal, P. Laguna, and J. P. Martínez, "The music database," pp. –.

[3] G. Savarese, P. M. Becher, L. H. Lund, P. Seferovic, G. M. C. Rosano, and A. J. S. Coats, "Global burden of heart failure," in *Cardiovascular Research*, vol. 118, pp. 3272–3287, 2022-12-01.

[4] T. pandas development team, "pandas-dev/pandas: Pandas," Feb. 2020.

[5] F. Pedregosa, G. Varoquaux, A. Gramfort, V. Michel, B. Thirion, O. Grisel, M. Blondel, P. Prettenhofer, R. Weiss, V. Dubourg, J. Vanderplas, A. Passos, D. Cournapeau, M. Brucher, M. Perrot, and E. Duchesnay, "Scikit-learn: Machine learning in Python," *Journal of Machine Learning Research*, vol. 12, pp. 2825–2830, 2011.

[6] J. D. Hunter, "Matplotlib: A 2d graphics environment," *Computing in Science & Engineering*, vol. 9, no. 3, pp. 90–95, 2007.

[7] M. L. Waskom, "seaborn: statistical data visualization," *Journal of Open Source Software*, vol. 6, no. 60, p. 3021, 2021.

[8] F. Plesinger, A. Ivora, E. Vargova, R. Smisek, J. Pavlus, P. Nejedly, V. Bulkova, R. Kozubik, J. Halamek, and P. Jurak", ""scalable, multiplatform, and autonomous ecg processor supported by ai for telemedicine center"," pp. –.

[9] "Smote," 2014.

[10] A. Bayes-Genis, K. F. Docherty, M. C. Petrie, J. L. Januzzi, C. Mueller, L. Anderson, B. Bozkurt, J. Butler, O. Chioncel, J. G. Cleland, R. Christodorescu, S. D. Prato, F. Gustafsson, C. S. Lam, and B. Moura, "Practical algorithms for early diagnosis of heart failure and heart stress using nt-probnp esc," *European Journal of Heart Failure*, vol. 25, no. 11, pp. 1891–1898, 2023.

[11] J. Ramírez, M. Orini, A. Mincholé, V. Monasterio, I. Cygankiewicz, A. B. de Luna, J. P. Martínez, P. Laguna, E. Pueyo, and V. Lionetti, "Sudden cardiac death and pump failure death prediction in chronic heart failure by combining ecg and clinical markers in an integrated risk model," *PLOS ONE*, vol. 12, no. 10, 2017-10-11.

Particle Size Measurement Using Acoustic Emission and Octave Band Analysis

1st Iveta Stetinova
Dept. of Control and Instrumentation
Faculty of Electrical Engineering
and Communication
Brno University of Technology
Brno, Czech Republic
xsteti04@vutbr.cz

2nd Stanislav Pikula
Central European Institute of Technology
Brno University of Technology
Dept. of Control and Instrumentation
Faculty of Electrical Engineering
and Communication
Brno University of Technology
Brno, Czech Republic
pikula@vut.cz

3rd Jiří Fialka
Central European Institute of Technology
Brno University of Technology
Dept. of Control and Instrumentation
Faculty of Electrical Engineering
and Communication
Brno University of Technology
Brno, Czech Republic
fialka@vut.cz

Abstract—**This paper investigates the application of Acoustic Emission (AE) for particle size measurement. AE is a non-destructive method that detects elastic waves generated by particle impacts. The study focuses on frequency-domain analysis using octave band analysis to examine how different particle sizes produce distinct AE signal responses.**

Index Terms—**Granulometry, particle size distribution analysis, acoustic emission, octave band analysis**

I. Introduction

Granulometry is the process of measuring and analysing the particle size distribution. It is used in various industries, including pharmaceutics, the chemical industry, and mining.

Various techniques, from traditional sieving and sedimentation to advanced laser diffraction, provide reliable results but often require extensive sample preparation, are time-consuming, or lack real-time monitoring capabilities [1].

Acoustic emission offers a non-destructive method by detecting elastic waves generated by particle interactions. These signals, analysed using different types of piezoelectric sensors, provide real-time monitoring with minimal sample preparation and the ability to operate in dynamic environments [2].

Studies have explored AE-based granulometry using different materials. Some researchers have used glass beads, smaller than 1 mm, in pneumatic conveying systems where particle velocity plays a significant role in AE signal generation [3]. Others have focused on metallic spheres in the millimetre to tens-of-millimetres range [4]. The choice of particle type affects impact dynamics and wave propagation.

Earlier research primarily analysed AE signals in the time domain, focusing on impact energy and peak amplitude [5]. This study instead emphasizes frequency-domain analysis. According to Hertzian contact theory, larger particles generate AE signals in lower frequencies (a few to tens of kHz), while smaller particles produce signals concentrated at higher frequencies (hundreds of kHz) [1]. This study examines the relationship between particle size and AE signal response in the frequency domain, offering insights for the practical application of AE-based granulometry in industrial settings.

II. Methods

To analyse AE signals in the frequency domain, an experimental setup was prepared, as shown in Figure 1, designed to capture acoustic emission signals generated by falling particles onto a waveguide.
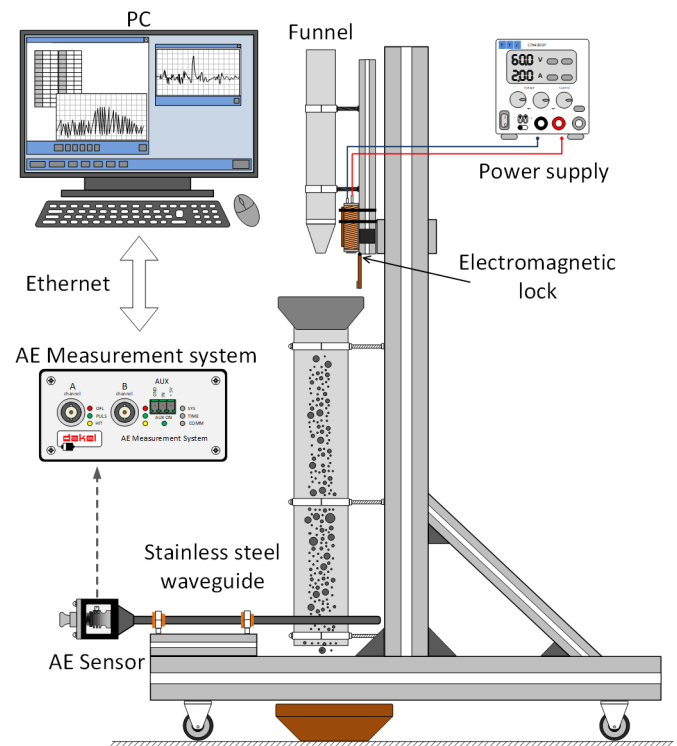
Fig. 1: Measurement setup (funnel with electromagnetic valve used to start particle flow, waveguide with AE sensor and AE measurement system controlled from PC).

The setup consists of:

- a funnel with an opening valve, controlled by an electromagnetic lock, used to regulate the particle flow.

For continuous flow measurements, the valve is initially closed and opens to begin the measurement.

- a round stainless steel waveguide with a diameter of 8 mm
- an Olympus V103 acoustic emission sensor with a resonant frequency of 1 MHz, the size of the contact area is 0.5 in (13 mm), output with BNC connector
- acoustic emission measurement card Dakel ZEDO-22
- computer with software for working with the Dakel ZEDO-22 measurement card

The measurement data was acquired using the ZEDO DAEMON software, which offers a range of options to configure, visualize, and process acoustic emission data.

A. Measurement parameters

Parameters set in ZEDO DAEMON software:

- Sampling frequency: 5 MHz
- Threshold trigger: 1 mV
- Pre-trigger: 5 ms
- Post-trigger: 20 ms
- Pre-amplifier gain: 34 dB
- Amplifier gain: 0 dB

The measured particles used in this experiment were bearing balls, categorized of five sizes, see Table I.

TABLE I: Weight and dimension of used bearing balls.

Size[a]	Weight (g)	Dimension (mm)
Size 1	0.002	0.800
Size 2	0.016	1.588
Size 3	0.131	3.175
Size 4	1.050	6.350
Size 5	8.383	12.700

[a]The same colours are used as in the graphs.

The dimensions of the bearing balls are apparent next to a common ruler in Figure 2.
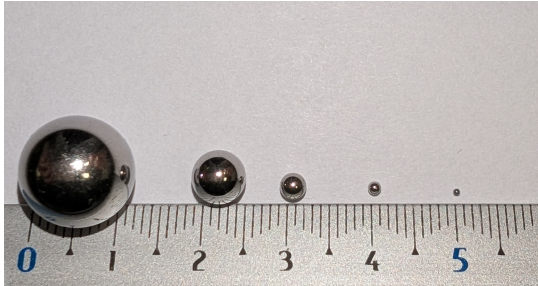
Fig. 2: Bearing balls used as particles generating AE (12.7 mm largest to 0.8 mm smallest).

B. Measurement process

The acquisition process was managed by ZEDO DAEMON software. The measurement was initiated in the software, and the bearing balls of each size were sequentially released onto the waveguide. To ensure consistency, 25 measurements were taken for each size.

Once the measurement was complete, the data acquisition was stopped programmatically and the collected data was exported for further analysis. The exported values were first processed in LabVIEW using the Octave Analysis VI, which computes the octave spectrum. This approach was chosen because of the wide frequency range in which AE data appears, allowing for a better representation of frequency-dependent characteristics. The processed data were then transferred to MATLAB for better visualization of all measurements.

In addition, the standard deviation was calculated across multiple measurements to determine the variability in the data.

III. RESULTS AND DISCUSSION

The AE signal data for a single impact is presented in Figure 3, showing that the smaller balls generate lower impact energy, while the larger balls produce higher impact energy.

(a)

(b)
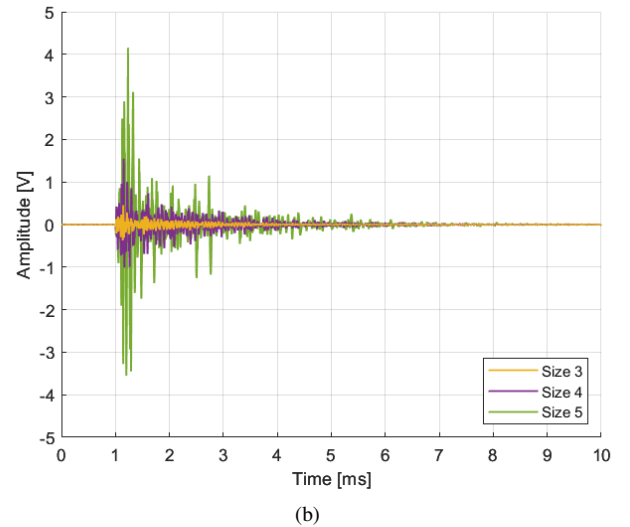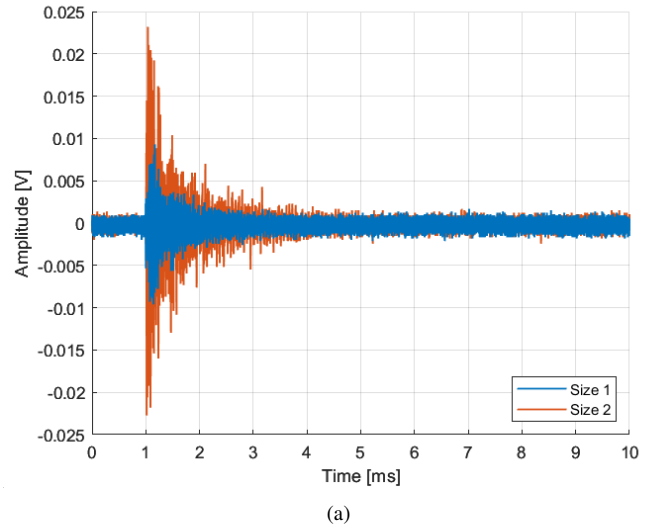
Fig. 3: AE Signal from single hit, (a) two smaller sizes (max amplitude 0.024 V), (b) three bigger sizes (max amplitude 4.1 V).

The range determined by the standard deviation is shown as a faded color region in the octave spectrum in Figure 4, indicating the variation around the average values.
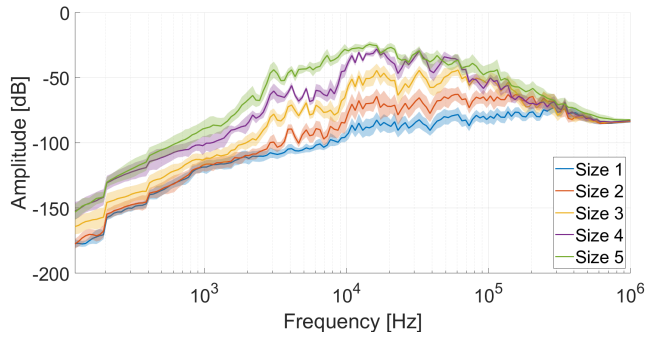
Fig. 4: Octave Spectrum

The graphs in Figure 3 indicate that each ball size generates a different level of impact energy according to its size. The octave spectrum in Figure 4 clearly shows that the amplitude in the octave spectrum is proportional to the impact energy of the ball. This means the graph mainly reflects the energy level rather than highlighting differences in frequency content.

To make the octave analysis more focused on the frequency rather than energy, the data were normalized. Specifically, the maximum impact energy of each ball was scaled to 1 V, and all other values in its spectrum were proportionally adjusted using the same factor. Afterwards, a new octave spectrum was calculated using the normalized values.
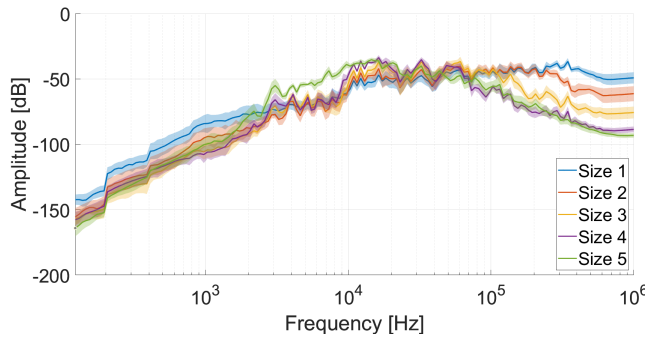
Fig. 5: Normalized Octave Spectrum

The normalized octave spectrum in Figure 5 shows that the largest particle generates stronger signals in the lower frequency range (around 2 to 10 kHz), while smaller particles are more prominent in the higher frequencies (above 100 kHz).

Based on the frequency range where the signal is most prominent, it may be possible to estimate the particle size. With further measurements and data processing, this relationship could be used to develop a size estimation method.

IV. CONCLUSION

This study explored the relationship between particle size and (AE) signal response using frequency-domain analysis. The results confirmed that larger particles generate AE signals at lower frequencies, while smaller particles exhibit higher-frequency components, in alignment with Hertzian contact theory. Octave band analysis proved that it could be useful

for distinguishing particle sizes based on their frequency characteristics.

There are potential factors influencing AE signal response, such as waveguide and sensor resonance effects, which could impact measurement accuracy. Future research could focus on optimizing the experimental setup by testing different waveguide materials and sensor configurations to improve signal differentiation.

REFERENCES

[1] Uher, Miroslav, and Petr Beneš. "Measurement of particle size distribution by the use of acoustic emission method." 2012 IEEE International Instrumentation and Measurement Technology Conference Proceedings. IEEE, 2012.
[2] Coombes, James Robert, and Yong Yan. "Experimental investigations into the use of piezoelectric film transducers to determine particle size through impact analysis." 2016 IEEE International Instrumentation and Measurement Technology Conference Proceedings. IEEE, 2016.
[3] Hu, Yonghui, et al. "On-line sizing of pneumatically conveyed particles through acoustic emission detection and signal analysis." IEEE transactions on instrumentation and measurement 64.5 (2014): 1100-1109.
[4] Schnabel, Stephan, et al. "Absolute measurement of elastic waves excited by Hertzian contacts in boundary restricted systems." Tribology Letters 65 (2017)
[5] Zhang, Guoqiang, et al. "Investigations into the sensing mechanism of acoustic emission sensors for particle size measurement in a particular case: normal incidence." Measurement Science and Technology 32.7 (2021): 075107.

IPv6 OSINT Network Analyzer

1st Maxim Nikulcha
Department of Telecommunications
Brno University of Technology
616 00 Brno, Czech Republic
230017@vut.cz

2nd Viet Anh Phan
Department of Telecommunications
Brno University of Technology
616 00 Brno, Czech Republic
243760@vut.cz

Abstract—At present time, Open Source Intelligence (OSINT) tools are used in various fields, including journalism, business analysis, cybersecurity, and networking. Although there are various tools available in the IPv6 domain, each tool has limitations in its features, which require the use of multiple applications to achieve a thorough analysis of the network. As a result, the process of effectively collecting IPv6 data often becomes quite challenging, which could compromise the reliability of the results. The IPv6 OSINT Network Analyzer seeks to address this challenge by merging the essential features of the currently available tools, with a particular focus on IPv6, into a single unified desktop application. This application enables the extraction of data across all layers of the TCP/IP protocol suite, retrieving MAC vendor information and geographic location from external APIs, as well as facilitating node identification, vizualization of network topology, and identification of blacklisted addresses. It also enables saving and loading results to a JSON file, making it convenient for future use. This paper serves as an introduction to the IPv6 OSINT Network Analyzer, exploring its functionalities and practical applications. In addition, it reflects on the insights gained from its implementation and outlines future directions for research and development.

Index Terms—OSINT, IPv6, PCAP, JAVA, JavaFX

I. INTRODUCTION

The introduction of IPv4, which provides essential addressing and routing functions, has markedly improved communication between devices on a global scale, resulting in a profound transformation of the international landscape. However, during the 1980s and 1990s, there was a significant increase in the number of computer networks, which brought to light various limitations inherent in IPv4, especially its limited address space, which was officially exhausted in January 2011. As a result, a determination was reached to commence the transition to a more sophisticated protocol, known as IPv6 [1].

The challenge associated with transitioning to new protocols lies in the fact that existing tools do not support them, a situation particularly evident with OSINT tools. Although there are currently numerous tools available, it is often necessary to combine them to effectively gather IPv6 data. The developed application effectively addresses the identified challenge by providing a comprehensive and integrated solution for the collection, analysis of IPv6 data, and visualization of the network topology.

.

The remainder of this paper is organized as follows. Section 2 provides the theoretical framework related to OSINT tools and presents a comprehensive overview of the instruments currently available within this domain, as well as the rationale for the decision to develop the IPv6 OSINT Network Analyzer. Section 3 delineates the software architecture and implementation of the IPv6 OSINT Network Analyzer. Section 4 offers an overview of the tool by elucidating its user interface and features. Section 5 illustrates a practical application of the tool within a specified network scenario. Finally, Section 6 concludes the paper.

II. BACKGROUND AND RELATED TOOLS

OSINT is characterized as "information that legally collected from free public sources" and is subjected to analysis in order to attain a comprehensive understanding of a particular individual, organization, or subject. The most significant surge in OSINT occurred at the outset of the 21st century, aligning with the widespread growth of Internet users and the emergence of social media platforms. OSINT can be classified into two distinct categories: passive and active. Passive OSINT refers to the process of acquiring information from public sources "without directly engaging with the target". Active OSINT, by contrast, involves "direct engagement with the target to extract" the necessary information [2].

The process from starting the data collection to the final result is referred to as the intelligence cycle and as can be seen from Fig. 1 consists of five key stages:
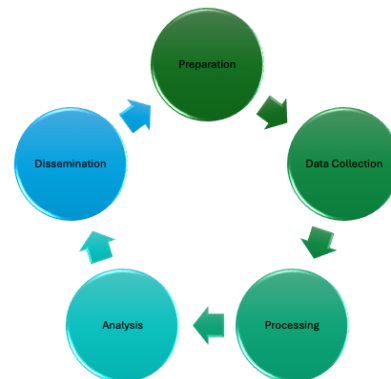

Fig. 1. Intelligence cycle

1) Preparation - this phase involves the assessment of requirements, including the establishment of task objectives and the identification of relevant data sources.
2) Data Collection - the process of gathering information from various open-sources.
3) Processing - storing and organizing data in a comprehensible manner.
4) Analysis - analysis of the collected data in alignment with the established objectives. This may involve identifying patterns and building timelines.
5) Dissemination - presentation of final outcomes utilizing visual aids, including reports and graphs.

These stages may be repeated if the results do not meet the established criteria [2].

Currently, there are several tools available in the domain of network scanning and IPv6 OSINT.

One of the tools in this context is the Network Mapper, commonly known as Nmap. This command-line network scanning utility that encompasses a variety of essential features, including the identification of devices within a network, the detection of active services, the collection of information regarding the operating system in use, and the execution of vulnerability assessments using Nmap Scripting Engine (NSE). Nevertheless, several functionalities are absent from the tools, including packet analysis, visualization (which necessitates supplementary add-ins), geolocation, and vendor information extraction. Additionally, there is limited capability for detecting IPv6 vulnerabilities and identifying Denial-of-Service (DoS) attacks [3].

Another widely utilized tool in the realm of OSINT is the-Harvester. This reconnaissance application is specifically engineered to collect data pertaining to a target's digital footprint, with an emphasis on domains, email addresses, IP addresses, and subdomains. The program is capable of autonomously aggregating data from a multitude of public sources, including search engines, DNS records, and various APIs. This capability not only enhances efficiency by conserving time but also broadens the range of data obtained, thereby assisting testers in the identification of vulnerable or overlooked assets, such as subdomains and public IP addresses. However, this tool is deficient in several key features, including packet analysis, node identification, detection of security vulnerabilities, and the identification of DoS attacks [4].

Consequently, it is evident that while each tool possesses a multitude of available features, they simultaneously exhibit certain deficiencies. Therefore, the decision was made to develop a new tool designed to effectively perform these tasks, with an emphasis on IPv6, all within a unified graphical user interface (GUI) application.

III. SOFTWARE ARCHIECTURE

The IPv6 OSINT Network Analyzer was created using the Java programming language, with the assistance of various open-source tools and libraries. At present, the program is only available on MacOS, but it is intended to be released for other systems as well.
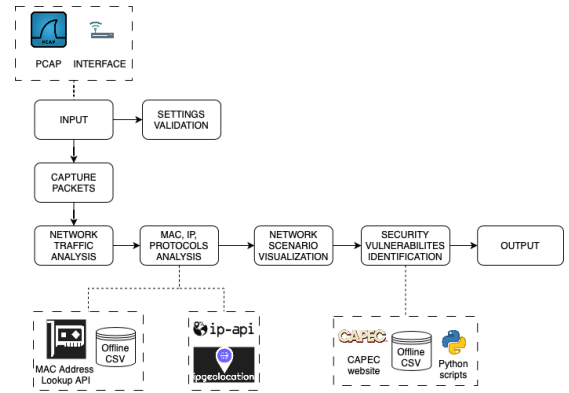
Fig. 2. High-level architecture diagram

Fig. 2 illustrates the high-level architecture diagram of the final product. Certain features have already been implemented within the program, while others remain under development. When initiating a new analysis, the user can select the data source from saved *.pcap* or *.pcapng* files or from a local network interface. Upon the selection of the data source, the analysis starts, encompassing a series of systematic steps. Below is a simplified algorithm that illustrates how the program processes from the starting point.

Algorithm 1 IPv6 Network Analyzer

1: Initialize packet capture from a network interface or load a PCAP file
2: Store all captured packets in memory
3: **for** each packet p in capturedPackets **do**
4:    **if** p is an IPv6 packet **then**
5:       Assign a unique identifier and extract the timestamp
6:       Extract source and destination MAC addresses
7:       Identify MAC vendors using a local CSV or API
8:       Extract source and destination IPv6 addresses
9:       Determine IP geolocation using external APIs
10:       Identify protocols at the link, network, transport, and application layers (IPv6-compatible)
11:       Analyze the packet content for known IPv6-specific vulnerabilities
12:       Map detected behaviors to CAPEC (Common Attack Pattern Enumeration and Classification) entries
13:    **end if**
14: **end for**
15: Identify unique devices (nodes) based on MAC and IPv6 addresses
16: Detect communication relationships between identified devices
17: Construct a network graph

Upon the completion of the analysis, the program generates a JSON file that contains two arrays: one comprising IPv6 packet objects and the other consisting of device objects, as depicted in Fig. 3. This file can be preserved and subsequently

Fig. 3. Output JSON format [5]

imported into the program or other JSON editing tools for further analysis of the traffic, as required.

The technical application architecture is organized into four sections by dividing the system into separate layers, with each layer assigned to specific tasks.

1) View - the frontend (FE), which is primarily responsible for creating UI components and presenting data to the user.
2) Entity - includes the definition of objects used in the project. For instance, the *IPv6Packet* object contains all pertinent information, such as the ID, timestamp, and details of each layer in the TCP/IP stack.
3) Logic - the backend (BE) and core of the application that is responsible for executing complex computations, including packet parsing, invoking external APIs, and identifying distinct nodes.
4) Controller - a bridge mainly used for transferring data between the View and the Logic.

Throughout development, a variety of tools and libraries were employed. The first of these is JavaFX, a robust library specifically developed for the creation of user interface applications that are compatible with various devices that operate on the Java platform [6]. The second tool, Scene Builder, is a software application designed to improve the efficiency of user interface design for applications utilizing JavaFX [7]. Furthermore, Pcap4J is used to facilitate the capture of network traffic and the analysis of packet content [8]. Furthermore, the Lombok library is incorporated to optimize the software development process by improving code readability and reducing verbosity through the application of custom annotations [9]. Lastly, OpenCSV and Jackson are libraries utilized for efficient reading and writing of data in CSV and JSON formats, respectively [10], [11].

IV. OVERVIEW OF CREATED TOOL

One of the notable advantages of the application is its user interface, which is updated systematically. This feature enables users to observe partial results from the outset, even while the analysis continues to run in the background. The main window consists of five main areas as shown in Fig. 4:
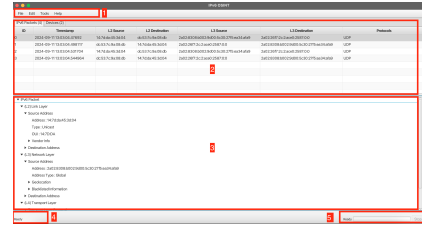
Fig. 4. Application - UI areas

1) Menu bar - allows the user to initiate various tasks, such as starting a new analysis or saving and loading previous analyses.
2) Table panel - provides the user with basic information about each packet or device.
3) Details panel - displays complete information about a packet or device.
4) Main status bar - shows the final analysis status. Currently supported statuses are ready, in progress, error, or stopped.
5) Progress bar - displays the progress of the analysis during runtime.

Another aspect of the system is the network graph accessible through the "Tools" menu. The graph provides a vizualization of the detected devices, identified by their respective IDs, and shows the connections between the nodes that engaged in communication during the analysis.

V. NETWORK SCENARIO EXAMPLE

In the testing scenario, real WiFi traffic was recorded in a specific location over a period of 10 minutes.

TABLE I
ANALYSIS OVERVIEW

Variable	Value
Packets	403
MAC addresses	9
IPv6 link local addresses	9
IPv6 global addresses	3
Protocols	4
Vendors	3
ISPs	5
Devices	9

After excluding the packets associated with the MAC address of the device used for the analysis, it can be observed that 403 packets were identified. In total, the analysis found nine different devices, one of which is the device on which the network analyzer was operating. In analyzing the results, the traffic data were filtered to eliminate any transmissions originating from the device under examination. As a result, the analysis focuses solely on traffic related to all other targeted devices.

- `maxims-macbook-air.local` - the device where the analysis was executed
- `prg03s12-in-x0a.1e100.net,`
  `prg03s10-in-x0a.1e100.net,`

`prg03s13-in-x0a.1e100.net` — Google servers located in Prague

- `czns1.vodafone.cz` — Vodafone router
- `maxims-ipad.local`, `lindas-macbook-air.local` — Apple devices on the local network
- `android.local`, `android-2.local` — Android devices
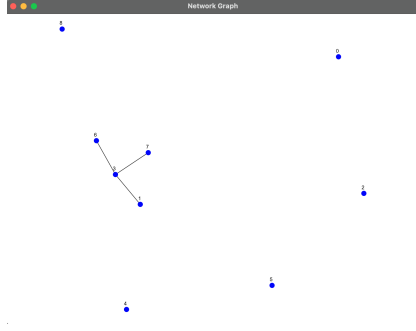
Fig. 5. Analysis - network graph

Fig. 5 depicts the network graph derived from the analysis. When the program generates the graphs, it searches for unique link-layer devices and identifies communication between the nodes based on the source and destination addresses. Subsequently, it draws the individual nodes in the graph and uses edges to represent the communication between the devices.

TABLE II
ANALYSIS PROCESSING TIME

Step	Time
Capture and traffic analysis	10 minutes
Geolocation	27 seconds
Devices	5 seconds
Blacklisted addresses	8 minutes 10 seconds
Total	18 minutes 42 seconds

In addition, it is important to outline the duration of the key steps involved in the analysis. The total analysis time was 18 minutes and 42 seconds. The first phase, which involved capturing packets and extracting all relevant IPv6 information, as well as fetching MAC vendors, took exactly 10 minutes. The second phase, which involved fetching the IP geolocation for all packet addresses, took 27 seconds. The next step, identifying unique devices and blacklisted addresses, took nearly as long as the packet capture phase. This occurrence may be due to several factors, including the network bandwidth during the analysis, since the process requires querying external APIs, as well as potential latency related to API responses and the execution of Python scripts within a Java environment.

Furthermore, it is beneficial to examine the distribution of packet utilization among various protocols that are compatible with IPv6, specifically ICMPv6 (a fundamental component of the protocol), as well as TCP, UDP, DNS, and DHCPv6, as illustrated in Fig. 6. The data indicate that UDP was utilized most frequently, while ICMPv6 was found to be the least
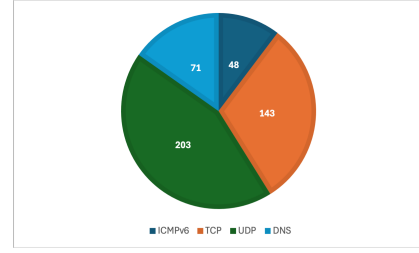
Fig. 6. Number of packets per IPv6 compatible protocols

prevalent. During analysis, the tool captured several ICMPv6 messages, including neighbor advertisement, neighbor solicitation, and router advertisement.

VI. CONCLUSION

This paper reported on the current developments of IPv6 OSINT Network Analyzer, a desktop application designed primarily to improve the capture and analysis of IPv6 network traffic. The development of the tool remains an ongoing process. There is still a lot of work to be done, and additional features need to be integrated into the program. These enhancements include refining the network vizualization graph, improving analysis performance, support on other operating systems, finding IPv6 security vulnerabilities, and mapping them to the CAPEC database.

Should you wish to download and try it, please reach out to the author to obtain permission to access the GitHub repository.

REFERENCES

[1] Popoviciu, Ciprian. "Transitioning to IPv6." Broadcast Engineering 53, no. 4 (April 1, 2011): 12–14. https://research-ebsco-com.ezproxy.lib.vutbr.cz/linkprocessor/plink?id=306489fe-26b3-3d96-90f6-4a173bb6fb28.

[2] C. Rafailă, F. Gurzău, C. Grumăzescu and I. Bica, "MTAFinder - Unified OSINT platform for efficient data gathering," 2023 15th International Conference on Electronics, Computers and Artificial Intelligence (ECAI), Bucharest, Romania, 2023, pp. 1-6, doi: 10.1109/ECAI58194.2023.10194004.

[3] Al-Khazaali, Z. et al, 2025. Characteristics of port scan traffic: A case study using nmap', Journal of Engineering and Sustainable Development, 29(1), pp. 26–35. doi:10.31272/jeasd.2638.

[4] Z. Terneva, I. Vladimirov and D. Nikolova, "Accessing LinkedIn and Google E-mail Databases Using Kali Linux and TheHarvester," 2021 56th International Scientific Conference on Information, Communication and Energy Systems and Technologies (ICEST), Sozopol, Bulgaria, 2021, pp. 59-62, doi: 10.1109/ICEST52640.2021.9483460.

[5] https://jsoncrack.com/editor (accessed on 1st of March, 2025)

[6] JavaFX: Getting Started with JavaFX. n.d. Online. Available at: https://docs.oracle.com/javase/8/javafx/get-started-tutorial/jfx-overview.htm#JFXST784 (accessed on 1st of March, 2025)

[7] JavaFX Scene Builder, n.d. Online. Available at: https://www.oracle.com/java/technologies/javase/javafxscenebuilder-info.html (accessed on 1st of March, 2025)

[8] https://github.com/kaitoy/pcap4j (accessed on 1st of March, 2025)

[9] https://github.com/projectlombok/lombok (accessed on 1st of March, 2025)

[10] https://mvnrepository.com/artifact/com.opencsv/opencsv (accessed on 1st of March, 2025)

[11] https://github.com/FasterXML/jackson (accessed on 1st of March, 2025)

There is no better time than now to be an **intelligent power management company.**

EAT•N

Powering Business Worldwide

We make what matters work.*

Evolving to meet the ever-changing needs of our world.

Building more efficient, sustainable power management solutions.

Powering Business Worldwide

Energy harvesting for UWB IIoT devices

1st Jan Ševčík
Faculty of Electrical Engineering and Communication
Brno University of Technology
Brno, Czech Republic
xsevci71@vutbr.cz

2nd Radovan Juráň
Faculty of Information Technology and Communication Sciences
Tampere University
Tampere, Finland
radovan.juran@vut.cz

Abstract—This paper focuses on the study and selection of suitable energy harvesting methods, considering specific application scenarios. It includes a comparison of various methods to identify the most optimal solutions and adjustments for efficient energy collection. Finally, the paper presents the design and development of a custom printed circuit board (PCB) featuring a chip that supports ultra-wideband (UWB) technology in accordance with the 802.15.4z standard. The system is powered by a battery, which extends its lifespan and ensures prolonged operation when the harvested environmental energy is sufficient.

Index Terms—UWB, Energy Harvesting, DWM3001, TEG, Solar panels, Energy storage, Batteries, Energy harvesting methods, Supercapacitors, IoT, RF energy harvesting, Low-power electronics

I. INTRODUCTION

Nowadays, our world faces increasing and new challenges in terms of environmental issues and the energy crisis. Term green energy is starting to become more important than ever before, and thanks to energy harvesting, it is possible to obtain energy from renewable sources such as solar cells, wind turbines, water flow, vibrations, RF energy (radio frequency), and many other methods. All of this leads to greater attention being paid to energy harvesting, which is a technology that allows the collection of energy needed to power devices by gradually gathering it from the surrounding environment, converting it into usable electrical power and possibly storing it for further usage. This leads to more eco-friendly device usage and lower maintenance costs.

In short Energy harvesting (EH) can be described as a revolutionary method for obtaining small amounts of energy and converting it into electrical power.

In case of battery-powered device energy harvesting can extend its lifespan, reducing material costs and time needed for maintenance of the devices. Devices which uses energy harvesting usually include IoT sensors, wearable electronics, smart buildings, sensors in harsh environments, and more. The significance of EH lies mainly in its ability to utilize energy that would otherwise be wasted or not obtained at all. For instance, sensors exposed to sunlight during the day can be powered by solar panels, while devices in motion can use piezoelectric generators to produce electricity from vibrations and movement. This can be beneficial mostly in remote ares or hard-to-reach locations. Examples of harvesting methods are shown in Fig. 1, with the exception of RF energy harvesting, which is currently mostly found in conference papers and test

devices, with only a few designs available on the market. Given the growing demand for reducing carbon footprints, increasing energy efficiency, and promoting sustainable development, EH has reached a peak in wider applications and can contribute to many new devices and systems where green energy plays can play role.
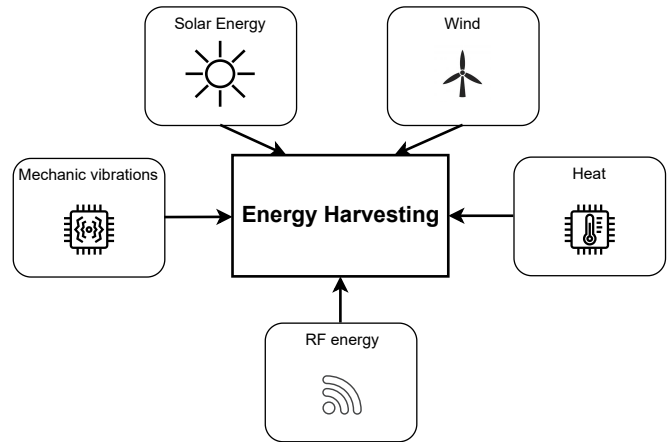
Fig. 1: Most commonly used harvesting methods

II. MAIN OBJECTIVES

Main goal of the work is to design system, research and study an ideally battery-powered, low-power device for the Industrial Internet of Things (IIoT) with possible use in real-time location systems (RTLS) with a focus on energy harvesting (EH). The main part of the work involves selecting the most appropriate EH method and exploring possible alternatives. The second goal focuses on the system design, where all experiments will be conducted on UWB tags integrated into system using the IEEE 802.15.4Z technology standard. This will combine Ultra-Wideband (UWB) technology with various energy harvesting methods to evaluate their suitability for specific scenarios.

The resulting model is developed using the DWM3001C module, with power requirements thoroughly verified and tested in laboratory conditions, ideally also under real-world conditions. The device will be able to properly harvest energy from the chosen method, convert it and store energy to extend battery life and power the system.

The final part of the work will focus on custom system design for specific applications and laboratory testing of the selected harvester. Additionally, it will involve studying and possibly testing RF energy harvesting from Wi-Fi, GSM, or other RF-based technologies, with potential integration into road vehicles. This follows a previous project that developed an onboard system for a vintage motorcycle [1] .

III. ENERGY HARVESTING METHODS

Energy can be usually obtained from human activity, other devices, or the surrounding environment. For example, mechanical movement during walking or passive energy generation, such as body heat, can be utilized. Energy from other devices can include waste heat or energy collected from RF signals, Wi-Fi, GSM, and other RF-based technologies. The amount of energy harvested from these sources is usually very small, but thanks to technological progress, it is expected to become more viable in the future.

Energy harvesting methods allows to collect usualy small amounts of energy and convert it into electrical energy. Usually its necessary to combine multiple harvesting methods to maximize the total harvested energy and compensate for their non-constant nature (e.g., sunlight, wind) and its small amounts.

Harvesting methods does not completely change the fundamental principles of power-efficient circuit design, but it can assist in power management and impact carbon footprint and longevity of the devices. However, it may also introduce challenges for some designers when meeting system requirements. Therefore, the goal is to properly match the power circuitry with the application circuits to achieve the best overall performance.

A. RF harvesting

One of the next option is RF energy harvesting which is particularly interesting, and this work will briefly explore its potential applications. However, the actual energy harvested from RF sources is currently quite low and has limited usability compared to the first three methods mentioned. In Table I, a comparison of these methods and their harvested power output is presented [2].

B. Solar harvesting

The most common type of energy harvester is the solar cell, which also serves as the primary energy source for the first revision of the system. Its good to match input impedance and try minimize losses on wiring to maximize harvested energy or use MPPT (maximum power point tracking) ensuring optimal energy extraction. Solar radiation is available in most geographic areas and enables efficient energy harvesting both outdoors and, in some cases, indoors. Thanks to continuous advancements in photovoltaic energy, cells are becoming slowly but steadily more efficient and cost-effective, further increasing their attractiveness for EH systems.

Source of Energy	Possible Power Harvested
Motion and Vibrations	
Human	$4\,\mu W/cm^2$
Industrial	$100\,\mu W/cm^2$
Temperature	
Human	$25\,\mu W/cm^2$
Industrial	$1\text{-}10\,mW/cm^2$
Light - Solar	
Indoor	$10\,\mu W/cm^2$
Outdoor	$10\,mW/cm^2$
RF	
GSM	$0.1\,\mu W/cm^2$
WiFi	$0.001\,\mu W/cm^2$

TABLE I: Overview of energy sources and their possible harvested power [2]

C. Other sources

Other energy harvesting sources like motion, vibrations, and temperature differences can be useful in specific cases but are not ideal in this scenario due to their nature. Motion-based EH depends on consistent movement, making it unreliable in static environments. Vibration can work well in industrial settings on during transportation, but is ineffective where vibrations are weak or inconsistent. Temperature-based EH usually requires stable heat gradients, which are rare in everyday conditions. This methods might be suitable for another systems.

D. RF harvesting

Another highly promising direction in the future of energy harvesting is the use of RF (radio frequency) energy. Harvesting energy from ambient radio signals, such as Wi-Fi or cellular networks, is proving to be particularly beneficial for small wireless sensors and IoT devices. The main advantage is the constant availability of RF signals in urban and indoor environments, allowing for stable power supply to low-power devices without frequent battery replacements. As wireless technologies continue to evolve, RF energy harvesting is expected to play an increasingly important role in the future.

IV. COMPONENTS

Next section will briefly describe chosen components, their functions and reasons for their usage and latest section will provide information about designing system and PCB.

A. DWM3001C

DWM3001C is ultra-wideband module from Qorvo uses UWB technology for IoT, industrial automation, and precise localization. It operates in the 6.5–8 GHz band (channels 6 and 9), with channel 9 (7987.2 MHz, 499.2 MHz bandwidth) preferred for global use. It features an integrated antenna, provides low power consumption (150 mA active, 1.4 µA standby), and supports SPI, UART, I2C, and GPIO. Measuring only 27×19 mm, it suits various applications and includes also Bluetooth. Data rates range from 850 kbps to 6.8 Mbps, with an operating temperature of -40 to +85 °C. As of 03/03/2025, module costs around 50 USD. [3]

B. BQ25504 - ULP boost converter with battery management

BQ25504 is an ultra-low-power boost converter with integrated battery management, designed for energy harvesting applications. It efficiently handles input power ranging from μW to mW making it suitable for harvesting energy from low-power DC sources like solar or thermoelectric generators (TEGs), and other ambient energy sources. Key features include a high-efficiency DC-DC boost converter operating from 130 mV, ultra-low quiescent current (330 nA), and a 600 mV cold start. It supports dynamic maximum power point tracking (MPPT) ensuring optimal energy extraction under varying conditions and stores energy in Li-ion batteries, supercapacitors, or conventional capacitors. It also provides battery charging, protection, and status output. Charge current is 0.1 A for charging chosen battery and battery charge voltage can differ from 2.5 V up to 5.25 V. Typical DC-DC conversion is up to 93%.

The converter features a programmable power tracking network [4]. As of 03/03/2025, its price on Mouser.com is 5.62 USD.

C. RF generators

Those generators work by collecting RF signals by an antenna (commonly referred to as a rectenna) and converting them into usable electrical energy. It is possible to utilize various frequency bands, such as GSM 868,MHz, WiFi 2.4,GHz, and many others, or even combine multiple bands for improved efficiency.

Since this technology is not yet widely adopted, only a few commercial RF energy harvesting solutions are currently available, primarily for the U.S. market, example of one RF harvesting module is Powercast P2110B which works on 915 MHz networks used usually in USA, Europe uses 868 Mhz [5]. An RF harvester may be considered for future system revisions after further research and evaluation.

D. Energy storage

Big portion of nowadays systems are usually battery powered, which allows them to stay working during power outages or are not connected to the power grid. Energy itself can be stored in capacitors, supercapacitors, or batteries (both rechargeable and non-rechargeable). Modern electronics primarily use rechargeable batteries due to their high capacity and suitability for long-term energy storage, while capacitors and supercapacitors help mitigate energy spikes.

Supercapacitors (SCs) store 10–150 times more energy per unit volume than conventional capacitors, charge and discharge faster than batteries, and offer significantly longer lifespans, enduring up to 1,000,000 cycles compared to 2,000–4,000 cycles for typical batteries. [6] In recent revision is used Li-Po AKYGA battery with 300 mAh capacity and is connected to the board by wires, product number is AKY0657 [7]. Which should provide device to run probably for about 81 hours with average power consumption per hour 2.86 mAh. Considered are duration of code for 0,05 sec, sleep time 1800 sec and consumption during execution about 60 mA and in sleep mode

850 nA. Typical self-discharge of this battery can be expected to be around 3-5% per month at room temperature.
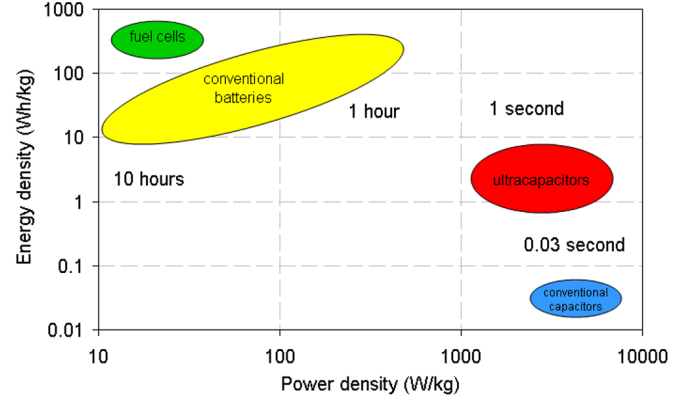
Fig. 2: Power density comparison [6]

V. DESIGNING SYSTEM

The board features the DWM3001C ultra-wideband module from Qorvo, integrating an antenna, accelerometer, power management, and an nRF52833 MCU with BLE. Derived from the DWM3001CDK, it includes an onboard J-Link debugger with SWD and UART interfaces, USB-C port for connectivity, and flexible power options, including a battery and energy harvesting by the BQ25504. The new design retains essential components while optimizing for future use by incorporating a TPS63051RMWT power regulator, removing an STM32-connected port, and adding test points for development. Programming is supported by a J-Link 6-pin connector (on reference board), first revision of the board is programmed by J-LINK EDU MINI segger [8] . The block diagram is shown in Fig. 3.
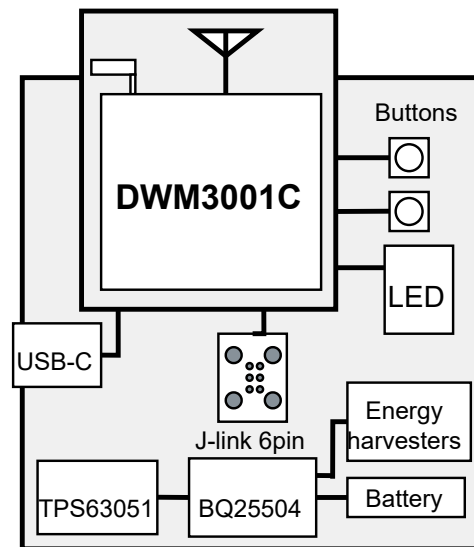
Fig. 3: Board block diagram

The initial steps involved studying the DWM3001CDK development board and its schematic. The board includes two switches (reset and boot wake-up), a programmable LED for debugging, and solder points for measurements. The new design replaces micro-USB with USB-C and retains J-Link for programming by 6 pin and edu segger. GPIO access is provided by two 4×2 connectors and a 13×2 Raspberry Pi-compatible header.

Power is managed by the TPS63051RMWT [9] regulator, replacing the discontinued XC925A33 [10], offering 90-95% efficiency. The BQ25504 energy harvester is used for solar charging, with battery connections by wires and offers up to 93% efficiency. The board follows a 4-layer design, which is now commonly used for many PCBs. All components are SMD with a package size of 0603 for easier assembly. The first revision of the board has dimensions of 46×42 mm, features a four-layer design (with GND and PWR as inner layers), and each component has a corresponding reference for easier assembly. The current revision of the board is shown in Fig. 4 and consists of the mentioned components. The next steps mainly involve testing the board and the system itself, as well as making layout adjustments. The board should remain a 4-layer design with a smaller size. The next steps also include evaluating the board's functions, primarily focusing on power management and consumption.

Additionally, a plastic outer shell will be designed for the system and 3D-printed. The shell should provide an simple mounting solution for various applications and simplify assembly.
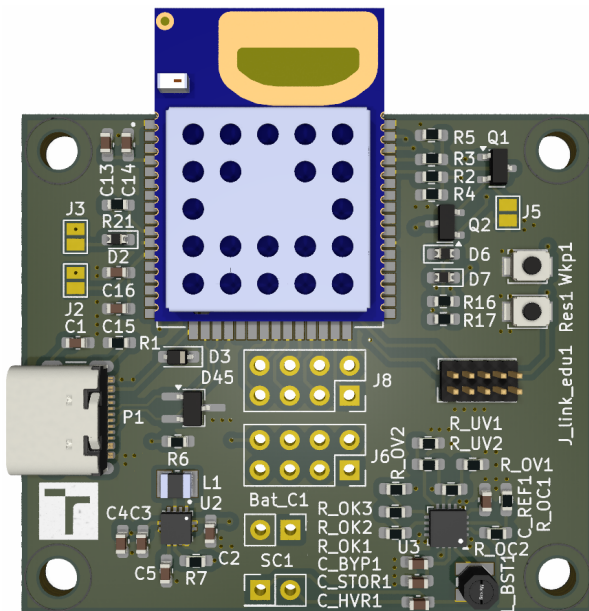
Fig. 4: Board PCB design

VI. CONCLUSION

The paper introduces the design an UWB-enabled board with energy harvesting capabilities. The main harvester in the current version is a solar panel with the battery located separately in a battery holder. Future revisions will include additional harvesters and improvements based on identified issues.

Along with the the next revision of the PCB and laboratory testing, the feasibility of RF energy harvesting will be investigated. Design changes may lead to an increased board size due to the addition of new components and harvesters. Lastly, a casing will be designed for the complete system, 3D-printed to accommodate all components and ensure suitability for various applications. The board will be tested with focus on energy harvesting and storage with possible use of the supercapacitors, followed by power consumption analysis and measuring battery life.

REFERENCES

[1] SEVCIK, Jan a JURAN, Radovan. Back to the Future: Developing an On-Board System for a Vintage Motorcycle. Online. In: Proceedings II of the 29st Conference STUDENT EEICT 2023: Selected papers. Brno University of Technology, Faculty of Electrical Engineering and Communication Technologies, 2023, s. 49-52. ISBN 978-80-214-6154-3. ISSN 2788-1334. Available at: https://doi.org/10.13164/eeict.2023.49. [accessed 2025-03-03].

[2] RAJU, Murugavel and GRAZIER, Mark, 2010. *ULP meets energy harvesting: A game-changing combination for design engineers.* Year. April 2010, pp. 1-8. Available at: https://www.mouser.com/pdfDocs/TI-ULP-meets-energy-harvesting-A-game-changing-combination-for-design-engineers.pdf. [accessed 2025-03-03].

[3] Qorvo. DWM3001C–Ultra-Wideband (UWB) Module with Low Energy (BLE) for Real-Time Location Systems. Qorvo. Available at: https://www.qorvo.com/products/p/DWM3001C. [accessed 2025-03-03].

[4] BQ25504 Ultra Low-Power Boost Converter With Battery Management For Energy Harvester Applications. Online. Ti.com. Available at : https://www.ti.com/lit/ds/symlink/bq25504.pdf?ts=1731428051286. [accessed 2025-03-03].

[5] Powercast Corporation. P2110B 915 MHz RF Powerharvester – RF Energy Harvesting and Wireless Power Module." Mouser Electronics. Available from: https://cz.mouser.com/datasheet/2/329/P2110B_Datasheet_Rev_3-3159474.pdf. [accessed 2025-03-03].

[6] B. Rajasekaran and K. Shirvekar, *A Survey on Supercapacitor Based Batteries* 2021 Third International Conference on Inventive Research in Computing Applications (ICIRCA), Coimbatore, India, 2021, pp. 180-187. Available from: https://ieeexplore.ieee.org/document/9544735. [accessed 2025-03-03].

[7] AKYGA Battery. AKY0657 - Li-Po; 3,7V; 300mAh battery Available from: https://www.tme.eu/cz/details/aky-lp752030/akumulatory/akyga-battery/aky0657/. [accessed 2025-03-03].

[8] SEGGER. "8.08.91 J-LINK EDU MINI – Compact Educational Debug Probe. Farnell. Available from: https://www.farnell.com/datasheets/2804162.pdf. [accessed 2025-03-03].

[9] Texas Instruments. TPS63051RMWT – High Efficiency Buck-Boost Converter. Texas Instruments. Available from: https://www.ti.com/product/TPS63051/part-details/TPS63051RMWT. [accessed 2025-03-03].

[10] Torex Semiconductor. XC9258A33CMR-G – Synchronous Step-Down Regulator. Mouser Electronics. Available from: https://mou.sr/3FyEAaU. [accessed 2025-03-03].

[11] *KiCad EDA A Cross Platform and Open Source Electronics Design Automation Suite* [online]. [accessed 2025-03-03]. Available from: ¡https://www.kicad.org/¿.

Multi-RCAT modem for Small-Scale PV Systems and Renewable Energy Communities

Alžbeta Kostelanská
Department of Telecommunications
Brno University of Technology
Brno, Czech Republic
xkoste13@vut.cz

Petr Mlýnek
Department of Telecommunications
Brno University of Technology
Brno, Czech Republic
mlynek@vut.cz

Lukáš Benešl
Department of Telecommunications
Brno University of Technology
Brno, Czech Republic
xbenes44@vut.cz

Ondřej Krajsa
Department of Telecommunications
Brno University of Technology
Brno, Czech Republic
krajsao@vut.cz

Michal Mahút
Department of Telecommunications
Brno University of Technology
Brno, Czech Republic
211263@vut.cz

Abstract—**In recent years, there has been a significant trend in the energy sector to build small-scale photovoltaic plants (PVPs). Such PV plants are a good tool to accelerate the drive towards zero-emission infrastructure in Europe. At the same time, however, they bring a lot of pressure to adapt the existing power grid to their unique requirements. This paper discusses the key features and typical communication technologies in Smart Grid systems, which can be utilized by small-scale PVPs. Based on the discussed features and challenges of small-scale PVPs, a modem prototype unit for reliable and secure communication is introduced. The proposed modem utilizes multiple wired and wireless technologies to ensure the best possible scalability and adaptability for most scenarios that may occur in Smart Grid communication scenarios.**

Index Terms—**PLC, Power Line Communication, Small-Scale PV, PVE, Renewable Energy, Energy Community**

I. INTRODUCTION

In Europe, the trend of increasing electricity generation from renewable sources has been very significant in the recent years. The main factor behind this are European Union's efforts to utilise renewables as efficiently as possible to build zero-emission infrastructure and buildings with the aim of achieving climate neutrality by 2050 [1]. Furthermore, by 2030, according to [1], 42.5% of the total energy consumed in the European Union should come from renewable sources. In the Czech Republic in 2023, according to [2], 44% of electricity was generated by burning fossil fuels, mainly coal. However, a significant increase in the adoption of photovoltaic power plants (PVPs) is also clear in the case of the Czech Republic at the same time. Additionally, PVPs made 4.2% of the total electricity generated. While the share of energy produced by PV plants with a power output above 100 kW has increased very slowly over the last years, the increase for PV plants with lower power output is very significant according to [3]. This trend shows a significant increase in small-scale PVPs with an output of up to 10 kW, whose total output more than doubled in 2023, indicating a significant increase in the number of

residential buildings that use small-scale PVPs to generate electricity. These small-scale PVPs have several significant advantages from a community energy perspective [4]. Despite the initial high cost, they are economically advantageous for households, mainly because of the long-term reduction in household utility costs.

Small-scale PVPs also provide means to enable energy independence of buildings and offer a pathway to zero-emission infrastructure. However, the biggest drawback of these installations is their impact on the overall distribution network and infrastructure, which may not be sufficiently prepared for large amounts of decentralised energy sources and may not be able to react quickly and flexibly enough to the generated electricity surpluses in case of unforeseen circumstances or fault conditions. These surpluses can have a bad impact on the balance of the distribution network. A reliable management system in the distribution network is needed to achieve this.

Such system requires reliable real-time communication between the PV inverter and the Smart meter or electricity meter. It is also necessary to ensure that the PV inverter can be regulated and possibly disconnected from the power grid in the event of power surpluses, to reliably prevent economic losses. For the monitoring purposes in decentralised grids, it is also advantageous to monitor changes, disturbances or possible faults on the grids as efficiently as possible and to send real-time reports of fault or atypical conditions. This can be achieved, for example, by using an appropriately chosen algorithm or artificial intelligence model as described in [5]. In addition, it is necessary that such communication is secured and cannot be tampered with or modified from the outside in any way, to prevent unwanted disconnections or connections of the PV inverter to the distribution grid, which could cause economic losses either on the side of the customer, i.e. in the case of small PV mostly households, or on the side of the distributor. As discussed in [6], communication between Smart
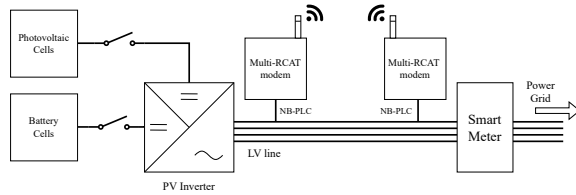
Fig. 1: Topology of PV Inverter and Smart meter system.

meter and PV inverter brings various challenges and problems. Typical communication scenario can be seen on fig.1.

II. COMMUNICATION TECHNOLOGY

The need for stable and reliable communication between devices in a Smart Grid network requires the implementation of a suitable communication protocol. It appears advantageous to implement a system that can support several independent communication technologies and is capable of switching between these technologies when stable connection cannot be guaranteed by some. For Smart Grid applications, a large variety of different communication technologies, both wired and wireless, are presently used. The communication protocols used in Smart Grid applications are often designed to ensure two-way communication between the smart devices in the network. The article [7] gives an overview of the advantages and disadvantages of the most commonly used technologies and standards.

A. Wired Technologies

For communication between smart devices in power grid applications it is advantageous to use PLC (Power Line Communication) technology. Its major advantage is the possibility of using the already established electrical infrastructure as a transmission medium. From [11] can be seen that the use of Narrowband PLC (NB-PLC) technology is a suitable candidate for the use case of Smart Grids and Community Energy. This technology is characterized by a narrow transmission bandwidth in VLF, LF and MF band (3–500 kHz), resulting in its resistance to noise and interferences and a relatively long transmission distance. In Europe, the CENELEC band (3-148,5 kHz) is used. High Data Rate (HDR) NB-PLC technology also offers the ability to transmit data with data rate up to 500 kb/s. Among other things, as described in [12] study, the use of NB-PLC technology appears to be advantageous in terms of possible coexistence with BB-PLC on a single line without cross-interference, the possibility of worldwide deployment of the device, as well as the optimisation of communication for energy sector applications using this technology.

Utilizing PLC technology as the main form of communication in the power grids can also be advantageous in terms of easy implementation of measurements on power lines. Study [8] proposes utilizing of PLC communication as tool for measuring and monitoring the degradation and ageing of power line cables. In [9] it is proposed that PLC technology

can be used as a tool for mapping the topology of an unknown low voltage power network.

Another possible wired technology implemented is communication using optical fibre as the transmission medium [7]. However, as mentioned in the article, compared to metallic cables, which are the transmission medium for PLC technology, optical fibers are more resistant to interference. At the same time, however, they are more expensive to build and more difficult to repair faults. The use of fibre optics necessitates the construction of new transmission infrastructure in locations. This presents a major disadvantage for deploying communications over this transmission medium for small-scale to medium-scale PVPs.

B. Wireless Technologies

In environments where the deployment of metallic or fiber communication technologies is not available, a variety of wireless technologies can be used. The advantages and disadvantages of the most used wireless technologies are summarized in [7]. Among the most widely used is the Zigbee protocol, which is an extension of the IEEE 802.15.4 standard. Bluetooth technology is also frequently deployed. Compared to Zigbee, its implementation is more challenging. The use of Sub-1GHz ISM band frequencies is also widespread. As stated by [7] and [10], the most used UHF bands are 412–475 MHz and 860–960 MHz. All the technologies mentioned so far transmit in the unlicensed ISM frequency band. However, the use of licensed bands can also be observed in Smart Grid networks, in particular LTE and 5G technology and its extensions for sensor and automated systems: LTE Cat-M and NB-IoT. Compared to unlicensed band technologies, these do not require the construction of a separate infrastructure. It is already available and managed by the mobile network providers in the deployment region. In this case, however, the disadvantage is the centralized nature of such communication, where communication must be carried out over the mobile operator's network, as mentioned in [7], which can negatively influence the real-time character of the communication.

III. PROPOSED PROTOTYPE UNIT

The proposed modem offers the possibility of utilizing several communication technologies commonly used in Smart Grids networks. This is very advantageous in case of its deployment in small-scale to medium-scale PV systems. Since in this case, as mentioned in section I, it is mainly PV plants located in residential buildings. In this case it is often not possible to ensure the presence and reliability of all frequently used communication technologies. At the same time, it is necessary to ensure reliable communication between the PV inverter, which connects the PV to the power grid network and transfers DC voltage from solar panels to AC voltage, and the associated electricity meter, which is built at the interface between the household power grid and the distribution grid, precisely for these objects. A reliable local communication needs to be built here to control the connection between the distribution grid and the home grid. The proposed modem
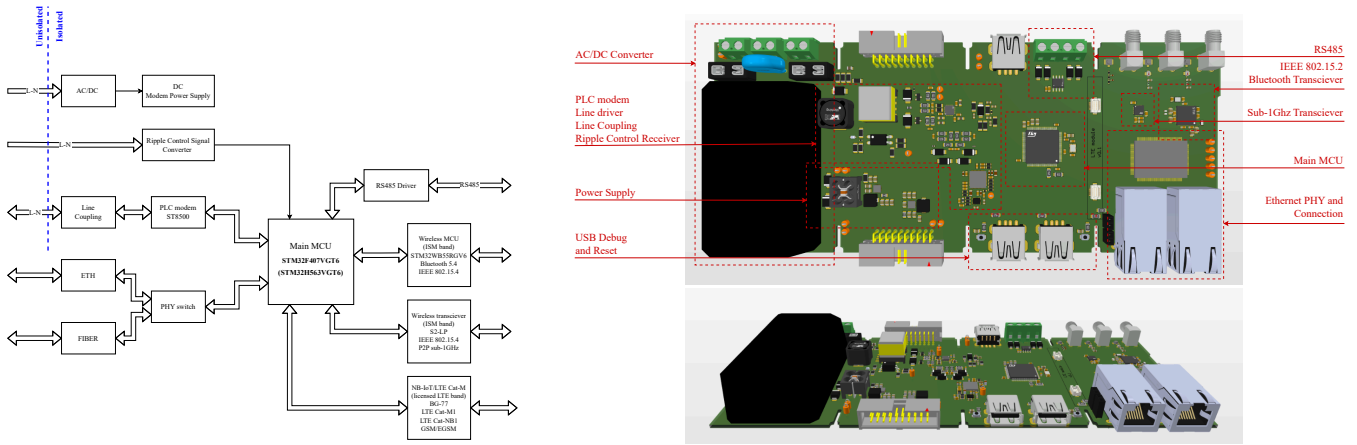
Fig. 2: (a) Block diagram of modem, and (b) the 3D model of the modem prototype.

can be described as a Multiple Radio and Cable Access Technology (Multi-RCAT) device.

Multi-RCAT devices provide the ability to communicate based on a combination of both wireless and wired communication technologies. The main advantage of the proposed modem is its capability to use multiple transmission technologies and the ability to switch between these technologies based on the specific requirements of the environment in which the modem is deployed. For the use with small-scale PVPs in Renewable Energy Communities implementing of one wired and wireless technologies is considered. The modem combines both wired and wireless communication within a local area network, making it a versatile device suitable for most typical deployment scenarios considered for the community energy scenario. In addition to that the proposed modem supports the possibility of receiving and digitalizing the Ripple Control signal, which is used in the Czech Republic for controlling and switching between tariffs in the Smart Grid network.

The modem acts as a communication link between the PV inverter and the associated meter. It provides a point-to-point connection between these two nodes on the local grid network. Additionally, the proposed modem provides the capability of controlling the consumption and production in small-scale PV plants and households based on the function of digitalized Ripple Control commands. Furthermore, the modem can also be used for statistical data collection and smart metering in the local network, or to record faults and line changes as previously mentioned in section II.

To provide the best flexibility, the proposed modem supports several different communication technologies, the use of which varies based on the deployment conditions. The modem is a hybrid device capable of providing both wired and wireless communications. Primarily wired communication is assumed. For community energy applications, the deployment of PLC technologies appears to be the most advantageous. As mentioned in section II, NB-PLC communication has major advantage in terms of the possibility to use the already present power lines as a transmission medium. NB-PLC technology

is also less susceptible to disturbances that may arise in the power grid due to the narrowband frequency transmission. Modem is proposed to utilise SiC PLC modem ST8500. According to the [14], this modem is prepared for deployment with The G3-PLC communication stack, which is standardized by G3-Alliance. This brings advantage in easy integration of the proposed modem with existing network and helps with quick development and future deployment of the prototype mode in real-life scenarios. Together with PLC technology, implementation of Ethernet communication is also considered.

In addition to the metallic link, the modem also considers the possibility of connecting to a fibre optic line for cases where these technologies are available, and their use is more advantageous due to increased interference on the power line. As previously discussed in section II, such communication is more reliable and stable, but needs dedicated fibre cabling.

In case of impossibility of using a wired connection, the modem also provides the possibility of wireless communication. To ensure redundancy, at least two wireless technologies are considered for each use-case, where at least one of them is always in the unlicensed frequency band. This is advantageous, for example, if there is no cable infrastructure in the deployed area, if the distance between the Smart meter and the PV inverter is too long, or the exact topology of the power grid is not known. LTE license band communication is utilized. Modem supports LPWAN standards LTE Cat NB2 and LTE CatM1 with help of wireless LPWAN module BG77. Both standards are characterised by the ability to transmit data over long distances with good coverage even in less accessible areas, possibly within buildings. In addition to that, both technologies have very high coverage rates in the Czech Republic. The modem also provides the possibility of wireless communication in the unlicensed frequency bands. For this purpose, communication protocol based on IEEE 802.15.4 standard in 2.4 GHz frequency band and Bluetooth communication are utilized. This function is provided by the wireless microcontrollers from the STM32WBx5 family. Lastly, point-to-point communication in Sub-1GHz band can be used. S2-

LP transceiver was selected, mainly because its relatively easy integration with SiC PLC modem ST8500. Together they can utilize G3-Hybrid communication stack, which is developed by G3-Alliance.

As already mentioned, the modem also provides the possibility of receiving Ripple Control signals, which are used as control commands in the power grid applications in the Czech Republic. The modem has the function of digitalizing these commands, which can subsequently be used in the control of small PV plants in households, as well as Renewable Energy Communities.

For dynamic switching between the available communication technologies, it is assumed to implement a failover function that ensures this switching with respect to the detected or expected interference in the network and selects the most suitable transmission protocol and transmission medium from the available ones. This redundancy in the system can ensure that there is no loss of information or failures caused by such losses. This can ensure and guarantee the best possible response of the system to sudden changes and prevent fault conditions caused by interference or leakage into the power grid that may occur in the energy communities utilizing Small-Scale PVEs.

IV. CONCLUSION AND FUTURE WORK

In this paper, key features of the reliable system for communication in small-scale PVPs Renewable Energy Communities and typical communication technologies employed in Smart Grid systems were discussed. The contribution of this article is threefold. Firstly, based on the discussed parameters developed prototype unit of the modem for this use case was introduced. The proposed modem, mainly aimed at providing safe and reliable communication between the PV inverter and the peripheral electrometer or Smart meter for small-scale PV systems, represents an important element in the energy distribution network considering the trend of increasing number of new small-scale PV systems primarily in residential areas. The presented modem combines several important functions that are essential for communication in networks of this kind. It provides a hybrid solution that assumes the possibility of real-time communication and response to changes in the network.

Secondly, by digitalizing Ripple Control commands used in the Czech Republic, the modem provides flexible and quick reaction to changes in the distribution network, either based on the expected energy balance, but also in case of unforeseen variations. Lastly, the modem provides a good tool for analysing the connectivity within the local energy network. Based on the measured parameters of the network, it could be possible to switch between the implemented communication technologies and select the most appropriate one to avoid communication failures and problems that may be caused by such failures.

Future work will be devoted to testing and validation of the proposed prototype for different scenarios that may arise in the case of small PV plants, with emphasis on communication reliability. The proposed unit will be used for measuring and testing of the communication between Smart meter and PV inverter in the typical scenarios. Reliability and security of the proposed prototype will be evaluated.

REFERENCES

[1] "Directive EU–2023/2413 EN–Renewable Energy Directive EUR-Lex," Europa.eu, 2023. https://eur-lex.europa.eu/eli/dir/2023/2413-/oj?locale=en (accessed Mar. 10, 2025).

[2] "Czech Republic - Countries & Regions," IEA. https://www.iea.org/-countries/czechia/energy-mix (accessed Mar. 10, 2025).

[3] "Energetika v číslech," Eru.gov.cz, 2025. https://eru.gov.cz/energetika-v-cislech (accessed Mar. 10, 2025).

[4] S. Garg and S. Tyagi, "A Comprehensive Review on Opportunities and Challenges of Grid Integration of Renewable Energy Resources," 2024 Second International Conference on Smart Technologies for Power and Renewable Energy (SPECon), Ernakulam, India, 2024, pp. 1-6, doi: 10.1109/SPECon61254.2024.10537518.

[5] M. Malik, M. M. Sati, A. Singh and N. Kumar, "Grid Integration Difficulties and Solutions for PV Solar Systems with AI Technique in a Homogeneous Environment," 2023 International Conference on Power Energy, Environment & Intelligent Control (PEEIC), Greater Noida, India, 2023, pp. 478-483, doi: 10.1109/PEEIC59336.2023.10451684

[6] P. Musil, P. Mlynek, L. Benesl, M. Mahút and M. Rusz, "Local Communication in Small-Scale PV Systems: Study on Inverter – Smart Meter PLC Communication," 2024 IEEE International Conference on Communications, Control, and Computing Technologies for Smart Grids (SmartGridComm), Oslo, Norway, 2024, pp. 529-534, doi: 10.1109/SmartGridComm60555.2024.10738078.

[7] V. C. Gungor et al., "Smart Grid Technologies: Communication Technologies and Standards," in IEEE Transactions on Industrial Informatics, vol. 7, no. 4, pp. 529-539, Nov. 2011, doi: 10.1109/TII.2011.2166794.

[8] Y. Huo, G. Prasad, L. Atanackovic, L. Lampe and V. C. M. Leung, "Grid surveillance and diagnostics using power line communications," 2018 IEEE International Symposium on Power Line Communications and its Applications (ISPLC), Manchester, UK, 2018, pp. 1-6, doi: 10.1109/ISPLC.2018.8360200.

[9] T. Erseghe, S. Tomasin and A. Vigato, "Topology Estimation for Smart Micro Grids via Powerline Communications," in IEEE Transactions on Signal Processing, vol. 61, no. 13, pp. 3368-3377, July 2013, doi: 10.1109/TSP.2013.2259826.

[10] N. Suhaimy, N. A. M. Radzi, W. S. H. M. W. Ahmad, K. H. M. Azmi and M. A. Hannan, "Current and Future Communication Solutions for Smart Grids: A Review," in IEEE Access, vol. 10, pp. 43639-43668, 2022, doi: 10.1109/ACCESS.2022.3168740.

[11] C. Cano, A. Pittolo, D. Malone, L. Lampe, A. M. Tonello and A. G. Dabak, "State of the Art in Power Line Communications: From the Applications to the Medium," in IEEE Journal on Selected Areas in Communications, vol. 34, no. 7, pp. 1935-1952, July 2016, doi: 10.1109/JSAC.2016.2566018.

[12] S. Galli, A. Scaglione and Z. Wang, "For the Grid and Through the Grid: The Role of Power Line Communications in the Smart Grid," in Proceedings of the IEEE, vol. 99, no. 6, pp. 998-1027, June 2011, doi: 10.1109/JPROC.2011.2109670.

[13] Z. Lipošćak and M. Bošković, "Survey of smart metering communication technologies," Eurocon 2013, Zagreb, Croatia, 2013, pp. 1391-1400, doi: 10.1109/EUROCON.2013.6625160.

[14] "ST8500-STMicroelectronics," STMicroelectronics, 2025. https://www.st.com/en/interfaces-and-transceivers/st8500.html (accessed Mar. 06, 2025)

Wireless node with Wi-Fi HaLow technology

Bc. Horčička Patrik

Brno University of Technology
Faculty of Electrical Engineering and Communication
Brno, Czech Republic
xhorci03@vutbr.cz

Abstract—**This paper presents the ongoing development of a wireless node and access point (AP) based on Wi-Fi HaLow (IEEE 802.11ah) technology, targeting long-range and low-power IoT applications. The project is currently underway and aims to design an affordable, fully open-source solution covering hardware and software aspects. The theoretical part compares Wi-Fi HaLow with other wireless technologies regarding range, energy efficiency, and integration with IP networks. Practically, the project includes PCB design, hardware integration, and preparation for firmware development. The wireless node has been fabricated and assembled; firmware development is currently in progress. Upon completion, the same methodology will be applied to the AP. The key contribution lies in the transparency, adaptability, and accessibility of the proposed open-source platform as an alternative to closed, proprietary systems.**

Index Terms—**Wi-Fi HaLow, 802.11ah, wireless sensor networks, wireless node, IoT, PCB design, Quectel FGH100M, sub-GHz**

I. INTRODUCTION

Wireless data transmission is essential to modern communication, enabling seamless data exchange between users and devices. In recent years, the increasing number of IoT devices and sensors has highlighted the need for efficient wireless connectivity solutions. The IEEE 802.11ah standard, also known as Wi-Fi HaLow, is a significant development in this context. It is designed to address these demands by offering low-power, long-range communication, making it particularly suitable for IoT applications.

Despite being introduced by the IEEE in 2017, Wi-Fi HaLow has only recently gained traction as companies begin to develop compatible hardware. This recent surge of interest in Wi-Fi HaLow, which operates in the sub-GHz spectrum, allowing for extended range, improved penetration through obstacles, and reduced power consumption, is a significant development in wireless communication. These features make it an ideal solution for large-scale sensor networks, industrial automation, and innovative city applications.

This paper examines the implementation of a wireless node and access point (AP) utilizing Wi-Fi HaLow technology. It explores the fundamental technical aspects of the standard, including its physical and Medium Access Control (MAC) layers, supported security protocols, and its advantages over other wireless technologies. Furthermore, it presents the conceptual design of a wireless node, discussing hardware selection, communication architecture, and data transmission between end

devices and a central server. Through this analysis, the paper aims to demonstrate the feasibility and potential applications of Wi-Fi HaLow in real-world deployments, instilling a sense of optimism about its practical use.

II. WI-FI HALOW TECHNOLOGY OVERVIEW

Wi-Fi HaLow is an extension of the IEEE 802.11 standard, specifically tailored for IoT applications. Unlike traditional Wi-Fi (IEEE 802.11n/ac/ax), which operates in the 2.4 GHz and 5 GHz bands, Wi-Fi HaLow utilizes the sub-1 GHz spectrum, enabling longer transmission distances and improved penetration through obstacles.

A. Key Features of Wi-Fi HaLow

- **Extended Range:** Transmission distances up to 1 km, surpassing conventional Wi-Fi technologies.
- **Low Power Consumption:** Optimized for battery-powered IoT devices, reducing energy usage through power-saving mechanisms like Target Wake Time (TWT).
- **High Device Capacity:** Supports up to 8191 connected devices per access point (AP), making it ideal for large-scale IoT deployments [2].
- **Secure Communication:** Implements WPA3 security, ensuring robust protection against network vulnerabilities [1].

B. Comparison with Other Wireless Technologies

Compared to LPWAN technologies such as LoRaWAN and Sigfox, Wi-Fi HaLow offers higher data rates (up to several Mbps under ideal conditions) [2] and native IP connectivity, eliminating the need for protocol translation gateways. Unlike Zigbee and Bluetooth Low Energy (BLE), which typically operate in the 2.4 GHz band with limited coverage (10–100 meters), Wi-Fi HaLow operates in the sub-1 GHz ISM bands and achieves significantly longer range (hundreds of meters to over 1 km in line-of-sight conditions), while maintaining comparable energy efficiency through mechanisms such as TWT.

Although exact numerical values vary based on regional regulations, environmental conditions, and implementation specifics, Wi-Fi HaLow demonstrates favourable trade-offs between throughput, range, power consumption, and scalability. A qualitative comparison with unlicensed LPWAN technologies is shown in Figure 1. Similarly, Figure 2 illustrates how

Wi-Fi HaLow positions itself against PAN and WAN technologies regarding coverage and application domains. Figure 3 presents a conceptual comparison with licensed LPWAN technologies, including NB-IoT (Narrowband Internet of things) and LTE-M.

Recent comparative studies [3] emphasize the practical advantages of IEEE 802.11ah in large-scale IoT deployments, particularly regarding real-time responsiveness and reduced system complexity. These findings suggest that Wi-Fi HaLow can bridge the gap between traditional Wi-Fi and constrained LPWAN systems in industrial and intelligent city environments.

Fig. 3. Comparison with licensed LPWAN technologies [2]

where the Microcontroller Unit (MCU) processes sensor data from interfaces and transmits it via the Wi-Fi HaLow module. The system is designed to operate autonomously with minimal power supply or battery energy consumption.

The key hardware components selected for the wireless node are:

- **Wi-Fi HaLow Module:** Quectel FGH100M, chosen to support the IEEE 802.11ah standard and low power operation [4].
- **MCU:** STM32L452RC, selected for its low-power processing capabilities and compatibility with IoT applications [7].
- **Power Management System:**
  - **DC/DC Converter:** MAX77827, selected primarily for its ultra-low quiescent current (only 6 µA) and exceptional efficiency, ideal for battery-powered IoT devices requiring minimal standby power [5].
  - **Battery Management System:** BQ25185, selected for its low quiescent current and support of high system loads [6].
- **Communication Interfaces:** UART, SPI, and I2C, allowing seamless integration with peripheral sensors and external systems.

B. AP Design

The AP was designed to facilitate high-speed data transmission between the Wi-Fi HaLow sensor network and the Internet, bridging these two domains. The AP integrates a dedicated control CPU responsible for managing the Wi-Fi HaLow module and the Ethernet interface, ensuring seamless Internet connectivity. Additionally, the AP is powered via a USB-C interface, utilizing a DC/DC converter to efficiently provide the required operating voltage.

The AP leverages an open-source software stack to ensure maximum flexibility, cost efficiency, and adaptability. The system is designed to run OpenWrt, a highly customizable Linux-based operating system tailored for networking applications. OpenWrt provides advanced routing capabilities,

Fig. 1. Comparison with unlicensed LPWAN technologies [2]

Fig. 2. Comparison with PAN and WAN technologies [2]

III. HARDWARE COMPONENTS

A. Wireless Node Design

The wireless node was designed to ensure efficient communication while minimizing power consumption. The selection of components and the overall architecture were crucial in achieving these objectives. The block diagram is shown in Figure 4. The wireless node consists of interconnected modules,

Fig. 4. Block diagram of Wireless node with Wi-Fi HaLow

Fig. 5. Wi-Fi HaLow communication infrastructure

security enhancements, and modular extensibility, making it an ideal choice for an open-source Wi-Fi HaLow AP. Should OpenWrt compatibility be limited, Raspbian (Raspberry Pi OS) can be used as an alternative.

The key hardware components selected for the AP are:

- **Wi-Fi HaLow Module:** Quectel FGH100M, chosen to support the IEEE 802.11ah standard and its low-power operation [4].
- **CPU:** Raspberry Pi Compute Module 4 (RPI-CM4), selected for its sufficient computational performance required for network routing tasks and its native support for Ethernet connectivity [8].
- **DC/DC Converter:** MAX77827, chosen primarily for its ultra-low quiescent current (only 6 µA) and exceptional efficiency, making it an optimal choice for battery-powered IoT applications that demand minimal standby power consumption [5].

IV. COMMUNICATION ARCHITECTURE

The communication infrastructure of the Wi-Fi HaLow standard is illustrated in Figure 5. External peripherals are connected to the wireless node via a wired interface, such as I2C, SPI, or other protocols. The wireless node communicates with an AP using a Wi-Fi HaLow wireless network. The AP acts as a bridge, allowing multiple independent wireless nodes to connect to the Internet. Data is transmitted through the AP to the Internet and then to servers, where it is stored and processed.

V. COMPARISON WITH COMMERCIAL SOLUTIONS

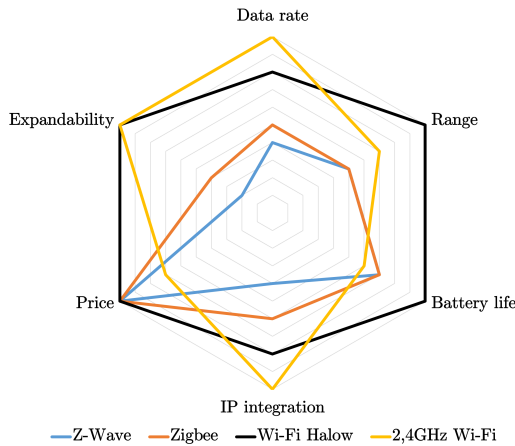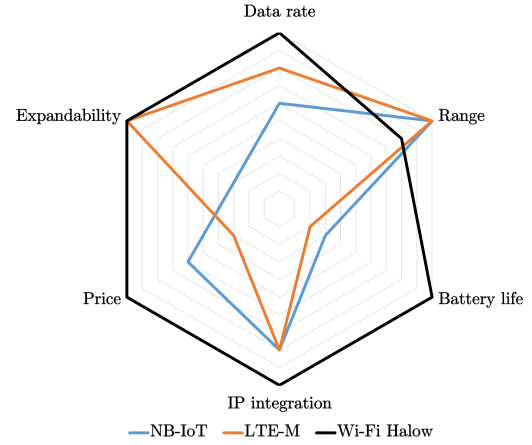While commercial Wi-Fi HaLow solutions typically support most of the features mentioned in the open-source design, their major drawback lies in their closed system architecture, which severely limits adaptability. These proprietary solutions are often significantly more expensive and provide minimal configurability, restricting users to predefined settings. Furthermore, not all technical details and security implementations are
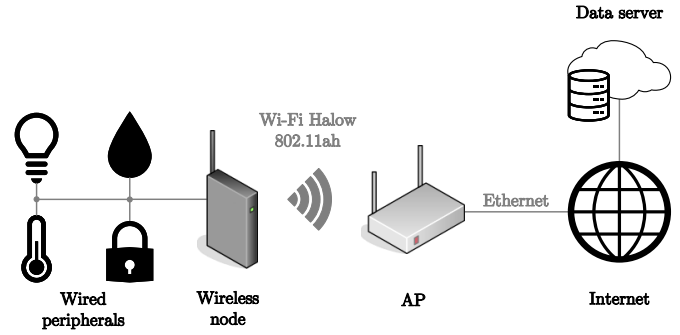
transparently disclosed, making it difficult for users to fully understand and modify the system according to their needs.

In contrast, the proposed open-source solution offers complete transparency and full access to all system components, allowing for extensive customization based on user requirements. One of the key advantages of this approach is its flexibility. Additionally, the absence of corporate licensing fees and proprietary restrictions significantly reduces costs, ensuring a more accessible and affordable alternative without sacrificing performance or security.

VI. PCB DESIGN AND IMPLEMENTATION

A custom PCB was developed to integrate all components into a compact, functional wireless node. The design process involved schematic development, PCB layout optimization, and prototyping to ensure efficient performance and reliability.

The device's core is the **STM32L452RC**, which is the primary MCU for data processing. Directly connected to the MCU is the **FGH100M Wi-Fi HaLow module**, which receives commands from the MCU to handle data transmission.

For power management, the PCB includes two dedicated pins for connecting a rechargeable battery. Charging is facilitated via a **USB-C port**, which also serves as an interface for external MCU control. The **USB-C voltage is regulated through the BQ25185 charging module**, which protects against Undervoltage and overvoltage while optimizing charging speed. The regulated output is then fed into a **DC/DC converter**, which steps down the battery voltage to **3.3V** to ensure stable operation of the board's components.

A dedicated **power switch** turns the system on and off as needed. Additionally, the board features **designated connection points** for external peripherals and an antenna connector for the Wi-Fi HaLow module.

A. PCB Layout Considerations

- **Compact Design:** The PCB layout was optimized to minimize footprint while maintaining signal integrity.
- **Power Optimization :** Power traces and planes were strategically routed to minimize energy losses and enhance efficiency.

- **Antenna Placement:** The antenna positioning was carefully designed to improve wireless performance and minimize interference.

B. 3D Model and Prototyping

A 3D model of the PCB was developed to visualize the final layout before manufacturing. The model of the wireless node is shown in Figure 6, and the model of the AP is shown in Figure 7. The prototypes will be tested under various real-world scenarios, including indoor/outdoor signal propagation, power consumption under different loads, and data transmission reliability over long-range communication links.
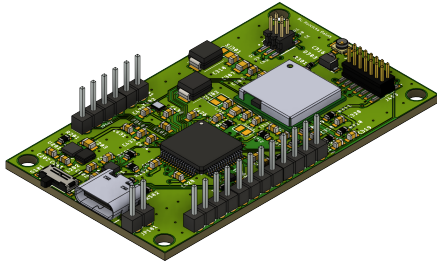
Fig. 6. Wireless node PCB design
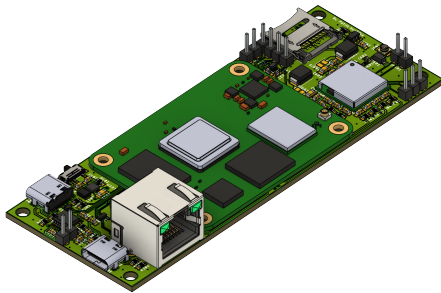
Fig. 7. AP PCB design

VII. CONCLUSION

This paper presents the design and partial implementation of a wireless node and AP based on Wi-Fi HaLow technology, demonstrating its potential for IoT applications. The proposed system architecture targets long-range connectivity, low power consumption, and seamless integration with IP networks, making it suitable for industrial, agricultural, and intelligent city environments.

The wireless node has been successfully fabricated and is currently undergoing component assembly. Firmware development and system programming will follow, accompanied by functional testing to verify operational parameters such as range, power consumption, and transmission reliability. Once validated, the same prototyping and evaluation methodology will be applied to the access point (AP), completing the system design loop.

This work constitutes a foundational step toward realizing a fully open-source Wi-Fi HaLow platform. Future efforts will focus on software integration, sensor interfacing, performance benchmarking, and validation in real deployment scenarios.

After functional testing, the complete hardware schematics, PCB layout files, and firmware source code will be publicly available under an open-source license.

Wi-Fi HaLow shows excellent promise as a next-generation wireless communication solution for IoT systems.

ACKNOWLEDGMENT

REFERENCES

[1] IEEE Organization, *IEEE Standard for Information Technology–Telecommunications and Information Exchange between Systems - Local and Metropolitan Area Networks–Specific Requirements - Part 11: Wireless LAN Medium Access Control (MAC) and Physical Layer (PHY) Specifications*, IEEE Std 802.11-2020 (Revision of IEEE Std 802.11-2016), 2021, pp. 1–4379, doi: https://doi.org/10.1109/IEEESTD.2021.9363693.

[2] Wi-Fi Alliance, *Wi-Fi CERTIFIED HaLow™ Technology Overview (2021)*, 2021, online, accessed: 2024-10-30, https://www.wi-fi.org/file/wi-fi-certified-HaLow-technology-overview-2021.

[3] M. Alam, N. Ahmed, R. Matam, and F. A. Barbhuiya, "Analyzing the suitability of IEEE 802.11ah for next generation Internet of Things: A comparative study," *Ad Hoc Networks*, vol. 156, pp. 103437, 2024. [Online]. Available: https://www.sciencedirect.com/science/article/pii/S1570870524000489. doi: https://doi.org/10.1016/j.adhoc.2024.103437.

[4] Quectel Wireless Solutions Co., Ltd., *FGH100M Wi-Fi HaLow Module Datasheet*, Rev. V1.0, 2023. [Online]. Available: https://www.quectel.com/product/fgh100m

[5] Analog Devices, *MAX77827: 2.5V to 5.5V, 3A Buck Converter*, Datasheet, 2021. [Online]. Available: https://www.analog.com/media/en/technical-documentation/data-sheets/max77827.pdf

[6] Texas Instruments, *BQ25185 Single Cell Charger with Low Iq and Power Path*, SLUSDT4B – APRIL 2019 – REVISED AUGUST 2020. [Online]. Available: https://www.ti.com/product/BQ25185

[7] STMicroelectronics, *STM32L4x2 Reference Manual (RM0394)*, Rev. 5, September 2022. [Online]. Available: https://www.st.com/resource/en/reference_manual/dm00151940.pdf

[8] Raspberry Pi Foundation, *Compute Module 4 Datasheet*, Rev. 1.0, October 2020. [Online]. Available: https://datasheets.raspberrypi.com/cm4/cm4-datasheet.pdf

Distributed Acoustic Sensing System Based on Dual Polarization 90-degree Optical Hybrid

Jan Bukovský
Department of Telecommunications
Brno University of Technology
Brno, Czech Republic
xbukov18@vutbr.cz

Petr Münster
Department of Telecommunications
Brno University of Technology
Brno, Czech Republic
munster@vut.cz

Abstract—**This work deals with the measurements with distributed acoustic sensing (DAS) systems using standard telecommunication optical fibers. In this work is also discussed the polarization fading suppresion using polarization diversity. As part of this work, measurements were made with an experimental DAS system. This DAS system used dual polarization 90-degree hybrid for polarization fading supression. During these measurements sinusoidal disturbance around the fiber was simulated. The method of data processing and the evaluation of the measured data are presented in the last part of this work.**

Index Terms—**DAS, polarization fading, polarization diversity, fiber optic sensor**

I. INTRODUCTION

Distributed acoustic sensing (DAS) systems are among the reflectometric distributed fiber optic sensors [1]. Distributed fiber optic sensors have several advantages over standard sensors. These sensors are resistant to electromagnetic disturbances and extreme temperatures, have a long operating range, and a single optical fiber can be converted into up to tens of thousands of independent sensors. The last advantage allows the mapping of various physical parameters along the fiber [2], [3].

DAS systems use fiber optic cables to measure the effect of strain and/or temperature changes along the fiber [1]–[3]. In most cases, standard telecommunication fiber optic cables are used as the sensor, so existing fiber optic networks can be used and converted to a distributed acoustic sensor capturing data in real time [4]–[6].

One of the important parameters of DAS systems is the spatial resolution. The spatial resolution $\Delta z_{\min}$ represents the ability to locate a section of fiber affected by temperature changes and/or strain. The spatial resolution value for OTDR-based systems is given by

$$\Delta z_{\min} = \frac{c \cdot \tau}{2 \cdot n},\qquad(1)$$

where c is the speed of light in vacuum, n is the index of refraction of the fiber core, and τ represents the pulse width of the incident light [2]. From this relation, it follows that the value of the spatial resolution is determined by the duration of the pulse sent into the fiber. Using shorter pulses will improve the spatial resolution value. However, by shortening the pulses, the power of the backscattered radiation will also be reduced

and therefore the signal-to-noise ratio will be reduced. As a result, there is a trade-off between the spatial resolution value and the maximum range of DAS systems [2], [3].

Either the intensity or the phase of the backscattered light due to Rayleigh scattering can be used to locate the location of the disturbance on the fiber. Therefore, DAS systems can be divided into systems based on intensity measurements or systems based on phase measurements [1], [7].

DAS systems based on intensity measurements have a simple structure and are cheaper than DAS systems based on phase measurements [1]. The disadvantage of these systems is that they can only locate the point of disturbance using intensity changes. However, the magnitude of the disturbance cannot be determined from the intensity changes, since there is no linear relationship between intensity and temperature changes or between intensity and applied strain [1], [8], [9].

Phase-based DAS systems have the advantage over intensity-based systems that by using phase changes, it is possible not only to locate the location of the disturbance acting on the fiber, but also to determine the magnitude of the disturbance [1], [3], [8]–[11]. More specifically, these systems can measure changes in temperature and/or applied strain (the absolute values of these parameters cannot be measured) [3], [10]. This is possible because the phase changes are linearly proportional to both the changes in temperature and the applied strain [1], [3], [8]–[11].

A. Polarization fading suppression

In fiber optic sensors, i.e. also in DAS systems, errors caused by polarization are common. The phenomenon causing these errors is referred to as polarization fading [12], [13]. Polarization fading occur for various reasons. Among these causes is the dependence of the polarization state (in a conventional single-mode fiber) on the fiber's birefringence. When the birefringence changes, e.g. due to external disturbance acting on the fiber, the polarization state of the light fluctuates randomly [12]. In systems using coherent detection, polarization fading occur when there is a polarization mismatch between the reference and the measured signal. Polarization mismatch between these signals occurs when the polarization states of the reference and measured signals are orthogonal to each other. Polarization fading generally cause a reduction in

the signal-to-noise ratio, and coherent systems may produce sections of fiber insensitive to the disturbance, leading to some unreliability of the measurement systems [2], [12], [13]. This unreliability is particularly problematic when DAS systems are used to detect bridge breaches and internal cracks and when monitoring the condition of pipelines and oil wells [2], [13].

There are several approaches to suppress polarization fading. In distributed sensing systems, polarization fading can be suppressed by using either polarization diversity, or orthogonal pulse pair, or polarization pulse encoding, or Faraday rotating mirror, or polarization maintaining fiber, or by using a polarization scrambler [2], [12], [13].

In the next chapter, the DAS setup is used to suppress polarization fading by using polarization diversity. The basic principle of the polarization diversity method is to divide the optical signal, before conversion to an electrical signal, into multiple light beams differing in polarization state. In most cases, the light beam is divided by polarizers or polarization beam splitters (PBS) into two or three beams with different polarization states [2], [12], [13]. In DAS systems, PBS is often used to split the beam into two orthogonal polarization states. These two signals are then combined to achieve suppression of polarization fading caused by a polarization state mismatch between the reference and the sensing arm at each location of the fiber under test (FUT) [2], [13]. Complete suppression of polarization fading caused by polarization mismatch between the reference and the measured signal can be achieved by splitting the signal into three beams with different polarization states [12].

II. EXPERIMENTAL SETUP

Measurements were made with a DAS system that should be able to suppress polarization-induced errors by using a dual polarization 90-degree hybrid. The used setup is shown in Figure 1. As can be seen in this figure, a narrow-linewidth laser was used as the light source. The emitted radiation was split into two branches using a coupler. In the first branch, the light wave is modulated by an acousto-optic modulator (AOM) with a frequency shift of 80 MHz. A pulse signal is supplied to the AOM. The pulse at the output of the AOM has a repetition rate of 10 kHz and a pulse width of 100 ns, corresponding to a spatial resolution of 10 m [14]. This pulse is further amplified by an optical amplifier and the amplified pulse is transmitted to the FUT. The FUT consisted approximately of a 250 m long fiber, 15 m of fiber wound on a PZ3-SMF2-O piezoelectric fiber stretcher and behind the fiber stretcher there was a coil with about 500 m of fiber. The fiber stretcher was supplied, from a functional generator Agilent 3350B, with a sinusoidal signal of different frequencies and amplitudes. The backscattered signal due to Rayleigh scattering then enters the 90-degree hybrid (from exail company) together with the signal from the second coupler branch. This second wave is used as a local oscillator (LO) in the 90° hybrid. In the 90° hybrid, the backscattered signal from the fiber is combined with the signal from the LO. The signals at the output of the 90° hybrid, representing

the in-phase and quadrature components for the two different polarizations, are fed to a 4-channel WL-BPD600MA-QUAD photodetector, which performs the conversion of the optical signals to electrical signals. These signals are further collected using a data acquisition (DAQ) system with a sampling frequency of 250 MHz. The signals obtained in this way are further processed.
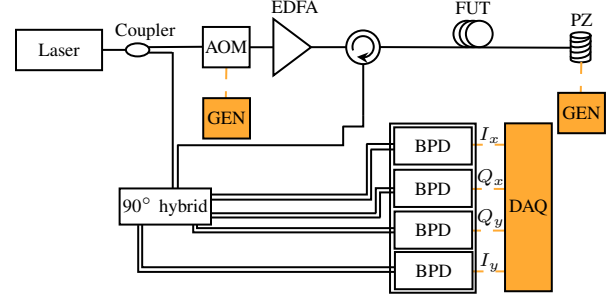
Fig. 1. Experimental setup of a DAS system with polarization diversity based on a dual polarization 90-degree hybrid.

III. BASIC PRINCIPLE OF PROCESSING MEASURED DATA

Since the frequency of the LO is different from the frequency of the signal originating from the measured fiber, it is necessary to convert the signals to baseband before calculating the signal magnitude and phase [14], [15].

After obtaining the in-phase and quadrature components in the baseband, the magnitude and phase of the backscattered signal can be calculated [14], [15].

To calculate the magnitude and phase of the backscattered light due to Rayleigh scattering using all signals obtained from the two polarizations, the following relationships apply

$$A_{\mathrm{s}} = \sqrt{I_x^2 + Q_x^2 + I_y^2 + Q_y^2}, \qquad (2)$$

$$\phi(t) = \arctan\left(\frac{Q_x + Q_y}{I_x + I_y}\right), \qquad (3)$$

where A_{s} is the signal magnitude, $\phi(t)$ is the phase of the signal, I_x is the in-phase component for the x polarization, I_y is the in-phase component for the y polarization, Q_x is the quadrature component for the x polarization, and Q_y is the quadrature component for the y polarization [16]. However, the relation (2) given in the article [16] is incorrect, since the signal magnitude calculation is based on the Pythagorean theorem and, as can be seen from the relation (3), the total value of the in-phase component is $I_x + I_y$ and the total value of the quadrature component is $Q_x + Q_y$ [17]. Therefore, the following relationship should be used to calculate the magnitude of the signal

$$A_{\mathrm{s}} = \sqrt{(I_x + I_y)^2 + (Q_x + Q_y)^2}. \qquad (4)$$

The calculation of signal magnitude and phase for a single polarization is given by

$$A_{\mathrm{s}} = \sqrt{I + Q}, \qquad (5)$$

$$\phi(t) = \arctan\left(\frac{Q}{I}\right), \qquad (6)$$

where I represents the in-phase and Q quadrature components of the signal [14], [15].

In the equations above, the arcus tangens function was used to obtain information about the signal phase. This function returns values in the range from $-\pi/2$ to $\pi/2$ [14].

Since the arcus tangens function only returns values within a certain interval, a phase unwrapping algorithm must be applied to the output of these function. After using this algorithm, the phase values can take values from $-\infty$ to ∞ [14], [16].

To obtain information about the phase changes on a given section of fiber, the following relation must be used

$$\Delta\phi = \phi_y - \phi_x, \qquad (7)$$

where $\Delta\phi$ represents the phase change on a given fiber segment, ϕ_x represents the phase on the xth channel of the fiber, and ϕ_y represents the phase on the yth channel of the fiber [14], [16].

In the article [14], it is noted that the distance between channels between which the phase change is computed can limit the spatial resolution, and therefore, channels between which the distance is less than or equal to the spatial resolution are typically chosen.

IV. RESULTS

With the DAS system described in the previous chapter, measurements were first performed with different settings of the simulated disturbance parameters. For all measurements was used 20 m gauge length. First, phase peak-to-peak measurements were performed with a simulated sinusoidal disturbance of 100 Hz for different voltage (U) amplitudes (0.05, 1, 3 and 6 V_{pp}) of this disturbance. Measured peak-to-peak phase (ϕ_{pp}) values for different polarizations are shown in Table I. From this table it can be observed that the values for different polarizations do not differ much at the same amplitude of simulated disturbance. The only exception are the values at a simulated disturbance amplitude of 6 V_{pp}. This exception was due to the fact that the phase values for polarization x and for sum of polarizations contained unwrapping errors. It can also be noticed from this table that the measured values vary roughly linearly with the amplitude of the simulated disturbance.

Next, phase peak-to-peak measurements were performed with a simulated sinusoidal disturbance of 6 V_{pp} amplitude for different frequencies (10, 100, 1000 and 2000 Hz) of this disturbance. Measured peak-to-peak phase values are shown in Table II. From this table, it can be observed that for simulated sinusoidal disturbances of 10 and 100 Hz, the peak-to-peak phase value was approximately the same. However, for disturbance frequencies of 1000 and 2000 Hz, the

TABLE I
SUMMARY OF PEAK-TO-PEAK PHASE VALUES OF DIFFERENT
POLARIZATIONS FOR DIFFERENT PEAK-TO-PEAK VOLTAGES OF THE
100Hz SINUSOIDAL DISTURBANCE

U (V)	ϕ_{PP_x} (rad)	ϕ_{PP_y} (rad)	$\phi_{\mathrm{PP}_{xy}}$ (rad)
0.05	0.822	0.825	0.786
1	16.022	16.41	16.367
3	47.703	48.122	47.689
6	89.085[a]	95.763	84.119[a]

[a]Unwrapped phase contained phase unwrapping errors.

TABLE II
SUMMARY OF PEAK-TO-PEAK PHASE VALUES FOR DIFFERENT
FREQUENCIES OF THE SINUSOIDAL DISTURBANCE

Frequency of Disturbance (Hz)	ϕ_{pp} (rad)
10	95.518
100	95.763
1000	8.657
2000	4.297

measured phase value was very different. For the 2000 Hz disturbance, the phase value was approximately half of the measured phase value for the 1000 Hz disturbance.

Furthermore, the measurement was performed at a simulated sinusoidal disturbance with a frequency of 10 Hz and an amplitude of 6 V_{pp} while rotating the optical connector. Part of the demodulated phase values obtained from this measurement is plotted in Figure 2. The figure shows that the demodulated phase values for polarization x do not resemble the simulated disturbance at all. In contrast, the demodulated phase values for the y polarization and for sum of polarizations resemble simulated disturbance. Figure 3 shows the overall view of the measured intensity for different polarizations during this measurement. From this figure it can be seen that for most of the measurement time the intensity for polarization x was very weak. After the third second of measurement, the signal from this polarization was almost lost. On the other hand, the signal from polarization y was strong at that moment, which resulted in suppression of polarization fading after summing the values obtained from both polarizations. The signal resulting from the summation of the values obtained from both polarizations is not constant since, as mentioned, the signal of polarization x was weak compared to the signal of polarization y. Another reason is that a decrease/increase in the intensity values of one polarization does not always lead to an increase/decrease in the intensity values of the other polarization. An example of this is the measurement time of approximately 16.5 s, when the intensity of both polarizations decreases simultaneously. On the other hand, after a measurement time of 5 s, the intensity values of polarization y increase and the intensity values of polarization x decrease.
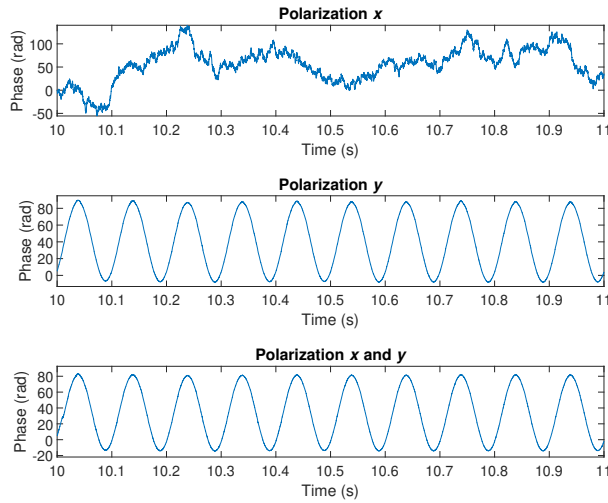
Fig. 2. Demodulated phase values for a generated disturbance with a frequency of 10 Hz and an amplitude of 6 V peak-to-peak.
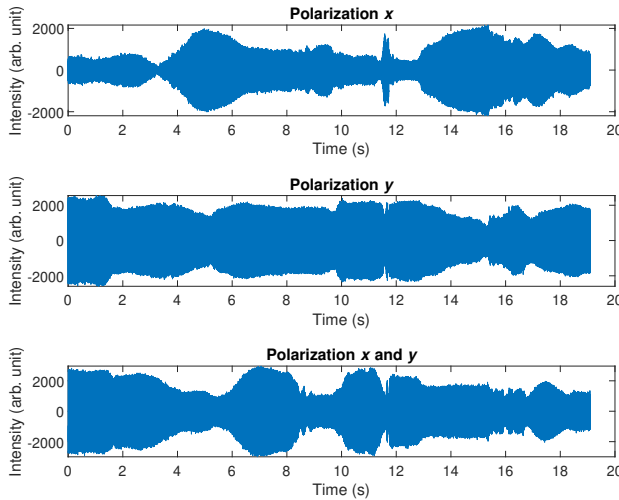

Fig. 3. Intensity changes caused mainly by the rotation of the optical connector.

V. CONCLUSION

DAS systems can use either the intensity or the phase of the backscattered light. With systems using intensity of backscattered light, it is only possible to locate the point on the fiber that is affected by the disturbance. With systems using phase of backscattered light, in addition to locating the point of disturbance, the change in the applied parameter (temperature or strain) can be determined. From the phase values of the backscattered signal it is then possible to reconstruct the disturbance almost accurately. The measured peak-to-peak phase values from both polarizations and from their sum were almost the same and varied roughly linearly with the amplitude of the simulated disturbance.

With experimental DAS system setup, the signal of one polarization was weak and the other was strong. Also, with this setup, there was not always an increase in the intensity values of one polarization when the intensity values of the other polarization decreased. Despite this, at no time were the intensity values of the both polarizations weak. As a result, by summing the values of both polarizations, the polarization fading can be suppressed.

REFERENCES

[1] S. Liu, et al., "Advances in phase-sensitive optical time-domain reflectometry," in Opto-Electronic Advances, vol. 5, no. 3, pp. 200078, 2022, doi: 10.29026/oea.2022.200078.

[2] X. Bao, and Y. Wang, "Recent Advancements in Rayleigh Scattering-Based Distributed Fiber Sensors," in Advanced Devices & Instrumentation, vol. 2021, no. 8696571, 2021, doi: 10.34133/2021/8696571.

[3] L. Palmieri, L. Schenato, M. Santagiustina, and A. Galtarossa, "Rayleigh-Based Distributed Optical Fiber Sensing," in Sensors, vol. 22, no. 18, pp. 6811, 2022, doi: 10.3390/s22186811.

[4] S. Hou, et al., "A method for visualizing urban road events using distributed acoustic sensing," in Urban Lifeline, vol. 2, no. 1, pp. 6, 2024, doi: 10.1007/s44285-024-00016-1.

[5] A. T. Turov, et al., "Comparison of the Sensitivity of Various Fibers in Distributed Acoustic Sensing," in Applied Sciences, vol. 14, no. 22, pp. 10147, 2024, doi: 10.3390/app142210147.

[6] N. J. Lindsey, et al., "City-Scale Dark Fiber DAS Measurements of Infrastructure Use During the COVID-19 Pandemic," in Geophysical Research Letters, vol. 47, no. 16, pp. e2020GL089931, 2020, doi: 10.1029/2020GL089931.

[7] K. I. Nishiguchi, "Phase unwrapping for fiber-optic distributed acoustic sensing," The 47th ISCIE International Symposium on Stochastic Systems Theory and Its Applications, Honolulu, 2016, pp. 81–87, doi: 10.5687/sss.2016.81.

[8] G. Tu, X. Zhang, Y. Zhang, F. Zhu, L. Xia and B. Nakarmi, "The Development of an Φ -OTDR System for Quantitative Vibration Measurement," in IEEE Photonics Technology Letters, vol. 27, no. 12, pp. 1349–1352, 2015, doi: 10.1109/LPT.2015.2421354.

[9] Y. Wang, R. Xu, Z. Deng, Y. Liang, J. Jiang and Z. Wang, "High-Performance Distributed Acoustic Sensing with Coherent Detection," 2022 IEEE 10th International Conference on Information, Communication and Networks (ICICN), Zhangye, China, 2022, pp. 485–488, doi: 10.1109/ICICN56848.2022.10006550.

[10] R. Crickmore, A. Godfrey, and C. Minto, "Strain monitoring using distributed Rayleigh sensing", Proc. SPIE 11199, Seventh European Workshop on Optical Fibre Sensors, 111991U, Limassol, Cyprus, 2019, doi: 10.1117/12.2539661.

[11] T. Lauber, and G. Lees, "Enhanced Temperature Measurement Performance: Fusing DTS and DAS Results," in IEEE Sensors Journal, vol. 21, no. 6, pp. 7948–7953, 2021, doi: 10.1109/JSEN.2020.3046339.

[12] L. Xiao, Y. Wang, Y. Li, Q. Bai, X. Liu and B. Jin, "Polarization Fading Suppression for Optical Fiber Sensing: A Review," in IEEE Sensors Journal, vol. 22, no. 9, pp. 8295–8312, 2022, doi: 10.1109/JSEN.2022.3161075.

[13] M. Ren, P. Lu, L. Chen and X. Bao, "Theoretical and Experimental Analysis of Φ -OTDR Based on Polarization Diversity Detection," in IEEE Photonics Technology Letters, vol. 28, no. 6, pp. 697–700, 2016, doi: 10.1109/LPT.2015.2504968.

[14] Z. Wang, et al., "Coherent Φ-OTDR based on I/Q demodulation and homodyne detection," in Optics Express, vol. 24, no. 2, pp. 853–858, 2016, doi: 10.1364/OE.24.000853.

[15] Y. Fu, N. Xue, Z. Wang, B. Zhang, J. Xiong and Y. Rao, "Impact of I/Q Amplitude Imbalance on Coherent Φ -OTDR," in Journal of Lightwave Technology, vol. 36, no. 4, pp. 1069–1075, 2018, doi: 10.1109/JLT.2017.2768587.

[16] Q. Yan, M. Tian, X. Li, Q. Yang and Y. Xu, "Coherent Φ-OTDR based on polarization-diversity integrated coherent receiver and heterodyne detection," 2017 25th Optical Fiber Sensors Conference (OFS), Jeju, Korea (South), 2017, pp. 1–4, doi: 10.1117/12.2265463.

[17] K. K. Sharma, "Modern Radar Signal Processor," in International Journal of Scientific & Engineering Research, vol. 8, no. 4, pp. 12–17, 2017, ISSN 2229-5518.

Implantable Medical Device for Measuring Vital Signs of Animals – Proof of Concept

Ondrej Lengal
Dept. of Microelectronics
Brno University of Technology
Brno, Czechia
230281@vut.cz

Jiri Haze
Dept. of Microelectronics
Brno University of Technology
Brno, Czechia
0000-0001-5670-4283

Abstract—**This paper presents the design of medical device implantable under the skin of animals for vital signs measurement (temperature and heartbeat) and wireless data distribution for health data review. This system utilizes a thermoelectric generator as an energy harvester and supercapacitor as an energy storage for long term operation without the need of system maintenance and Bluetooth Low Energy module for data transfer to any Bluetooth compatible device. Design also includes passive RFID tag for identification. The system is presented as proof of concept with commercially available electronic components.**

Keywords—battery management, DC-DC converter, energy harvesting, Bluetooth Low Energy, vital sign measurement, supercapacitor, proof of concept

I. INTRODUCTION

As technology is moving forward, new ways of health monitoring and improvements are proposed. In recent years, the market was dominated by smart watches for humans, smart collars for larger pets and other *in vitro* (wearable) devices which were designed for health monitoring. These devices are able to measure and distribute the vital sign data of subject through wireless communication (i.e. Bluetooth) while also staying reasonably compact and non-invasive. When it comes to health prediction or disease treatment, history of the vital signs is a crucial information. The accuracy of said medical evaluation depends also on the completeness of the information history, so the best practice would be to wear the device all the time, which may cause a discomfort.

In vivo (implantable) medical devices, contrary to *in vitro* applications, offer more compact but invasive way of health improvements. These devices are usually used for stimulation or even as substitution for organs inside the body. One such popular application is cardiac pacemaker which maintains an even heart rate. Biggest concern for these devices is the energy source, because including non-rechargeable energy element will lead for multiple instances of surgery for mere change of the energy element, while including rechargeable energy element may pose health risk of the materials used, but also the question on what recharging technique to use for chosen energy element.

In this paper, we present a proof of concept for implantable medical device designed for vital signs (temperature and heartbeat) measurement of pets while dealing with problems of both wearable and implantable devices by combining their strengths and facing their weaknesses with new technologies

such as thermoelectric energy harvesting and utilization of the supercapacitor.

II. SYSTEM DESIGN

A. Required system parameters

- Temperature and heartbeat measurement
- Periodic measurement (every 5 – 10 minutes)
- Autonomous regime
- Bluetooth compatibility
- Long lifespan
- Small area of the whole system
- RFID tag

B. Energy harvesting

Multiple techniques of energy harvesting were proposed. Such techniques include body-centric, environment-centric, wireless and hybrid energy harvesting as shown in [1]. One promising way of body-centric energy harvesting is thermoelectric generator (TEG) as shown in [2]. TEGs can be designed to occupy small area while still generating reasonable amount of energy from small temperature gradient although with low output voltage. These generators were recently used as energy sources for both wearable and implantable devices.

Multiple papers focus on using TEGs as energy source implanted under the skin into subcutaneous tissue (fat layer) where quite significant temperature gradient between outer skin and muscle layer is located [3], [4]. Our device is also designed for implantation into subcutaneous tissue with TEG energy harvesting in mind.

When using energy harvesting in wearable or implantable medical devices, it is necessary to capture the maximum power from the energy harvester by correct impedance matching. In this design, the MPPT (Maximum Power Point Tracking) uses technique called FOCV (Fractional Open-Circuit Voltage) set at 50 % which is recommended value for TEGs as shown in [1].

C. Battery management

Energy source output is often not suitable for system and requires additional circuitry to convert the energy to suitable form. Energy source output also needs to be monitored and controlled so the battery and the rest of the system is protected. These functions are accomplished by battery management system. This part manages effective transfer of energy from energy source to storage element, protection of storage element

from overcharging, suitability of supply voltage for the rest of the system. General description of battery management as energy chain is shown in [5]. This chain includes power module, energy storage element, battery (energy storage element), converter (if necessary), power management and load (rest of the system).

Power module is used for effective energy transfer between energy source and battery. When TEG is used as an energy source, power module includes boost converter to increase output voltage of TEG to optimal value for battery charging and use MPPT to capture maximum power as discussed above.

The choice of energy storage element is a crucial point in design. Lot of conventional batteries are quite big and use dangerous materials which make them not suitable for implantable devices. One promising choice for energy storage element is a double layer capacitor, often called supercapacitor. This type of capacitor has a large capacity despite maintaining small size. Supercapacitor can also withstand many more charge cycles than conventional batteries as shown in [6], which makes it even more suitable for implantable devices.

Main purpose of converter is to change output voltage of energy storage element to suitable value for the load (i.e. buck converter – voltage stepdown). It is also possible to lower energy consumption of the system if lower acceptable supply voltage is used, but this may lead to problems, especially when high current demand occurs. Also keep in mind that no converter is 100 % effective.

Power management has two functions: overcharge protection of energy storage element and ensuring suitable output voltage for the load.
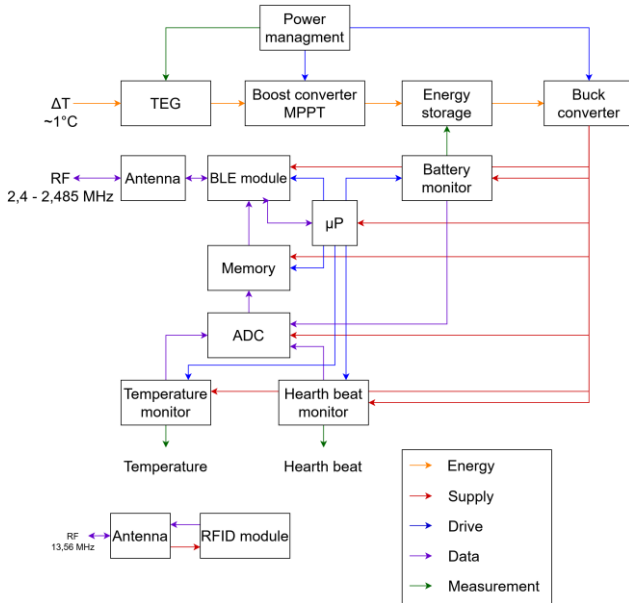
Fig. 1. Proposed system overview

D. Measurement system

For device to be able to measure, collect and send the data wirelessly, a number of modules are necessary to include in the design. In our case, these modules are: heart rate monitor, temperature monitor, battery monitor, microprocessor, analog to digital converters (ADCs), Bluetooth Low Energy (BLE) module and antenna.

In today's popular wearable devices a heart rate monitor consist of a LED and optical sensor as is shown in [7]. This technique is called PPG (photoplethysmography) may be also usable for implantable devices.

For temperature monitor, conventional way of temperature acquisition with measuring current flow thought BJT thermal transistor is used.

Battery monitor measures voltage and self-discharge current on the energy storage element for evaluating state of health of the energy storage.

Microprocessor drives the entire system, so low power operation and sleep mode can be ensured.

ADCs converts the analog value of the monitors to digital form. BLE module sends processed data out through antenna. It is necessary to include impedance matching and harmonic filters (if necessary) between the BLE module and antenna.

E. RFID tag

Quick subject recognition is also desirable quality. Rather than using Bluetooth for this function, which may take considerable amount of energy, a passive RFID system is an excellent choice. This system is supplied directly by RFID reader and is fully autonomous from rest of the system. RFID system consists of two components: antenna and RFID module.

III. PROOF OF CONCEPT

The system described in the last chapter is assembled of commercially available components (see Table I) to prove the function and to measure energy consumption of the proposed system. Proof of concept system does not include buck converter to keep the system robust and resilient to any voltage drops created by sudden current demands. Fig. 2 shows a schematic diagram of proof of concept with chosen components which most of the time substitute multiple system parts.

A. Electrical components and their function

BQ25570 from Texas Instruments is component designed to efficiently extract power generated of high output impedance DC sources like TEGs. This integrated circuit encapsulates power module (boost charger) with MPPT and power management circuit. This chip will store the generated energy into small supercapacitor CPH2225A from Seiko Instruments.

MAXM86161 form Analog devices uses PPG technique to measure heartbeat frequency and converts the data to digital form. TMP117 form Texas Instruments measures temperature by voltage difference created on BJT transistor and also processes the data to digital form.

TABLE I. COMPONENT SUBTITUTION FOR SYSTEM PARTS

Components for Proof of Concept	
System part	*Component*
Power module (with MPPT), Power management	BQ25570
Energy storage element	CPH2225A
Heart rate monitor (with ADC)	MAXM86161
Temperature monitor (with ADC)	TMP117
Microprocessor, BLE modul, Battery monitor (with ADC)	BlueNRG-232
Impedance matching, harmonic filter for BlueNRG transciever	BALF-NRG-02D3
Bluetooth antenna	2021LL00R2400A
RFID module	RF37S114

Microprocessor BlueNRG-232 drives the entire system. By I^2C communication, it stores and sends data from heartbeat and temperature monitors. Using its own ADCs, the processor measures voltage on the supercapacitor and the voltage on shunt resistor to evaluate leakage current of the supercapacitor. Serial Wire Debug interface is used for microprocessor programming.

BALF-NRG-02D3 is a balun specially designed for BlueNRG transceiver. Its main function is to match the impedance between BlueNRG and Bluetooth antenna 2012LL00R2400A from YAGEO Company.

Passive RFID module RF37S114 from Texas Instruments is responsible for identification of subject.

B. Printed circuit board design

Proof of concept circuit is situated on two-layer PCB (top layer for routes, bottom for ground plane) with the dimensions of 28 x 21,5 cm (see Fig. 3 and 4). Board was designed with manufacturer component layout recommendations in mind.

The board features number of pins for measurement and supply voltage inputs. It also includes resistors labeled R01-9 used for component detachment if such action is needed.

IV. CONCLUSION

Proposed proof of concept is the first step in effort to design small, maintenance free medical chip for pet health overview for popular use. While not all components used in the proof of concept are designed for implantation or very low power consumption, it gives general idea of where the technology is developed enough and where improvements must be done in order to start designing the final product.

The following projects will focus on developing new vital signs monitors for long-term implantation (such as glucose monitor), suitable thermoelectric generator to meet the power and area demand and further component integration while focusing on power consumption.
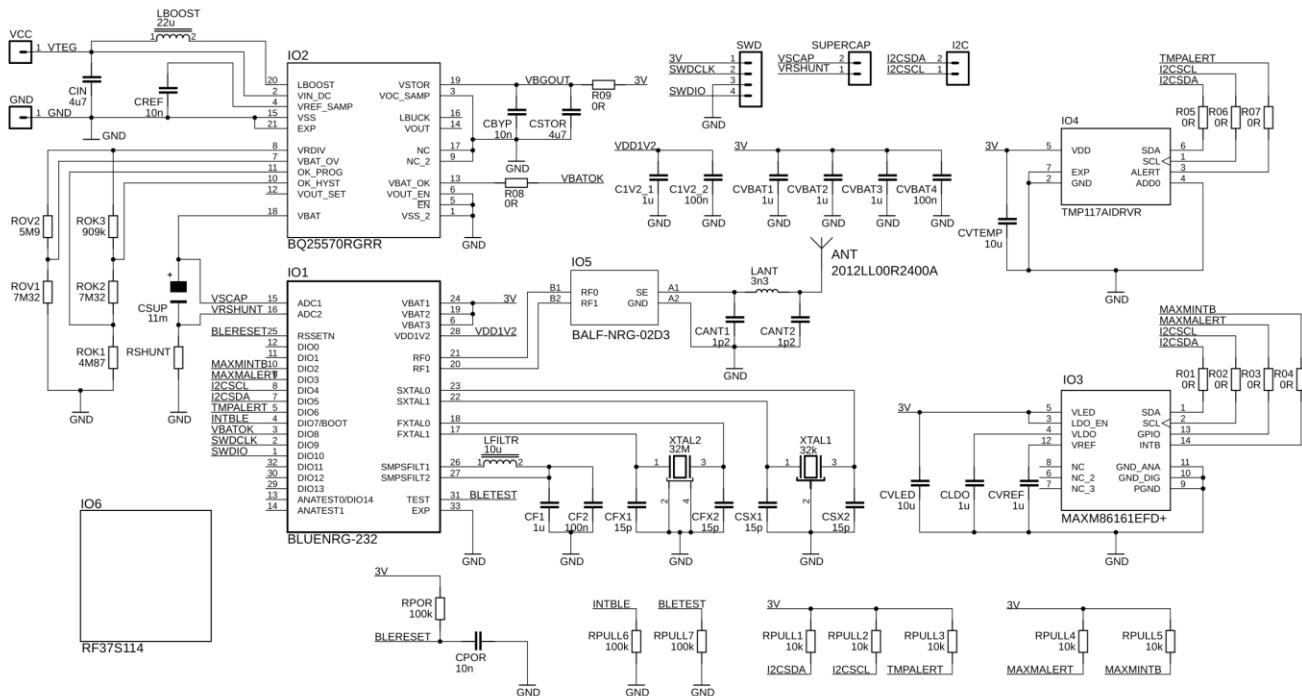
Fig. 2. Schematic diagram of Proof of Concept
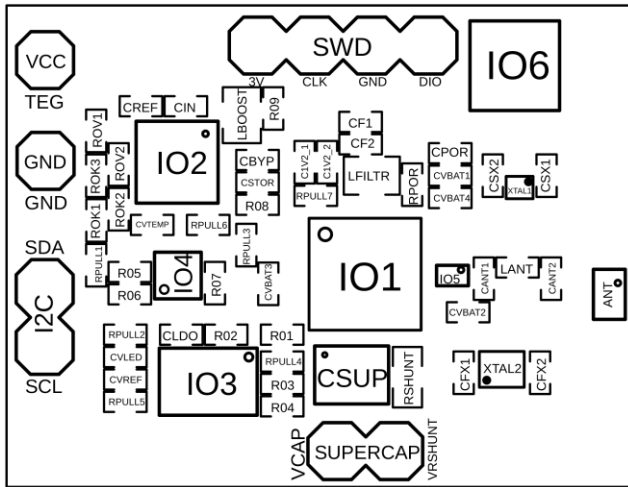
Fig. 3. PCB component layout
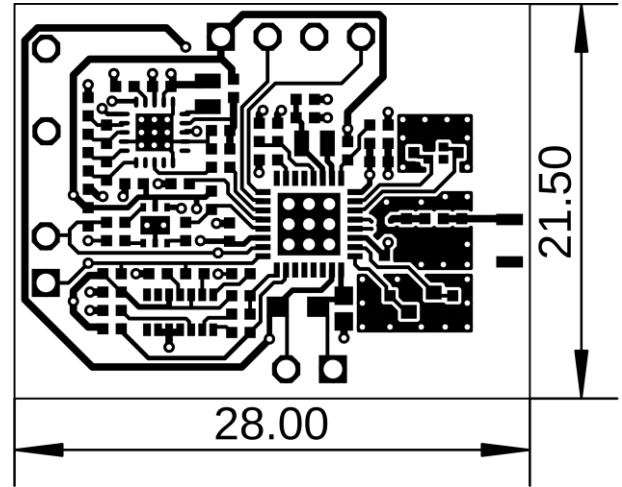
Fig. 4. PCB routes layout with dimensions in milimeters

REFERENCES

[1] M. M. H. Shuvo, T. Titirsha, N. Amin, and S. K. Islam, "Energy Harvesting in Implantable and Wearable Medical Devices for Enduring Precision Healthcare," *Energies*, vol. 15, no. 20, p. 7495, Oct. 2022, doi: https://doi.org/10.3390/en15207495.

[2] A. Zhang and L. Zhu, "A Promising Way of Energy Harvesting for Implantable Medical Devices – Thermoelectric Generator (TEG)," *2021 International Conference on Smart City and Green Energy (ICSCGE)*, pp. 22–25, Nov. 2021, doi: https://doi.org/10.1109/icscge53744.2021.9654315.

[3] T. Janes *et al.*, "Thermoelectric Energy Harvesting for Implantable Medical Devices," *2021 43rd Annual International Conference of the IEEE Engineering in Medicine & Biology Society (EMBC)*, pp. 1547–1550, Nov. 2021, doi: https://doi.org/10.1109/embc46164.2021.9630243.

[4] Y. Rao, M. Voss, T. Bechtold, and D. Hohlfeld, "Implantable Thermoelectric Generator with High Aspect Ratio Thermolegs and Integrated Voltage Converter," pp. 206–209, Dec. 2023, doi: https://doi.org/10.1109/powermems59329.2023.10417479.

[5] H. J. Bergveld, W. S. Kruijt, and P. H. L. Notten, *Battery Management Systems*. Dordrecht: Springer Netherlands, 2002. doi: https://doi.org/10.1007/978-94-017-0843-2.

[6] M. Şahin, F. Blaabjerg, and A. Sangwongwanich, "A Comprehensive Review on Supercapacitor Applications and Developments," *Energies*, vol. 15, no. 3, p. 674, Jan. 2022, doi: https://doi.org/10.3390/en15030674.

[7] A. Boukhayma, A. Barison, S. Haddad, and A. Caizzone, "Earbud-Embedded Micro-Power mm-Sized Optical Sensor for Accurate Heart Beat Monitoring," *IEEE Sensors Journal*, vol. 21, no. 18, pp. 19967–19977, Sep. 2021, doi: https://doi.org/10.1109/jsen.2021.3098861.

Diagnostic Oscilloscope with Artificial Intelligence

1st Martin Knob
Department of Radio Electronics
Brno University of Technology
Brno, Czech Republic
221054@vut.cz

2nd Jan Kufa
Department of Radio Electronics
Brno University of Technology
Brno, Czech Republic
kufa@vut.cz

Abstract— **This paper describes the design and implementation of an oscilloscope that can recognise individual measurement signals, communication protocols, and buses based on machine learning (ML), a subset of artificial intelligence (AI). The oscilloscope is compact and fully portable. The device is powered by a battery, making it energy self-sufficient. The oscilloscope data can be visualised with a smartphone using the Scoppy app. The Raspberry Pi Pico W microcontroller can be connected via Wi-Fi or USB. The processing of the measured signals is not done in real time, but from exported data using MATLAB. A graphical user interface (GUI) has been designed in MATLAB for data processing using ML.**

Keywords—Oscilloscope, microcontroller, machine learning, signal, protocol, bus.

I. INTRODUCTION

The digital oscilloscope is a key instrument not only in electrical engineering. The oscilloscope is used in the design of various electronic circuits, signal analysis and overall signal visualisation. Nowadays, Digital Storage Oscilloscope (DSO) are the most widely used.

This paper deals with the design of an oscilloscope that can recognise individual signals, communication buses and protocols using machine learning algorithms. There are many oscilloscope manufacturers on the market, but according to the available information, none of them has an oscilloscope that can recognise different types of communication protocols and buses. Commercially available oscilloscopes can only decode one type of communication protocol or bus, but cannot independently recognise which type of communication protocol or bus it is.

Conventional oscilloscopes usually require an external power supply and are large and heavy, making them unportable and limiting their use. For this reason, the proposed DSO has been extended to include a battery that powers the oscilloscope, making it portable and independent of mains power, allowing the oscilloscope to be used almost anywhere. Despite the use of a battery, the oscilloscope retains its compact size and is fully portable. In this oscilloscope, the FSCOPE-500K microcontroller extension board was used as the input block of the oscilloscope [1]. The Raspberry Pi Pico W microcontroller was used for this board, allowing us to connect to the oscilloscope via Wi-Fi and visualise the measured data on, for example, a mobile phone that everyone carries with them nowadays.

II. OSCILLOSCOPE IMPLEMENTATION

In order for the oscilloscope to recognise individual communication protocols and buses, it is important that it can measure them at all. Therefore, when designing and selecting components, it is important to focus on parameters such as bandwidth, vertical resolution, sampling frequency, input impedance and maximum input voltage. All of these parameters have their own importance and are important to consider for quality data measurement. If the oscilloscope cannot measure at a sufficient speed, or if it does not meet the other parameters mentioned, the recorded data may not be of sufficient quality and the ability of ML to recognise a particular bus type or protocol would be compromised.

In Fig. 1 we can see the block diagram of the whole device. The measured signal is sensed by the probes connected to the FSCOPE-500K microcontroller extension board, which is used as the input block of the oscilloscope. A Raspberry Pi Pico W microcontroller is connected to this board. Power is supplied by a DFR1026 circuit connected to a 3500 mAh Li-Po battery with a nominal voltage of 3.7 V. The connection to the device, which can be a smartphone or a PC, can be realised in two ways. We can connect via the micro-USB connector or via Wi-Fi. On the connected device, e.g. PC, we export the measured signal that we want to detect using ML and in the created GUI in MATLAB we detect the measured signal.
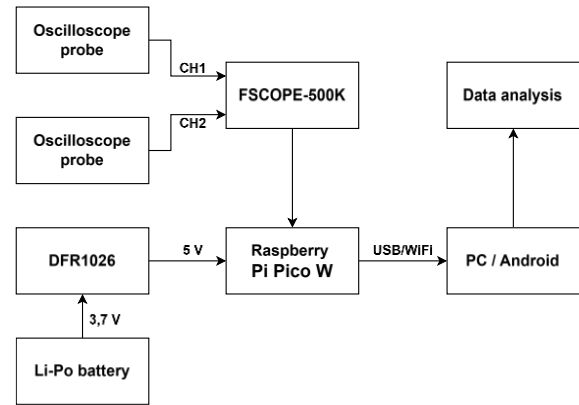
Fig. 1. Block Diagram of All Components of the Entire Device

A. FSCOPE-500K

The microcontroller extension board was used as an input block for the FSCOPE-500K oscilloscope. The microcontroller chosen for this expansion board was the Raspberry Pi Pico W. This microcontroller was chosen for its good 12-bit analog-to-digital converter (ADC), compatibility with the FSCOPE-500K and the possibility of wireless connectivity using Wi-Fi [1]. One of the most important parameters in the selection of the microcontroller was its built-in ADC, as this ADC is used for oscilloscope measurements and thus determines the vertical resolution of the oscilloscope.

The oscilloscope can measure two channels simultaneously. The sampling rate of the oscilloscope is 500 kS/s for single channel measurements [1]. If two channel measurements are required, the sampling rate is halved to 250 kS/s [1]. Another important parameter is the bandwidth. For this oscilloscope it is 150 kHz, which is sufficient for most communication protocols and buses [1]. The input impedance is 1 MΩ with a capacity of 22 pF [1]. The vertical resolution is 12 bits, determined by the ADC converter of the microcontroller. Another important parameter in oscilloscopes is the input voltage, which here is only ±6 V when using 1x probes [1].

If we need to measure signals with larger amplitudes, we need to use other probes. The probes are connected to the oscilloscope via BNC connectors. These connectors allow us to use probes that are commonly used in professional oscilloscopes. The use of a good quality probe is crucial for a correct measurement, so it was important to choose a BNC connector, thanks to which we have many types of probes available. The oscilloscope has an AC/DC coupling switch that can be operated by a switch on the outside of the case. The oscilloscope can measure in many modes such as YT, FFT, FFT + YT, X-Y, XY + YT mode [2].

The visualization of measured signals and all other oscilloscope settings, including data export, is done through the Scoppy application. The data export is in „.csv" format, where this file contains 2048 samples. This data export is important for further processing of the measurement data and evaluation of the bus type or communication protocol using machine learning.

B. Microcontroller

As mentioned above, this device uses the Raspberry Pi Pico W microcontroller. The „W" variant was deliberately chosen because of the use of wireless connectivity, specifically the single-band 802.11n Wi-Fi interface [3]. The basic version of the Raspberry Pi Pico offers the same parameters but lacks the ability to connect wirelessly without an external module. The microcontroller is attached to this board via a pin-rail and is not directly powered, due to the possibility of a future upgrade to a Raspberry Pi Pico 2 W. This microcontroller has sufficient power and number of IO pins. It also has a relatively low power consumption, which gives it a long battery life. All these parameters make this microcontroller a suitable choice for this purpose.

C. Power Management

This DSO does not require an additional power source. It is powered by a battery. This power supply is managed by the DFR1026 module, an integrated charge and discharge module for lithium batteries [4]. A 3.7 V nominal Li-Po battery is connected to the input of the DFR1026. The output of the module is connected via a switch to the VSYS pin of the microcontroller, supplying power to the oscilloscope. The VSYS pin of the Raspberry Pi Pico W is the main power pin of this microcontroller, to which we can supply voltages from 2.3 V to 5.5 V [3]. The output of the power supply module is 5 V. The battery can be connected directly to this pin, but thanks to the module, the battery can also be charged directly, with a micro-USB connector added to the module for this purpose.

In addition, the DFR1026 includes battery protection circuitry that is essential for battery operation. Specifically, lithium battery protection such as over-current, over-voltage, over-temperature and short-circuit protection [4]. It also provides battery charge/discharge indication in the form of 4 LEDs. The indications provided by these LEDs are shown in the following tables. In TABLE I. we can see the different states of indication when the battery is discharging. In TABLE II. we can see the indication states using the LEDs when the battery is charging.

TABLE I.   DISCHARGE MODE [4]

Electricity C(%)	D1	D2	D3	D4
C ≥ 75%	ON	ON	ON	ON
50% ≤ C < 75%	ON	ON	ON	OFF
25% ≤ C < 50%	ON	ON	OFF	OFF
3% ≤ C < 25%	ON	OFF	OFF	OFF
0% < C < 3%	1.5Hz Flashing	OFF	OFF	OFF

TABLE II.   CHARGING MODE [4]

Electricity C(%)	D1	D2	D3	D4
Full	ON	ON	ON	ON
75% ≤ C	ON	ON	ON	0.5Hz Flashing
50% ≤ C < 75%	ON	ON	0.5Hz Flashing	OFF
25% ≤ C < 50%	ON	0.5Hz Flashing	OFF	OFF
C < 25%	0.5Hz Flashing	OFF	OFF	OFF

The DFR1026 can be charged from 4.6 V to 5.4 V, making it ideal for charging via USB using the micro-USB connector [4]. Batteries can be charged with up to 2.1 A. Discharge current can be up to 3.5 A [4]. All of these parameters make the DFR1026 a good choice for battery-powered oscilloscopes.

D. Battery

The oscilloscope is powered by a lithium polymer battery. This type of battery was chosen because of its high energy density and low self-discharge. This particular battery has a capacity of 3500 mAh and a nominal voltage of 3.7 V [5]. Li-Po batteries must be charged using the CCCV method. This is a method of charging where the battery is first charged at a constant current and then at a constant voltage. This charging is performed by the DFR1026 module. Lithium polymer batteries are susceptible to overcharging and undercharging, hence the need for protection circuitry, all of which is contained in the DFR1026. Even though this battery reaches quite a large capacity, it still maintains a compact size. Specifically, it measures 56 mm in width and 65.5 mm in length [5]. The thickness of this battery is only 7.2 mm [5]. These compact dimensions have allowed the battery to be conveniently integrated into the top of the case.

E. The measured power consumption of the oscilloscope.

As this is a battery powered device, it is important to know its power consumption. The power consumption was measured using the INA3221 module and the ESP32 microcontroller, with the measured data sent over the serial link and exported as a „.csv" file using a Python script. One such measurement is shown in Fig. 2. The measurement lasted 677 seconds and the readings were sent every 100 ms. On average, the device consumes 126 mA at a battery voltage of 4 V. The average power consumption is about 506 mW, only at the beginning the consumption is higher due to the Wi-Fi connection.
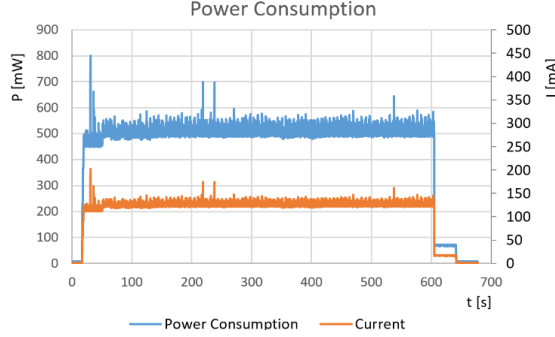
Fig. 2.   Graph of the measured energy consumption and current

This measurement was taken during normal use of an oscilloscope connected via Wi-Fi. After switching off the oscilloscope, the current draw was still around 17 mA, which is caused by the DFR1026 module, which uses 4 LEDs to indicate the battery status for 30 seconds after switching off the oscilloscope, corresponding. This measurement was taken with a fully charged battery, so all 4 LEDs were lit and the current draw after switching off the oscilloscope was higher. If the battery was more discharged and fewer information LEDs were lit, the consumption after switching off the oscilloscope would be lower. Despite the consumption of around 500 mW, the oscilloscope lasts quite a long time on the battery, estimated at more than 20 hours of continuous operation. When the battery runs out, the scope can still be used without a Wi-Fi connection. Simply connect the scope via USB to a mobile phone, for example.

F. The design of the oscilloscope enclosure

A suitable enclosure for the oscilloscope had to be designed. This was done in Fusion 360. The design of this oscilloscope is shown in Fig. 3., with holes on the front for BNC connectors to which the probes are connected. Also on the front are holes for AC/DC link switches and LEDs for Wi-Fi and trigger indication. There are also labels for each of these parts. On the side of the case, we find a switch for switching on the oscilloscope, a signal LED and a micro-USB hole for communication with the microcontroller. At the rear there is a micro-USB hole for charging the battery and a place for the DFR1026 module, including a hole for the LED on this module.

Fig. 3.   Designed oscilloscope enclosure

On the top cover there is a hole for the strap for attaching the probes and a hole for the button on the DFR1026 module. The top cover also has a recess for the Li-Po battery. This cover was printed on a 3D printer from PLA material. The fully assembled oscilloscope is shown in multiple views in Fig. 4. All the labels are easy to read, and the construction looks durable.

Fig. 4.   Assembled oscilloscope: a) Front view b) Side view c) Rear view

In Fig. 5 we can see the assembled oscilloscope with the cover open. The main parts of the oscilloscope are numbered. Number 1 is the microcontroller, 2 is the FSCOPE-500k, 3 is the BNC connectors, 4 is the AC/DC coupling switches, 5 is the DFR1026 module, 6 is labelled micro-USB for charging. Number 7 is the LEDs, 8 is the oscilloscope start switch and under number 9 is the Li-Po battery embedded in the top cover of the oscilloscope.
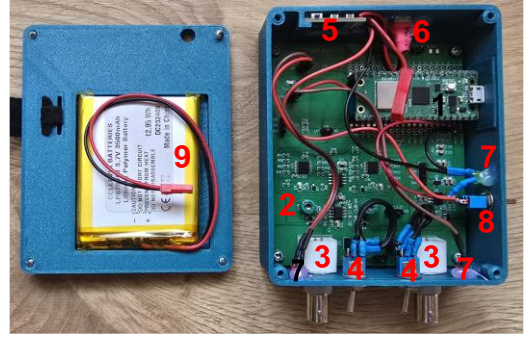
Fig. 5.   Uncovered oscilloscope

G. Application for Oscilloscope Control

The data display and oscilloscope setup is done using the Scoppy application. It is a control application for the FSCOPE-500K extension board. Several measurement modes can be set in the application, such as YT, FFT, FFT + YT, X-Y, XY + YT mode [2]. The application offers many settings, just like a classic oscilloscope. It is clear and intuitive. From Scoppy we can export the measured data in .csv format, which is essential for further processing. The application also outputs parameters such as Vmin, Vmax, Vpp, Freq, Time and Duty during real-time measurements [2]. These parameters can be enabled for both channels at the same time. It is also possible to make measurements with cursors. An example of the environment in this application is shown in Fig. 6.

Fig. 6.   Example of the Scoppy application interface [2]

III. RECOGNITION OF BUS TYPES AND PROTOCOLS

ML is used to recognise signals, communication protocols and buses. It also enables efficient classification and identification of individual protocols. The implementation of this recognition is done using MATLAB. Specifically, the Machine Learning Toolbox implemented in MATLAB is used. This toolbox contains several algorithms such as KNN, SWM, Decision Trees, Bagged Trees, Naive Bayes and others that can be used.

Good quality data for learning ML algorithms is crucial for their proper functioning. Data collection was performed using an oscilloscope on various communication protocols and periodic signals. After the data collection, the algorithm was taught with this measured data. A script called TrainModel.m was created for learning. After running this script, we are asked to select the folder containing the data for learning a particular protocol, signal or bus. After selecting the data, the name of the signal class must be entered. Once the signal class has been specified, the data is loaded, and we are asked to confirm that we want to retrain the model. If we confirm to retrain, the data will be saved in TrainedModel.mat. Another script called classifySignal.m is used to classify the signal based on the pre-trained data.

Signals, communication protocols and buses are not recognised in real time, but only from the „.csv" file exported from the oscilloscope. For ease of use, a GUI has been created in MATLAB. An example of this GUI is shown in Fig. 7, where a) shows the startup screen. After clicking on „Vybrat soubor", we have to select the file in „.csv" format that we want to recognise. After selecting the file, it will be loaded, rendered and the file name will be written in the GUI, as we can see in Fig. b). After clicking on the „Rozpoznat signál" button, the signal is recognised and the name of the communication protocol or bus is printed in the GUI. This can be seen in Fig.7 c), where it is specifically I2C.

Fig. 7. Example of GUI for signal recognition in MATLAB

The ML detection algorithm is universal in order to be as versatile as possible. At present, data acquisition from I2C bus, IR protocols for controlling TVs from JVC, LG, Panasonic and Samsung companies and periodic signals has been performed. The I2C algorithm recognised with 100% success every time, even CLK from DATA, it was no problem to distinguish CLK for I2C from a rectangular periodic signal. For IR protocols for TV control, the algorithm was sometimes confused between Samsung and JVC, with a success rate of around 70%. Periodic signals such as sine, triangle and rectangle were used to learn the algorithm from two generators. The first generator used was the ICL8038, which is a DIY generator kit. The second generator
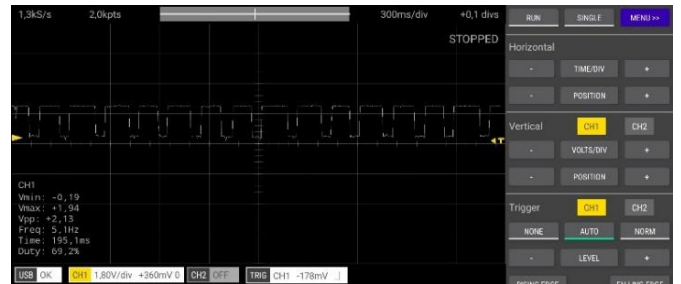
used was an Agilent 33220A laboratory generator. The algorithm also recognised which generator it was in most cases. The database of measured signals is not yet very large, but it is constantly being expanded. The plan is to extend the database by recognising other communication buses and protocols such as SPI, UART and many others.

IV. CONCLUSION

The aim of this work was to design and build an oscilloscope that could recognise different signals, communication protocols and buses based on machine learning. The oscilloscope has been designed and implemented. The microcontroller extension board was used as the input block of the FSCOPE-500k oscilloscope for the implementation. A Raspberry Pi Pico W microcontroller was used for this extension board, allowing the oscilloscope to be connected to both USB and WiFi. The oscilloscope was also extended with a DFR1026 module, which is used to power the oscilloscope and charge the 3500 mAh Li-Po battery implemented in the oscilloscope. In addition, a case was designed for the oscilloscope to protect the oscilloscope's components and allow for easy portability and increased durability. This case was produced using a 3D printer. BNC connectors protrude from the case to connect the probes for both channels. AC/DC link switches and signal LEDs for Wi-Fi, trigger and oscilloscope power-on status are also extruded. There are also LEDs to indicate battery charge status. There are also two micro-USB connectors on the oscilloscope. One is for charging the battery and the other is for USB connection to the microcontroller. Machine learning recognition of individual signals, communication buses and protocols is not performed in real time, but from an exported „.csv" file. This ML recognition is implemented using MATLAB, where a graphical user interface for signal, communication protocol and bus recognition has been created for this purpose. The ML algorithm was trained on periodic signals, I2C bus and IR communication protocols from different companies. The recognition success rate for I2C and periodic signals was 100% and for IR protocols was about 70% so far, with the Samsung IR protocol occasionally being confused with JVC. ML Algorithm can even distinguish for periodic if it is a DIY generator or a lab generator.

References

[1] FScope-500k DIY OSCILLOSCOPE. Online. FHDM store. Dostupné z: https://store.fhdm.xyz/fscope-500k. [cit. 2024-12-28].

[2] Scoppy. Online. FHDM. Dostupné z: https://oscilloscope.fhdm.xyz/. [cit. 2025 01-01].

[3] Pico-series Microcontrollers. Online. Raspberry Pi. Dostupné z: https://www.raspberrypi.com/documentation/microcontrollers/pico-series.html. [cit. 2024-12-18].

[4] FARNELL. DFR1026. Online. Farnell. Dostupné z: https://cz.farnell.com/dfrobot/dfr1026/integrated-module-dc-dc-lithium/dp/4457329. [cit. 2025-03-06].

[5] CELLEVIA BATTERIES. Specification Approval Sheet. Online. TME. Dostupné z: https://www.tme.eu/Document/f1936d672f413b5ca76f8cb2f88109bd/ACCU-LP675568.pdf. [cit. 2025-03-11]

Opportunistic ambient temperature sensing using commercial microwave links

1st Jan Hejna
Department of Telecommunications
Brno University of Technology
Brno, Czech Republic
xhejna02@vutbr.cz

2nd Petr Musil
Department of Telecommunications
Brno University of Technology
Brno, Czech Republic
xmusil56@vutbr.cz

3rd Matěj Ištvánek
Department of Telecommunications
Brno University of Technology
Brno, Czech Republic
xistva02@vutbr.cz

Abstract—**This paper discusses the utilization of Commercial Microwave Links (CMLs) for opportunistic air temperature measurement. This opportunistic sensing method uses the existing dense infrastructure of microwave telecommunication devices without the additional cost of extending the meteorological network. This method provides extensive spatial coverage, especially in areas with low meteorological density. The research presented here investigates the factors influencing temperature of the devices, analyzes their correlation with reference meteorological station data, and evaluates the capability of a neural network model to accurately predict ambient temperature using this opportunistic sensing method.**

Index Terms—**Opportunistic sensing, Commercial Microwave Links (CMLs), ambient temperature estimation, neural networks, Long Short-Term Memory (LSTM), correlation analysis, temperature prediction.**

I. Introduction

Meteorological data play an essential role in various fields including agriculture, transportation, energy management, environmental protection, and urban planning. Accurate temperature measurements are crucial for monitoring weather conditions, predicting climatic trends, and mitigating the effects of extreme weather events. However, conventional temperature monitoring methods, which predominantly rely on dedicated meteorological stations, face significant limitations due to high installation, operational, and maintenance costs. These limitations often lead to sparse spatial coverage of monitoring networks.

Commercial Microwave Links (CMLs), which are extensively deployed for telecommunications, offer an innovative solution to this problem through opportunistic sensing. Opportunistic sensing is a cost-effective method that leverages various parameters inherently recorded by telecommunication devices, including temperature, signal strength, and operational indicators, to estimate ambient temperature without deploying additional dedicated meteorological equipment. The widespread availability of CML infrastructure across urban and suburban areas provides extensive spatial coverage without additional deployment costs. Furthermore, microwave link-based sensing can effectively bridge spatial gaps present in traditional meteorological networks, enhancing the resolution and reliability of weather monitoring.

The following figure illustrates the comparison between the density distribution of professional meteorological stations measuring temperature and the significantly denser network of CML infrastructure available across urban and suburban regions in the Czech Republic, highlighting the potential of this opportunistic approach.
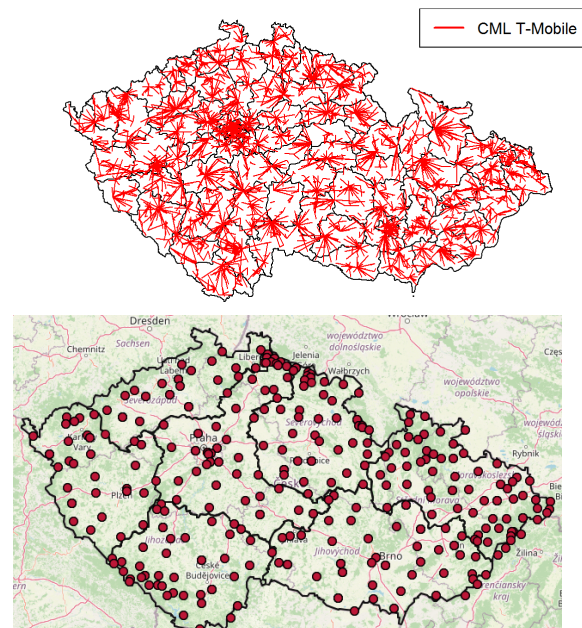

Fig. 1. Distribution comparison: CML infrastructure (top) vs. meteorological stations (bottom) in the Czech Republic.

II. Principle of Opportunistic Temperature Measurement

Commercial Microwave Links (CMLs) are telecommunication systems primarily used for high-capacity data transmission between fixed points. These devices contain built-in temperature sensors intended for internal hardware monitoring. Opportunistic sensing exploits these internal temperature sensors for estimating ambient temperatures, after accounting for multiple influencing factors such as direct solar radiation, environmental reflections, and device-generated heat.

The measured device temperature is influenced by:

- **Device-generated Heat** (t_U): Heat generated by electronic components within devices.
- **Solar Radiation** (t_S): Heat gained from direct solar radiation and reflected radiation, strongly dependent on sun position and sensor orientation.
- **Environmental reflections** (t_E): Temperature offset due to convective heat transfer from surrounding surfaces and structures.

By subtracting these temperature increments from the measured device temperature (t_{MU}), we obtain the estimated ambient temperature (t_A):

$$t_A = t_{MU} - (t_U + t_S + t_E) \tag{1}$$

The figure below illustrates these influencing factors, providing a clear visual explanation of how device-generated heat, solar radiation, and environmental reflections impact the measured temperature of microwave link devices.
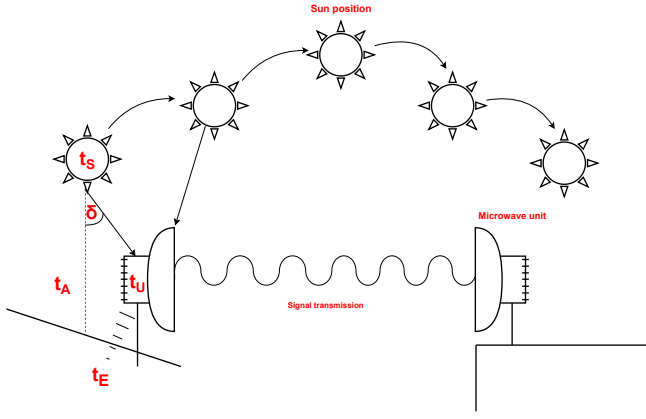
Fig. 2. Key factors affecting measured temperature of the device

A. Analysis of Influencing Factors on Measured Temperatures

The practical utilization of Commercial Microwave Links (CMLs) for opportunistic temperature sensing requires a deeper understanding of how different influencing factors. Although the theoretical influences of internal device heat, solar radiation, and environmental reflection have been identified, it is crucial to thoroughly examine their interactions and variability under practical, real-world conditions.

Solar radiation stands out as one of the most dominant influences, with the device's azimuth orientation, defined by its alignment relative to cardinal directions, playing a crucial role. Temperature measurements are typically taken at the rear side of the parabolic antenna, which can partially shield the sensor from direct solar exposure, thereby mitigating some of the effects of solar radiation. However, even devices placed in close proximity may exhibit substantially different temperature profiles throughout the day due to varying degrees of exposure. Figure 3 clearly illustrates how differences in azimuth orientation can shift the timing of peak temperatures by several hours, emphasizing the importance of considering

device placement, orientation, and the shielding effect of the antenna in interpreting temperature data.
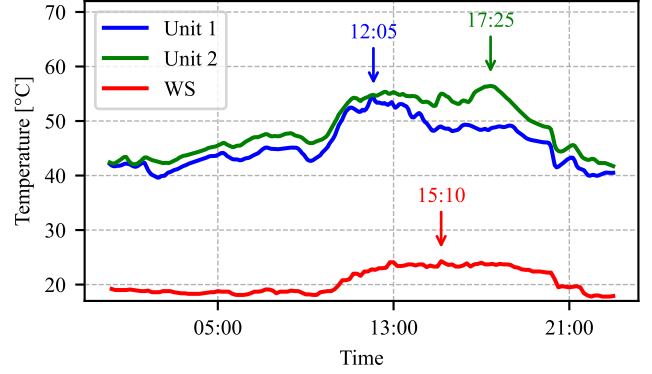

Fig. 3. Effect of azimuth orientation on peak temperature shifts.

Device-generated heat (t_U) is a critical factor influencing temperature measurements (t_{MU}) obtained from commercial microwave links (CMLs). To accurately assess this effect, we leveraged data from a reference meteorological station positioned very close to the microwave device, providing ambient temperature (t_E). Ambient temperature measurements (t_E) from this nearby station allowed precise subtraction of external temperature effects. To further improve accuracy, we specifically analyzed data collected during nighttime periods, effectively eliminating influences from direct solar radiation (t_S) and environmental heat reflections (t_E). This approach ensured that the residual heat (temperature offset $t_{MU} - t_E$) observed and presented in Figure 4 could be attributed primarily to internal heat generation (t_U) within the device itself.
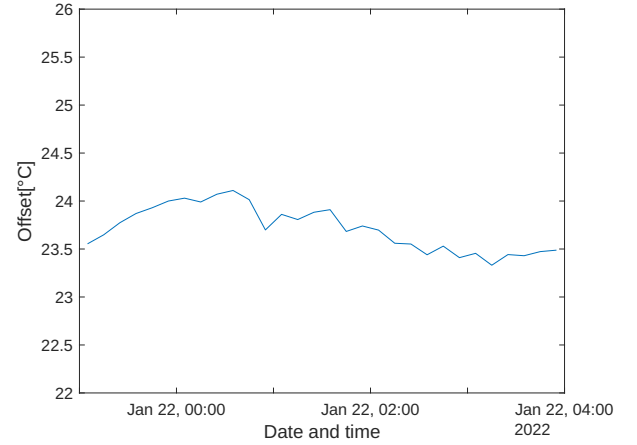

Fig. 4. Quantification of device-generated heat.

Weather events, particularly precipitation, introduce additional complexity. The strength of the microwave signal itself becomes another critical parameter, as fluctuations in signal strength can reliably indicate the occurrence of rainfall. Rain events, depicted in Figure 5, significantly reduce the device temperature due to direct cooling effects, with subsequent

147

evaporation prolonging this cooling period. The blue line (MU) represents the temperature measured at the microwave unit, while the red line (WS) corresponds to the temperature recorded at the weather station. The black curve (Rain) indicates precipitation levels, showing the correlation between rainfall events and the cooling effects observed in both temperature measurements. Thus, integrating signal strength data provides valuable context for interpreting temperature variations and accurately distinguishing between temperature changes due to rainfall and other environmental effects.
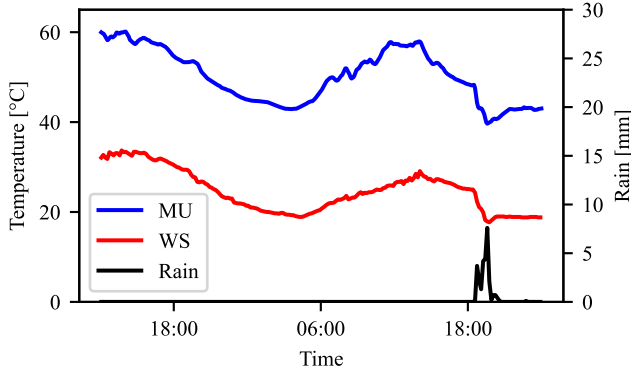
Fig. 5. Impact of rainfall on device temperature.

B. Challenges in Opportunistic Sensing

The opportunistic use of Commercial Microwave Links (CMLs) for ambient temperature sensing offers significant advantages in terms of cost-efficiency and spatial coverage. However, several practical challenges need to be addressed to enhance the accuracy and reliability of temperature measurements.

One of the critical challenges arises from the vertical placement of microwave link devices. Standard meteorological stations typically measure temperature at a height of around two meters above the ground(h_{WS}), whereas microwave link devices require direct line-of-sight for transmission. As a result, they are installed on the rooftops of high-rise buildings or mounted on towers that can reach heights of up to 60 meters above ground level(h_{MU}). Determining the precise installation height of microwave link devices is often difficult due to the lack of available data. This issue complicates the correlation between temperature measurements from microwave links and actual ambient temperatures near the surface, as temperature can vary significantly with altitude. Figure 6 illustrates this discrepancy, highlighting the differences in installation heights between microwave links and standard meteorological stations.

Another significant issue arises from the installation environment of microwave devices. These devices are often mounted on buildings that also house various heat exchangers. For example, rooftop air conditioning units may elevate the local temperature, leading the device's internal sensor to record higher values than the actual ambient conditions. Such offsets,
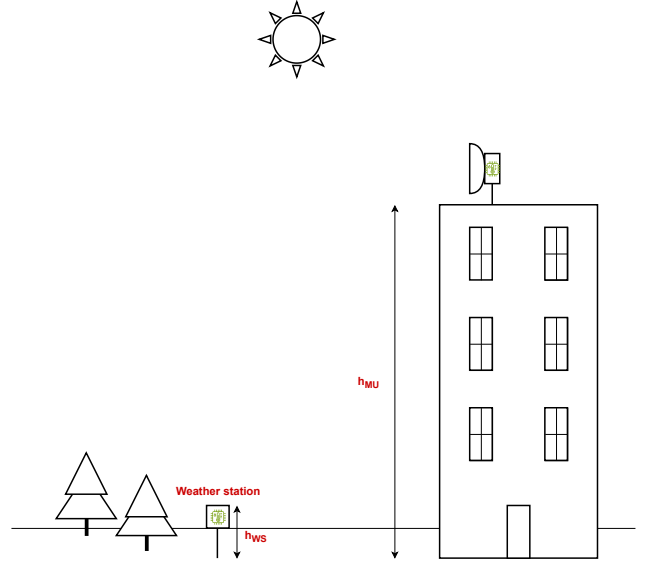

Fig. 6. Height difference between microwave link devices and weather stations.

if not properly corrected, can introduce systematic errors in temperature estimation models and ultimately degrade the quality of ambient temperature predictions.

III. DATA ANALYSIS AND PREDICTION

This chapter focuses on analyzing the correlation between temperatures measured by CMLs and adjacent meteorological stations, followed by evaluating the performance of a neural network model trained for temperature prediction based on the CML data.

A. Correlation Analysis

To validate the capability of CML devices to measure ambient temperature, a detailed correlation analysis between device temperatures and adjacent meteorological station measurements was performed.Several statistical metrics were calculated, including Pearson's, Kendall's, and Spearman's correlation coefficients, across multiple devices from October 2021 to September 2022. The results, summarized in Table I, demonstrate consistently strong correlations. The Pearson correlation coefficient ranged from 0.780 to 0.920, indicating a very good linear relationship between device-measured and actual ambient temperatures. Spearman's rank correlation, which assesses monotonic relationships, also reflected robust correlations (0.774 to 0.927). These results confirm the potential of CML-based sensing as a reliable opportunistic temperature measurement method.

Date	Pearson	Kendall	Spearman	No. of values
2021-10	0.837	0.705	0.856	4463
2021-11	0.780	0.605	0.774	4320
2021-12	0.909	0.743	0.888	4464
2022-01	0.877	0.695	0.852	4464
2022-02	0.806	0.699	0.838	4032
2022-03	0.904	0.755	0.906	4457
2022-04	0.912	0.767	0.915	4320
2022-05	0.883	0.719	0.885	4464
2022-06	0.892	0.739	0.905	4318
2022-07	0.920	0.779	0.927	4464
2022-08	0.901	0.743	0.904	4464
2022-09	0.883	0.735	0.892	4320

TABLE I

CORRELATION ANALYSIS OF TEMPERATURE DATA FROM A CML AND A NEARBY WEATHER STATION

B. Neural Network Prediction

Following the promising correlation analysis results, a neural network model, specifically a Long Short-Term Memory (LSTM) network, was implemented and trained using one year of temperature data sampled every 10 minutes from multiple CML devices and their adjacent meteorological stations. LSTM was chosen due to its ability to effectively capture temporal dependencies in sequential data, making it well-suited for temperature prediction. The dataset included input features such as device temperature, solar radiation indicators, azimuth, and temporal factors. The trained model achieved high prediction accuracy, as summarized in Table II.

Metric	Value
Mean Absolute Error (MAE)	0.584 °C
Mean Squared Error (MSE)	0.744 °C^2
Root Mean Squared Error (RMSE)	0.863 °C
Coefficient of Determination (R^2)	0.989

TABLE II
RESULTS OF THE TRAINED MODEL.

The following two graphs in Figure 7 provide a visual representation of the performance of the trained model. The scatter plot compares the predicted values from the model with the actual values measured by nearby meteorological stations. The graph supports the high accuracy of the model, with only slight deviations. The residual histogram, which depicts the distribution of prediction errors, shows a symmetric distribution centered around zero, indicating that most prediction errors are small and the model exhibits minimal systematic bias.
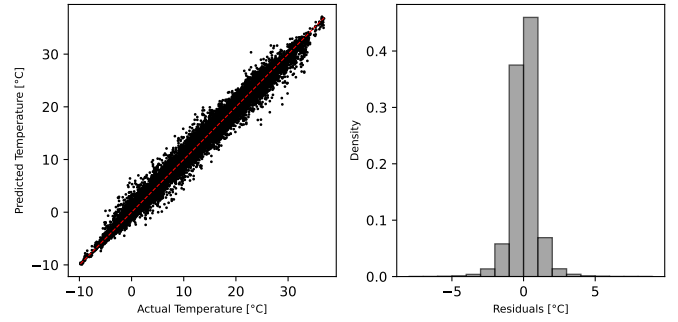

Fig. 7. Comparison of actual and predicted temperature values.

IV. CONCLUSION

This paper demonstrates the feasibility of using Commercial Microwave Links (CMLs) for opportunistic ambient temperature sensing. The analysis confirmed a strong correlation between device-measured temperatures and reference meteorological data, with key influencing factors such as solar radiation, azimuth orientation, and device-generated heat being systematically evaluated. Furthermore, a neural network model successfully predicted ambient temperature with high accuracy, achieving an MAE of 0.584°C. While challenges such as installation height variability and environmental heat sources remain, CML-based sensing presents a cost-effective and scalable alternative for enhancing meteorological networks, particularly in regions with sparse weather station coverage.

REFERENCES

[1] M. Fencl, "CML network operated by T-Mobile," in *CML network in Czech Republic* [online]. Praha: Martin Fencl, 2015. Dostupné z: https://rpubs.com/fenclmar/91451.

[2] CHWALA, Christian a Harald KUNSTMANN. Commercial microwave link networks for rainfall observation: Assessment of the current status and future challenges. *WIREs Water* [online]. 2019, 6(2), e1337. DOI: 10.1002/wat2.1337. Dostupné z: https://wires.onlinelibrary.wiley.com/doi/10.1002/wat2.1337

[3] S. Hochreiter and J. Schmidhuber, "Long Short-Term Memory," *Neural Computation*, vol. 9, pp. 1735–1780, 1997, DOI: 10.1162/neco.1997.9.8.1735.

[4] J. Hejna, "Secure Web Application for Surface Temperature Monitoring Based on Machine Learning Methods," *Bachelor's thesis* [online]. Brno: Brno University of Technology, Faculty of Electrical Engineering and Communication, Department of Telecommunications, 2023. Supervisor: Petr Musil. Available at: http://hdl.handle.net/11012/210374 [Accessed: Mar. 5, 2025].

[5] T. T. K. Tran, S. M. Bateni, S. J. Ki, and H. Vosoughifar, "A review of neural networks for air temperature forecasting," *Water*, vol. 13, no. 9, p. 1294, 2021. DOI: 10.3390/w13091294. Dostupné z: https://www.mdpi.com/2073-4441/13/9/1294

[6] L. W. de Vos, A. M. Droste, M. J. Zander, A. Overeem, H. Leijnse, B. G. Heusinkveld, G. J. Steeneveld, and R. Uijlenhoet, "Hydrometeorological Monitoring Using Opportunistic Sensing Networks in the Amsterdam Metropolitan Area," *Bulletin of the American Meteorological Society*, vol. 101, no. 2, pp. E167–E182, Feb. 2020. DOI: 10.1175/BAMS-D-19-0091.1. Dostupné z: https://doi.org/10.1175/BAMS-D-19-0091.1

Anomaly Detection in Networks Using Noise Spectrum Analysis of Network Devices

Oliver Varga
Faculty of Electrical Engineering
Brno University of Technology
Brno, Czechia
xvarga20@vutbr.cz

Ing. et Ing. Petr Musil
Faculty of Electrical Engineering
Brno University of Technology
Brno, Czechia
musilp@vutbr.cz

Abstract—This document presents a novel anomaly detection system based on analyzing power line communication (PLC) noise to differentiate between various network conditions. By leveraging a decision tree classifier, the system classifies measured data into four different states: idle, normal traffic (25 Mbit/s), higher-bandwidth traffic (460 Mbit/s), and DoS attack scenarios. Experimental results demonstrate that this approach is effective in distinguishing DoS attack conditions from normal operations, although some limitations still remain. A key limitation is that a DoS attack aimed at the measuring system may cause it to freeze, preventing real-time analysis by the proposed system.

Index Terms—DoS/DDoS, electrical signal, machine learning, network anomaly detection, noise, PLC

I. Introduction

In modern networking environments, it is essential that performed operations are reliable and secure. In order to achieve these essentials, some traditional network monitoring techniques work with packet inspection and traffic analysis. These methods, however, may be limited due to encryption, privacy concerns, or network complexity. An alternative approach involves taking advantage of power consumption characteristics and the impact they inevitably impose on electromagnetic noise patterns.

Power Line Communication (PLC) technology enables data transmission over electrical power lines while also generating characteristic noise signals that can be directly influenced by the connected devices, such as routers. By capturing and further analyzing these fluctuations in electrical noise, it is possible to infer network behavior and detect network anomalies such as cyber attacks or unauthorized activities [1].

This research aims to explore the feasibility of using PLC modems as a nonintrusive method to analyze noise fluctuations for anomaly detection in data networks, where the primary objectives are:

- To investigate the relationships between data network activity and noise spectrum variations.
- To develop a machine learning model for classifying normal and anomalous behavior.
- To implement a prototype system capable of detecting anomalies in real time.

II. Methodology

In this section, we describe the methodology used to detect data network anomalies based on the changes in the electrical noise spectrum of PLC networks. The approach consists of steps like data collection, feature extraction, and machine learning-based classification.

For the purposes of analyzing changes to the electrical noise caused by network devices, such as routers, distributed PLC modems of the company MaxLinear were used. These modems allow measurements of the frequency characteristics of generated noise in the electrical network, utilizing the Multiple Input Multiple Output (MIMO) method [1].

A. Experimental Setup

The experimental setup consists of a network topology (Fig. 1) where two PLC modems are used to measure electrical noise characteristics under different circumstances. The chosen topology includes:

- Two PLC modems connected to two different extension cords to form a communication link.
- A network router.
- Two computers, one generating network traffic and the other receiving it.
- A third computer generating a high traffic load using Denial of Service (DoS) tools.

Software applications that were used during measuring include Java and Wireshark to ensure proper functionality of the SpiritConfigTool.jar and iPerf3 speed testing tool to simulate network traffic between the computers.
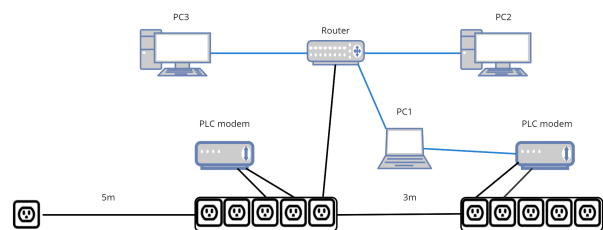

Fig. 1. Measurement Topology.

B. Data Collection and Processing

The measured data of generated noise belong in the 1.8-80 MHz frequency range. In order to capture these measurements, the proprietary application `SpiritConfigTool.jar` was used to allow our computer to save each measurement in the `.csv` format in the form of two files, one for Channel 1 and the second for Channel 2. In each file, the first column represents the measured values of frequency in MHz, and the second column represents captured noise values in dBm/Hz.

The data is collected under four conditions. Firstly, a condition where no network activity is generated. Secondly, a simulation of regular data transmission is performed. Thirdly, a network traffic condition of the highest possible bandwidth, in our case 460 Mbit/s. Lastly, a simulated DoS/DDoS attack causing high network load is performed. Data from both channels is then combined, and statistical features such as mean, maximum, minimum, and standard deviation are extracted. During these simulations, the load on the router's CPU is also monitored.

C. Machine Learning Approach

In order to classify network conditions based on noise spectrum features, a decision tree classifier was employed. For model training purposes, four labels were assigned based on the network conditions they represent. The **Idle** label corresponds to a scenario where no network activity was present, and CPU load remained below 1%. The **Normal** label represents network traffic at a rate of 25 Mbit/s with a maximum CPU load of 1%. Additionally, the **High Traffic** label was introduced for network conditions with a data rate of 460 Mbit/s. Lastly, the **Attack** label was designated for scenarios involving simulated DDoS attacks, characterized by extreme network congestion and CPU load fluctuations of up to 72%.

The performance of the model is evaluated using:

- Accuracy of classification.
- Confusion matrix to analyze misclassifications.
- Comparison of predicted and actual labels for different network conditions.

III. RESULTS

This section presents the experimental results obtained from the proposed anomaly detection system and discusses their implications.

A. Experimental Results

The measured dataset was used to train and evaluate a Decision Tree Classifier due to its simplicity and interpretability.

The collected data were analyzed to determine the effectiveness of the proposed model in distinguishing between different network conditions. The dataset was divided into training, testing, and validation sets in a way that ensures fair representation of all four network traffic states. The model's accuracy was evaluated on both the test and validation sets.

The average accuracy of the testing set in 5-fold cross-validation was 76.67% and the validation set accuracy was 80%.

The results so far indicate that the model performs well in distinguishing between high-bandwidth traffic (460 Mbit/s) and attack conditions. However, the differentiation between idle and low-bandwidth traffic (25 Mbit/s) proved to be less accurate, likely due to similarities in noise characteristics. This issue could be mitigated by expanding the dataset and incorporating additional features in the future.

B. Proposed Anomaly Detection System Prototype

As a system of anomaly detection, we implement a simple Python script that reads created `.csv` files by the BPL modem measuring application and uses our trained model to timely mark the network communication as disrupted by an incoming DoS attack.

However, a critical limitation of this prototype was observed during testing: if a DoS attack targets the PC running the measurement application, the application freezes completely, preventing any further data collection and analysis.

C. Comparison with Existing Approaches

Compared to traditional traffic-based anomaly detection systems, our method offers a unique approach by relying on power line communication noise analysis. This approach provides a nonintrusive alternative that can be deployed in environments with restricted access to network device interfaces.

D. Limitations and Future Work

Despite promising results, a few limitations still exist:

- The used dataset is limited in size, potentially affecting the generalizability of the model.
- The system currently classifies anomalies based on predefined conditions but may require adaptation for detecting emerging attack patterns.
- Real-time deployment and optimization need further evaluation to assess feasibility in dynamic network environments.
- A critical limitation of the proposed system, when a DoS attack targets the PC running the measurement application, the application freezes. This results in the Python script being unable to access new measurement data, effectively preventing analysis of network conditions in real time.

Future work will focus on expanding the dataset, exploring different measurement topologies to enhance model generalizability, and evaluating alternative machine learning models for improved data classification performance.

IV. CONCLUSION

This paper presented an experimental anomaly detection system based on power line communication noise analysis. To classify different data network conditions, including idle, normal, higher bandwidth, and attack scenarios, a decision tree

classifier was implemented and trained. The results demonstrated that the approach is capable of differentiating between attack conditions and normal operations, although some challenges still remain.

The proposed system works nonintrusively by analyzing electrical noise in real time, eliminating the need to directly access the interfaces of network devices. However, limitations such as dataset size and application stability under DoS attacks highlight areas for improvement. Future efforts and work will focus on expanding the dataset, refining the machine learning model, and improving the real-time deployment capabilities.

REFERENCES

[1] A. Schwager, D. Schneider, W. Baschlin, A. Dilly, and J. Speidel, "MIMO PLC: Theory, measurements and system setup," in *Proc. IEEE Int. Symp. Power Line Commun. Appl. (ISPLC)*, Udine, Italy, 2011, pp. 48-53.
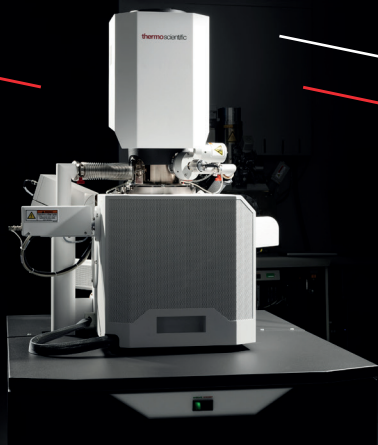
Can Neural Networks spot the Sponge?

Matej Gradoš[1,2], Christof Paar[3], Muhammad Bilal Zafar[4,5], and Gregor Leander[5]

[1]Brno University of Technology, Brno, Czech Republic
[2]Tampere University, Tampere, Finland
[3]Max Planck Institute for Security and Privacy, Bochum, Germany
[4]UAR Research Center for Trustworthy Data Science and Security
[5]Ruhr University Bochum, Bochum, Germany

Abstract—**Cryptographic hash functions ensure data integrity and security in modern cryptographic systems. They are a core mechanism for digital signatures, authentication protocols, and blockchain technology, designed to make their output impossible to predict. Inspired by machine learning's ability to approximate complex functions, we trained models of varying complexity to assess whether they can learn and replicate the behavior of cryptographic hash functions. Our study evaluates the extent to which these models are able to approximate the underlying mathematical operations, shedding light on potential vulnerabilities and theoretical limits of machine learning in cryptographic contexts.**

Index Terms—**Hash functions, neural networks, machine learning, cryptanalysis**

I. BACKGROUND

Hash functions are components for many critical information security applications, including the generation and verification of digital signatures, key derivation, and pseudorandom bit generation [1]. A key property of hash functions is their high sensitivity to input modifications, which makes their outputs highly unpredictable, allowing hash values to serve as unique digital fingerprints [2]. This sensitivity is fundamental to essential security features, including preimage resistance, also known as **one-wayness**, referring to the difficulty in determining any input from its hashed output. Second preimage resistance refers to the infeasibility of finding two distinct inputs producing the same hash. Lastly, a hash function is considered collision-resistant if finding two different inputs that produce the same hash output is infeasible. Although these functions are robust, their complexity can make them challenging to understand and analyze.

Secure Hash Algorithm 3 (SHA-3) currently represents the latest standardized advancement in cryptographic hash functions [1]. SHA-3 and its SHAKE128 and SHAKE256 variants derived from Keccak, introduce an innovative structure that sets it apart from earlier hashing schemes. While SHA-1 and SHA-2 utilize the Merkle-Damgård construction [3], SHA-3 implements Keccak's innovative sponge construction. Following message preprocessing, which segments the message into blocks and applies padding, the sponge construction operates in two sequential phases:

1) **Absorbing phase** processes the message blocks x_i.
2) **Squeezing phase** calculates and produces an adjustable length output.

The core computational element of SHA-3, the Keccak-f function, is frequently referred to as the Keccak-p permutation due to its bijective nature, mapping each b-bit input to a unique b-bit output. A Keccak-p permutation round consists of five sequential transformation steps: θ, ρ, π, χ, and ι. These steps systematically manipulate the state array through linear transformations providing diffusion and symmetry breaking, while nonlinear transformations introduce confusion properties crucial for cryptographic security.

II. MOTIVATION

Machine learning (ML) has demonstrated remarkable success in modeling complex functions across various domains. Deep neural networks (DNNs) have proven particularly effective at tackling challenging tasks that were once thought to require human-level intelligence. While they have been widely applied in areas such as classification [4], pattern recognition [5], or disease outbreak modeling [6], their potential in cryptographic tasks remains an emerging and promising field of research.

Numerous studies proposed hash functions based on neural network architectures [7], [8], [9], leveraging their ability to provide security through nonlinearity, high sensitivity, and adaptability. These approaches build on the neural networks' highly nonlinear architecture. The ability to model complex bit mappings provides an excellent foundation for creating secure, efficient, and collision-resistant cryptographic hash functions. Beyond hashing, a recent study explored how deep neural networks (DNNs) can be integrated into broader cryptographic functionalities, such as encryption, authentication, and watermarking. However, a key challenge arises from the fundamental difference between traditional cryptographic systems, which rely on discrete Boolean operations, and DNNs, which operate on continuous real-valued inputs [10].

Given the opposing characteristics of machine learning and cryptographic security, we aim to explore the boundaries of ML's predictive power. In this paper, we pose a fundamental question: **Can machine learning predict the output of a cryptographic hash function SHA-3?**

We aim to train the neural network on fundamental principles of hash functions and leverage its nonlinear characteristics instead of developing a more sophisticated hashing method that integrates existing solutions with abstract enhancements.

III. Contribution

To transform these theoretical foundations, we developed a prototype that effectively captures the essence of the Keccak algorithm. This simplified SHA-3 hash function, also referred to as a "*toy function*", reduces the state size from 1600 bits to 25 bits, omits suffixes, padding, and uses only 12 rounds compared to the full version's 24 rounds to simplify the demonstration of core concepts. These are all available modifications, discussed in [1], [2], also provided in the first column of Table I. The implementation's simplified state size of 25 bits is arranged as a 5×5 grid of lanes, preserving the essential mathematical principles of the original algorithm.

TABLE I: Valid state sizes with parameters n_r, w and l

State size b [bits]	25	50	100	200	400	800	**1600**
Number of rounds n_r	12	14	16	18	20	22	**24**
Lane w [bits]	1	2	4	8	16	32	**64**
l	0	1	2	3	4	5	6

A. Dataset

To explore the behavior of the reduced SHA-3 implementation, all possible 25-bit binary values were generated. This approach ensures complete coverage of the 25-bit state space, which consists of 2^{25} distinct values ranging from 0 to $(2^{25} - 1)$. Generating, and subsequently hashing all possible values allowed us to perform a comprehensive validation of the hash function implementation using Dirichlet's drawer principle [2]. The Dirichlet's drawer principle, known as the pigeonhole principle, states that if more items are distributed than there are containers to hold them, at least one container must contain more than one item [11].

B. Neural Network

A constructed neural network represents a sequence of three fully connected layers, each composed of linear transformations, followed by nonlinear Rectified Linear Unit (ReLU) activation functions [12]. The neural network input layer's dimensionality corresponds to the bit length of the binary inputs processed by the hash function. Similarly, the output layer's dimensionality matches the 25-bit representation of the hash function's output.

IV. Experimental results

A. Impact of Optimizer Algorithm on Loss

Our experiment examines the effectiveness of various optimizer algorithms in minimizing the Mean Squared Error (MSE) loss function during model training. The neural network was trained on a dataset comprising 512 sample pairs of unhashed and hashed data for 50 epochs. Experimental results demonstrate that optimizer selection significantly influences model performance metrics.

As shown in Fig. 1, Stochastic Gradient Descent (SGD) [13] and Adam [14] displayed robustness to variations in learning rate and hidden layer dimensionality, offering a wider range of optimal configurations. However, SGD and Nesterov-Accelerated Adaptive Moment Estimation (NAdam) [15] were more sensitive to changes in learning rate values. Adaptive gradient-based optimizers, specifically Adagrad [16] and Adadelta [17], maintained consistent performance across the learning rate values. A positive correlation was observed between hidden layer dimensionality and error reduction, with increased dimensionality generally resulting in decreased MSE loss. The Adam optimizer consistently outperformed alternative algorithms, exhibiting lower error metrics across diverse hyperparameter configurations. Therefore, it was chosen as the default optimization algorithm for subsequent experiments, leveraging its robust learning capabilities with an optimal learning rate of 0.001.
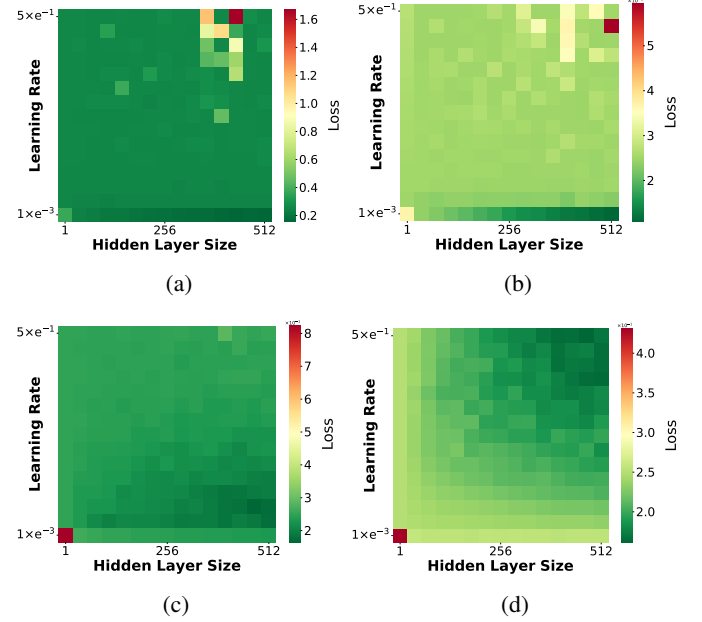

Fig. 1: Heatmap visualization comparing loss values across optimization algorithms (a) Adam, (b) Nadam, (c) Adagrad, (d) SGD. Each heatmap shows how loss varies with different combinations of learning rate and hidden layer size.

B. Impact of Input Complexity and Hidden Layer Size on Loss and Accuracy

Performance was systematically evaluated across input complexities and hidden layer dimensionalities. Each configuration underwent training for 50 epochs on a dataset of 16384 combinations of unhashed and hashed samples. Loss values highlighted regions where the network struggled to learn the step mappings between unhashed inputs and their corresponding hashed outputs. Accuracy metrics indicated the model's ability to predict hashed outputs from unhashed inputs within the dataset correctly.

Our analysis revealed a clear correlation between architectural capacity and performance. Hidden layers with reduced dimensionality demonstrated insufficient capacity to model

complex input-output mappings effectively. While smaller hidden layers failed to handle complex input relationships, larger architectures provided adequate representational capacity. Networks with hidden layer sizes of 512, 1024, and 2048 neurons performed well across both simple and complex input samples. The accuracy heatmap in Fig. 2 shows that as input complexity increases, model accuracy generally improves, particularly for larger hidden layer configurations—represented by green cells in the visualization. This trend suggests that more complex inputs may contain distinctive patterns that facilitate more effective learning by models with sufficient capacity.
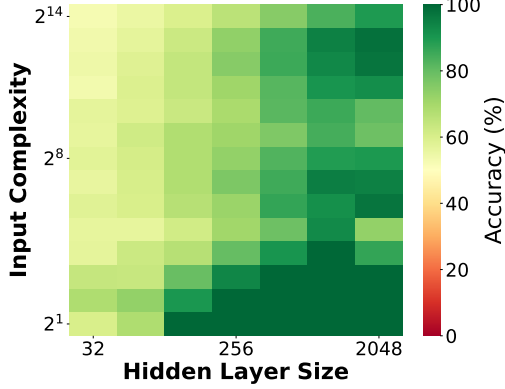
Fig. 2: Heatmap visualizes the relationship between model accuracy, hidden layer size, and input complexity. The color gradient represents accuracy levels, with darker green indicating higher accuracy and red signifying lower accuracy.
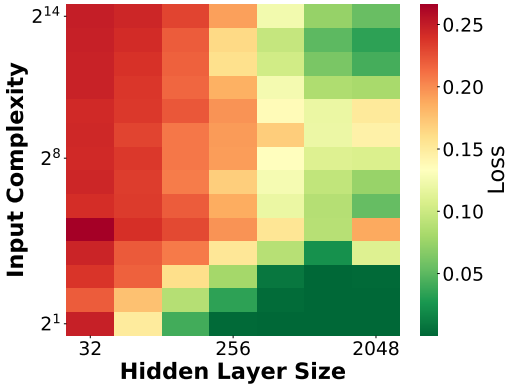
Fig. 3: Heatmap visualizes the loss values in relation to input complexity and hidden layer size. The color gradient represents magnitude of the loss, with red indicating higher loss and green denoting lower loss.

C. Model Performance in Training and Generalization Across Multiple Rounds

We analyzed the correlation between the complexity of the SHA-3 cryptographic hash function and the learning capability of neural networks. The analysis involved incrementally increasing the number of Keccak-p permutation rounds, starting
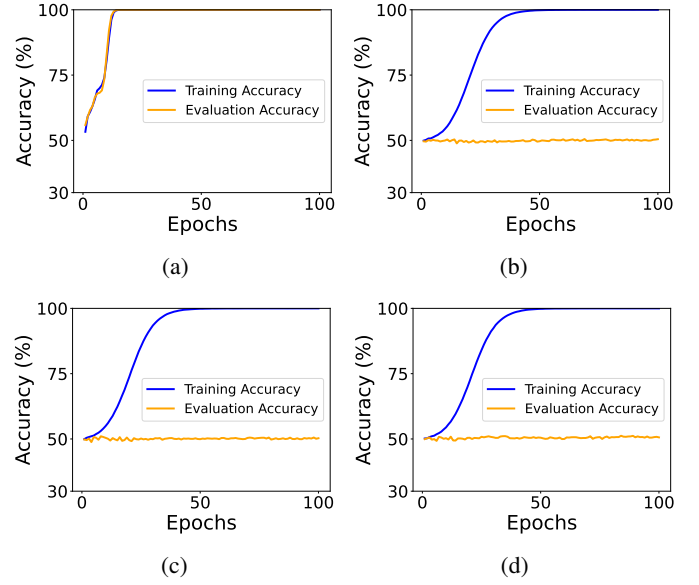
Fig. 4: Training and evaluation accuracy over epochs for increasing number of Keccak-f rounds. Plots graph the divergence between training accuracy (blue) and evaluation accuracy (orange) as the number of Keccak-f rounds increases. (a) 1 round, (b) 2 rounds, (c) 6 rounds, and (d) 12 rounds.

from Round 1 (denoted as Round 0 in existing literature) and continuing up to Round 12. A neural network with a fixed architecture comprising three fully connected layers and a hidden layer of 1024 neurons was trained for 100 epochs using 8192 samples, with 95% allocated for training and 5% for evaluation.

Fig. 4 illustrates the model's performance across multiple rounds of the SHA-3 toy function during training and generalization, demonstrating its ability to learn step mappings even as complexity increases. After the first five permutation steps, training and evaluation accuracy align relatively closely, reaching near 100%. However, as the number of rounds increases, the network's ability to generalize drops. Over the span of 12 rounds of the SHA-3 toy function, training accuracy remains high, while evaluation accuracy stagnates near 50%, suggesting potential overfitting.

As evidenced by the widening gap between training and evaluation accuracy, the decline in generalization can be attributed to the phenomenon of network data memorization [18]. The increasing complexity of SHA-3 permutations leads to intricate transformations. Hence, the model begins to store specific training samples instead of learning and extracting generalizable patterns. As a result, the model fits the training data perfectly but struggles with unseen samples, evident from the widening gap between training and evaluation accuracy.

V. CONCLUSION

This work investigates the feasibility of learning hash functions using neural networks, specifically questioning whether teaching a neural network the underlying cryptographic trans-

formations inside the hash function is possible. From an implementation standpoint, experimenting with a reduced version of the SHA-3 hash function provided a more manageable starting point for exploring this approach.

Across the experiments we found that the choice of optimizer can significantly impact the model's performance. Across various learning rates and hidden layer sizes, the Adam optimizer consistently excelled compared to other optimizer algorithms. Larger neural networks, with 512, 1024 and 2048 neurons, achieved high accuracy on inputs of higher complexity. This suggests that neural networks can learn Keccak-p permutation step mappings quite effectively. However, these models struggled to generalize across multiple Keccak-f function rounds. Although they performed well during training, their accuracy dropped significantly when tested on more challenging inputs. This can indicate various limitations in capturing the patterns of cryptographic hash functions.

Results of this exploratory work open several promising avenues for further research at the intersection of neural networks and cryptographic hash functions. The observed divergence between training and evaluation accuracy suggests the need for more robust machine learning approaches. Potential future steps include the exploration of advanced regularization techniques specifically designed for learning bit mappings of cryptographic hash functions.

REFERENCES

[1] NATIONAL INSTITUTE OF STANDARDS AND TECHNOLOGY, "FIPS PUB 202: SHA-3 Standard: Permutation-Based Hash and Extendable-Output Functions." Online. August 2015. Available: http://dx.doi.org/10.6028/NIST.FIPS.202.

[2] C. Paar and J. Pelzl, "Understanding Cryptography: A Textbook for Students and Practitioners," 2nd ed., Springer-Verlag GmbH, DE, part of Springer Nature, 2024. ISBN: 978-3-662-69006-2 (Print), 978-3-662-69007-9 (eBook). Available: https://doi.org/10.1007/978-3-662-69007-9.

[3] EITCA INSTITUTE, "How does the Merkle-Damgård construction operate in the SHA-1 hash function, and what role does the compression function play in this process?" Online. Published: June 15, 2024; Accessed: December 4, 2024.

[4] R. Féraud and F. Clérot, "A methodology to explain neural network classification," Neural Networks, vol. 15, no. 2, pp. 237-246, April 2002.

[5] A. Patil and M. Rane, "Convolutional Neural Networks: An Overview and Its Applications in Pattern Recognition," in Information and Communication Technology for Intelligent Systems, T. Senjyu, P. N. Mahalle, T. Perumal, and A. Joshi, Eds. Singapore: Springer, 2021, vol. 195, pp. TBD.

[6] M. Barman, M. Panja, N. Mishra, and T. Chakraborty, "Epidemic-guided deep learning for spatiotemporal forecasting of Tuberculosis outbreak." Online. Available: https://doi.org/10.48550/arXiv.2502.10786.

[7] S. Lian, J. Sun, and Z. Wang, "Secure hash function based on neural network," Neurocomputing, vol. 69, no. 16–18, pp. 2346–2350, July 2006.

[8] M. Turčaník and M. Javurek, "Hash Function Generation by Neural Network," in 2016 New Trends in Signal Processing (NTSP), 2016, pp. 1–5. Available: https://doi.org/10.1109/NTSP.2016.7747793 .

[9] S. Lian, Z. Liu, Z. Ren, and H. Wang, "Hash Function Based on Chaotic Neural Networks," in 2006 IEEE International Symposium on Circuits and Systems (ISCAS), 2006, p. 4. Available: https://doi.org/10.1109/ISCAS.2006.1692566 .

[10] D. Gerault, A. Hambitzer, E. Ronen, and A. Shamir, "How to Securely Implement Cryptography in Deep Neural Networks" Cryptology ePrint Archive, Paper 2025/288, 2025.

[11] M. Ajtai, "The Complexity of the Pigeonhole Principle," in [Proceedings 1988] 29th Annual Symposium on Foundations of Computer Science, 1988, pp. 346–355. Available: https://doi.org/10.1109/SFCS.1988.21951.

[12] A. K. Dubey and V. Jain, "Comparative Study of Convolution Neural Network's ReLU and Leaky-ReLU Activation Functions," in Applications of Computing, Automation and Wireless Systems in Electrical Engineering, S. Mishra, Y. Sood, and A. Tomar, Eds., Lecture Notes in Electrical Engineering, vol. 553, Springer, Singapore, 2019. Available: https://doi.org/10.1007/978-981-13-6772-4_76.

[13] S. Amari, "Backpropagation and Stochastic Gradient Descent Method," in Neurocomputing, vol. 5, no. 4, pp. 185–196, 1993. Available: https://doi.org/10.1016/0925-2312(93)90006-O

[14] D. P. Kingma and J. L. Ba, "Adam: A Method for Stochastic Optimization," in Proceedings of the 3rd International Conference on Learning Representations (ICLR), San Diego, CA, USA, May 2015. Available: https://arxiv.org/abs/1412.6980

[15] T. Dozat, "Incorporating Nesterov Momentum into Adam," in Proceedings of the International Conference on Learning Representations (ICLR) Workshop Track, San Juan, Puerto Rico, May 2016. Available: https://openreview.net/pdf?id=OM0jvwB8jIp57ZJjtNEZ

[16] J. Duchi, E. Hazan, and Y. Singer, "Adaptive Subgradient Methods for Online Learning and Stochastic Optimization," in Journal of Machine Learning Research (JMLR), vol. 12, pp. 2121–2159, Jul. 2011. Available: https://jmlr.org/papers/v12/duchi11a.html

[17] M. D. Zeiler, "ADADELTA: An Adaptive Learning Rate Method," in Proceedings of the 6th International Conference on Learning Representations (ICLR), Scottsdale, AZ, USA, May 2012. Available: https://arxiv.org/abs/1212.5701

[18] N. Carlini, C. Liu, Ú. Erlingsson, J. Kos, and D. Song, "The Secret Sharer: Evaluating and Testing Unintended Memorization in Neural Networks," in Proceedings of the 28th USENIX Security Symposium, Santa Clara, CA, USA, Aug. 2019, pp. 267–284. Available: https://www.usenix.org/conference/usenixsecurity19/presentation/carlini

Web application for secure file transfer

1st Vít Horký
Department of Telecommunications
FEEC, Brno University of Technology
Brno, Czech Republic
221971@vut.cz

2nd Tomáš Caha
Department of Telecommunications
FEEC, Brno University of Technology
Brno, Czech Republic
tomas.caha1@vut.cz

Abstract—**This paper focuses on the design and implementation of a web application capable of securely transferring files over the Internet. It aims to be an open-source solution for handling more complex tasks that are underserved by tools freely available on the internet. The application prioritizes ease of use by incorporating integration with Microsoft Single Sign-on (SSO) and provides easy future extensibility for use with multiple storage providers by abstracting its storage layer.**

Index Terms—**file transfer, web application, SSO, .NET, Blazor**

I. INTRODUCTION

In an increasingly digital world, the ability to securely transfer data between individuals and/or organizations is a fundamental requirement. From this naturally arises the need to send multiple, possibly large, files securely and easily over the internet. An example use case could be a remote worker, who routinely transfers files larger than the maximum limit of an email attachment. With the ever-increasing prevalence of digital media on the internet and the rapid projected growth of virtual reality [1], which requires sizable 3D models, there is a requirement for a robust solution to this problem.

The output of this paper is a web-based tool that supports common workflows that arise from this need. The many other ways of sending files over the internet result in certain compromises, which this tool attempts to eliminate. Examples of these limitations include restrictions on the maximum size of email attachments, which is typically between 20 to 50 MB for common providers [2]. One solution to this limitation is using cloud providers to store data. This comes with potentially large costs when storing large amounts of data. There are also some organizations concerned with data security and privacy protection issues that prevent them from using the cloud [3]. A way of solving these issues is giving the users full ownership and management of their data, which can be achieved by letting them host a solution for themselves on their own servers. The proposed web application aims to achieve this and presents a secure and easy-to-use interface for external access from outside the user's network.

As the task of transferring large files over the internet is neither new nor uncommon, existing solutions were examined for common functionality. Like similar web-based tools, the proposed one also makes extensive use of email as a way to send its users information. The two main workflows that this tool supports are: 1. uploading files and sending someone a download link and 2. sending a request for a file upload to someone.

In principle, this web application is intended to reside on the user's network with access to the internet and store all incoming and outgoing files. Focus was placed on the ability to replace the file storage layer, with local filesystem storage and FTP being implemented. For security, the website supports authentication using SSO which is a technology allowing users to securely authenticate using only one set of credentials for multiple websites [4]. Microsoft was chosen as a provider for SSO.

II. EXISTING SOLUTIONS

Part of this work was also comparing existing solutions to find their differences and possibly identify areas for improvement. The focus was on tools generally available on the internet with free and paid solutions both considered. There were generally two groups of solutions identified that broadly fall into categories for personal/small organization use and for larger organizations.

The first category focuses on ease of use and simple user interfaces, with a free plan that is limited and a monthly subscription that increases storage capacity and holding time. All solutions in this category do not offer the ability to store files locally and are instead hosted in the cloud. The functionality to make requests to receive files is also limited, with one website not supporting it at all and one marking the functionality as 'Beta'.

The second category contains only one web application which seems to be targeted towards larger organizations with more extensive workflows and more complex integration to other systems. From this stems a different licensing approach which is a yearly subscription and scales by the number of users. The solution also lacks support for many storage protocols and by default stores data on a local disk. The only other supported protocols are FTP and NFS.

The main shortcoming found is the lack of any popular open-source solution. This problem has security and data integrity implications, as the user cannot be entirely certain the data is handled properly. The second problem found is that all but one surveyed web applications are hosted on the cloud by their provider which creates similar problems with data integrity and limits the maximum capacity of storage and time before automatic deletion. The web application that runs

on a user-provided server offers limited support for different storage types.

The solutions compared were: Úschovna.cz, Posílej.cz, Liquidfiles.com and WeTransfer. A more detailed comparison can be seen in Table I.

III. Design and implementation

As mentioned before, two primary workflows of this web application are: 1. Uploading files to a server and giving an individual the link to download them, and 2. Creating a request for another individual, which they can use to upload files. Both of these are slightly different processes that require different considerations and are also logically separated on the final website.

The first one, being simpler to implement, is also more common among free tools online, as discussed in the previous section. When uploading files, the user fills in the title and a short message which will be reflected in the resulting email sent to the recipient. The user can fill in as many email addresses as they please and a message with the link will be sent to all of them. The user is also shown the generated hyperlink which can be copied and sent by any other means.
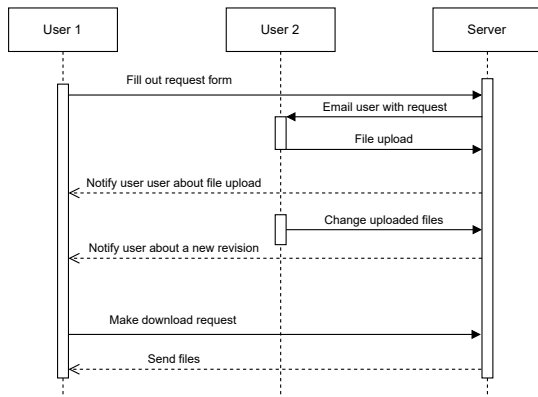
Fig. 1. Sequence of steps for requesting files from another user

The second workflow, which is intended as a way for making requests to individuals external to the organization, is the more complex one. A diagram containing a possible sequence of events is in Fig. 1. As seen in the diagram, the process can send multiple email messages throughout depending on whether the user specified that they want to be notified about successful file uploads. More than one email can be sent because this process also supports creating revisions. This means a user can resubmit the form with different files in it, for example, if they made a mistake.

The other feature differentiating this process from a simple file upload is the need to discern when multiple individuals are specified as recipients of one request. This is handled by creating multiple slots that can be uniquely identified and are connected to an email address to which the file request was sent. Then they can be separately accessed by users to whom the request was sent. This is achieved by sending a slightly different email to each user, each one containing a link identifying the person it was sent to.

As already mentioned, the functionality to update files when they are already uploaded is a supported feature. This simplifies the management of storage because it removes the need for users to delete and recreate file uploads if they make a mistake. Also, it is a necessary functionality for file requests which allows users to make revisions after the fact. This update doesn't concern only files and can be used to edit the title and message. In the case of a request link, an email with an updated title, message and list of files is sent again if so configured.

All of these features are designed and implemented with a certain degree of configurability in mind. The website's settings, not including basics like email and storage configuration, also include a way to influence how these processes behave. One setting determines if a person who is not authenticated can upload files. By default, they are not, but it could sometimes be beneficial to allow guest users to do so. However, care should be taken not to allow large amounts of anonymous individuals to fill up the storage and bring down the website.

Other configurations are related to allowing or preventing users from viewing and editing the files they uploaded. By default, they can both view and edit the files already created, but when disabled, the users either see a read-only list of the files or a message informing them that they successfully uploaded their files.

As previously stated, it is configurable if an unauthenticated user can upload files into the system, but making requests for files is gated entirely behind a log-in. Authentication for users is handled by redirecting them to Microsoft Single sign-on. This simplifies account management and storage, which also increases data security because the web application does not need to store passwords in any form. There is also a concern about limiting which users can access this website. This can be handled by restricting logins to specific email domains. This is achieved by creating a whitelist containing domains from which users can log in and a separate whitelist for full email addresses. Fortunately, the email address is one piece of information that Microsoft SSO provides in the login process; therefore it can be used to implement the whitelist filtering.

The management of uploaded files, request links, and slots is handled by a separate page containing two separate tables for upload links and request links. Basic information like the title and the message sent to the email recipient is shown. The page also includes the time created, the last time uploaded and information about file contents split into size and a list of extensions. Also, functionality for managing links and slots is provided via buttons for deletion, download, and displaying a detailed view.

The last and very important part of this project's design is an interchangeable storage layer. It is achieved by abstracting all file operations using an interface of common methods, which is the only way for the website to interact with underlying implementations. The interface consists of a small number of methods for inserting a file, reading its contents, listing directory contents, etc. Its full structure can be seen in Fig. 2.

TABLE I
COMPARISON OF EXISTING SOFTWARE

Software	Upload	Request	Maximum file size	Time limit	Self-hosted	Open-source
Úschovna.cz	YES	NO	30GB or 50GB (paid)	14 or 90 days (paid)	NO	NO
Posílej.cz	YES	BETA	40GB or 100GB (paid)	21 days or ∞ (paid)	NO	NO
Liquidfiles	YES	YES	∞	∞	YES	NO
WeTransfer	YES	YES	2GB or ∞ (paid)	7 days or ∞ (paid)	NO	NO
This project	YES	YES	∞	∞	YES	**YES**

There is currently an implementation using the FTP protocol, and one leveraging existing file APIs of .NET. It is an important part of this interface that it is asynchronous, which is in anticipation of many implementations that require the network for their function.
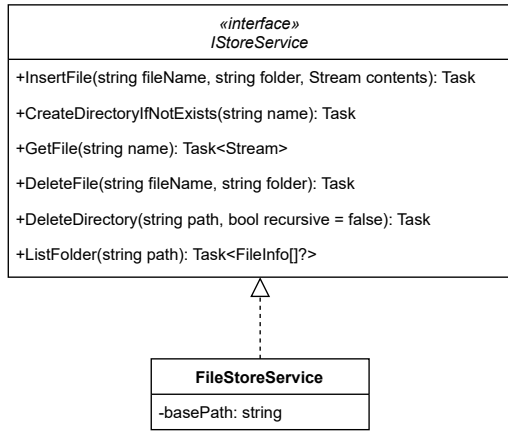
Fig. 2. Storage interface with methods and class implementing it

A. Implementation

The website was implemented using .NET Blazor, which is an extensive framework for developing interactive websites using only C# and Razor components [5]. The framework works in two modes; one is fully client-side in the browser running in WebAssembly. This mode requires sending a large binary blob to the browser before the website becomes interactive; it also requires maintaining an API (Application Programming Interface) on the server side for communication. The second mode, called Interactive Server, was selected because it removes the need to download the large WebAssembly binary, which reduces load times, and makes running server-side code as simple as calling a function, simplifying development. This mode works by Blazor automatically sending messages by WebSocket on interactions and the server responding by rendered HTML (Hypertext Markup Language) which is inserted into the DOM (Document Object Model).

To make the user interface consistent, a front-end library was used, Blazorise, which supplies many common components that are already styled. For this, it in turn uses the Bootstrap library.

SQLite was chosen as the database for data persistence. It stores information about users, request links, upload links, and request link upload slots in similarly named tables. The entity relationships can be seen in Fig. 3
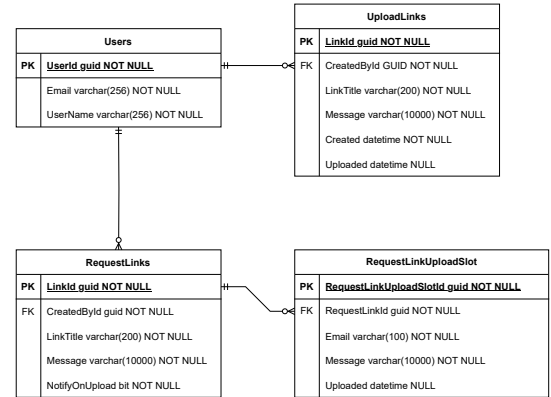

Fig. 3. Entity relationship diagram of database

B. Email

The ability to send email messages is one of the more critical features of this web application. It also has some security implications, because of the existence of email injections, which allow attackers to inject links, scripts, or other content into an email from a trusted domain. These types of attacks can happen to any web application that takes input and creates an email message from it. The mitigation for this type of attack is proper validation and sanitization of user inputs.

The body of the email messages is rendered using Razor; this simplifies the implementation of email templates and automatically encodes all rendered strings, which improves resilience against injection attacks. The contents of an email are the sender's name if logged in, or the sender's email address, if not. Also, when sending someone files or uploading files as a response to a request, a list of them is provided, containing their names, sizes, and a button redirecting to a place to download them.

C. Configuration

As already discussed, the website allows for configuration on deployment. The settings are stored in a JSON (JavaScript

Object Notation) file, which is accessed by the program. An example of a configuration can be seen in Listing 1

```
{
    "ConnectionStrings": {
    "Db": "Datasource=main.sqlite3"
    },
    "EmailSenderSettings": {
    "SenderEmail": "notify@example.com"
    },
    "FileStoreConfiguration": {
    "FileStoreService": {
      "BasePath": "folder/"
    }
    },
    "SmtpSettings": {
    "Host": "email_server.example.com",
    "Port": 1025
    },
    "ClosedLinkCanView": true,
    "ClosedLinkCanReopen": true,
    "AllowedDomains": ["vut.cz"],
    "AllowedEmails": ["user@example.com"]
}
```

Listing 1. Example configuration

IV. Usage

This section demonstrates the application's usage and shows the user interface for sending files. Fig. 4 shows an example of an upload submission ready to be sent. There were 3 files uploaded with total size of 133.2 KB, but there is no limit on the number of files or their size, except for the size of the storage the web application has access to. The configuration is the same as in Listing 1, so the user can view and edit already created links.

Fig. 4. Finalized form for file upload ready to be submitted

The email sent to recipients listed in a previous form, containing the name of the sender, title, message, and list of files with their sizes and names, can be seen in Fig. 5
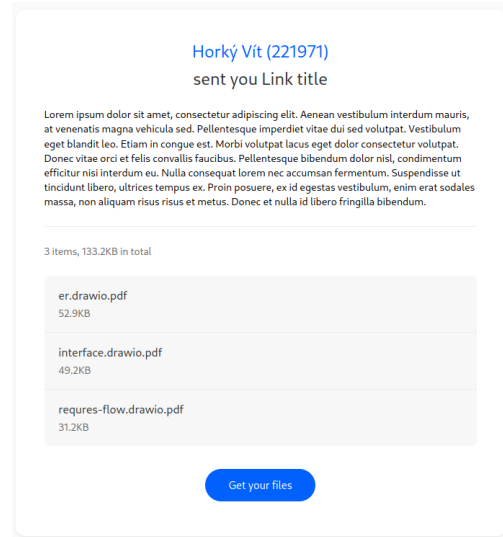
Fig. 5. Email message notifying a person of someone sending them files

V. Conclusion

This paper briefly compared the existing solutions for large file transfer over the internet, focusing on comparison between web apps. The lack of an open-source solution was highlighted as the main problem.

A web application using .NET Blazor was designed and implemented supporting the transfer of files by uploading them to the server. Making requests for files to multiple individuals is also supported. This web application compares favorably to other solutions, which can be seen in Table I. Most importantly, it is the only open-source solution in the comparison. The web application supports FTP and local filesystem as storage providers and handles authentication using Microsoft SSO.

The code was published on GitHub under an MIT license, accessible from: https://github.com/Ederen1/Dipl

Future improvements on this project could focus on adding other implementations of the storage interface or adding multiple SSO providers, so users don't need a Microsoft account to log in.

References

[1] Nokia. (2023) Into the metaverse: How the evolution of vr and ar will impact the network. Online. [Online]. Available: https://www.nokia.com/metaverse/impact-of-metaverse-on-the-network/

[2] A. Zapisotskyi. (2019) Recommended maximum email size and proven ways to optimize it. Online. [Online]. Available: https://mailtrap.io/blog/email-size/

[3] D. Chen and H. Zhao, "Data security and privacy protection issues in cloud computing," in *2012 International Conference on Computer Science and Electronics Engineering*, vol. 1, 2012, pp. 647–651.

[4] A. Wittman. (2024) What is single sign-on (sso)? how does sso work? Online. [Online]. Available: https://www.oracle.com/cz/security/identity-management/single-sign-on-sso/

[5] L. L. et al. (2024) Asp.net core blazor. Online. [Online]. Available: https://learn.microsoft.com/en-us/aspnet/core/blazor/

Design of a secure data transmission system in NB-IoT environment

1st Daniel Kluka
Department of Telecommunications
Brno University of Technology
Brno, Czech Republic
xkluka00@vutbr.cz

2nd Petr Musil
Department of Telecommunications
Brno University of Technology
Brno, Czech Republic
xmusil56@vutbr.cz

Abstract—**This work presents the design and implementation of a secure data transmission system for an IoT-based weather station using NB-IoT (Narrowband Internet of Things). The system integrates multiple sensors to measure environmental parameters such as temperature, humidity, atmospheric pressure, light intensity, precipitation, and air quality. A key focus is on ensuring energy-efficient, long-term operation in remote environments while maintaining data security through encryption and secure protocols. The proposed solution utilizes MQTT over NB-IoT for reliable data transmission, with results demonstrating efficient power management and stable connectivity.**

Index Terms—**NB-IoT, IoT protocols, weather station, security, automation, sensors, electronic components**

I. Introduction

Accurate meteorological data are essential for environmental monitoring and weather forecasting. Traditional weather stations rely on wired communication or high-power wireless networks, which are not optimal for remote, battery-powered deployments. This work focuses on designing a secure, energy-efficient weather station using NB-IoT, a low-power wide-area network (LPWAN) technology, to enable long-range data transmission with minimal energy consumption. The system incorporates robust sensors and security mechanisms to ensure reliable data collection and transmission. The collected data are processed, analyzed, and visualized using suitable platforms to provide actionable insights and demonstrate the system's capabilities.

The primary objectives of this project are:

- Development of a low-power, autonomous weather station for remote deployment.
- Integration of multiple sensors for comprehensive environmental monitoring.
- Secure data transmission using MQTT and TLS encryption over NB-IoT.
- Optimization of energy consumption to extend battery life.

II. Modern weather stations

Mentioned environmental parameters represent basic data that mankind has been trying to measure for centuries. With the passage of time, a number of measuring instruments have been developed, and their measurement principles have been improved. However, in modern times, it is necessary to look at the measurement of meteorological quantities in a more comprehensive way. With rapidly changing and less predictable meteorological conditions, there are increasing demands for accurate and on-time measurements that can predict changes.

Professional weather stations are becoming more and more accessible to ordinary users, who receive early warnings of weather changes and, at the same time, care about the quality of the environment in which they live and thus protect their health. However, their prices can be high, which can be a deciding factor for ordinary users. One of the many aims of this project is therefore to create a weather station that meets the demands and requirements of a professional weather station at a fraction of its price.

III. Internet of Things

All physical addressable devices that are connected to a network and communicate with each other are part of a working concept called the Internet of Things. These are, for example, devices in the smart home, industry, medicine, or transport, and can be connected using central units and intelligent control systems. The Internet of Things connects physical devices called 'objects' with objects in the virtual world, which form a virtual code describing the state of the device and is based on communication technologies.[1]

A. NB-IoT

The technology is used for cellular network devices and services with indoor or outdoor coverage, long battery life, and high-density connectivity. It has a narrow bandwidth of 200 kHz with half-duplex transmission. Peak downlink and uplink speeds are 26 Kbps and 66 Kbps, respectively, with a latency range of 1600 ms to 10,000 ms. The UE bandwidth is 200 kHz with a maximum transmission power of 23 dBm to 33 dBm. Due to the high latency range, it may not be an ideal choice for applications where a high emphasis is placed on response, and it suits stationary applications with occasional data sending and low transmission speed. There is a high level of noise in the transmitted signal, and therefore it transmits small data and not large data streams.[2][3]

B. MQTT

The MQTT, also known as Message Queuing Telemetry Transport, is an IoT protocol. Communication with MQTT

is established between devices using TCP. The two main components of MQTT are the MQTT Broker (central server) and MQTT Client (publisher). The client is the one who sends (publishes) messages to the broker. The received data from the client to the broker is then sent to subscribed clients. Due to its reliability and ability to handle high latency, it is recommended for a large number of clients. MQTT is mainly used in automation, smart homes, the automotive industry, and in the health service.[4][5]

IV. System design and implementation

Many electronic components and sensors were tested during the development of the weather station prototype. Not all of them worked reliably, and therefore it was necessary to find replacements that would be reliable and meet the desired purpose and requirements. These include, for example, the TPS63020 3.3 V power supply with automatic buck-boost function, which supports input voltages from 1.8 V to 5.5 V. In the context of a weather station, this is the most reliable method of power transfer with fluctuating battery and solar panel input voltages.

A. Hardware Architecture

The weather station in fig. 1 consists of the following key components:

- **ESP32-S3 DevKitC-1**: Microcontroller responsible for sensor data acquisition and communication.
- **Quectel BC660K-GL**: NB-IoT module enabling long-range data transmission.
- **Sensors**: DS18B20 (temperature), VEML7700 (light intensity), SDS011 (air quality), Vaisala WXT536 (multi-parameter weather sensor).
- **Power Management**: Solar panel with a TP4056 battery management system and TPS63020 voltage regulator.

Fig. 1. Weatherstation created for this project.

B. Sensors

The DS18B20 digital temperature sensor from UMW Youtai Semiconductor in a waterproof design is a replica of the popular and accurate DS18B20 sensor from Maxim Integrated.

The DS18B20 measures temperature in degrees Celsius with a resolution of 9 to 12 bits. It is powered by a One Wire bus, which has the advantage of being powered by only one data wire. The operating temperature is from -55 °C to +125 °C with an accuracy of ±0.4 °C (range -10 °C to +70 °C). Due to its waterproof property, it can be used in environments with excessive humidity.[6]

The VEML7700 is a high precision digital light intensity sensor from Vishay. It is manufactured and sold in several versions, for example, in a small transparent housing or in a small transparent housing mounted directly on the circuit board. For this project, the latter version was chosen, which includes a high-sensitivity photodiode, a low-noise amplifier, and a 16-bit A/D converter. The VEML7700 provides a measurement range from 0 to 120,000 lux with a resolution of 0.0036 lux ([lx] - lumen per square meter [lm/m²]). The sensor is also suitable for operating temperatures from -25 °C to +85 °C.[7]

The SDS011 laser dust sensor is designed to monitor dust particles in the air with a diameter greater than 0.3 micrometers [μm]. The sensor measures particles PM2.5 and PM10, which are 2.5 μm and 10 μm in diameter. This value is given in micrograms per cubic metre [μg/m³]. The SDS011 has a low power consumption of less than 4 mA in sleep mode. It can measure dust particles with an accuracy of 0.3 μm and the measurement range is from 0 μg/m³ to 999.9 μg/m³. The operating temperature of the sensor is from -10 °C to +50 °C and the atmospheric pressure is from 86 kPa to 110 kPa. It uses a UART bus or PWM for its communication.[8]

The WXT536 is one of the professional and high-end multi-parameter sensors that can simultaneously measure air temperature, humidity, pressure, precipitation, and wind. The low current consumption makes the sensor suitable for projects using solar panels. Vaisala's sensor series exceeds the IEC60945 marine standard and is a versatile device suitable for monitoring multiple environmental variables with high accuracy. Its rugged design and wide compatibility allow it to be used in a variety of applications including meteorology, industry, and research.[9]
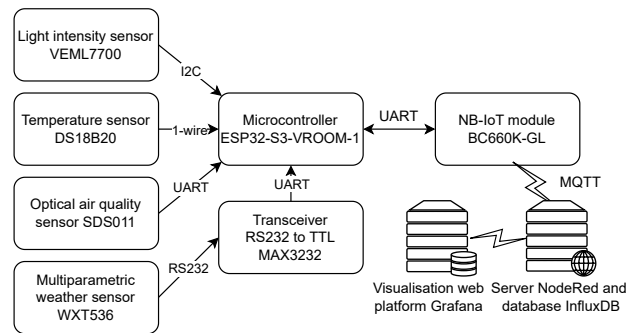

Fig. 2. Weatherstation software block scheme.

C. Software and Communication

The system is programmed using Arduino IDE, with sensor data processed locally before being transmitted via MQTT over NB-IoT. Data integrity and confidentiality are ensured using TLS encryption. The data is sent to a remote server for storage and visualization using Node-RED, InfluxDB, and Grafana.

The main measurement algorithm is able to initialize all sensors and continuously measure the actual values from the sensors. A function is also available to measure the average values of the four measurements, which are later sent via the NB-IoT module Quectel BC660K-GL to the Node-Red server via the MQTT broker Mosquitto. The project also tested the implementation of the MQTT broker HiveMQ.

Within the source code, several functions have been created that work with the batteries and optimize the operation of the weather station so that it does not consume too much power. The algorithm checks several parameters at runtime and adjusts the measurement frequency accordingly, which is advantageous when saving batteries on cloudy days or when using the batteries fully on sunny days.

The algorithm is also capable of estimating the actual charging current based on the solar panel parameters and light intensity. At the beginning of the source code, several macros are created, and they can be set at will by the user, to start individual modes of operation or to virtually disconnect the HW modules used by the weather station. If a sensor fails to initialize, the algorithm automatically continues without the particular sensor. This principle accounts for the possibility that a sensor has been disconnected or damaged.

Measurements can be taken every minute, and between measurements, the sensors and BC660K-GL are completely disconnected from the power supply, and the ESP32S3 microcontroller is in deep sleep mode. When the measurement is switched on, the microcontroller is first initialized, and it is checked that the battery is charged to at least 3.3 V. If the battery is charged, the measurement is performed, and the data are sent. If not, the microcontroller is put into sleep mode again. Data are sent every 6 minutes and are stored in a buffer in the RTC memory of ESP32-S3.

D. Node-RED, InfluxDB, and Grafana

The Quectel BC660K-GL is used to send data through the MQTT Mosquitto server to Node-RED in fig. 3.
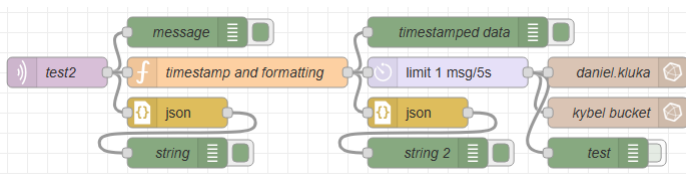

Fig. 3. Created flow on the NodeRED server, which processes the data and stores them in the InfluxDB database.

An MQTT message containing 6 measurements is sent to the server. The server processes these measurements into the form in which they will be entered into the InfluxDB time series database. Since all operating time data is measured in the weather station, it is possible to calculate the exact time in milliseconds when each measurement was taken.
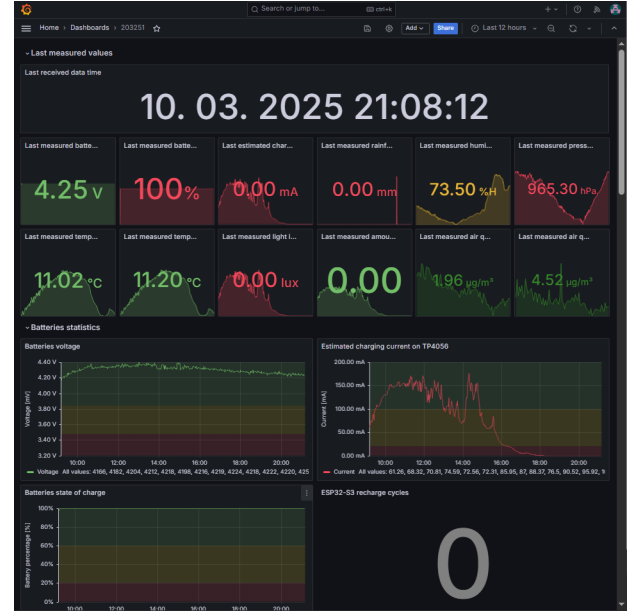

Fig. 4. Grafana dashboard created to visualise measured data.

The data entered into the database are further visualised via the Grafana platform in fig. 4, where all the necessary graphs of meteorological variables as well as diagnostic operational data are created. Grafana highlights the last measured (current) values, but also graphs in which data in any time interval are visualised with color thresholds.

V. NETWORK CONSUMPTION EVALUATION

TABLE I
PHASES OF MQTT MESSAGE TRANSMISSION IN AN NB-IoT NETWORK

Phase	Size	Source
Random Access + RRC Setup	200–300 B	3GPP TS 36.331, TS 36.321
NAS Attach (Request/Accept)	300–400 B	3GPP TS 24.301, TS 23.401
PDCP + RLC + MAC headers	50–150 B	3GPP TS 36.323, TS 36.322, TS 36.321
IP + TCP headers	40–60 B	RFC 791, RFC 793
TCP handshake + teardown	200–300 B	GSM IoT Guide
MQTT CONNECT + CONNACK	30–100 B	MQTT 3.1.1 (OASIS)
MQTT PUBLISH + PUBACK	202–232 B	MQTT 3.1.1, RFC 793
MQTT DISCONNECT (vol.)	10–20 B	MQTT 3.1.1
RRC Release (vol.)	∼500 B	3GPP TS 36.331
MQTT message (payload)	182 B	–
Total (typical)	**1000–1500 B**	–

The Quectel BC660K-GL module is fully powered off and restarted in each measurement cycle, which requires a complete signaling procedure for registration in the NB-IoT network. It then establishes a TCP connection and sends an **MQTT message of size 182 B** using the User Plane (not the Control Plane CIoT), meaning that the IP and TCP layers are included. For example, with a sending frequency of 24

messages per day, a total of 720 transmissions are performed per month.

As a result, the monthly data consumption ranges from **0,47 MB** (under optimal conditions), through **0,81 MB** in a typical scenario, up to **1,15 MB** when retransmissions or higher protocol overhead are present. According to Table I, a key factor is the signaling and protocol overhead, which often significantly exceeds the payload size, and when messages are sent every 6 minutes, the monthly usage can increase to **8,12 MB** (or **3,31 MB** if the module remains registered in the network).

VI. POWER OPTIMIZATION

To extend battery life, the following strategies were implemented:

- Duty cycling to put the ESP32-S3 into deep sleep between measurements.
- Selective power control of sensors using transistor.
- Adaptive transmission frequency based on environmental conditions.

Logic has been implemented that measures how much in percentage the batteries are charged, and if the battery value is higher than 80%, the weather station measures normal meteorological data (temperature, humidity, pressure, light values) and diagnostic data (battery charge level in mV and in %, length of initialization, length of measurement, total ESP cycle length, length of registration to the network, estimated recharge current of the weather station, recharge cycle counter) every minute and air quality every 6 minutes. However, if the battery charge drops below 80%, measurement and data sending frequency will be 10 times greater.

This weather station control implements a lightweight battery saving mode. The strong save mode has also been implemented, but it is clear from the measured diagnostic data that it has not been triggered even once. The weather station has been on the roof since mid-January, and due to the gentle battery management, it has not been fully discharged once. The TP4056 charging module works exceedingly well, but lacks the MPPT function that would take full advantage of the solar panel. In poor lighting conditions in January, the battery dropped to 3.72 V in fig. 5, but it took the weather station up to 9 days to discharge to that level. As can be seen from the graphs, there has been nice, bright weather since January 29, which has recharged the weather station and kept the batteries at a good level of charge.

VII. CONCLUSION

The project proposed a weather station (fig. 1) solution that provides the user with the necessary meteorological data using NB-IoT technology and a battery-friendly design. The developed algorithm interacts with the developed sensor library and implements the measurement methods. The ESP32-S3 collects data from the sensors, stores them in memory, and then sends them to the Node-RED server through the BC660K-GL and the MQTT broker. The data are then written to the InfluxDB database and clearly visualized on the Grafana platform.
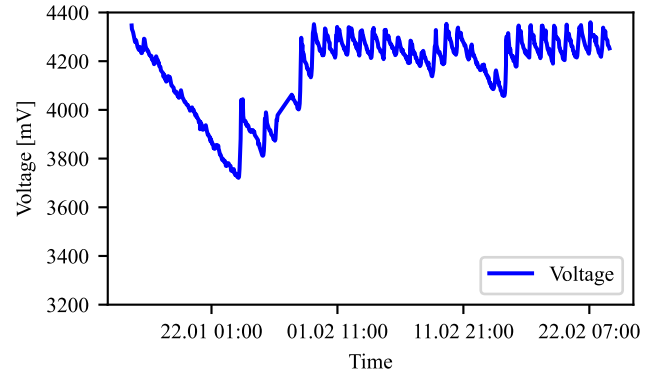

Fig. 5. Battery charging efficiency during cloudy days (2025-01-15 to 2025-01-23) and sunny days (2025-01-23 to 2025-02-23) with a sending frequency of 24 messages per day.

From the measured data in fig. 6, it is clear that the weather station meets the demands and requirements placed on professional weather stations and thus achieves high accuracy and robustness.
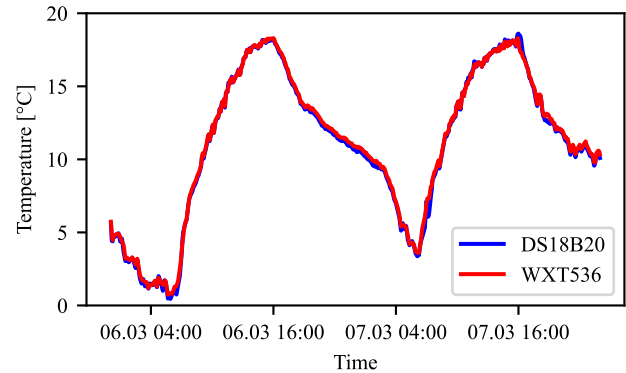

Fig. 6. Differences in measurement between DS18B20 and WXT536.

REFERENCES

[1] D. Kluka, 'Modular Streaming System with a Cloud Storage," Bachelor's thesis, (supervisor: L. Kratochvíla), Faculty of Electrical Engineering and Communication, Department of Automation and Measurement Technology, Brno University of Technology, Brno, Czech Republic, 2023, 87 pages. [Online].

[2] Portal PROMWAD, 'Low Power Wireless Technologies for Your Future Device: Selection Guide," 2024-04-15. [Online].

[3] Portal VelosIOT, 'Different LPWAN Technologies Explained," 2023-06-12. [Online].

[4] Portal A1 Digital, 'IoT Protocols: A Comprehensive Guide for Enterprises," 2024. [Online].

[5] Portal Geeks for Geeks, 'Introduction of Message Queue Telemetry Transport Protocol (MQTT)," 2024-02-26. [Online].

[6] Distributor láskakit, 'DS18B20 Digital waterproof temperature sensor 1m," 2024. [Online].

[7] Distributor láskakit, 'Light Intensity Sensor VEML7700, I2C," 2024. [Online].

[8] Distributor láskakit, 'Nova PM SDS011 Optical Air Quality Sensor PM2.5 PM10," 2024. [Online].

[9] Vaisala, 'WXT530 Series User Guide," 2024. [Online].

Privacy-Preserving Face Recognition Using Noised Eigenvectors

1st Bruce L'Horset
Software Engineering
Paris Institute of Digital Technology
Paris, France
bruce.lhorset@eleve.isep.fr

2nd Charles Mailley
Software Engineering
Paris Institute of Digital Technology
Paris, France
charles.mailley@eleve.isep.fr

3rd Elodie Chen
Software Engineering
Paris Institute of Digital Technology
Paris, France
elodie.chen@eleve.isep.fr

4th Sara Ricci
Department of Telecommunication
Brno University of Technology
Brno, Czech Republic
0000-0003-0842-4951

Abstract—**Widespread face recognition systems raise significant privacy concerns due to potential data exposure, especially with centralized data storage.**

We propose a privacy-preserving framework integrating k-same pixelation, Principal Component Analysis (PCA), and Differential Privacy (DP).

Our pipeline applies k-same smoothing for initial feature averaging, uses PCA for dimensionality reduction while preserving essential facial features, and adds Laplace noise to the resulting projection vectors to achieve DP. This method masks biometric information, operating efficiently in the lower-dimensional PCA space, aiming to balance privacy protection with the utility needed for identity verification.

Evaluations on the LFW dataset quantitatively analyze this trade-off using MSE and SSIM metrics. Results confirm integrating DP enhances privacy. Crucially, experiments show adding noise to lower-dimensional projection vectors preserves utility better than noising higher-dimensional eigenfaces.

We identified parameters (k=10, PCA ratio=0.19, ϵn=0.24) yielding a practical balance (Avg. MSE 1499, Avg. SSIM 0.38), enabling effective machine recognition on the anonymized data and demonstrating the framework's viability.

Index Terms—**K-Same Pixel, Eigenface, Laplace Noise Addition, Differential Privacy, Facial Recognition, Biometric Authentication.**

I. INTRODUCTION

Face recognition (FR) [5] is ubiquitous in modern security, authentication, and surveillance systems. However, this reliance raises significant privacy concerns due to potential misuse or exposure of sensitive biometric data, leading to risks like identity theft, especially when centralized. Addressing these risks requires robust privacy-preserving techniques to effectively balance security and system utility. While traditional encryption protects stored data, it is often too computationally intensive for demanding real-time FR applications.

Alternatives like Differential Privacy (DP) [1] and k-anonymity [4] offer promising directions. These methods introduce controlled noise or anonymization, aiming to protect individual identities while still permitting necessary aggregate analysis or verification tasks. This paper develops and evaluates a specific framework integrating such techniques for practical, privacy-enhanced face recognition deployment.

A. Contribution

In this work, we propose a privacy-preserving framework applying: (1) K-Same pixelation for smoothing facial characteristics, (2) Principal Component Analysis (PCA) [3] for dimensionality reduction and feature extraction, and (3) controlled Laplacian noise for anonymization, aiming to balance privacy and recognition utility. Our scheme enhances [1] by incorporating K-Same pixelation and experimental results favouring eigenvectors over eigenfaces.

We developed a user-friendly Graphical User Interface (GUI) to apply different anonymization levels and visualize the privacy-utility trade-off. Evaluation using Mean Squared Error (MSE) and Structural Similarity Index Measure (SSIM) metrics helps identify optimal approaches for secure face recognition.

II. ARCHITECTURE AND ANALYSIS METHOD

The system has been built using the Flask package in Python, enabling deployment as either a website server or a desktop application. Flask provides a straightforward and standardized way to create websites in Python, clearly separating the front-end components from the back-end logic.

The primary goal of this application is to serve as an experimental tool, allowing users to adjust various parameters to generate noised images, attempt to reconstruct the resulting images and verify the existence of a user in the database. The secondary goal is to provide users with optimal parameters for each step of the noised image generation process. To accomplish this, the application includes analyses and graphs that justify the choice of specific parameter values.
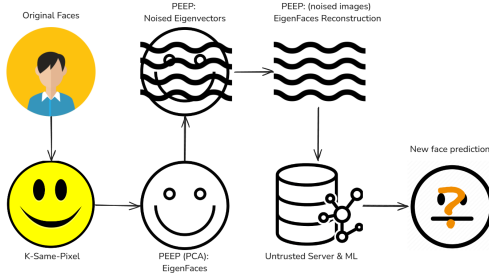
Fig. 1. Anonymization Process Schematic

The image anonymization process follows the steps illustrated in Fig. 1. Starting with a list of front-facing photos, the anonymization mechanism applies 1) K-same pixel method, 2) PCA and, finally 3) differential privacy and, finally 4) create noised images. This produces a list of anonymized images that can be stored in an untrusted database. On the other hand, to evaluate the privacy-utility trade-off, the final step involves reconstructing the user's face and comparing the reconstructed image with the original photo provided.

The PCA algorithm generate both eigenfaces and eigenvectors. Noised images are reconstructed from noised eigenvectors using the existing PCA model, while eigenfaces are used solely for visual verification purposes.

III. BACK-END AND FRONT-END ARCHITECTURE

The Controller object orchestrates the various steps of image processing. This approach enables an autonomous workflow for the GUI application while also allowing the creation of multiple analysis objects. These objects can be used to develop and test functions independently.

The back-end application starts by taking a data set as input. PCA is used to extract eigenfaces and eigenvectors from the input images. DP mechanism is then applied on eigenvectors. Using the precomputed PCA model and the noised eigenvectors, noised images are then reconstructed, enhancing security and privacy.
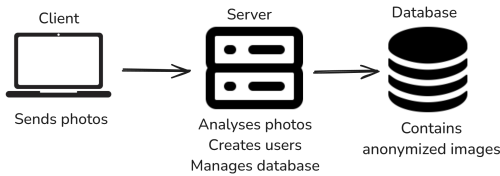
Fig. 2. Front-End Architecture

For the front-end, the application runs locally, meaning the client, server, and database are all managed on the user's laptop. However, in a web-based implementation, the database would reside on untrusted third-party servers, as illustrated in Fig. 2. The database used is a simple SQLite file containing a single table with two columns: the user ID and the anonymized images.
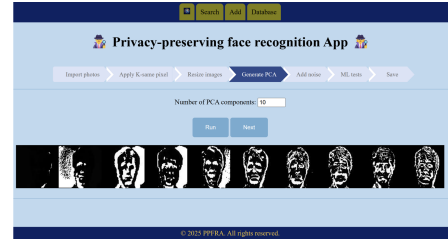
Fig. 3. Screenshot of the application

Fig. 3 shows the front-end application layout. The application comprises three main functional components: adding new users to the database, verifying if a user exists within the database, and managing the database's contents. The new user page enables the creation of new users using the PEEP method, requiring a set of front-facing photos of the same individual. The database management page allows users to display, remove, or attempt reconstruction of stored images.

IV. EXPERIMENTAL RESULTS

This section details the experimental setup, parameter selection, and analysis of the trade-off between privacy and utility conducted on the Labeled Faces in the Wild (LFW) dataset. LFW was chosen for its representation of faces in less constrained, real-world conditions, providing a robust testbed for our privacy preserving pipeline.

A. Metrics Definition

To evaluate the quality of image reconstruction and the impact of anonymization, we use two primary metrics: Mean Squared Error (MSE) and Structural Similarity Index Measure (SSIM).

Mean Squared Error (MSE): The MSE quantifies the pixel-wise difference between the original and reconstructed images. It is calculated as the average of the squared intensity differences for all pixels. A lower MSE value indicates a higher fidelity reconstruction, meaning the reconstructed image is closer to the original. High MSE values suggest significant distortion.

Structural Similarity Index Measure (SSIM): The SSIM assesses the perceived similarity between two images by considering luminance, contrast, and structure. SSIM values range from -1 to 1, where 1 signifies perfect similarity. Values closer to 1 indicate that the structural information, crucial for visual perception and potentially recognition, is well preserved.

In our privacy-preserving context, these metrics serve a dual purpose. Before noise addition, low MSE and high SSIM validate the PCA reconstruction quality. After noise addition for differential privacy, we aim for a controlled increase in MSE and decrease in SSIM. The goal is to find a balance where MSE is high enough to hinder human visual recognition, while SSIM remains sufficient for machine-based recognition systems. This balance is explored through parameter tuning.

B. Experimental Setup Overview

Our pipeline applied to the LFW dataset involved several steps. We used a subset of LFW containing individuals with at least 20 images each, ensuring sufficient data per subject for subsequent analysis. The core steps included K-Same pixelation, PCA dimensionality reduction, and Differential Privacy noise addition. The selection of parameters for each step was guided by analyzing their impact both quantitatively (metrics trends) and qualitatively (visual results), as detailed in the following subsections.

C. K-Same Pixelation Analysis

The K-Same pixel technique averages pixel values across 'k' images of the same subject, providing initial smoothing and anonymization. We analyzed the effect of varying 'k' on reconstruction metrics (MSE/SSIM after this step, before PCA/noise). The trend graph 4 shows how distortion (MSE) increases and similarity (SSIM) decreases as 'k' increases. Based purely on finding an intersection point between hypothetical MSE/SSIM thresholds on this trend graph, a value like k=9 might appear optimal. Visual inspection of the resulting images for different 'k' values on Fig. 5 further illustrates the trade-off between the smoothing effect and the preservation of distinct facial features.
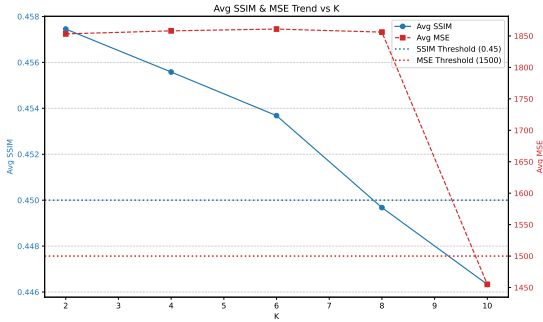
Fig. 4. MSE/SSIM of k-value trend graph

Fig. 5. K-Same Visual Impact

D. PCA Dimensionality Reduction Analysis

Principal Component Analysis (PCA) reduces data dimensionality. We evaluated the reconstruction quality (MSE/SSIM, measured *before* noise addition) versus the number of principal components retained (expressed as a ratio of available components). The trend graph 6 shows reconstruction fidelity improving with higher ratios. Visual analysis of the graph suggests that an approximate optimal ratio could be around 0.55. However, visual examples on Fig. 6 demonstrate that

perceptual gains can become marginal beyond a certain point, while computational load increases. This analysis helps identify ratios that capture essential features without unnecessary overhead.
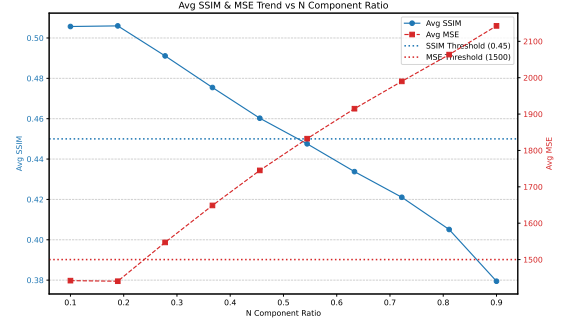

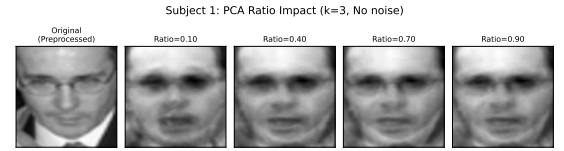Fig. 6. MSE/SSIM of PCA Component ratio trend graph

Fig. 7. PCA Component ratio Visual Impact

E. Differential Privacy Noise Analysis

Laplace noise was added to the projection vectors (coefficients obtained from PCA) to ensure ϵ-differential privacy. Adding noise to these lower-dimensional vectors is preferred over adding noise directly to eigenfaces for better utility preservation. The privacy parameter epsilon (ϵ) controls the noise level: lower ϵ means more noise and stronger privacy guarantees. Trend graph 8 shows MSE increasing and SSIM decreasing as ϵ gets smaller (more noise). Observation of the graph indicates that a value of approximately 0.2 for ϵ appears relevant, as the MSE and SSIM curves intersect while remaining within their respective acceptable thresholds. Visual examples on Fig. 9 illustrate the increasing image distortion with lower ϵ values.
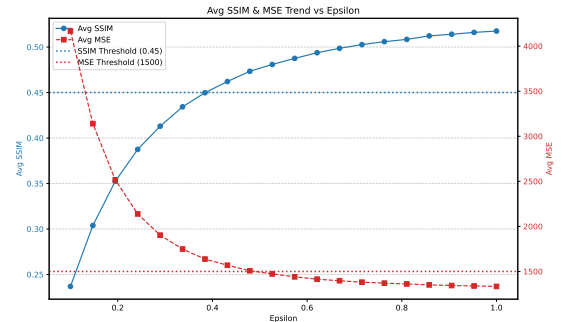

Fig. 8. MSE/SSIM of k-value trend graph

Fig. 9. K-Same Visual Impact

F. Selected Parameter Combination

While individual analyses (Sections IV.C, IV.D, IV.E) might suggest specific optimal points for each parameter (like k=9 from Fig. 4), the final parameter selection must consider their combined effects on both privacy and utility. A multi-objective perspective, potentially visualized through a density and scatter plot showing performance across combinations on Fig. 10, is necessary. This visualization helps identify Pareto optimal points or regions that satisfy specific constraints (e.g., minimum acceptable utility, maximum tolerable distortion).
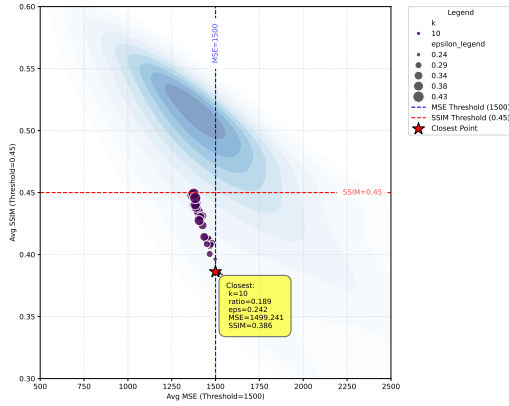
Fig. 10. Privacy-utility performance density graph for various (k, ratio, ϵ)

Based on such an analysis, aiming for robust machine recognition while ensuring significant visual distortion, the combination k=10, PCA ratio=0.19, and ϵ=0.24 (marked with a star in Fig. 10) was selected for the main experiments reported in this paper. This specific parameter set resulted in an average MSE of 1499 and an average SSIM of 0.38 across the processed LFW subset.

G. Machine Recognition Utility

A crucial aspect is evaluating whether the anonymized images, despite the introduced distortions resulting from the chosen parameters (k=10, ratio=0.19, ϵ=0.24), remain useful for automated tasks like face recognition. We trained a simple Convolutional Neural Network (CNN) model exclusively on the anonymized LFW images produced by our pipeline. The training process of the CNN model is illustrated in Fig. 11, showing the convergence of accuracy and loss over epochs, indicating successful learning on the anonymized data.
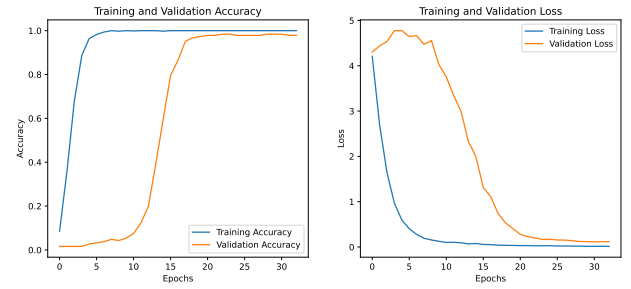

Fig. 11. Accuracy and Loss on anonymized LFW ML training

The model's performance was assessed on a held-out test set of similarly anonymized LFW images. It achieved a classification accuracy of 98%.

H. Privacy-Utility Discussion

The results using k=10, PCA ratio=0.19, and ϵ=0.24 on LFW represent an operating point selected via multi-parameter analysis (Fig. 10). Measured MSE (1499) and SSIM (0.38) quantify privacy (distortion), while ML accuracy (98%) quantifies utility. This demonstrates feasibility on datasets like LFW, retaining utility for automated systems. Achieving a different balance (e.g., stronger privacy or maximum utility) necessitates further exploration guided by trade-off visualizations (Fig. 8, Fig. 10), as the optimal choice depends on application needs.

V. CONCLUSION

Our framework, using K-Same pixelation, PCA, and Differential Privacy on projection vectors, anonymizes LFW dataset faces while maintaining ML recognition utility. Achieving a suitable balance required careful parameter selection (k=10, ratio=0.19, ϵ=0.24), guided by multi-objective analysis of the privacy-utility trade-off. Applying noise to vectors proved advantageous, and results underscore the need for dataset-specific tuning.

Future Work: Further research could investigate alternative anonymization methods (pixelation, transforms, noise types, adaptive approaches) to explore different privacy-utility profiles. Optimizing ML models using robust architectures for enhanced recognition on anonymized data is another direction. Finally, developing automated techniques for selecting optimal parameters based on specific requirements would improve practical application.

REFERENCES

[1] Chamikara MA, Bertok P, Khalil I, Liu D, Camtepe S. Privacy preserving face recognition utilizing differential privacy. Computers & Security. 2020 Oct 1;97:101951.

[2] Dosselmann R, Yang XD. A comprehensive assessment of the structural similarity index. Signal, Image and Video Processing. 2011 Mar;5:81-91.

[3] Kim KI, Jung K, Kim HJ. Face recognition using kernel principal component analysis. IEEE signal processing letters. 2002 Feb;9(2):40-2.

[4] Meden B, Emersic Z, Struc V, Peer P. k-Same-Net: k-Anonymity with generative deep neural networks for face deidentification. Entropy. 2018 Jan 13;20(1):60.

[5] Taskiran M, Kahraman N, Erdem CE. Face recognition: Past, present and future (a review). Digital Signal Processing. 2020 Nov 1;106:102809.

Post-Quantum Cryptography in V2X Communication

Filip Wagner

Department of Telecommunications
Faculty of Electrical Engineering and Communication
Brno University of Technology
Brno, Czech Republic
xwagne11@vutbr.cz

Abstract—This work describes the current trends, specifications, and adoption rate of Cooperative Intelligent Transportation Systems (C-ITS) and Post-Quantum Cryptography (PQC). It investigates the possibility of implementing PQC signatures in C-ITS to ensure safety in the Post-Quantum era. To reach this objective, the security architecture in C-ITS, along with all of its requirements, is presented. To ensure a high level of security, only the PQC algorithms selected by the National Institute of Standards and Technology (NIST) for further standardization are considered. Individual algorithms are compared with the currently used Elliptic Curve Digital Signature Algorithm (ECDSA) to evaluate the impact of changing the algorithms. A recommendation on the most suitable algorithms is provided.

Index Terms—— C-ITS, V2X, OBU, RSU, ECDSA, PQC, Dilithium, SPHINCS$^+$, Falcon

I. INTRODUCTION

Cooperative Intelligent Transportation Systems (C-ITS) have a leading role in modern data-driven infrastructure. The focus on their importance can be outlined by the EU Directive from 2010 [1]. In parallel, the European Telecommunications Standards Institute has released their Technical Specification (ETSI TS) [2] regarding the technology. Implementation of C-ITS is further supported by organizations i.e. CAR 2 CAR Communication Consortium (C2C-CC), that also take part in the standardization process [3].

In terms of security, C-ITS should be treated as a safety-critical system, since its faulty operation could lead to human harm. Another challenging specific of the automotive industry is the relatively long lifetime of vehicles. Cryptography implemented there should be safe, or able to adapt for the next up to 20 years since being introduced to the market [4].

Post-Quantum Cryptography (PQC) presents algorithms, that so far have proven to be resistant to attacks enabled by quantum computing. The threat involves the usage of Shor's algorithm to solve prime factorization and discrete logarithm problems in a polynomial time and Grover's algorithm to ease brute-force attacks [5]. In specific cases Grover's algorithm can be improved into a more efficient Brassard–Høyer–Tapp algorithm (BHT algorithm) [6]. Initially mentioned Shor's algorithm requires fundamental changes in asymmetric cryptography, while the others only seem to increase the required amount of bits of security for all cryptographic tools.

II. DEPLOYMENT OF C-ITS IN PRACTICE

Most common C-ITS transmissions happen between On-board units (OBU) present in the vehicles and stationary Roadside units (RSU) or other OBUs. This network offers two-way communication between the infrastructure and its users. Sharing information can lead to safer and more efficient traffic usage.

A. Security Architecture in C-ITS

As was described in the previous section, C-ITS carries signs of a safety-critical system. Not only that makes security a key aspect of C-ITS development. It also has a significant impact on the whole infrastructure, which makes it a valuable asset requesting protection. C-ITS further faces challenges of privacy protection, because the system operates with the location of its users.

To satisfy the security requirements, all messages are currently signed with the Elliptic Curve Digital Signature Algorithm using the curve P-256 (ECDSA-256). Legitimate users can be validated while having their privacy secured through the implementation of a specific public key infrastructure as shown in Fig. 1. In this system, each user is supplied with multiple pseudonymous authorization certificates, that can be
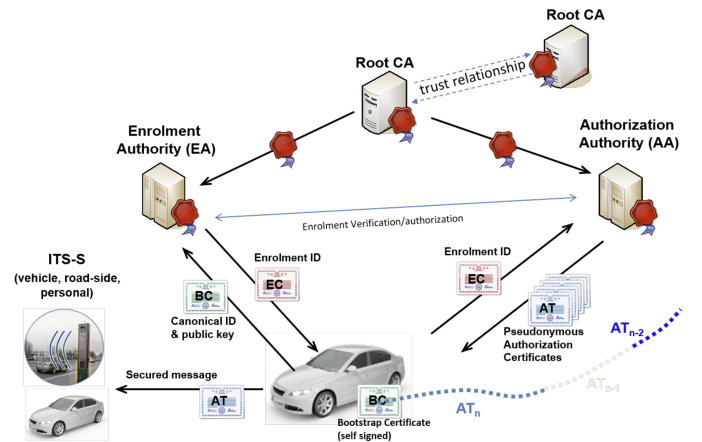

Fig. 1. Public key infrastructure of C-ITS [7]

used arbitrarily. This approach renders individuals' communication unlinkable to anyone but their authorization authority. Each certificate also specifies its usage, therefore unauthorized users, respectively unauthorized certificates cannot be used for signing restricted types of messages (requesting traffic light priority, etc.).

B. C-ITS Initiatives

The cooperative deployment of C-ITS technologies in Europe is coordinated by the C-Roads initiative [8]. The platform is co-funded by the EU, however non-EU countries participate too and are included in the 19 core members of the initiative. Based on their 2023 report, C-ITS deployment was taking place in 54 European cities and the EU contribution amounted to 400 million euros [9].

In the Czech Republic, one of the core members, there are in total 7 projects DT0 – DT6 deploying C-ITS technologies as part of C-Roads initiative [8]. The project DT2 is focused on covering the Brno city whose C-ITS coverage can be seen in Fig. 2. In 2023 the Czech Republic reported in total 379 RSUs and 1930 OBUs installed [9].

C. C-ITS Messages

Current standards define multiple messages in C-ITS. The most common ones are Cooperative Awareness Messages (CAM), which broadcast information about the position, velocity, steering, and other parameters of a vehicle. Other widely used messages offer information about the road, weather, local regulations, congestion, accidents, available lanes, and the traffic lights' status. More restricted types of messages are used by emergency services or public transport to request priority at traffic lights.

III. Adoption of Post-Quantum Cryptography

Since quantum computers capable of cracking currently used asymmetric cryptography do not seem to be available in

Fig. 2. C-ITS roadside stations in Brno

the foreseeable future, the popularity of PQC is limited by the further computational and memory constraints it introduces. Based on the screening of NCSA in Illinois in June 2023, only 0.029 % SSH connections used PQC [10]. Its usage is currently mostly limited only to research and testing purposes in order to set standards for future implementation.

However, this research is essential to ensure safety in the future. The National Institute of Standards and Technology (NIST) has declared a competition to pick the best PQC algorithms and provide their standardization [11]. The open call concluded with picking CRYSTALS-Kyber as the suitable key encapsulation mechanism and CRYSTALS-Dilithium, SPHINCS+, and FALCON for signatures [12].

IV. Available PQC Algorithms

Since signing is the most common cryptographic procedure executed in C-ITS, this paper will focus solely on finding and discussing the alternative for the currently used ECDSA-256.

A. CRYSTALS-Dilithium

Dilithium has been standardized by NIST in Federal Information Processing Standards Publication (FIPS) 204 under Module-Lattice-Based Digital Signature Algorithm (ML-DSA). The signature scheme is based on the module learning with errors problem. Dilithium resembles Schnorr-like signature by being derived from a proof of knowledge protocol. Through Fiat-Shamir heuristic, the random choice of the verifier is derived from the signed message making it an uninteractive signature scheme [13].

B. SPHINCS+

SPHINCS+ is a hash-based signature scheme standardized in FIPS 205 as Stateless Hash-Based Digital Signature Algorithm (SLH-DSA). The security of SPHINCS+ is derived from the hardness of finding preimages of hash functions. It utilizes Winternitz One-Time Signature Plus (WOTS$^+$) in the eXtended Merkle Signature Scheme (XMSS). Resulting XMSS trees form a hypertree, whose signature is used to authenticate the public key of the forest of random subsets (FORS) [14].

- WOTS$^+$ – The private key is a random value, that is hashed n times to produce the public key. To sign a message, a $x < n$ is derived from it and a value of the private key hashed $n - x$ times is revealed. This scheme is not reusable.
- XMSS – Connects WOTS$^+$ in a tree, where each node can be used for one signature, while they share the root as a common public key.
- Hypertree – To limit number of WOTS$^+$ pairs required, individual smaller XMSS trees are connected in a hypertree.
- FORS – Utilizes the whole structure, so that a message can be signed by hashing and splitting in multiple pieces first. Each piece is then signed with a different Merkles' tree.
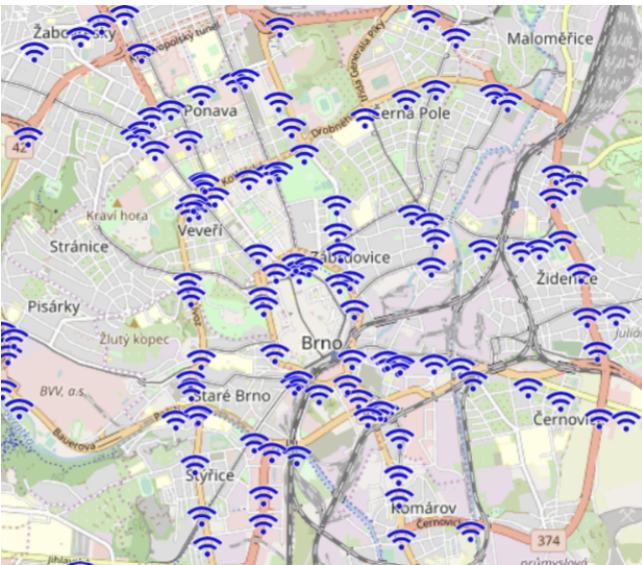
This signature scheme in its architecture focuses on re-usability of one-time signatures by making them individually insignificant.

C. Falcon

Unlike the previously mentioned schemes, Falcon did not receive NIST standardization yet. However, it has been chosen to receive one as FIPS 206 under FN-DSA, which stands for FFT (fast-Fourier transform) over NTRU-Lattice-Based Digital Signature Algorithm. Falcon utilizes Gentry-Peikert-Vaikuntanathan Framework (GPV framework), where public and private keys are matrixes generating orthogonal lattices modulo q. The signature is a small vector, that multiplied with the transposed public key gives the hash of the signed message. Without the knowledge of the private key, it is unfeasible to find a vector small enough to be accepted as a valid signature [15].

In Falcon, the GPV framework is executed on NTRU Lattices with Ducas-Prest fast Fourier nearest plane sampler as the trapdoor algorithm [15]. The chosen framework is an improvement from its predecessor, which was vulnerable to key-recovery attacks [16], while NTRU Lattices and preferred sampler allow for smaller signatures and public keys.

V. Comparison of the Algorithms

In order to choose the best PQC algorithm to replace the currently used ECDSA-256, the key parameters must be identified. From the space complexity point of view, the most sensitive value is the size of the signature, that is present in every message. As described in ETSI TS 103 097 [17] public key is present in the certificate, which in case of CAM is sent only once per second. However, the communication should withstand messages extended with the certificate. The last considered size is of the private key, that gets stored on the device, is distributed via the PKI and gets involved in the computations. Table I compares presented algorithms with currently used ECDSA-256 and its more secure versions [4]. With the exception of Dilithium-2, all presented PQC algorithms have their qubits of security equal to half of their classical bits of security. Dilithium-2 has presumed 85 qubits of security and would need to be attacked using BHT algorithm [18].

Another problem would be the time complexity of signing messages and verifying signatures. As seen from the Table I, Falcon is the most memory efficient with its signatures. However, it seems to have up to 30 times longer [18] signing time for short messages, than Dilithium on the same level of security. The difference in signature verifying times is negligible.

VI. Limits of C-ITS Technologies

Currently, the C-ITS uses *GeoNetworking Secured Packet* header to include signatures [19]. Within it, a *SignedData* section is present with *signature* component of type *Signature* as defined in IEEE Std 1609.2 [17]. This specification allows only the use of ECDSA and SM2 signature algorithms [20].

TABLE I
MEMORY CONSTRAINTS OF SIGNATURE ALGORITHMS

Algorithm	Private key size (bytes)	Public key size (bytes)	Signature size (bytes)	Bits of security
Classical Algorithms				
ECDSA-256	32	64	64	≈ 128
ECDSA-384	48	96	96	≈ 192
ECDSA-512	64	128	128	≈ 256
Post-Quantum Algorithms				
Dilithium-2	2528	1312	2420	≈ 128
Dilithium-3	4000	1952	3293	≈ 192
Dilithium-5	4864	2592	4295	≈ 256
SPHINCS$^+$-128	64	32	17088	≈ 128
SPHINCS$^+$-192	96	48	35664	≈ 192
SPHINCS$^+$-256	128	64	49856	≈ 256
Falcon-512	1281	897	666	≈ 128
Falcon-1024	2305	1793	1280	≈ 256

Therefore, to implement PQC signatures a new standard must be defined.

Another concern would be the size difference of signatures. Regular CAM messages, that can be simulated in the Vanetza testing environment are in size smaller than the signature of the most memory-efficient PQC algorithm described [21]. A helpful solution in the future could be message fragmentation, which is allowed in C-Roads specifications for MAPEM messages to inform about complex intersections [22].

VII. Conclusion

This paper has analyzed the current state-of-the-art in C-ITS and PQC with the vision of making C-ITS quantum-resistant by implementing PQC algorithms. NIST-recommended PQC algorithms were compared with the currently used ECDSA. In addition, the previous chapter reviewed signature standards in C-ITS, which would need to be reworked since they do not allow new signature methods.

The most memory efficient out of the presented ones is Falcon, which in the case of the signed message carrying a certificate still uses a little over 12 times more memory than the currently used ECDSA.

While Falcon may have been the most memory efficient, it is exceeded in signing time in the case of short messages by Dilithium, which seems to be thirty times faster. The importance of their benefits should be a subject of further research to establish, which parameter is more limiting for adapting the current infrastructure.

REFERENCES

[1] "Directive 2010/40/EU of the European Parliament and of the Council of 7 July 2010 on the framework for the deployment of Intelligent Transport Systems in the field of road transport and for interfaces with other modes of transport", 2010.

[2] European Telecommunications Standards Institute "Etsi ts 102 731 v1.1.1. Technical Specification", 2010.

[3] CAR 2 CAR Communication Consortium, "Basic system profile" 2020.

[4] N. Lohmiller, S. Kaniewski, M. Menth, T. Heer, "A Survey of Post-Quantum Cryptography Migration in Vehicles" in IEEE Access, vol. 13, pp. 10160-10176, 2025.

[5] L. Chen, S. Jordan, Y. Liu, D. Moody, R. Peralta, R. Perlner and D. Smith-Tone, "Report on Post-Quantum Cryptography", April 2016.

[6] G. Brassard, P. HØyer, A. Tapp, "Quantum cryptanalysis of hash and claw-free functions" 1998.

[7] B. Lonc and P. Cincilla "Cooperative its security framework: Standards and implementations progress in europe" in 2016 IEEE 17th International Symposium on A World of Wireless, Mobile and Multimedia Networks (WoWMoM), page 1–6, June 2016.

[8] Centrum dopravního výzkumu, v. v. i. "ITS knihovna", 2024.

[9] Alina Pinkelnig, Damaris Anna Gruber "Annual deployment overview report 2023", 2024.

[10] J. Sowa, B. Hoang, A. Yeluru, S. Qie, A. Nikolich, R. Iyer and P. Cao "Post-quantum cryptography (pqc) network instrument: Measuring pqc adoption rates and identifying migration pathways", 2024.

[11] National Institute of Standards and Technology "Submission requirements and evaluation criteria for the post-quantum cryptography standardization process", Post-Quantum Cryptography, 2016.

[12] National Institute of Standards and Technology "Pqc standardization process: Announcing four candidates to be standardized, plus fourth round candidates", Post-Quantum Cryptography, 2022.

[13] National Institute of Standards and Technology "Module-Lattice-Based Digital Signature Standard", August 2024.

[14] National Institute of Standards and Technology "Stateless Hash-Based Digital Signature Standard", August 2024.

[15] T. Prest, P. Fouque, J. Hoffstein, P. Kirchner, V. Lyubashevsky, T. Pornin, T. Ricosset, G. Seiler, W. Whyte and Z. Zhang "Falcon: Fast-Fourier Lattice-based Compact Signatures over NTRU", October 2020.

[16] P. Q. Nguyen and O. Regev "Learning a parallelepiped: Cryptanalysis of GGH and NTRU signatures", EUROCRYPT, 2006.

[17] European Telecommunications Standards Institute "ETSI TS 103 097 V2.1.1 Technical Specification", 2021.

[18] M. Raavi, S. Wuthier, P. Chandramouli, Y. Balytskyi, X. Zhou and S. Chang "Security Comparisons and Performance Analyses of Post-quantum Signature Algorithms", 2021.

[19] European Telecommunications Standards Institute "ETSI EN 302 636-4-1 V1.3.0 European Standard", 2017.

[20] Intelligent Transportation Systems Committee of the IEEE Vehicular Technology Society "IEEE Standard for Wireless Access in Vehicular Environments—Security Services for Application and Management Messages", 2022.

[21] Raphael Riebl "Vanetza project documentation" 2024.

[22] C-Roads Platform, Working Group 2 "Technical AspectsC-ITS European Handbook for MAPEM and SPATEM Creation Release 2.0.9", 2023.

Online recursive least square parameter estimation for PMS machine

Bc. Adam Kečkéš
dept. of Control and Instrumentation
Brno University of Technology
Brno, Czech Republic
xkecke01@vutbr.cz

Abstract—**This paper presents the simulation results of the Recursive Least Squares (RLS) algorithm for estimating key motor parameters, including stator resistance and inductances. The algorithm is implemented and tested in MATLAB Simulink to evaluate its accuracy and adaptability under varying operating conditions. The results demonstrate the effectiveness of RLS in real-time parameter estimation, highlighting its potential for improving motor control precision and system stability.**

Index Terms—**Motor control, parameter estimation, recursive least squares, stator resistance, inductance estimation, real-time estimation.**

I. Introduction

Motor control is a fundamental aspect of modern electrical engineering and automation, as electric motors are essential in both industrial and consumer applications. With increasing demands for precision, efficiency, and adaptability, the need for advanced control strategies has also grown. Modern control methods, supported by power electronics, enable the optimization of motor performance across a wide range of applications, from high-precision robotic actuators to large-scale industrial drives. [5] [3]

A key challenge in motor control system design is the variability of motor parameters. Factors such as stator resistance, winding inductance, and magnetic flux can change due to varying operating conditions, including temperature fluctuations, load variations, and component aging. These changes can significantly impact control accuracy, drive efficiency, and system stability. [5] [3]

The objective of modern motor control is not only to ensure reliable drive operation but also to enable real-time adaptation to parameter variations. The development of fast and accurate parameter estimation techniques plays a crucial role in optimizing motor performance under diverse operating conditions. [5] [3]

II. PMSM Modeling and control

A. PMSM model

PM machine control is usually achieved using Park's transformation. This method reduces the three-phase "abc" machine equations to a 2-D model as follows:

$$u_d = R_s i_d + L_d \dot{i_d} - N\omega_e i_q L_q$$
$$u_q = R_s i_q + L_q \dot{i_q} + N\omega_e(i_d L_d + \psi) \tag{1}$$

Equation 1 describes the electrical subsystem for a PMSM model. This equation can also be written in state space form:

$$\begin{bmatrix} \dot{i_d} \\ \dot{i_q} \end{bmatrix} = \begin{bmatrix} -\frac{R_s}{L_d} & \frac{\omega_e L_q}{L_d} \\ -\frac{\omega_e L_d}{L_q} & -\frac{R_s}{L_q} \end{bmatrix} \begin{bmatrix} i_d \\ i_q \end{bmatrix} + \begin{bmatrix} \frac{1}{L_d} & 0 \\ 0 & \frac{1}{L_q} \end{bmatrix} \begin{bmatrix} u_d \\ u_q - \omega_e \psi \end{bmatrix} \tag{2}$$

Here, R_s is the stator resistance, L_{dq} are the machine $q-$ and $d-$axis inductances, ω_e is the machine electrical speed, and i_{dq} and u_{dq} are the machine $q-$ and $d-$axis currents and voltages, respectively. Symbol $\dot{\ }$ represents Laplace differential operator. The electromagnetic torque is given by

$$T = \frac{3}{2}N(i_q(i_d L_d + \psi) - i_d i_q L_q) \tag{3}$$

where N is the number of machine poles and ψ is the rotor magnetic flux. For a motor modeled in this way, it is essential to know its nominal parameters, which will later be identified. These parameters are listed in the Table I.

Maximum permanent magnet flux linkage	0.035	Wb
Number of pole pairs	3	-
Stator d-axis inductance, L_d	0.6	mH
Stator q-axis inductance, L_q	0.65	mH
Stator resistance per phase, R_s	0.25	Ω
Rotor inertia	0.65	$kg \cdot cm^2$

TABLE I
TABLE OF PMSM PARAMETERS

B. Discretization of the PMSM Model

Since the system will be implemented on a development kit containing a microcontroller, discretization of the PMSM model is necessary. A general time-invariant system is given in state-space representation as:

$$\dot{x}(t) = Ax(t) + Bu(t),$$
$$y(t) = Cx(t) \tag{4}$$

Using a zero-order hold (ZOH) sampler with a sampling period T_s, the system equations can be transformed into the discrete domain as:

$$x(kT_s + T_s) = A_d(kT_s) + B_d u(kT_s),$$
$$y(kT_s) = C_d x(kT_s), \tag{5}$$

where the discrete-time matrices are defined as:

$$A_d = e^{AT_s},$$
$$B_d = \int_0^{T_s} e^{As} ds B, \qquad (6)$$
$$C_d = C$$

The matrices A_d and B_d can be discretized using the integral of the state transition matrix Ψ, defined as [2]:

$$\Psi = \int_0^s T_s^{A_s} ds \simeq \sum_{i=0}^{n} \frac{A^i T_s^{i+1}}{(i+1)!}, \qquad (7)$$

which leads to the following approximations:

$$A_d = I + A\Psi,$$
$$B_d = \Psi B. \qquad (8)$$

As n approaches infinity, the approximation error converges to zero. For $n = 0$, the approximation corresponds to the Euler forward method, which replaces the derivative with the finite difference approximation [2]:

$$\dot{x}(t) \approx \frac{x(t + T_s) - x(t)}{T_s}. \qquad (9)$$

Using the motor equations in the d-q coordinate system, the state-space representation of the system can be written as:

$$\frac{d}{dt}\begin{bmatrix} i_{sd} \\ i_{sq} \end{bmatrix} = \underbrace{\begin{bmatrix} a_{11} & a_{12} \\ a_{12} & a_{22} \end{bmatrix}}_{A}\begin{bmatrix} i_{sd} \\ i_{sq} \end{bmatrix} + \underbrace{\begin{bmatrix} b_{11} & b_{12} \\ b_{21} & b_{22} \end{bmatrix}}_{B}\begin{bmatrix} u_{sd} \\ u_{sq} \end{bmatrix}, \qquad (10)$$

where:

$$A = \begin{bmatrix} -\frac{R_s}{L_d} & \frac{\omega_e L_q}{L_d} \\ -\frac{\omega_e L_d}{L_q} & -\frac{R_s}{L_q} \end{bmatrix}, \quad B = \begin{bmatrix} \frac{1}{L_d} & 0 \\ 0 & \frac{1}{L_q} \end{bmatrix}, \qquad (11)$$

with:

$$\overline{u}_{sq} = u_{sq} - \omega_e \psi_m. \qquad (12)$$

The discretized model using the Euler forward method is then expressed as:

$$\begin{bmatrix} i_{sd}(k+1) \\ i_{sq}(k+1) \end{bmatrix} = A_d \begin{bmatrix} i_d(k) \\ i_q(k) \end{bmatrix} + B_d \begin{bmatrix} u_d(k) \\ \overline{u}_{sq}(k) \end{bmatrix}, \qquad (13)$$

where:

$$A_d = \begin{bmatrix} a_{11d} & a_{12d} \\ a_{12d} & a_{22d} \end{bmatrix} = \begin{bmatrix} -\frac{R_s T_s}{L_d} + 1 & \frac{\omega_e L_q T_s}{L_d} \\ -\frac{\omega_e L_d T_s}{L_q} & -\frac{R_s T_s}{L_q} + 1 \end{bmatrix},$$
$$B_d = \begin{bmatrix} b_{11d} & b_{12d} \\ b_{21d} & b_{22d} \end{bmatrix} = \begin{bmatrix} \frac{1}{L_d} T_s & 0 \\ 0 & \frac{1}{L_q} T_s \end{bmatrix}. \qquad (14)$$

C. PMSM control

For the control of PMS machine to reach desired speed setpoint, a cascaded control structure with PI controllers was designed according to [1]. The control structure consists of two current controllers for i_d and i_q, whose outputs are the voltage components V_d and V_q, and a speed controller regulating the rotor speed. This cascaded structure for a PMSM motor ensures fast current control in the inner loop, while the outer speed loop adjusts the torque reference. The PI controllers in the current loop regulate the stator currents in the rotating d-q reference frame, allowing for precise control of electromagnetic torque and minimizing steady-state error. The speed controller generates the required current references based on the speed error, ensuring smooth and efficient motor operation. These controllers are tuned to ensure phase margin safety within the range of $30 - 60°$. The controllers are discretized into their equivalent discrete models, using a sampling period of $T_s = 50$ μs and a transport delay of $\frac{3}{2}T_s = 75$ μs.

III. PMSM ELECTRICAL PARAMETERS

The main factor affecting stator winding resistance is temperature. Since most windings are made of copper, their resistance changes with temperature, described by:

$$R_{r\ at\ T_{act}} = R_{r\ 75°C} \left(\frac{235 + T_{act}}{310} \right) \qquad (15)$$

Resistance also depends on the current frequency due to the skin effect, which causes current to concentrate near the conductor's surface. This effect increases at higher frequencies but can be reduced by increasing the conductor's surface area. In AC motors, where the frequency is usually below a few hundred hertz, the stator windings are often made of stranded copper wire, minimizing the skin effect, which is usually negligible in synchronous motors. [4]

Another factor influencing machine parameters is magnetic saturation. When the stator and rotor cores experience strong magnetic fields, their inductance decreases due to a nonlinear current-to-flux characteristic. [5]

Saturation primarily affects the $q-$axis inductance, while the $d-$axis inductance is already somewhat reduced due to permanent magnet flux. However, with large negative $d-$axis currents (as in flux weakening), the $d-$axis inductance increases. Conversely, the q-axis inductance is higher at low $q-$axis currents but decreases as saturation occurs at higher currents. Additionally, cross-saturation occurs when the d-axis flux influences the q-axis flux and vice versa, making both inductances dependent on both currents. [5]

IV. PROPOSED ALGORITHM

A. Linear regression

The structure of the model is given by:

$$y(k) = \varphi(k)^T \theta \qquad (16)$$

In statistics, this is also known as linear regression, where we assume that the state-space representation in equations 14 is linear in θ. The vector $\varphi(k)$ is referred to as the regression vector. The vector θ represents unknown parameters and is primarily used for model parameterization. [2]

Since the currents i_{sd}, i_{sq} are measured almost instantaneously and their values are available in the next computational cycle, the model can utilize the currents from the previous step $k - 1$. A challenge arises with the applied voltages u_{sd}, u_{sq}. These voltages are processed by an inverter before reaching the motor, introducing a delay caused by the

computational time of the controller and the dynamics of power semiconductor devices. As a result, the actual applied voltage to the motor experiences a two-step delay, meaning that the voltages used at the current time step were computed in step $k - 2$.

$$\begin{bmatrix} i_{sd}(k) \\ i_{sq}(k) \end{bmatrix} = \underbrace{\begin{bmatrix} a_{11d} & a_{12d} \\ a_{21d} & a_{22d} \end{bmatrix}}_{A_d} \begin{bmatrix} i_{sd}(k-1) \\ i_{sq}(k-1) \end{bmatrix} + \underbrace{\begin{bmatrix} b_{11d} & b_{12d} \\ b_{21d} & b_{22d} \end{bmatrix}}_{B_d} \begin{bmatrix} u_{sd}(k-2) \\ \overline{u}_{sq}(k-2) \end{bmatrix}. \quad (17)$$

This model can be rewritten in the linear regression form:

$$y(k) = \begin{bmatrix} i_{sd}(k) & i_{sq}(k) \end{bmatrix}, \qquad \theta = \begin{bmatrix} a_{11d} & a_{12d} \\ a_{21d} & a_{22d} \\ b_{11d} & b_{12d} \\ b_{21d} & b_{22d} \end{bmatrix},$$

$$\varphi^T(k) = \begin{bmatrix} i_{sd}(k-1) & i_{sq}(k-1) & u_{sd}(k-2) & \overline{u}_{sq}(k-2) \end{bmatrix}$$

$$\omega_e(k) = \frac{\omega_e(k) + \omega_e(k-1)}{2}. \quad (18)$$

Using Euler's forward method the motor parameters can be extracted from the unknown parameter vector θ as follows:

$$R_s = \frac{2 - a_{11d} - a_{22d}}{b_{11d} + b_{22d}},$$
$$L_d = \frac{T_s}{b_{11d}}, \quad (19)$$
$$L_q = \frac{T_s}{b_{22d}}.$$

B. Recursive least square with forgetting factor

Since the matrix θ stores all values from the beginning of the measurement, new values are stored with decreasing weight, meaning that changes in the system may not be reflected in the identified parameters. To address this, a so-called Forgetting Factor is introduced, which prioritizes newer values while gradually discarding older data. However, the downside is that the system may no longer converge reliably.

Based on this approach, the loss function [2] can be modified as follows:

$$V(\theta, k) = \frac{1}{2} \sum_{i=1}^{k} \lambda^{k-i} [y(i) - \varphi^T(i)\theta(k)]^T [y(i) - \varphi^T(i)\theta(k)]. \quad (20)$$

The variable λ is called the Forgetting Factor and is within the range $(0, 1)$, with typical values between 0.95 and 0.99. The most recent data points are weighted by λ, whereas older data points, n steps behind, are weighted by λ^n.

An advantage of using a λ of 0.99 is that values in the matrix P do not grow indefinitely but instead stabilize at a high value. Using the same approach as in the constant-variable method without a Forgetting Factor, a recursive algorithm can be derived. This algorithm is presented below.

---

1) $\varepsilon(k) = y(k) - \varphi^T(k)\hat{\theta}(k - 1)$

2) $K(k) = \frac{P(k-1)\varphi(k)}{\lambda(k)+\varphi^T(k)P(k-1)\varphi(k)}$

3) $P(k) = \lambda^{-1}(k) \left(P(k-1) - K(k)\varphi^T(k)P(k-1) \right)$

4) $\hat{\theta}(k) = \hat{\theta}(k-1) + K(k)\varepsilon(k)$

5) $k = k + 1$

6) Repeat step 1

V. Simulation and Results

The three-phase PMSM model from equation 1 is reused in MATLAB/Simulink to analyze the performance of Recursive Least Squares (RLS) with a forgetting factor in parameter identification. This model allows simulation with different inductance values (L_d, L_q), providing a more precise evaluation.
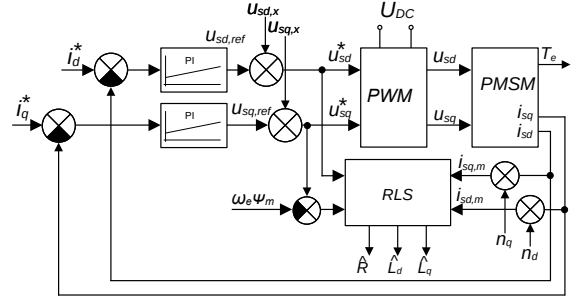

Fig. 1. Vector control structure with RLS parameter identification

Figure 1 shows the inner current loop of vector control with the parameter identification block. Identification signals $u_{sq,x}$ and $u_{sd,x}$ must vary to ensure persistent excitation [2]. These signals are generated as a Pseudo-Random Binary Sequence (PRBS), switching between $\pm 0.5V$ with approximately 50% probability per sample. The simulation includes a noise component (n_d, n_q) representing real current sensor noise. The motor's full current range is 6A, with noise at $\pm 0.17\%$ of the full range, modeled assuming a high-quality current sensor. The sampling period is $T_{vz} = 0.05$ ms.

The forgetting factor λ significantly influences identified parameters. A lower value increases noise and speeds up forgetting. The following values were used for RLS:

$$\lambda = 0.999 \qquad P = \begin{bmatrix} 0.1 & 0 & 0 & 0 \\ 0 & 0.1 & 0 & 0 \\ 0 & 0 & 0.1 & 0 \\ 0 & 0 & 0 & 0.1 \end{bmatrix}$$

$$\theta = \begin{bmatrix} 1 & 1 \\ -1 & 1 \\ \frac{1}{1.5 \cdot L_d} T_{vz} & 0 \\ 0 & \frac{1}{1.5 \cdot L_q} T_{vz} \end{bmatrix} \quad (21)$$

In the following figures, a simulation is conducted where the load torque (T_L) and motor parameters change in steps. At $t = 0.5s$, T_L increases from $0.2Nm$ to $0.3Nm$. At $t = 1s$, the inductances L_d and L_q increase by approximately 8%,
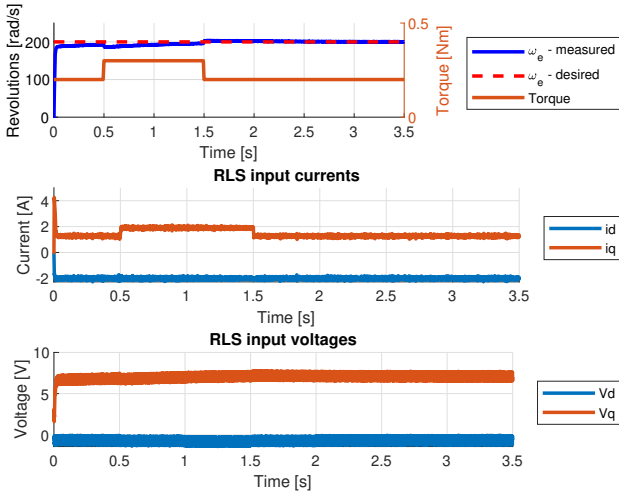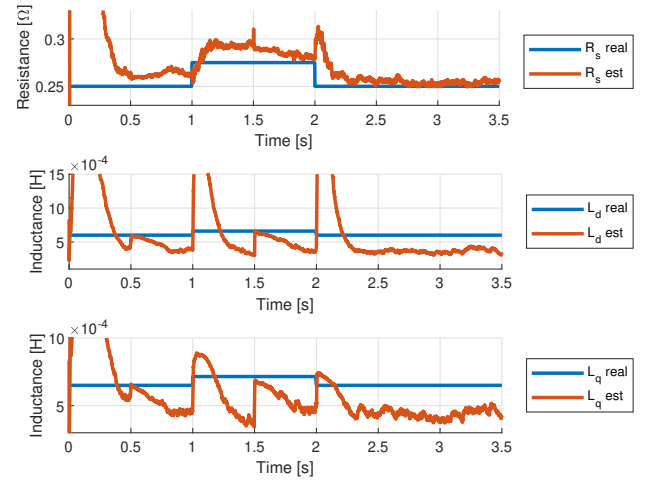
Fig. 2. Electrical motor speed and torque

Fig. 3. Change of estimated and real parameters

Fig. 4. Simulation results: (a) motor speed and torque, (b) estimated vs real parameters

followed by a 20% increase in the resistance R_s. At $t = 1.5s$, T_L returns to $0.2Nm$, and at $t = 2s$, all motor parameters revert to their initial values. This procedure validates the functionality of the RLS online parameter identification.

During transient states caused by changes in load torque, minor overshoots occur, demonstrating how the algorithm effectively adjusts and refines the estimation of motor parameters. As observed in the graphs, significant peaks primarily appear during abrupt changes in the electrical parameters of the motor. Since all three parameters are modified simultaneously, the resulting peaks are more pronounced. In real-world applications, such sudden parameter changes are unlikely; however, they are simulated in this study to rigorously test the robustness and adaptability of the algorithm.

In steady-state conditions, the identification error for each estimated parameter converges to $e_{R_s} = 1.64\%$, $e_{L_d} = 35.15\%$, and $e_{L_q} = 29.48\%$. Residual errors attribute highly to measurement noise, numerical approximation, and the adaptation speed of the recursive least squares (RLS) algorithm.

Furthermore, the longer the system remains in steady-state, the smaller the resulting error, as the estimation has more time to refine. Additionally, the final error is influenced by the choice of the forgetting factor λ, which affects the balance between adaptation speed and parameter stability.

VI. CONCLUSION

This study explored the implementation of an online parameter estimation approach for Permanent Magnet Synchronous Machines (PMSM) using the Recursive Least Squares (RLS) algorithm with a forgetting factor. The methodology was tested in MATLAB/Simulink under varying operating conditions, including step changes in load torque and motor parameters.

The results demonstrate the effectiveness of the RLS algorithm in adapting to parameter variations, particularly in estimating stator resistance and inductances in real-time. The identified parameters exhibited steady-state errors, with $e_{R_s} =$

1.64%, $e_{L_d} = 35.15\%$, and $e_{L_q} = 29.48\%$. These deviations are influenced by factors such as sensor noise, numerical approximation, and the tuning of the forgetting factor λ.

A key observation is that the duration of steady-state operation significantly impacts the accuracy of parameter estimation, as longer observation periods allow for improved convergence. Moreover, the choice of λ directly affects the trade-off between fast adaptation and estimation stability, highlighting the importance of proper tuning for optimal performance.

In future work, an adaptive forgetting factor approach could be explored to dynamically adjust λ based on real-time system conditions, further improving estimation accuracy. Additionally, experimental validation on actual PMSM hardware could provide deeper insights into the practical implementation and robustness of the proposed method.

REFERENCES

[1] KEČKÉŠ, Adam. *Modeling and Simulation of AC Electric Motor Control.* Brno: Brno University of Technology, Faculty of Electrical Engineering and Communication, Department of Automation and Measurement Technology, 2023, 72 pages. Bachelor's thesis. Supervisor: Ing. Ondřej Bartík.

[2] NEUGEBAUER, Henrik. *Parameter Identification of a Permanent Magnet Synchronous Motor.* Master´s Thesis. Gothenburg, Sweden: Chalmers University of Technology, 2012.

[3] Rafaq, M. S., & Jung, J.-W. (2020). *A Comprehensive Review of State-of-the-Art Parameter Estimation Techniques for Permanent Magnet Synchronous Motors in Wide Speed Range.* In IEEE Transactions on Industrial Informatics (Vol. 16, Issue 7, pp. 4747–4758).

[4] Sul, S. K. (2011). *Control of electric machine drive system.* Hoboken. N.J.: Wiley-IEEE Press. ISBN 978-0-470-59079-9.

[5] UNDERWOOD, Samuel J a HUSAIN, Iqbal. *Online Parameter Estimation and Adaptive Control of Permanent-Magnet Synchronous Machines.* Online. In: *IEEE Transactions on Industrial Electronics.* 2010, s. 2435-2443. ISSN 0278-0046. Available from: https://doi.org/10.1109/TIE.2009.2036029. [cit. 2025-03-06].

Simulation of Electrical Energy Demand Across Various Types of Users for Energy Communities

Tomáš Vaculík
Faculty of Electrical Engineering and Communication
Brno University of Technology
Brno, Czechia
xvacul39@vutbr.cz

Abstract—**Prediction of energy demand within energy communities is important for choosing optimal solutions and thus ensuring profitability. Such predictions may be obtained using simulations. The purpose of this paper is to explain key factors in the simulation of electrical energy demand data, with respect to the specific Czech conditions and to offer possible approaches as well as present its usage in simulations of energy communities.**

Keywords—*electrical energy demand, energy communities, simulation of energy flow, consumer profiles*

I. Introduction

Since second half of year 2024 the Czech legislation [1] has been through significant changes in regards to energy communities. Various types of subjects may become members of an energy community in Czechia. Among these members may arise various combinations of producers, consumers and prosumers, where prosumers stand for a subject both producing and consuming electricity. The fundamental idea of energy communities is to share abundances of produced energy among its members in mutually beneficial conditions. It is wise for the subjects interested in forming an energy community, to make a thorough analysis of energy balance, to ensure profitability. For production of electricity, photovoltaics are, due to subsidy programs, a favorable source of energy although different electrical energy sources are permissible. Whereas the data representing electricity production from photovoltaic sources are easily obtainable using various software. The data of energy consumption rely strongly on the characteristic of a specific subject.

II. Characteristics of Various Consumer Subjects

The consumer base within an energy community might be very diverse depending on various types of users. Each connection point has specific conditions related to grid parameters, used appliances and different user behavior. It is clear, that the electricity demand profiles will differ between households, municipal buildings, office buildings and small companies, while all of the enumerated might take part in community energetics in Czechia.

One of the parameters that is helpful for predicting electricity demand in given points of connection is its supply type diagram class and its tariff rate. These parameters reflect the probability profile of electricity demand in specific points of connection and might be obtained e.g. by electricity supplier. The Czech energy market operator provides the data representing proportional consumption for individual supply type diagram classes in one-hour intervals for individual past months possibly years [2]. These data are gathered by measurements on a representative group of electricity consumers. Two types of data are provided. First normalized, are used mostly for energy bills forecast. Second recalculated used for electricity demand predictions.

III. Possible Approaches of Energy Demand Simulation

A. Stochastical approach

Stochastical approach is based on creating a probability function, that generates outcome data based on set parameters such as annual consumption, number of phases connected to the grid and supply type diagram class. These parameters may be set depending on the type of consumer. For simulating households electricity demand, inverse proportion may be used. That means the peaks of relatively lower value (consumption) will appear for a longer period of time and on the contrary, the peaks of relatively greater value will appear for a shorter period of time. This might not be the case for all of the potential participants within given community and needs further optimization. The probability of a peaks being generated would be dependent on the supply diagram class. The computational time is quick as well as parametrization, on the other hand simulating more diverse consumption using this approach is a problem [3].

B. Simulation of individual appliances

This approach considers simulation of individual appliances, where individual models are created for each device based on its parameters such as operating diagrams, average consumption, average time of use of device and its usage throughout the day. Appling this approach to a large scale project may be unnecessarily complicated. To simplify this method, simulations may be done for individual groups, representing appliances of similar parameters. Combination of both is also possible. For example, simulation of individual electrical machine's demand within a company and the building's demand using representative groups.

Input data may be gained by expert estimation or measurement. An experiment had proven, that using simulation of groups representing specific appliances, may reach high correlation with data obtained by measuring, when measured data are used for parametrization of individual groups. Simulation time and time needed for creating models are short [3].

C. Simulation of electrical circuit units within an energy community

Up to this point the outputs of the simulations were merely data of active power P being supplied by the superior electrical system to load in time t. This approach allows us to describe the physical phenomena occurring in the system. Model in MATLAB Simulink was created for these reasons. Other than simulation of energy consumption, simulation of energy production from photovoltaics and simulation of different metrics is possible within this model, allowing for easy simulation of energy communities [4].

Energy communities in Czechia work on the energy sharing principle. That means, producers participating in energy sharing do not have to share their local distribution grid with consumers within their group of sharing. They can use distribution grid instead, although specific criteria needs to be met [1][5].

For purposes of this paper, functionalities of this model will be explained on an example. Simple scheme of an example of energy community is shown in Fig. 1. Scheme represents sharing electricity from photovoltaic to two consumers, with the usage of distribution grid.

To simulate the behavior of distribution grid within Simulink, 3-phase voltage source was used in combination with impedance. Value of impedance is chosen based on the voltage
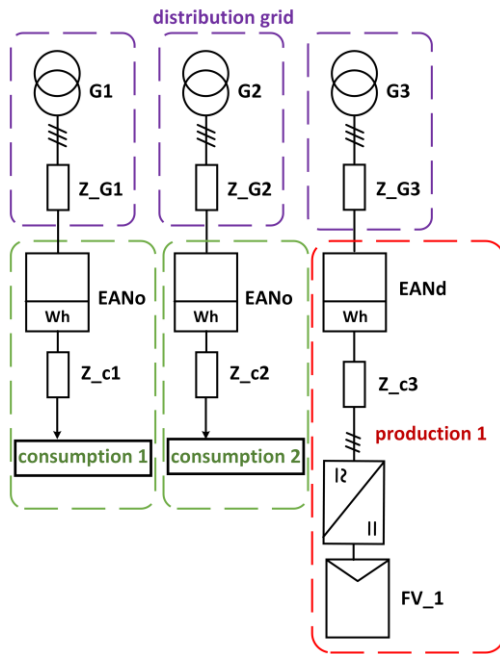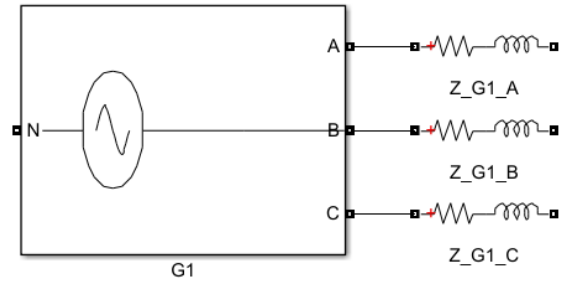
Fig. 2 Connection to distribution grid represented by voltage source and impedance

level of distribution grid following IEC TR 60725 [6]. Representation of connection to distribution grid in Simulink is shown in Fig. 2 with 3-phase transformer on the left and impedance on the right.

For measurements, block was created with the ability to measure instantaneous values of voltages and currents in 3-phase electrical system for individual phases. Multiplication of these provides instantaneous power flow in individual phases. Further algorithms are used for sorting to positive and negative registers respecting two different types of metric. Chosen sampling frequency of 1 second corresponds with the measuring window of electricity revenue meters. As an output, this block provides a matrix of instantaneous power in time in the place of measurement. Additional algorithm has to be applied on this matrix to get data of energy flow. Since energy is shared in 15-minutes intervals [5][7], it is appropriate for such algorithm to respect this fact. This block is in Fig. 1 represented by "EANo" for consumption metering and "EANd" for production metering. Representation of this block within Simulink model is in Fig. 3.

For production of electricity, block representing photovoltaic source was created. Algorithm simulates photovoltaics irradiance, based on which signal of power is generated based on specified parameters of the photovoltaics. Supporting block then converts this signal to electrical current based on current voltage in the point of connection of the photovoltaics. Phase shift of generated electrical current is adjusted to grid voltage to ensure maximum active power generation. Representation of this algorithm in Simulink is in Fig. 4.

For simulation of consumption within this model, block representing load profile was created. Signal of consumed active power in time is generated using approach mentioned in

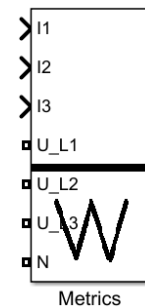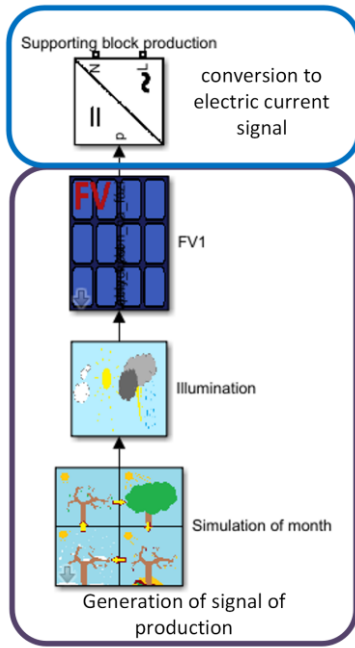Fig. 1 Schematics of an example of energy community

Fig. 3 Block representation of metrics in Simulink

Fig. 4 Representation of algorithm simulating electricity production from photovoltaic source in Simulink

Fig. 5 Representation of model of consumption in Simulink

III.B. Algorithm is divided into four parts, each simulating individual group representing appliances of similar parameters. In work describing this approach [4], only domestic consumption was taken into consideration, although model allows for changes and various types of consumptions may be simulated. This signal is again used as an input for a current source, which with the help of supporting block ensures maximum active power consumption in given point of connection. Different consumptions may be simulated separately in individual phases. Representation of consumption model in Simulink model is in Fig. 5.

Using these blocks, energy community from Fig. 1 was simulated. Full scale model of Simulink schematics is not shown for its size. Parameters for electricity production and consumption were set randomly since they are not important for showing functionality of this model.

Energy balance of the simulated community is in Fig. 6. Outputs provided by Simulink are shown in shades of gray. Algorithm was applied on them to obtain 15-minute average values, represented by red color for consumption 1, green color for consumption 2, blue color for production 1. These values could be then used for calculation of shared energy using allocation keys, described in [5]. No specific type of metric was applied in this case, as no prosumers are included in this example hence no distortion could be observed.
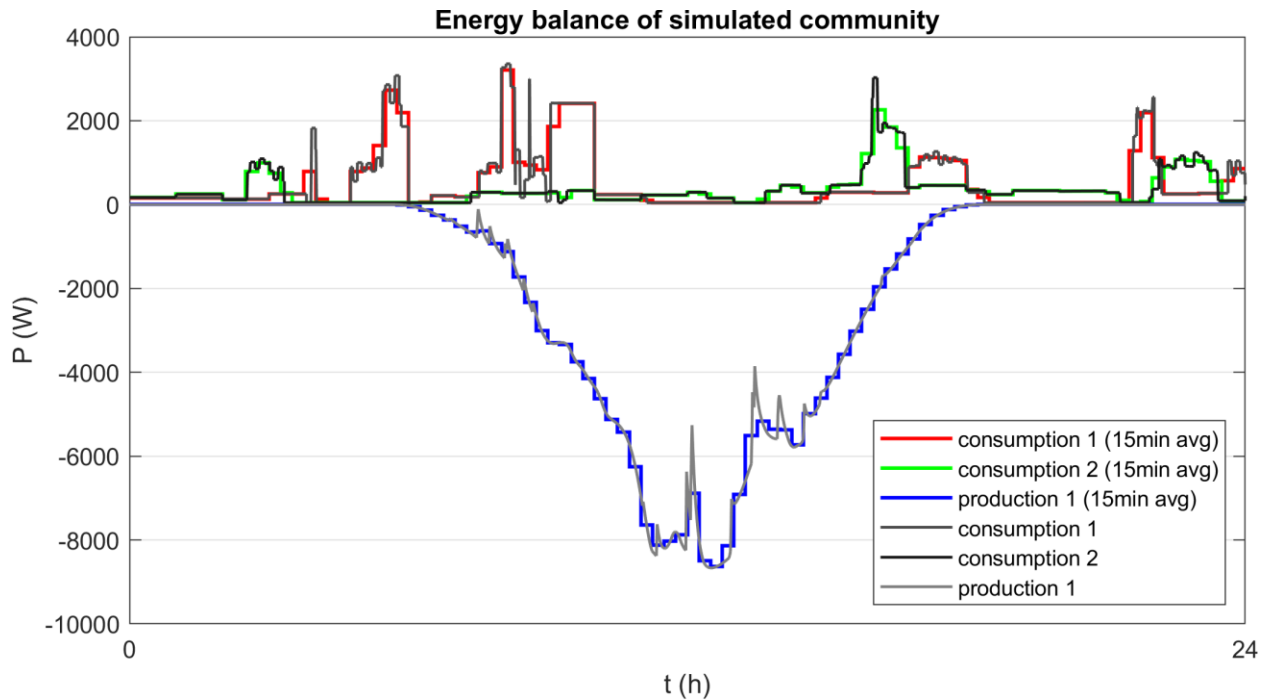
Fig. 6 Energy balance of simulated community

This balance is only one of many data outputs we may get from this model. Simulation of electrical circuit units using model in Simulink may provide much more data than previous methods. It might be used for e.g. individual metrics comparison [4], analysis of voltage changes within local distribution grid, etc. Supporting blocks of production and consumption may be also changed to simulate other than strictly active power consumption and production.

This approach on the other hand requires more time for creation of individual models, parametrization and post processing of obtained outputs. Requirements on computational power are also much higher, although some functionalities such as time of the year simulation may be inactivated to lower computation time. Model uses simulation time of one second, this is a positive in case we want to observe dynamics of the system. For practical application on energy balance prediction within energy communities, simulation time, this short is not needed. This approach also lacks the ability to predict consumption based on supply type diagram and expert estimate needs to be used.

IV. Conclusion

Advantages and disadvantages of each approach were described individually. When choosing which approach to choose, we should think about what kind of output data we need. Stochastical approach (section III.A) and Simulation of individual appliances (section III.B) are optimal for basic simulations of 15 minutes intervals of energy consumption. Simulation of electrical circuit units (section III.C) might be used for more complex analysis of physical processes.
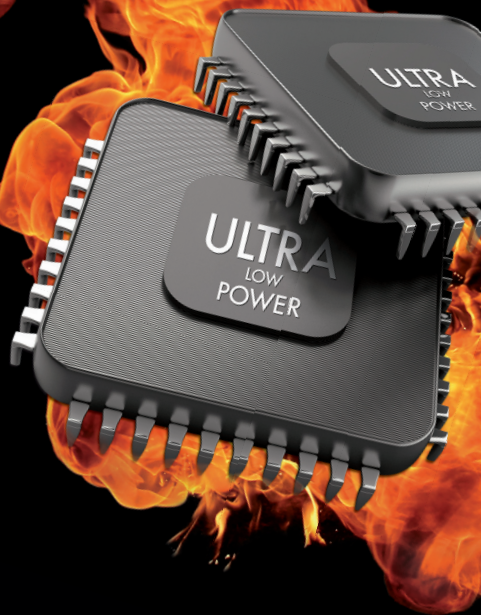
Acknowledgment

References

[1] ČESKÁ REPUBLIKA, Zákon č. 458/2000 Sb. o podmínkách podnikání a o výkonu státní správy v energetických odvětvích [Act No. 458/2000 Coll., on Business Conditions and Public Administration in the Energy Sectors], (in Czech), Zákony pro lidi.cz, 2000. [Online]. Available: https://www.zakonyprolidi.cz/cs/2000-458. [Accessed: Jul. 10, 2024].

[2] OTE, Statistika - typové diagramy dodávek elektřiny [Statistics – Standard Load Profiles of Electricity Supply], (in Czech), [Online]. Available: https://www.ote-cr.cz/cs/statistika/typove-diagramy-dodavek-elektriny/prepoctene-tdd?date=2024-12-31. [Accessed: Mar. 3, 2025].

[3] J. Kaňa, Bilance elektřiny v typologicky lokální soustavě energetického společenství s výrobnou elektřiny [Electricity Balance in a Typologically Local System of an Energy Community with Electricity Production], Bachelor's thesis, Faculty of Electrical Engineering and Communication, Brno Univ. of Technology, Brno, Czech Republic, 2022, pp. 21-38, [Online]. Available: https://www.vutbr.cz/studenti/zav-prace/detail/142388.

[4] T. Vaculík, Technicko-ekonomický rámec začleňování individuálních a komunitních výroben [Techno-Economic Framework for the Integration of Individual and Community Power Plants], Bachelor's thesis, Faculty of Electrical Engineering and Communication, Brno Univ. of Technology, Brno, Czech Republic, 2022, pp. 21-32, [Online]. Available: https://www.vut.cz/studenti/zav-prace/detail/159563.

[5] EDC, Elektroenergetické datové centrum [Electricity Data Centre], (in Czech), [Online]. Available: https://www.edc-cr.cz/pro-uzivatele-edc/#videonavody-dokumenty-ke-stazeni. [Accessed: Mar. 5, 2025].

[6] INTERNATIONAL ELECTROTECHNICAL COMMISSION, IEC TR 60725:2012 – Consideration of Reference Impedances and Public Supply Network Impedances for Use in Determining the Disturbance Characteristics of Electrical Equipment Having a Rated Current ≤75 A per Phase, 3rd ed., 2012.

[7] ČESKÁ REPUBLIKA, Vyhláška č. 359/2020 Sb. o měření elektřiny [Decree No. 359/2020 Coll. on Electricity Metering], (in Czech), Sbírka zákonů České republiky, Jan. 1, 2021. [Online]. Available: https://www.zakonyprolidi.cz/cs/2020-359. [Accessed: Mar. 5, 2025].

Extraction of RC parameters for the ECM model of the Li-Ion battery

Daniel Moravčík
Department of Electrical and Electronic Technology
Brno University of Technology
Brno, Czech Republic
xmorav46@vut.cz

Petr Vyroubal
Department of Electrical and Electronic Technology
Brno University of Technology
Brno, Czech Republic
vyroubal@vut.cz

Abstract— **This paper deals with the issue of extracting the parameters of a Li-ion battery's equivalent electrical circuit using Electrochemical Impedance Spectroscopy. It examines the principle of the EIS method and possible procedures for extracting the equivalent circuit. The study is complemented by the development of a free desktop application capable of extracting these parameters, with its output format directly aligning with the required inputs for the Ansys Fluent simulation software.**

Keywords— lithium-ion batteries, ECM model, EIS, Matlab, Ansys Fluent, Nelder-Mead, EC-Lab

I. INTRODUCTION

Batteries have become an everyday part of human life. However, gradual technological progress has required increasingly greater demands on their properties, safety and reliability, especially in special applications, in which case their inappropriate properties could pose a high risk of danger. For these, but also other financial reasons for testing, it is increasingly necessary to simulate their properties, which makes it possible to predict their behavior.

This is one of the reasons why this article deals with the extraction of RC parameters of a Li-ion battery, with which it is possible to simulate its properties and behavior before using the battery in various applications under various conditions.

Currently, there are several programs for extracting RC parameters of electrochemical systems independent of simulation programs, through which it is possible to simulate the behavior of Li-ion batteries. However, a major disadvantage is their incompatibility in terms of the required data with simulation software. Therefore, within the framework of this work, a program was designed and created that allows parameters to be extracted in a format required by the simulation software Ansys Fluent.

II. EQUIVALENT CIRCUIT MODEL

Modeling a Li-ion battery using an equivalent electrical circuit (ECM) is the most widely used method for simulating its behavior. This approach establishes an analogy between the chemical processes within the battery and the electrical components of the circuit [1]. Depending on the complexity of the modeling, the battery can be represented by various equivalent circuits. However, the Ansys software, for which the following program is designed, supports only two types of models: the Thévenin equivalent electrical circuit and its improved version. The latter is based on the first but includes an additional RC pair, allowing for a more accurate representation of the complex impedance and electrochemical behavior of the battery..
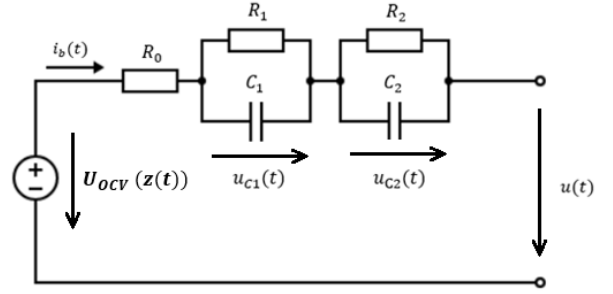

Fig. 1.   Improved Thévenin equivalent circuit [2]

The improved Thévenin model consists of a series connection of the open-circuit voltage source U_{ocv}, a series resistor R_0, and two RC pairs, which describe transient phenomena within the battery. Each component in the circuit depends on the state of charge (SoC), ambient temperature, and battery aging. The resistor R_0 represents the internal resistance of the battery, while the first parallel combination of R_1 and C_1 accounts for electrochemical polarization effects caused by the formation of the SEI layer. Meanwhile, a combination of elements R_2 and C_2 characterize concentration polarization effects at the interface between the electrolyte and electrodes [3].

III. ELECTROCHEMIC IMPEDANCE SPECTROSCOPY

This method of obtaining information about the parameters of a Li-ion battery's equivalent electrical circuit is based on the impedance response of the examined system. Unlike time-domain analysis, the response is observed as a function of the frequency of the system's electrical excitation. The principle of this method lies in exciting the electrochemical source using a harmonic electrical signal (voltage or current) while monitoring its response in the form of variations in the output signal at different excitation frequencies [4].

According to Ohm's law, impedance is defined as the ratio of electrical voltage to current. Since the excitation is a harmonic signal with time-varying values, impedance can be expressed as:

$$Z = \frac{\tilde{U}}{\tilde{I}} = \frac{U_0 e^{j0}}{I_0 e^{-j\phi}} = \frac{U_0}{I_0} e^{j\phi} = Z_0 e^{j\phi} , \qquad (1)$$

Where $\tilde{U}$ represents the test voltage (phasor), $\tilde{I}$ denotes the test current (phasor), and U_0, I_0 are their amplitude values. The value Z_0 expresses the absolute value (modulus) of the impedance and φ represents the phase shift between electric voltage and current.
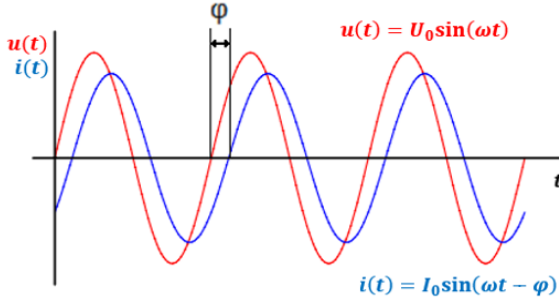

Fig. 2. Excitation and output signal in the EIS method [5]

If there were no phase shift, the impedance would consist solely of a real component. However, electrochemical systems, such as Li-ion batteries, also exhibit a capacitive nature, which results in a phase shift. As a consequence, impedance comprises both real and imaginary components, which vary with frequency.This variation is captured by the Nyquist diagram, which represents impedance in the complex plane.
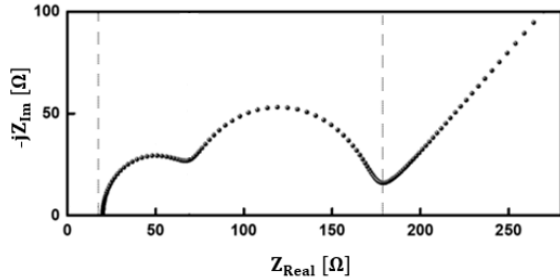

Fig. 3. Impedance response of an electrochemical system [6]

IV. EXTRACTION OF SUBSTITUTION ELEMENTS

The extraction of equivalent circuit parameters from the impedance characteristics can be performed using two approaches. The first is the numerical approach, which applies impedance curve fitting to numerically compute the parameters of the equivalent circuit.The second option is the analytical approach, where the parameters are determined directly by reading and calculating from the Nyquist diagram, based on the geometry of the impedance curve.

A. Numerical extraction approach

The numerical extraction of equivalent circuit parameters is performed using optimization methods, which operate by iteratively computing the parameters of a predefined equivalent circuit. The values of these parameters are continuously optimized through a numerical algorithm, which aims to minimize the error between the measured impedance and the calculated impedance of the model.This approach utilizes impedance equations corresponding to the chosen equivalent circuit model. The impedance value for the improved Thevenin equivalent circuit is given by:

$$Z = R_0 + \frac{R_1}{1+j\omega R_1 C_1} + \frac{R_2}{1+j\omega R_2 C_2} \; , \qquad (2)$$

where R_0 represents the value of the series resistor. The parameters R_1 and C_1 form the first parallel RC pair, while R_2 and C_2 denote the resistance and capacitance of the second parallel RC pair.

B. Analytical extraction approach

The values of R_0, R_1, and R_2 can be determined directly by identifying the point where the system begins to exhibit capacitive behavior and from the diameters of the semicircles in the impedance characteristic.
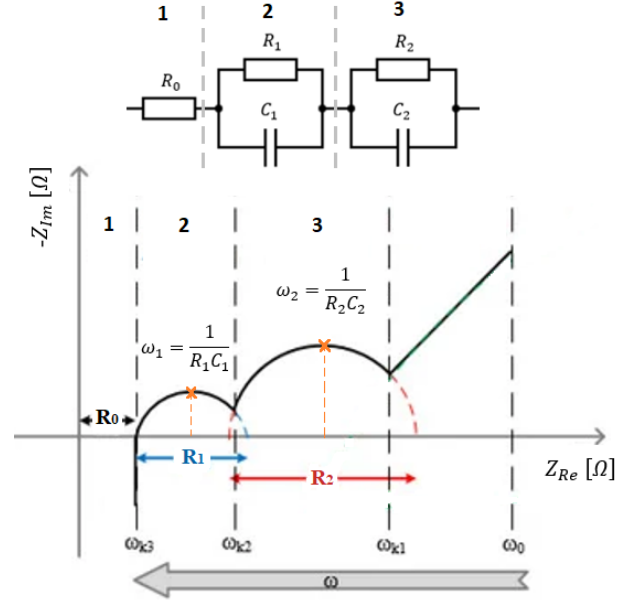

Fig. 4. Analytical parameter extraction [7]

Based on the known frequencies of the local maxima of the semicircles, the capacitance values for each pair can then be calculated using the following equation:

$$C = \frac{1}{R\omega} = \frac{1}{R 2\pi f_{max}} \; , \qquad (3)$$

where C represents the capacitance value of the capacitor, R represents the resistance value of the resistor, and f_{max} represents the frequency of the driving signal at which the imaginary component of the impedance reaches a local maximum.

V. SOFTWARE DESIGN

Building on the theoretical part of the work, the focus is on creating a desktop application for extracting parameters from measured impedance values using the EIS method. Since the developed program uses specific mathematical functions and a graphical user interface, the programming language Matlab was chosen for its creation. The program is exported as a desktop application, which does not require Matlab with a license for execution but can be run through the free Matlab Runtime application.

A. Basic description of the program

The program was designed to allow the import of data from electrochemical impedance spectroscopy, then fit and calculate the values of equivalent circuit parameters from the measured imported data for various charge levels of a Li-Ion battery. It created polynomial functions from these calculated values at different charge levels for each equivalent circuit element and exported the calculated polynomial coefficients into a format required by the Ansys Fluent simulation program.
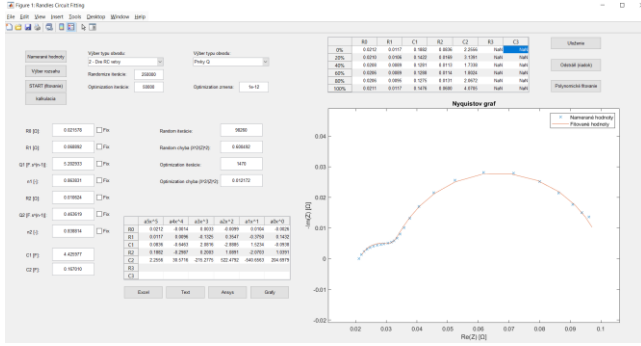

Fig. 5. Graphical interface of the created program

B. Data import and processing

To extract the RC parameters from the impedance characteristics of a Li-Ion battery, three basic quantities need to be known: the real component of the impedance, the imaginary component of the impedance, and the frequency of the driving signal at which the given impedance value was measured. Since the impedance characteristic is measured using a laboratory potentiostat (VMP3 Multichannel Potentiostat), the program is configured to import a text file containing three columns of values along with their names (frequency, real component, imaginary component).

```
freq/Hz           Re(Z)/Ohm        -Im(Z)/Ohm
1,0001000E+004    1,3715076E-002   -9,9485964E-003
6,8029990E+003    1,3442756E-002   -6,7705349E-003
4,6280000E+003    1,3626825E-002   -4,3528383E-003
3,1480005E+003    1,3773568E-002   -2,6797978E-003
2,1398601E+003    1,3930511E-002   -1,4909939E-003
1,4555454E+003    1,4124190E-002   -6,2459911E-004
```

Fig. 6. Input data format from EIS measurement

The program then generates a Nyquist plot and allows the user to select the desired range for fitting using the cursor in the graph. The option to select the range is also important due to the requirements of Ansys Fluent, which does not account for the induction of the supply wiring or the Warburg element, both of which appear in the graph at low and high frequencies, and need to be removed from the fitting range.

C. Setting up a equivalent circuit

The Ansys Fluent software requires parameters for an enhanced Thevenin model, which consists of a series resistor and two RC pairs. The program is therefore adapted to this requirement; however, for various purposes, it allows fitting of the Thevenin circuit with one to three RC pairs. The program

also allows the use of CPE (Constant Phase Element) elements instead of capacitors, which enables more accurate fitting of the impedance curve and better describes the imperfections in the capacitive behavior of the battery. However, this is an additional feature of the program, as Ansys requires capacitors, not CPE elements, which can be subsequently converted into pseudo-capacitors. These, however, do not have a clear physical interpretation corresponding to capacitors. This means that when converting CPE to pseudo-capacitance, the fitting error would be greater than when using standard capacitors.

D. Fitting process

The impedance characteristics of a Li-ion battery represent a nonlinear dependency, which is why a nonlinear regression algorithm was necessary. The program uses the Nelder-Mead optimization method, which does not rely on derivatives in its calculations and is fast enough for the given type of fitting. However, this method is sensitive to initialization parameters, and poor initial values can cause the algorithm to converge to an incorrect local minimum. For this reason, the optimization method is complemented by a randomization algorithm, which generates a large number of random combinations of input values, with the best combination subsequently used as the initial set of values for the nonlinear regression algorithm.
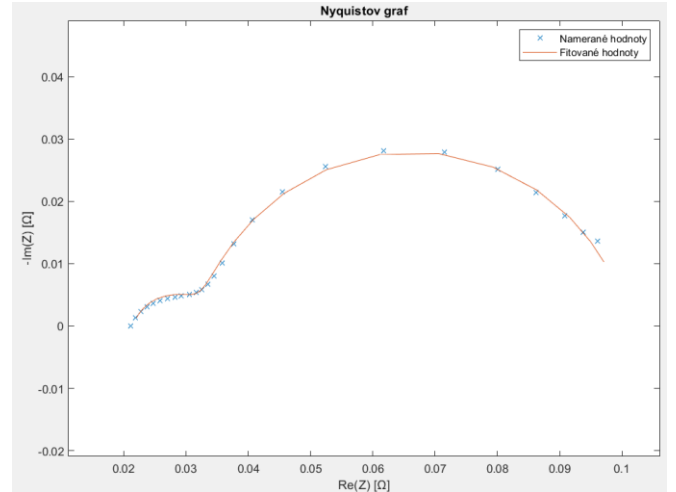

Fig. 7. Example od fitting measured data

The entire algorithm is based on evaluating the error between the measured impedance and the impedance of the currently optimized equivalent circuit. If a new combination of parameters with a smaller error than the current best error is found, the current most accurate values are replaced with these new values. The number of cycles required depends on the complexity of the nonlinear nature of the impedance characteristics and the desired fitting accuracy. To determine the error, the program uses the least squares method with a weighted sum of squares, which ensures more accurate results as it takes into account the greater uncertainty at higher impedance values [8]. This is achieved by dividing the square of the impedance difference by the square of the measured impedance value:

$$\chi^2 = \frac{\sum_{i=1}^{n} |Z_{mer}(f_i) - Z_{sim}(f_i)|^2}{|Z_{mer}(f_i)|^2}, \tag{4}$$

where Z_{mer} represents the value of the measured impedance and Z_{sim} represents the value of the simulated (fitted) impedance at a given frequency f.

E. Polynomial function creation and export

To ensure direct compatibility of the fitted parameters with the Ansys Fluent software, the program was designed to allow the continuous saving of fitted parameters for six different charge levels of the battery. For each charge state, the program then calculates a polynomial function for each circuit parameter.
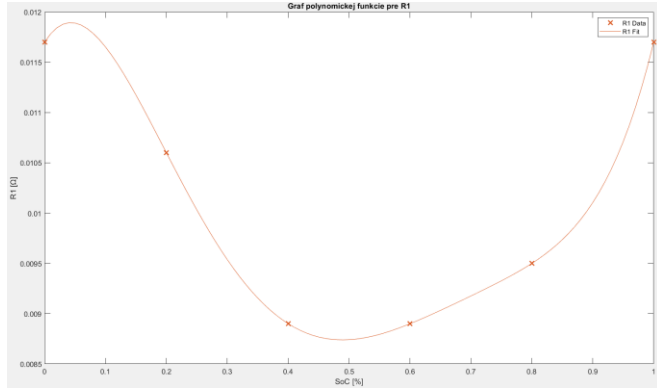

Fig. 8. Example of the resulting polynomial function

The result is five polynomial functions of the sixth degree, which the program allows to be displayed for visual inspection and exported in text, excel, or journal format.

	a5x^5	a4x^4	a3x^3	a2x^2	a1x^1	a0x^0
R0	-0.2081	0.4907	-0.3793	0.1053	-0.0078	0.0219
R1	-0.2213	0.5119	-0.3500	0.0373	0.0277	0.0053
C1	-527.8740	1370.8174	-1242.1407	449.6086	-50.4044	0.2043
R2	2.6690	-6.4482	5.7115	-2.1967	0.3207	0.0042
C2	681.4814	-1826.4135	1752.6258	-703.1707	99.0091	0.6824

Fig. 9. Sample of exported polynomial function data

Since there are thirty values that need to be entered independently into Ansys Fluent, the simplest way is to use the journal format, which Ansys can import, allowing the parameter values to be automatically overwritten in the required simulation software icons.

VI. PROGRAM VALIDATION

The accuracy of the fitting in the developed program was verified using the EC-Lab software, which is specifically designed for evaluating the impedance characteristics of chemical systems. The verification was carried out on the impedance characteristics of two Li-Ion batteries, specifically the Panasonic NCR18650 and LG 18650 MG1 types.

SoC [%]	100	80	60	40	20	0
ΔR_0 [Ω]	-0,000003	0,000001	-0,000004	0,000004	0,000002	-0,000003
ΔR_1 [Ω]	0,000004	-0,000001	0,000004	0,000005	0,000004	0,000000
ΔC_1 [F]	-0,000452	-0,000422	0,000025	-0,000303	0,000369	0,000077
ΔR_2 [Ω]	-0,000001	0,000000	0,000000	0,000000	0,000002	0,000000
ΔC_2 [F]	-0,000038	0,000029	-0,000005	-0,000040	0,000044	0,000036

Fig. 10. Absolute error values of the created program

All parameter results from the individual impedance curves were extracted under the same iterative conditions. To calculate the error in the results of the developed program, the absolute error between the EC-Lab results and the results from the developed program was computed. The absolute errors between the given results reached minimal values, which are caused by rounding, as EC-Lab rounds the results to one decimal place fewer.

VII. CONCLUSION

This paper describes the basic principle of the equivalent electrical circuit of a Li-ion battery and electrochemical impedance spectroscopy, which represent one of the methods for simulating battery behavior. It also explains the differences between the basic approaches to extracting the parameters of the equivalent circuit from the impedance characteristics.

In the practical part, a program was designed and developed for extracting these parameters, which uses the numerical Nelder-Mead optimization method and is specifically tailored to meet the input data requirements of Ansys Fluent software. Finally, the program was validated using EC-Lab software. The validation results showed that the developed program operates correctly and can be used to simulate the Li-ion battery in the Ansys Fluent environment.

REFERENCES

[1] MENG, J. et al. Overview of Lithium-Ion Battery Modeling Methods for State-of-Charge Estimation in Electrical Vehicles. *Applied Sciences* [online]. 2018, 8(5) ISSN 2076-3417. Available at: doi:10.3390/app8050659

[2] NIKOLIAN, A. et al. Classification of Electric modeling and Characterization methods of Lithium-ion Batteries for Vehicle Applications [online]. December 2014. Available at: https://www.researchgate.net/publication/266739163_Classification_of_Electric_modeling_and_Characterization_methods_of_Lithium-ion_Batteries_for_Vehicle_Applications

[3] HE, H., XIONG, R. and FAN, J., Evaluation of Lithium-Ion Battery Equivalent Circuit Models for State of Charge Estimation by an Experimental Approach. *Energies* [online]. 2011, 4(4), 582-598. ISSN 1996-1073. Available at: doi:10.3390/en4040582

[4] TATARKOVIČ, M., BRONCOVÁ, G., KRONĎÁK, M. *Identification of Li-ion Elektroimpedanční spektroskopie a její využití v chemické analýze* [online]. Ústav analytické chemie, Fakulta chemicko-inženýrská, VŠCHT Praha, Chemické listy 106, 1067-1074, 2012. Available at: http://www.chemicke-listy.cz/docs/full/2012_11_1067-1074.pdf

[5] Stanovení kinetických parametrů pomocí metody elektrochemické impedanční spektroskopie [online]. In: VYSOKÁ ŠKOLA CHEMICKO-TECHNOLOGICKÁ V PRAZE. 23 September 2009. Available at: https://old.vscht.cz/kat/download/lab_eis.pdf

[6] CHOI, Woosung, Heon-Cheol SHIN, Ji Man KIM, Jae-Young CHOI a Won-Sub YOON. Modeling and Applications of Electrochemical Impedance Spectroscopy (EIS) for Lithium-ion Batteries. Journal of Electrochemical Science and Technology [online]. 2020, 11(1), 1-13. ISSN 2093-8551. Available at: doi:10.33961/jecst.2019.00528

[7] ABASPOUR, Marzia, Krishna R. PATTIPATI, Behnam SHAHRRAVA a Balakumar BALASINGAM. Robust Approach to Battery Equivalent-Circuit-Model Parameter Extraction Using Electrochemical Impedance Spectroscopy. *Energies* [online]. 2022, **15**(23). ISSN 1996-1073. Available at: doi:10.3390/en15239251

[8] BIOLOGIC. EC-Lab Software Users Manual [online]. August 2014 Available at: https://mmrc.caltech.edu/BioLogic%20Echem/ECLab%20Manuals/EC-Lab%20software%20user%27s%20manual.pdf

Predictive Model of Household Consumption in Conjunction with Complementary Electricity Generation

1st Libor Pavlík
Brno university of technology
Faculty of electrical engineering and communication
Brno, Czechia
230411@vutbr.cz

2nd Lukáš Radil
Brno university of technology
Faculty of electrical engineering and communication
Brno, Czechia
radil@vutbr.cz

Abstract—The growing importance of decentralized energy sources and the concept of community energy present new challenges in predicting and optimizing electricity consumption. This work builds on previous research and focuses on enhancing predictive models of electricity consumption by incorporating photovoltaic systems (PV) in residential homes.

Index Terms—energy consumption prediction, community energy, electricity sharing,

I. INTRODUCTION

To effectively plan and optimise energy supply, it is essential to use predictive models of electricity consumption that allow for more accurate estimation of energy needs under different conditions. This work focuses on extending and improving existing models with an emphasis on the integration of PV in single-family houses and the development of a simple Graphical User Interface (GUI) in MATLAB environment [1].

II. DEMAND DIAGRAM MODEL

The model of the consumption diagram, which was developed and detailed examined in the framework of the thesis Household consumption diagram model [2], that is a probabilistic model that takes into account the number of people and their occupancy and uses probabilistic approaches to model energy consumption with 1-second granularity, taking into account the number of occupants and their presence in the household. Emphasis has been placed on the use of freely available data and to account for socio-economic factors, allowing for a better understanding and prediction of energy consumption behaviour.

In developing the model, current methods of creating household consumption diagrams were analysed and their advantages and disadvantages were identified. Subsequently, a methodology was proposed that allows the simulation of energy consumption with high accuracy. A key requirement for this data was a high sampling rate, which is important to ensure sufficient simulation accuracy. The simulation results were verified and compared with reference data.

A. Input data

The input data for this model are a combination of freely available datasets and reference measurements that include information on individual appliance consumption, demographic characteristics of households, behavioural patterns, and time trajectories of energy consumption. The emphasis is on transparency and reproducibility of the model. The combination of different data sources allows to simulate not only the consumption of individual appliances but also the total household consumption.

B. Model verification and data validation

For verification and validation of the model results, data obtained from PREdistribuce are used, which include measurements of medium voltage (MV) and low voltage (LV) MV/NV transformer outlets from panel houses and measurements of consumption of individual flats in Prague. Measurement data from German households are also used to refine the results and increase their accuracy. These data have a high sampling rate, which is in the order of minutes, which allows improving the quality of the simulated household energy consumption predictions. The combination of these different metered data provides higher accuracy when compared to real consumption.

TABLE I
COMPARISON OF DATASETS TO VALIDATE RESULTS

Datasets name	File name	Sampling frequency
German household	`nemecko.csv`	1 minute
PREDistribuce	`predi.csv`	5 minutes

C. Demand model

The model developed takes into account various aspects of household consumption, ranging from basic constant consumption to the complex interactions between occupant behaviour and appliance operation.

For better clarity, the model can be divided into two main parts. In the first part algorithm and code structure of the

model, which includes two classes containing all the necessary attributes and functions to simulate consumption. This part provides the basic functionality of the model, including the definition of the appliances and their functions for the consumption simulation. In the second part is the file that runs each part of the classes and controls the flow of the simulation. This file modifies the simulation parameters, allows interaction with the user and ensures that all simulated scenarios

III. SIMULATION OF PV POWER GENERATION WITH PVLIB LIBRARY

The PV_LIB library is intended for analysis, simulation and design of photovoltaic systems. It uses to model the performance of PV systems, which includes the prediction of energy production, estimating panel efficiency and evaluating the effect of factors such as illumination, temperature and panel orientation. The library was originally developed for the Python language and was ported to the MATLAB environment [3]. The mathematical models for simulating the performance of solar panels are adapted to be able to provide results similar to the real ones. Thus, the models account for climatic and operating conditions.

A. Prediction of energy production based on TMY

PV_LIB allows the prediction of energy production based on historical solar radiation data, temperatures and other factors. This data is contained in typical meteorological data Year (TMY) files [4]. To obtain them, it is possible to use the online tool PVGIS (Photovoltaic Geographical Information System). Developed by the Joint Research Centre of the European Commission, which provides information and data for analysing the performance of photovoltaic (solar) systems [5].

B. Outputs of PV model

One of its main functions is to calculate the electricity production from photovoltaic panels. This calculation is based on a geographical location entered by the user, which determines the amount of solar of solar radiation available in a given area.

PV_LIB also allows different configurations of PV systems to be simulated in order to to determine which setup is the most advantageous. The user can test different tilt angles and orientations of the panels, and the tool will automatically calculate the optimal values that maximize production energy [5].

IV. IMPLEMENTING MODELS INTO THE APPLICATION

The application will implement scripts for simulating household and photovoltaic systems, it will export the simulated data and display them in a user-friendly interface. Furthermore, the application will allow aggregation of data to different time intervals, on a per second basis, minute and 10-minute periods, thus ensuring flexibility in analysis and visualisation results. One of the core features of the application is its ability to aggregate simulation data across different temporal resolutions — namely, 1-second, 1-minute, and 10-minute intervals. This

functionality provides a high degree of flexibility for both visualization and analysis.The use of 1-second intervals is particularly advantageous when detailed system behavior is of interest. Such a high-resolution time base allows for the precise capturing of fast dynamics in household consumption patterns or PV system outputs — including sudden power spikes, voltage fluctuations, or inverter reaction times

A. Application graphic section

The AppDesigner tool is responsible for the functioning and design of the application, the first step of this process is to create a basic application environment that will contain all the necessary controls for effective interaction with the user. The application controls are systematically divided into three main groups, allowing for clear organization and easy navigation between the different functions of the application.

- General Settings - this group is focused on setting simulation parameters, rendering graphical outputs and selecting the month for simulations,
- consumption Simulations - this section is used to select the period and the number of households,
- PV simulation - this group sets the GPS (Global Positioning System) coordinates, inclination and azimuth, etc.

Each of these groups focuses on specific tasks provided by the application, such as household simulation, data visualization, and simulation parameter settings, among others.

B. General settings

This group focuses on the configuration of basic simulation parameters that are common for multiple elements of the application. The user can set several parameters here. The exact elements are month selection, interval length, rendering of simulation progress, plotting of graphs.

C. PV simulation

The last group of components contains the PV plant simulation setup and basic information for obtaining TMY data. The parameters in this control are panel selection, inverter selection, number of panels in series, number of strings, panel angle and azimuth settings.

D. Consumption simulations

This group includes components for controlling, setting and adjusting the simulation of household consumption. The period selection element is a control that allows to set the period for which the electricity consumption will be generated. The user can choose between two modes. Weekday, where the simulation adapts its algorithms to match the typical behaviour of people and appliance usage on weekdays. And Weekday, where the simulation algorithms are optimized for the weekend when people's behavior is different.

Furthermore, a content component to select the number of iterations that the accuracy of the simulation.

The last component of this page is a numerical selector for the number of households for which to simulate the resulting consumption.
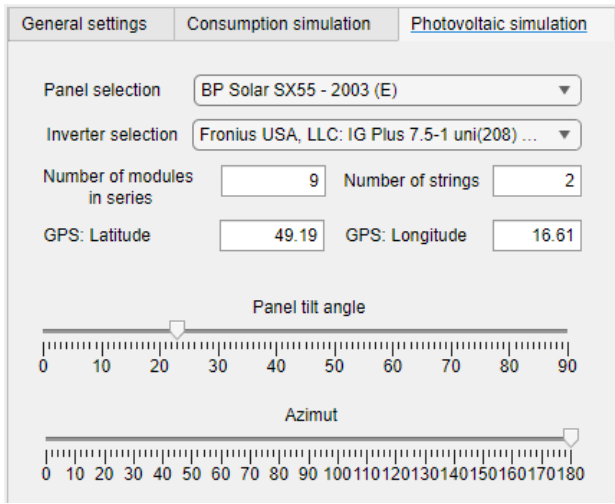
Fig. 1. Designed GUI for setting up a photovoltaic power plant

E. Application control

The last important part of the GUI is the ability to save to .csv. For this purpose, a Save to .csv button is created that downloads the data from the simulation and prepares it for export in CSV format.
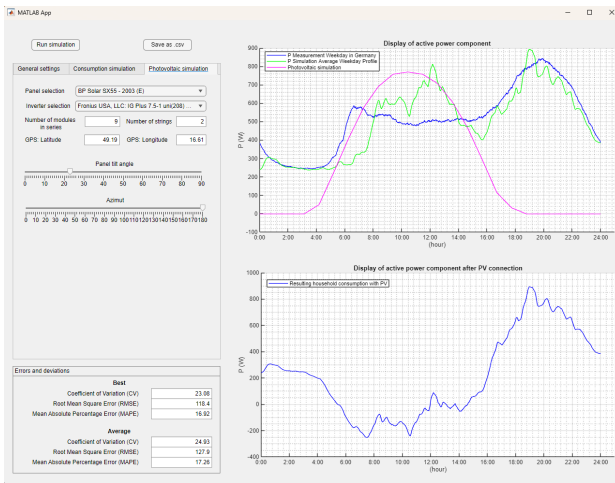

Fig. 2. Overall designed GUI applications

V. APPLICATION OPERATION

After pressing the Run Simulation button, all variables are restarted to ensure a clean start of the simulation. This is followed by saving all user options and finally the progress_bar function is run to coordinate the execution of other parts of the application (e.g. the nemecko.m script for the simulation, plotting graphs, etc.).

VI. 1 ST. SIMULATION AND PV SYSTEM CONFIGURATION

The simulation was carried out for a representative group of 200 households based on the model described in [2]. The simulation was performed for the month of July, which was
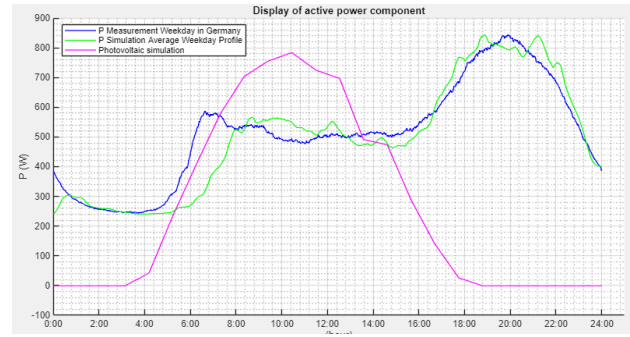

Fig. 3. Displayed active power of all components in 1 st. configuration

chosen to represent the period with intense solar radiation. The number of iterations for this simulation was set to 10 in order to improve the stability and accuracy of the results. The PV plant model included two stringers, each containing nine panels of the BP Solar SX55 - 2003 type. The output energy was further processed by a Fronius IG Plus 7.5-1 uni(208) inverter. A more detailed configuration of the PV system can be found in Fig. 1 IV-C.

VII. 1 ST. SIMULATION RESULTS AND ANALYSIS

The resulting waveforms of both simulations are shown in Fig. 3 V, where they are compared with real measured data from Germany. The plot shows only a minimal deviation between simulated and real values, which is confirmed by the following error bars: CV = 21.18, RMSE = 108.6, MAPE = 14.23. Bottom figure on Fig. 2 IV-E further shows the resulting course at the level of the whole object, i.e. the consumption point. It shows that the PV plant designed in this way is optimally sized - it minimizes the energy overflows to the distribution grid while covering its own consumption. The main advantage of the proposed application is the possibility to efficiently estimate the appropriate size of the PV system with respect to the number of load points, while maintaining high simulation accuracy.
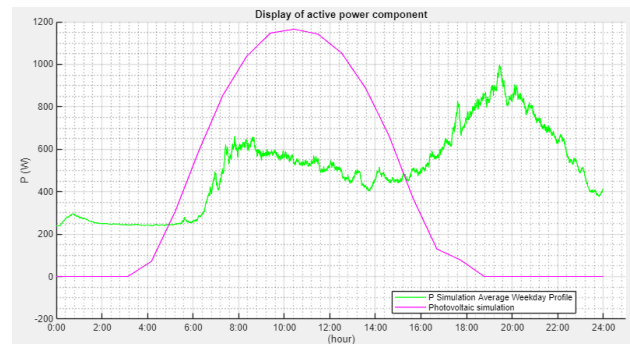

Fig. 4. Displayed active power of all components in 2 nd. configuration

VIII. 2 ND. SIMULATION AND PV SYSTEM CONFIGURATION

For the second test, a Sharp ND-187U1F panel was used in combination with a HiSEL Power – HiSEL-K 4000 inverter

(208V), responsible for processing the generated energy. The panel configuration consisted of four strings, each with two panels. The consumption simulation was again performed for 200 households, but this time with six iterations and using a higher time resolution with 1-second intervals.

IX. 2 ND. SIMULATION RESULTS AND ANALYSIS

From the plotted results, it is evident that reducing the time step to one second significantly improved the accuracy and variability. Thanks to the probabilistic model described in [2], the resulting load curve exhibits a distinctly different shape, more accurately capturing realistic variations in household behavior.

X. DATA VALIDATION

The data validation for the household consumption model is thoroughly described in [2]. Validation for the photovoltaic model is available in [3]. This application utilizes their original source codes and integrates their functions into a unified user interface, offering users convenient access to both models within a single environment.

XI. CONCLUSION

The practical implementation combines the theoretical knowledge explored in an earlier master thesis in the field of energy consumption modelling with energy production modelling using PV_LIB supported by the PV_GIS library.

The application is developed in the AppDesigner environment in MATLAB. Both graphical and computational aspects have been considered in its development, while the adjustment of the calculations focuses on data aggregation. The graphical part of the application is designed to be user-friendly and intuitive, allowing easy interaction with the different modules and visualization of the results. The application also includes a data export option. The application includes an integrated reporting system to help users avoid errors in their work.

The result is a link between the prediction of PV generation and the estimation of consumption based on the behaviour of the household users. The generated values are then merged to produce the resulting waveform shown in Fig. 2 IV-E. This graph illustrates how the consumption of a customer site changes after the integration of a PV plant.

REFERENCES

[1] MATLAB©. Develop Apps Using App Designe online. MATLAB ©, 2024. Available at: https://www.mathworks.com/help/matlab/app-designer.html

[2] Bočan, T. Households consumption diagram model. Brno, CZ, 2024. Master thesi. BRNO UNIVERSITY OF TECHNOLOGY, FACULTY OF ELECTRICAL ENGINEERING AND COMMUNICATION. Available at: https://www.vut.cz/www_base/zav_prace_soubor_verejne.php?file_id=267742

[3] Laboratories, S. N. MATLAB PV_LIB Toolbox online. 2018. Available at: https://github.com/sandialabs/MATLAB_PV_LIB

[4] Centre, J. R. PVGIS Typical Meteorological Year (TMY) Generator online. 2024.Available at https://joint-research-centre.ec.europa.eu/photovoltaic-geographical-information-system-pvgis/pvgis-tools/pvgis-typical-meteorological-year-tmy-generato_en

[5] Centre, J. R. PVGIS Tools online. 2022. Available at: https://re.jrc.ec.europa.eu/pvg_tools/en/

Semi-Automatic Spot-Welding Machine for contacting battery cells

Bc. Martin Martincek
Department of Electrical and Electronic Technology
Brno University of Technology
Brno, Czech Republic
220847@vut.cz

doc. Ing. Petr Vyroubal Ph.D.
Department of Electrical and Electronic Technology
Brno University of Technology
Brno, Czech Republic
vyroubal@vut.cz

Abstract—**This article describes a design of a machine developed for manufacturing of a battery systems by joining singular battery cells by resistance spot-welding method. The document shows the main design parts and modules and discusses their function and implementation. The article also briefly talks about common joining methods used for joining the battery cells, their principles and the advantages and disadvantages.**

Keywords—spot-welding, resistance, welding, battery, cells, contacting, spot, welding

I. INTRODUCTION

In today's era of electrification of industry and households, the need for electrical energy sources is constantly increasing. In the case of mobile devices or where it is not possible to be connected to the grid, a battery consisting of electrochemical cells take over. However, to create the desired energy source, the individual cells must be connected to each other to create a battery assembly with the required parameters. When creating these battery assemblies, various cell connection technologies can be used. Each of the available technologies is suitable for certain types of electrochemical cells and has its own advantages and disadvantages. The choice of the right technology also depends on the target application of the device on which the battery will be used. The biggest differences between the available cell joining technologies include the resulting electrical resistance, mechanical strength of the joints, thermal resistance of the joints and the thermal load on the cell itself during the joining process.

II. JOINING METHODS

The joining of electrochemical cells is crucial in the production of batteries or battery systems. The quality of the resulting product depends on the success of this process. Whether it is performance, safety or battery life, each of these qualities can be critical in production.

Each individual cell has a nominal voltage and is capable of delivering a certain amount of current. Thanks to the possibility of connecting multiple cells, it is possible to assemble the resulting battery system, the parameters of which can be set using the series or parallel connection of the individual cells. When cells are connected in series, an assembly is created with a voltage equal to the sum of the individual nominal voltages of the cells, Fig. 1 a). When connected in parallel, Fig. 1 b), on the contrary, the voltage does not increase, but the total charge of the system increases, as well as the maximum current that the system is capable of delivering, both peak and continuous.
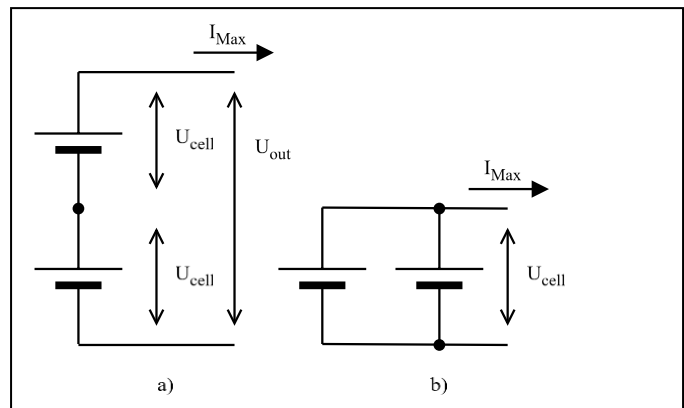

Fig. 1. Different configurations of connecting multiple cells in battery system: a) Series configuration and b) Parallel configuration.

High-quality and reliable cell connection also ensures uniform distribution of current and voltage, preventing local overheating of connected elements or singular cells of the battery assembly. Reducing the thermal load on the cells and the overall system is important in minimizing wear, maintaining long service life and reducing safety risks of the entire battery system. There are several basic methods used to create a reliable inter-element connection. One of the most common methods is welding, which can be performed in a variety of ways, differing mainly in the way heat is generated and the resulting connection.

A. Resistance welding

Resistance welding is one of the basic techniques, in this method the connection between the cells is created using high current pulses, which creates local heating and melting battery tab and a joining element which is often a thin metal strip made of nickel plated steel [2]. After the subsequent cooling of both metals, a solid conductive connection is formed between them. In this method most of the heat created by the passing current is concentrated in the place with the greatest electrical resistance, which in this case is the contact interface between the two connecting conductors. Due to the commonly used high values

of the flowing current, it is possible to deliver a large amount of thermal energy in a short time. Thanks to this short exposure time the generated heat does not spreads onto the surrounding parts of the battery cell body, which helps to minimize the thermal load on the spot-welded cell. During the resistance welding, the main focus is to keep the electric resistance between the welding electrodes and the nickel strip as low as possible, while the resistance between the nickel strip and the cell tab must be much higher. This ensures that the majority of the applied voltage drop and the highest temperature increase is localized at this point.[2]
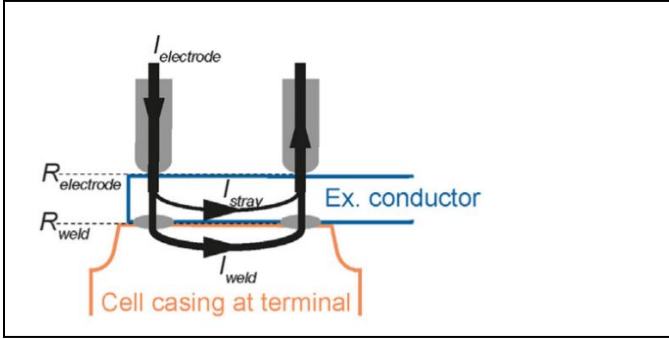

Fig. 2.   Resistance welding on a cylindrical cell with a nickel strip [1].

B. Ultrasonic welding

Ultrasonic welding is also a commonly used technique, in which the energy of mechanical vibrations at high frequency, usually 15 kHz and above, is used to create a frictional bond between two or more materials [2]. The materials are pressed together, with one of them being fixed and the others vibrating at the frequency of the ultrasonic transducer.

This type of welding does not cause contamination problems because oxides and contaminants on the surface of the materials are disrupted by the ultrasonic vibrations, resulting in the exposed metal surface. A major advantage of ultrasonic welding is the ability to join dissimilar materials and multiple layers of materials [2]. Another advantage is an ability to create a connections inside the cell [2]. This method is highly dependent on the hardness of the material and the roughness of its surface, so softer materials such as copper or aluminum are suitable, but steel with higher hardness presents a slightly greater obstacle for this method [2].

C. Laser welding

Main advantage of this method is that it is a non-contact method that uses a focused beam of light to create a connection. By focusing the beam on the desired point, the two metals being welded are melted in a short time and then cooled again to form a joint between the two materials [2]. Typically, a pulsed low-power neodymium laser is used, that can be focused onto a small area, combined with a short exposure time, helps prevent unnecessary overheating of the surrounding area of the welded joint. When making joints using this method, it is necessary to use a material whose surface has low reflectivity and high absorption for the wavelength of the laser used, and to maintain high purity of the surfaces of the welded materials.[2]

III. DESIGN

The device described in this article is designed to automate most of the contacting process and requires minimal user intervention. The final device is designed to be used on all battery cells of various sizes and types that are suitable for the use of resistance welding technology.

The user can set welding parameters consisting of the power rating level, which is a relative value to the total power that the device can deliver, the pressure force on each cell during the spot-welding process, and the number of pulses or welding duration time in milliseconds. These parameters ultimately determine the quality of the resulting welded joints.

The machine consist of a system of modules and can be divided into several parts, the most important of which are: Welding current source module, Central Computer and User Interface and Three-Dimensional Arm Positioning System. The diagram below shows the relationship between the individual modules.
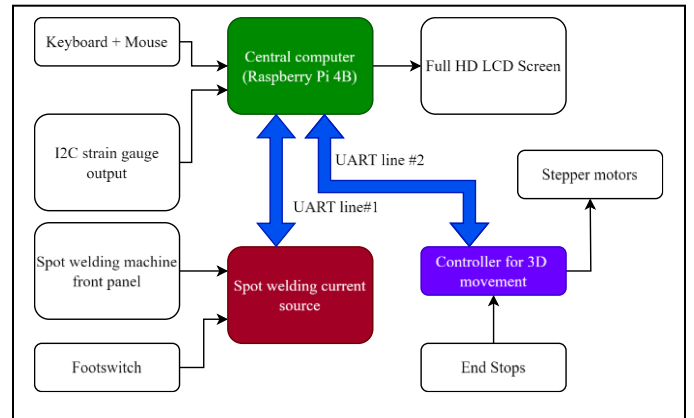

Fig. 3.   Individual modules of the system and their linkage.

A. Welding current source module

This module is a separately functional device originally developed for manual spot welding using a special contacting pen. The main hardware parts are shown in Fig. 4 below.
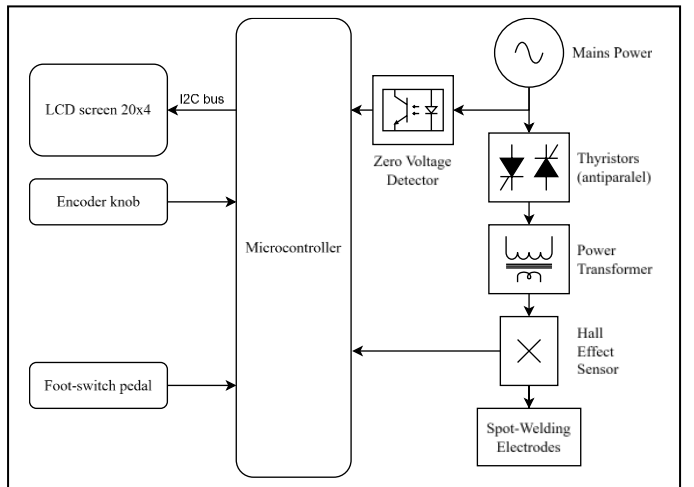

Fig. 4.   Welding current source main hardware sections.

It consists of a power transformer, specially modified so that the output open-circuit voltage is around 3 V, but at the same time so that the output current can reach high values, because the output is short-circuited during normal operation. These parameters are obtained by replacing the secondary winding of the transformer with three turns of a thick 35 mm2 copper wire.

Fig. 5. The custom power transformer modified for high current output.

The output power is phase-controlled by a thyristor regulator, which consists of two antiparallel thyristors, that uses a zero-crossing voltage detector for synchronization and timing. The magnitude of the output welding current is then measured by contactless Hall effect sensor, which serves as feedback for the timing of the phase regulation.
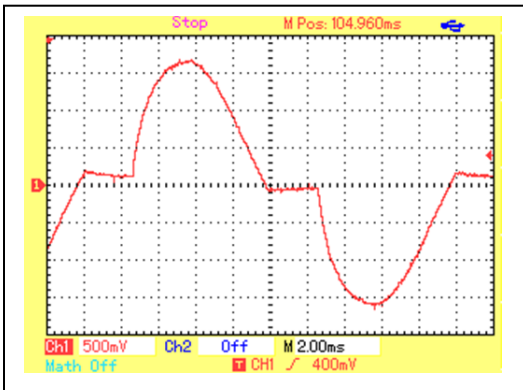

Fig. 6. The closed-circuit voltage waveform measured at the output of the power transformer with medium output power set.

This whole welding current module is being controlled by a small ARM microcontroller, the microcontroller also communicates with the central computer from which it receives the welding parameters and commands. This module also includes a foot pedal, which is a safety feature, because the user must keep their foot on this pedal throughout the entire welding process and if it is released, welding will stop.

As mentioned, this module is capable of standalone manual operation, which does not involve communication with a central computer and therefore welding parameters are not received over the serial line. Instead, they are set using a rotary encoder and LCD display located on this module.

B. Central Computer and User Interface

The central processing unit of the whole system is designed to be a miniature development board Raspberry Pi but it can be replaced by any standard personal computer with an operating system and python installed. The central computer communicates with the other modules via serial line and controls them by sending commands and parameters.

On the central computer there is an application that provides a graphical user interface to set up and control the welding process. The user interface application displays the feed from the camera located above the welding area.
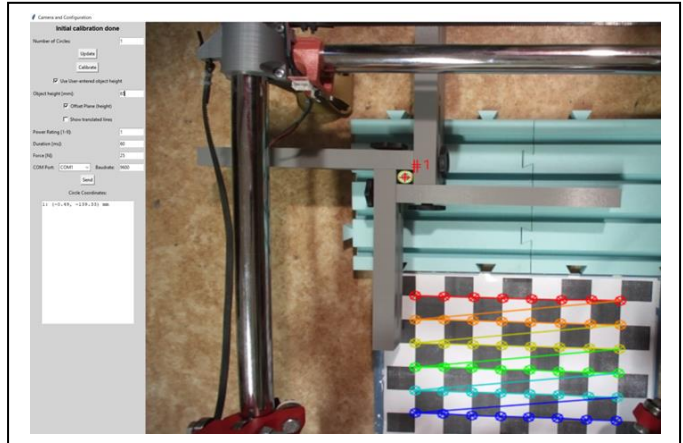

Fig. 7. The graphical user interface application in the central computer.

The camera feed provides two-dimensional coordinates of all the points that the camera sees and projects to the screen. To use the coordinates for positioning the CNC arm onto the position of the cells, the screen coordinates need to be recalculated to the corresponding three-dimensional real-world coordinates.

This conversion is calculated using Zhang's camera calibration method [3], which involves calibrating the camera against a calibration board with a chessboard pattern with known dimensions. This procedure does not need to be done at the beginning of every spot-welding process if the calibration data can be loaded from a previous calibration and if the camera position has not changed since then.

The output from this calibration method is a transformation matrix which is saved to a local file and then being used throughout the entire operation of the device until the next calibration procedure is performed.

To set up the spot-welding process, the user needs to type in the app the number of the cells that are to be spotwelded and mark the locations of their terminals on the screen. In addition, the user must also enter the welding parameters, which consist of the welding power rating level, number of pulses or welding time and required downward force during the spot-welding.

C. Three-Dimensional Arm Positioning System

To create precise and repeatable spot-welded joints, precise movements are critical and for this purpose a CNC (computer numerical control) system is used that allows movement in three axes using dual stepper motors and their endstop switches. The assembly used in this device is an open-source project called "MPCNC" (mostly printed CNC). The acronym means that the parts of the assembly are mostly printed from polymer material using an additive manufacturing printer.

The CNC mechanism is controlled by the controller made up of MKS Gen V1.4 control board, which uses open-source firmware Marlin to decode incoming commands from the

central computer and then use stepper motors to move the moving arm to the exact position in the specified trajectory. cell.
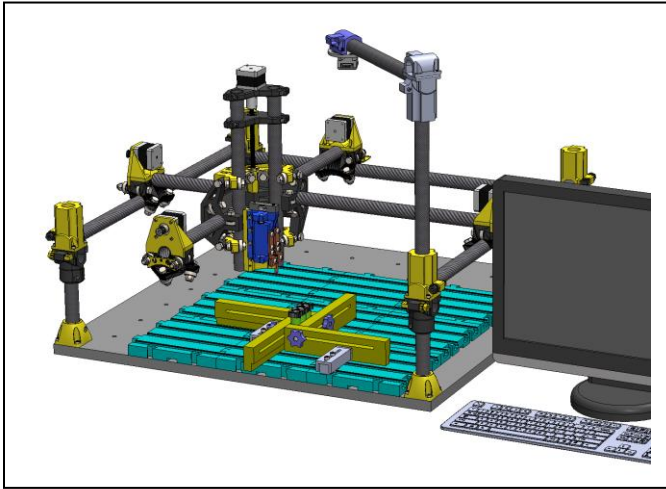

Fig. 8. Model of the CNC assembly setup for spot welding of a cylindrical cells.

The moving arm copper welding electrodes and a downward pressure force sensor module mounted to it. The force module is responsible for sensing the downward force pushing onto the tab of the battery cell that is being spot welded. The force module consists of a load cell that uses built in strain gauges that change their electrical resistance based on the mechanical stress they are subjected to.
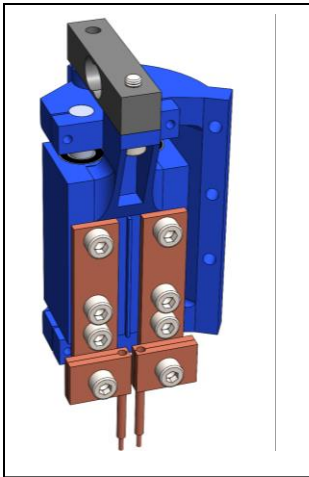

Fig. 9. The moving arm with welding electrodes and the attached load cell as force sensor.

The output signal is processed by an ADC (analog-to-digital converter) and then via I2C (Inter-Integrated Circuit) bus sent to the central computer as a feedback value of the downward welding force.

In the preparation stage of the welding process, the central computer sends a command to move the moving arm to the XY position of the cell that's going to be spot-welded. After arriving at the position, the computer goes into a loop where it sends a command to move the arm on Z axis about 0.5 mm down and checks the received value of the downward force and when the force reaches a required force value previously set by a user, the

arm stops and holds its position. After that the welding starts and then the arm continues to the next cell.

IV. RESULTS

This device is currently in the testing process. Initial test results are shown in Fig. 10, where two cells with a spot welded joints to the nickel strip are shown.

Fig. 10. Spot-welded connections on cylindrical cells of size 18650, maximum power output on the left, and low power output on the right.

The cell on the left was spot-connected with maximum power and the cell on the right with medium power. The cell on the left shows visible discoloration of the nickel strip, indicating slight overheating of the nickel but a good welded joint. The cell on the right does not show this discoloration even though a spot weld has been made, but this joint does not achieve the same mechanical strength and low contact resistance as the spot welded joint on the left.

The spot-welding machine described in this article was designed to achieve high-quality, repeatable cell connections. This claim cannot yet be confirmed or proven because the device is still in the testing process and the study to check the repeatability of the connections has not yet been completed, but initial results suggest this. With the correct tuning of the welding parameters, it would be possible to produce battery systems with top-notch parameters with minimal user intervention.

REFERENCES

[1] M.J. Brand, P.A. Schmidt, M.F. Zaeh, A. Jossen, Welding techniques for battery cells and resulting electrical contact resistances, J. Storage Mater. 1 (2015) 7–14.

[2] Lee, SS, Kim, TH, Hu, SJ, Cai, WW, & Abell, JA. "Joining Technologies for Automotive Lithium-Ion Battery Manufacturing: A Review." Proceedings of the ASME 2010 International Manufacturing Science and Engineering Conference. ASME 2010 International Manufacturing Science and Engineering Conference, Volume 1. Erie, Pennsylvania, USA. October 12–15, 2010. pp. 541-549. ASME. https://doi.org/10.1115/MSEC2010-34168.

[3] Burger, Wilhelm. (2016). Zhang's Camera Calibration Algorithm: In-Depth Tutorial and Implementation. 10.13140/RG.2.1.1166.1688/1.

Efficient Optimization through Normalized Variable Scaling and Selective Term Pruning

Jan Sedlář

Department of Control and Instrumentation
Faculty of Electrical Engineering and Communication
Brno University of Technology
Brno, Czechia
xsedla1x@vutbr.cz

Abstract—**This paper presents an innovative pruning algorithm designed to enhance computational efficiency of optimization-related tasks by reducing the number of computations. The algorithm, which is based on optimization variable normalization and subsequent term pruning according to a set relative threshold, offers balance between accuracy and computational complexity of the solution, making it suitable for performance-critical applications. The trade-off between accuracy and complexity in this approach is expressed by metrics of Pareto efficiency and relative efficiency.**

Index Terms—**selective term pruning, cost function optimization, variable normalization, computational efficiency, system control optimization, model reduction**

I. Introduction

This paper proposes an innovative approach to large-scale real-time optimization problems that reduce computational complexity. The efficiency of the algorithm is achieved by normalizing the optimization variables in a range of [-1, 1], ensuring that the objective function, which is expressed as a sum of terms consisting of normalized variables and numerical coefficients, has a bounded contribution. The objective function expressed in this way enables the use of an algorithm that can assess the impact of each summation term on the overall value of the objective function and its differentiations and omit those terms that have negligible influence from further calculations. By selectively pruning the coefficients, the optimization solution presents a significantly lower computational complexity problem than the original problem, while preserving the accuracy of the results. The efficiency of the algorithm is demonstrated on a nonlinear model predictive control (NMPC) of a permanent magnet synchronous motor (PMSM) represented as a state-space model, where state predictions with recursive nature exponentially enlarge the optimization problem, and fast dynamics require real-time computations at a microsecond level. However, this algorithm is broadly applicable to many large-scale optimization problems, not necessarily gradient-based, involving high-dimensional functions, such as trajectory planning, machine learning, or process control.

II. Illustrative Example of a Large-Scale Optimization Problem

Predictive control of dynamic systems is a popular approach to managing complex processes described by a suitable model and incorporating some constraints placed upon various quantities present in the system. Consider a system with nonlinear dynamics described by discrete-time state-space matrices (1). [1]

$$\boldsymbol{x}(k+1) = \boldsymbol{A}\boldsymbol{x}(k) + \boldsymbol{B}\boldsymbol{u}(k) + \boldsymbol{f}(\boldsymbol{x}(k), \boldsymbol{u}(k)) \quad (1)$$

Where $\boldsymbol{x}(k)$ denotes the state vector, $\boldsymbol{u}(k)$ the control inputs vector, $\boldsymbol{A}$ and $\boldsymbol{B}$ are discrete-time state matrices and $\boldsymbol{f}(\boldsymbol{x}(k), \boldsymbol{u}(k))$ represent the nonlinear dynamics of the system. In the context of PMSM the states of the model include currents i_d, i_q in dq space and speed ω, while voltages u_d, u_q applied to the motor represent the inputs of the model. The goal of the predictive controller is usually to minimize a given objective (or cost) function J over the length of the prediction horizon N, typically formulated as (2). Λ represents here the function that penalizes the state and the input values and E penalizes the states in the final step of the prediction horizon. The problem is usually subjected to constraints such as: $x(k+1) = \boldsymbol{A}\boldsymbol{x}(k) + \boldsymbol{B}\boldsymbol{u}(k) + \boldsymbol{f}(\boldsymbol{x}(k), \boldsymbol{u}(k))$, initial conditions, and bounds on inputs and states (e.g. $|x_1|, |f(x_2)| \leq X_{max}$). [2]

$$J(\boldsymbol{x}(k), \boldsymbol{u}(k)) = \sum_{m=k}^{N+k-1} \Lambda(\boldsymbol{x}(m), \boldsymbol{u}(m)) + E(\boldsymbol{x}(m)) \quad (2)$$

A significant challenge is to find a minimum of such nonlinear function when the length of the prediction horizon N increases. The equations for future states are obtained via a recursive substitution of the original equation into itself, potentially causing an exponential growth of the number of terms present with growing N. Considering (1) for $k = 1$, the state values for $k = 2$ will be obtained as shown in (3).

$$\boldsymbol{x}(2) = \boldsymbol{A}(\boldsymbol{A}\boldsymbol{x}(0) + \boldsymbol{B}\boldsymbol{u}(0) + \boldsymbol{f}(\boldsymbol{x}(0), \boldsymbol{u}(0))) +$$
$$+ \boldsymbol{B}\boldsymbol{u}(1) + \boldsymbol{f}(\boldsymbol{x}(1), \boldsymbol{u}(1)) \quad (3)$$

Furthermore, in an application like PMSM control, the objective function is non-convex with multiple local minima

due to nonlinear dynamics present in the model and constraints placed upon the quantities. Those facts make such a problem expensive to solve in a very short time. This example motivates the innovative approach to such problems through variable normalization and selective coefficient pruning proposed in this paper.

III. NORMALIZED OPTIMIZATION VARIABLES

The underlying principle of this algorithm that allows the terms of the objective function to be pruned is the normalization of the optimization variables in a range of [-1, 1]. This allows all the variables contained in the function to be represented equally and also enhances the numerical stability of the algorithm and can speed up its convergence. [3] [4] Controller tuning can also focus on the relative priority of each variable rather than their magnitudes. This uniformity of the optimization problem is achieved by applying a linear scaling formula (4) to each quantity present in the objective function.

$$x_{\text{norm}} = 2 \frac{(x - x_{\min})}{x_{\max} - x_{\min}} - 1 \tag{4}$$

The function J for N of arbitrary but predetermined size can be rewritten as a sum of terms consisting of variables and a numerical coefficient weighing the particular term, as shown in (5) for the case of model predictive control. Here, x_i represents the states of the model with $i \in [0, n_x]$ and n_x being the total number of states and similarly u_j represents the input of the model with $j \in [0, n_u]$ and n_u being the total number of inputs, k is the step of the prediction horizon with length N. $M \in \mathbb{R}$ is the numerical coefficient of the term, γ_i and δ_{jk} are indicators that denote whether a state or input is present in the respective term ($\rho_i, \sigma_{jk} \in \{0, 1\}$). Note that such a term can contain only values of x_i from the first step of the prediction horizon (the currently available values), but inputs throughout the length of the horizon.

$$M \prod_{i=1}^{n_x} \rho_i x_i(0) \cdot \prod_{j=1}^{n_u} \prod_{k=0}^{N-1} \sigma_{jk} u_j(k) \tag{5}$$

Without applying the normalization formula to the variables first, the term would take values over an unbounded range. However, if the normalization principle is introduced, the maximum absolute value of each term of the function is given purely by its numerical coefficient. The maximal contribution of each term to the overall function value is therefore determined only by the absolute value of its coefficient. This principle does not only apply to the objective function of the controller, but also to its differentiations with respect to the optimization variables, too, and can be successfully utilized in gradient-based optimization solvers. This fact allows for a reduction of the number of terms that need to be computed during the optimization step. If a sensitivity analysis of the contribution of the coefficients to the overall J is performed, terms with $\text{abs}(M)$ below a determined threshold can be pruned. The threshold value is highly dependable

on the desired accuracy target and computational complexity reduction demands and is chosen as a balance between these two. If a problem would span over a small magnitude, i.e. all numerical coefficients would contribute to the function value with approximately the same amount, this approach would naturally not be applicable. However, this particular case is highly probable only for low-complexity optimization problems, where the need for term pruning is not significant.

IV. COEFFICIENTS IMPACT IN OBJECTIVE FUNCTION

In NMPC of PMSM the dominance of large-magnitude coefficients in the objective function (and its differentiations) exemplifies the efficiency of the application of term pruning. For a better understanding of the underlying problem, a set of discrete-time equations are listed that describe the non-linear dynamics of PMSM (6), as well as the constraints placed on the quantities (7). The pure numerical coefficient that multiplies each term present in the equations is represented here by c_{0-9}.

$$i_d(k+1) = c_0 i_d(k) + c_1 \omega(k) i_q(k) + c_2 u_d(k) \tag{6a}$$
$$i_q(k+1) = c_3 i_q(k) - c_4 \omega(k) i_d(k) + c_5 u_q(k) - c_6 \omega(k) \tag{6b}$$
$$\omega(k) = \omega(k) + c_7 i_q(k) + c_8 i_d(k) i_q(k) - c_9 \tag{6c}$$

$$u_d^2 + u_q^2 \leq U_{max} \tag{7a}$$
$$i_d^2 + i_q^2 \leq I_{max} \tag{7b}$$

The recursive expansion over the length of the prediction horizon of the controller yields thousands of terms. As the controller tries to find an optimal control signal for each step of the horizon, the number of optimization variables and the gradient of the function also scale up with longer horizons. The complexity of the core optimization problem while omitting constraints (7) for $N = 3$ is visualized in 1. The total of 1,126 terms of the cost function are divided into logarithmic bins plotted along the x-axis of the graph in logarithmic scale. The x-axis therefore represents the absolute value of the coefficients' magnitude. The total number of coefficients present in each bin is represented by the color saturation of the bin. The height of each bin illustrates the impact of the encompassed coefficients on the value of the cost function and is also plotted on a logarithmic scale. The yellow line represents the cumulative sum of the coefficients, i.e. the value of the cost function. It can be clearly seen that only the biggest coefficients have a significant impact on the value. A dotted line demonstrates the potential pruning threshold and is equal to $1/1000$ of the largest coefficient present.

Note that in 1 only the standard coefficients of the cost function are represented. The ones generated by constraining functions are omitted for the sake of clarity. From this graph, it can be assumed that the relative pruning threshold denoted δ with respect to the largest coefficient present can be safely chosen in the range of $\delta = [10^3, 10^4]$. The former bound would be a direct representation of the dotted line in the graph.
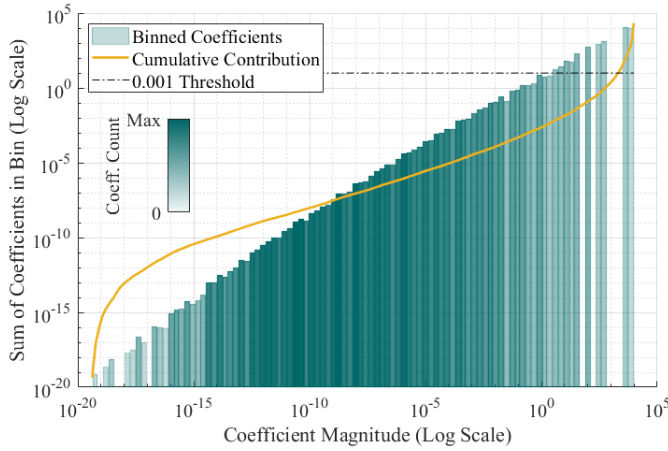
Fig. 1. Impact of Coefficients on Cost Function (Binned)

V. PRUNING THRESHOLD

The selection of the pruning threshold often requires a trade-off between computational complexity reduction and precision. Two quantitative parameters were designed to indicate this trade-off and to reflect suitability of the selected threshold for different applications. Both metrics take on positive values with larger magnitudes, indicating better trade-offs.

Pareto Efficiency-Inspired Metric (PEM) is defined by (8) and is based on Pareto efficiency, a fundamental idea in multiobjective optimization and economics. [5] Pareto efficiency describes a concept where reallocating resources to improve one objective cannot be achieved without degrading another. It is represented by the first term of the multiplication in formula (8) and measures an Euclidean distance of the current (pruned) solution to some ideal point which would yield zero error and zero computational complexity, represented by subtracting zeros in the denominator. N_{pruned} and N_{original} indicate the total number of terms of the pruned and original unpruned cost function respectively, MAE stands for *mean absolute error* of the current solution, $|\overline{C_{\text{original}}}|$ represents the mean of the absolute values of the outputs of the original cost function, and CD stands for *crowding distance*. The term (9) assesses the density of solutions in the trade-off space, and it is used so that PEM encourages the spread of viable pruning thresholds. This strategy aligns with the diversity aspect of Pareto efficiency. PEM combines these two components to evaluate how well a pruning threshold balances the computational complexity and accuracy of the solution.

$$\text{PEM} = \frac{1}{\sqrt{\left(\frac{N_{\text{pruned}}}{N_{\text{original}}} - 0\right)^2 + \left(\frac{\text{MAE}}{|\overline{C_{\text{original}}}|} - 0\right)^2}} \cdot \frac{1}{1 + CD} \quad (8)$$

$$\text{CD} = \left|\frac{N_{\text{pruned},i+1} - N_{\text{pruned},i-1}}{N_{\text{original}}}\right| + \left|\frac{\text{MAE}_{i+1} - \text{MAE}_{i-1}}{|\overline{C_{\text{original}}}|}\right| \quad (9)$$

The Euclidean distance term in PEM prioritizes solutions close to the ideal (minimal complexity and error), making it sensitive to overall trade-off quality. The crowding distance discourages clustering at extremes (over-pruning or under-pruning), favoring intermediate thresholds. This is ideal when a solution that balances multiple goals is required (e.g., optimizing speed versus optimizing accuracy).

Relative Efficiency Metric (REM) balances the trade-off in a slightly different way. The numerator of the expression (10) increases the REM indicator when the total computational complexity of the solution is reduced, while the denominator utilizes the normalized *mean absolute error* of the solution, directly emphasizing the accuracy relative to the best-case error. The term is also regularized by ϵ to avoid singularities, with small magnitudes such as $\epsilon = 0.01$ being recommended.

$$\text{REM} = \frac{\frac{N_{\text{original}} - N_{\text{pruned}}}{N_{\text{original}}}}{\frac{\text{MAE} - \text{MAE}_{\text{min}}}{\text{MAE}_{\text{max}} - \text{MAE}_{\text{min}}} + \epsilon} \quad (10)$$

REM is more suited to performance-critical applications, where accuracy is the primary concern and computational complexity reduction is secondary, as long as it stays within a reasonable limit.

VI. PRUNING EFFICIENCY

For the real-life PMSM problem discussed in the previous chapter, a statistical analysis was performed. A dataset of $n = 1000$ entries was created for different input sequences which were evaluated using six different cost functions. The pruned functions with relative thresholds of 100, 1000, 10^4, 10^5 and 10^6 were compared to the original. In contrast to the case in Chapter IV, here, also the constraining functions (7) were included in the computations. The resulting functions constisting of regular part (2) and the constraints were pruned by the respective threshold.

The comparison of pruning threshold selection in the simulated PMSM application can be seen in I. Various statistical metrics were used to differentiate between the results: r is the Pearson correlation coefficient, $\bar{d}$ stands for *mean difference* and represents the average bias of the pruned solution, s_d is the standard deviation of differences, MAE is the *mean absolute error* measuring the average magnitude of the error, RMSE stands for *root mean squared error* penalizing larger errors more heavily and finally MRE is the *mean relative error* which is used to contextualize errors relative to the magnitude of the original values.

TABLE I
COST FUNCTION PRUNING THRESHOLD COMPARISON TO UNPRUNED
COST FUNCTION

δ	100	1000	1E+04	1E+05	1E+06
$\bar{d}$	111.6655	3.3757	-0.0556	0.0209	0.0065
s_d	50.7002	5.0960	0.4595	0.0448	0.0160
MAE	111.6655	4.7109	0.3397	0.0362	0.0117
RMSE	122.6259	6.1105	0.4626	0.0494	0.0173
MRE	18.3812	0.6666	0.0486	0.0053	0.0011
CC	119	181	246	337	454
REM	0.94	17.75	69.37	**84.11**	81.08
PEM	7.50	**11.41**	9.12	6.55	5.04

The original cost function consisted of 2399 terms in the form of (5), while pruning the used threshold significantly reduced these counts, expressed by CC (coefficient count) in I. Based on the REM and PEM metrics for these cases, it can be determined which threshold settings should be preferred in this application. If the goal of the control engineer was to prioritize the robustness and precision of the algorithm, a relative threshold of approximately $\delta = 10^5$ would provide better results than other threshold values tested. In contrast, if the speed of convergence were prioritized over the optimality of the solution of the function, a threshold of $\delta = 1000$ would be selected.

A visual representation of the entire dataset for two different threshold values, namely $\delta = 10^3$ and $\delta = 10^4$, was created using the Bland-Altman plot 2. The differences in the cost function from the unpruned version are plotted against the x-axis, which represents the mean magnitude of the pruned and original cost function. The mean values of the differences are displayed as blue and red lines in the graph, and ideally they should align with zero. This is achieved much more accurately by the cost function pruned by $\delta = 10^4$, as expected. The lower relative threshold also displays a higher deviation from the mean, although compared to the magnitude of the cost function on the x-axis and the respective entry for the mean relative error in I, the average error is less than 1%. Magnifying the threshold by a factor of ten improves the accuracy of the solution approximately by the same factor in this case.
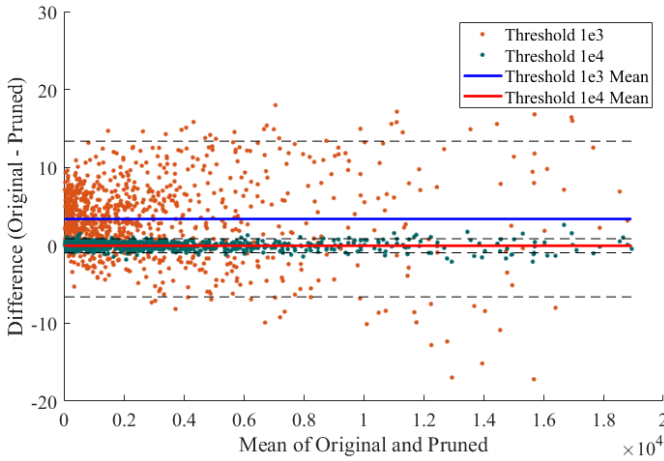

Fig. 2. Bland-Altman Comparison of $\delta = 10^3$ and $\delta = 10^4$

It is also important to note that even with the highest testes threshold (i.e. $\delta = 10^6$) the complexity was reduced by a factor larger than 5. Indicating that even in applications where the accuracy of the solution is highly prioritized, computational demands can still be lowered. For the case of $\delta = 1000$, the reduction factor is greater than 13. This represents a potential $13\times$ speed-up of the optimization solver run while introducing only a slight suboptimality to the solution.

VII. Application in Optimization

Although in the previous chapter a simple evaluation of the cost function was discussed, the approach of variable normalization and term pruning can be utilized in many algorithms. Population-based methods can utilize the term reduction of the cost function, while gradient-based methods benefit from the reduction of the gradient computation complexity. It should also be noted that optimization methods are often iterative in nature. The total time reduction of the evaluations is therefore amplified by the total number of iterations performed while searching for an optimum of a function.

The term-pruning approach proposed in this paper systematically reduces computational complexity in optimization-related tasks. The effectiveness of the algorithm was evaluated using statistical metrics including two indicators – *Pareto Efficiency Metric* and *Relative Efficiency Metric* – reflecting the key factor of complexity-accuracy trade-off. The approach aims to simplify the computations while preserving the essential accuracy and making it adaptable to various applications, demonstrated on predictive permanent magnet synchronous motor control.

References

[1] T. Geyer, *Introduction*, ch. 1, pp. 1–28. John Wiley & Sons, Ltd, 2016.
[2] J. Richalet, A. Rault, J. Testud, and J. Papon, "Model predictive heuristic control: Applications to industrial processes," *Automatica*, vol. 14, no. 5, pp. 413–428, 1978.
[3] S. Boyd and L. Vandenberghe, *Convex Optimization*. Cambridge, UK: Cambridge University Press, 2004.
[4] J. Nocedal and S. J. Wright, *Numerical Optimization*. New York, NY, USA: Springer, 2nd ed., 2006.
[5] A. Mas-Colell, M. D. Whinston, and J. R. Green, *Microeconomic Theory*. Oxford: Oxford University Press, 1995. Chapter 16: Equilibrium and Its Basic Welfare Properties, pp. 547–554.

Towards Varroa destructor mite detection using a narrow spectra illumination

1st Samuel Bielik
Department of Control and Instrumentation
Brno University of Technology
Brno, Czech Republic
Samuel.Bielik@vut.cz

2nd Šimon Bilík
Institute for Research and Applications of Fuzzy Modeling
University of Ostrava
Ostrava, Czech Republic
simon.bilik@osu.cz

Abstract—**This paper focuses on the development and modification of a beehive monitoring device and *Varroa destructor* detection on the bees with the help of hyperspectral imagery while utilizing a U-net, semantic segmentation architecture, and conventional computer vision methods. The main objectives were to collect a dataset of bees and mites, and propose the computer vision model which can achieve the detection between bees and mites.**

Index Terms—**Honey bee, Varroa destructor, Semantic segmentation, Hyperspectral imaging, Multispectral imaging**

I. Introduction

Bees are one of the most important creatures in the world, so humanity has to protect them. One of the bee diseases is varroosis, which is caused by *Varroa destructor*. Overpopulation of this mite in beehive can ruin a whole beehive. Mechanical monitoring of the beehives is time-consuming. *Varroa destructor* mites are much smaller than bees and they have similar color with the bees, so it can be very hard to detect this mite on body of the bee using common visible light. This paper describes a new approach to *Varroa destructor* monitoring in the beehives with utilizing illumination with particular wavelengths. Our goal is to detect mites on bees which are flying into the beehives.

II. Related Works

Kim Bjerge et. al. [1] developed device for automatic beehive inspection, which consists of camera and illumination unit. The device is mounted on the entrance of the beehive, where the bees pass through the parallel tunnels, which constraint their velocity and direction of movement. The research team also analysed 19 different wavelengths of visible and near infrared light in the range between 375 - 970 nm. The best wavelengths for resolution between bees and Varroa mites were considered as 450, 570 and 780 nm. The images are processed outside of the device and are not processed in real time. The algorithm first finds bees while using the Implicit shape model, and afterwards, it tries to find a Varroa mites on the segmented bees only using the convolutional neural network. The proposed solution also allows counting of the bees.

In article [2], Zina-Sabrina Duma et. al. aimed to determine the best wavelengths to distinguish between bees and mites

from hyperspectral data captured using the Specim IQ camera. The bees and mites were illuminated by a custom multispectral LED unit, where brightness of individual LED wavelengths was adapted to Specim IQ hyperspectral camera chip sensitivity. To find the best wavelengths, the authors utilized the Principal component analysis (PCA) with K-means++ followed by the Kernel flow partial least squares. The best wavelengths were considered as 493, 499, 508 and 797 nm.

U-net is a semantic segmentation architecture proposed by Olaf Ronneberger et. al. [3]. Semantic segmentation is a computer vision task in which the model assigns every pixel to a particular category. In U-net architecture, every cell in decoder is combined with corresponding cell from encoder. The predictions of the model are more exact thanks to this. One cell consists of two convolutional layers and max pooling layer in encoder or upsampling convolution in decoder. Every convolution si followed by ReLu activation function. This architecture does not have fully connected layer.

III. Materials and methods

A. Experimental hardware

To collect a dataset, we modified an existing beehive monitoring device Fčielka-Thor 2000, which is described in [4]. The current version is Fčielka-Thor 3000 (Figure 1).

We modified the illumination unit (Figure 2), which now comprises three rows, each containing 24 LEDs emitting at 500 nm (turquoise), 780 nm (infrared) as proposed in [2], and cold white for the general purposes. This unit is controlled by three PWM modules consisting of two parallelly connected MOSFET transistors AOD4184A, Raspberry Pi Pico and Raspberry Pi 4B. We measure the emitted light spectra of the utilized LEDs, which is shown in the Figure 3. Our goal was to propose serial-parallel connection, in which the LED voltage is 0.1 V lower than declared LED maximum in datasheet.

Photos were captured by Raspberry Pi HQ camera with the removed IR filter from the sensor. In the previous version, photos were captured continuously, and only image frames different from the last one were saved on the disk. In this version, the device waits for the button-triggering signal, and on each trigger, it takes three photos of three different illumination (white, infrared and turquoise). The photos are

Fig. 1. Fčielka-Thor 3000 mounted on the beehive.

Fig. 2. LED illumination unit.

processed with the image calibrator module after the capture. The device also contains microphone and environment sensors (such as temperature, humidity and CO_2), but these data were not used in the current research.

In the expected use-case, the bees will walk through the tunnels, which will separate them for an easier processing. Bees will be captured from the above in three different images using one selected illumination.

B. Dataset

Our dataset consists of 647 photos and is divided into 2 main parts: Photos of dead bees and dead mites before treatment and after treatment with fumigation. Both parts have 3 categories: Bees, mites and bees with mites. Bee and mite samples were collected in November 2024 and during the dataset capture, they were approximately 2-3 weeks old.

All samples were collected in the location of Těšínky, CZ. More details about the dataset are shown in Table I. To collect the dataset, we used around 25 bees and 20 Varroa mites in
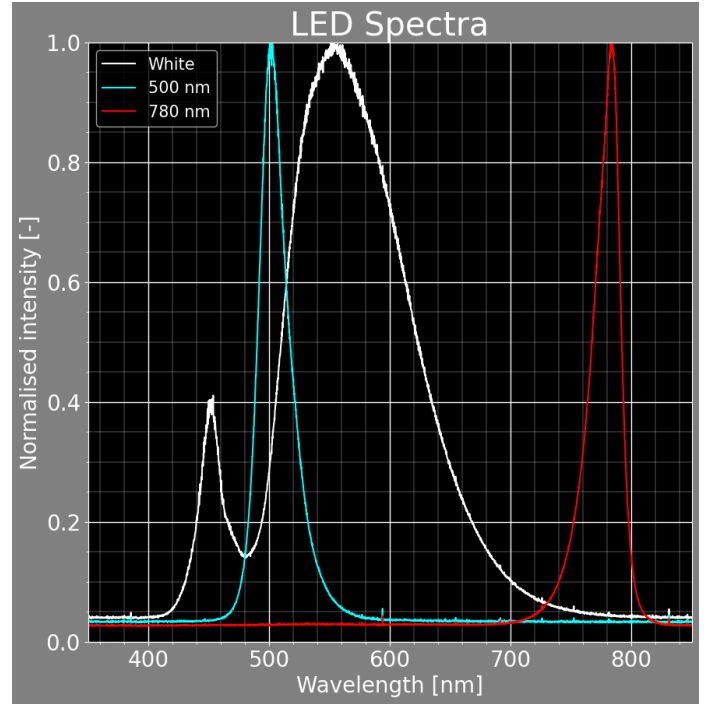

Fig. 3. Measured LED spectra.

total. The photos of bees were taken from ventral, dorsal, left and right side. An example of all illumination of our dataset is shown in Figure 4. All images have a uniform size of 1116×300 pixels.

The dataset can be found in [5]. To utilize the dataset for the U-net training, we annotated it in LabelStudio tool [6]. Export format was set as the three channels image, where every channel belongs to another category (blue - background, green - bee and red - mite). Because the bees were dead, we could use the same masks for the each of the illumination colors. Images were also annotated in the YOLO dataset format using the bees and mites classes.

TABLE I
NUMBER OF PHOTOS IN EACH CATEGORY

Category	Mite	Bee	Bee with mite
Before treatment	78	110	113
After treatment	113	113	120

C. Evaluation metrics

To evaluate the U-Net segmentation masks and the mite detections, we designed our own metric called Satisfied Bee Metric (SBM). As we just need to know, if the mite is present on the bee and we do not have to know its exact position, use of the common metrics could be misleading.

For every mite in prediction, the algorithm looks for intersection with the mite in the corresponding ground truth image. If a match occurs, the detection is considered as a true positive case. If a no intersection is found, it is considered
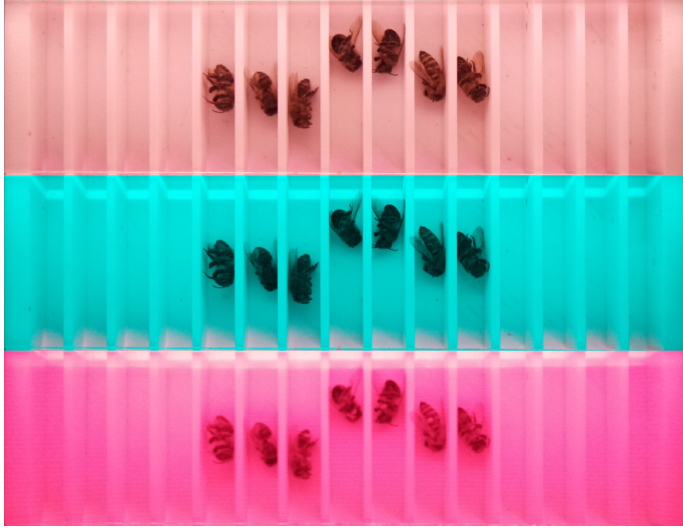
Fig. 4. Example of photos in dataset.

as a false positive case. Afterwards, the algorithm takes every mite in ground truth image and searches intersection in the predicted image. If an intersection is found, nothing happens as the mite was counted in previous search, but if not, this case is considered as a false negative.

IV. EXPERIMENT DESCRIPTION

A. Conventional computer vision based approach

As the mites under turquoise illumination almost coincide with bees, we also tried conventional methods without an use of a neural network. Conventional methods have an advantage in their speed and explainability but they also have a great disadvantage - as the live bees will move, such measurements and experiments will be challenging. These problems will result in different positions of bees in infrared and turquoise image. As we do not have a dataset on live bees, the experiments were performed only with static bees.

After capturing the photos, we convert them into grayscale format and we subtract a background static image from the captured photo. Afterwards, we make an absolute value of these intermediate results and we perform binary thresholding. In the next step, we multiply the infrared image by two, and we subtract it from the previously modified image. Finally, we perform a morphological opening and binary thresholding again. Pixels with the True value belong to Varroa mites and those with the False value belong to the background or bees. The proposed algorithm is shown in the Figure 6. Sadly, this approach did not perform as expected, because it is quite hard to define the right thresholds, which are different in every image. Besides it, the performance of our proposed model could be decreased by dirty from pollen or some another insect which can go through tunnels to beehive, for example ants. This method have also a lot of false positive and false negative cases, so we utilized only the results from semantic segmentation, which is described in the section bellow. We assume, that machine learning algorithm will be better, because

our proposed conventional method works only with individual pixels, while machine learning method see every pixel value in some context.

B. Semantic segmentation based approach

In order to find the *Varroa destructor* mites, we utilized a modified U-net semantic segmentation framework available from [7]. For training, a Cross entropy loss is used. The network was trained on a computer with CPU AMD Ryzen 5 5600X with 64 GB RAM and GPU NVIDIA GeForce GTX 1060 with 3GB RAM. We trained 40 epochs in total, with batch size=1, learning rate=0.0001. The size of the images was scaled to 0.5 in both dimensions. 10% of the images were used as validation data. One epoch training took about 2:20 - 2:40 minutes. Because the Varroa mite is not visible in the turquoise images, we decided to train the model only on images of bees illuminated by infrared color.

V. EXPERIMENTAL RESULTS

In Figure 5 is shown the output of our model trained on infrared data (780 nm). Our model was trained by 40 epochs. The results were achieved during the epoch 20. Table II left shows a confusion matrix for this model on every image of training data. Table II right shows confusion matrix on every training image without the individual mites, because in real case scenario, mites will occur on the bees.
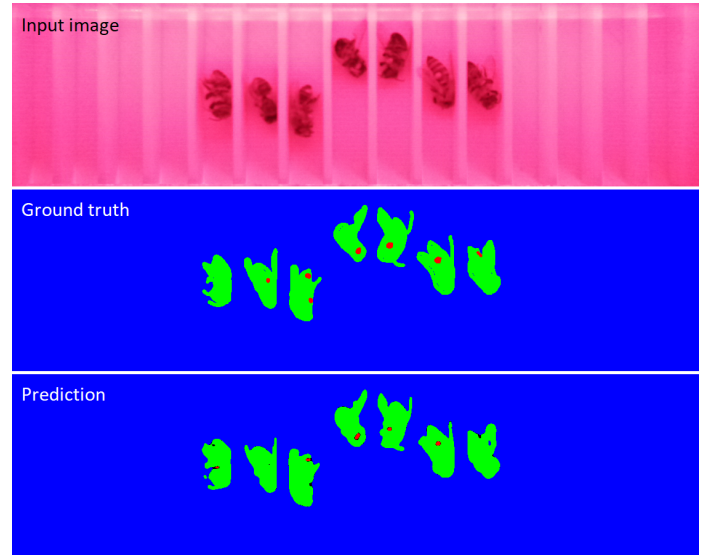

Fig. 5. Output of the U-net model.

TABLE II
CONFUSION MATRIX OF U-NET WITH (LEFT) AND WITHOUT (RIGHT)
INDIVIDUAL VARROA MITES

-	Predicted	
GT	TP=1893	FN=588
	FP=207	TN=0

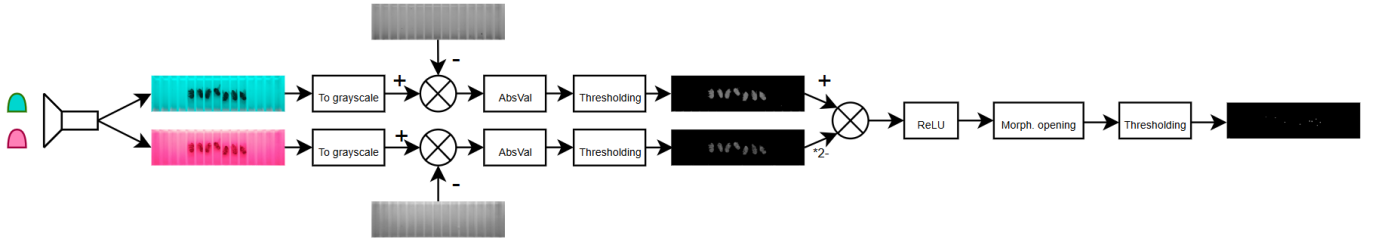| -	Predicted	
GT	TP=954	FN=513
	FP=204	TN=0

Fig. 6. Algorithm of conventional computer vision based approach.

VI. Discussion

The goal of our research is to detect the *Varroa destructor* mites as much accurate as possible. On the other hand, the false positive detections should be kept low as the false alarms tasks the beekeeper and they might result in an unnecessary interventions to the hive. Based on this assumption, we record the detected object as Varroa mite only in the case that it contains more pixels than a certain threshold. As greater the area of mite is, the bigger is the confidence of our model. Such filtered results are shown in Table III. We can see that the number of false positive cases rapidly decreases up to about 5% of the original value, but we also increased the number of false negative cases. The probability, that our model will detect real mite is around 55% as shown in Equation 1, which has to be improved in our future research.

$$\frac{TP}{TP + FN} = \frac{806}{806 + 661} = 55\% \tag{1}$$

TABLE III
Confusion Matrix of U-net without mites smaller than 20 pixels

-	Predicted	
GT	TP=806	FN=661
	FP=10	TN=0

Our model reaches inference time to process one capture from 5 up to 6 seconds when using the rPi 4B with Bullseye 64-bit OS and 4GB of RAM. This should be improved by using a more powerful computational hardware, or a rPi in combination with the HW accelerator.

VII. Conclusion

In this paper, we modified an existing beehive monitoring device to capture images of the bees illuminated by turquoise, infrared, and cold white color. Afterwards, we collected a dataset of photos of dead bees and mites. We utilized these photos to train an U-net, a semantic segmentation architecture. As a result, we reached the probability 55% that our model will assign real mite pixels to the *Varroa destructor* class. We also tried a conventional computer vision based approach, but the results were not satisfactory and the real use would be limited as our proposed approach requires two overlaying captures of bees under various illumination conditions. Such overlay would not be possible in the real conditions as the bees will move and besides the reasons described in Section IV-A, it would increase the inaccuracy of this approach.

In our future research, we would like to accelerate our model and improve its accuracy. The high false negative rate is the most problematic aspect of our study, but in our future research, we will try to combine more illuminations in order to better distinguish mites from the background and bees. In combination with an improved loss function, these factors could improve the accuracy and reduce the false negative cases.

For a practical application, a metric for planning the medical intervention depending on the number of detected mites has to be tested or developed. Such metric has to be developed in cooperation with a veterinary expert, but it could be based for example on the metric presented by [1] in a similar experimental setup.

We also would like to collect a dataset on live bees with a new Raspberry Pi Camera 3 with autofocus, which would solve the blury outputs while capturing in the IR band.

References

[1] Per Kryger, Kim Bjerge, Carsten Frigaard, Peter Mikkelsen, Thomas Nielsen, and Michael Misbih. A computer vision system to monitor the infestation level of varroa destructor in a honeybee colony. *Computers and Electronics in Agriculture*, 164, 07 2019. doi:10.1016/j.compag.2019.104898.

[2] Zina-Sabrina Duma, Tomáš Zemčík, Šimon Bilík, Tuomas Sihvonen, Peter Honec, Satu-Pia Reinikainen, and Karel Horak. Varroa destructor detection on honey bees using hyperspectral imagery. *Computers and Electronics in Agriculture*, 224:109219, 07 2024. doi:10.1016/j.compag.2024.109219.

[3] Olaf Ronneberger, Philipp Fischer, and Thomas Brox. U-net: Convolutional networks for biomedical image segmentation. *CoRR*, abs/1505.04597, 2015. URL: http://arxiv.org/abs/1505.04597, arXiv:1505.04597.

[4] Jakub Nevláčil, Šimon Bilík, and Karel Horak. Raspberry pi bee health monitoring device, 04 2023. doi:10.48550/arXiv.2304.14444.

[5] Samuel Bielik, Simon Bilik, and Tomas Zemcik. Bee dataset but-hs2, 2025. URL: https://www.kaggle.com/dsv/10996316, doi:10.34740/KAGGLE/DSV/10996316.

[6] Maxim Tkachenko, Mikhail Malyuk, Andrey Holmanyuk, and Nikolai Liubimov. Label Studio: Data Labeling Software, 2020-2022. Open source software available from https://github.com/heartexlabs/label-studio. URL: https://github.com/heartexlabs/label-studio.

[7] Alexandre Milesi. Pytorch-unet. https://github.com/milesial/Pytorch-UNet, 2018. Accesed: 2025-01-15.

Metaheuristic Planner for a Swarm of UAVs

1st Jan Čtvrtníček
Department of Control and Instrumentation
Brno University of Technology
Brno, Czech Republic
xctvrt06@vutbr.cz

2nd Jiří Janoušek
Department of Theoretical
and Experimental Electrical Engineering
Brno University of Technology
Brno, Czech Republic
xjanou09@vutbr.cz

Abstract—Unmanned Aerial Vehicles (UAVs) have become an important component in various applications, such as filmmaking or area surveillance. Many modern applications employ autonomous flight of UAV swarms, which offer advantages but also pose constraints. This paper is focused on research and testing of different metaheuristic algorithms used for swarm path planning. Specifically, this study compares the performance of Genetic Algorithm (GA), Ant Colony Optimization (ACO), Tabu Search (TS) and Gravitational Search (GS) in solving UAV path planning problem. The proposed path planner aims to generate near-optimal trajectories for area coverage while avoiding collisions within the swarm.

Index Terms—UAV, metaheuristic, swarm, path planning, optimization

I. Introduction

From home filmmaking or hobby flying to building inspection or military use, Unmanned Aerial Vehicles (UAVs) have become an integral component of modern technological applications. Among these applications, area surveillance was chosen as the focus of this research paper. This domain of usage has many different options, ranging from single UAV flying in parallel lines to swarms of UAVs using complex path planning.

Creating optimal paths for multiple UAVs can become an increasingly difficult task with the growing size of the swarm. Using exact methods guarantees optimality within a finite computational time, but the time to find this solution is often too long to be usable in normal use cases. Metaheuristic algorithms are a great alternative to exact methods, since they focus on finding near-optimal solution while maintaining short computational times.

The focus of this article is to explore different metaheuristic algorithms and compare their capabilities used in swarm path planning. Metaheuristic algorithms are generic in their nature and can be easily modified to plan near-optimal paths. The optimal solutions can be decided on a number of criteria, for example the shortest flight path or lowest energy consumption.

This research is motivated by the need for efficient UAV swarm coordination to enhance coverage efficiency while minimizing computational cost and energy consumption. Given the limited flight endurance of UAVs, finding an optimal solution is a great asset when exploring large areas and enables UAVs to work more effectively. By systematically evaluating different metaheuristic techniques, this research aims to provide insight into their strengths, weaknesses, and applicability in UAV swarm coordination.

II. Metaheuristics

A metaheuristic is a general framework providing a set of rules and strategies for developing heuristic optimization algorithms, regardless of the specific problem. As the name suggests, metaheuristic algorithms belong to a broader category of heuristics, which are mathematical and computational techniques designed to find solutions more quickly compared to classic methods. However, a key limitation of heuristic approaches is the reliance on prior knowledge about the problem being solved. This results in an algorithm tailored for a specific problem, making them ineffective if the problem's parameters or criteria change [1], [2], [3].

Metaheuristic algorithms extend heuristic methods, with the prefix "meta" implying higher-level or beyond-heuristic approach. Unlike heuristics, metaheuristics are problem independent, allowing them to be applied across a wide range of optimization problems. However, compared to exact numerical methods, metaheuristics do not guarantee finding the global optimal solution for a given problem. Instead, they are used to produce satisfactory solutions much faster and with lower computational effort [4], [5].

Technical literature offers various criteria for classifying metaheuristic algorithms. Some of the most common classifications are:

- Nature-inspired vs. non-nature-inspired
- Single-solution vs. population-based
- Deterministic vs. stochastic
- Local search vs. global search

These classifications often overlap and primarily serve more as an indicator of the algorithm's inspiration or functional capabilities. For instance, Ant Colony Optimization (ACO) is a population-based method inspired by foraging of ants looking for food.

The classification approach depicted in Fig. 1 is based on multiple technical sources. It is widely used due to its simplicity and clear outline for algorithm division. Another addition to the diagram shown in figure 1 could be implementing hybrid algorithms, which have recently gained popularity for their effectiveness when solving optimization problems. These algorithms are created by implementing features of two or more different metaheuristic methods from other categories,

combining their strengths while avoiding downfalls. However, hybrid algorithms fall outside the scope of this article and will not be examined [4], [5]. For purposes of this article, one algorithm from each category (evolutionary, swarm, physics-based and human-based algorithms) is chosen and implemented for UAV path planning with subsequent evaluation.
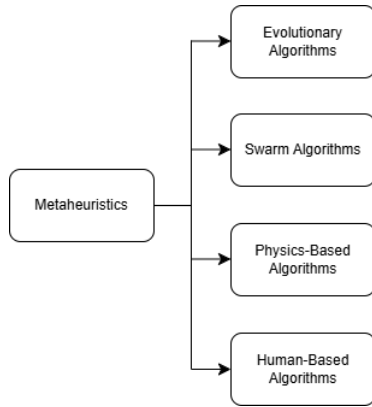

Fig. 1. Metaheuristic Algorithms Classifications [4] [5]

A. Evolutionary Algorithms

Evolutionary algorithms are a class of metaheuristics inspired by the process of natural evolution. The different algorithms belonging to this category are all based on a concept, where individuals within a population compete for a limited amount of resources and only the fittest survive. The cycle of evolutionary algorithms involves initialization of population containing possible solutions and subsequent evolution through selection, mutation and recombination. The termination condition can be either finding an acceptable solution or reaching the limit of iterations. The concept of evolutionary algorithms can be applied to a variety of problems that require finding maximal or minimal solution. The fitness of current population can be determined by different criteria, but for purposes of path planning, the shortest path will be considered the best. Some common algorithms would be Genetic Algorithm (GA), Evolutionary Strategies (ES) or Differential Evolution (DE) [4], [6], [7].

B. Swarm Algorithms

Swarm Algorithms belong to a category of population-based artificial intelligence inspired by the behaviour of animals, such as ants, bees or birds. Essential part of these algorithms is the cooperation of decentralized self-organized systems, where individuals interact with their environment and subsequently share this information with each other to achieve a common goal. The process of swarm algorithms mainly consists of exploration and search. During exploration phase the goal of individual particles is to move through the defined space and using different communication channels detect, verify and broadcast data to their neighbours. Subsequently during search phase each individual in the swarm determines the best direction in which they should travel by combining the collective

data of the swarm. Swarm algorithms are generally different from each other, but they share some common denominators, which are:

- Decentralization - there is no centralized control over the system and each agent follows simple rules based on local information and interactions with neighbours
- Self-organization - individuals interact with their environment and each other to form a structure from the collective behaviour of the system
- Adaptation - system is capable of adapting to changes in environment by adapting the behaviour of individuals or creating new behavioural structures

Examples of swarm algorithms are Ant Colony Optimization (ACO), Particle Swarm Optimization (PSO) and Bee Colony Optimization (BCO) [4], [8].

C. Physics-Based Algorithms

Physics-Based Algorithms are a type of metaheuristics inspired by physical or chemical laws and principles. By exploiting concepts such as energy or force, they guide the search for optimal solutions in defined problem space. When solving more complicated tasks some simpler metaheuristic algorithms can fall short of finding an acceptable solution. Using complex principles of physics or chemistry, physics-based algorithms offer a unique approach to optimization for complicated problems with large search spaces and multiple goals, from scheduling to image processing. Instances of these algorithms are Gravitational Search Algorithm (GSA), Electromagnetic Field Optimization (EMO or EFO) and Big Bang-Big Crunch (BB-BC) [4], [9].

D. Human-Based Algorithms

Metaheuristics based on human behaviour are a class of optimization techniques applying aspects of human intelligence, including knowledge and experience. Using human aspects is effective when solving complex problems, and these algorithms can often find high-quality solutions faster than other more traditional optimization techniques [4]. This category of metaheuristics can be difficult to classify, mainly due to lack of usable sources. Different articles often disagree on classification of algorithms. For the purpose of this research Tabu Search (TS), Cultural Algorithm (CA) and Harmony Search (HS) were chosen as examples of this category.

III. UAV PATH PLANNING

Autonomous UAV path planning is an essential task in various applications, including building inspections or area surveillance. There are several approaches to path planning and this article is focused on area surveillance (coverage of an area) using a swarm of UAVs.

The goal of a coverage path planner is to create a flightpath that will cover the entirety of target environment while considering UAV's motion restrictions and sensor's characteristics. Different methods can be applied for this type of planner, but the best way for a metaheuristic-based planner is to divide the given area into regular cells. The size of these cells

is determined by the flight altitude of a UAV and sensor characteristics (field of view (FOV) and aspect ratio). This coverage footprint is calculated using equations (1), (2) and (3).

$$D = 2 \cdot x \cdot \tan\left(\frac{\theta}{2}\right) \tag{1}$$

$$A = \frac{D}{\sqrt{1+r^2}} = \frac{2 \cdot x \cdot \tan\left(\frac{\theta}{2}\right)}{\sqrt{1+r^2}} \tag{2}$$

$$B = r \cdot A = \frac{2 \cdot r \cdot x \cdot \tan\left(\frac{\theta}{2}\right)}{\sqrt{1+r^2}} \tag{3}$$

Here, D represents footprint diagonal and A and B are footprint width and height, θ is the field of view, x is flight altitude and r is aspect ratio [10], [11].

A. Polygon division

As previously stated, the best approach for metaheuristic-based planner is to generate a set of exploration points within given polygon. There are multiple approaches to creating points for a swarm of UAVs. One approach is to divide the polygon into a certain number of smaller sub-polygons given by the number of used UAVs and subsequently create points inside these sub-polygons. Another option is to create cells for the entire polygon and dividing these into clusters using clustering algorithms. Point sampling can also be achieved by applying different methods, such as square or hexagonal grid, or Poisson disk division. Since exploring multiple options for polygon division would be beyond the scope of this article, an approach based on Poisson disk division and k-means clustering was chosen.

IV. Metaheuristic path planner

The goal of this article is to create coverage path planner using metaheuristic algorithms. The task of visiting every point generated within the polygon is known as Travelling Salesman Problem (TSP) and research of metaheuristic algorithms was aimed to cover this task. Testing was done on a non-convex polygon with 5 UAVs specifically using GA, ACO, GSA and TS. The fitness of these algorithms was evaluated by the total length of a path.

A. Genetic Algorithms (GA)

Genetic Algorithm is a global search optimization technique inspired by the principles of natural selection and evolution. This process is simulated through the operators of selection, mutation and recombination on a given population. The population of possible candidate solutions, where each candidate is usually coded as a binary string called a chromosome. For TSP each candidate would correspond to a cell in polygon. The initial population is randomly generated and through generations (iterations) new trajectories originate [12].

The final planner utilizing GA, as shown in Fig. 2, demonstrates partial success in path planning. Despite parameter
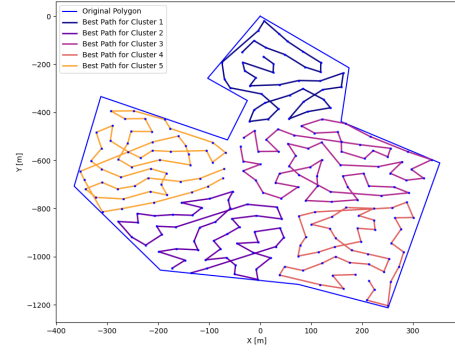

Fig. 2. Genetic Algorithm Paths

refinement, the resulting trajectories are not optimal enough and intersect. Using GA has proven to be a viable approach, but some improvements are necessary to improve solutions. Implementing elitism (picking best individuals from the population for crossover) could significantly improve path planning.

B. Ant Colony Optimization (ACO)

Ant Colony Optimization is a swarm based metaheuristic mimicking the foraging behaviour of ants. Ants are social insects living in colonies and their behaviour is driven by the common goal of colony survival. When searching for food, ants initially explore their surroundings in a random manner, leaving a trail of chemical pheromones. Other ants can smell this pheromone and decide, with a certain probability, to follow this trail. ACO implements this behaviour. When using this for TSP, paths between points have each their pheromone level (all same at the beginning). When creating a path, points are selected with a probability based on the distance and pheromone level. After a trajectory is created, it is evaluated by its length and pheromones between points are updated [13].
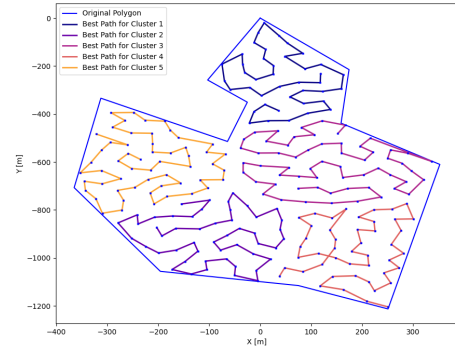

Fig. 3. Ant Colony Optimization Paths

The planner utilizing ACO, as shown in Fig. 3, generates near-optimal trajectories, even with basic parameter settings. During testing, the best results were achieved with higher number of individuals in the swarm and fewer iterations. Swarm algorithms appear to be highly effective for coverage path planning, since they create large number of solutions within a relatively short time.

C. Gravitational Search Algorithm (GSA)

Gravitational Search Algorithm is based on the law of gravity. In this system each agent is considered an object and his performance is measured by his mass. These objects then attract each other by the force of gravity. This force causes a global movement towards heavier objects and these heavy masses correspond to good solutions. By adjusting gravitational constant, the system should be refined to find better solutions [14].
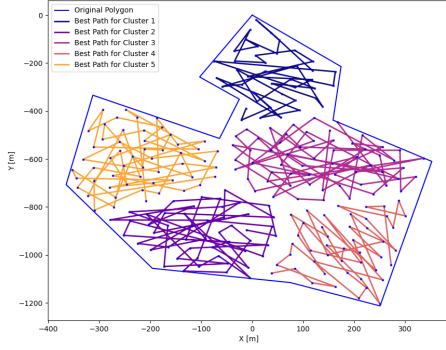

Fig. 4. Gravitational Search Algorithm Paths

The final implementation of GSA shown in Fig. 4 clearly demonstrates its failure in generating optimal coverage paths. Although the algorithm did not perform as expected, it may still have potential applications. This algorithm proved to be highly sensitive to parameter tuning, as even minor adjustments resulted in significant behaviour changes.
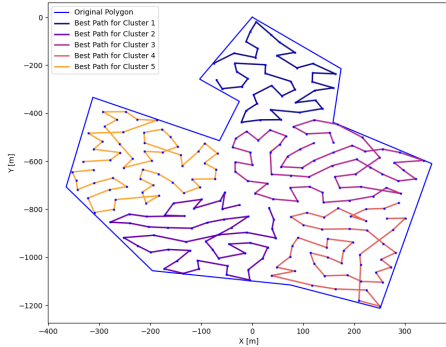
D. Tabu Search (TS)

Fig. 5. Tabu Search Paths

Tabu Search is a local search method using the concept of human memory for solving optimization problems. By utilizing "smart" search and flexible memory, TS is often able to avoid falling into local minimum. Compared to other algorithms, TS starts from one solution or point from which it moves toward the optimal solution. The main part of this algorithm is aforementioned memory, which consists of short-term, mid-term and long-term. Short-term memory is a list of recent solutions, which cannot be revisited before expiration time. Next mid-term memory is a set of rules guiding the

system toward promising areas. And lastly, long-term memory focuses on diversification of the search space and forces the system to explore new areas [15].

The resulting planner, shown in Fig. 5, demonstrates promising path planning performance. The final algorithm generates paths that approximate near-optimal solutions. With further refinements, this algorithm can be viable solution for UAV path planning.

V. CONCLUSION

This research focused on coverage path planning using metaheuristic algorithms. A test software was developed, incorporating Genetic Algorithm, Ant Colony Optimization, Gravitational Search Algorithm and Tabu Search. These algorithms were selected as representatives of their respective classes to ensure diverse testing scope. Each algorithm was initially implemented and refined to achieve an optimal state for comparison. Experimental results show that ACO has the best capabilities for path planning, while TS and GA have both demonstrated potential, but would require further adjustments. GSA had the worst results, likely due to improper adaptation to the TSP or its inefficiency in solving this type of task.

REFERENCES

[1] K. Sörensen and F. W. Glover, "Metaheuristics", in Encyclopedia of Operations Research and Management Science, Boston, MA: Springer US, 2013, pp. 960-970.
[2] V. Fulber-Garcia, "Heuristics vs. Meta-Heuristics vs. Probabilistic Algorithms", Baeldung, 02024. .
[3] "Heuristic (computer science)", Wikipedia: the free encyclopedia, 02001-. .
[4] S. M. Almufti, A. Ahmad Shaban, Z. Arif Ali, R. Ismael Ali, and J. A. Dela Fuente, "Overview of Metaheuristic Algorithms", Polaris Global Journal of Scholarly Research and Trends, vol. 2, no. 2, pp. 10-32, Apr. 2023.
[5] V. Tomar, M. Bansal, and P. Singh, "Metaheuristic Algorithms for Optimization: A Brief Review", in RAiSE-2023, 2024, p. 238-.
[6] Y. S. Perera, D. A. A. C. Ratnaweera, C. H. Dasanayaka, and C. Abeykoon, "The role of artificial intelligence-driven soft sensors in advanced sustainable process industries: A critical review", Engineering Applications of Artificial Intelligence, vol. 121, 2023.
[7] D. D. Martinelli, "Generative machine learning for de novo drug discovery: A systematic review", Computers in Biology and Medicine, vol. 145, 2022.
[8] S. Poudel, M. Y. Arafat, and S. Moh, "Bio-Inspired Optimization-Based Path Planning Algorithms in Unmanned Aerial Vehicles: A Survey", Sensors, vol. 23, no. 6, 2023.
[9] E. Rashedi, H. Nezamabadi-pour, and S. Saryazdi, "GSA: A Gravitational Search Algorithm", Information Sciences, vol. 179, no. 13, pp. 2232-2248, 2009.
[10] T. Cabreira, L. Brisolara, and P. R. Ferreira Jr., "Survey on Coverage Path Planning with Unmanned Aerial Vehicles", Drones, vol. 3, no. 1, 2019.
[11] S. Srinivasan, "Calculating a drone camera's image footprint OR How I learned to love tan again", Technology for Wildlife Foundation, 02019. .
[12] G. Nagib and W. Gharieb, "Path planning for a mobile robot using genetic algorithms", in International Conference on Electrical, Electronic and Computer Engineering, 2004. ICEEC '04, 2004, pp. 185-189.
[13] C. Blum, "Ant colony optimization: Introduction and recent trends", Physics of Life Reviews, vol. 2, no. 4, pp. 353-373, 2005.
[14] E. Rashedi, H. Nezamabadi-pour, and S. Saryazdi, "GSA: A Gravitational Search Algorithm", Information Sciences, vol. 179, no. 13, pp. 2232-2248, 2009.
[15] A. Amuthan and K. Deepa Thilak, "Survey on Tabu Search metaheuristic optimization", in 2016 International Conference on Signal Processing, Communication, Power and Embedded System (SCOPES), 2016, pp. 1539-1543.

MediaPipe FaceMesh use in 3D model-based remote gaze tracking

1st Marek Paták

Institute of Automation and Computer Science
Brno University of Technology
Brno, Czech Republic
217872@vutbr.cz

2nd Pavel Škrabánek

Institute of Automation and Computer Science
Brno University of Technology
Brno, Czech Republic
pavel.skrabanek@vut.cz

Abstract—**This paper presents a model-based approach for remote 3D gaze tracking with unrestricted head movement. The system utilizes MediaPipe FaceMesh for facial landmark detection and RGB-D data from an Intel RealSense D435i camera to estimate gaze direction. A modified Daugman's Integro-Differential Operator serves as a baseline for iris center localization. To simplify screen-camera calibration, a custom camera holder was designed.**

Index Terms—*remote gaze tracking, mediapipe, daugman*

I. INTRODUCTION

Gaze tracking is the process of predicting where a person is looking in real-time, offers a powerful window into human attention and interest. Because gaze can reveal cognitive focus, gaze tracking and estimation techniques have been widely studied and applied across diverse fields. In the advertising market, analyzing eye gaze allows researchers to understand customer preferences and develop more engaging content. Within Human-Computer Interaction (HCI), gaze serves as a valuable input modality, either replacing traditional inputs like a mouse and keyboard or augmenting them to facilitate more intuitive and natural interaction.

3D model-based remote gaze tracking methods solves this issue by calibrating invariant eye features and estimating spatial eye parameters. These approaches leverage the known structure of the eyeball and the principles of spatial geometric imaging models, which is done by combining image and depth information. Usual aproach is to use the Kinect sensor which directly estimate the head pose and gradient based method for iris center estimation [1] [2].

To create more general solution, we will use MediaPipe FaceMesh, which is a convolutional neural network with architecture designed for real-time high-fidelity facial landmark detection, which architecture is based on MobileNetV2 [3], featuring customized blocks optimized for real-time performance. It produces 478 3D facial landmarks, representing the facial surface [4].

We will leverage landmarks from MediaPipe to get the head pose by solving Perspective-n-Point (PNP) pose computation problem. PnP solves the problem of rotation and translation that minimizes the reprojection error from 3D-2D point correspondences (Fig. 1) using camera intrinsic parameters. We use SQPnP solver, a fast and globally convergent non-polynomial PnP solver [5].
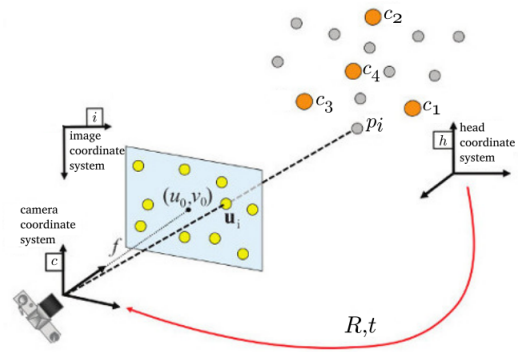

Fig. 1. PNP problem vizualization [6]

II. MATERIAL AND METHODS

A. 3D eye model

The eyeball system (Fig. 2) is approximated by two intersecting spheres: the eyeball and cornea. Both rotate around the eyeball center to change gaze direction [1]. The optical axis $\boldsymbol{n}_o$ is defined by the line connecting the eyeball center $\boldsymbol{e}$, cornea center $\boldsymbol{c}$, and pupil center $\boldsymbol{p}$. The cornea-to-eyeball center distance r_{ce} in adults is approximately 9.2 mm [7]. The gaze direction is represented by the visual axis $\boldsymbol{n}_v$. The deviation angle $\kappa = (\alpha, \beta)$ between the optical and visual axes remains constant as the eyeball rotates around its center. However, the actual gaze direction as well as the offset of the eyeball from the coordinates origin (center of rotation of the head) $\boldsymbol{v}_{he}$ are subject-specific. We summarize the subject-specific in the vector:

$$\boldsymbol{\theta} = (\alpha, \beta, \boldsymbol{v}_{he}) \tag{1}$$

B. Head pose estimation

To model the head, a head coordinate system is introduced with its origin at the center of rotation of the head. The Z-axis points forward from the face, the X-axis extends to the
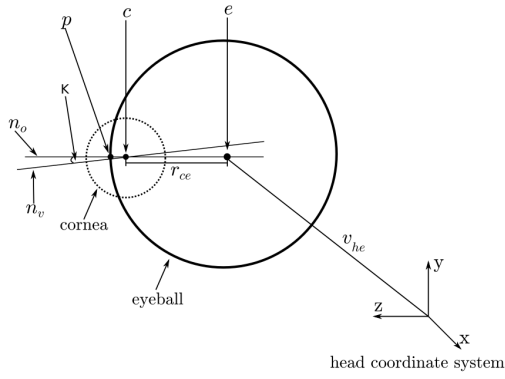
Fig. 2. 3D eye model

left, and the Y-axis points upward. A point in this system is represented as (x_h, y_h, z_h). While head shapes vary among individuals, the rotation center is approximately at nose level [8]. Under this assumption, the nose's x_h, y_h coordinates are set to zero. Its z_h coordinate is initially estimated and later refined using a few images of the subject with different head poses.

A simplified 3D model of the head can be obtained from six landmarks: the right and left eye corner, nose, right and left mouth corner, and chin (Fig. 3). We obtain the facial landmarks from images using the MediaPipe FaceMesh in (x, y, z) format, where x and y are normalized image coordinates, and z represents relative depth [4]. The x, y coordinates are converted to image coordinates x_i and y_i as:

$$x_i = xw \tag{2}$$
$$y_i = yh \tag{3}$$

where w and h are the image width and height, respectively.

The camera coordinates x_c, y_c can be obtained from image coordinates as:

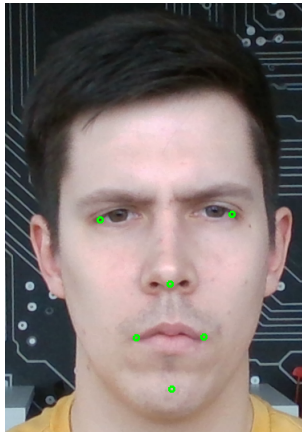$$x_c = (x_i - c_x)z_i/f \tag{4}$$
$$y_c = (y_i - c_y)z_i/f \tag{5}$$

Fig. 3. Example of key facial landmarks

where x_i and y_i are the image coordinates, respectively, z_i is the depth, c_x and c_y are X and Y coordinates of the camera principal point, and f is the focal length of the camera lens.

Points can be transformed from head coordinates to camera coordinates as:

$$\begin{bmatrix} x_c \\ y_c \\ z_c \\ 1 \end{bmatrix} = \begin{bmatrix} r_{11} & r_{12} & r_{13} & t_x \\ r_{21} & r_{22} & r_{23} & t_y \\ r_{31} & r_{32} & r_{33} & t_z \\ 0 & 0 & 0 & 1 \end{bmatrix} \begin{bmatrix} x_h \\ y_h \\ z_h \\ 1 \end{bmatrix} \tag{6}$$

where x_c, y_c, and z_c are camera coordinates, r_{ij} for $i, j \in \{1, 2, 3\}$ are elements of the rotation matrix $\mathbf{R}$, t_i for $i \in \{x, y, z\}$ are elements of the translation vector $\mathbf{t}$. The rotation matrix $\mathbf{R}$ and translation vector $\mathbf{t}$ are estimated using the SQPnP solver.

C. Iris center estimation

We compare two methods for estimating the iris center: MediaPipe landmarks, and Daugman's Integro-Differential Operator.

1) MediaPipe: The last ten landmarks predicted by the MediaPipe correspond to the corners of the iris and the center of the iris for each eye (Fig. 4). To obtain the 3D coordinates of the iris center, the normalized coordinates x, y of the iris center are converted to the image coordinates using (2) and (3), respectively, and $z_i = z$.

2) Daugman's Integro-Differential Operator: Daugman's integro-differential operator searches for the most significant change in the sum of pixel intensities along circles of increasing radius in a grayscale image. This search is performed for all pixels within a specified area, and the iris center is estimated as the pixel with the highest operator response [9].

In this case, the search area is a quadrilateral defined by the iris corner landmarks of the given eye. Since the upper and lower parts of the iris are often occluded by eyelashes, integration is performed only over the quarter circles on the left and right sides of the iris (Fig. 4). The estimated iris center position in the sense of the X and Y axes is given in image coordinates, while the depth is obtained, as described above.
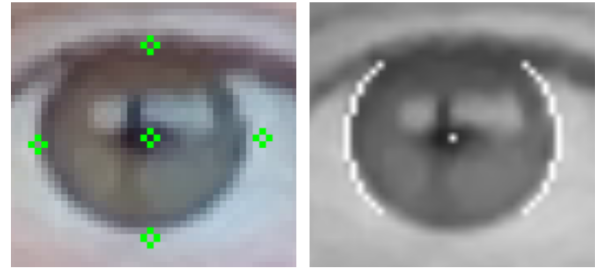

Fig. 4. MediaPipe iris landmarks on the left and modified Daugman algorithm on the right

D. Camera/screen calibration

The Intel RealSense D435i camera is used for image acquisition. A simple camera holder model is designed for capturing
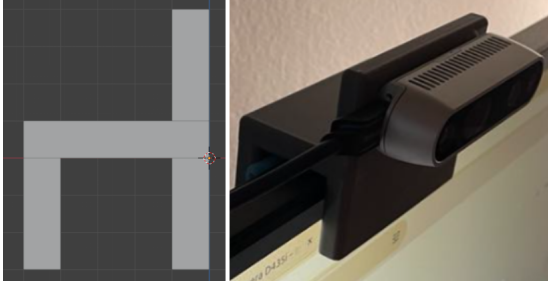
Fig. 5. Cam holder model on the left and real world use case on right

front-facing images, intended to be mounted at the center top of the screen (Fig. 5). The holder is easily 3D-printable.

For screen camera calibration, a point and vector in the camera coordinate system are determined to compute the subject's gaze intersection with the screen. The camera holder ensures parallel alignment of the image and screen planes, setting the screen plane normal $n_s = (0, 0, 1)$.

The offset vector from the RGB sensor's depth start point to the screen center is $v_{cs} = (32.5, 30, -30.85)$, derived from the camera datasheet [10], model parameters, and screen bezel. A point on the top-left corner of the screen is given by $s = v_{cs} + (m_w/2, 0, 0)$, where m_w is monitor width in mm. The monitor plane constant is then computed as:

$$d = -(n_s \cdot s) \tag{7}$$

where $\cdot$ is the dot-product.

E. Gaze estimation

The eyeball center in camera coordinates is computed as:

$$e = Rv_{he} + t \tag{8}$$

Using the eyeball and pupil center, the normalized optical axis is determined as:

$$n_o = \frac{(p - e)}{|p - e|} \tag{9}$$

The cornea center is then obtained by:

$$c = e + r_{ce} n_o \tag{10}$$

The visual axis is given by:

$$n_v = \begin{pmatrix} \cos(\gamma + \alpha)\sin(\delta + \beta) \\ \sin(\gamma + \alpha) \\ -\cos(\gamma + \alpha)\cos(\delta + \beta) \end{pmatrix} \tag{11}$$

where γ and δ describe the optical axis.

With the cornea center, visual axis, and the parametric line equation, the distance from the cornea center to the screen along the visual axis is computed as:

$$t = -\frac{n_s \cdot c + d}{n_s \cdot n_v} \tag{12}$$

The intersection of the gaze with the screen is then given by:

$$i = c + n_v t \tag{13}$$

Before determining the Point of Regard (PoR) on the screen, the intersection is normalized to screen dimensions:

$$i_n = \left(\frac{s_x - i_x}{m_w}, \frac{i_y - s_y}{m_h} \right) \tag{14}$$

where m_w and m_h are the monitor width and height, respectively, in mm. Finally, the PoR is obtained as:

$$g = (i_{nx} r_w, i_{ny} r_h) \tag{15}$$

where r_w and r_h are the resolution width and height, respectively, in pixels.

F. Subject specific calibration

To calibrate subject-specific parameters (1), the user is asked to look at 9 evenly distributed points c with known screen position. The subject-dependent eye parameters are then estimated by minimizing the gaze prediction error:

$$\theta^* = \arg\min_\theta \sum_{i=1}^{9} |g_i - c_i|^2 \tag{16}$$

subject to

$$\theta_l < \theta < \theta_h. \tag{17}$$

The upper and lower limits are chosen to match the possible structure of the human head and eye. Differential evolution is used to solve this optimization problem, ensuring a comprehensive search of the solution space while avoiding local minima.

G. Proposed solution

Our proposed solution consists of three parts (Fig. 6). First, five aligned RGB-D images are captured for feature extraction, where the averaged results provide R and t from head pose estimation and p from iris center estimation. In the second part, these parameters, combined with subject-specific θ, yield the gaze direction described by c and n_v. Finally, the PoR g is determined by intersecting the gaze direction line with the screen, using screen-camera calibration parameters. The PoR is computed separately for each eye, and the final PoR is obtained as their average.
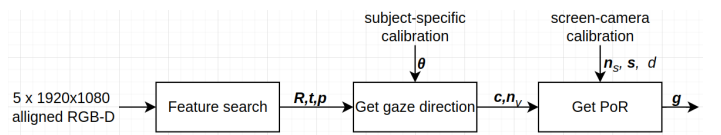

Fig. 6. Pipeline of the proposed solution

H. Dataset

The datasets are stored as .json files, where each testing/calibrating point is stored as an object. Each object has five keys: index, x, y, color_image, test_image. The index stores the index of a point. Keys x and y store the given coordinate of a displayed point (ground truth). Color_image is an array that stores five RGB images of the subject looking at the point losslessly encoded as base64 strings. Depth_image is an array that stores five depth images corresponding to the color images, also losslessly encoded as base64 strings.

I. Test plan

To evaluate the proposed solution, one subject performed the calibration and testing procedure. During testing, the subject sequentially looked at 50 points evenly distributed across ten columns and five rows, with the order randomized for each trial. The test was repeated three times. Throughout both calibration and testing, the subject was free to move their head naturally while ensuring it remained within the camera's field of view.

To evaluate the estimation quality of the proposed method, the angular error is calculated as the absolute difference between the estimated PoR and the ground truth from dataset. Since the conversion to 3D camera space is identical for both methods, the average time required to obtain the 2D coordinates is measured to assess time complexity.

III. Results

The mean, median and standard deviation of the angular errors are summarized for the MediaPipe and Daugman's operator in the Table I and II, respectively.

TABLE I
MEAN, MEDIAN, AND STANDARD DEVIATION OF ANGULAR ERRORS FOR
MEDIAPIPE ON THE TESTING DATASETS.

Dataset	Mean [°]	Median [°]	Std [°]
1.	9.49	8.34	5.12
2.	8.63	8.61	3.92
3.	10.68	10.58	4.72

TABLE II
MEAN, MEDIAN, AND STANDARD DEVIATION OF ANGULAR ERRORS FOR
DAUGMAN'S OPERATOR ON THE TESTING DATASETS.

Dataset	Mean [°]	Median [°]	Std [°]
1.	9.55	8.58	5.04
2.	8.63	8.73	3.80
3.	10.72	10.13	4.78

The average time required to obtain the 2D coordinates using MediaPipe and Daugman's operator is 3×10^{-3} and 40 ms, respectively.

IV. Discussion

The results summarized in Table I and II show that the gaze estimation quality of both methods is comparable. MediaPipe achieved slightly better mean and median values. The high standard deviations reflect the distribution of test points across the entire monitor, where points near calibration positions tend to yield more accurate estimates than those in less-covered areas.

The inference time of the two tested methods differs by four orders of magnitude (40 ms for Daugman's operator vs. 3×10^{-3} ms for MediaPipe). The high time complexity of Daugman's operator is due to its iterative search over multiple pixels and circle radii. In contrast, MediaPipe is optimized for real-time applications.

V. Conclusion

This study demonstrated that MediaPipe is a suitable solution for 3D model-based gaze tracking, as it effectively estimates both head pose and iris center position. The method was tested under challenging conditions, allowing unrestricted head movement, which introduces angular distortions in iris images. To assess its applicability for iris center estimation, MediaPipe was compared with Daugman's integro-differential operator, with results confirming its sufficient accuracy.

A key advantage of MediaPipe is its real-time optimization, enabling the extraction of all necessary data for gaze estimation in a single inference. The precision of the proposed method is comparable to other approaches that do not restrict head movement [11], [12]. However, further research into more precise calibration procedures and more advanced head models for head pose estimation could lead to significantly improved results.

REFERENCES

[1] J. Liu, J. Chi, H. Yang, and X. Yin, "In the eye of the beholder: A survey of gaze tracking techniques," Pattern Recognition, vol. 132, p. 108944, Dec. 2022, doi: 10.1016/j.patcog.2022.108944.

[2] K. Wang and Q. Ji, "Real time eye gaze tracking with Kinect," in 2016 23rd International Conference on Pattern Recognition (ICPR), Dec. 2016, pp. 2752–2757. doi: 10.1109/ICPR.2016.7900052.

[3] M. Sandler, A. Howard, M. Zhu, A. Zhmoginov, and L.-C. Chen, "MobileNetV2: Inverted Residuals and Linear Bottlenecks," Mar. 21, 2019, arXiv: arXiv:1801.04381. doi: 10.48550/arXiv.1801.04381.

[4] "Face landmark detection guide — Google AI Edge," Google AI for Developers. Accessed: Mar. 04, 2025. [Online]. Available: https://ai.google.dev/edge/mediapipe/solutions/vision/face_landmarker

[5] G. Terzakis and M. Lourakis, "A Consistently Fast and Globally Optimal Solution to the Perspective-n-Point Problem," in Computer Vision – ECCV 2020, A. Vedaldi, H. Bischof, T. Brox, and J.-M. Frahm, Eds., Cham: Springer International Publishing, 2020, pp. 478–494. doi: 10.1007/978-3-030-58452-8_28.

[6] "OpenCV: Perspective-n-Point (PnP) pose computation." Accessed: Mar. 05, 2025. [Online]. Available: https://docs.opencv.org/4.x/d5/d1f/calib3d_solvePnP.html

[7] I. T. C. Hooge, D. C. Niehorster, R. S. Hessels, D. Cleveland, and M. Nyström, "The pupil-size artefact (PSA) across time, viewing direction, and different eye trackers," Behav Res, vol. 53, no. 5, pp. 1986–2006, Oct. 2021, doi: 10.3758/s13428-020-01512-2.

[8] N. Yoganandan, F. A. Pintar, J. Zhang, and J. L. Baisden, "Physical properties of the human head: Mass, center of gravity and moment of inertia," Journal of Biomechanics, vol. 42, no. 9, pp. 1177–1192, Jun. 2009, doi: 10.1016/j.jbiomech.2009.03.029.

[9] E. M. Arvacheh and H. R. Tizhoosh, "IRIS Segmentation: Detecting Pupil, Limbus and Eyelids," in 2006 International Conference on Image Processing, Oct. 2006, pp. 2453–2456. doi: 10.1109/ICIP.2006.312773.

[10] "Intel RealSense D400 Series Product Family Datasheet," Intel® RealSense™ Developer Documentation. Accessed: Mar. 06, 2025. [Online]. Available: https://dev.intelrealsense.com/docs/intel-realsense-d400-series-product-family-datasheet

[11] K. A. Funes Mora and J.-M. Odobez, "Person independent 3D gaze estimation from remote RGB-D cameras," in 2013 IEEE International Conference on Image Processing, Sep. 2013, pp. 2787–2791. doi: 10.1109/ICIP.2013.6738574.

[12] K. A. Funes Mora and J.-M. Odobez, "Gaze estimation from multimodal Kinect data," in 2012 IEEE Computer Society Conference on Computer Vision and Pattern Recognition Workshops, Jun. 2012, pp. 25–30. doi: 10.1109/CVPRW.2012.6239182.

Automatic Landing of an Unmanned Aerial Vehicle Using Visual Markers

Tomáš Frigyik
Department of Control and Instrumentation
Brno University of Technology
Brno, Czech Republic
xfrigy00@vut.cz

Abstract—This paper deals with the creation and implemenetation of an algorithm for automatic landing of an unmanned multicopter vehicle using visual markers, incorporating pre-built detection libraries and a suitably equipped vehicle in a simulator. This paper also deals with an introduction to ROS 2 tools, an introduction to localization markers and a PX4 control system for unmanned aerial vehicles as well as the commissioning of software and hardware equipment, the marker detection, its evaluation and design.

Keywords—landing, multicopter, marker, ArUco, detector, ROS 2, PX4, Pixhawk, controller

I. INTRODUCTION

The basic situations that a drone should be able to handle are takeoff, flight itself and solving problems during the flight, and landing. The aim of this work is to create an algorithm that will solve some of these situations. Specifically, it concerns the automatic landing of an unmanned vehicle of the multicopter type. This work deals with software tools and frameworks such as ROS 2, RViz, Gazebo and also PX4, and PX4 bridge. The reader will be introduced to the hardware used within the unmanned vehicle, communication within individual hardware elements, and communication between them. This work also deals with the library for creating applications-ARToolKit and the solution of localization markers ArUco. The drone model will also be shown, the marker scanning algorithm and the evaluation of the scanning landing algorithm will be described, the design and use of the controller, the course of regulation and its evaluation will also be described, some critical states during landing will also be described. At the end of this paper, the further course of the work will be presented.

II. SOFTWARE TOOLS AND FRAMEWORKS

A. ROS 2

To create a landing algorithm based on visual marker detection, it is necessary to create a system that will ensure the launch of the drone landing algorithm, automatic marker detection, arrival over the marker and regulation of the drone's position over the marker throughout the landing process. Because the entire landing system requires multiple partial blocks, such as camera scanning, marker detection and controller and at the same time it is necessary to ensure communication between these blocks, it is appropriate to use the ROS 2 program, which allows individual functional blocks to exchange the necessary information. Part of the communication can take place through nodes. Nodes are able to send data to the desired topic and are also able to subscribe data from the desired topics. Since data are not exchanged directly between nodes, a communication link must be established. Such a connection is provided by a topic. In some cases, it is necessary to trigger an action based on a client request at a given time, while such a request does not occur often. Within ROS 2 are for this type of communication used services. [1]

If it is necessary to display data from a topic and there is no need to process it, it is more time-efficient to just listen to the data from the topic with the *ros2 topic echo* command. If it is necessary to know the number of publishers, subscribers and message type on a given topic, it is possible to use the command *ros2 topic info /topic_name* and the necessary information will be displayed in the terminal. However, if it is necessary to know what a specific message looks like, it is possile to first use the command *ros2 topic info* to find out the message type and then the command *ros2 interface show msg_type*. To find out the content of the message, it is possible to use the repository from ROS 2, common interfaces. If the topic to which messages need to be published is known, along with the message type and content, the command *ros2 topic pub topic_name message_type arguments* can be used to publish the message. This command is useful in case of need to publish the same messages on the topic for a longer period of time by users. In case it is necessary to find out the frequency of data publication, it is possible to use the command *ros2 topic hz topic_name*. This information can be useful when choosing a camera for a given system due to the selection of a suitable camera speed.

In the RViz tool, it is possible to visualize data that is being worked with in ROS 2 or data from the simulator.

B. Gazebo

Gazebo is a simulator which offers libraries and cloud services that make simulation easier. Except of a robot simulation, it enables messaging, service mediation, data logging, sensor models, implementation of model physics, and creation of 3D applications. This simulator was used for testing of the landing algorithm for the drone. [2]

C. Marker Detection Software

The aruco_ros package from PAL Robotics was used to detect optical markers and calculate relative positions. This

software allows the detection of a single marker, multiple markers, or a whole dictionary of markers of different sizes simultaneously. In this work, single marker detection was used, but since multiple markers of different sizes were present, multiple detector instances were used. [3]

D. Firmware PX4 and PX4 bridge

The PX4 autopilot system is open source, other advantages include modularity in application development, the possibility of connectivity with built-in computer vision tools, free use, the possibility of using the ecosystem of supported devices, and implemented safety measures in case of failures. This system is configurable, but its configuration is not necessary in this work. [4]

The main goal of the PX4 bridge is to transfer all the data that is on the MAVLink to ROS 2. It is also desirable that there is no need to deal with MAVLink communication and that all the software that exists on the drone can be used only with ROS 2.

III. HARDWARE AND COMMUNICATION

The main hardware elements of the multicopter are the NUC and Pixhawk, which are connected using the MAVLink protocol, with communication taking place using the UART / USB interface.

A. Hardware

An aerial vehicle with more than two rotors is called a multicopter. There are several types of multicopters, the most common configurations being tricopters with three rotors, quadcopters with four rotors, hexacopters with six rotors, and octocopters with eight rotors. Propellers are attached to the individual rotors, with which the rotors create lift. The direction of flight and the speed of the multicopter can be controlled by controlling the speed of the individual rotors.

NUC is a small compact computer format that consists of a case, power supply, motherboard, RAM and data storage. The user can add RAM, SSD or HDD storage and peripherals. An operating system can be installed on the NUC, on which the ROS 2 program is installed in this work. Although the NUC has small dimensions, it offers relatively high performance and portability, low energy consumption and is environmentally friendly.

Pixhawk creates a set of open hardware standards in the form of schematics that contain components and their interconnections, according to which drone systems are developed. The Pixhawk drone controller is a device for autonomous flight that uses computer vision. The Pixhawk controller can be loaded with various firmwares such as PX4.

In the framework of landing based on optical marks, it is necessary to provide the drone position controller with information about where the given optical marker is located, relative to which the drone position will be regulated. For this purpose, a camera was used

B. Communication

One of the most important building blocks of the system is the communication protocol, through which individual elements can exchange data or indicate the state they are in. If the communication is set up correctly, the data will arrive at the right object or at the right place, have the right shape, parts are not deleted from them and will arrive at the right time. This work uses communication protocols such as the UART and MAVLink and the MAVSDK library, which enables communication between the PX4 bridge and the MAVLink protocol. The UART / USB bus is used for the connection between the NUC and the Pixhawk. In this case, the MAVLink communication protocol is used for both NUC-Pixhawk communication and connection between the Pixhawk and the laptop. The laptop allows MAVLink to be configured and can also serve as a ground station for the drone. The camera communicates with the NUC using the USB standard.

IV. LOCALIZATION MARKERS

For an unmanned vehicle, precise positioning is an essential element, whether during flight as a target position or when landing. As part of positioning, the drone can use GPS data for movement, but with an accuracy of 2 to 5 meters, this may not always be enough, and for specific maneuvers such as landing, it is advisable to consider the use of optical, or in other words, localization markers, each with a unique design.

A. Solutions

There are several visual marker solutions, including open-source solutions available to the ROS community. They include ARTag, ArUco, AprilTag, and Stag. The individual solutions differ mainly in the size of the library and the reliability of detection. Some optical marker solutions, whose individual segments are square, are based on the open-source software library for creating augmented reality applications-ARToolKit. With the help of this library, it is possible to determine the position of the marker relative to the camera coordinate system in real time. It is also possible to track any square pattern of the marker. [5]

ArUco is also based on ARToolKit. The advantage of this solution is the creation of an option for the user, thanks to which it is possible to configure their own library so that it contains only the required number of markers according to needs and therefore it is not necessary for the library to contain all possible markers. The markers in the user-configured library are generated so that they have the largest possible Hamming distance and therefore the largest possible differences between them. Thanks to a smaller marker library, this solution provides a reduction in the time required for the detection of a given marker. Compared to QR markers, ArUco provides a higher level of detectability. [5]

V. SIMULATION AND MARKER DETECTION

A. Drone model and simulation

For the simulation, the Gazebo Garden simulator was used on the Ubuntu 22.04 operating system and a drone model was provided. The essential device that the drone is equipped with is a camera, which can be used to capture optical marks. The drone model from the Gazebo simulator is created in the form of coordinate systems created on the drone components. These are the drone chassis, rotors, and camera, RViz visualizes data

that can be worked with in ROS 2. It is possible to listen to data transmitted from the camera using a combination of the *ros2 topic list* and *ros2 topic echo* commands. For this work, ArUco optical markers were used, which had to be inserted into the simulator. In Fig. 1 are shown the markers inserted into the simulator.

Fig. 1. Drone model with a cascade of ArUco markers in the Gazebo simulator

B. Capturing markers

To capture optical markers, it is first necessary to properly configure each detector by providing information about the camera used, and the ID and size of the marker detected. Messages can be provided using the publisher node. The type of message required can be found using the *ros2 interface show sensor_msgs/msg/CameraInfo* command. As can be seen from Fig. 2, the output of the detector in RViz shows the detection of the markers.

Fig. 2. Marker detection, output from the RViz

To initiate takeoff, the takeoff service must be called using the *ros2 service call* command. A list of available services can be viewed using the *ros2 service list* command. The output from the detector in the terminal is shown in Fig. 3. The detector indicates the relative position with respect to the camera coordinate system. As can be seen, the detector indicates almost zero distance from the camera in the x and y axis directions and a distance of 16 cm in the z axis direction.

Fig. 3. Output of the aruco detector in the terminal

C. Evaluation of captured data

Two square markers, one small with a size of 0.15 m and one large with a size of 0.58 m, were used for detection, with a separate detector for each. The small marker is not reliably detectable above 1.6 meters, because at greater distances its pattern becomes more difficult for the detector to recognize and was used at a height from 0 to 1.51 meters, while the large marker at a height from 1.6 to 4.71 meters. As shown in Fig. 4, as the size of the marker decreases or the drone moves away from it, the accuracy of detection decreases, as the detector can no longer reliably extract key features of the pattern, such as corners and edges, needed for accurate distance calculation. The absolute error was calculated from the height measurements provided by the drone model in the simulation, which reflects the real data of the drone's distance from the camera, and from the height calculated by the detectors.
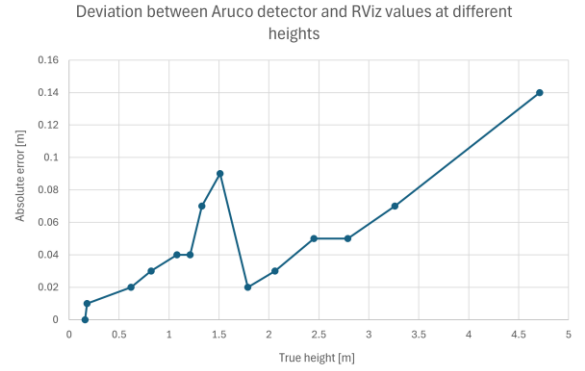

Fig. 4. Accuracy of the Aruco detector

VI. LANDING

A. Landing algorithm

The landing algorithm contains 3 marker detectors that detect the marker in three different height ranges, an action client and an action server and camera info publisher. If any of the detectors recognizes a pattern for the set marker in the camera output data, the action client starts automatic landing using optical markers by sending a goal to the action server. The relevant Aruco detector calculates the relative distance of the marker to the camera, the deviation in the x and y axes is manually calculated so that the drone lands in the center of the marker system with an unchanging layout. The ouput from the detector, the total deviation from the center of the marker system, is the input for the controller, which regulates the speed so that the desired horizontal distance of the drone to the marker, set in the algorithm code, is achieved. At the same time, the landing is set so that the drone, after reaching the minimum horizontal distance in the x and y axes, begins to descend to the height specified by the action goal, while during the descent the algorithm regulates the deviation in the x and y axes by adjusting the speeds. After reaching the desired height, it sets the speed value in the z-axis direction to 0, stops descending and continues to regulate the deviations in the x and y axes.

The algorithm calculates the difference between two consecutively received distances from the detectors throughout its operation. If during landing the processed data is noisy and the difference between two consecutive values is greater than the set threshold value, the action server cancels the goal. The

algorithm also evaluates whether the marker is detected in the current altitude range. If the marker is not detected for longer than the set threshold time, the action server also cancels the goal. If the goal is canceled, the action server sends its canceled status to the action client, sends commands to set zero speeds on all axes, and prevents the drone from descending further. The algorithm ensures that the drone lands at the required height at which it is unlikely that the drone will deviate in the x and y axes after calling the action land. Such a height is currently determined by the simulator, considering the size of the markers, at 0.4 m. Subsequently, the action land is called, which ensures that the drone lands on the ground.

B. Controller design and regulation process

So far, a controller is used for regulation, which contains a proportional component Kp = 0.5. The controller analyzes data regarding the position in the x and y axes of the detector output. Since the detector output indicates the deviation in the x and y axes, the controller multiplies the deviation on each axis by the value of the proportional component and sets the speed. As the detector operates in the image frame and the drone moves in its own robot frame, a transformation is needed. The x-axis of the image frame corresponds to the negative y-axis of the robot frame. Therefore, the drone's speed in the y direction is computed as the negative of the Aruco detector's output in the x direction, scaled by the proportional component. Analogously, the speed of the drone in the x axis direction. As shown in Fig. 5, the automatic landing was initiated at a horizontal distance of 1.06 m and the required control deviation of 0.05 m was achieved after 6.5 seconds. The oscillation at the start of automatic landing was originally larger, but by adjusting the algorithm and gradually increasing speed along a ramp during the drone's acceleration, the amplitude of this oscillation was reduced.
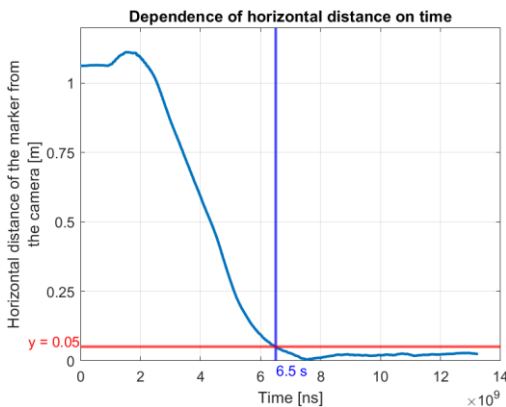

Fig. 5.   Regulation process

C. Landing evaluation

The drone lands above the marker and stops at the required height at which it is possible to launch the action land for touchdown. The algorithm for automatic landing is functional, although not yet maximally effective, but already usable for the simulator and for testing with a real hardware.

VII.   CONCLUSION AND FUTURE WORK

The automatic landing algorithm was implemented and tested in a simulator, it is not yet maximally effective due to the use of a simple, but still sufficient controller, but it is also ready for testing with real hardware in real conditions in which other critical states such as action server failure will be eliminated. Also, because the detection of the aruco detector works on the principle of finding edges and subsequently determining the ID of the marker that contains the given pattern, it is possible to insert aruco markers into the white fields of other markers and thus create a system of nested markers that are more compact than the originally used cascade of markers. The principle of finding edges of the ArUco detector in the image is shown in Fig. 6, inserting the ArUco marker into another ArUco marker is shown in Fig. 7.
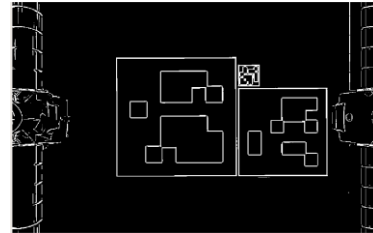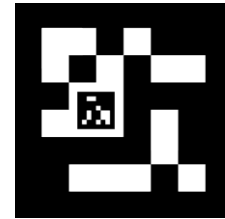

Fig. 6.   Debug output in the RViz

Fig. 7.   ArUco marker inside another ArUco marker

REFERENCES

[1]   *ROS2 Tutorials*. Online. ROS 2 Documentation. 2022. Available from: https://docs.ros.org/en/humble/Tutorials.html. [cit. 2025-03-14].

[2]   *GAZEBO*. Online. GAZEBO. 2022. Available from: https://gazebosim.org/home. [cit. 2025-03-14].

[3]   *Aruco_ros*. Online. GitHub. 2008. Available from: https://github.com/pal-robotics/aruco_ros. [cit. 2025-04-03].

[4]   *PX4 Autopilot User Guide*. Online. PX4 Autopilot User Guide. 2022. Available from: https://docs.px4.io/main/en/. [cit. 2025-03-14].

[5]   KALAITZAKIS, Michail; CARROLL, Sabrina; AMBROSI, Anand; WHITEHEAD, Camden a VITZILAIOS, Nikolaos. Online. In: *Experimental Comparison of Fiducial Markers for Pose Estimation*. 2020. IEEE, 2020, s. 781-788. ISBN 978-1-7281-4278-4. Dostupné z: https://ieeexplore.ieee.org/document/9213977. [cit. 2025-03-14].

Evaluation Possibilities of the Tafel Extrapolation Method

1st Silvia Bátorová
Department of Electrical and Electronic Technology, FEEC
Brno University of Technology
Brno, Czech Republic
xbator05@vutbr.cz

2nd Miroslav Zatloukal
Department of Electrical and Electronic Technology, FEEC
Brno University of Technology
Brno, Czech Republic
zatloukal@vut.cz

Abstract—**The paper explores possible evaluation methods of Tafel slopes on polarization curves. These methods might be suitable for cases where data evaluation beyond the possibilities of regular measuring software is desirable.**

Keywords—*corrosion potential, Tafel slopes, Butler-Volmer equation*

I. INTRODUCTION

In corrosion measurement, Tafel extrapolation is a common method of evaluation. The process involves a three-electrode set-up immersed in electrolyte, consisting of a saturated calomel reference electrode, a platinum counter electrode, and a metallic sample serving as the working electrode. The resulting data carry information about the rate and tendency of corrosion of the measured sample.

In order to get the necessary information from the measured data, there exist some analytical tools built into the measurement programs. However, these tools may sometimes be insufficient, requiring an alternative evaluation method. This paper explores the possibilities of evaluating the data beyond the usual needs of regular measurements.

II. THEORY

Tafel extrapolation is an electrochemical method used in corrosion measurements. It measures the value of corrosion current density i_{corr} (representing the rate of corrosion) across different values of corrosion potential E_{corr} (representing the tendency of the material to corrode). The result is a graph depicting two polarization curves, which represent the cathodic and anodic reactions. The linear regions on these curves are called Tafel regions.

The corrosion current density is found at the intersection of the Tafel lines, while the corrosion potential is located at the lowest point of the polarization curves, where the cathodic reaction turns into anodic [1]. These two variables are crucial in determining the nature of corrosion of the measured sample. Additionally, they can be used in measurements taking place over time, where they may help determine the change in corrosion behavior of the measured material, such as formation of passivation layers.
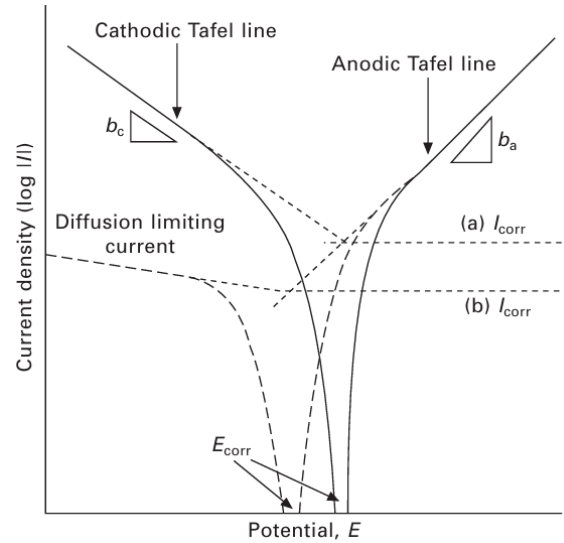
Fig. 1. Tafel extrapolation method on polarization curves [1]

The characteristic shown in Figure 1 is described by the Butler-Volmer equation (1):

$$i = i_0 \cdot \left\{ exp\left(\frac{\alpha_a nF\eta}{RT}\right) - exp\left(\frac{-\alpha_c nF\eta}{RT}\right) \right\} \qquad (1)$$

Where i is instantaneous current density and i_0 is exchange current density (in this case equal to i_{corr}). n is electron number (for this case the number 2 was chosen due to the most likely nature of the occurring chemical reactions). η is overpotential, F is Faraday constant, R is gas constant and T is absolute temperature [1,2]. α_a and α_c are anodic and cathodic transfer coefficients, linked to Tafel slopes b_a and b_c by (2):

$$b = \frac{2.303RT}{\alpha nF} \qquad (2)$$

The transfer coefficients are a number between 0 and 1 and are critical in determining the rate of the reaction [3,4].

III. Linear region detection in Matlab

The first approach includes the creation of a MATLAB program, which can detect linear regions on the polarization curves and fit a line through these regions. Then, on the intersection of these linear regions, a resulting value of corrosion current density can be determined. The program also determines the value of corrosion potential as the lowest point of the characteristic. That allows for easy, automated determination of desired values, while providing an opportunity for further calculations and improvements.

The polarization curves are first split into cathodic and anodic sections at E_{corr}. Then, the linear regions on each side are identified. A sliding window of 10 data points is used, with the program assessing the linearity of each segment. The 10 point window size was chosen empirically, as larger windows caused issues with proper linearity assessment. For each window, the program fits a straight line to the data and a mean square error (MSE) of the fit is calculated. The most linear regions are identified by selecting segments where the MSE value is below 0.5 %. The threshold of 0.5% MSE ensures a balance between determining the most linear regions while avoiding excessive sensitivity to small variations. The linear regions are subsequently fitted with lines, so the value of i_{corr} can be visually identified (the value is also calculated). The part of the code calculating the linear regions of the anodic branch is in Figure 2. The resulting graph is in Figure 3.

```
num_windows_anodic = length(x_anodic) - window_size + 1;
anodic_errors = zeros(num_windows_anodic, 1);

% Sliding regression for anodic branch
for i = 1:num_windows_anodic
    x_window = x_anodic(i:i+window_size-1);
    log_y_window = log_y_anodic(i:i+window_size-1);
    % Linear regression in semi-log space
    coeffs = polyfit(x_window, log_y_window, 1);
    log_y_fit = polyval(coeffs, x_window);
    % MSE
    anodic_errors(i) = mean((log_y_window - log_y_fit).^2);
end

% Most linear region in anodic branch
threshold_anodic = quantile(anodic_errors, 0.005);
anodic_linear_indices = find(anodic_errors < threshold_anodic);

% Combination of linear windows into one
x_anodic_linear = [];
log_y_anodic_linear = [];
for i = 1:length(anodic_linear_indices)
    idx = anodic_linear_indices(i);
    x_anodic_linear = [x_anodic_linear;
    x_anodic(idx:idx+window_size-1)];
    log_y_anodic_linear = [log_y_anodic_linear;
    log_y_anodic(idx:idx+window_size-1)];
end
```

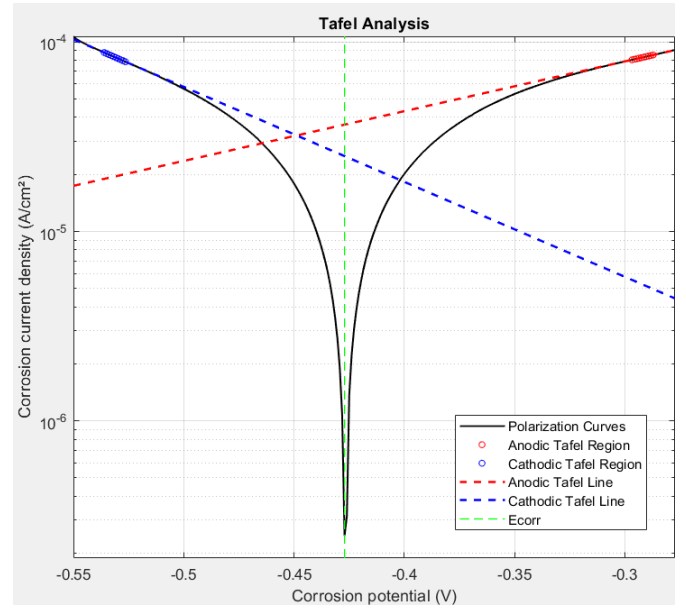Fig. 2. Linear region detection of anodic branch

Fig. 3. Resulting graph from the MATLAB program

Unfortunately, the method comes with certain limitations. In particular, the anodic and cathodic regions do not have identical slopes, which means that the value of i_{corr} does not correspond to E_{corr}. One option is to assume symmetry based on one of the slopes, such as the cathodic slope, though this solution is not ideal. Alternatively, the value of i_{corr} could be calculated as a mean value of i_{corr} of the anodic and cathodic branches. Nevertheless, achieving more precise data evaluation requires an alternative approach.

IV. Butler-Volmer equation calculation in Excel

The second method aims to utilize the Butler-Volmer equation (B-V equation) and fit it to the measured data. The fitting is achieved with the use of Excel Solver, a program within Excel used for advanced calculations. The program changes the variables of the B-V equation in order to make it fit as closely as possible to the gathered data. The result is a set of data, which aligns almost perfectly with the measurement, and it can be further used for additional data analysis.

The calculation process begins with finding E_{corr} and setting the data range to ± 200 mV around that point. The range is set in order to focus on the most important part of the data to make the fitting more accurate. Consequently, Excel Solver is activated to fit the B-V equation to the measured data. The result is an expression with automatically calculated values of i_{corr}, α_a and α_c.

The main advantage of this approach is that the obtained results tend to be more accurate, since they relate more closely to theoretical findings. At the same time, the method allows for filling in the data that are missing in some of the measurements. An example of the approach being used for incomplete measurements is in Figure 4. An example of the measured data is in Table 1.
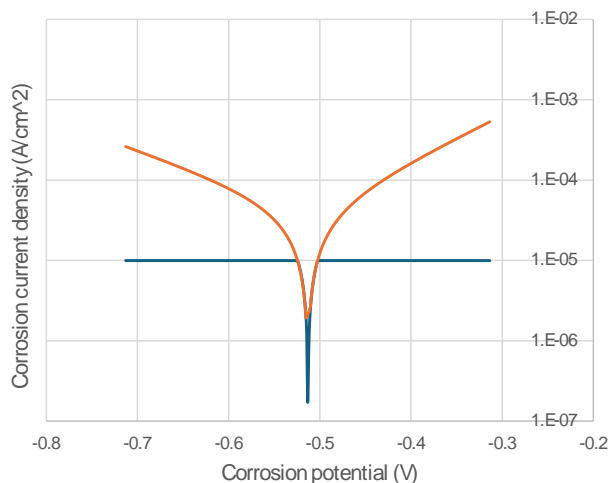
Fig. 2. B-V equation (orange) used for filling in missing data (blue)

TABLE I.   AN EXAMPLE OF MEASURED DATA

Incomplete data set		Complete data set	
E_{corr} (V)	i_{corr} ($\mu A/cm^2$)	E_{corr} (V)	i_{corr} ($\mu A/cm^2$)
-0.404	9.99	-0.650	141.94
-0.403	9.99	-0.649	139.77
-0.402	9.99	-0.648	138.43
-0.401	9.99	-0.647	136.57
-0.400	9.99	-0.646	135.07
-0.399	9.99	-0.645	133.76
-0.398	9.90	-0.644	132.39
-0.397	9.94	-0.643	130.52
-0.396	9.42	-0.641	128.97
-0.395	9.14	-0.640	127.72
-0.394	8.57	-0.639	126.53
-0.393	8.04	-0.638	125.18
-0.392	7.48	-0.637	123.81
-0.390	6.91	-0.636	122.89
-0.389	6.31	-0.635	121.55
-0.388	5.76	-0.634	120.24
-0.387	5.20	-0.633	119.26
-0.386	4.64	-0.632	118.23
-0.385	4.05	-0.631	117.19
-0.384	3.47	-0.630	116.12
-0.383	2.87	-0.629	115.30
-0.382	2.29	-0.628	114.32

The incorrect measurement was caused by inaccurate current limits being set up during the measurement, resulting in the data points above a certain current threshold being omitted and replaced by a constant line at the threshold. Previously, the incomplete measurements could not be included in the measurement results, but with certain calculation modifications, an estimate of the missing data can be created.

For the estimation to be most representative, the values of α_a and α_c are taken from the properly set measurements, each of their means are calculated and the resulting values are used in the equation estimation. The only value changing in the fitting is the i_{corr}. The mean values of α_a and α_c are 0.167 and 0.121, respectively. A mean of all measurements was selected instead of a sample-specific mean due to the limited number of correct measurements available (9). While a global mean might be more statistically reliable, it may not accurately reflect sample-specific differences. Additionally, accuracy could be influenced by the amount of data points missing or the stability of α_a and α_c values. This method also assumes perfect linearity of the polarization curves, meaning unexpected corrosion reactions (such as passivation) would not be represented well.

V. DISCUSSION

The aim of this paper is to explore the possible ways of analyzing polarization curves with the Tafel extrapolation method. In certain circumstances, the evaluation tools in standard measuring software may be insufficient. For instance, some programs only offer Tafel slope analysis performed by manually picking out the linear regions on the polarization curves. However, the obtained results come with an unacceptable amount of uncertainty, which is why an automatic evaluation was necessary to be created.

Two approaches are explored, in particular automated calculation programs in MATLAB and Excel. The former detects linear regions of the polarization curves and calculates essential variables, while the latter utilizes the Butler-Volmer equation to represent the measured data, with the important variables being part of the equation itself. Both methods have their advantages and disadvantages, though for this situation the second method was preferable due to its higher accuracy and option to correct previously unusable measurements. Both of these approaches may be modified for further analysis of the data based on specific needs.

Future work could involve further accuracy assessment and comparison of the two methods. A larger amount of correct data measurements could provide the possibility of employing sample-specific mean values of α_a and α_c, which may provide better estimation accuracy.

215

REFERENCES

[1] S. Hiromoto, "Corrosion of metallic biomaterials," In: M. Niinomi (Ed.) *Metals for biomedical devices.* Cambridge, UK: Woodhead Publishing Limited, 2010, ISBN 978-1-84569-924-6

[2] E. J. F. Dickinson, A. J. Wain, "The Butler-Volmer equation in electrochemical theory: Origins, value, and practical application," *Journal of Electroanalytical Chemistry,* vol. 872, Apr. 2020, doi: 10.1016/j.jelechem.2020.114145

[3] P. Pedeferri, Corrosion Science and Engineering, Cham, Switzerland: Springer Nature Switzerland, 2018, ISBN 978-3-319-97625-9

[4] P. Khadke, T. Tichter, T. Boettcher, F. Muench, W. Ensinger, C. Roth, "A simple and effective method for the accurate extraction of kinetic parameters using differential Tafel plots," *Scientific Reports*, vol. 11 (1), 2021, doi: 10.1038/s41598-021-87951-z

Design and Implementation of an Educational CubeSat Constellation

Clyde Mavhundu
Department of Radio Electronics FEEC
Brno University of Techonology Technicka 12
Brno, Czech Republic
clydetmavhundu@gmail.com

Jiří Veverka
Department of Radio Electronics FEEC
Brno University of Techonology Technicka 12
Brno, Czech Republic
xvever12@vutbr.cz

Abstract—The development of satellite constellations has advanced global communication, Earth observation, and research. CubeSats have emerged as a cost-effective, scalable solution, particularly for educational applications. This Paper explores the design and implementation of an educational satellite constellation consisting of three 1U CubeSats. The constellation operates in the UHF band using the AX.25 protocol for real-time communication and telemetry transmission. The design process for the satellite subsystems includes commercial off-the-shelf (COTS) components explicitly selected to meet design requirements. The Paper also examines inter-satellite communication, mission design, and system performance, adding to the growing field of low-cost satellite deployments emphasizing their educational potential.

Keywords—CubeSat, Satellite constellation, On-Board Computer (OBC), AX.25 protocol, telemetry, Communication systems (COM).

I. Introduction

A constellation is a network of multiple satellites working together in coordinated orbits to achieve a common mission. These satellites operate as a system to provide continuous global coverage, increased data collection, or redundancy. Some common applications are:

- Earth Observation-Disaster response, Weather Control.

- Communication-Internet services.

- Science and Research in Astronomy.

- Defence and Surveillance.

Among the many types of small satellites, CubeSats have gained attention due to their modularity, affordability, and ease of development. These attributes make CubeSats attractive for educational and research applications, enabling students to gain practical experience with satellite technology, mission planning, and system engineering. This thesis presents the design and implementation of an educational CubeSat Constellation consisting of three simplified 1U CubeSats, typically (100x100x100mm), mass <2kgs, intended for real-time telemetry and communication with a ground station. The constellation is designed to operate in the UHF band, utilizing the AX.25 protocol to facilitate reliable data transmission. In contrast to the limited coverage capacity of a solitary satellite, a constellation enables greater coverage and improved mission reliability by ensuring that in the event of a failure or communications blackout in one satellite, the remaining satellites are capable of independent data transmission. Furthermore, the utilization of inter-satellite communication through the RFM98W LoRa transceiver facilitates the relaying of data between satellites, thereby ensuring redundancy and enhancing the probability of successful data delivery. The CubeSat architecture follows the CubeSat Design Specification (CDS) Revision 14 which was published in February 2020. The Design Standard is maintained by the California Polytechnic State University (Cal Poly) [1]. The document defines the dimensions, interfaces, weight and other design requirements for CubeSats. The project includes Schematics, structural and printed circuit board (PCB) design. The Paper draws inspiration from the 2P-sized PocketQube Satellite Demonstrator [2] in the department STEM Laboratory.

II. Cubesat Systems.

Similar to larger satellite systems, CubeSats consist of multiple subsystems that work together to ensure mission success. Each CubeSat in the constellation contains several key subsystems[3]. The Structure acts as a housing for all the components, providing mechanical support and protection. The on-board computer (OBC) acts as the central processing unit, managing data processing, telemetry, and command execution while payloads represent the mission objectives, such as scientific experiments. The Communication System (COM) handles data transfer between the CubeSat, the ground station and other satellites. Finally, the Electrical Power System (EPS) provides power to all subsystems.

A. Structure Design

First, the structure of each CubeSat is designed to be lightweight and durable, focusing on the easy integration of subsystems. CubeSat frames are typically constructed using high-strength alloys, i.e. aluminium 6061, providing mechanical stability and resistance to thermal variations. The structure provides housing for PCBs and satellite components. The outer surface of the CubeSat is equipped with solar panels to harvest energy from the Sun, while an antenna is included for efficient communication with the ground station. For this design, the structure was created using SolidWorks (as shown in Fig. 1).

Finite Element Analysis (FEA) was performed to evaluate the structural integrity under various stress conditions. In the context of the static analysis, both aluminium 6061 and Polylactic Acid (PLA) were used. The former was utilized considering real flight considerations, while the latter was employed for the purpose of basic comparison with our educational prototypes. The structure will be 3D printed using a lightweight PLA, as it is not required to be orbit worthy. The 3D printing process will allow for rapid iteration and adjustment to the design, optimizing for weight, durability, and ease of assembly. The final structure will then be assembled with all subsystems, ensuring that each component fits within the CubeSat's 1U standard form factor. For secure assembly, the structure incorporates precisely placed mounting holes designed for 3M ISO flat head screws and nuts.
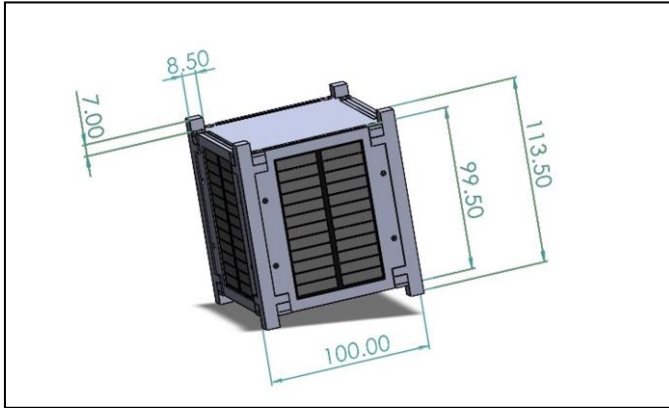

Fig. 1. Designed model of the CubeSat structure in SolidWorks. Units in (mm)

B. On-Board Computer (OBC)

The On-Board Computer (OBC) serves as the central processing unit for each CubeSat in the constellation, handling mission data processing, telemetry management, and command execution from the ground station. The Black Pill development board, which features an STM32F411CEU6 microcontroller [5] was the preferred option. This microcontroller is well-suited for space applications due to its low power consumption, high processing speed, and extensive peripheral support. The 32-bit STM32F411CEU6 Microcontroller features an ARM Cortex-M4 processor (100MHz, 512KB Flash, 128KB RAM) and a floating-point unit (FPU) which enhances scientific computations and data analysis onboard by enabling faster and more accurate processing of floating-point operations. It supports multiple protocols (I2C, SPI, UART, CAN, USB) (as seen in Fig. 2). I2C and SPI enable communication with sensors and POWER management units. UART facilitates easy debugging access. The RF module is connected via SPI. An External EEPROM for Data Logging ensures mission-critical data is stored safely. Even in the event of power resets it retains sensor readings, telemetry, and event logs even without power. This allows the system to recover lost data and resume operations once communication is restored. Temporary communication failures can occur due to signal interference, obstructions, or satellite positioning, making onboard data storage essential for preserving mission data. The Black Pill's small size and weight make it ideal for educational CubeSats, where minimizing mass is crucial.
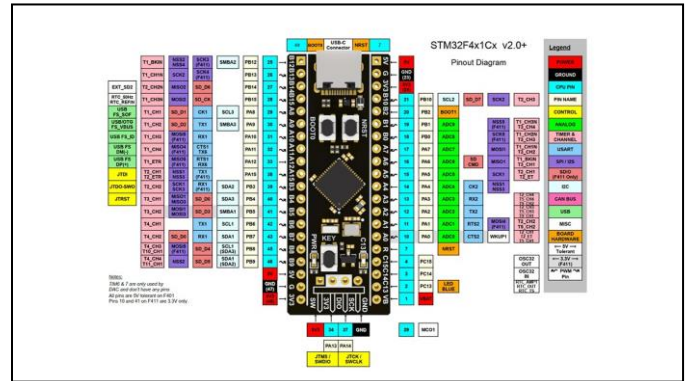

Fig. 2. STM32F411CEU6 Pin out Diagram, The figure shows the pin configuration of the STM32F411CEU6 microcontroller, essential for connectivity. Source: BlackPill development board DFRobot [4].

C. Payloads

The CubeSat constellation was equipped with multiple sensors for real-time telemetry, inter-satellite communication and system monitoring. These include the DS18B20 digital temperature sensor, the 3in1 MPU-9250 inertial measurement unit (IMU) and the INA219 current sensor.

Temperature Sensor – DS18B20

The system was designed to incorporate a DS18B20 digital temperature sensor to monitor internal temperatures. It operates on a 1-Wire communication protocol, making it easy to integrate with the onboard computer. With an accuracy of ±0.5°C and an operating range of -55°C to +125°C, it ensures that electronic components remain within safe temperature limits. The sensor is connected to the OBC via a GPIO.

Attitude Determination Sensors – 3in1 MPU-9250

To determine the orientation of the CubeSat, the system includes the 3in1 MPU-9250 Inertial Measurement Unit (IMU). This sensor integrates an accelerometer, gyroscope and magnetometer to provide accurate attitude data. The accelerometer measures linear motion, while the gyroscope measures rotational speed. The magnetometer senses the earth's magnetic field, helping to stabilise the attitude. The IMU communicates with the OBC via I2C.

Current Sensor – INA219

Two INA219 current sensors were integrated into the system with the objective of monitoring power consumption at critical points within the Electrical Power System (EPS). The first sensor is positioned between the Maximum Power Point Tracking (MPPT) module and the TP4056 charge controller, while the second is situated between the TP4056 charge controller and the Low Dropout (LDO) voltage regulator. The primary function of the first sensor is to assess the efficiency of solar energy conversion and battery charging by monitoring power transfer from the MPPT to the charge controller. The second sensor, situated after the charge controller, ensures accurate tracking of power supplied to the voltage regulator and, ultimately, to the system's load. They operate over an I2C interface and can measure currents up to 3.2A with a 12-bit

resolution. By tracking sudden current spikes, the INA219 helps identify faults such as short circuits or excessive power drawsIt helping track potential overcurrent conditions that can lead to system failures. The INA219 sensor can also be used to measure voltage levels at critical locations in the power system. In this system however , the sensors were not used for this intention. Voltage data, combined with current readings, can allow for accurate power calculations ($P = V \times I$), enabling better energy management and system diagnostics.

The OBC and sensor suite (as shown in Fig. 3), enables precise telemetry and efficient energy distribution. These features are essential for maintaining the constellation's functionality.
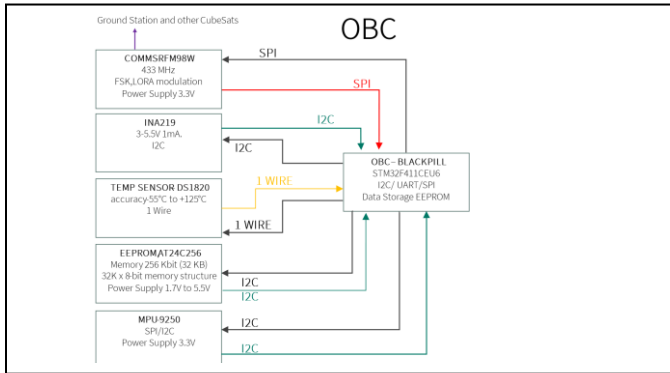

Fig. 3.   Block Diagram of OBC and Sensors

D. Communication systems (COM)

The RFM98W RF transceiver [6] was selected as the primary communications module for the CubeSat constellation because it is a high performance RF transceiver module operating in the required UHF band (410 to 525 MHz) and designed for long range, low power communications. It features LoRa (Long Range) modulation, for robust communications with a high signal-to-noise ratio, even in challenging environments. Its low power consumption of only 120 mA in transmit mode and 11 mA in receive mode makes it ideal for power-constrained CubeSat missions. The RFM98W can be connected to an antenna through an SMA connector soldered onto the PCB. Integrated via SPI, it provides seamless communication with the Ground Station and the other CubeSats. The RFM98W supports LoRa (Long Range) modulation, enabling low-power, long-range communications with a high signal-to-noise ratio. This is critical for CubeSat applications where maintaining a stable link with the ground station is essential. Compared to other RF modules such as the NRF905, the RFM98W offers superior range and signal penetration, ensuring reliable satellite communications. The RFM98W enables inter-satellite communication (as shown in Fig. 4). Use of Packet-Switched Communication or Addressed Broadcast Communication where each message carries a unique identifier (address) to ensure correct reception prevents interference between CubeSats.

AX.25 Protocol Compatibility

The RFM98W supports the AX.25 protocol, a standard for packet-based telemetry and command transmission in amateur radio satellites. Each CubeSat transmits telemetry data, sensor readings, using AX.25 packets. AX.25 ensures reliable data exchange by incorporating error detection and correction mechanisms to minimise data loss in noisy space environments. It also provides efficient addressing and routing, enabling easy ommunication between the CubeSat and ground stations.
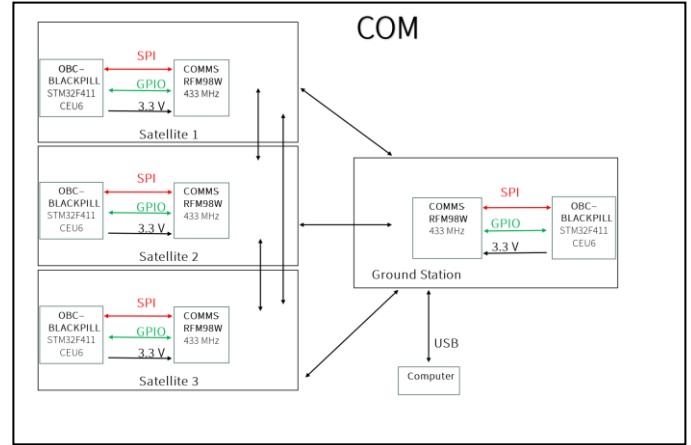

Fig. 4.   Block Diagram of COM;

E. Electrical Power System (EPS)

The EPS is responsible for generating, storing, and distributing power to all CubeSat components. The system was designed to ensure a reliable power supply,considering the Power output of the all the Components (Table 1). The EPS (as shown in Fig. 3) consists of:

- Power generation using solar panels - Power is generated using 4x6W 90x60mm solar panels mounted on the outside of the CubeSat. These panels are connected in 2S2P configuration (2 in series, 2 in parallel). A Maximum Power Point Tracking (MPPT) system optimises power harvesting under varying light conditions.

- Power storage using a Li-ion battery - The EPS uses a single cell 3.7V (Li-ion) 3000mAh Li-ion battery. This battery stores excess energy generated by the solar panels and provides power during normal operation.

- Charge Controller (TP4056) - The charge controller receives power from the four solar panels or an external charger and manages battery charging with a wide input voltage range of 4.5V to 6V and a charge current of up to 1A. It features automatic charging, overvoltage protection and charge status indication.

- Power Distribution with Voltage Stabilizer - The XC6206P332MR LDO voltage regulator provides a fixed 3.3V output, ensuring stable power to low-voltage components. This helps maintain consistent performance across all subsystems.

- Current Monitoring with INA219 Sensor - The current sensors measure current at two key points: between the MPPT and the TP4056 charge controller and between the TP4056 charge controller and the LDO voltage regulator. Operating via I2C, they provide real-time current measurements up to 3.2A and ±1% accuracy.

	Component	Current	Power (P = V × I)
1	STM32 Blackpill (MCU)	300mA	0.99W
2	Dallas DS18B20 (Temp Sensor)	1.5mA	0.005W
3	MPU-9250 (IMU)	1.5mA	0.005W
4	RFM98W (Radio Module)	10.3mA	0.034W
5	INA219 (Current Sensor1)	1mA	0.0033W
6	INA219 (Current Sensor2)	1mA	0.0033W
7	EEPROM (AT24C256)	1mA	0.0033W
8	XC6206P332MR (Voltage Regulator)	1mA	0.0033W
9	Additional Power Losses (Est.)	-	0.05W
	Total	**317.3**	**1.0472W**

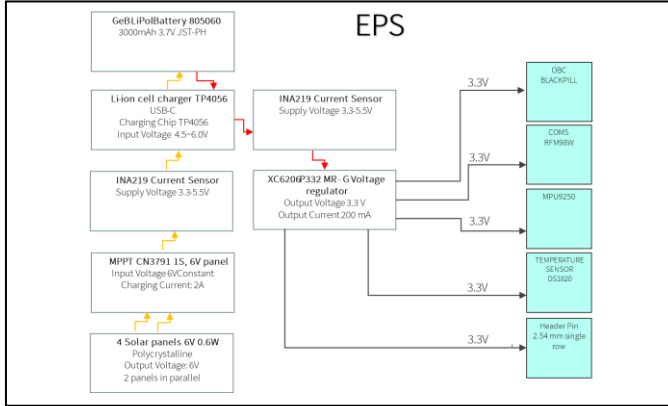a. *Power Output of Satellite Components*

Fig. 5.   Block Diagram of EPS

III. GROUND STATION AND SOFTWARE

The ground station, similar to the CubeSats, is designed to receive telemetry via an RFM98W RF module and antenna operating at 433MHz. This configuration is connected to a computer via USB to enable communication and send commands to the CubeSat constellation.

The software architecture of the CubeSat constellation is developed using the STM32CubeIDE [7] with an RTOS managing concurrent tasks. Key modules include telemetry and data logging, command processing and power management to ensure efficient operation and autonomous decision making. The AX.25 protocol is used for reliable communication.

IV. CONCLUSION

This paper demonstrates the design of a constellation of three 1U CubeSats operating in the UHF band and using the AX.25 protocol. This CubeSat system enables students to explore satellite to ground station communications, telemetry transmission and inter-satellite communications. By integrating commercial off-the-shelf (COTS) components, the project demonstrates the potential, affordability and scalability of modular designs in educational CubeSat development. The modularity of the system, the focus on reliable inter-satellite communication, and the integration of power management, sensors and efficient data transfer contribute to its educational value. This constellation not only serves as a tool for satellite communications, but also provides insight into spacecraft operations, including power management and data processing. Future work could include scaling the CubeSat constellation, improving communication protocols and adding additional payloads for scientific research.

REFERENCES

[1] California Polytechnic State University, CubeSat Design Specification, Revision 14, 2020. [Online]. [cit. 2025-03-07]. Avaliable at *https://www.cubesat.org/cubesatinfo*

[2] Ing. Jiří VEVERKA, Educational PocketQube Satellite Demonstrator Výukový satelit formátu PocketQube [Online]. Avaliable at https://dspace.vut.cz/items/eeac98a4-ac06-4efb-8408-8f066adab5f9

[3] A. Povalač. Nanosatellite Design and Electronics. Brno: Brno University of Technology, Faculty of electrical engineering and communications, 2021.

[4] STM32F411 BlackPill development board DFRobot [Online]. Available from https://nz.mouser.com/new/dfrobot/dfrobot-stm32f411-blackpill-board/

[5] Black Pill STM32F411CEU6 microcontroller [Online]. [cit. 2025-03-07]. Avaliable at *https://www.st.com/resource/en/datasheet/stm32f411ce.pdf*

[6] The RFM98W RF transceiver [Online]. [cit. 2025-03-07]. Avaliable at *https://www.hoperf.com/modules/lora/RFM98PW.html*

[7] STM32CubeIDE User Guide [Online]. [cit. 2025-03-07]. Available at: https://www.st.com/resource/en/user_manual/dm00629856-stm32cubeide-user-guide-stmicroelectronics.pdf].

Lumped Parameter Method for Prediction of Sound Absorption Coefficient of Loudspeaker Placed in Closed Enclosure

Š. Skvaril
Faculty of electrical engineering and communication
Brno University of Technology
Brno, Czech Republic
xskvar08@vut.cz

Abstract— **This paper presents a comparative analysis of a theoretical lumped parameter model used to compute the acoustic impedance of a loudspeaker placed in closed enclosure, which acts as a low-frequency absorber. The analysis aims to validate the theoretical predictions by examining the system's mechanical and acoustic parameters. The influence of diaphragm compliance, mass, and damping on acoustic impedance is explored. Additionally, an impedance tube measurement is used to experimentally verify the theoretical results. The methodology, measurement procedure, and laboratory setup are described in detail. Results indicate that the lumped parameter approach provides a reliable estimation for specific frequency ranges, with deviations attributed to non-ideal structural and material properties.**

Keywords—Sound waves, acoustic impedance, acoustics, resonator, sound absorption

I. INTRODUCTION

Low-frequency noise is one of the biggest challenges in acoustics today. Acoustic engineers dealing with noise in residential spaces near traffic or industry are faced with the problem of low-frequency noise that is not effectively attenuated by conventional building materials. Residents are thus disturbed even when complying with the regulations. Low-frequency sound also causes significant problems in small music studios and listening rooms, where standing waves and resonances significantly affect the frequency response of the room at low frequencies. Such example of standing wave problem can be seen in Fig. 1, which shows result of simulation used FDTD numerical method [1] for small shoebox-shaped room.
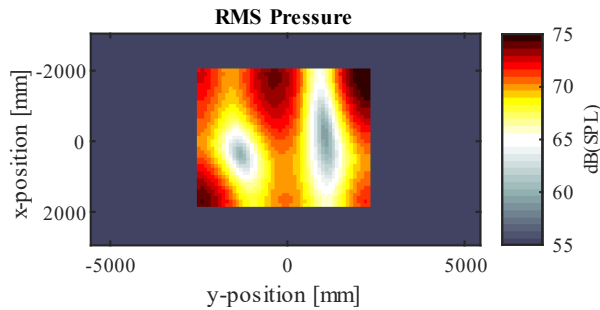

Fig. 1. FDTD simulation of spatial distribution of sound field in horizontal plane for 2nd axial mode in y direction at 68 Hz in room with dimensions of 5 x 4 x 3 m.

Conventional porous absorbers, such as foam and fiberglass panels, become ineffective at low frequencies unless they are significantly thick, often exceeding 50 cm in depth [2]. This practical limitation necessitates the use of alternative solutions such as resonant absorbers, including Helmholtz resonators and membrane absorbers, which are specifically designed to target narrow frequency bands. However, precise design of such devices is somewhat difficult as not all of physical properties are known during their design and construction. On the other hand, the loudspeaker diaphragm has all its essential properties measured and provided by the manufacturer. Using these, the lumped parameter method can be used to successfully predict its absorptive properties.

The effectiveness of these absorbers depends on their acoustic impedance, or more accurately, how well the impedance of loudspeaker diaphragm is matched to the acoustic impedance of air. Impedance matching is crucial for effective sound absorption of such device [3].

This work evaluates a theoretical lumped parameter model for predicting the acoustic impedance of a loudspeaker mounted on closed enclosure and compares it with experimental measurements conducted using an impedance tube setup. The impedance tube method allows precise measurement of the absorption characteristics of materials and structures within the low-frequency range, providing a reliable means of validation.

II. LUMPED PARAMETER MODEL

A. Mechanical properties of loudspeaker

The lumped parameter model simplifies the complex vibration behaviour of translation mechanical system by assigning its physical properties to components of electrical circuit. Mass of the system translates to inductance, compliance translates to capacity and mechanical losses to resistance. Most loudspeaker manufacturers list these parameters as M_{ms}, C_{ms} and R_{ms}.

R_{ms} is often not listed, however it can be calculated from mechanical quality factor Q_{ms} as [4]:

$$R_{\mathrm{ms}} = \frac{2\,f_s M_{\mathrm{ms}}}{Q_{\mathrm{ms}}}, \tag{1}$$

where f_s is resonant frequency of loudspeaker.

When loudspeaker is mounted onto enclosure, the air enclosed in the cavity acts as an additional compliance. This compliance is in this work noted as C_{enc}. Value of this compliance is calculated as [5]

$$C_{enc} = \frac{V}{\rho_0 c_0^2}, \tag{2}$$

where ρ_0 is air density (1.29 kg/m^3), c_0 is speed of sound in air (344 m/s) and V is the enclosed volume behind the loudspeaker diaphragm. When all mechanical variables are known, then acoustic impedance of entire system can be calculated by solving equivalent circuit. The equivalent electro-mechanical model of the circuit is shown in Fig. 2.
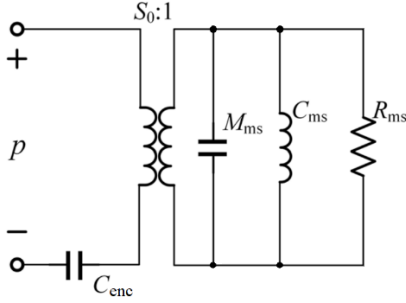

Fig. 2 Equivalent electro-mechanic circuit model of loudspeaker driven by external acoustic pressure

First, the acoustic impedance of the loudspeaker diaphragm itself must be calculated, which is done using

$$Z_d = \frac{R_{ms}}{S_d} + \frac{j \omega M_{ms}}{S_d} + \frac{1}{j \omega C_{ms} S_d}, \tag{3}$$

where $\omega = 2\pi f$ is the angular frequency, j is imaginary unit and S_d is the effective area of loudspeaker diaphragm.

After that, compliance of enclosure can be added using:

$$Z_{lspk} = Z_d + \left(\frac{S_d}{j \omega C_{enc}}\right). \tag{4}$$

Because, the whole resonant structure is placed and measured in impedance tube the of known cross-section area, as described in next part of this paper, it is important to take into account the transformation of acoustic impedance between the diaphragm surface and the cross-section area of the impedance tube. Acoustic impedance of the entire system is then calculated using [6]:

$$Z_x = Z_{lspk} \left(\frac{S_0}{S_d}\right), \tag{5}$$

where S_0 is the cross-section area of the impedance tube. Acoustic impedance of the entire system can be converted into absorption coefficient values using [7]:

$$\alpha = \frac{4\rho_0 \ c_0 \ Re(Z_x)}{(\rho_0 c_0 Re(Z_x))^2 + (Im(Z_x))^2}. \tag{6}$$

B. Prediction of absorption coefficient of real structure

Using the above equations, the absorption coefficient values were calculated for a specific loudspeaker type. The Dayton Audio PC105-8 was selected. Its mechanical parameters are listed in the table below.

TABLE I Mechanical Properties of loudspeaker selected for verification

Dayton PC105-8			
Table column subhead	*Symbol*	*Value*	*Unit*
Moving mass	M_{ms}	4.2	g
Mechanical compliance	C_{ms}	0.84	mm/N
Mechanical Quality factor	Q_{ms}	2.29	-
Resonant frequency	f_s	84.8	Hz
Mechanical losses	R_{ms}	0.97	kg/s
Diaphragm area	S_d	52.8	cm²

The resulting absorption coefficient values for enclosure volume of 4 liters are shown in Fig. 3.

Lumped parameter model allows quick investigation of influence of changes in the structure to final sound absorption coefficient values. For example, if an additional mass is added to the mass of the moving diaphragm, the effect on the resulting sound absorption coefficient can be determined. The calculation was performed for three different variants, each with an increasing mass of 2.5 g. (See in Fig. 4.)

The values of the sound absorption coefficient do not reach the value of 1, because this is a calculation of acoustic impedance of the entire system. Only the area of the loudspeaker diaphragm is acoustically active, which is approximately 6% of the total cross-section area of the impedance tube.
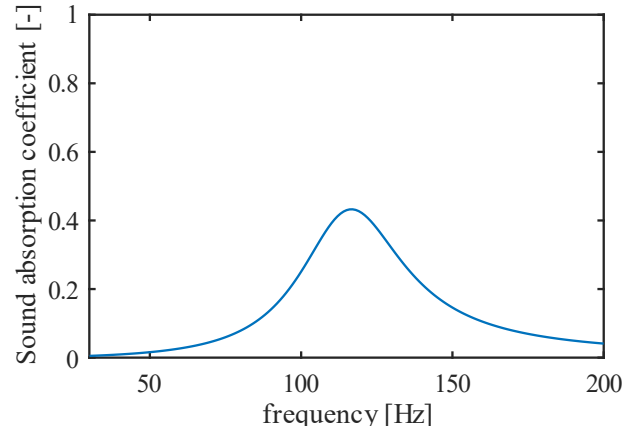

Fig. 3 Calculated sound absorption coefficient of complete system with Dayton PC105-8 placed in enclosure with volume of 4 liters
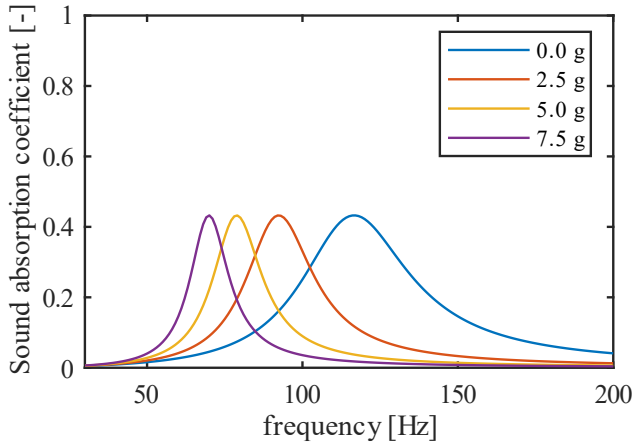
Fig. 4 Calculated sound absorption coefficients for different values of added mass

III. Verification Measurements

A. Measureement technique

Measurement using impedance tube method was conducted. The impedance tube used in this study has a square cross-section of 30 cm x 30 cm, that allows testing of larger samples. The impedance tube is made of MDF board with thickness of 18 mm plated with 3 mm thick metal sheets. This ensures high reflection and sound insulation even for low frequencies. Driving loudspeaker is located on one side of the tube whereas a highly reflective surface, where specimen shall be placed, on the other. As illustrated in Fig.6.
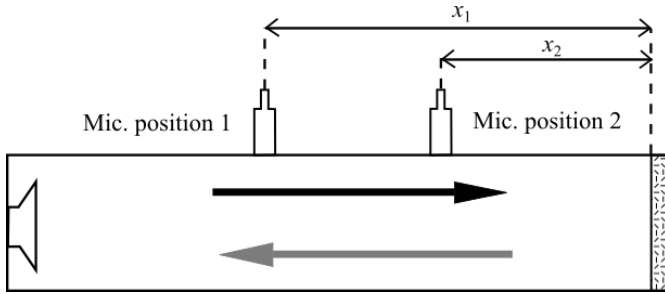

Fig. 5 Diagram of impedance tube that uses transfer function method of measurement of acoustic impedance

The impedance tube has two positions for microphones. The microphones pick up the acoustic pressure at their respective positions and then the transfer function between those two positions is calculated using

$$H_{12} = \frac{P_2 P_1^*}{P_1 P_1^*} \ , \tag{7}$$

where P_1 and P_2 are Fourier transforms of acoustic pressures acting on the microphones. The * symbol stands for complex conjugate [8]. H_{12} is then used to compute the reflection coefficient using

$$r = \frac{H_{12} - e^{-jk_0(x_1 - x_2)}}{e^{jk_0(x_1 - x_2)} - H_{12}} e^{2jk_0 x_1} \tag{8}$$

where x_1, x_2 are distances of microphones from the measured sample, k_0 is the wavenumber. The reflection coefficient is then used to compute absorption coefficient using [8]

$$\alpha = 1 - |r|^2. \tag{9}$$

B. Measurement of sound absorption coefficients and comparsion to theoretical model

A prototype was created for comparative measurement of the absorption coefficient. MDF board with thickness of 16 mm was used for the enclosure. The internal dimensions are 20 cm x 20 cm x 10 cm and thus the volume is 4 liters. There are four openings for future experiments with coupled Helmholtz resonators, which were sealed with 3D printed plugs during the measurement. Its photograph is shown in Fig. 6.

Fig. 6 Photograph of the absorber prototype.

If we compare the calculated values of the absorption coefficient with the measured ones, a slight deviation can be observed, mainly in the shift of the resonant frequency towards higher values, see Fig. 7. This is probably due to the fact that the loudspeaker unit partially fills the internal volume of the enclosure. Therefore, the volume is actually slightly smaller than 4 liters, which leads to a decrease in compliance and therefore the resonant frequency increases.

Furthermore, the maximum absorption value is slightly lower, which is probably due to additional losses inside the enclosure, since the volume of enclosure was represented only by ideal compliance without resistance which would include losses caused by leaks and other imperfections. Another reason for inaccuracies may be deviations in real TS parameters, which may be slightly different from the data provided by the manufacturer.

However, these are relatively small deviations and this is a very promising initial step in the case of the design of a specific acoustic element.
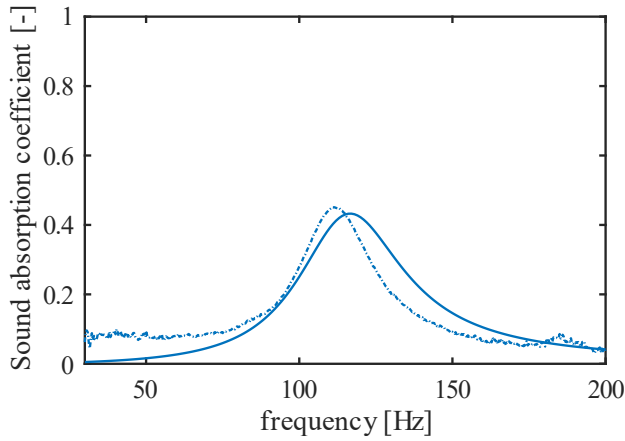
Fig. 7 Comparison of measured and calculated absorption coefficients. Dotted line shows measured values.

When additional weights are added to the theoretical model and to the prototype, then high accuracy of the prediction be observed when comparing measured and predicted values. It can even be observed that the deviation in both resonance frequency and maximum value of the absorption coefficient decreases in comparison with the initial state. (see Fig. 8)
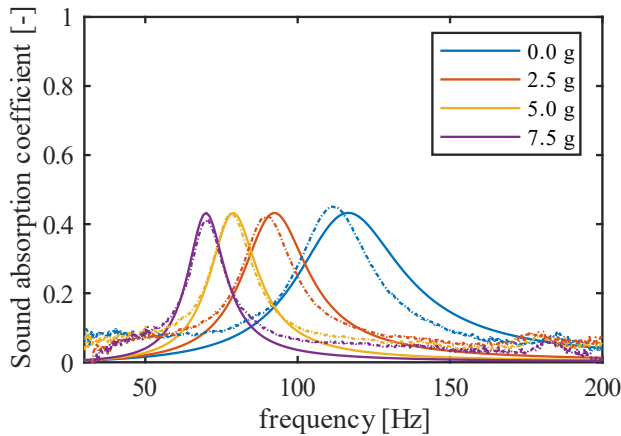

Fig. 8 Comparison of measured and calculated absorption coefficients with added mass. Dotted line shows measured values.

IV. CONCLUSION

The lumped parameter model provides a useful approximation of the acoustic impedance of a loudspeaker diaphragm acting as a low-frequency absorber. This approach effectively captures the fundamental impedance characteristics at low frequencies, where mass, compliance, and resistance play a crucial role in defining the acoustic behaviour of the system. Acoustic impedance values are then used for prediction of absorption coefficients where theoretical predictions align well with experimental results obtained from the impedance tube setup, demonstrating the model's reliability for practical applications in low-frequency sound absorption.

One of the key advantages of the lumped parameter model is its ability to provide insights into the behaviour of absorbing structures with minimal computational complexity. By tuning parameters, such as diaphragm mass, compliance, and damping, it is possible to design absorbers optimized for specific frequency ranges. This makes the model particularly useful for applications in room acoustics, and architectural noise control, where effective low-frequency absorption is required.

Future work should focus on extending the model to incorporate more complex structures and configurations. One potential area of exploration is the application of the lumped parameter approach to bass-reflex loudspeaker enclosures, which exhibit additional resonant behaviours due to the interaction between the port and the internal air volume. Another promising direction is the investigation of shunt resistance applied to loudspeaker terminals, which can provide additional control over the system's impedance characteristics and further enhance absorption performance. [6]

One promising direction for further research is the application of the lumped parameter model in the design and analysis of acoustic metamaterials. [9] Acoustic metamaterials are engineered structures with unique wave-manipulating properties, often achieving negative effective mass or bulk modulus, leading to unconventional sound absorption and wave propagation characteristics. By incorporating the lumped parameter approach, researchers can model the interaction of resonant elements within metamaterials, predicting their impedance characteristics and optimizing them for targeted frequency ranges. For instance, arrays of membrane-based absorbers with precisely tuned mass and compliance could be designed to achieve extreme low-frequency absorption in compact structures. [10] Additionally, combining lumped parameter modelling with metamaterial concepts such as locally resonant units or tuned Helmholtz-like inclusions can lead to advanced noise reduction solutions for architectural acoustics, aerospace applications, and underwater acoustics, where traditional absorbers are impractical due to size constraints [1].

REFERENCES

[1] *k-Wave: A MATLAB toolbox for the time domain simulation of acoustic wave fields [online].* Copyright ©. Available from: http://www.k-wave.org/manual/kwave_user_manual_1.1.pdf

[2] COX, T.; D'ANTONIO, P. *Acoustic absorbers and diffusers: theory, design and application. Third edition*. Boca Raton: CRC Press, Taylor & Francis Group, [2017]. ISBN 978-1-4987-4099-9.

[3] KIM, Y. *Sound propagation: an impedance based approach. Hoboken*, N.J.: Wiley, c2010. ISBN 978-0-470-82583-9

[4] DICKASON, V. *The loudspeaker design cookbook. 6th ed., new, expanded*. Peterborough: Audio Amateur Press, 2000. ISBN 1-882580-33-8.

[5] ZHANG P., CONG, C., TAO, J. *et al. Dual frequency sound absorption with an array of shunt loudspeakers*. Sci Rep 10, 10806 (2020). https://doi.org/10.1038/s41598-020-67810-z

[6] LI, Xin; CAO, Zhigang; LI, Zihao a LIU, Bilong. *Sound absorption of a shunt loudspeaker on a perforated plate*. Online. Applied acoustics. 2022, roč. 193, s. 108776. ISSN 0003-682X.

[7] MORSE, Philip M. a INGARD, K. Uno. *Theoretical acoustics*. Princeton: Princeton University Press, 1986. ISBN 0-691-02401-4.

[8] ISO 10534:1996, *Acoustics – Determination of sound absorption coefficiend in impedance in impedance tubes*

[9] NORRIS, A.; HABERMAN, M. *ACOUSTIC METAMATERIALS*. *Online*. The Journal of the Acoustical Society of America. 2012, roč. 132, č. 4. ISSN 0001-4966. [cit. 2024-04-05].

[10] LISSEK, H; BOULANDET, R and RENÉ, P.. *Shunt loudspeakers for modal control in rooms, 2009*

Comparing variant calling tools for genomic analysis of patients predisposed to Kidney Disease

1st Jana Neuwirthová
Department of Biomedical Engineering
Faculty of Electrical Engineering and Communication
Brno, Czech Republic
274451@vut.cz
0009-0000-5292-5468

2nd Jana Indráková
Institute of Molecular and Clinical Pathology and Medical Genetics,
Faculty of Medicine, University of Ostrava,
Ostrava, Czech Republic
jana.indrakova@fno.cz

3rd Valentýna Provazník
Czech Institute of Informatics, Robotics and Cybernetics, Czech Technical University in Prague
Faculty of Medicine, University of Ostrava,
Ostrava, Czech Republic
0000-0002-3422-7938

4th Jana Schwarzerová
Department of Biomedical Engineering
Faculty of Electrical Engineering and Communication
Brno, Czech Republic
Molecular Systems Biology (MOSYS),
Department of Functional and Evolutionary Ecology
Vienna, Austria
Institute of Molecular and Clinical Pathology and Medical Genetics,
Faculty of Medicine, University of Ostrava,
Ostrava, Czech Republic
0000-0003-2918-9313

Abstract— **This study compares various variant calling tools for the analysis of genomic data from patients predisposed to kidney disease and evaluates algorithms for identifying genetic variants that may contribute to the pathogenesis of these conditions. The aim is to assess the performance of these tools, focusing on their sensitivity and specificity in detecting specific pathogenic variants. The study tests three variant calling tools on genomic data from four selected patients sequenced at the University Hospital Ostrava. It compares different variant calling approaches, emphasizing their impact on the accuracy and efficiency of identifying relevant genetic variants. The tools were selected based on their widespread usage, strong benchmarking performance in prior studies, and compatibility with the Sarek pipeline, making them the most modern approaches in variant calling, suitable for both research and clinical applications. As part of this study, high-throughput sequencing data will be analysed, and methods for variant detection will be evaluated at different levels of precision and sensitivity.**

Keywords — Variant calling tools, kidney disease, next generation sequencing, genetic variants

I. Introduction

Kidney disease (especially chronic kidney disease, CKD) is becoming an increasingly significant global health issue [1]. Research has shown that, in addition to environmental factors, genetic factors play a crucial role in disease progression—especially mutations in single genes [2],[3]. Understanding the primary cause of the disease and accurately identifying genetic variants are essential for improving diagnostics and advancing personalized medicine. Therefore, precise mapping and analysis of genomic data are crucial for gaining deeper insights into the disease's pathogenesis [4].

Genetic CKD encompass a large group of disorders with diverse clinical presentations. Mutations in approximately 450 genes have been identified as the cause of monogenic kidney diseases [5]. Among the most common hereditary genetic variants associated with kidney disease are polycystic kidney disease (PKD) and Alport syndrome [4].

PKD is an inherited disorder characterized by the formation of multiple cysts in the kidneys, gradually impairing their function. There are two main forms: autosomal dominant (ADPKD) and autosomal recessive (ARPKD). In ADPKD, a mutation in just one of the two parental alleles is sufficient to cause the disease, making it more common. It typically manifests in adulthood and is most often caused by mutations in the PKD1 (over 80% of cases) and PKD2 genes, which encode polycystin 1 and 2. In contrast, ARPKD follows a recessive pattern of inheritance, requiring mutations in both alleles of the gene to manifest. This variant is rarer but often more severe, usually appearing perinatally or in early childhood. It is primarily caused by mutations in the PKHD1 gene, which encodes the protein fibrocystin. Defects in these proteins disrupt cell signaling and growth regulation, leading to excessive kidney cell division and cyst formation [5], [6].

After ADPKD, Alport syndrome is the second most common cause of monogenic renal failure [7]. This rare hereditary disease primarily affects the kidneys but can also impact the eyes

and ears. It is caused by mutations in the genes encoding the α chains of collagen IV, a key component of basement membranes in various tissues, including the renal glomeruli, retinal cells, and the inner ear. The most common mutation occurs in the COL4A5 gene on the X chromosome (X-linked inheritance), making the condition more prevalent and severe in males. However, Alport syndrome can also follow an autosomal dominant (AD) or autosomal recessive (AR) inheritance pattern. These forms typically present with milder symptoms and result from pathogenic variants in the COL4A3 and COL4A4 genes [7].

Accurate variant calling [8], combined with next-generation sequencing (NGS) technology, is essential for genomic analysis in kidney disease. It enables the identification of genetic variants in DNA sequences (e.g., single nucleotide variants (SNVs), deletions, and insertions) that may contribute to the development [8] and progression of renal disorders. Given the strong genetic component of many kidney diseases, precise variant detection is crucial for improving diagnosis, prognosis, and treatment selection in affected patients.

Therefore, this study focuses on comparing different variant calling tools for the detection of genetic variants in patients predisposed to kidney disease. Genetic data from four selected patients, who underwent NGS sequencing at the University Hospital Ostrava, were analyzed. The study evaluates the performance of these three variant calling tools—DeepVariant [9], Strelka2 [10], and HaplotypeCaller [11]—integrated within the Sarek pipeline (version 3.4.2) [12]. The selection of DeepVariant, Strelka2, and HaplotypeCaller reflects their current popularity and performance in clinical and research contexts. All three are supported by the Sarek pipeline, which ensures reproducibility and standardization. The primary goal is to assess their accuracy and efficiency in identifying genetic variants, as this has a significant impact on the further analysis and interpretation of genetic data in both clinical practice and research.

While previous benchmarking studies have evaluated variant calling tools across various conditions and datasets [13], [14], few have focused on their performance in clinically relevant cohorts with kidney disease. Moreover, comparative analyses using real-world clinical sequencing data remain limited, particularly in the context of tools integrated within standardized pipelines such as Sarek. This highlights the originality and relevance of our study, which specifically addresses the use of these tools for genetic analysis in kidney disease patients.

II. COHORT DATA

In this study, genomic data from next-generation sequencing (NGS) were analyzed for four patients suspected of having a genetic kidney disease. Sequencing was performed using the NovaSeq Illumina platform, generating a large number of short DNA fragments (reads) representing sections of the original DNA.

Following sequencing, the FastQ data were processed using open-source bioinformatics tools—DeepVariant [9], Strelka2 [10], and HaplotypeCaller [11]—integrated within the Sarek pipeline [12] (version 3.4.2). The individual reads were

then assembled, and specific genetic variants were identified by aligning the sequences to the reference human genome GRCh38 (HG38).

III. METHODS

A. Library preparation and sequencing

Library preparation for sequencing on the NovaSeq Illumina platform is a key step in NGS. The input material is isolated genomic DNA from a biological sample, which must be of high quality to avoid contamination or degradation. Due to the short-read nature of the sequencer, the isolated DNA is fragmented using specific restriction enzymes or other fragmentation methods (e.g., sonication), producing fragments of the desired size. Adapters are then added to the DNA fragments, followed by amplification using polymerase chain reaction (PCR) with specific primers.

After amplification, quality control is performed, typically via electrophoresis (e.g., gel-based or capillary electrophoresis), to select fragments within the size range of 300–600 base pairs. Once the library passes quality control, it is denatured into single-stranded DNA (ssDNA), which is then hybridized to complementary sequences on the sequencing flow cell. After the DNA fragments are bound to the flow cell, amplification occurs, which is important for generating a strong signal for sequencing on the Illumina NovaSeq 6000Dx sequencer.

For setting up the sample sheet for sequencing, the Basespace platform was used. The run description should include approximately 1% PhiX. The input DNA concentration should be set to 250 pM. The instrument platform should be set to NovaSeq 6000/6000Dx, with secondary analyses selected as Basespace. The read lengths should be set as follows: Read1: 151, Index1: 8, Index2: 8, Read2: 151.

B. Bioinformatic analysis

Following sequencing, the raw FastQ data were processed using a suite of open-source bioinformatics tools, including DeepVariant v 1.8.0 [9], Strelka v-2.9.10 [10], and HaplotypeCaller [11] (– GATK4), all of which are integrated within the Sarek pipeline [12] (version 3.4.2). The Sarek pipeline is a comprehensive workflow designed to automate the analysis of genomic data, particularly for next-generation sequencing (NGS). It incorporates a range of tools, such as GATK, BWA-MEM, and others, to perform alignment, variant calling, and other essential steps in genomic analysis.

After processing the raw sequencing data through the Sarek pipeline, individual reads were aligned to the reference human genome GRCh38 (HG38), which was selected for its comprehensive annotation, high-quality sequence, and wide acceptance in clinical genomics for human variation studies. Although alternative genomes, such as GRCh37 or newer versions like GRCh39, are available, GRCh38 remains the preferred choice in clinical settings due to its more accurate representation of complex genomic regions [15].

After alignment, Specific genetic variants, such as single nucleotide polymorphisms (SNPs) and insertions/deletions (INDELs), were identified and filtered for high confidence. The variant annotation process was then performed by utilizing

several widely recognized databases. These included ClinVar which was used to assess clinical significance, allowing classification of variants as pathogenic, likely pathogenic, benign, or of uncertain significance. The gnomAD database was used to population allele frequencies, essential for filtering out common benign variants and highlighting rare, potentially pathogenic ones. In addition, dbSNP database was used to identify known SNPs and determine whether detected variants had been previously documented in the population.

To ensure the accuracy and reliability of the identified variants, we applied several critical filtering parameters. These included the variant name, chromosomal position, and coordinate for precise genomic mapping, as well as variant class (e.g., SNP, INDEL) and genotype (homozygous or heterozygous) to assess the nature and inheritance pattern of each alteration. Variants classified as pathogenic or likely pathogenic were prioritized for further analysis. Furthermore, a minimum read depth threshold was used to ensure sufficient sequencing coverage and reduce the likelihood of false-positive calls. By combining these criteria, only high-confidence variants with a higher probability of clinical relevance were retained for downstream interpretation.

The filtered results from the Sarek pipeline were then further analyzed and visualized using an in-house method. This included the evaluation of the overlap of detected variants across different sample sets. The variant intersections were visualized and analyzed in R Studio (version 3.4.2), a widely used environment for statistical computing and data visualization. Through custom scripts, we assessed the shared and unique variants among different conditions, providing insight into the biological significance of the detected genetic alterations.

IV. RESULTS AND DISCUSSION

This study compared three open-source tools for variant calling: DeepVariant, Strelka2, and HaplotypeCaller. We focused on parameters that could provide useful information about the sensitivity of detecting pathological genetic variants. The key comparative parameters included Variant Name, Chromosome, Coordinate, Variant Class, Genotype, Impact, Consequence, Clinical Significance, Variant Frequency, and Read Depth.

A. Comparison of Variant Callers

To evaluate the performance of each tool, we first pre-processed the variant data by extracting relevant features and merging the datasets. This allowed us to assess the overlap and differences in variant detection across the three methods. The common and unique variants detected by each tool were visualized using a Venn diagram, highlighting the agreement and discrepancies among the callers (see Fig 1). The HaplotypeCaller tool detected the most variants (2556), followed by DeepVariant (2517), and finally Strelka2 (2457). The relatively small number of unique variants detected by individual tools (HaplotypeCaller – 25, DeepVariant – 4, Strelka2 – 9) and the high number of common variants detected by all three tools (2424) indicate a high level of concordance in variant detection.

A boxplot analysis was conducted to compare the Read Depth (see Fig 2) and Variant Frequency distributions (see

Fig 3) among the three tools. Read Depth, an important metric indicating the reliability of a called variant, was analysed across the different tools to determine if any systematic biases or differences exist.
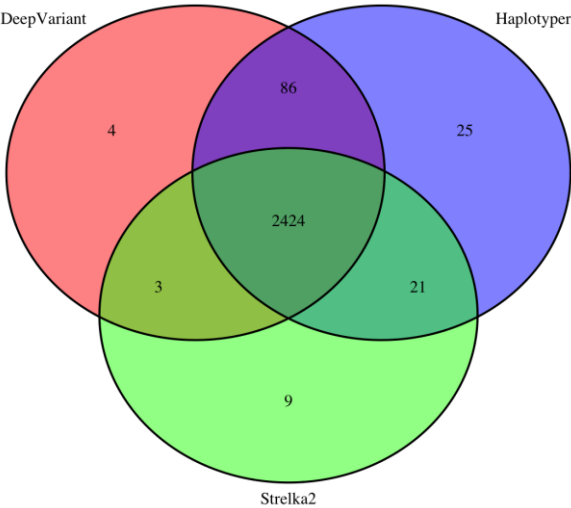

Fig 1. Venn diagram showing the overlap of variants detected by DeepVariant, HaplotypeCaller, and Strelka2

Similarly, Variant Frequency distributions were examined to assess whether certain tools tended to report higher or lower variant frequencies.
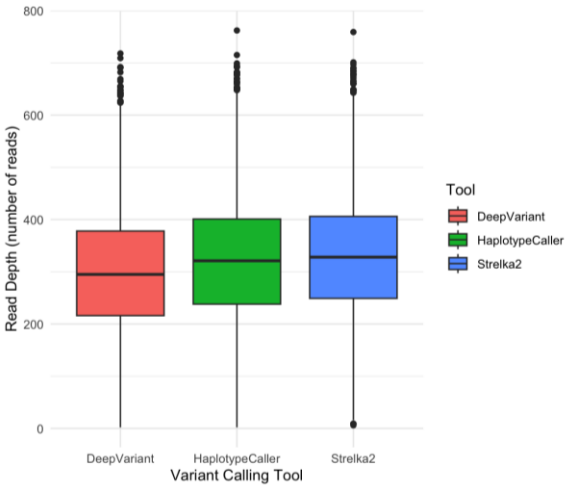

Fig 2. Boxplot comparing Read Depth across different variant calling tools

A comparison of Read Depth Across Variant Calling Tools (Fig 2) shows that slightly higher medians are observed for Strelka2 and HaplotypeCaller, indicating that these tools detect variants with higher read depth. However, the difference compared to DeepVariant is not significant. In the assessment of Variant Frequency (Fig 3), no substantial difference is observed between the tools, demonstrating their consistency and similar reliability of results.
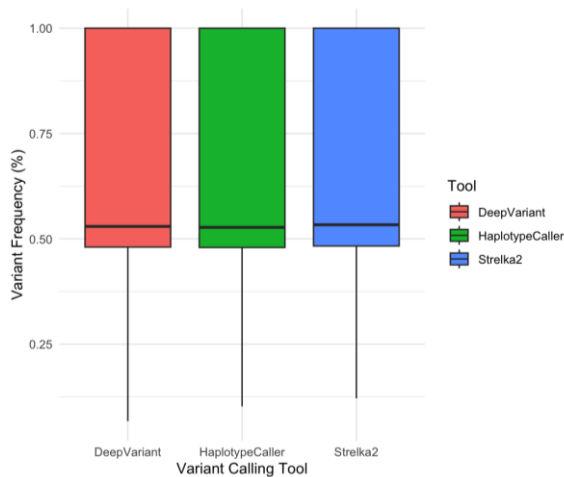
Fig 3. Boxplot comparing Variant Frequency across different variant calling tools

B. Variant Classification and Clinical Significance

A bar plot was generated to illustrate the distribution of Variant Classes across the three tools, helping to identify whether certain tools favor specific types of variants (e.g., single nucleotide variants vs. insertions/deletions – see Fig 4).
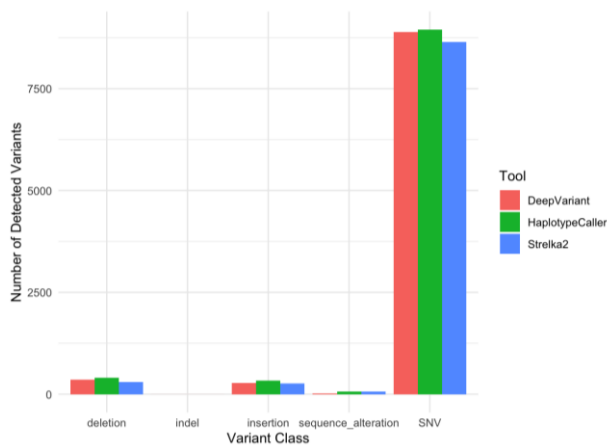

Fig 4. Bar plot of Distribution Variant Classes across calling tools

The most frequently detected variant class across all three tools was clearly single nucleotide variants (SNVs). Deletions, insertions, and sequence alterations were represented to a significantly lesser extent. All three tools exhibit a very similar distribution of variants; however, HaplotypeCaller consistently detected slightly more variants than the other tools.

The clinical significance of the detected variants was another crucial aspect of the analysis. To enhance the clarity of the results, we focused only on the two most frequently occurring clinical significance categories and visualized them using a bar plot (see Fig 5). This allowed for a clearer interpretation of how often each tool identified variants classified under these critical categories.

The most frequently detected Clinical Significance category is benign, which dominates across all three tools (DeepVariant, HaplotypeCaller, and Strelka2). The second most common category is N/A (variant of unknown meaning), where there are

slight differences among the tools — HaplotypeCaller detected slightly more variants in this category than DeepVariant and Strelka2. Strelka2 could be considered the best in this analysis, as it detected the fewest variants of unknown meaning, which may indicate better classification accuracy. However, the overall distribution of clinical significance categories is very similar among the tools, suggesting consistency in their classification and comparable performance in terms of clinical relevance.
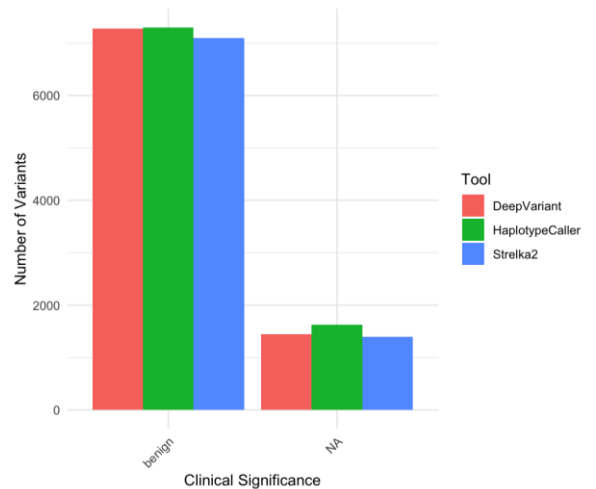

Fig 5. Bar plot showing the top 2 Clinical Significance categories across different variant calling tools

C. Findings and Implications

The comparison revealed that while there is a substantial overlap in the detected variants, each tool also identified unique variants, emphasizing the importance of tool selection in clinical and research settings. Differences in Read Depth and Variant Frequency suggest that each tool applies slightly different filtering or sensitivity settings. Additionally, variations in Clinical Significance classification highlight potential discrepancies in how each tool prioritizes or annotates genetic variants.

These findings highlight the importance of selecting and validating variant calling tools carefully, as different algorithms can produce variable results that affect clinical decisions. In clinical genomics, combining multiple tools is crucial for an accurate genetic profile. Future work should investigate ensemble approaches that integrate multiple callers to improve variant detection accuracy and robustness.

V. CONCLUSION

In this study, we evaluated three widely used variant calling tools — DeepVariant, Strelka2, and HaplotypeCaller integrated into the Sarek pipeline (v3.4.2) for genomic data analysis. The analysis was based on sequencing data from four patients suspected of having genetic kidney diseases, compared to the human reference genome GRCh38 (hg38). Key parameters, including Variant name, Coordinate, and Chromosome, were compared across the tools. These are crucial for accurately identifying and localizing genetic variations. Variant name

identifies the specific genetic change, Coordinate pinpoints its exact location on the genome, and Chromosome places the variant in its correct chromosomal context.

The results showed that all three tools were effective in variant detection, with HaplotypeCaller outperforming the others in all evaluated parameters. It identified the largest number of matching variants, demonstrating superior sensitivity and efficiency in detecting genetic variants within the given dataset. This greater number of variants detected by HaplotypeCaller could be attributed to enhanced sensitivity, although further validation is needed to confirm the clinical relevance of these additional variants. In comparison, DeepVariant performed similarly to HaplotypeCaller but identified slightly fewer variants. Strelka2, while still providing valuable results, was the least effective in this study across all evaluated metrics.

Findings indicate HaplotypeCaller is the most sensitive and reliable tool for variant detection. It demonstrated superior sensitivity in detecting a broader range of genetic variants, as evidenced by its ability to identify the largest number of matching variants across the dataset. In terms of reliability, HaplotypeCaller showed consistency in the quality of its results across key metrics such as variant frequency, read depth, and clinical significance, making it the preferred choice for identifying genetic variants in clinical and research settings.

While previous benchmarking studies have evaluated variant calling tools across various conditions and datasets [13], [14], few have focused on their performance in clinically relevant cohorts with kidney disease. Moreover, comparative analyses using real-world clinical sequencing data remain limited, particularly in the context of tools integrated within standardized pipelines such as Sarek. This highlights the originality and relevance of our study, which specifically addresses the use of these tools for genetic analysis in kidney disease patients.

It is important to consider some potential limitations of this study. The small sample size and lack of diversity within the patient population may limit the generalizability of the results. The findings are based on data from only four patients, which may not fully capture the complexity of genetic variations in a broader population. Therefore, results should be interpreted with caution, and further research with larger, more diverse samples is needed, including a broader range of data types and genomic studies, to provide a more comprehensive evaluation of each tool's performance.

REFERENCES

[1] Guo, J., Liu, Z., Wang, P., Wu, H., Fan, K., Jin, J., Zheng, L., Liu, Z., Xie, R. and Li, C. (2025). Global, regional, and national burden inequality of chronic kidney disease, 1990–2021: a systematic analysis for the global burden of disease study 2021. *Frontiers in Medicine, 11*, p.1501175.

[2] Huang, Z. Y., Liang, L. N., Li, Y. M., Xu, K., & Li, X. Y. (2022). Genetic, environmental and other risk factors for progression of retinitis pigmentosa. *International Journal of Ophthalmology, 15*(5), 828.

[3] Yan, X., Xu, Z., Zhang, P., Sun, Q., Jia, Y., Qin, T., ... & Xiao, Z. (2023). Non-driver mutations landscape in different stages of primary myelofibrosis determined ASXL1 mutations play a critical role in disease progression. *Blood Cancer Journal, 13*(1), 56.

[4] Hildebrandt, F. (2010). Genetic kidney diseases. *The Lancet, 375*(9722), 1287-1295. ISSN 0140-6736.

[5] Connaughton, D. M., & Hildebrandt, F. (2020). Personalized medicine in chronic kidney disease by detection of monogenic mutations. *Nephrol Dial Transplant, 35*(3), 390-397.

[6] Bergmann, C., Guay-Woodford, L. M., Harris, P. C., Horie, S., Peters, D. J. M., et al. (2018). Polycystic kidney disease. *Nature Reviews Disease Primers, 4*(1). ISSN 2056-676X.

[7] Savige, J., Ariani, F., Mari, F., Bruttini, M., Renieri, A., et al. (2019). Expert consensus guidelines for the genetic diagnosis of Alport syndrome. *Pediatric Nephrology, 34*(7), 1175-1189. ISSN 0931-041X.

[8] Koboldt, D. C. (2020). Best practices for variant calling in clinical sequencing. *Genome Medicine, 12*(1). ISSN 1756-994X.

[9] Meng, G., Han, L., Li, Y., & Wu, H. (2024, March). Optimization of Deepvariant Software for Domestic Heterogeneous Platforms. In *2024 5th International Seminar on Artificial Intelligence, Networking and Information Technology (AINIT)* (pp. 382-388). IEEE.

[10] Kim, S., Scheffler, K., Halpern, A.L., Bekritsky, M.A., Noh, E., Källberg, M., Chen, X., Kim, Y., Beyter, D., Krusche, P., & Saunders, C.T. (2018). Strelka2: fast and accurate calling of germline and somatic variants. *Nature Methods, 15*(8), 591-594.

[11] Salem, R.M., Wessel, J., & Schork, N.J. (2005). A comprehensive literature review of haplotyping software and methods for use with unrelated individuals. *Human Genomics, 2*, 1-28.

[12] Garcia, M., Juhos, S., Larsson, M., Olason, P. I., Martin, M., Eisfeldt, J., DiLorenzo, S., Sandgren, J., De Ståhl, T. D., Ewels, P., & Wirta, V. (2020). Sarek: A portable workflow for whole-genome sequencing analysis of germline and somatic variants. *F1000Research, 9*, 63.

[13] Hwang, S., Kim, E., Lee, I., & Marcotte, E. M. (2015). Systematic comparison of variant calling pipelines using gold standard personal exome variants. *Scientific Reports, 5*(1). ISSN 2045-2322.

[14] Stepanian, J., Saldaña, D., Mahecha, D., Mazabel, L., & Diaz, J. (2024). Variant calling pipelines benchmark for whole exome sequencing in clinical context. *medRxiv*.

[15] Guo, Y., Dai, Y., Yu, H., Zhao, S., Samuels, D. C., et al. (2017). Improvements and impacts of GRCh38 human reference on high throughput sequencing data analysis. *Genomics, 109*(2), 83-90. ISSN 0888-7543.

Dequantized signal from two parallel quantized observations

Vojtěch Kovanda
Dept. of telecommunications
Brno University of Technology
Czech Republic
xkovan07@vutbr.cz

Abstract—**We propose a technique for signal acquisition that uses a combination of two devices with different sampling rates and quantization accuracies. Subsequent processing involving sparsity-based regularization enables us to reconstruct the input signal at such a sampling frequency and with such a bit depth that were not possible using the two devices independently. Objective tests show the evaluation of the proposed method in comparison with the alternatives.**

Index Terms—**Dequantization, bit depth, multichannel, audio, optimization, sparsity, analog-to-digital conversion.**

I. Introduction

In analog-to-digital (A/D) conversion, two qualities play a crucial role. The sampling frequency determines how broad the signal spectrum is that can be acquired, while the number of bits used for representing signal samples governs their accuracy [1]. In any particular application, a combination of a sampling frequency and a quantization step that are adequate is required. For demanding applications, however, a proper combination of the parameters can imply a high sale price of the A/D conversion unit.

In this paper, we propose a system that overcomes the described property via employing two parallel signal acquisition branches. One branch consists of an A/D converter with a high sampling frequency but a coarse quantization. The second branch involves a significantly more accurate quantizer; nevertheless, it operates at a low sampling frequency. The scheme of the system is in Fig. 1. The goal is to reconstruct a signal as close to the original signal as possible, given the two different observations $\mathbf{y}_1, \mathbf{y}_2$.

If the proposed concept proves beneficial, it could allow employing cheaper components to provide an acquisition quality comparable to high-end devices. Seen from another side, the approach could even make possible acquisitions that would not be accessible with a single converter; in this sense, our approach can be understood as superresolution in time and/or in sample value domains. Naturally, estimating the original signal from $\mathbf{y}_1, \mathbf{y}_2$ is not straightforward and comes at the cost of computation.

Related work. Increasing the sampling frequency and the quantization resolution of an A/D converter has always been
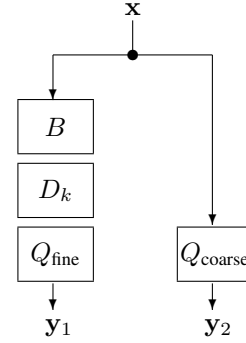
Fig. 1. Scheme of the parallel conversion. In one branch, the original signal $\mathbf{x}$ goes through an anti-aliasing filter B, then the subsampling operator D_k, and finally the quantization with a high-resolution Q_{fine}, producing the observation $\mathbf{y}_1$. The second branch does not alter the sampling frequency and only quantizes the signal with a low-resolution Q_{coarse}. Note that in practice, $\mathbf{x}$ would come in as an analog signal; in our treatment, $\mathbf{x}$ already is assumed in the discrete time.

of interest to the signal processing community. The parallel branches in Fig. 1 do not represent an entirely new idea: As regards the sampling speed, the physical limit of a sampling device can be bypassed via involving multiple A/D converters that are time-interleaved. Such an idea is actually a special case of the so-called multirate filterbank A/D conversion concept [2], [3]. To increase the resolution in value (i.e., the final quantization accuracy) within the A/D conversion, a similar trick of an array of quantizers with different offsets in value can be applied [4]. In the converters of classical design, such as Σ–Δ, the resolution is exchanged with speed [1].

In the mentioned approaches, no property of the analog signal is utilized, except its bandwidth. Additional signal characteristics can yet be exploited for the increase of sampling frequency or resolution, as a postprocessing step. This has been demonstrated in various signal processing fields, such as image superresolution [5], audio dequantization [6] or compressive sampling [7], [8]. An approach to increasing the sampling frequency of the A/D conversion has been presented in [9]. The authors showed that when the observed signal from a low-frequency A/D converter is understood as the subsampled version of a desired signal sampled at a high frequency, it can be estimated via optimization involving the signal sparsity

assumption in a proper representation system. A side effect of increasing the effective bit depth is even demonstrated, thanks to inherent oversampling. The dequantization of audio has also been studied using different prior assumptions [6], [10]–[13]. However, these methods only rely on a single channel, which is in contrast to our approach, which combines two parallel sources of quantized audio information to achieve dequantization. We are not aware of any other multichannel dequantization method.

II. METHOD

The proposed means of signal acquisition are shown in Fig. 1. The parameters affecting the observations $\mathbf{y}_1, \mathbf{y}_2$ are:

- The sampling frequency of the right-hand branch.
- The sampling frequency of the left-hand branch; in our study it is k-times lower, due to the downsampler denoted D_k. (Utilizing a non-synchronized downsampler might bring additional benefits, but our simulation is based on digitized signals at the input.)
- The bit depths of the quantizers Q_{fine} and Q_{coarse}.
- The properties of the low-pass filter B.

Due to the involvement of lossy components in the acquisition, the estimation of $\mathbf{x}$ back from $\mathbf{y}_1, \mathbf{y}_2$ is clearly an ill-posed problem. As such, a kind of regularization has to be introduced. As one of the options, we will make use of the sparsity of an audio signal in the time-frequency domain in this paper. Therefore, our recovery task can be written as

$$\hat{\mathbf{x}} = \underset{\mathbf{x} \in \mathbb{R}^L}{\arg \min} \quad \lambda \|A\mathbf{x}\|_1 + \imath_{\Gamma_{\text{fine}}}(D_k B\mathbf{x}) + \imath_{\Gamma_{\text{coarse}}}(\mathbf{x}). \quad (1)$$

The operator A transforms a time-domain audio signal from $\mathbb{R}^L$ to the time-frequency domain $\mathbb{C}^P$ [14], and the sparsity of such a representation is quantified by the convex ℓ_1-norm $\|\cdot\|_1$ [15]. The functions $\imath_{\Gamma_{\text{fine}}}$ and $\imath_{\Gamma_{\text{coarse}}}$ are the indicator functions [16] taking value ∞ when $D_k B\mathbf{x} \notin \Gamma_{\text{fine}}$ and $\mathbf{x} \notin \Gamma_{\text{coarse}}$ enforcing the estimate to lie within the quantization levels corresponding to the operators Q_{fine} and Q_{coarse}, respectively. The indicator functions thus secure consistency of the solution with the observations, while the sparsity-related term promotes natural audio signals. Finally, the scalar $\lambda > 0$ is a weight which clearly could be omitted (i.e., $\lambda = 1$) in theory, but it can be used to influence the convergence of the practical numerical algorithm.

The problem (1) is convex and since it contains three terms, an advanced solver should be utilized. We make use of the Condat–Vũ algorithm (CVA) [17], [18], which utilizes proximal operators [16] corresponding to the functions involved in (1). The CVA for our problem is given in Alg. 1.

The asterisk denotes the adjoint of a linear operator; the adjoint of B is simply a filtering with the impulse response flipped in time. The operator $\text{clip}_\lambda(\cdot)$ clips the input vector elementwise such that the output samples reside in the interval $[-\lambda, \lambda]$.

As for the scalars τ, σ, the convergence of CVA is guaranteed if it holds $\tau\sigma\|A^*A + (D_kB)^*(D_kB) + Id^*Id\| \leq 1$. Using the properties of operator norms, we can arrive at a weaker

---

Algorithm 1: Condat–Vũ algorithm (CVA) solving (1)

Choose parameters $\tau, \sigma, \rho > 0$ and initial values
$\mathbf{x}^{(0)} \in \mathbb{R}^L, \ \mathbf{u}_1^{(0)} \in \mathbb{C}^P, \mathbf{u}_2^{(0)} \in \mathbb{R}^{L/k}, \mathbf{u}_3^{(0)} \in \mathbb{R}^L$.
for $i = 0, 1, \ldots$ **do**

$\quad \tilde{\mathbf{x}}^{(i+1)} = \mathbf{x}^{(i)} - \tau(A^*\mathbf{u}_1^{(i)} + B^*D_k^*\mathbf{u}_2^{(i)} + \mathbf{u}_3^{(i)})$

$\quad \mathbf{x}^{(i+1)} = \rho\tilde{\mathbf{x}}^{(i+1)} + (1-\rho)\mathbf{x}^{(i)}$

$\quad \tilde{\mathbf{u}}_1^{(i+1)} = \text{clip}_\lambda(\mathbf{u}_1^{(i)} + \sigma A(2\tilde{\mathbf{x}}^{(i+1)} - \mathbf{x}^{(i)}))$

$\quad \mathbf{u}_1^{(i+1)} = \rho\tilde{\mathbf{u}}_1^{(i+1)} + (1-\rho)\mathbf{u}_1^{(i)}$

$\quad \mathbf{p}_2 = \mathbf{u}_2^{(i)} + \sigma D_k B(2\tilde{\mathbf{x}}^{(i+1)} - \mathbf{x}^{(i)}) \ \% \text{ auxiliary}$

$\quad \tilde{\mathbf{u}}_2^{(i+1)} = \mathbf{p}_2 - \sigma \, \text{proj}_{\Gamma_{\text{fine}}}(\mathbf{p}_2/\sigma)$

$\quad \mathbf{u}_2^{(i+1)} = \rho\tilde{\mathbf{u}}_2^{(i+1)} + (1-\rho)\mathbf{u}_2^{(i)}$

$\quad \mathbf{p}_3 = \mathbf{u}_3^{(i)} + \sigma(2\tilde{\mathbf{x}}^{(i+1)} - \mathbf{x}^{(i)}) \ \% \text{ auxiliary}$

$\quad \tilde{\mathbf{u}}_3^{(i+1)} = \mathbf{p}_3 - \sigma \, \text{proj}_{\Gamma_{\text{coarse}}}(\mathbf{p}_3/\sigma)$

$\quad \mathbf{u}_3^{(i+1)} = \rho\tilde{\mathbf{u}}_3^{(i+1)} + (1-\rho)\mathbf{u}_3^{(i)}$

end

(still sufficient) condition $\tau\sigma(2 + \|\mathbf{b}\|_1^2) \leq 1$, where $\|\mathbf{b}\|_1$ is the ℓ_1-norm of the impulse response corresponding to B. Also, we have utilized the assumption that A corresponds to a tight Parseval frame, which is achieved via a suitable selection of transfrom parameters [19], see below our particular choice. The parameter ρ has to satisfy $\rho \in]0, 2[$.

III. EXPERIMENT

For the numerical experiment, we selected recordings of solo instruments. Such signals exhibit a great time-frequency sparsity, which the proposed reconstruction is regularized with. We used 83 excerpts selected from the Good-sounds dataset[1] containing various instruments, each playing several musical scales, such as violin, flute, saxophone, and clarinet. All audio is originally sampled at 48 kHz, in the 24-bit resolution (further on, we use the abbreviation bps for 'bits per sample'). The excerpts are between 10 and 20 seconds long. Audio has been peak-normalized before any processing to make the most of the available dynamic range.

Regarding the acquisition channels (see Fig. 1), Q_{coarse} operates at a bit depth varying between 4 and 16 bps, while the bit depth of Q_{fine} ranges between 10 and 24 bps. The quantization is uniform (linear PCM), as is typical in audio [1]. We use the mid-riser distribution of quantization levels, in line with [6]. In all experiments, the downsampling factor $k = 4$ is fixed, as is the low pass filter B, which has been designed by the Matlab Filter Designer as an FIR filter using the equiripple method. Note that for the purpose of the reconstruction, however, the properties of B are not crucial; actually, the proposed system would be applicable even if the filter were not present. The parameters of the operator A are: the 2048-sample-long Hann window, the window shift of 512 samples, and 4096 frequency channels. The Algorithm 1 used $\tau = 1$, $\sigma = 0.5$ and $\rho = 0.8$.

[1] https://www.upf.edu/web/mtg/good-sounds

A. Objective evaluation

We measure the performance of the algorithms using objective metrics: the common signal-to-distortion ratio (SDR) and the objective difference grade (ODG) provided by the PEMO-Q computational psychoacoustic model [20]. The ODG scale ranges from -4 to 0 (worst to best). These metrics are used for comparing our estimate $\hat{x}$ with reference signal x. We also evaluate SDR and ODG of the quantized signal observation x_Q and an estimate given by a different dequantization method compared with the reference signal x to judge the effectiveness of our method. The estimate we are comparing with is obtained by using the Chambolle–Pock algorithm (CPA) considering only single channel observation x_Q; the CPA was taken from [6]. We compare the results with the same bits per sample.

The results are presented in Fig. 2 and 3 in a condensed way. Instructions on how to read the graphs are in the captions.

As an example, take the case of 4 bps of the y_2 branch and 16 bps of the y_1 branch. As the y_1 branch is downsampled by a factor of 4, the effective number of bits of this combination is $4\,\text{bps} + \frac{1}{4} \cdot 16\,\text{bps} = 8\,\text{bps}$. Our reconstruction provides an average SDR of 43.09 dB which we compare with the reconstruction given by the CPA (i.e., $\text{CP}(x_Q)$) using the same number of effective bits resulting in an average SDR of 37.02 dB. From the graph, we can see that the 8-bit x_Q without processing provides an average SDR of 29.25 dB. The same combination of bit depths but this time in terms of the ODG scale, we see that our method provides an average ODG of -2.70. Using the CPA with the same bps increases the ODG of x_Q from -3.18 to -2.51. On the other hand, combinations with a higher effective number of bits in our reconstruction, for example 14 bps, are not better than using CPA, as we can see from the graph.

B. Computational considerations

Algorithm 1 was run for 200 iterations. With regard to the SDR plots, the maximum SDR achieved within these 200 iterations is presented. In particular cases, a small additional SDR improvement can be obtained by running more than 200 iterations; nevertheless, increasing the iteration count does not bring an improvement in most cases; typically, it is the other way round. Such an interesting effect is due to the presence of the ℓ_1 norm in (1): After reaching a good SDR within the constraints given by Γ_{fine} and Γ_{coarse}, the ℓ_1 norm starts to prevail, and as a lower $\|Ax\|_1$ is promoted, the signal is pushed towards lower quantization decision levels, therefore worsening the SDR [6]. The same effect is observable in the strip corresponding to the CPA in Fig. 2, since the CPA utilizes the ℓ_1 norm as well. The described effect is nevertheless not present in the ODG scores, and no significant improvement typically occurred with a greater number of iterations. Thus, the ODG value was computed based on the iteration no. 200.

Note that in Alg. 1, the parameter λ appears solely in connection with the clip operator. For each particular combination of the bit depths of the quantizers, a different choice of λ is advantageous as it speeds up the convergence and yields better results. Finding a right λ requires hand-on tuning, but we took advantage of values published in [6] as the starting point.

For a 19-second-long excerpt, a single iteration of the CVA takes about 0.18 second on a PC with Intel 3.6 GHz CPU and 64 GB RAM. Thus, the excerpt was reconstructed in about 40 seconds, i.e., twice the realtime.

IV. CONCLUSION

We have shown the possibility of reconstructing the desired signal from two parallel acquisition branches. Our algorithm scored well in both objective and subjective tests. In the future, testing at higher sampling rates is necessary.

The advantage of our algorithm further lies in the fact that by combining common converters with bit depths such as 4, 8, or 16 bps, we are able to achieve signal quality that would correspond to a less common converter with a bit depth of, for example, 9 bps.

Further extensions come naturally. For example, our approach exploits the simplest form of sparsity available; one could think about employing advanced signal priors such as the social sparsity [21] or the phase-consistency [22]. In such cases, only parts of the CVA algorithm would change. Generalization to nonuniform quantization would be straightforward. We have demonstrated the concept in the field of audio; however, the concept is general enough to be translated to image or video processing fields, with suitable regularizers. Finally, the concept allows increasing the sampling frequency beyond the frequency physically available in a device [9], i.e., superresolution.

Codes for Matlab are publicly available.[2]

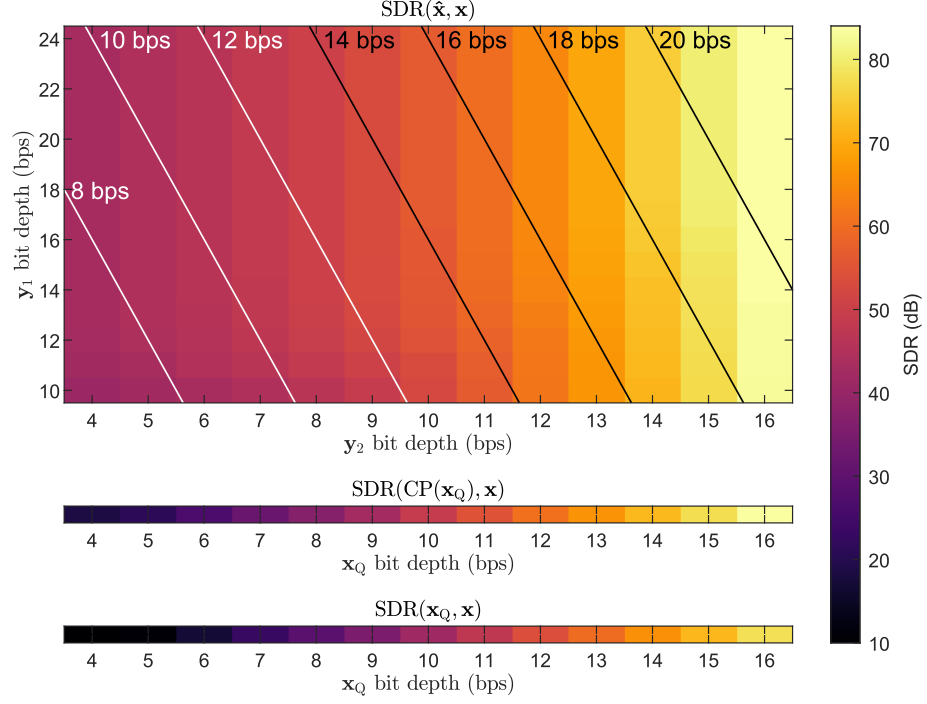[2] https://github.com/rajmic/parallel-dequantization

Fig. 2. Dequantization results in terms of the SDR; averages across test signals are presented. Each field in the main grid corresponds to a combination of bit depths in the two branches. The lines in the graph represent the combinations with the same number of effective bits. The colors code the SDR value of our reconstruction $\hat{\mathbf{x}}$ related to the original signal $\mathbf{x}$ (a lighter color indcates a closer estimate). The horizontal strip just below the main grid shows the SDR of the single channel reconstruction, $CP(\mathbf{x}_Q)$. The bottom strip presents the SDR of $\mathbf{x}_Q$ without postprocessing.
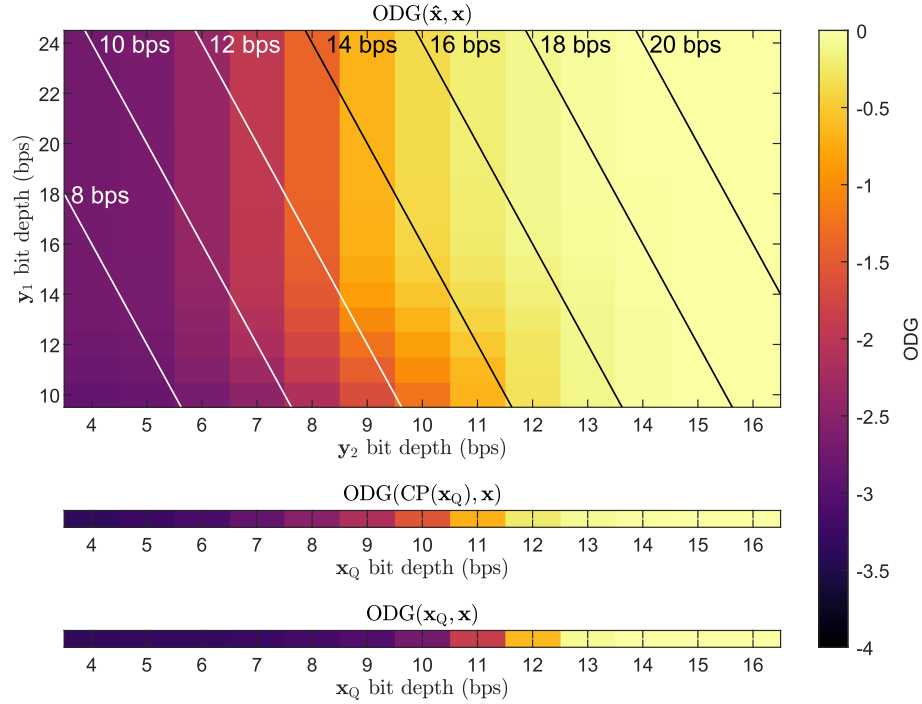

Fig. 3. Dequantization results in terms of the ODG, presented in analogy with Fig. 2.

References

[1] J. Watkinson, *The Art of Digital Audio*, Focal Press, 2001.

[2] A. Petraglia and M.A.A. Pinheiro, "Effects of quantization noise in parallel arrays of analog-to-digital converters," in *Proceedings of IEEE International Symposium on Circuits and Systems – ISCAS '94*, 1994, vol. 5, pp. 337–340.

[3] P. Lowenborg and H. Johansson, "Quantization noise in filter bank analog-to-digital converters," in *The 2001 IEEE International Symposium on Circuits and Systems (ISCAS)*, 2001, vol. 2, pp. 601–604.

[4] Jian Gao, Peng Ye, Hao Zeng, Zhixiang Pan, Yu Zhao, Hao Li, and Jie Meng, "Theory of quantization-interleaving adc and its application in high-resolution oscilloscope," *IEEE Access*, vol. 7, pp. 156722–156732, 2019.

[5] Filip Šroubek, Jan Flusser, and Gabriel Cristóbal, "Super-resolution and blind deconvolution for rational factors with an application to color images," *The Computer Journal*, vol. 52, no. 1, pp. 142–152, 2009.

[6] Pavel Záviška, Pavel Rajmic, and Ondřej Mokrý, "Audio dequantization using (co)sparse (non)convex methods," in *2021 IEEE International Conference on Acoustics, Speech and Signal Processing (ICASSP)*, Toronto, Canada, 2021, pp. 701–705.

[7] Emmanuel J. Candes and Michael B. Wakin, "An introduction to compressive sampling," *IEEE Signal Processing Magazine*, vol. 25, no. 2, pp. 21–30, 2008.

[8] Marie Mangová, *Increasing Resolution in Perfusion Magnetic Resonance Imaging Using Compressed Sensing*, Ph.d. thesis, Brno University of Technology, 2018.

[9] Aldo Baccigalupi, Mauro D'Arco, Annalisa Liccardo, and Rosario Schiano Lo Moriello, "Compressive sampling-based strategy for enhancing ADCs resolution," *Measurement*, vol. 56, pp. 95–103, 2014.

[10] C. Brauer, Z. Zhao, D. Lorenz, and T. Fingscheidt, "Learning to dequantize speech signals by primal-dual networks: an approach for acoustic sensor networks," in *2019 IEEE International Conference on Acoustics, Speech and Signal Processing (ICASSP)*, May 2019, pp. 7000–7004.

[11] Lucas Rencker, Francis Bach, Wenwu Wang, and Mark D. Plumbley, "Sparse recovery and dictionary learning from nonlinear compressive measurements," *IEEE Transactions on Signal Processing*, vol. 67, no. 21, pp. 5659–5670, Nov. 2019.

[12] P. T. Troughton, "Bayesian restoration of quantised audio signals using a sinusoidal model with autoregressive residuals," in *Proceedings of the 1999 IEEE Workshop on Applications of Signal Processing to Audio and Acoustics. WASPAA'99 (Cat. No.99TH8452)*, Oct. 1999, pp. 159–162.

[13] Hyun-Wook Yoon, Sang-Hoon Lee, Hyeong-Rae Noh, and Seong-Whan Lee, "Audio dequantization for high fidelity audio generation in flow-based neural vocoder," in *Proc. Interspeech 2020*, Shanghai, China, Oct. 2020, pp. 3545–3549.

[14] Karlheinz Gröchenig, *Foundations of time-frequency analysis*, Birkhäuser, 2001.

[15] David L. Donoho and Michael Elad, "Optimally sparse representation in general (nonorthogonal) dictionaries via ℓ_1 minimization," *Proceedings of The National Academy of Sciences*, vol. 100, no. 5, pp. 2197–2202, 2003.

[16] Patrick L. Combettes and Jean-Christophe Pesquet, "Proximal splitting methods in signal processing," *Fixed-Point Algorithms for Inverse Problems in Science and Engineering*, vol. 49, pp. 185–212, 2011.

[17] Laurent Condat, "A generic proximal algorithm for convex optimization—application to total variation minimization," *Signal Processing Letters, IEEE*, vol. 21, no. 8, pp. 985–989, Aug. 2014.

[18] B. C. Vũ, "A splitting algorithm for dual monotone inclusions involving cocoercive operators," *Advances in Computational Mathematics*, vol. 38, no. 3, pp. 667–681, Apr. 2013.

[19] O. Christensen, *An Introduction to Frames nad Riesz Bases*, Birkhäuser, Boston-Basel-Berlin, 2003.

[20] R. Huber and B. Kollmeier, "PEMO-Q—A new method for objective audio quality assessment using a model of auditory perception," *IEEE Trans. Audio Speech Language Proc.*, vol. 14, no. 6, pp. 1902–1911, Nov. 2006.

[21] M. Kowalski, K. Siedenburg, and M. Dörfler, "Social sparsity! neighborhood systems enrich structured shrinkage operators," *Signal Processing, IEEE Transactions on*, vol. 61, no. 10, pp. 2498–2511, 2013.

[22] Tomoro Tanaka, Kohei Yatabe, and Yasuhiro Oikawa, "PHAIN: Audio inpainting via phase-aware optimization with instantaneous frequency," *IEEE/ACM Transactions on Audio, Speech, and Language Processing*, vol. 32, pp. 4471–4485, 2024.

Hausdorff Distance for P wave Alignment in ECG with Intracardiac Validation

1st Richard Redina

Department of Biomedical Engineering,
Faculty of Electrical Engineering
and Communication,
Brno University of Technology,
International Clinical Reseach Center
St. Anna's University Hospital
Brno, Czech Republic
0000-0002-4901-0504

2nd Adrian Luca

University Hospital of Lausanne,
Lausanne, Switzerland
0000-0002-0040-8191

3rd Jakub Hejc

International Clinical Reseach Center
St. Anna's University Hospital
Brno, Czech Republic 0000-0001-5743-9960

4th Marina Filipenska

Department of Biomedical Engineering,
Faculty of Electrical Engineering
and Communication,
Brno University of Technology,
Brno, Czech Republic
0000-0003-1366-8336

Abstract—The accurate alignment of P waves on surface electrocardiograms (ECG) is crucial to evaluating atrial electrical activity, particularly in patients with arrhythmias. This study introduces a novel P wave alignment method based on the Hausdorff distance, validated against intracardiac electrograms (EGM). The detection process incorporates a wavelet transform for QRS complex identification and dynamic pattern matching using the Hausdorff distance and Pearson's correlation coefficient. Statistical analysis was performed using F and t tests to compare variances and mean shift values between the correlation and Hausdorff distance methods over various pattern durations. The results indicated that there were no significant differences between the two methods, apart from extreme cases (the p-values of the F test ranged from 0.003 to 0.265, and the p-values of the t test ranged from 0.079 to 0.661). The findings suggest that both metrics perform similarly, offering reliable alternatives for the alignment of P waves in clinical and research applications. The proposed approach has the potential to enhance P wave detection, improving the precision of atrial signal analysis in patients with atrial arrhythmias.

Index Terms—Arrhythmia, Hausdorff distance, P wave alignment, Wavelet Transform, Intracardiac Electrograms

I. Itroduction

Accurate alignment of P waves in surface electrocardiograms (ECG) is critical for the assessment of atrial electrical activity, particularly in patients with cardiac arrhythmias. The precise identification of P-wave onset and its offset provides valuable information on atrial conduction and arrhythmogenic mechanisms. However, standard signal processing techniques often struggle with robust alignment due to low amplitude, noise interference, and variations in morphology between patients. [1]

In this study, we propose a novel approach for the alignment of P waves based on Hausdorff distance, a metric commonly applied in shape comparison and pattern recognition [2]. Using this geometric measure, we aim to improve the robustness of P-wave detection in complex ECG signals. A key objective of this work is to assess whether the Hausdorff distance-based method can achieve at least comparable performance to the widely used correlation-based approach. To validate our method, we utilize intracardiac electrograms (EGMs) as a reference, specifically the local activation time (LAT) recorded from intracardiac electrodes. This enables an objective comparison between ECG-derived surface P waves and the true electrical activation of atrial tissue [3].

The proposed methodology has the potential to enhance the accuracy of P wave alignment in clinical and research settings, particularly for patients with atrial arrhythmias where standard algorithms may be insufficient. In the following sections, we detail the methodological framework, present experimental results, and discuss the implications of our findings for improved atrial signal analysis.

II. Methods

This study introduces a new pipeline for the alignment of the P wave in surface ECG using the Hausdorff distance (HD). To validate the approach, intracardiac electrograms (EGM) serve as a reference standard. First, P waves are detected using a wavelet transform, with QRS complexes providing

temporal anchoring. The local activation times (LAT) are then identified from intracardiac signals recorded through a coronary sinus catheter. The alignment of the P wave is performed by segmenting the signal between consecutive LATs based on the Hausdorff distance [4], a geometric measure designed to compare two-dimensional curves. As a control, the P wave intervals are compared with the simple temporal difference between the LAT peaks in intracardiac recordings. The following subsections describe the dataset, preprocessing steps, and methodological details.

A. Data

The study used preliminary data from 47 patients selected from the publicly available dataset [5]. This database consists of recordings from patients with various arrhythmias and includes both surface electrocardiograms (ECG) and intracardiac electrograms (EGM). Both signals were sampled at frequency 2 kHz. For this analysis, only segments corresponding to the sinus rhythm were included, ensuring a consistent physiological baseline for the alignment of the P wave.

The dataset provides annotated markers that indicate the onset of local activation in coronary sinus leads. These annotations were used as reference points to approximate P wave positions. Given that it is assumed that the catheter position remains stable throughout the recording, the spatial relationship between the reference annotation and the corresponding P wave location should remain consistent within each patient.

B. P wave alignment

The detection of P waves follows a structured multistep approach, integrating advanced signal processing techniques to enhance atrial activity patterns while ensuring robustness across different signal conditions.

The process begins with the identification of the QRS complex, achieved through bandpass filtering to remove baseline wander and high-frequency noise, wavelet transform-based feature extraction to enhance morphology, and adaptive thresholding to detect dominant R peaks. The precise location of the R peak is then adjusted to align with the most prominent spike in the signal, ensuring consistency between beats.

Given that the patient is in sinus rhythm, the P wave is expected to occur within a physiologically consistent interval before each QRS complex. To define this region, a fixed time window is selected that precedes the detected R peak, with possible adjustments based on variability between patients. This region is systematically analyzed to identify the location of the P wave.

The first P wave in the signal is detected using a Mexican hat wavelet transform [6], applied to emphasize the local curvature characteristics of P waves, enhancing their distinction from surrounding activity. A peak detection algorithm is then used to identify the most prominent maximum within the transformed representation, corresponding to the likely position of the first P wave.

Following automatic detection, the identified P wave position undergoes a visual inspection for confirmation and potential refinement. This step allows for manual verification and adjustment if necessary, ensuring that the reference P wave is correctly localized before further processing.
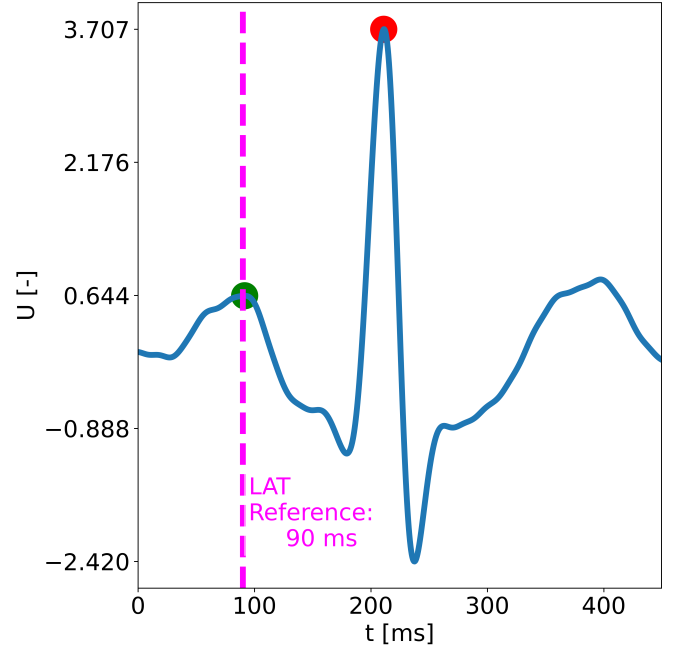

Fig. 1. ECG signal sample with detected R-peak (red) and first P-peak (green). A reference vertical line (magenta) marks a key time point, with the corresponding time indicated in milliseconds. The time axis is displayed in milliseconds, and the signal amplitude is shown in normalised units (U).

Subsequent P waves are detected using the initial detected P wave as a reference pattern. the duration of the pattern is dynamically adjusted within a time window ranging from 190 to 230 ms [7], with the peak P positioned at the center of the window. The pattern search is conducted in the temporal region following each detected R peak. Within this search window, both the maximum correlation and minimum Hausdorff distance are computed to evaluate the alignment of the candidate P wave with the reference pattern. Given the assumption that the reference P wave should be approximately consistent in position throughout the ECG signal, the shift between the reference position of the initial P wave and the detected position of subsequent P waves is also quantified, providing an indication of the localization accuracy.

C. Metrics used

To evaluate the alignment of the P wave, we employ the Hausdorff distance (HD) as the primary metric, supplemented by correlation analysis for comparison.

The Hausdorff distance is a measure of the dissimilarity between two point sets, commonly used in shape analysis. Given two sets of points $A = \{a_1, a_2, \ldots, a_m\}$ and $B = \{b_1, b_2, \ldots, b_n\}$, the directed Hausdorff distance is defined as:

$$d_H(A, B) = \max \left(\sup_{a \in A} \inf_{b \in B} \|a - b\|, \sup_{b \in B} \inf_{a \in A} \|b - a\| \right) \quad (1)$$

where $\|\cdot\|$ denotes the Euclidean norm. This metric captures the largest discrepancy between two sets, making it suitable for assessing differences in P wave alignment.

As our objective is to minimize the discrepancy between the detected and reference P wave boundaries, we propose modifying the Hausdorff distance formulation accordingly. Specifically, we replace the operator $\max\{\cdot\}$ with $\min\{\cdot\}$, ensuring that the measure reflects the closest rather than the furthest deviation between the two sets, resulting in the new formula:

$$d_H^{\text{mod}}(A, B) = \min\left(\sup_{a \in A} \inf_{b \in B} \|a - b\|, \sup_{b \in B} \inf_{a \in A} \|b - a\|\right) \quad (2)$$

This modification better aligns the metric with the goal of precise P wave alignment by emphasizing minimal deviations instead of worst-case discrepancies.

For validation, we also compute the Pearson correlation coefficient to compare the detected P wave intervals with the reference intervals derived from intracardiac LAT measurements. Given two sequences $X = (x_1, x_2, ..., x_n)$ and $Y = (y_1, y_2, ..., y_n)$, the Pearson correlation coefficient is defined as

$$r = \frac{\sum_{i=1}^{n}(x_i - \bar{x})(y_i - \bar{y})}{\sqrt{\sum_{i=1}^{n}(x_i - \bar{x})^2}\sqrt{\sum_{i=1}^{n}(y_i - \bar{y})^2}} \quad (3)$$

where $\bar{x}$ and $\bar{y}$ represent the mean values of X and Y, respectively. A high correlation indicates strong agreement between the delineated and reference intervals.

D. Statistical analysis

To evaluate the differences between the shift measurements obtained using correlation and Hausdorff distance across various pattern duration, two statistical tests were employed. First, the F-test was used to compare the variances of the shifts for each method. This test assesses whether there are significant differences in the variability of changes between the two metrics. Subsequently, the Student's t-test was applied to compare the mean shift values between correlation and Hausdorff distance for each pattern duration. This test evaluates whether the observed differences in the means are statistically significant. A significance threshold of $p < 0.05$ was established for both tests, indicating statistical evidence of differences between methods.

III. RESULTS

In this preliminary study, a total of 513 P waves were analyzed. For each P-wave, two sets of shifts were computed on the basis of correlation and Hausdorff distance across various pattern durations. To assess statistical differences between these two sets of shifts, we performed both an F-test to compare variances and a t-test to compare means.

The results of these tests (Table I) did not reveal significant differences between the two methods for most of the pattern durations, as indicated by the p-values. However, a more noticeable divergence appears for the longest window duration

(240 ms), probably due to portions of the QRS complex being included in the pattern, which may affect similarity measures and shift estimations.

Figures 2 and 3 illustrate the alignment of the P wave based on both matching criteria. The results show that both methods produce comparable P-wave positions, with slight variations in the detected alignment.

Figures 4 and 5 present the distribution of the computed shifts (in milliseconds) for the alignment of the P wave. Figure 5 displays the distribution of the shifts obtained by maximizing the correlation coefficient, while Figure 4 shows those derived from minimizing the modified Hausdorff distance. In both cases, the red dashed line represents the mean shift, which is slightly negative: -0.13 ms for correlation-based alignment and -0.41 ms for Hausdorff distance-based alignment. Despite this small offset, both methods yield consistent P wave detections, demonstrating their robustness for delineation in this context.
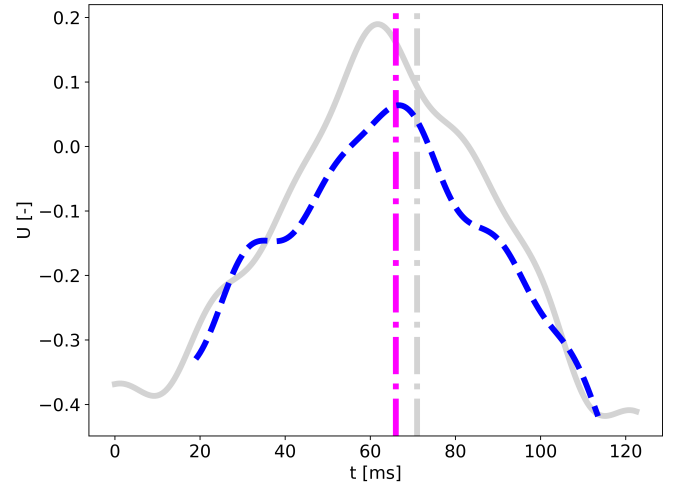

Fig. 2. Visualization of P wave alignment based on the best correlation match. The ECG signal (gray) is shown with the P wave pattern (blue, dashed). The magenta dashed line indicates the optimal alignment shift, while the light gray dashed line marks the reference position. The time axis is in milliseconds (ms), and the signal amplitude is normalized.

TABLE I
P-VALUES OBTAINED FROM F-TEST AND T-TEST FOR DIFFERENT PATTERN DURATION. THE TESTS WERE PERFORMED TO EVALUATE STATISTICAL DIFFERENCES IN THE ANALYZED SIGNALS ACROSS VARYING WINDOW LENGTHS.

Pattern duration	F-test	t-test
190	0.1201	0.3941
200	0.0896	0.4077
210	0.1047	0.3087
220	0.0823	0.1025
230	0.0490	0.0340
240	0.0004	0.0133

IV. DISCUSSION

A. Comparison of Distance Metrics

The results of this study highlight that both the Hausdorff distance and the correlation coefficient yield similar shift
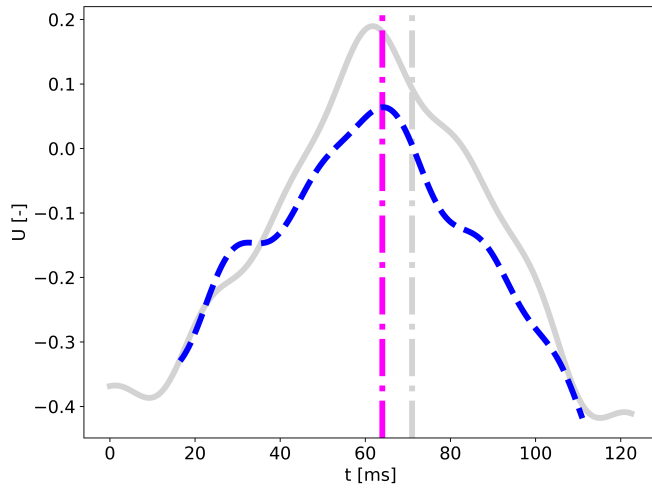
Fig. 3. P wave alignment using the best Hausdorff distance match. The padded ECG signal (gray) is displayed with the P wave pattern (blue, dashed). The magenta dashed line represents the optimal shift based on the Hausdorff distance, while the light gray dashed line indicates the reference position. Time is given in milliseconds (ms), and the signal amplitude is normalized.
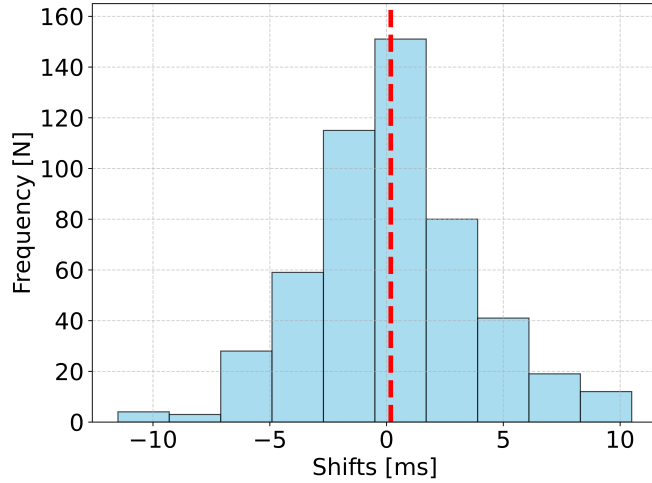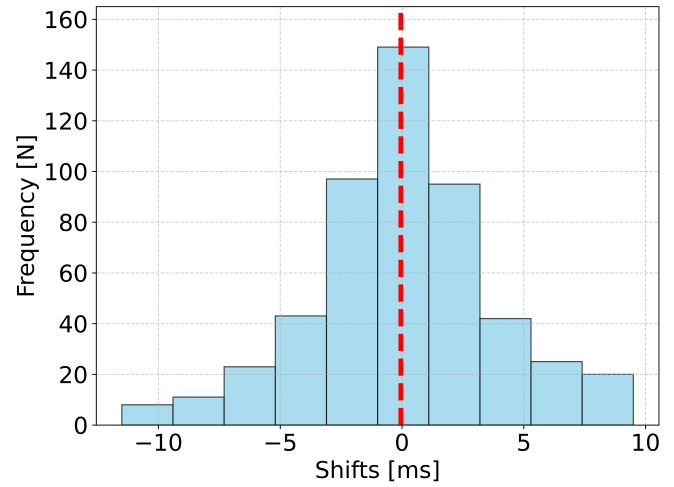

Fig. 5. Distribution of the shifts (in ms) calculated using the modified Hausdorff distance coefficient for the P wave alignment with pattern duration 210 ms. The mean shift is indicated by the red dashed line (-0.053 ms).

tion coefficient in conjunction with intracardiac electrograms as a reference, we ensure a more accurate alignment of the surface ECG P waves with the true electrical activation of the atrium, especially in patients with arrhythmias. This improves the reliability of the location of the P wave, which is critical to assessing atrial conduction and detecting arrhythmogenic patterns.

C. Statistical Analysis Interpretation

The lack of significant differences in the results of the F-test and the t-test further supports the idea that both metrics, the correlation and the Hausdorff distance, perform similarly in terms of mean changes and variance. These statistical results indicate that, for the tested pattern durations, both methods yield comparable alignment accuracies, making them viable alternatives for clinical and research purposes. Future studies may explore whether the inclusion of additional patient-specific factors could further differentiate the performance of these metrics.

D. Implications for Atrial Arrhythmia Research

The findings of this study provide important implications for the investigation of atrial arrhythmias. An accurate and robust alignment of the P wave is essential to understand the mechanisms of arrhythmogenesis in the atria. By offering an effective method for alignment, this approach could contribute to better predictions of arrhythmic events, improved patient outcomes, and more precise atrial signal analysis. Furthermore, the use of intracardiac electrograms as a reference allows for a more objective evaluation of surface ECG signals, improving the credibility and precision of the results.

Fig. 4. Distribution of the shifts (in ms) calculated using the correlation coefficient for the P wave alignment with pattern duration 210 ms. The mean shift is indicated by the red dashed line (0.179 ms).

distributions for the alignment of the P wave, suggesting that either metric can be used effectively for this purpose. Although the Hausdorff distance has the advantage of focusing on the minimum deviations between P wave peaks, the correlation metric also provides a reliable measure of alignment. Both methods provide complementary insights into the accuracy of P wave detection, indicating their utility in clinical applications, particularly in the context of atrial arrhythmias.

B. Robustness of the Methodology

The proposed methodology demonstrates significant robustness in the detection and alignment of P waves in complex ECG signals, even with the challenges posed by noise and low-amplitude signals. Using the Hausdorff distance and correla-

V. LIMITATIONS

A. Generalizability of the findings

The analysis in this study was based on a relatively small subset of 47 patients, all of whom were selected from a pub-

licly available data set. Although the results are promising, the sample size and limited demographics of the patients can affect the generalizability of the findings. Importantly, the study population consisted of pediatric patients, who generally exhibit a more regular propagation of the atrial depolarization wave. This intrinsic stability may contribute to more consistent results in this cohort. However, these findings do not necessarily translate to adult patients, particularly those with atrial pathologies that could alter conduction patterns. It is possible that the performance of the proposed method could vary in larger cohorts or different patient populations, particularly those with more diverse arrhythmias or other confounding factors.

B. Signal quality and noise interference

Although the proposed method demonstrates robustness against low-amplitude and noise signals, challenges related to signal quality remain. For example, surface ECG signals may suffer from artifacts caused by muscle contractions, baseline drift, or motion. These factors can negatively impact the accuracy of P wave detection, particularly in patients with poor signal quality. Further refinement of the signal processing pipeline, including more advanced filtering techniques, could help mitigate these challenges.

C. Variable Pattern Duration

In this study, the detection of the P wave was performed using a series of pattern durations rather than a fixed duration. Different pattern lengths were analyzed to evaluate how the chosen duration affects the alignment metrics in various settings. This approach allowed for a comprehensive assessment of the method's performance under different conditions. The results suggest that an adaptive selection of pattern duration, based on the characteristics of the ECG signal, could further enhance the accuracy of alignment in various scenarios.

D. Manual verification

Although automatic detection of P waves is followed by visual inspection and manual verification, this step introduces potential bias and subjectivity. the need for manual adjustment can lead to inconsistencies, particularly in a larger clinical setting with high patient throughput. Automating this verification step would reduce human error and streamline the process, making the method more feasible for widespread clinical use.

E. Intracardiac EGM as reference

The reliance on intracardiac electrograms (EGM) as the reference standard is a strength of the study, providing a highly accurate measure of electrical activation of the atrium. However, the use of intracardiac electrodes is invasive and not always feasible in routine clinical practice. Thus, while this approach offers high precision in alignment, its practical application may be limited to specific research settings or cases that require invasive monitoring. Alternative non-invasive methods to improve surface ECG alignment should be explored.

VI. Conclusion

This study presents a novel approach to alignment of P waves in surface ECG signals using the Hausdorff distance, validated against intracardiac electrograms. Both the Hausdorff distance and the correlation coefficient were found to yield similar results in terms of shift distribution, demonstrating their effectiveness in accurately aligning P waves. Despite certain limitations, such as the reliance on manual verification and fixed pattern duration, the proposed method shows promise for improving P wave detection, particularly in patients with arrhythmias. This approach offers valuable information for the analysis of atrial signals and could improve the clinical understanding of arrhythmogenic mechanisms, with potential applications in both research and patient care.

References

[1] L. Saclova, A. Nemcova, R. Smisek, L. Smital, M. Vitek, and M. Ronzhina, "Reliable P wave detection in pathological ECG signals," Scientific Reports, vol. 12, no. 1, p. 6589, Apr. 2022, doi: https://doi.org/10.1038/s41598-022-10656-4.

[2] O. U. Aydin et al., "On the usage of average Hausdorff distance for segmentation performance assessment: hidden error when used for ranking," European Radiology Experimental, vol. 5, no. 1, Jan. 2021, doi: https://doi.org/10.1186/s41747-020-00200-2.

[3] J. Hejč, M. Vítek, M. Ronzhina, M. Nováková, and J. Kolářová, "A Wavelet-Based ECG Delineation Method: Adaptation to an Experimental Electrograms with Manifested Global Ischemia," Cardiovascular Engineering and Technology, vol. 6, no. 3, pp. 364–375, Apr. 2015, doi: https://doi.org/10.1007/s13239-015-0224-z.

[4] L. S. Fainzilberg, "ECG averaging based on Hausdorff metric," Int. J. Bioelectromagn., vol. 5, no. 1, pp. 236–237, 2003.

[5] R. Ředina, Jakub Hejc, D. Pospíšil, M. Ronzhina, P. Novotná, and Z. Starek, "Arrhythmia Database with Annotated Intracardial Atrial Signals from Pediatric Patients Undergoing Catheter Ablation," Computing in Cardiology (CinC), 2012, Dec. 2022, doi: https://doi.org/10.22489/cinc.2022.282.

[6] M. Ali, S. Mohsen, and M. M. Abo-Zahhad, "ECG signals compression using dynamic compressive sensing technique toward IoT applications," Multimedia tools and applications, vol. 83, no. 12, pp. 35709–35726, Sep. 2023, doi: https://doi.org/10.1007/s11042-023-17099-7.

[7] S. A. Guidera and J. S. Steinberg, "The signal-averaged P wave duration: A rapid and noninvasive marker of risk of atrial fibrillation," Journal of the American College of Cardiology, vol. 21, no. 7, pp. 1645–1651, Jun. 1993, doi: https://doi.org/10.1016/0735-1097(93)90381-a.

Sampling Configuration Analysis for the Design of Spherical Microphone Array

Matej Liska
Department of Telecommunications
Brno University of Technology
Brno, Czech Republic
xliska19@vut.cz

Abstract—**This paper investigates optimal microphone placement in spherical microphone arrays by analyzing spherical sampling designs. The placement of microphones on a sphere significantly influences the accuracy of sound pressure estimation and field reconstruction. Various sampling strategies, including the Lebedev quadrature and t-designs, are examined for their effectiveness in spherical surface sampling. To assess their uniformity and suitability, these designs are compared by efficiency and using statistical measures such as mean spacing, standard deviation and spherical cap discrepancy. The results provide a quantitative basis for selecting optimal microphone placements in spherical arrays designed for spatial sound field analysis.**

Index Terms—**optimal sampling, spherical microphone arrays, spherical t-designs, spatial & uniform distribution analysis**

I. Introduction

The design of spherical microphone arrays is a critical research area across various disciplines, including acoustics, beamforming, spatial filtering techniques, and spatial audio capture and rendering. Similar to other fields where spatial sampling is essential for digital processing, the design of microphone arrays involves determining optimal configurations that balance system complexity with the accuracy of the reconstructed sound field. Specifically, the positions of microphones within a spherical array determine the sampling points, which, in turn, influence the precision of sound pressure field reconstructions. The challenge lies in identifying the most effective configuration of microphones to achieve the desired accuracy while minimizing the number of microphones to reduce system complexity and cost [1]. In this study, we focus on spherical microphone arrays designed to capture the sound field in terms of spherical harmonics up to the 4th degree, due to limitations. A detailed explanation of these limitations can be found in Section III.

Sampling theorems, such as the Nyquist theorem [2], which are commonly applied to time and space, offer valuable insights into the design of microphone arrays. These theorems assert that to achieve perfect reconstruction from samples, the underlying function must be band-limited. In the context of spherical arrays, this translates to requiring the sampled function to be order-limited or representable by a finite number of spherical harmonics [3].

The application of sampling theorems on the sphere is thus analogous to traditional sampling in time or space, with the key difference being the use of spherical harmonics as the basis functions for the approximation of the sound pressure. The general problem of spatial sampling can be framed within the context of quadrature methods, where the aim is to compute an approximation of the integral of a function using a summation over discrete samples. In this case, the function is the sound pressure over the unit sphere, and the challenge is to identify an optimal set of sample points and associated weights that allow for accurate integration, or equivalently, reconstruction of the function from the samples.

Sec. II provides background on sampling order-limited functions. Sec. III describes the system design. Sec. IV presents an overview of quadrature sampling schemes. Sec. V and VI provide statistical and Cap Discrepancy analysis. Sec. VII compares and validates the proposed modifications. Sec. VIII concludes the paper.

II. Sampling and Efficiency of Square-Integrable Order-Limited Functions

Quadrature schemes, derived from the theoretical framework of square-integrable functions on the unit sphere, can be described as $L^2(\mathbb{S})^2 = \{\int_{\mathbb{S}^2} |f|^2 \, d\Omega < \infty\}$. Functions within this class can be represented as expansions in terms of the orthonormal basis of spherical harmonics on $\mathbb{S}^2$ [4]. The spherical harmonics are presented as a weighted sum of a set of basis functions, also forming the Fourier basis for functions on the sphere. The explicit form of the spherical harmonics is given by [5]:

$$Y_n^m(\theta, \phi) \equiv \sqrt{\frac{2n+1}{4\pi} \frac{(n-m)!}{(n+m)!}} P_n^m(\cos\theta) e^{im\phi}, \quad (1)$$

where ! represents the factorial function, P_n^m are the associated Legendre functions, $m \in \mathbb{Z}$ is an integer denoting the function degree and $n \in \mathbb{N}$ is a natural number denoting the function order, θ represents elevation and ϕ azimuthal angle.

As previously mentioned, quadrature methods are designed to approximate the integral of a given function through a summation over samples of that function [1]. In this context, if we truncate the expansion, we can define a finite subset of spherical harmonics up to degree N as $\Pi^N = \text{span}\{Y_n^m(\theta, \phi) : 0 \leq n \leq N, -n \leq m \leq n\}$. By uti-

lizing these spherical harmonics, any function in Hilbert space $f \in L^2(\mathbb{S}^2)$ can be expressed as:

$$f(\theta, \phi) = \sum_{n=0}^{N} \sum_{m=-n}^{n} c_{nm} Y_n^m(\theta, \phi), \qquad (2)$$

where the coefficients c_{nm} can be found via inner products with the basis functions, which was described in [6] as:

$$c_{nm} = \int_{\mathbb{S}^2} f(\theta, \phi) \bar{Y}_n^m(\theta, \phi) \, d\Omega. \qquad (3)$$

The coefficient decay rate depends on the smoothness of f, which determines the convergence rate of the spherical harmonics expansion. A quadrature method seeks to approximate the integral of a function $f(\theta, \phi)$ by utilizing a discrete set of sample points (θ_q, ϕ_q) on the unit sphere, along with corresponding sampling weights α_q, where Q represents the total number of samples. In this context, the function $f(\theta, \phi)$ can be exactly reconstructed on the sphere $\mathbb{S}^2$ through the inverse spherical Fourier transform. Substituting the spherical harmonic $Y_{n'}^{m'}(\theta_q, \phi_q)$ for $f(\theta, \phi)$ and assuming the Dirac delta functions over the sphere $\delta_{nn'}\delta_{mm'}$ for the Fourier coefficients c_{nm} [1], this process leads to following expression:

$$\sum_{q=1}^{Q} \alpha_q Y_{n'}^{m'}(\theta_q, \phi_q) \bar{Y}_n^m(\theta_q, \phi_q) \approx \delta_{nn'}\delta_{mm'}. \qquad (4)$$

For order-limited functions, this approximation holds exactly within a specified order range, preserving the orthogonality of spherical harmonics in an ideal sampling scheme. From the spherical harmonic expansion, it is evident that an effective quadrature scheme must integrate all spherical harmonics up to a degree N, corresponding to the space Π^N. McLaren [7] used this principle to define the efficiency of quadrature schemes, which is the ratio of the number of spherical harmonics L that the scheme integrates exactly to the total degrees of freedom in the quadrature setup. For a quadrature rule with Q integration points, the degrees of freedom is $3Q$, as each integration node specifies coordinates (θ_q, ϕ_q) and a weight w_q. Ensuring exact integration of all spherical harmonics up to degree N gives $L = (N + 1)^2$, leading to the efficiency formula:

$$E = \frac{(N + 1)^2}{3Q} 100. \quad [\%] \qquad (5)$$

III. Description of the System Design

Our system utilizes Time-Division Multiplexing (TDM) [8] for microphone data acquisition, supporting up to 16 microphones per TDM line. The maximum spacing between microphones on the same line is constrained to 50 mm for proper synchronization. A custom flexible-rigid PCB was designed to daisy-chain 16 microphones to the FPGA, with each USB-C connection measuring approximately 13,4 mm. This reduces the available spacing, resulting in a final maximum distance of 23,2 mm between microphone capsules, defining the inner dimensions of the spherical structure.

The FPGA used for data sampling and high-frequency clock signal generation currently supports two TDM lines, enabling

a total of 32 microphones. This setup focuses on a spherical configuration with at least 25 microphones for 4th-order sound field sampling. The final diameter of the 15 mm thick sphere will be determined in Section 6. The system allows data transfer using FTDI chip [9] to Matlab via a single USB cable for power and data transmission. A detailed description of system prototype is provided in [10].

IV. Quadrature Sampling Schemes

A perfectly uniform distribution ensures that no region is disproportionately represented, which is essential for applications such as spherical harmonic analysis. Uniformity is a fundamental concept in spherical sampling, referring to the even distribution of points across the sphere's surface. In the context of quadrature-based sampling, we aim to approximate integrals over the sphere using weighted sums of function values at specific sample points. The choice of sampling scheme directly impacts the accuracy of these approximations.

A. Lebedev sampling

The Lebedev quadrature method [11] constitutes a well-established approach for determining optimized point distributions for numerical integration over the unit sphere. Specifically designed to facilitate Gaussian quadrature on $\mathbb{S}^2$, this method achieves high-order accuracy while minimizing the number of required sampling points. However, as the Lebedev scheme prioritizes quadrature precision, the resulting point sets do not necessarily exhibit strict spatial uniformity, and the associated quadrature weights are not uniformly distributed across all points. For instance, considering the 26-point Lebedev rule with the 7th degree precision from [7], the efficiency, as determined via Eq. (5), could be calculated as:

$$E = \frac{(7 + 1)^2}{3 \cdot 26} 100 = 82.05\%. \qquad (6)$$

B. Spherical t-designs

If we impose the standard requirement that a quadrature is exact for all spherical harmonics up until degree N in the case of equal weights we arrive at the spherical designs. The platonic solids can be seen as spherical designs. Sampling distributions based on the platonic solids offer uniform distributions of samples, with a simple equation to compute the spherical Fourier transform. However, they are available only for a limited number of configurations to maximum second order and 20 number of points.

Hardin and Sloane [12] extend the t-designs of the platonic solids to a larger set of sampling configurations, for some t value and a corresponding degree N. Based on their approach, it is possible to obtain our desired configuration for 25 to 32 points on sphere. Its energy calculated via Eq. (5) is shown in Fig. 1 – 3-degrees of freedom.

It should be noted that the original McLaren formula Eq. (5) was used to determine E, assuming three degrees of freedom per node. However, if the fixed equal weights were interpreted as a reduction in degrees of freedom and each point will have only two degrees of freedom. This adjustment reflects
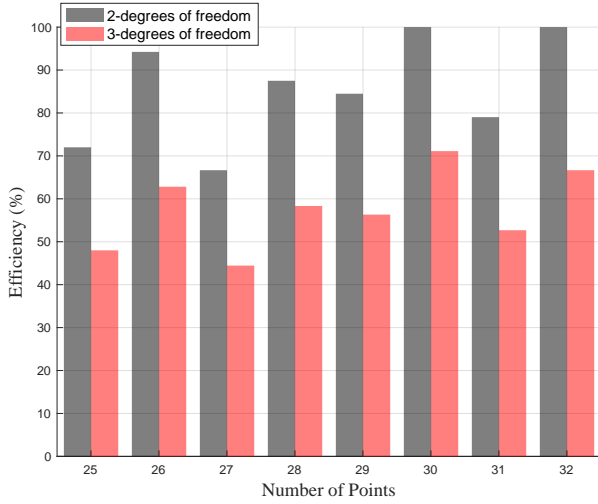
Fig. 1. Efficiency of t-designs (25-32 points) by Hardin & Sloane.

TABLE I
COMPARISON OF SPHERICAL GRID UNIFORMITY BASED ON PAIRWISE
EUCLIDEAN DISTANCES.

Design	Mean	Standard Deviation
Hardin & Sloane - 25 points	1.042	0.552
Hardin & Sloane - 26 points	1.040	0.553
Hardin & Sloane - 30 points	1.035	0.557
Womersley - 26 points	1.040	0.553

The results indicate that all four designs demonstrate similar levels of grid uniformity, with slight variations in the standard deviation of pairwise Euclidean distances. These small discrepancies suggest that the spatial distributions of the points in each design are closely aligned, with no significant deviations in uniformity. The differences observed in the mean and standard deviation values are marginal, implying that each design is similarly effective in achieving an even distribution across the sphere. However, based on the histogram of pairwise Euclidean distances generated by Matlab software, the 26-point t-design from Hardin & Sloane and the 26-point design from Womersley exhibit the most uniformly spread points on the sphere, as shown in Fig. 2.

Among the evaluated designs, the 25-point t-design demonstrated the lowest uniformity in distribution. Therefore, to enhance our analysis, we will focus on computing the spherical cap discrepancy for the 26-point Hardin & Sloane design, the 26-point Womersley design, and the 30-point Hardin & Sloane design.

VI. SPHERICAL CAP DISCREPANCY ANALYSIS

To further evaluate the uniformity of selected spherical point sets, we compute the *spherical cap discrepancy* (SCD) using the method described in [14]. SCD quantifies the deviation of a point distribution from a perfectly uniform reference measure on the sphere. It is defined as the supremum of the absolute difference between the empirical distribution of points and the uniform measure over all spherical caps.
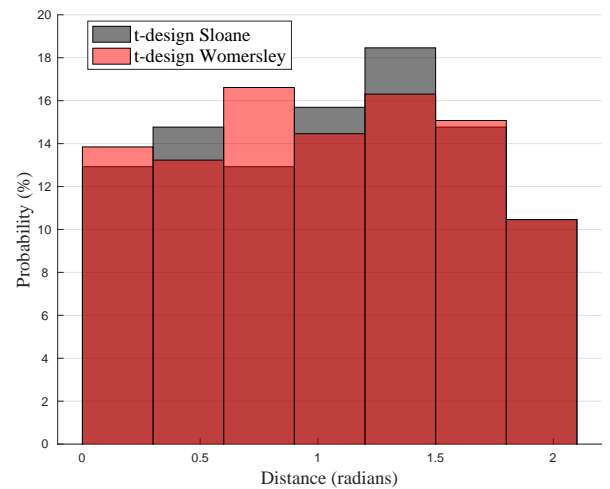
a fundamental trade-off in the design of spherical sampling grids: while equal-weight quadrature rules ensure numerical stability and ease of implementation, they inherently limit the degrees of freedom available for function approximation and integration accuracy. In practical applications, such as beamforming and spherical harmonics decomposition, achieving a balance between uniform spatial distribution and optimal weight allocation is crucial. After recalculation with two degrees of freedom, the value of E would be 66% in the worst-case scenario for a 27-point design. In contrast, the best values of E are observed in spherical designs with 30 and 32 points.

All calculated efficiencies with 2-degrees of freedom are shown in Fig. 1.

Another viable class of t-designs is provided by Rob Womersley's constructions [13], which, like those from Hardin & Sloane's database, yield identical efficiency when evaluated using McLaren's formula Eq. (5). However, to rigorously assess their uniformity, alternative metrics such as Euclidean pairwise distances and spherical cap discrepancy must be considered. These methods will be explored in the following section.

V. STATISTICAL APPROACH TO SPHERICAL DESIGNS

Based on the efficiency, calculations presented in the previous section, the 25-point, 26-point, and 30-point t-design quadratures were selected, with a focus on maximizing the possibilities of a larger t-value while minimizing the number of points. In the following section, we will conduct a statistical comparison of four distinct designs: three derived from Hardin & Sloane's t-designs and one from Womersley's configurations. This comparison will be performed using pairwise Euclidean distances between the points on the sphere. The resulting mean and standard deviation of these distances will be computed and summarized in Tab. I.

Fig. 2. Comparison of Euclidean distances.

Given a finite set of points $\mathcal{X} = \{x_1, \ldots, x_N\}$ on the unit sphere $\mathbb{S}^2$, the spherical cap discrepancy $D_C(\mathcal{X})$ is computed as:

$$D_C(\mathcal{X}) = \sup_{C \subset \mathbb{S}^2} \left| \frac{|\mathcal{X} \cap C|}{N} - \frac{\sigma(C)}{\sigma(\mathbb{S}^2)} \right|, \qquad (7)$$

where C is any spherical cap, $|\mathcal{X} \cap C|$ represents the number of points within the cap, and $\sigma(C)$ is the surface area measure of the cap relative to the total area of the sphere. A lower SCD indicates a more uniform point distribution, as it suggests the point set approximates the uniform measure more closely. In the following analysis, we used Matlab scripts from [14] to compute SCD, the results are in Tab. II.

TABLE II
COMPARISON OF SPHERICAL CAP DISCREPANCY.

Design	Spherical Cap Discrepancy
Hardin & Sloane - 26 points	0.123
Hardin & Sloane - 30 points	0.103
Rob Womersley - 26 points	0.135

The Womersley 26-point design exhibits the highest discrepancy among the tested grids, making it the least uniform and unsuitable for our further applications.

VII. IMPACT OF MODIFICATIONS AND COMPARISON OF OPTIMAL SPHERICAL DESIGNS

The Hardin & Sloane t-designs, specifically the 30-point and 26-point configurations, were selected for their superior spherical uniformity, evaluated using efficiency calculations, Euclidean distances, and spherical cap discrepancy. However, a key challenge arises as both designs include a point at the bottom of the sphere (0° azimuth, 0° elevation), a position required for securing the physical array, such as a stand or hanging support for the microphones.
For simplicity, this paper focuses on 26-point design, with future work exploring potential modifications of the 30-point design. The distribution of the 26-point design is shown in Fig. 3.

A. Consideration for Removing the Bottom Point

A straightforward solution is the removal of the bottom point, transforming the array into a 25-point configuration. While this modification enhances practical implementation, it may degrade spherical uniformity. The impact of this change is evaluated by analyzing the resulting Euclidean distances, efficiency, and discrepancy metrics.

B. Alternative Approach: Adding a New Position for the Stand

Another alternative is relocating the stand to a different position within the array where no microphone is placed, preserving uniformity. However, this adjustment would necessitate recalculating azimuth and elevation values, as it shifts the reference coordinate system. Initial evaluations focus on bottom point removal, with further research considering stand relocation as a potential optimization strategy.
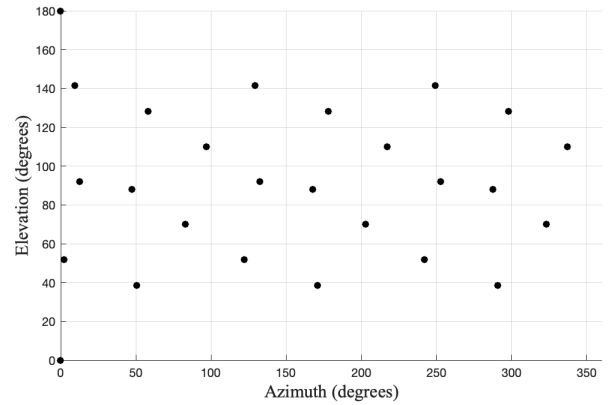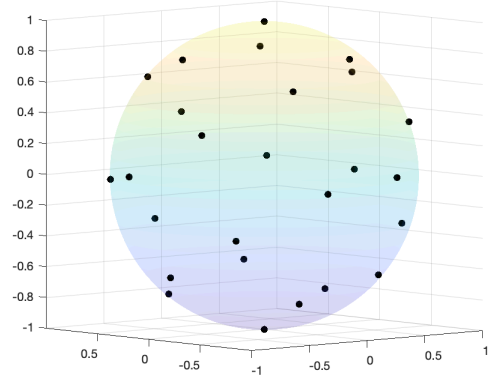

Fig. 3. 26-point Hardin & Sloane design on sphere.

C. Comparison of 25-point Designs

To assess the impact of modifying spherical point distributions, three different 25-point designs were analyzed based on efficiency via Eq. (5), mean and standard deviation of Euclidean distance, and spherical cap discrepancy. The first design was derived from the Hardin & Sloane 26-point configuration by removing the bottom point to accommodate structural constraints. The second design represents the original Hardin & Sloane 25-point configuration, serving as a benchmark for optimal spherical uniformity. The third design follows a similar modification approach but originates from the 26-point Lebedev grid, where the bottom point was removed to form a comparable 25-point structure. The results are listed in Tab. III.

TABLE III
COMPARISON OF MODIFIED DESIGNS WITH 25 POINTS.

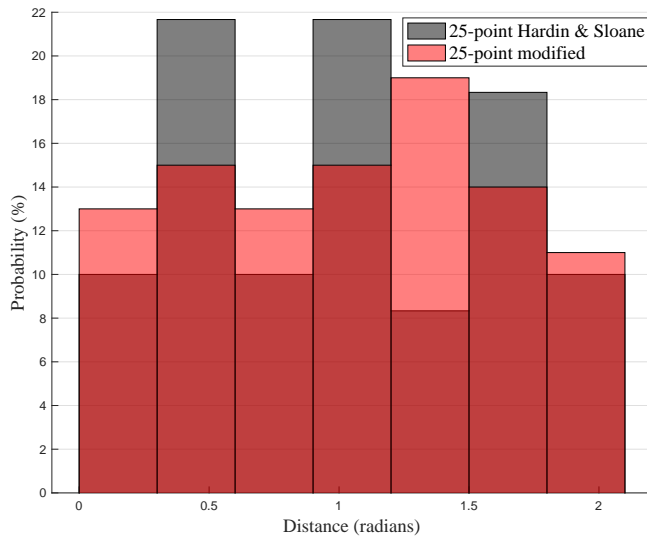| Design	Eff [%]	Mean	Standard Deviation	Spherical Cap Discrepancy
H & S: 25-point	72	1.042	0.552	0.126
H & S: modified	72	1.040	0.553	0.145
Lebedev: modified	65	1.040	0.553	0.180

Fig. 4. Distribution of distances over 25-point designs.

Calculations show that the original Hardin & Sloane 25-point design has high efficiency and the lowest spherical cap discrepancy, ensuring superior theoretical uniformity. However, Euclidean distance probability indicates that our modified 25-point Hardin & Sloane design achieves better distribution of distances between capsules, as visualized in Fig. 4.

This improved distribution of distances is essential for our application, where equal microphone spacing ensures consistent clock signal distribution and data acquisition in the system described in Section III. Despite a reduction in efficiency, the modified design offers more evenly spaced capsules, making it the optimal choice for our very first implementation.

VIII. Conclusion

This paper initially explored spherical sampling techniques for microphone placement, emphasizing the importance of uniformity in spherical arrays for spatial sound field analysis. We introduced our hardware design and compared the Lebedev 26-point grid with t-designs from Hardin & Sloane and Rob Womersley. Efficiency was evaluated using Eq. (5), along with metrics such as Euclidean distances, mean spacing, standard deviation, and spherical cap discrepancy.

Based on these evaluations, a 25-point modified design was selected, which demonstrated improved Euclidean distance distribution while maintaining practical performance and spherical uniformity. The selected design was 3D modeled for printing, with an outer diameter of 112 mm and is shown in Fig. 5.

The model houses an FPGA and flexible PCB for data acquisition, which will be further validated through experimental measurements to assess real-world performance.

Fig. 5. 3D model of modified 25-point design.

References

[1] B. Rafaely, "Sampling the Sphere," in Fundamentals of Spherical Array Processing, vol. 16. Springer, Switzerland, 2019.

[2] J. G. Proakis and D. K. Manolakis, Digital Signal Processing, 4th ed. Prentice Hall, New Jersey, 2006.

[3] H. Groemer, Geometric Applications of Fourier Series and Spherical Harmonics. Cambridge University Press, New York, 1996.

[4] K. E. Atkinson and W. Han, Spherical Harmonics and Approximations on the Unit Sphere: An Introduction. Springer-Verlag, Berlin, Heidelberg, 2012.

[5] E. G. Williams and J. A. Mann, Fourier Acoustics: Sound Radiation and Nearfield Acoustical Holography. Academic Press, London, 1999.

[6] C. H. L. Beentjes, "Quadrature on a spherical surface," Mathematical Institute, University of Oxford, Oxford, UK, 2016. [Online]. Available: https://cbeentjes.github.io/files/Ramblings/QuadratureSphere.pdf

[7] A. D. McLaren, "Optimal numerical integration on a sphere," Mathematics of Computation, vol. 17, pp. 361–383, 1963.

[8] Cirrus Logic, "Time Division Multiplexed Audio Interface: A Tutorial," AN301 User Manual, rev. 1, Sept. 2006.

[9] Future Technology Devices International Ltd., "Instructions on including the D2XX driver in a VS Express project," TN_153 Technical Note, rev. 1.1, June 2018. [Online]. Available: https://ftdichip.com/wp-content/uploads/2020/08/TN_153-Instructions-on-Including-the-D2XX-Driver-in-a-VS-Express-2013-Project.pdf

[10] M. Liska and J. Tomešek, "FPGA-based sound acquisition prototype from MEMS microphone array," in Proceedings of the 30th Conference STUDENT EEICT 2024, Brno University of Technology, Faculty of Electrical Engineering and Communication, 2024.

[11] V. I. Lebedev, "Quadratures on a sphere," USSR Computational Mathematics and Mathematical Physics, vol. 16, pp. 10–24, 1976.

[12] R. H. Hardin and N. J. A. Sloane, "McLaren's improved snub cube and other new spherical designs in three dimensions," Discrete and Computational Geometry, vol. 15, no. 4, pp. 429–441, 1995.

[13] R. Womersley, "Efficient spherical designs with good geometric properties," [Online]. Available: http://web.maths.unsw.edu.au/ rsw/Sphere/-EffSphDes/index.html [Accessed: Dec. 23, 2015].

[14] H. Heitsch and R. Henrion, "An enumerative formula for the spherical cap discrepancy," Journal of Computational and Applied Mathematics, vol. 390, 2021.

Brighter Together

automotive   comms-infrastructure   industrial   mobile   smart-city   smart-home

NABÍZÍME

- **placenou stáž**, která Tě bude bavit a je
  - atraktivní
  - motivující
  - flexibilní
  - podporující Tvé studium
- **full - time** poté, co úspěšně dostuduješ
- **témata diplomových prací**, ze kterých si rozhodně vybereš
- **workshopy**
- **NXP Cup**: největší mezinárodní soutěž autonomních autíček v Evropě, které se můžeš zúčastnit

O NÁS

NXP Semiconductors se prostřednictvím inovací zasazuje o chytřejší, bezpečnější a udržitelnější svět. Jakožto světová jednička v embedded řešeních, NXP posouvá hranice v oblastech automobilového průmyslu, IoT, mobilních a komunikačních infrastruktur.

www.nxp.com

Implementation Aspects of Car-sharing Applications

1st Minh Tran
Department of Telecommunications
Brno University of Technology
Brno, Czech Republic
0009-0003-4096-1957

2nd Petr Dzurenda
Department of Telecommunications
Brno University of Technology
Brno, Czech Republic
0000-0002-4366-3950

Abstract—The concept of shared vehicles is becoming increasingly popular. Currently, there are several organizations, such as Google and Apple, that offer applications for car-sharing key management and vehicle access via a mobile app. However, these platforms are often not suitable for legacy vehicles, data processing is outsourced to third parties, and technical documentation is missing. All of this limits the scalability, increases privacy issues, and reduces the trustworthiness of the system. In this paper, we provide details on the implementation of our car-sharing solution, identifying key implementation challenges, security risks, and technological limitations. We propose an optimization technique that reduces the authentication time by 81%, making the solution practical for automotive applications. The experimental results verify the performance of our application and demonstrate its reliability in facilitating secure vehicle access in just 1.5 seconds.

Index Terms—Access Control, Authentication, Android, Mobile Application, Car-sharing, Software Development

I. Introduction

One of the rapidly growing markets within the automotive industry is car-sharing. Factors such as rising travel costs, the overall cost of living, and an increasing emphasis on environmental sustainability contribute to this trend. Car-sharing allows multiple individuals to collectively use a transportation vehicle, eliminating the need for each individual to own one. This model not only saves on the time and financial resources required to acquire a vehicle, but also reduces the costs associated with its maintenance. Although the option of public transport is worth considering, cars often prove to be a more practical choice, particularly in areas with unreliable public transportation, when privacy is a concern, or when transporting larger items. Although car-sharing is not a new concept, many existing systems are limited in functionality. They lack support for legacy vehicles, do not offer offline solutions, their data is outsourced to third parties, and often provide inadequate documentation and implementation details. These shortcomings present opportunities for researchers to develop faster, more secure protocols and technologies for end users and companies using car-sharing services.

A. Contribution and Paper Structure

In this paper, we build on our previous work in car-sharing applications [1], [2]. Our car-sharing concept overcomes the

issues mentioned in current solutions. The end-users are provided with a mobile application that serves as the user's entry point into the system and an authentication element for vehicle access. In this paper, we focus on the technological barriers, implementation aspects, and security risks associated with the practical development of such systems. The contribution of this paper consists of three main parts:

- providing *analysis of popular commercial car-sharing solutions*, their features, strengths and weaknesses.
- defining the *implementation methodology* and describing the practical implementation of the car sharing system.
- *evaluating the developed system* speed, reliability, security, and possible attack vectors.

The paper is organized as follows. Section II analyzes existing commercial car-sharing solutions and presents our previous work on car-sharing applications. Section III provides details on the implementation of our Android application as the primary user authentication element for vehicle access. Section IV presents our experimental results. Section V focuses on the security aspects of our implementation and possible attack vectors. In the last section, we conclude this work.

II. Preliminaries

A. Existing Commercial Solutions

Existing car-sharing technologies using keyless entry offer various features but also come with limitations. The targeted users are mostly organizations that have a large fleet of cars to rent. On the other hand, there are some systems for Peer-to-Peer (P2P) usage [3]. Almost all modern platforms use a mobile application as an entry point to the system using Bluetooth Low Energy (BLE) or Near Field Communication (NFC) for authentication. Unfortunately, technical documentation is very rarely provided. Many car-sharing solutions depend on online communication, such as Zipcar [4], which requires an internet connection for access. A major advantage of online systems is real-time management. In contrast, the disadvantage is that loss of connectivity prevents access to the vehicle. BLE-based platforms, on the other hand, work offline, ensuring access even without an Internet connection, although they may require additional hardware for legacy vehicles. Apple [5] and Google [6], in collaboration with the Car Connectivity Consortium [7], provide a digital key standard for cars used by major manufacturers such as BMW,

Mercedes, Škoda, Hyundai, or Volkswagen. Data management is outsourced to a third party, making this solution prone to security and privacy risks. Although it offers seamless access to new vehicles via NFC or BLE, it is incompatible with legacy cars. In contrast, WorldWideMobility [8] offers a solution that works with legacy vehicles, providing more flexibility for older car models. However, the disadvantage is that this approach requires access to the Internet to interact with the vehicle. Table I presents a summary of the most used systems.

TABLE I
COMPARISON OF CAR SHARING SYSTEMS

	Apple/ Android Car key	Car4Way	World Wide Mobility	Zipcar	Our Solution
Legacy car support	No	No	Yes	No	Yes
P2P	Yes	Yes	Yes	No	Yes
Fleet	No	No	Yes	Yes	Yes
BLE	Yes	Yes	Yes	Yes	Yes
NFC	Yes	No	No	Yes	No
White paper	Yes	No	No	No	Yes
Orgs	Yes	Yes	Yes	Yes	Yes
End users	Yes	Yes	No	No	Yes
Smartwatch	Yes	No	No	No	Yes
Offline mode	Yes	No	No	No	Yes
3rd party Outsource	Yes	Yes	Yes	Yes	No

None of the solutions from the table above provide all essential features together, whereas our approach offers them all. It also operates independently of third-party services, which minimizes potential risks associated with external services.

B. Offline Keyless Vehicle Entry for Car-sharing using Privileged Access Tokens

In this section, we outline the architecture of the access control system [1], including its communication channels and cryptographic core. Next, we present our implementation of the cryptographic core within our mobile application and its integration throughout the entire system.

1) System Architecture: The whole system architecture, including the cryptographic core, has been presented in [2]. The system is depicted in Figure 1. It consists of four main components: two servers, car-sharing mobile application, and a rental car with a control unit.

- **Identity manager** server is responsible for managing authentication tokens, vehicle access keys, and user registration via SMS or QR codes. It also generates vehicle identifiers. It communicates with the reservation manager and the mobile application via TCP/IP.
- **Reservation manager** server manages vehicle reservations, allowing users to interact with the car-sharing system via the website. It synchronizes data with the mobile application via TCP/IP and exchanges information with the rental car's control unit about booked users.
- **Mobile application** serves as the primary interface for users to authenticate against a rental car using BLE. It

also provides information about the user's reservations, including vehicle ID, appearance, reservation duration, and location of the reserved vehicles.
- **Rental car with control unit** is responsible for authenticating users using the verification protocol, ensuring secure access to the vehicle.
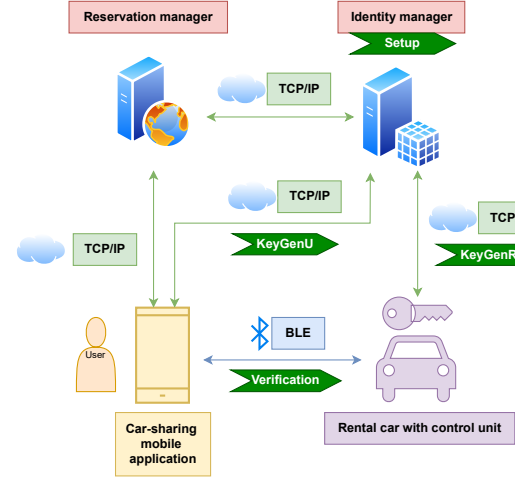

Fig. 1. The system architecture and communication channels.

2) Cryptographic core: The cryptographic core features a lightweight and secure access control protocol tailored for car-sharing. The protocol is efficient in terms of speed and energy use, ideal for mobile vehicles. It includes four algorithms:

- `Setup` - Executed by the Identity Manager, it calculates the system master key.
- `KeyGenR` - Used by the control unit and identity manager to generate the control unit's key by hashing its ID with the master key (SHA-256).
- `KeyGenU` - Executed by the user, identity manager, and reservation manager to compute the user's key. It uses the User Authentication Token (ATU), containing user info, vehicle ID, and permissions. The user's key is calculated as a hash of the master key and the ATU hash (SHA-256).
- `Verification` - Executed by the user and control unit when sending commands, such as unlocking a car:
    1) The user and control unit exchange random challenges and the control unit's ID.
    2) The user computes a session key from the user key, challenges, and a constant value.
    3) The user encrypts and sends the ATU, including the command, using AES-256 in GCM mode.
    4) The control unit verifies the token type, access list, and reconstructs the user's key. It decrypts the ATU and compares the hashes to authenticate the user.

III. IMPLEMENTATION DETAILS

The core of our application includes a BLE module for communication, REST API infrastructure, a database, and a bottom navigation architecture. The stand-alone library handles our cryptographic protocols and connects data flow. The mobile

application also implements Google Maps for car location, a notification system, and a user-friendly interface.

The application, developed in Android Studio with Java and Kotlin, uses Model View ViewModel (MVVM), Model-View-Intent (MVI) architectural patterns, and Dagger for dependency injection. This ensures clear separation of concerns, reactive data flow, and improved maintainability. The application targets Android version 34, with a minimum requirement of version 26, covering 95.7% of Android devices.

A. Application architecture

The application consists of the following layers:

1) Data Layer: The data layer handles all data-related tasks, including storage, server communication, and device interactions. It also manages data transformation like encryption and decryption. Key components include:

- **Retrofit**: Used for server communication to handle registration, login, and syncing vehicle reservations.
- **BLE**: The application acts as a Generic Attribute Profile (GATT) server, with the control unit as the client. The application uses `BluetoothLeScanner` for device detection and `BluetoothGatt` for data exchange, with a Received Signal Strength Indicator (RSSI) of -70 dBm.
- **ROOM Database**: Manages authentication tokens and reservation data.
- **MobileKeyLibrary**: Handles the cryptographic core of the system.

2) Domain Layer: The domain layer defines business logic and ensures consistent application of rules independent of infrastructure. It includes:

- **Interfaces**: Define methods for classes with implementations in the data layer.
- **Data Models**: Represent objects, like the User class, and handle business logic like authentication and challenge generation.

3) UI Layer: The UI layer displays data and captures user actions. Key components include:

- **Activities/Fragments**: Manage navigation and contain UI elements. Four activities are used: `ActivationActivity`, `WizardActivity`, `MainActivity`, and `AuthenticationActivity`.
- **Views**: Build responsive UI layouts with XML and `ConstraintLayout`, interacting with `ViewModels`.
- **ViewModels**: Manage dynamic data changes using `LiveData` and `StateFlows` for consistency across configuration changes.

B. Application features

Our application has four main features. These features, along with their corresponding activities and potential navigation, are illustrated in Figure 2.

- **Device Registration**: The first step in using the car-sharing features is registering the user's device, which requires an internet connection. Users can register by
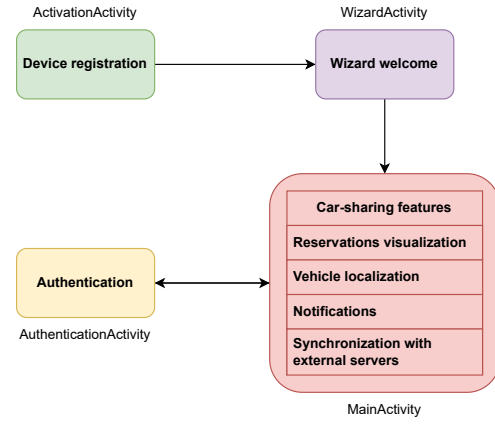

Fig. 2. Application features.

scanning a QR code using the Google ML Kit library, which sends verification data to the Identity manager via REST API. If successful, the device is registered, and account information is stored in the ROOM database. Alternatively, users can enter a phone number to receive an SMS code. After entering the code, the Identity manager verifies it via REST API, and upon success, the device is registered.

- **Wizard Welcome**: After registration, users are directed to the Wizard welcome activity, which provides information about the application and requests necessary permissions (e.g., Bluetooth, notifications, location). After confirming permissions, the application calls the Reservation manager via REST API to download reservation data, which is stored in the ROOM database.
- **Car-Sharing Features**:
    1) *Reservation Visualization*: Reservations are displayed on the main screen as cards showing the vehicle's picture, ID, and reservation time; see Figure 3 (on the left).
    2) *Vehicle Localization*: Each vehicle sends real-time location data to the Reservation manager, shown on the Google map; see Figure 3 (on the right).
    3) *Notifications*: Notifications about reservation status changes are sent via Firebase by the Reservation manager. Notifications are displayed regardless of its lifecycle (i.e., running, background, or closed).
    4) *Synchronization with External Servers*: To ensure the latest reservation data, synchronization occurs when the main screen is opened or manually triggered via swipe gestures.
- **Authentication**: Users can send commands to open or close the vehicle. Upon selecting an option, an authentication screen appears, requiring enabled Bluetooth. After successful authentication, users return to the main screen.

C. Optimization of authentication time

The authentication protocol itself, specifically the verification part, takes only 2.7 ms, as depicted in Table II,
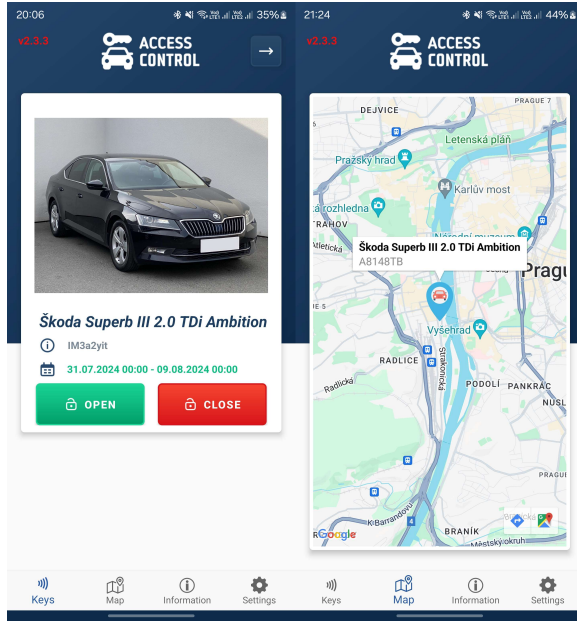
Fig. 3. Main screen (left) and map screen (right).

but problems can arise when it is incorporated into actual hardware. In our case, this scenario indeed transpired. The core of the issue was that a control unit enters sleep mode when no authentication is occurring to save as much electricity as possible. This introduces a delay in the overall authentication time. The control unit must wake up first and then initiate an authentication session. Authenticating with a control unit in sleep mode takes around 8 seconds, which is unacceptable. To resolve this issue, we implemented a functionality that requests a connection to wake up the device. Whenever a user opens the main screen with reservations, the active vehicle (the one displayed on the screen) is sent a connection request to ensure it wakes up before authentication begins. Thanks to this approach, we reduced authentication time by 81%, bringing it down to a total of 1.5 seconds.

IV. EXPERIMENTAL RESULTS

For our testing scenario, we used a combination of a mobile phone Samsung Galaxy S23 Ultra (CPU: Qualcomm Snapdragon 8 Gen 3 (3,39 GHz), RAM: 12 GB, OS Android 14), and a smartwatch Samsung Galaxy Watch5 Pro (CPU: Exynos W920 (1.18 GHz), RAM: 1.5 GB, WearOS 4). The vehicle authentication unit uses the PIC24FJ256GA406 processor, which is programmed in the XC16 language using the MICROCHIP MPLAB X development environment. The mbedtls-mbedtls-2.23.0 library is used for cryptographic operations used in communication between the user's mobile application and the authentication unit. In order to evaluate the performance of our implementation, we conduct tests on both Android devices, specifically focusing on the authentication protocol algorithms themselves as presented in Table II and the whole authentication process, including data transfer through BLE as illustrated in Figure 4.

TABLE II

BENCHMARKS IN MILLISECONDS OF THE AUTHENTICATION PROTOCOL ALGORITHMS

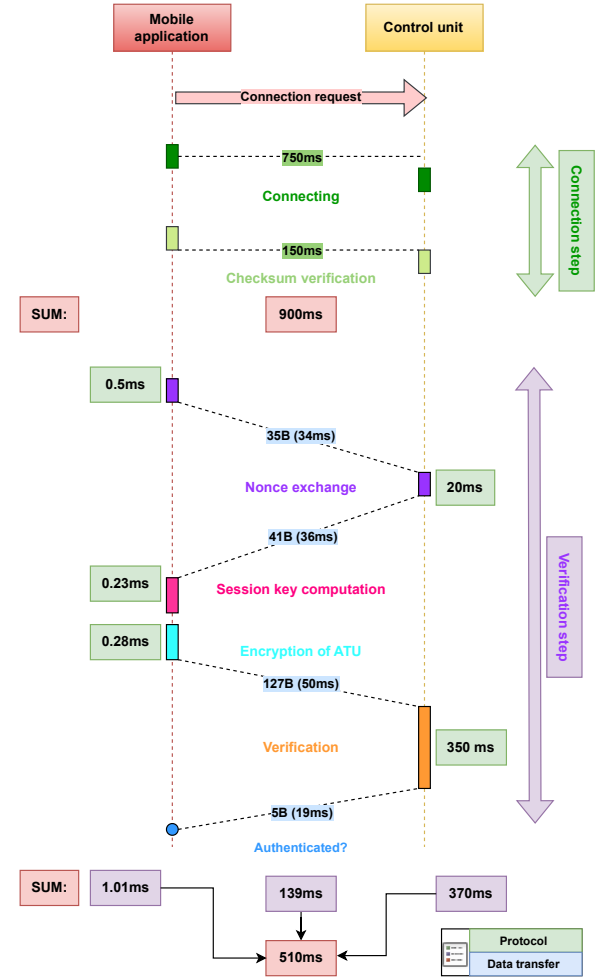|	Setup	KeyGenR	KeyGenU	Verification
Mobile	0.4	0.46	0.3	2.7
Smartwatch	5.8	47	25	90

Fig. 4. Sequence diagram of authentication process.

Connecting the mobile application to the control unit requires approximately 750 ms, while checksum verification adds around 150 ms, bringing the total pre-authentication time to 900 ms. The authentication process averages 510 ms, with the verification step being the most time-consuming. The data transfer time between the mobile device and the control unit is relatively efficient and does not introduce significant delays. However, when comparing the verification speed on the mobile phone or smartwatch to that of the control unit, it becomes evident that the control unit acts as a performance bottleneck, limiting overall efficiency. Optimizing the verification process on the control unit or improving the connection establishment process could significantly boost authentication speed.

Figure 5 illustrates the transfer times for BLE, NFC, and Wi-Fi. The BLE time is based on our actual measurements,
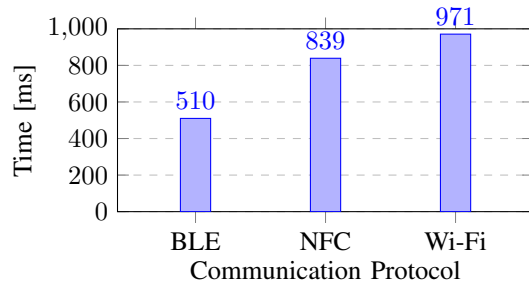
Fig. 5. Comparison of transfer times for BLE, NFC, and Wi-Fi.

while the NFC and Wi-Fi times are theoretically computed using percentage differences derived from the study [9], which employs a similar authentication protocol. Since their work closely aligns with our use case, we used their observed trends to estimate the expected times for NFC and Wi-Fi under comparable conditions.

V. SECURITY EVALUATION

We assess the security of our mobile application by focusing on the protection of reservation data and private keys stored on the mobile device. We also consider potential attackers, attack vectors, and mitigation strategies. Our security model is structured as follows:

- **User-driven attack**: Users have one primary attack vector to prolong the reservation time. To achieve this, an attacker would need to modify the ROOM database. The database enforces strict access controls through Data Access Objects (DAOs), which limit data access and modification. Since ROOM operates on top of SQLite, it benefits from SQLite's robust data integrity and transaction features, ensuring consistency. Unauthorized data modification is challenging. If data were modified, the authentication protocol controls the hash of the ATU; if the hash is altered (e.g., due to a modified reservation time), authentication would fail.
- **Service provider-driven attack**: This entity can modify all reservation data. We assume the service provider is not malicious, as such behavior is unbeneficial.
- **Third party-driven attack**: For this entity, we must secure the Confidentiality, Integrity, and Availability (CIA) triad [10].
  1) An attacker may attempt to access and modify data. Local data in the ROOM database is protected, as described earlier. We assume that external servers also handle data securely.
  2) BLE communication is secured using AES encryption to prevent eavesdropping and Man-In-The-Middle (MITM) attacks. Additionally, the authentication protocol uses random challenges to defend against replay attacks.
  3) Private keys are protected using the Android `Keystore` system, which securely stores cryptographic keys in a hardware-backed or trusted ex-

ecution environment. The `Keystore` ensures that private keys are never exposed to applications or malicious entities, safeguarding cryptographic operations from key extraction attacks.

Although most attack vectors are mitigated, the system lacks secure pairing between the mobile application and the control unit, leaving it vulnerable to device spoofing. To mitigate this, implementing secure pairing using certificates would enhance security [11]. Additionally, since the ROOM database is not encrypted, data stored on the device could be exposed in case of physical access or rooting. Encrypting the ROOM database would help mitigate this risk.

VI. CONCLUSION

This paper presents the design and implementation of a mobile application for secure car authentication via BLE. We analyzed existing commercial solutions and proposed a novel architecture with a robust cryptographic core for optimized BLE communication. Our solutions provide all the missing features of the existing commercial solutions. It integrates legacy car support, offline functionality, possibility for smartwatch extention, available technical documentation, and broader accessibility, making it overall more comprehensive. The application featured seamless usability alongside high-security standards. We achieved an 81% reduction in authentication time, enhancing practicality for automotive use. Experimental results confirm efficient, reliable authentication, while security analysis shows resilience against threats.

REFERENCES

[1] Dzurenda, P., Ilgner, P., Tran, M., Malina, L., Kristof, P., Makarov, A., Loutocký, P. & Kasl, F. Offline Keyless Vehicle Entry for Car-sharing using Privileged Access Tokens. *ICUMT 2024 – The 16th International Congress On Ultra Modern Telecommunications And Control Systems (ICUMT)*. pp. 1-8 (2024)

[2] Dzurenda P, Malina L, Loutocky P, Kasl F, Kristof P, Hajny J. Towards to Lightweight and Secure Access Control Systems for Car-Sharing Services. *ICUMT 2022 – The 14th International Congress On Ultra Modern Telecommunications And Control Systems*. pp. 104-109 (2022)

[3] Prieto, M., Stan, V., Baltas, G. New insights in Peer-to-Peer carsharing and ridesharing participation intentions: Evidence from the "provider-user" perspective. *Journal of Retailing and Consumer Services*. Volume 64, 102795 (2022). https://doi.org/10.1016/j.jretconser.2021.102795.

[4] Zipcar, [Online]. Available: https://www.zipcar.com/

[5] Apple, "Add your car key to Apple Wallet on your iPhone or Apple Watch." [Online]. Available: https://support.apple.com/en-us/118271

[6] Android, "Car keys, reimagined." [Online]. Available: https://www.android.com/digital-car-key/

[7] CarConnectivity, "Share Digital Car Keys Globally Using Secure And Private Technology" [Online]. Available: https://carconnectivity.org/

[8] WorldWideMobility, "Car sharing software: Used by the major car sharing services." [Online]. Available: https://worldwidemobility.io/our-solutions/carsharing-software

[9] Texl, Filip. *Přístupový systém pro aplikaci carsharing*. Online. Bachelor's Thesis. Brno: Brno University of Technology, 2023. Available at: https://theses.cz/id/36rnz9/.

[10] Samonas, S., Coss, D. The CIA strikes back: Redefining confidentiality, integrity, and availability in security. *Journal of Information System Security*. Volume 10, Issue 3 (2014).

[11] Zhang, Y., Weng, J., Dey, R., Jin, Y., Lin, Z., Fu, X. Breaking Secure Pairing of Bluetooth Low Energy Using Downgrade Attacks. *29th USENIX Security Symposium (USENIX Security 20)*. pp 37-54 (2020). https://www.usenix.org/conference/usenixsecurity20/presentation/zhang-yu.

NB-IoT over NTN: Evaluating TBS and Elevation Angle Effects on Communication Reliability

1st Radim Dvořák
Department of Telecommunications
Brno University of Technology
Brno, Czech Republic
xdvora2g@vutbr.cz

2nd Pavel Palurík
Department of Telecommunications
Brno University of Technology
Brno, Czech Republic
pavel.palurik@vut.cz

2nd Martin Štůsek
Department of Telecommunications
Brno University of Technology
Brno, Czech Republic
martin.stusek@vut.cz

2nd Pavel Mašek
Department of Telecommunications
Brno University of Technology
Brno, Czech Republic
masekpavel@vut.cz

Abstract—**With the ever increasing size of the IoT market that utilizes 5G-IoT technologies, NB-IoT and LTE Cat-M, the variety of applications and the demand for functionality are increasing. Due to terrestrial constraints, 5G-IoT technologies cannot be applied globally to suit all use cases such as maritime asset tracking. With the introduction of Non Terrestrial Networks to the 5G ecosystem the newly estabilished standard NB-IoT over Sattelite could cover various use cases. This paper aims to explore the influence of the elevation angle of the gNodeB located in LEO (Low-Earth Orbit) related to the end-user device, as well as the TBS (Transport Block Size) configuration quantified by a Block Error Rate (BLER). A simulation in MATLAB 5G Toolbox was performed and the elevation angle with TBS changed in granual steps. The results show that the BLER drops significantly with higher elevation angles as well as increases with increasing orbital height of the gNodeB. The TBS influences the success rate of the communication link where the BLER decreases with smaller TBS configuration.**

Index Terms—**IMT-2020, 5G+, IIoT, 5G-IoT, mMTC, Non-Terestrial Networks, URLLC, NB-IoT, LTE Cat-M, LEO, MEO, GEO**

I. Introduction

In recent years, the rise of IoT market has introduced various different use-cases and demands from the private sector. While the current infrastructure in place is theoretically sufficient for most use-cases some applications are not possible with today's deployment either due to the demands on the network (high speed applications in remote areas) or the location (rural areas without coverage). The announcement of the integration of NTN (Non-Terrestrial Networks) into the 5G standards by the 3GPP aims to cover the latter, therefore allowing connectivity for applications in areas without coverage [1]–[4].

Currently, the standard is under revision and we are yet to see the extent of the full specification. While still being under revision, the direction it aims to focus on is clear, NB-IoT (Narrowband-IoT) over NTN. Standard NB-IoT focuses on low-throughput, high latency communication with high reliability of transmission making the ideal candidate to be the first technology to adopt an NTN alternative [1], [4].

However, as the terrestrial communication strongly differs from the non-terrestrial in all aspects, the challenge is modifying the current NB-IoT technology to accomodate these changes while enabling compability with systems currently in operation while keeping the distinguished features of the NB-IoT, such as reliability, in place. For a successful data transfer the UE (User Equipment) has to be able to reach the orbital gNodeB on the NPRACH (Narrowband Physical Random Access Channel) channel and it has to be able to receive information on the NPDCCH (Narrowband Physical Downlink Control Channel) in the least [1], [5], [6].

The main motivation of this paper is to explore an aspect of the NTN communication based on the overhead satellite (containing the base station gNodeB) location with respect to the UE located on the Earth's surface. The key aspect being the block error rate (BLER) based on the relative angle deviation of the orbital gNodeB from the UE upward position.

The paper aims to provide a comprehensive overview on the influence of varying parameters TBS (Transport Block Size), the amount of repetitions used and the satellite orbital altitude on general behaviour of the NTN systems that are to become a part of the 6G standard with regards to the success rate of the communication (BLER). As a output of the paper the recommended settings of each parameter for different applications are presented.

In this paper, firstly an introduction to the NB-IoT over NTN is presented as well as the key differences between a TN and NTN networks. Further, main issues with adapting the NB-IoT to NTN are presented. Second part focuses on the simulation scenarios in MATLAB 5G Toolbox for NTN, which was utilized as the simulation environment. Furthermore the results are presented in the third section and in the fourth section we conclude the paper.

II. Narrowband IoT over NTN

NB-IoT over Non-Terrestrial Networks (NTNs) is an emerging technology that extends the reach of IoT connectivity

beyond terrestrial infrastructure using satellite and aerial networks.

NB-IoT is a low-power, wide-area network (LPWAN) technology designed for massive IoT applications, offering efficient, low-cost, and extended coverage. However, terrestrial networks have limitations in remote, rural, and maritime areas. To overcome these, as of 3GPP Release 17, NB-IoT is integrated with NTNs, including satellite communications (LEO, MEO, GEO), high-altitude platforms (HAPS), and UAVs [2], [6].
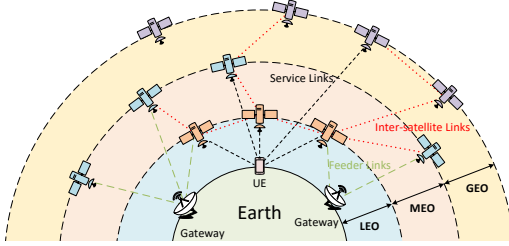

Fig. 1. NTN network topology.

The integration of NB-IoT with NTNs has been a focus of 3GPP (Third Generation Partnership Project), particularly in Release 17 and 18, which address the technical adaptations needed to ensure reliable IoT connectivity via satellites and other non-terrestrial platforms [2], [7].

In Release 17 an official support for NB-IoT and LTE-M over NTN has been added. The main focus of the addition is focused on LEO (Low-Earth Orbit) and GEO (Geostationary Orbit) satellite applications. As a part of the standard, common challenges related to the high altitude communication, such as timing synchronization, doppler shift compensation and power control enhancements, are addressed to allow for efficient and reliable communication. Furthermore some part of the current terrestrial standards had to be modified to adapt for a different type of communication environment such as random access procedures, HARQ (Hybrid Automatic Repeat ReQuest) retransmission strategies and paging optimizations [6].

Release 18 further built on top of the grounds set by Release 17, further improving the communication chain and broadening the application range of the NB-IoT over NTN. The support for faster moving objects was added (e.g. fast-moving satellites) as well as resource allocation and network synchronization was optimized to allow for efficient usage of allocated spectrum. While multiple feateres were added the complexity of the end-user devices was stripped down further improving the power efficiency of the modules.

A. Challenges of Switching from TN to NTN

One of the primary challenges in NB-IoT over NTNs is the significantly greater path loss experienced in satellite communication compared to terrestrial networks. The increased distance between IoT devices and satellites, particularly in Geostationary Earth Orbit (GEO) and Medium Earth Orbit (MEO) constellations, leads to higher free-space path loss,

necessitating power-efficient transmission mechanisms. Additionally, atmospheric conditions, such as tropospheric and ionospheric disturbances, can introduce further signal degradation, affecting link reliability and data transmission efficiency [8], [9].

According to the current specifications by the 3GPP, orbit altitudes of 600 km and 1200 km in LEO region are considered with an S-band carrier frequency of 2 GHz. However, even in LEO 600 km scenario the distance, depending on the elevation angle (EL), can easily exceed 1900 km of distance between UE and the gNB, which causes significant channel path loss and introduces noise [6].

The SNR of the channel is defined according to the 3GPP as:

$$SNR = EIRP + \frac{G}{T} + 10log(k) - FSPL - SF \\ - SL - AL - PL - 10log(BW) \tag{1}$$

where the inputs are $\frac{G}{T}$ gain-to-noise temperature ratio, boltzman constant k, free-space path loss $FSPL$, shadow fading SF, atmospheric loss AL, polarization loss PL and the total bandwidth of the system BW [8].

At lower LEO altitudes the pathloss, considering the free-space model, ranges from 154 dB (90° elevation angle) to 164 dB (10° elevation angle) which is on the edge of maximum link budget allowed for terrestrial NB-IoT systems.

Additional challenge in NTN networks is that unlike terrestrial networks, where base stations are stationary, NTNs involve satellites or high-altitude platforms that move relative to IoT devices. Low Earth Orbit (LEO) satellites, in particular, travel at velocities of approximately 7.5 km/s, resulting in substantial Doppler shifts that affect carrier frequency synchronization. NB-IoT devices, originally designed for static or low-mobility applications, must incorporate advanced frequency tracking algorithms and adaptive timing compensation techniques to mitigate these effects [6], [9].

In terrestrial NB-IoT networks, random access procedures rely on a well-defined synchronization and contention-based access model. However, in NTNs, satellite beam handovers, higher latency, and fluctuating channel conditions complicate Random Access Channel (RACH) procedures. Moreover, satellite systems experience frequent variations in user density across beams, requiring dynamic resource allocation strategies to optimize spectrum utilization and avoid network congestion [7], [10].

B. Transport Block Size in NTNs

Considered all key points mentioned above, the Transport Block Size (TBS) plays a crucial role in determining the efficiency and reliability of NB-IoT transmissions, particularly when operating over non-terrestrial networks. Unlike terrestrial deployments, where TBS selection is primarily influenced by radio conditions and network congestion, NTNs introduce additional factors that necessitate a more dynamic and adaptive approach. The increased propagation delay in NTNs, especially in geostationary satellite systems, has a direct impact

on hybrid automatic repeat request (HARQ) mechanisms, as retransmissions over long distances can lead to significant performance degradation. To compensate for this, larger TBS values are often preferred in order to reduce retransmission overhead and maximize spectral efficiency. However, this approach introduces trade-offs in terms of error resilience and power consumption, particularly in scenarios where signal fading and high path loss are dominant [1], [2].

Satellite-based NB-IoT communications also experience considerable variations in channel conditions due to atmospheric attenuation, beam coverage transitions, and elevation angle effects. In such cases, smaller TBS values may be more advantageous, as they reduce the likelihood of errors and minimize retransmission delays. However, relying exclusively on small transport block sizes results in excessive protocol overhead, thereby reducing overall throughput. Additionally, the high Doppler shift experienced in LEO satellite communications further complicates TBS selection, as larger blocks may be more susceptible to errors if frequency synchronization is not well maintained. In contrast, in GEO and MEO systems, where Doppler effects are relatively less severe but latency is higher, larger TBS values can be leveraged to improve efficiency while ensuring sufficient error correction through robust modulation and coding schemes [8], [9].

Another critical consideration in TBS optimization is power consumption. Since most NB-IoT devices rely on battery power and are designed to operate for extended durations, excessive retransmissions due to suboptimal TBS selection can significantly impact device longevity. A balance must be struck between energy efficiency and data transmission reliability, ensuring that power constraints do not compromise communication effectiveness. [2], [5].

Closely tied to this is the concept of repetitions, where the same transport block is transmitted multiple times to improve decoding probability under poor signal conditions. While repetitions increase reliability—especially for small TBSs in low-SNR environments—they also lead to higher spectral occupancy and elevated power consumption due to prolonged radio activity. Conversely, selecting a larger TBS in unfavorable conditions may reduce the need for repetitions but risks a higher block error rate (BLER), potentially triggering costly retransmissions. Thus, an intricate relationship exists: larger TBSs generally require higher SNR to avoid repetition, while smaller TBSs tolerate more repetitions but at the expense of energy efficiency. Optimizing this trade-off demands context-aware scheduling mechanisms that dynamically adjust both TBS and repetition factors based on link-layer metrics and application-level latency and power constraints. In this regard, cross-layer optimization between the MAC and physical layers becomes pivotal for achieving sustainable and robust NB-IoT connectivity [2], [5].

To address these challenges, adaptive TBS selection algorithms that take into account real-time satellite beam conditions, link quality, and mobility patterns are essential. The emerging approaches such as machine learning-based predictive models for transport block adaptation offer promising avenues for enhancing the efficiency of NB-IoT transmissions over NTNs. By dynamically adjusting TBS values based on signal quality metrics and network load conditions, these techniques can optimize the trade-offs between power efficiency, latency, and throughput, ultimately improving the feasibility of deploying NB-IoT in satellite-based communication systems [2].

III. Simulation Scenarios

To evaluate the performance of NB-IoT over Non-Terrestrial Networks (NTNs), we conducted simulations that analyze the impact of key network parameters—including elevation angle, satellite altitude, and transport block size (TBS)—on system performance. The purpose of the simulation was to provide a comprehensive insight into the communication success rate, under varying parameters. The results were captured in terms of Block Error Rate (BLER), which quantifies the reliability of data transmission under varying conditions.

The simulation environment was setup in MATLAB 5G Toolbox and was designed to reflect realistic NTN deployment scenarios in urban areas, considering key aspects such as orbital altitude, channel impairments, and propagation characteristics. All the simulations consider a single LEO orbit base station with a single UE located on the Earth's surface.
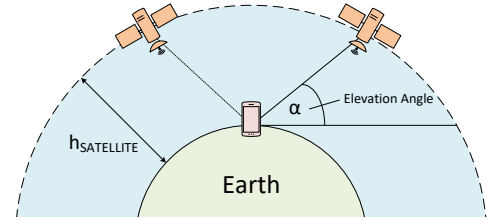

Fig. 2. Visualization of simulation scenario.

The selected static parameters for all the simulations were set as follows:

- EIRP of the sattelite - 44 dBm.
- EIRP of the UE - 23 dBm.
- Rician fading model - K factor of 10.
- RX Noise figure of 6 dB.
- RX antenna temperature of 270 K.
- Carrier Frequency 2 GHz.
- Number of Transport Blocks 500.

The first simulation scenario focuses on the BLER of the communication channel based on the orbital altitude of the gNodeB to show the impact of the orbital altitude on the channel propagation success rate. For the scenario only orbital heights in the LEO region were considered, specifically altitudes of 600 km, 800 km and 1200 km were selected. The simulation was performed with elevation angles ranging from 10° to 170° with respect to the UE's position on the Earth's surface. To emphasize on the system's performance and reveal the stability of the communication link, multiple repetitions configurations, namely 1, 2, 4, 8, 16, 32, 64 and 128, were simulated. For the simulation, the TBS size of 408 bits ($I_{SF} = 5$, $iMCS = 4$) was selected as the default value

for all simulation iterations to keep the results focused on the height and elevation angle of the satellite.

Second simulation showcases the influence of varying TBS configuration on the system's performance. In this scenario, the satellite altitude of 800 km was selected. In each iteration, the TBS of the system was altered and performance quantified by BLER was evaluated. Complementary to the first scenario, multiple repetition configurations were utilized.

IV. RESULTS DISCUSSION

The first scenario focuses on relationship of BLER with regards to the number of repetitions utilized as well as the over-head satellite altitude.

The results of the simulation scenario are plotted in figures 3, 4, 5 and 6.

As seen in figures 3, 4 and 5, the elevation angle with respect to the UE plays a big role in communication link success rate. The results show an increase of BLER in low elevation angles, due to the highest distance of travel and possible obstacles in an urban area impeding the successful data transmission. While the BLER is the highest at the lower angles, approaching 100%, it is lowest, as expected, at elevation angles close to the 90° mark which represents the state where the satellite is directly over-head the UE with the shortest distance of the propagation channel and the least of obstacles.

The success rate also heavily depends on the number of repetitions allowed by the communication channel. Although the channels with lower repetitions configuration present some BLER even in higher elevation angles, in general, with the increasing number of repetitions the BLER decreases accordingly as the added repetitions increase the probability of successful data transmission through the channel. This relationship is clearly visible in figure 5 but applies to all of the presented configurations.
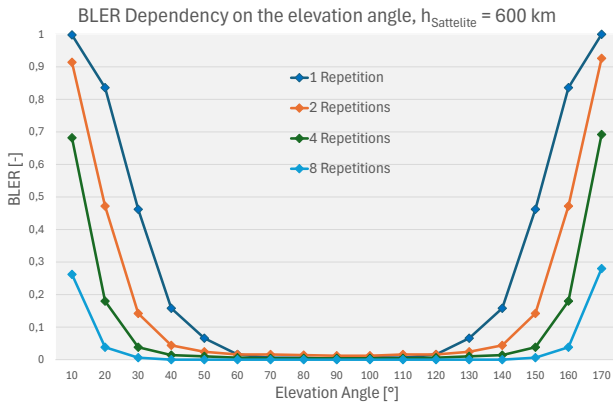

Fig. 3. Relationship of BLER and number of repetitions with satellite altitude of 600 km.

Satellite altitude plays an enormous role in the success rate of the communication channel. Figure 6 presents the comparison in BLER for different satellite altitudes with a configuration of a maximum of 1 repetition. Due to the longer distance between the UE and the overhead eNodeB, the BLER
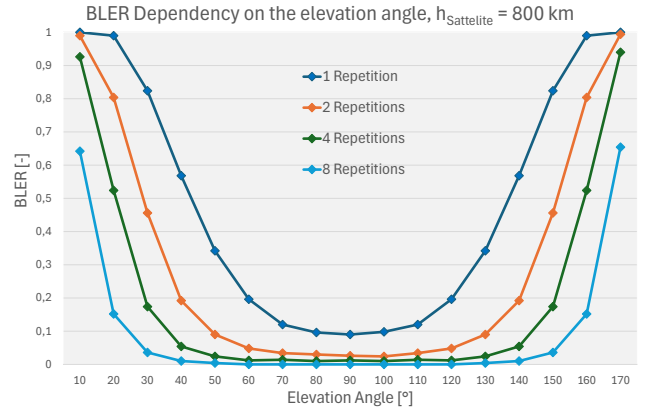

Fig. 4. Relationship of BLER and number of repetitions with satellite altitude of 800 km.
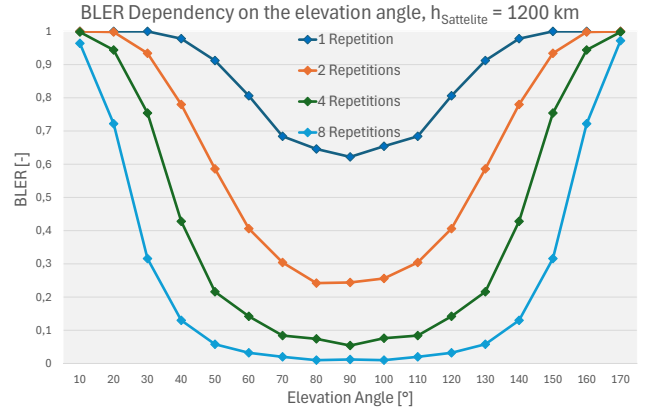

Fig. 5. Relationship of BLER and number of repetitions with satellite altitude of 1200 km.

increases with higher altitudes, while it decreases with lower altitudes. Considering the best-case scenario (i.e. elevation angle of 90°), the BLER for the satellite altitude of 600 km is 0%, however for the increased altitude of 1200 km it approaches 62,2%.
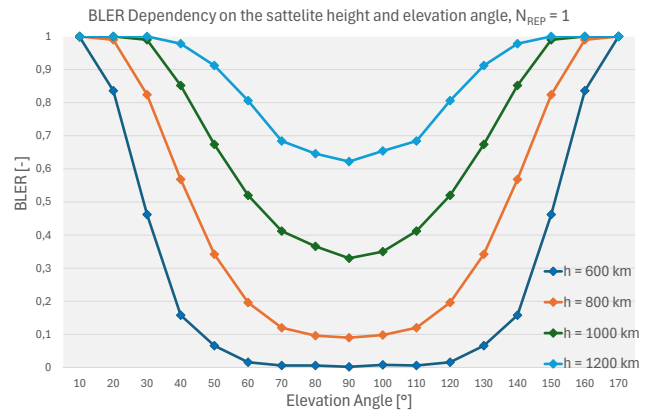

Fig. 6. Comparison of BLER based on different satellite altitudes.

The second simulation focused on the influence of the TBS settings on the BLER. For this simulation a satellite altitude

of 800 km was selected and parameters I_{SF} and $iMCS$ were modified in steps, to achieve the desired configuration of TBS according to the 3GPP specification [11]. The results of the simulation are displayed in figure 7.

Figure 7 clearly shows that the selection of the TBS has a significant influence on the success rate of the data transmission of the communication link. As the TBS increases the communication becomes more prone to errors due to the higher amount of bits transmitted within each message and therefore has to be retransmitted, which in return increases the energy consumption of the user end-device. With lower TBS the error rate is considerably lower. To further demonstrate the simulation environment has allowed to set up arbitrary TBS sizes, via the parameters I_{SF} and $iMCS$, that are undefined by the 3GPP, where the maximum TBS defined is 680 bits (85 bytes) [11].

As expected, the lowest TBS setting of 16 bits has the highest probability of being successfully decoded by the receiver potentially saving energy of the UE. However, this setting significantly limits the throughput at the expense of communication channel reliability. For cases where the elevation angle is higher than 50°the channel can reliably deliver data with TBS of up to 256 bits which has a significant impact on data throughput. The simulation was performed for repetition values of up to 4 where the reliability improved significantly, at the expense of the UE power consumption, to values of up to BLER 4.2% for elevation angle 40°and 14.6% for elevation angle of 30°.
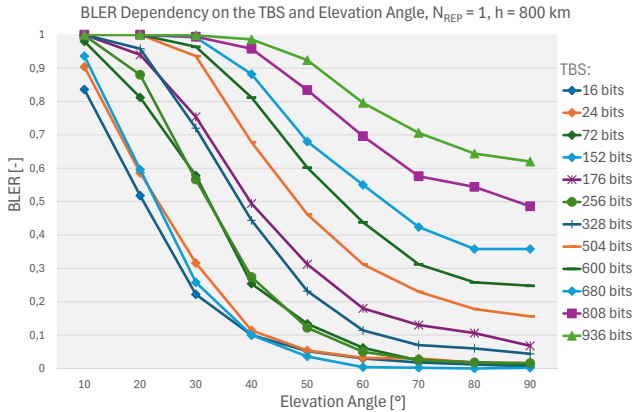

Fig. 7. Comparison of BLER based on different TBS.

V. Conclusion

In summary, the design and configuration of the communication architecture for non-terrestrial networks (NTN) require a meticulous and context-aware approach. While lower satellite altitudes—such as Low Earth Orbit (LEO) at 600 km—offer improved link reliability and the potential for higher data rates, they necessitate a denser satellite constellation due to shorter fly-over durations, during which a user terminal (UE) remains in direct contact with a satellite. In contrast, higher-altitude LEO systems (e.g., 1200 km) provide extended coverage time per satellite, allowing for a sparser constellation,

but impose greater challenges in link budget and necessitate the use of more robust modulation and coding schemes to ensure communication reliability.

A pivotal factor influencing system performance is the selection of the *Transport Block Size* (TBS). Lower-altitude applications can typically support larger TBS values (e.g., 680 bits at 600 km LEO) while maintaining acceptable reliability—evidenced by a BLER below 10% at elevation angles above 50°—whereas higher-altitude systems benefit from using smaller TBS values to increase the likelihood of successful decoding. Proper tuning of TBS plays a critical role in minimizing unnecessary repetitions, which are otherwise required to compensate for poor link quality, thereby conserving the energy budget of battery-powered devices.

To address the variability of link conditions inherent to satellite-based communication, *adaptive TBS selection mechanisms* should be employed. These mechanisms enable dynamic adjustment of the TBS based on instantaneous radio conditions, thereby enhancing link reliability while reducing the number of required repetitions. For instance, at elevation angles below 40°, smaller TBS values are recommended to maintain reliability, while at higher angles, larger TBS values can be employed more effectively. As a concrete example, for a satellite altitude of 800 km, it is advisable to limit the TBS to 152 bits or lower for elevation angles under 40°, as the block error rate approaches the 10% threshold in this regime (see Fig. 7).

Future work will further investigate the interplay between satellite density, coverage continuity, and adaptive resource allocation strategies to guide the development of energy-efficient and robust IoT-oriented NTN architectures.

References

[1] O. Liberg, M. Sundberg, Y.-P. E. Wang, J. Bergman, J. Sachs, and G. Wikström, *Cellular Internet of Things: From Massive Deployments to Critical 5G Applications*, second edition ed. Academic Press, 2020.

[2] I. Marin, "Introduction to 3GPP and 3GPP 5G Releases 15, 16 and 17," online. [Online]. Available: ¡https://society5.com/miot-5g/5g-3gpp-releases-15-16-17/¿

[3] X. Lin, "An Overview of 5G Advanced Evolution in 3GPP Release 18, year=2022," *IEEE Communications Standards Magazine*, vol. 6, no. 3, pp. 77–83.

[4] M. Roubíček, O. Zeman, P. Mlýnek, and P. Mašek, "NB-IoT Capacity; 2020."

[5] R. Barbau, V. Deslandes, G. Jakllari, J. Tronc, J.-F. Chouteau, and A.-L. Beylot, "NB-IoT over GEO Satellite: Performance Analysis," in *2020 10th Advanced Satellite Multimedia Systems Conference and the 16th Signal Processing for Space Communications Workshop (ASMS/SPSC)*, 2020, pp. 1–8.

[6] S. N. K. Veedu, M. Mozaffari, A. Höglund, E. A. Yavuz, T. Tirronen, J. Bergman, and Y.-P. E. Wang, "Toward Smaller and Lower-Cost 5G Devices with Longer Battery Life: An Overview of 3GPP Release 17 RedCap," *IEEE Communications Standards Magazine*, vol. 6, no. 3, pp. 84–90, 2022.

[7] O. Ledesma, P. Lamo, and J. Fraire, "Trends in lpwan technologies for leo satellite constellations in the newspace context," *Electronics*, vol. 13, p. 579, 01 2024.

[8] M. Conti, A. Guidotti, C. Amatetti, and A. Vanelli-Coralli, "Nb-iot over non-terrestrial networks: Link budget analysis," in *GLOBECOM 2020 - 2020 IEEE Global Communications Conference*, 2020, pp. 1–6.

[9] M. Conti, S. Andrenacci, N. Maturo, S. Chatzinotas, and A. Vanelli-Coralli, "Doppler impact analysis for nb-iot and satellite systems integration," in *ICC 2020 - 2020 IEEE International Conference on Communications (ICC)*, 2020, pp. 1–7.

[10] S. Cluzel, L. Franck, J. Radzik, S. Cazalens, M. Dervin, C. Baudoin, and D. Dragomirescu, "3gpp nb-iot coverage extension using leo satellites," in *2018 IEEE 87th Vehicular Technology Conference (VTC Spring)*, 2018, pp. 1–5.

[11] 3GPP, "Lte; evolved universal terrestrial radio access (e-utra); physical layer procedures," 3GPP, Tech. Rep. TS 36.213 version 14.2.0 Release 14 (2017/04), 2017.

Trends And Challenges Of Hydrometallurgical Recycling Of Lithium-ion Batteries

Jiří Báňa
Department Of Electrical and Electronic Technology
Brno University of Technology
Brno, Czech Republic
0000-0002-8119-979X

Tomáš Kazda
Department Of electrical and Electronic Technology
Brno University of Technology
Brno, Czech Republic
0000-0003-1973-02Z

Abstract— **Hydrometallurgical recycling of lithium-ion batteries (LIBs) is becoming a key technology for the sustainable recycling of critical materials such as lithium, cobalt and nickel. This article focuses on new trends and challenges in hydrometallurgical processes, including the development of leaching reagents or new separation processes, and increasing overall recycling efficiency. Innovations such as the use of biological and organic leaching methods are discussed. The main challenges include reducing the environmental impact, improving economic efficiency.**

Keywords— Li-ion battery, recycling, hydrometallurgy

I. Introduction

LIBs generally consist of five key components: the cathode, anode, electrolyte, separator, and casing. The cathode features an aluminum current collector coated with an active material, usually a lithium-containing transition metal oxide. The anode is typically made of graphite on a copper current collector, though lithium titanate ($Li_4Ti_5O_{12}$ or LTO) may sometimes take place. Nowadays, silicone is often added into anode to increase capacity. The casing is commonly constructed from aluminum or stainless steel, while the separator is usually composed of polymeric materials such as polyethylene (PE), polypropylene (PP), or a combination of both. [1][2]

LIBs operate on intercalation and deintercalation process. During charging, lithium ions move from the cathode to the anode via the electrolyte, intercalated between graphene layers of graphite while electrons travel through the external circuit. During discharge, the process reverses—lithium ions return to the cathode structure as electrons flow through the circuit. The principle is illustrated in equation below. LCO was chosen as the cathode material for this equation. [3][4]

$$LiCO_2 \xrightarrow{Discharge} Li_{1-x}CO_2 + xLi^+ + xe^-$$
$$C_6 + xLi^+ + xe^- \xrightarrow{Charge} Li_xC_6$$
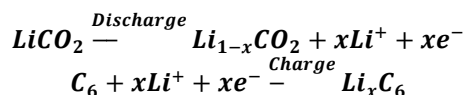
Since commercialization of LIBs in 1991, their demand has surged, driven by electric vehicles (EVs), portable electronics, and energy storage systems. The push for EV adoption to reduce carbon emissions has fuelled rapid LIB growth, with global demand projected to reach 4,700 GWh by 2030. By then, an estimated 11 million metric tons of spent LIBs will accumulate, rising to 340,000 metric tons annually by 2040.

Recycling these batteries is crucial, as they contain valuable metals like Li, Ni, Co, Mn, Al, and Cu. Recovering these materials supports a sustainable supply chain, turning waste into wealth. Additionally, improper disposal poses environmental and health hazards, making efficient LIB recycling essential for resource recovery and pollution reduction.[5]

Pyrometallurgical processes, such as the Umicore method, are particularly high-temperature smelting. Spent LIBs, along with flux and slagging agents, are processed in a shaft furnace, where electrolytes evaporate, organic components pyrolyze, and reduction smelting produces metal alloys (Cu, Co, Fe, Ni), while Li, Al, and Mn transfer to slag. Toxic compounds are captured using Ca, Na, and ZnO_2, with gas purification systems ensuring further treatment. In Fig. 1 is shown pyrometallurgical recycling process of by Umicore.

Roasting, an alternative method, involves exothermic reactions between gases and solids, where carbon acts as a reducing agent, heating cathode materials to form alloys and carbon residue. Metal oxide reduction depends on carbon input, controlling valence states.

Despite its advantages (simplicity), pyrometallurgy has limitations: Li, Al, and Mn require additional hydrometallurgical processing, graphite (12-21%), organics like electrolyte etc. (~15%), and plastics (~7%) are not recovered, and overall efficiency is below 50%. Additionally, it is ineffective for LFP battery recycling and poses challenges in waste gas cleaning[6][7][8][9]
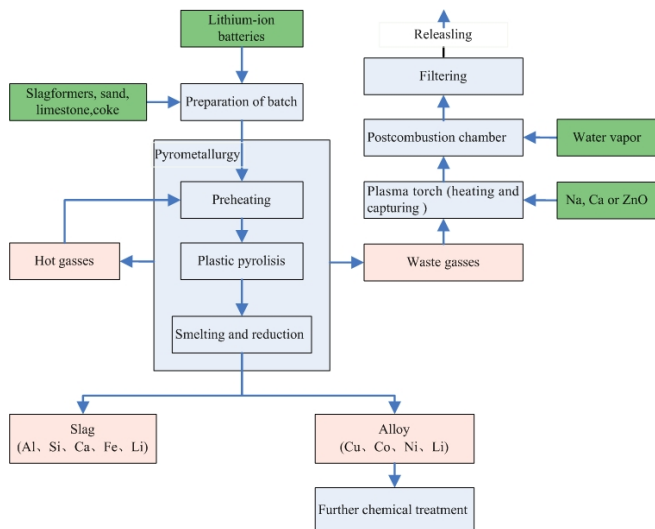
Fig. 1.   Pyrometallurgical recycling process of by Umicore[10]

The hydrometallurgical process is a key commercial method for recycling metals from spent LIBs, involving multiple steps to recover valuable materials efficiently. Initially, the batteries are ground in an inert atmosphere to evaporate electrolyte solvents, which are then collected through condensation. Supercritical CO_2 is used to extract lithium salts. The crushed material undergoes further separation, with ferrous components removed magnetically and electrodes isolated from separators using airflow.

Heating the material to 400–600°C eliminates binders, separating current collectors from active material particles. Graphite anode material and Cu/Al current collectors are extracted, while lithium is leached from the cathode material. The active material dissolves in an acid mixture, where heavy metals are separated using various leaching techniques, including oxalates, organic acids (citric or acetic acid), or concentrated mineral acids (sulfuric, hydrochloric, and nitric acid).[11][12][13]
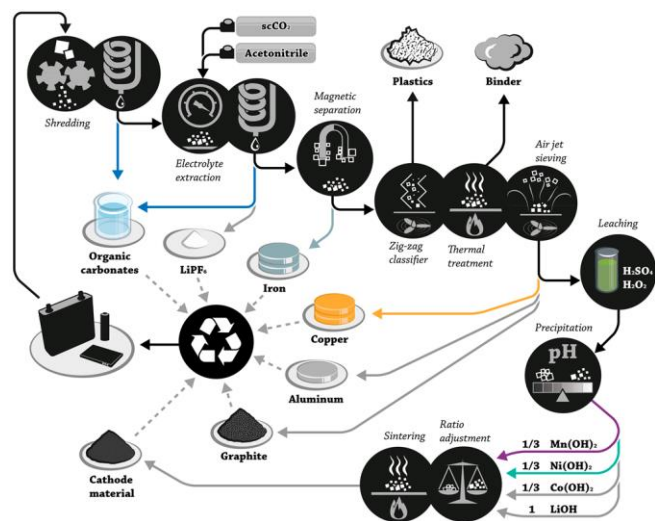

Fig. 2.   Hydrometallurgical recycling process by Duesenfeld

Leaching enables metal recovery through extraction, precipitation, or electrodeposition. However, lithium ions are often lost as waste, mostly if output is only black mass for recycler, leading to significant resource loss. Additionally, hydrometallurgy generates substantial wastewater containing chemical residues, necessitating proper treatment. The recovery of certain metals, particularly lithium, remains challenging due to their high solubility and reactivity. Despite these limitations, hydrometallurgy is a widely used and promising approach for sustainable LIB recycling.[11][12][13]

II.   CHALLENGES OF LIB RECYCLING

By 2031, the European directive mandates, that over 70% of a LIBs weight must be recycled. Additionally, all recycling processes must meet minimum material recovery targets, including 95% for cobalt, copper and nickel, and 80% for lithium. [14] Thus pyrometallurgical process will not be suitable for recycling in EU and more and more focus in the future will be on new environmentally friendly approaches of hydrometallurgical recycling process.

Electric vehicles use a wide variety of battery configurations, cell types, and chemistries, making recycling challenging. Different vehicle manufacturers have adopted various designs, leading to diverse disassembly needs, especially concerning automation. The variations in size, format, and cell chemistry affect materials reclamation and the overall economics of recycling. For example, prismatic and pouch cells have planar electrodes, while cylindrical cells are tightly coiled, complicating electrode separation.

Currently, automotive battery packs are manually dismantled for repurposing or recycling, requiring qualified personnel and specialized tools due to their weight and high voltage. However, there's a shortage of skilled technicians, with only a small percentage of motor technicians trained to service EVs. In countries with high labor costs, manual dismantling may be uneconomical. Furthermore, vehicle designs, while optimized for safety and performance, often compromise recyclability, making manual disassembly time-consuming and inefficient.[15]

Another drawback of hydrometallurgical recovery process graphite recovery, which is typically sold at a low price, with unclear prospects for economically or sustainably viable applications. Proper recycling method for graphite purity and capacity will be necessary in the future.

The use of inorganic acids raises concerns about safety, secondary pollution, and equipment corrosion during leaching. Additionally, the dissolution of electrolytes in acids generates secondary pollutants like hydrofluoric acid (HF) in wastewater and gases, which require expensive treatment. [16]
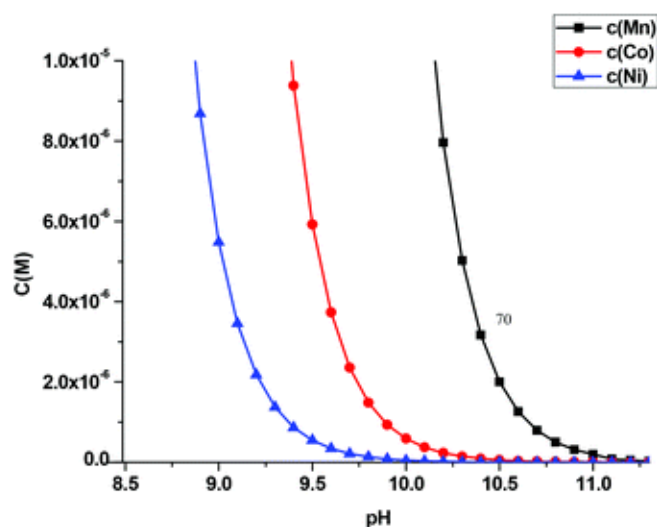
Fig. 3.   pH range of precipitation of Mn, Co and Ni [17]

Separating metals nickel, manganese, and cobalt is also challenging due to their similar properties. Precipitation of these metals is within a short pH range, see Fig. 3. Organic acids offer an alternative, as they are easier to degrade and recycle, reducing secondary waste.[16]

Removing the current collector foil in batteries is challenging, especially due to the use of polyvinylidene fluoride (PVDF) as a binder for cathode material. While PVDF offers good electrochemical stability and binding ability, its removal at through pyrolysis creates toxic gases demanding to filter out from the waste gases. Dissolution of PVDF using NMP (N-methyl-2-pyrrolidone) posing environmental and safety concerns. Moreover, solvents like NMP are expensive, dangerous, and require special engineering, raising costs of recycling process. To mitigate these issues, alternatives to PVDF must be found. Recent suggestions involve using green solvents for PVDF removal, but heat treatment must be avoided to prevent HF formation and fluorinated compounds. As manufacturers would switch to alternative binders, the process of binder removal could be simplified, reducing harmful by-products and costs. [18]

III. NEW TRENDS IN RECYCLING

Biometallurgical processes rely on microorganisms to convert insoluble compounds into soluble forms, but generally achieve low leaching efficiencies for Co and Li, even with extended leaching times and the use of Fe^{2+} as a catalyst. Fungal leaching is the preferred alternative due to its wide pH tolerance, resistance to toxins and efficient leaching by organic acids in fungal metabolites. However, although it is environmentally friendly and operates under mild conditions, its slow kinetics and low pulp density limit its industrial viability. While parameter optimization can increase efficiency, the process is still time consuming, which poses a problem for large-scale applications. [19]

Deep eutectic solvents (DES) are a class of green solvents formed by mixing two or more components, resulting in a

lower melting point than the individual substances due to strong hydrogen bonding. DESs typically consist of a hydrogen bond acceptor (HBA), such as a quaternary ammonium salt, and a hydrogen bond donor (HBD), like an alcohol or carboxylic acid. These solvents are low in toxicity, cost-effective, biodegradable, and highly efficient at dissolving metal oxides, making them a promising alternative to traditional mineral or organic acids in LIB recycling.

A key advantage of DESs is their dual role as both leaching reagents and reducing agents. Their strong coordination ability, reducibility, and acidity enable efficient metal oxide dissolution, particularly for Co, Ni, and Mn. Unlike conventional hydrometallurgical methods, DESs eliminate the need for additional reducing agents like H_2O_2, reducing costs and environmental impact. Various DES formulations, such as choline chloride (ChCl) combined with ethylene glycol (EG), urea, or oxalic acid, have demonstrated high metal recovery efficiencies. For example, ChCl/EG DES achieved a 99.3% Co leaching rate at 220°C, while ChCl/urea DES reached 95% Li and 98% Co recovery at 180°C. Additionally, ChCl/oxalic acid DES enabled direct Li and Co recovery with over 96% efficiency, separating metal oxalates simply by temperature control. These findings underscore DESs' potential as a sustainable, efficient, and eco-friendly alternative for LIB recycling. Downside of this technology could be higher temperature demand resulting in higher energy consumption. [5][20]

Non-thermal plasmas (NTPs) can break down PVDF polymer chains by generating high-energy particles during discharge, which disrupt C-F bonds through the oxidation effects of OH radicals, leading to deactivation. This method enables direct recycling of intact aluminum foil and significantly shortens processing time, making it an efficient and clean technique for removing cathode materials. NTPs could decompose cathode materials and metal current collectors, achieving a separation rate of 95.69% under experimental conditions with 300 W discharge power at 80°C for 35 minutes. Combination of plasma with ultrasonic separation, reaching a cathode material separation rate of 96.8% under optimal conditions with an ultrasonic frequency of 13.56 MHz, 100 W power, and a 10-minute processing time in an oxygen atmosphere. [21]

Another difficulty of hydrometallurgical recycling is the effective regeneration of LFP cathode material, which has recently become more popular due to its stability and low cost. Since LFP does not contain precious metals such as Co or Ni, recycling this material is unprofitable and inefficient in terms of yield. [22]

Another hydrometallurgical recycling method, electro-dissolution, has been used to extract both lithium carbonate and cobalt in the form of cobalt metal or cobalt oxide (CoO). Similarly, electrowinning has been used to simultaneously recover cobalt and nickel metals with purities of

approximately 96% and 94%, respectively, from chemically leached NMC cathodes. These techniques eliminate hazardous chemicals, thus contributing to a more sustainable industry. However, there are still gaps in electrochemical recovery. Unlike some conventional methods, electrochemical approaches have not yet been applied to mixed chemical batteries or to the recovery of non-cathode materials. [23]

Direct recycling, possibly a next step in hydrometallurgical recycling is a sustainable recycling method that maintains the composition and structure of electroactive materials without breaking them down into elemental forms. It uses processes like Li addition and crystal lattice reconstruction, minimizing the need for strong acids or bases. This method reduces energy and chemical inputs, helping create a more sustainable recycling ecosystem.

Pre-separation treatment is crucial for ensuring the purity of electroactive materials before regeneration. It involves sorting, disassembling, and mechanically processing batteries, as well as removing binders. Direct recycling focuses on harvesting cathode/anode materials, separating them from current collectors and polymers, and restoring their electrochemical properties. Solvents like NMP, DMF, DMAC, and DMSO are used to remove PVDF binder, with ultrasonic technology improving dissolution efficiency by up to six times.

The efficiency of direct recycling varies based on technology, input material quality, and extraction methods, with recycling efficiency reaching 90-100% when binders are also recycled. This method is also suitable for LFP cathodes. Downside of this technology is need in volatile organic solvents to dissolve PVDF and need in manual separation of battery parts. [18] [24][25]

IV. CONCLUSION

LIB recycling is a topic that will become increasingly important in the future. Recycling technologies are evolving with time and seeking efficiency, lowering recycling costs and increasing environmental friendliness. New approaches increasing environmental friendliness, yet lacking scaling ability.

REFERENCES

[1] L. S. Martins, L. F. Guimarães, A. B. Botelho Junior, J. A. S. Tenório, and D. C. R. Espinosa, "Electric car battery: An overview on global demand, recycling and future approaches towards sustainability", *Journal of Environmental Management*, vol. 295, 2021.

[2] E. Foreman, W. Zakri, M. Hossein Sanatimoghaddam, A. Modjtahedi, S. Pathak, A. G. Kashkooli, N. G. Garafolo, and S. Farhad, "A Review of Inactive Materials and Components of Flexible Lithium-Ion Batteries", *Advanced Sustainable Systems*, vol. 1, no. 11, 2017.

[3] X. Yuan, H. Liu, and J. Zhang, *Lithium-Ion Batteries: Advanced Materials and Technologies*. CRC Press, 2016.

[4] Y. Wu, *Lithium-Ion Batteries: Fundamentals and Applications*. CRC Press, 2015.

[5] Y. Dong, H. Ji, X. Wu, N. Zheng, J. Wang, G. Ji, Y. Chen, G. Zhou, and Z. Liang, "Trends of sustainable recycling technology for lithium-ion batteries: Metal recovery from conventional metallurgical processes to innovative direct recycling", *MetalMat*, vol. 1, no. 1, 2024.

[6] B. Makuza, Q. Tian, X. Guo, K. Chattopadhyay, and D. Yu, "Pyrometallurgical options for recycling spent lithium-ion batteries: A comprehensive review", *Journal of Power Sources*, vol. 491, 2021.

[7] A. Pražanová, V. Knap, and D. -I. Stroe, "Literature Review, Recycling of Lithium-Ion Batteries from Electric Vehicles, Part I: Recycling Technology", *Energies*, vol. 15, no. 3, 2022.

[8] G. Qu, J. Yang, H. Wang, Y. Ran, B. Li, and Y. Wei, "Applicability of the reduction smelting recycling process to different types of spent lithium-ion batteries cathode materials", *Waste Management*, vol. 166, pp. 222-232, 2023.

[9] C. Yi, Y. Yang, T. Zhang, X. Wu, W. Sun, and L. Yi, "A green and facile approach for regeneration of graphite from spent lithium ion battery", *Journal of Cleaner Production*, vol. 277, 2020.

[10] S. Wang, Y. Tian, X. Zhang, B. Yang, F. Wang, B. Xu, D. Liang, and L. Wang, "A Review of Processes and Technologies for the Recycling of Spent Lithium-ion Batteries", *IOP Conference Series: Materials Science and Engineering*, vol. 782, no. 2, Mar. 2020.

[11] A. Zanoletti, E. Carena, C. Ferrara, and E. Bontempi, "A Review of Lithium-Ion Battery Recycling: Technologies, Sustainability, and Open Issues", *Batteries*, vol. 10, no. 1, 2024.

[12] F. Larouche, F. Tedjar, K. Amouzegar, G. Houlachi, P. Bouchard, G. P. Demopoulos, and K. Zaghib, "Progress and Status of Hydrometallurgical and Direct Recycling of Li-Ion Batteries and Beyond", *Materials*, vol. 13, no. 3, 2020.

[13] S. Nowak and M. Winter, "The Role of Sub- and Supercritical CO2 as "Processing Solvent" for the Recycling and Sample Preparation of Lithium Ion Battery Electrolytes", *Molecules*, vol. 22, no. 3, 2017.

[14] "Regulation (EU) 2023/1542 of the European Parliament and of the Council of 12 July 2023 concerning batteries and waste batteries, amending Directive 2008/98/EC and Regulation (EU) 2019/1020 and repealing Directive 2006/66/EC." .

[15] G. Harper, R. Sommerville, E. Kendrick, L. Driscoll, P. Slater, R. Stolkin, A. Walton, P. Christensen, O. Heidrich, S. Lambert, A. Abbott, K. Ryder, L. Gaines, and P. Anderson, "Recycling lithium-ion batteries from electric vehicles", *Nature*, vol. 575, no. 7781, pp. 75-86, Nov. 2019.

[16] X. Ma, Z. Meng, M. V. Bellonia, J. Spangenberger, G. Harper, E. Gratz, E. Olivetti, R. Arsenault, and Y. Wang, "The evolution of lithium-ion battery recycling", *Nature Reviews Clean Technology*, vol. 1, no. 1, pp. 75-94, 2025.

[17] H. Zou, E. Gratz, D. Apelian, and Y. Wang, "A novel method to recycle mixed cathode materials for lithium ion batteries", *Green Chemistry*, vol. 15, no. 5, 2013.

[18] D. Thompson, C. Hyde, J. M. Hartley, A. P. Abbott, P. A. Anderson, and G. D. J. Harper, "To shred or not to shred: A comparative techno-economic assessment of lithium ion battery hydrometallurgical recycling retaining value and improving circularity in LIB supply chains", *Resources, Conservation and Recycling*, vol. 175, 2021.

[19] W. Lv, Z. Wang, H. Cao, Y. Sun, Y. Zhang, and Z. Sun, "A Critical Review and Analysis on the Recycling of Spent Lithium-Ion Batteries", *ACS Sustainable Chemistry & Engineering*, vol. 6, no. 2, pp. 1504-1521, Feb. 2018.

[20] G. Azimi and K. H. Chan, "A review of contemporary and emerging recycling methods for lithium-ion batteries with a focus on NMC cathodes", *Resources, Conservation and Recycling*, vol. 209, 2024.

[21] W. Yang, Z. Tong, X. Bu, and L. Dong, "Research progress on the separation of cathode materials from metal current collectors of spent lithium-ion batteries", *Journal of Industrial and Engineering Chemistry*, 2024.

[22] C. B. van Beek, E. Yilmaz, and D. H. A. Boom, "Sustainable Hydrometallurgical LFP Battery Recycling: Electrochemical Approaches", *ChemSusChem*.

[23] J. G. Sederholm, L. Li, Z. Liu, K. -W. Lan, E. J. Cho, Y. Gurumukhi, M. J. Dipto, A. Ahmari, J. Yu, M. Haynes, N. Miljkovic, N. H. Perry, P. Wang, P. V. Braun, and M. C. Hatzell, "Emerging Trends and Future Opportunities for Battery Recycling", *ACS Energy Letters*, vol. 10, no. 1, pp. 107-119, Jan. 2025.

[24] J. Wu, M. Zheng, T. Liu, Y. Wang, Y. Liu, J. Nai, L. Zhang, S. Zhang, and X. Tao, "Direct recovery: A sustainable recycling technology for spent lithium-ion battery", *Energy Storage Materials*, vol. 54, pp. 120-134, 2023.

[25] Y. Ji, E. E. Kpodzro, C. T. Jafvert, and F. Zhao, "Direct recycling technologies of cathode in spent lithium-ion batteries", *Clean Technologies and Recycling*, vol. 1, no. 2, pp. 124-151, 2021.

Early fire detector using GAS FET

Adam Dvorský
Department of Microelectronics
Brno university of technology
Brno, Czech Republic
xdvors12@vutbr.cz

Abstract— **This work aims to evaluate available commercial fire alarm solutions on the market in the Czech Republic. Based on the specified parameters, the pros and cons of these systems were evaluated. Another point was the research of new solutions that show promising parameters for further development and increasing the reliability of these devices. The selected type of gas sensor is sensitive layers on the FET structure.**

Keywords— fire detector, GAS FET, sensitive layer

I. INTRODUCTION (HEADING 1)

The latest trend in the construction industry is the construction of smart homes. Buildings of this type have become very popular and their demand is growing rapidly. This progress is possible thanks to the great and rapid development of electronics. One of the most desired needs is the development in the field of fire protection. The most valuable is the protection of health, lives and, last but not least, property. Any fire must be detected as soon as possible and this incident must be immediately reported to the owner or designated authorities, i.e. the fire department. In the concept of smart cities, it is appropriate to connect these detection systems in one building into one unit to ensure correct detection and quick localization. There are errors in today's systems that cause fake alarm triggering and thus unnecessary visits by firefighters, who cannot intervene in other, more necessary cases. Furthermore, after merging into one unit, it is possible to monitor the detection process and thus determine the spread of fire in the building. The goal is therefore to determine the composition of various types of emissions that may occur in a given building. Based on this composition, develop an effective detection method based on gas sensing, temperature detection, etc. To save costs, it is advisable to ensure low consumption of the developed detection system.

II. PRINCIPLE OF BASIC DETECTORS

Today, the most common types of fire detectors are detectors based on temperature sensing, optical and ionization. Each of these types has a different detection speed and detection medium.

A thermal smoke detector consists of a control unit and a temperature sensor, which is located inside the detection chamber. When the temperature changes, the air moves and the warm air rises upwards, towards the ceiling. The temperature sensor detects an increase in temperature above the alarm level and a report is initiated. This sensor itself has the greatest disadvantage in rooms where the temperature is higher. It can declare a false alarm even if there is no fire in the room. The

advantage of this sensor is the possibility of using it in areas with high dust, where the sensor is not blocked. For this reason, it is advisable to install a different type of detector in these rooms.

The second type of detector is an optical detector. This detector works with an infrared beam of light. The beam source and the detector are off-axis. When particles pass through, the beam is refracted and then comes into contact with the detector. According to the described function, this detector cannot be used in dusty areas, where frequent false alarms may occur.
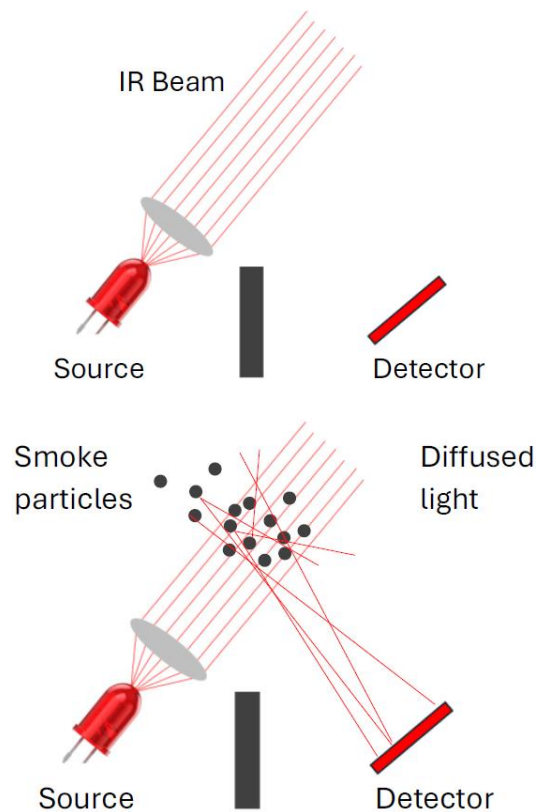

Fig. 1. Optical smoke detector functions

The last mentioned detector is ionization. This detector is the most complex in its design. It contains an ionization chamber with a weak radioactive element connected to two electrodes. The air is ionized in this part and a free electron is created. A weak current source is then created between the electrodes, where free electrons are attracted to the positive electrode and a positive atom to the negative electrode. When particles enter,

positive ions are attracted by these particles, the current is interrupted and the control circuit detects the possibility of fire. This type of detector is the most sensitive, where the sensor can detect even weak smoke from just a small flame. A significant disadvantage is the frequent detection when unwanted particles enters the chamber.
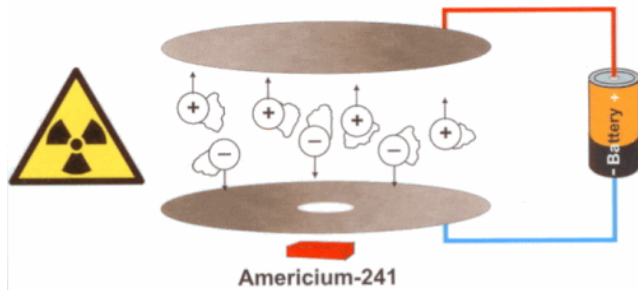

Fig. 2. Ionization smoke detector funstions

There may also be special types of detectors, combined, which consistof two different detection methods. This improves the system against false detections.

III. Combustion products

Every combustion reaction produces certain gases and their concentrations. It all depends on the material that is subjected to this reaction. The largest proportion contained in the flue gas is the compound CO and NO2. For example, in an open fire, when so-called good combustion occurs, the release of CO gas is smaller. On the contrary, in incomplete combustion, the production of CO gas is significantly higher.

The formation of other aerosols during combustion cannot be ignored. These aerosols, as well as water vapor, are the most common reason for the unreliability of detection and alarm. When water vapor is detected, a false alarm can be triggered, which can lead to the departure of the responsible rescue services. The most common representative in combustion was the element carbon. Therefore, the created design will be thwarted by the detection of mainly carbon.

It is necessary to include changes in the air pressure in the room where the combustion takes place. When a fire occurs, it is necessary to take into account two different scenarios. In the first case, a fire may develop in a closed room. In such a case, when the air temperature in this room increases, a state occurs, according to the equation of state ideal gas law, when the hot gas expands and thus increases the pressure in the room. During the combustion process, it is consumed, which reduces the pressure again. When substances are burned, combustion products are produced, which again increase the pressure in the room. The production of combustion products increases the pressure in the room more than the oxygen decreases. In the second case, it is necessary to take into account leaks in the room, open doors and windows. Thanks to these leaks, the pressure in the room does not increase, as there is a flow of gases and a distribution of pressures.

During combustion, the air is heated and its specific gravity changes. As a result, warmer air rises, while cooler air falls. This phenomenon creates a flow and accumulation of heat in the upper parts of the room.

Thanks to this knowledge, when designing a new detection system, we know that we don't need to take into account the changing pressure in the room. Only the increase in temperature and the presence of carbon.

IV. Gas FET

The technology of gas sensors based on FET transistors (GasFET) has been gaining increasing attention in recent years due to its high sensitivity in detecting various gases. GasFET sensors are based on the conventional structure of field-effect transistors (FETs), with the key element being a sensing layer deposited on the gate electrode or floating gate of the transistor. This sensing layer is able to interact with gas molecules in the surrounding environment, which leads to physicochemical changes in its structure.

When gas is absorbed, the surface charge in the sensing layer changes, which affects the distribution of the electric field in the transistor structure. This phenomenon changes the potential between the control and floating gates, thereby affecting the channel conductivity between source and drain. In the case of a floating gate (FG-GasFET), a long-term change in charge can occur due to electron capture, which allows the detection of even low gas concentrations with high signal stability.
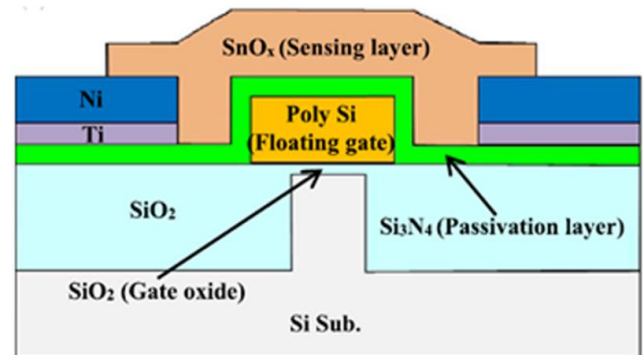

Fig. 3. Schematic cross-sectional view [8]

Depending on the material of the sensing layer used, for example the semiconductor tin oxide (SnO2), mentioned in the article [8], zinc oxide (ZnO) or graphene, different levels of selectivity and detection limits for specific gases can be achieved. Thanks to the possibility of integration into common CMOS semiconductor technologies and low energy requirements, GasFET sensors represent a promising solution for applications in smart sensors, industrial gas monitoring and medical diagnostics.

The mentioned article presents several technological solutions to this problem. The most promising seems to be the formation of the sensing layer structure directly on the floating gate in the form of a thin layer.

V. Output Current Change

For the correct design of a GasFET gas sensor, it is crucial to understand the change in the output current ID as a function of the material of the sensitive layer. This parameter directly affects the detection capabilities of the sensor, since the change in potential in the sensitive layer caused by gas adsorption affects the threshold voltage Vth, and thus the overall

conductivity of the transistor. The calculation of ID allows us to quantify the difference in electrical response between different materials of the sensitive layer and thus optimize the selection of the material for maximum sensitivity to the detected gas.

In the following section, the calculation of SnO2 as the material of the sensitive layer was used. It was chosen because of its use in many sources about these gas sensors. The gas pressure was chosen to be an average state, i.e. 1000 hPa, and the temperature was also room temperature, since this is a sensor that is tasked with detecting gases in the event of a fire, when the room pressure and temperature values are not increased in any way.

A. Calculation for SnO2 and pure graphene

Initial equation: Calculation of ID current in linear mode.

$$I_D = \mu C_{ox} \frac{W}{L} \left[(V_{GS} - V_{th})V_{GS} - \frac{V_{DS}^2}{2} \right] \tag{1}$$

Where μ is the charge carrier mobility in the channel, C_{ox} is the capacitance of the gate oxide per unit area, W and L are the width and length of the channel, V_{GS} is the gate-source voltage, Vth is the threshold voltage of the transistor. In this mode, I_D current is proportional to V_{DS} voltage.

The threshold voltage Vth is affected by the surface potential of the sensing layer Φ_s, which varies depending on CO adsorption. The relationship can be approximated by the Schottky-Mott equation:

$$V_{th} = \gamma \left(V_{th0} - \frac{q}{C_{ox}} \Delta \Phi s \right) \tag{2}$$

Where γ is the capacitance ratio between the sensing layer and the gate, V_{th0} is the original threshold voltage before gas exposure, Cox is the oxide capacitance, and $\Delta\Phi_s$ is the change in surface potential caused by CO adsorption.

The change in surface potential can be calculated from the Langmuir absorption isotherm and Poisson's equation.

$$\Delta \Phi s = \frac{kT}{q} \ln \left(\frac{P}{P_0} \right) \tag{3}$$

Where P is the current partial pressure of the analyzed gas in the environment, P_0 is the reference pressure, corresponding to the maximum possible gas concentration at which the sensing layer is completely covered by molecules of the examined gas. If this ratio is close to zero, we can say that there are very few particles of molecules in the gas. If the surface is completely saturated, the ratio is close to one.

For the initial calculation, average values for the FET transistor and tabulated values of the permittivity of the materials used are selected. The results are in Table 1.

TABLE I. Results

Material	SnO2	Graphene
C [F/m²]	1,15 x 10⁻²	4,25 x 10⁻³
γ	0,92	0,81
ΔV_{th} [V]	-0,64	-0,15
I_D [µA]	0,552	7,65

In this case, the output current ID was calculated for a GasFET transistor with a SnO_2 and graphene-based sensing layer. The calculations showed that for a gate voltage of $V_{GS} = 2$ V, the I_D value for SnO2 is approximately 0,552 µA, while for graphene it reaches 7,65 µA. This difference suggests that graphene provides higher conductivity and greater sensitivity to changes caused by gas adsorption, making it a more suitable material for CO detection. The results show that the correct choice of sensing layer significantly affects the performance of the sensor and its ability to accurately detect the presence of the target gas. The detection ability of graphene can be increased by appropriate additives. The most promising is doping with nitrogen or platinum. Higher sensitivity can also be achieved by changing the transistor parameters and technological production of the sensitive layer.

VI. CONCLUSION

This article aims to outline the essence of the problem in the field of fire detection. The main task is to improve the detection system, which will thus have the ability to detect a fire at an early stage of its development. It is also assumed that these sensors will be calibrated against false alarms. This is possible thanks to the use of an alternative gas sensor, which was selected based on the detected smoke compounds during combustion.

Initial calculations, when all the gate parameters and the size of the sensitive layer are the same, have shown that graphene is a more promising material for detecting CO gas. A possible improvement in the parameters of the sensitive layer is doping graphene with, for example, nitrogen, platinum. Its major disadvantage is its high price. When saving lives and property, the purchase price may not play a large role compared to the cost of the aforementioned lives and property.

By combining multiple sensors, it could be possible to remove interfering elements and thus prevent false alarms.

REFERENCES

[1] Jack, Kufre Esenowo, Adigun, Abdulraheem Sholagbade, Adewale, Faith Adesina a Inyang, Aniekan Ben. Improved Fire Safety and Protection Model for Smart Buildings with Internet of Things. ACM International Conference Proceeding Series, 2021. ISBN 978-145038734-7.

[2] Li, Xiaolu, Sánchez del Río Saez, José, Ao, Xiang, Yusuf, Abdulmalik a Wang, De-Yi. Highly-sensitive fire alarm system based on cellulose paper with low-temperature response and wireless signal conversion. Chemical Engineering Journal, 2022. DOI: 10.1016/j.cej.2021.134108. ISSN 13858947.

[3] Kumaran S., Arunachalam S., Surendar V. a Sudharsan T. IoT based Smoke Detection with Air Temperature and Air Humidity; High Accuracy with Machine Learning. Proceedings of the 3rd International Conference on Artificial Intelligence and Smart Energy, ICAIS 2023, 2023. DOI: 10.1109/ICAIS56108.2023.10073920. ISSN 978-166546216-7.

[4] Jack, Kufre Esenowo, Adigun, Abdulraheem Sholagbade, Adewale, Faith Adesina a Inyang, Aniekan Ben. Mproved Fire Safety and Protection Model for Smart Buildings with Internet of Things. ACM International Conference Proceeding Series, 2021. DOI: 10.1145/3508072.3508115. ISSN 978-145038734-7.

[5] VOJÁČEK, Antonín. Detektory kouře - princip & IO Freescale. Automatizace.hw.cz [online]. 2006 [cit. 2023-08-25]. URL: https://automatizace.hw.cz/clanek/2006091701

[6] D. Gutmacher, U. Hoefer a J. Wöllenstein. Gas sensor technologies for fire detection [online]. Volume 175, 2012. Sensors and Actuators B: Chemical [cit. 2023-10-14]. ISSN 0925-4005. URL: doi:https://doi.org/10.1016/j.snb.2011.11.053

[7] JAROSLAV, Chyský Prof. Ing. CSc.; KAREL, Hemzal Prof. Ing. CSc. a kolektiv. Technický průvodce - Větrání a klimatizace. Praha, 1993.

[8] HONG, Seongbin; WU, Meile; HONG, Yoonki; JEONG, Yujeong; JUNG, Gyuweon et al. FET-type gas sensors: A review. Online. Sensors and Actuators B: Chemical. 2021, roč. 330. ISSN 09254005. URL: https://doi.org/10.1016/j.snb.2020.129240. [cit. 2024-04-20].

[9] LEENAERTS, O.; PARTOENS, B a PEETERS, F. M. Adsorption of H2O, NH3, CO, NO2, and NO on graphene: A first-principles study. Online. American Physical Society. 2008, roč. 77, č. 11, s. 6. URL: https://link.aps.org/doi/10.1103/PhysRevB.77.125416. [cit. 2025-03-16].

Effects of gate boosting on gate oxide reliability and lifetime estimation of commercially available MOSFETs

Pavel Tomíček

Department of Microelectronics
Brno University of Technology
Brno, Czech Republic
xtomic05@vutbr.cz

Jaroslav Boušek

Department of Microelectronics
Brno University of Technology
Brno, Czech Republic
bousek@vut.cz

Abstract - **This paper presents a method of estimating gate oxide reliability and lifetime of commercially available MOSFETs. The estimation is calculated for the specific condition that is present when gate boosting is used as a gate driving method. The effects of overvoltage are presented as well as calculation of the expected lifetime of a MOSFET when gate boosting is used.**

Keywords - MOSFET, gate oxide reliability, lifetime, gate boosting

I. Introduction

The gate of metal-oxide-semiconductor field effect transistor can be driven in a variety of ways. All of them limit the voltage that is connected between gate and source electrode below the maximum value specified by the manufacturer of the MOSFET to ensure its reliability and long lifetime. The reason for this is that the gate oxide that is present between the gate metallization and channel can be easily damaged, and breakdown can occur. However, the novel gate driving method called gate boosting relies on momentarily increasing the gate-source voltage to a value often much higher than the maximum value specified by the manufacturer. In this paper the effects of this overvoltage on the gate oxide are studied and calculation for the estimated lifetime is presented.

II. Gate boosting

Gate boosting is a novel gate driving technique, that significantly increases the switching speed of varieties of solid-state switching devices including MOSFETs. Typical applications include instrumentation for experimental physics research such as driving magnets for particle accelerators or Pockels cells drivers [1]. In these applications it is usually critical to generate pulses with slew rate of the edges as fast as possible.

The switching speed of a MOSFET is determined by the duration it takes the gate capacitance to charge. This duration is in turn determined by three devices: MOSFET and its parasitics, gate driver and the interconnect between them. The switching speed can be improved by careful design and optimalization of any of the three devices. But ultimately there is a limit to the switching speed. Assuming ideal interconnect and gate driver, then the switching speed of the MOSFET can be approximated using RLC low pass filter driven by a square wave.
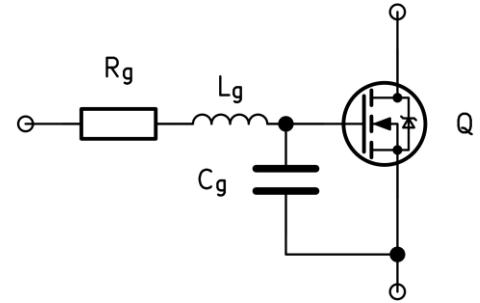

Fig. 1. Equivalent circuit under consideration for gate-boosting

In figure 1 the RLC low pass filter and an ideal MOSFET are shown. Resistance R_g and inductance L_g are caused by the bond wire, leads and gate contact on the die itself. Capacitance C_g is the gate capacitance. The resonant frequency and damping factor determine the gate current and therefore the switching speed.

To switch faster it is necessary to increase the resonant frequency, while ensuring proper damping. Usually, it is beneficial to set the damping factor such that the response of the filter is critically damped or slightly underdamped as this doesn't hinder the switching speed while also not causing the gate oxide to be overstressed [2]. Tuning of the damping factor is possible by adding additional series resistance in the form of a discrete resistor connected in series with the gate.

Utilizing gate boosting it is possible to bypass the switching speed limit imposed by the RLC filter and use the properties of the filter to an advantage. This is demonstrated in figures 2 and 3. In the figures an RLC filter was driven by V_{drive} voltage which is the output of an ideal gate driver. The parameters of parasitic components are $R_g = 2\ \Omega$, $L_g = 13$ nH and $C_g = 3,9$ nF. These values are representative of an IRFPC60 MOSFET transistor in a TO-247 package [3]. The maximum value of gate voltage V_{GSmax} is 20 V. This value shouldn't be exceeded to ensure that the MOSFET is operated under conditions that are tested by the manufacturer and guarantee reliability [4].
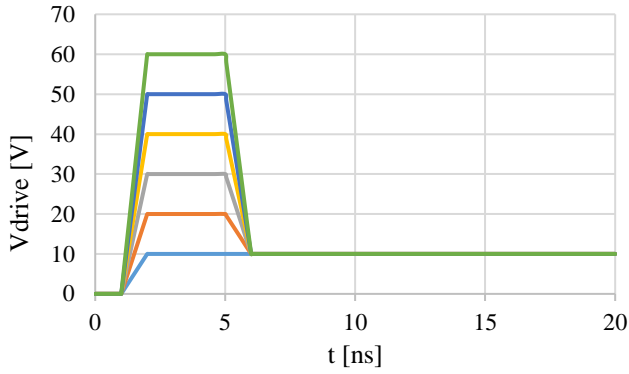
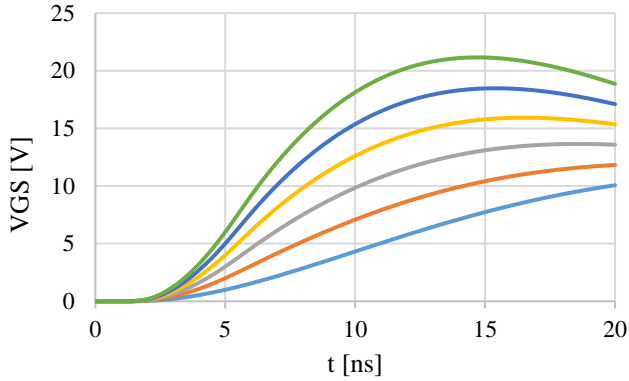Fig. 2. V_drive on the output of gate boosting driver circuit.

Fig. 3. V_GS on the die of the driven MOSFET.

Because the filter has a low pass frequency response the voltage across the gate V_{GS} doesn't rise instantly but gradually. By momentarily increasing the drive voltage V_{drive} to a value significantly bigger than V_{GSmax} we can charge the gate significantly faster. But if the combination of pulse amplitude and duration of V_{drive} is sufficient then V_{GS} exceeds V_{GSmax} which can lead to reduced reliability.

Measurement of this phenomenon was performed on IGBT transistor in TO-247 package. The transistor was partly decapsulated using fuming nitric acid and voltage was measured directly on bond wire. [5]
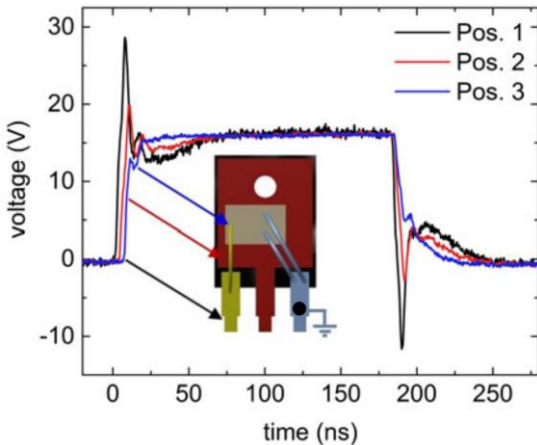
Fig. 4. Voltage measurement on decapsulated IGBT along the gate bond wire [5]

The measurement along the bond wire shows that the bond wire along with the gate capacitance acts as a low pass filter. As such the spikes and overvoltage on the outside of the transistor do not propagate to the die. But it is impractical to decapsulate a transistor to verify proper filtering. This along with the fact that the optimal V_{drive} pulse amplitude and duration relies on difficult to measure parasitic parameters of transistor creates a risk that the gate oxide is being stressed in application reducing reliability. Thus, gate boosting is currently unsuitable for most applications as they usually require long and reliable operation.

III. GATE OXIDE RELIABILITY AND BREAKDOWN

Reliability of a MOSFET is dependent on many factors. If we consider the effects of gate boosting some of the problems that can arise are following gate oxide breakdown, lift-off of bond wire due to increased thermal stress and latch-up in certain transistor structures [6]. Only the degradation of the gate oxide caused by voltage stressing the oxide is considered in this paper.

The gate oxide is a dielectric, typically made from SiO_2, and its insulating properties are key to the operation of the MOSFET. As with any dielectric, the voltage connected to the insulating barrier creates an electric field across the barrier. If the magnitude of the created electric field is higher than the dielectric strength (also called critical intensity) the barrier immediately undergoes breakdown and loses its insulating properties. Therefore, the device suffers catastrophic failure and no longer functions.

It might seem that if a field with lower intensity is connected to a barrier, then breakdown cannot occur. However, the voltage connected to oxide is slowly degrading the barrier even if the intensity is lower than the dielectric strength and eventually breakdown occurs. This phenomenon is due to its time dependency called time-dependent dielectric breakdown TDDB.

Usually, TDDB is divided into two categories: extrinsic and intrinsic. These determine the cause of the breakdown. Extrinsic breakdown is caused by the defects in the gate oxide that are created during the complex manufacturing process of the MOSFET. Intrinsic breakdown occurs even in a perfectly manufactured oxide as it is dependent on the oxide structure itself. The type of TDDB that is more likely to occur in a given device is dependent on the thickness of the oxide and the magnitude of the electric field. Devices with thicker oxide, such as discrete power MOSFETs, tend to suffer from extrinsic breakdown. Thin oxide devices with large electric fields across the oxide, such as modern logic FETs, are more likely to undergo intrinsic breakdown. [7]

Modeling of both intrinsic and extrinsic breakdown can be done using effective oxide thickness. In this model the defects of the extrinsic breakdown are thought to have a higher electric field across them for a given applied voltage. This simplifies the subsequent calculation because it merges both types of breakdowns into one. The effective oxide thickness is less than the actual oxide thickness.[8]

Analyzing the intrinsic and extrinsic breakdown is usually done with accelerated aging testing. That is testing under high temperature and voltage stress. Two typical tests are Constant voltage stress (CVS) and Vramp test. The first type is suitable for measuring TBBD. The second type is useful for fast

production screening of transistor to detect faulty or "weak" oxide that would drastically impact the lifetime of the transistor. As TBBD is a statistical phenomenon it is necessary to measure many samples to determine it accurately. The minimum number of samples is defined in a Jedec JP-001 standard for foundry processes [9].
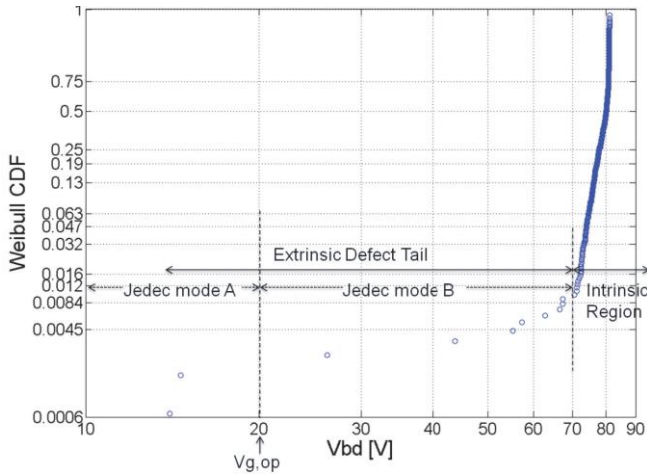

Fig. 5. Cumulative distribution function of a Vramp test for a thick gate oxide (t_{ox} = 100 nm) [8]

On figure 5 the results of a Vramp test are presented. The results form three regions called Jedec mode A, B and C. In the region Jedec mode A transistors with severe defects in gate oxide, that fail under V_{GS} smaller than V_{GSmax} are sorted. These transistors are automatically discarded by the manufacturer. Jedec mode C contains transistor with "ideal" gate oxide that does not have defects and such they undergo intrinsic breakdown. In between these regions is the most problematic region of Jedec mode B. These transistors undergo extrinsic breakdown, and their population is quite low due to the ever-improving manufacturing process. However not all of them are discarded by the manufacturer [8].

So, if the user wants to use gate boosting it is necessary to statistically evaluate the limited reliability data that the manufacturer provides. Otherwise, there is a risk that gate boosting will cause a premature failure of MOSFETs with "weak" gate oxide.

IV. MEASUREMENT OF TDDB USING CVS AND GATE BOOSTING

The measurement of TDDB is critical in evaluating the lifetime of a MOSFET. Typically, the TDDB is measured using constant voltage stress under accelerated aging conditions. This means higher temperatures in the range of 150 °C to 200 °C and V_{GS} such that the magnitude of the electric field across the oxide is in the range of 8 MVcm^{-1} to 10 MVcm^{-1}. This is equal to roughly double the V_{GSmax} rating for a given MOSFET.

These two conditions are achieved using a thermal chamber for increasing temperature and a suitable power supply capable of delivering a high enough voltage. The typical experimental setup is in figure 6. Ten MOSFETs under test are placed on a single PCBs and several PCBs are placed in a single thermal chamber. Failure of gate oxide causes an increase in current flow into a current to voltage converter and is recorded using a datalogger. As the test is DC only the MOSFETs are necessary to be placed inside the thermal chamber. Instrumentation can be situated outside the thermal chamber and is not subject to increased temperature. This setup is very simple and allows for economic testing of large number of components. [8]

Testing with gate boosting requires experimental setup that is not as simple. It is necessary to place the gate driver as close as possible to the MOSFET due to the high frequency nature of the drive voltage. This means that the driver is exposed to elevated temperatures, reducing its lifetime considerably. This can be solved by heating the DUT using methods based on conduction of heat instead of air convection. For example, by connecting the heatsink tab of a TO-220 package to a heating element. Another issue is that every DUT needs its own driver circuit, increasing the cost significantly.

V. LIFETIME ESTIMATION FOR GATE BOOSTING

Evaluation of the lifetime for gate boosting is similar to an evaluation of accelerated testing conditions that the manufacturer already does. However, the manufacturer doesn't provide the "raw" data, but only some reliability guarantees for a certain mission profile. For example, if a MOSFET has V_{GS} equal to V_{GSmax} and is at maximum operating temperature of 175 °C then 1 ppm of transistors will fail in 10 years [10]. Each manufacturer has a different specification. The minimum allowable values are set in Jedec JP-001 and AEC Q101
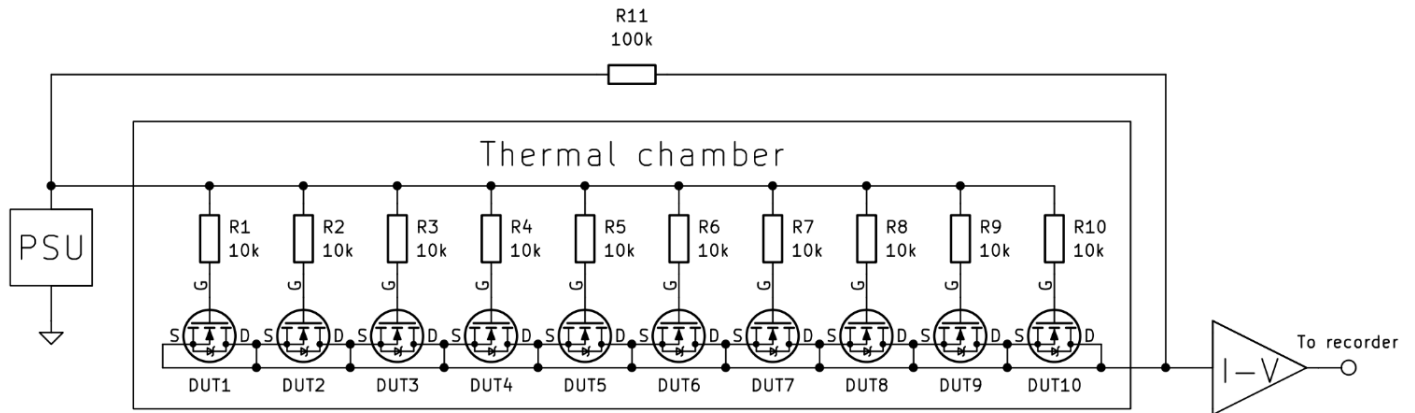

Fig. 6. Experimental setup for measuring TDDB using constant voltage stress at elevated temperature [8]

standards with the latter being stricter for the automotive industry.

As such several assumptions of MOSFET and the reliability need to be made. For the MOSFET itself these assumptions apply: the MOSFET has a thick gate oxide (>20 nm) [10], breakdown will be caused by an extrinsic defect [8], electric filed across the oxide is smaller than 9 MV/cm [10]. Reliability assumptions are based on AEC Q101. This is that the MOSFET must have less than 1 ppm failure rate after 1000 hr at maximum temperature of 175 °C and with V_{GS} equal to V_{GSmax}.

The goal is to calculate an estimated lifetime t_{est} at several values of V_{GS} at ambient temperature of 25 °C. First the acceleration factor AF is calculated from Arrhenius equation [9]

$$AF = e^{\frac{E_a}{k_B}\left(\frac{1}{T_A}-\frac{1}{T_{MAX}}\right)} = e^{\frac{0,5 \cdot 1,602 \cdot 10^{-19}}{1,38 \cdot 10^{-23}}\left(\frac{1}{25+273}-\frac{1}{175+273}\right)}$$

$$AF = 679 \ [-] \tag{1}$$

E_a is activation energy and is given in [9] as 0,5 eV. Next the AF is used with the lifetime at maximum temperature to scale the lifetime to ambient temperature

$$t = t_{175°C}AF = 1000 \cdot 679 = 679000 \ hr \tag{2}$$

TDDB for low-field across gate oxide is determined using the thermochemical E-model for low fields [11].

$$t_{BD} = t_1 e^{-\gamma E_{OX}} \tag{3}$$

Of these parameters only field acceleration parameter γ is known [10]. To determine other values, it would be necessary to measure the TDDB. Nevertheless, the equation can still be used to scale the lifetime t. The modified equation does not have other device parameters except for γ, t_{OX} and V_{GSmax}.

$$t_{GB} = te^{\gamma(E_{OX}-E_{OX25°C})} = te^{\gamma\left(\frac{V_{GSmax}}{t_{OX}}-\frac{V_{GS}}{t_{OX}}\right)}$$

$$t_{GB} = te^{\frac{\gamma}{t_{OX}}(V_{GSmax}-V_{GS})} \tag{4}$$

Of these parameters only the gate oxide thickness t_{OX} is not specified. It is possible to measure the thickness by decapsulating the MOSFET and making a microsection using an SEM. But it is more appropriate to make an educated guess based on available literature. This is because regular electrical engineers don't have access to SEM.

TABLE I Gate oxide thickness for various values of V_{GSmax}

V_{GSmax} [V]	t_{OX} [nm]	Reference
12	33	[10]
20	100, 40-80	[8]

For V_{GSmax} the oxide thickness is in range from 40 nm to 100 nm. The smaller value will be used as it will result in worst case scenario.

$$t_{GB} = te^{\frac{\gamma}{t_{OX}}(V_{GSmax}-V_{GS})} = 679000e^{\frac{4,5 \cdot 10^{-8}}{40 \cdot 10^{-9}}(20-30)} = 107 \ hr \tag{5}$$

For V_{GS} equal to 30 V the 1 ppm failure rate at room temperature drops to 107 hours from 679000 hours. This is a massive drop and shows that it is extremely important to ensure proper design of gate boosting driver which if possible will not stress the gate oxide.

But the higher V_{GS} is applied to the gate for a brief moment. Assuming cumulative degradation of the gate oxide, that is the sum of duration of all individual pulses t_{OVtot} with amplitude equal to V_{GS} will have the same effect as if V_{GS} was DC applied to the gate for duration t_{OVtot}. We can derive the lifetime for pulsed applications. We will assume that the pulse frequency is 100 kHz and duration of gate boost for a single pulse t_{OV} is 5 ns. The duty cycle of the duration of gate boost D is determined by

$$D = f_{sw}t_{ov} = 100 \cdot 10^3 \cdot 5 \cdot 10^{-9} = 500\mu \tag{6}$$

Using the duty cycle we can determine the lifetime of the MOSFET when used in application t_{APP}

$$t_{APP} = \frac{t_{GB}}{D} = \frac{107}{500 \cdot 10^{-6}} = 214000 \ hr \tag{7}$$

The MOSFET will be able to work for 214000 hours or approximately 24 years with a 1 ppm failure rate. This lifetime is large enough for most applications and shows that gate boosting is a technique that could be implemented even in applications that require reliable operation.

Further research should aim to verify the calculation with measurement and provide more accurate models. But such work should keep in mind, the need to calculate lifetime by regular electrical engineers with limited access to test data, device parameters and special laboratory equipment.

VI. CONCLUSION

In this paper the effects of a novel gate driving technique called gate boosting on the gate oxide of MOSFET transistor are presented.

It is shown that properly designed gate driver utilizing gate boosting does not stress the oxide above its V_{GSmax} rating and as such does not lead to a decrease in reliability when compared to conventional gate driving methods. However, the design relies on many parasitic parameters that are very difficult to characterize. Another issue is measuring the gate voltage on the die itself to verify proper design. This culminates in a risk that the MOSFETs gate oxide is being stressed above its V_{GSmax} rating and thus will fail prematurely.

Measurement of TDDB under gate boosting conditions is difficult and requires an unconventional experimental setup. Typical setup for measurement using CVS method is unsuitable due to several factors. Primarily due to the possible difference between DC and pulsed oxide stress. Due to the nature of gate boosting the proposed setup is severely constrained and would be difficult to implement in a large-scale measurement.

Gate oxide reliability is investigated and based on several assumptions the effects of overvoltage on the gate oxide are calculated. The results show that even when the gate oxide is stressed with voltage larger than V_{GSmax} reliable operation is possible due to the very low duty cycle of stress above V_{GSmax}. Expected lifetime for a 1 ppm failure rate is calculated to be

approximately 24 years, which is suitable for most applications. It should be noted, that the calculation assumes that the effect of gate oxide stress is cumulative.

REFERENCES

[1] V. Senaj, T. Kramer, M. Sack, and A. A. del Barrio Montañés, "Sub-Nanosecond Switching of HV SiC MOS Transistors for Impact Ionisation Triggering", in *12th International Particle Accelerator Conference (IPAC 2021)*, Online: CERN, 2021, pp. 4454-4456. doi: 10.18429/JACoW-IPAC2021-THPAB340.

[2] M. Azizi, J. J. V. Azizi, and T. Huiskamp, "Ultrafast Switching of SiC MOSFETs for High-Voltage Pulsed-Power Circuits", *IEEE Transactions on Plasma Science*, vol. 48, no. 12, 2020, doi: 10.1109/TPS.2020.3039372.

[3] *IRFPC60: Power MOSFET*, Rev C. Vishay Siliconix, 2022.

[4] *Designing in MOSFETs for safe and reliable gate-drive operation: AN90001*, Rev. 1.1. Nexperia, 2024.

[5] M. Hochberg, M. Sack, and G. Mueller, "Analyzing a gate-boosting circuit for fast switching", in *2016 IEEE International Power Modulator and High Voltage Conference (IPMHVC)*, San Francisco, CA, USA: IEEE, 2016, pp. 171-175.

[6] M. Hochberg, "A high-voltage pulsed power modulator for fast-rising arbitrary waveforms", Dissertation thesis, Karlsruhe, 2019.

[7] A. Ghetti, "Gate Oxide Reliability: Physical and Computational Models", in *Predictive Simulation of Semiconductor Processing*, Springer Berlin, 2004, pp. 201–258.

[8] T. Kopley, M. Ring, C. Choi, and J. Colbath, "Combined Vramp and TDDB analysis for gate oxide reliability assessment and screening", in *2015 IEEE International Integrated Reliability Workshop (IIRW)*, South Lake Tahoe, CA, USA: IEEE, 2015, pp. 138-142. doi: 10.1109/IIRW.2015.7437087.

[9] *FOUNDRY PROCESS QUALIFICATION GUIDELINES: JP001.01*. JEDEC, 2004.

[10] E. Efthymiou, P. Rutter, and P. Whiteley, "A methodology for projecting SiO_2 thick gate oxide reliability on trench power MOSFETs and its application on MOSFETs VGS rating", *Microelectronics Reliability*, no. 58, 2016.

[11] H. Chenming and L. Qiang, "A Unified Gate Oxide Reliability Model", in *1999 IEEE International Reliability Physics Symposium Proceedings*, San Diego, CA, USA: IEEE, 1999, pp. 47-51.

Parametrization of equivalent circuit models for lithium-ion batteries using galvanostatic intermittent titration technique

Marek Sedlařík
Department of Electrical and Electronic Technology
Faculty of Electrical Engineering and Communication, Brno University of Technology
Brno, Czech Republic
Marek.Sedlarik@vut.cz

Petr Vyroubal
Department of Electrical and Electronic Technology
Faculty of Electrical Engineering and Communication, Brno University of Technology
Brno, Czech Republic
vyroubal@vut.cz

Martin Mačák
Electric Vehicle Technologies
Transport Technologies
AIT Austrian Institute of Technology GmbH
Vienna, Austria
Martin.macak@ait.ac.at

Martin Šedina
Department of Electrical and Electronic Technology
Faculty of Electrical Engineering and Communication, Brno University of Technology
Brno, Czech Republic
martin.sedina1@vut.cz

Tomáš Kazda
Department of Electrical and Electronic Technology
Faculty of Electrical Engineering and Communication, Brno University of Technology
Brno, Czech Republic
kazda@vut.cz

Abstract— **This study presents an experimental methodology for parameterizing an Equivalent Circuit Model (ECM) of lithium-ion (Li-ion) batteries using the Galvanostatic Intermittent Titration Technique (GITT). ECMs are widely used for battery modeling due to their ability to approximate battery behavior with relatively low computational complexity. However, their accuracy strongly depends on precise identification of internal resistances and time constants, which define transient responses related to charge transfer and diffusion processes. In this work, a 3RC ECM configuration is employed to capture both fast and slow relaxation effects, enabling a more detailed characterization of the battery's dynamic behavior. The experimental procedure consists of applying controlled current pulses followed by relaxation periods, during which voltage recovery is analyzed to extract key parameters. To refine the extracted values and ensure an optimal match between the model and measured voltage response, an iterative optimization process is applied, minimizing the discrepancy between simulated and experimental data. The proposed approach significantly enhances the accuracy of ECM parameterization, leading to a more reliable representation of lithium-ion battery dynamics across different States-of-Charge (SOC). The findings of this study contribute to improved state estimation, enhanced predictive maintenance, and more effective battery management strategies, ultimately supporting the optimization of energy storage systems and advancing battery performance modeling.**

Keywords — Li-ion battery, SOC, Estimation, ECM, GITT

I. Introduction

Lithium-ion (Li-ion) batteries are a fundamental technology in modern energy storage systems, offering high energy density, long cycle life, and stable electrochemical performance. Their role is particularly significant in applications requiring efficient and reliable power delivery, such as electric vehicles (EVs) and stationary energy storage. As the demand for energy storage solutions continues to increase, precise modeling of Li-ion battery behavior is essential for optimizing performance, ensuring safety, and extending operational lifespan.

The dynamic behavior of Li-ion batteries is affected by complex electrochemical processes influenced by State-of-Charge (SOC), temperature and aging effects [1, 2]. Accurate estimation of internal states, including SOC and State-of-Health (SOH), is essential for real-time battery management [3]. While SOC can be inferred from voltage and current measurements under controlled conditions and SOH can be estimated through long-term performance metrics, direct measurement of these parameters remains impractical in real-world applications. Therefore, mathematical models are widely used to approximate battery behavior [4, 5, 6, 7], providing a foundation for predictive control and diagnostics.

Equivalent Circuit Models (ECMs) are widely used for this purpose due to their balance between computational efficiency and fidelity [7]. These models approximate the battery's electrical characteristics using circuit elements such as resistors, capacitors, and voltage sources, enabling the representation of both transient and steady-state behavior [7, 8]. Among the various ECM configurations, first-order (1RC) and second-order (2RC) models are commonly employed, as they effectively capture the key electrical response of Li-ion cells while maintaining relatively low computational complexity [8].

In the paper [9] by M. Lagnoni et al., the ECM and the Physics Based Model (PBM) are compared using a 60 Ah prismatic graphite/lithium-iron-phosphate battery. The ECM is significantly faster and easier to calibrate, while the PBM achieves higher accuracy at high currents but requires complex parameterization and longer computation times. However, the accuracy of these models depends on precise parameter identification, which remains a challenge in battery modeling.

Various techniques are employed for ECM parameter estimation, with Electrochemical Impedance Spectroscopy (EIS) and Hybrid Pulse Power Characterization (HPPC) being among the most widely used. EIS analyzes a battery's impedance response across a range of frequencies, providing detailed insights into charge transfer resistance and diffusion processes, though its reliance on specialized equipment limits its practicality [10, 11]. HPPC estimates internal resistance and transient response by applying controlled current pulses at different SOC. While widely used in automotive and energy storage applications, it lacks the temporal resolution needed to capture long-term diffusion effects [12, 13, 14]. A promising alternative is the Galvanostatic Intermittent Titration Technique (GITT), which enables high-resolution characterization of battery dynamics by analyzing voltage relaxation after controlled current pulses. Unlike HPPC, GITT provides a more detailed extraction of diffusion-related parameters and time constants, improving the accuracy of ECM parameterization [15, 16, 17]. M. Mohamed et al. in [18] review advancements in parameter estimation techniques for 1RC and 2RC ECMs of Li-ion batteries, including methods based on GITT. This method is described as effective for detailed characterization across various SOC levels, independent of complex equipment, and suitable for comprehensive OCV and SOC studies, despite its longer test duration and lower resolution at extreme SOCs.

This study presents an experimental framework for ECM parameter identification based on GITT analysis, focusing on the 3RC model configuration. By leveraging the high-resolution data obtained through GITT, we aim to refine parameter extraction methodologies and improve the accuracy of ECM representations of Li-ion batteries. The increased complexity of the 3RC model enables a more detailed characterization of battery dynamics, particularly in capturing multi-time constant transient responses. The findings of this study contribute to the development of more reliable battery models, ultimately enhancing battery management strategies and energy storage optimization.

II. Experiment

A. Measurement

The experiment was conducted on Li-ion batteries with lithium-nickel-manganese-cobalt oxide (NMC) as the cathode material and graphite as the anode material. The parameterization of the ECM was performed using the GITT. The pulse test consisted of a 5-minute current pulse followed by a 1 hour relaxation period, ensuring adequate voltage stabilization before the next pulse. This protocol was chosen based on preliminary measurements, which indicated that

sufficient relaxation time is required for reliable extraction of RC parameters.

The experiment was conducted in a controlled environment, and the procedure is schematically represented in fig. 1. The test sequence began with a Constant-Current (CC) charge at 0.2 C up to 4.2 V, followed by a Constant-Voltage (CV) charge at 4.2 V until the current dropped to 68 mA. After a 1 hour rest period, the discharge phase commenced using 0.3C CC pulses of 5 minute duration, each followed by a 1-hour rest period to capture the voltage relaxation behavior. The cycling continued until the battery voltage reached the cut-off voltage of 2.7 V, at which point the test was terminated.
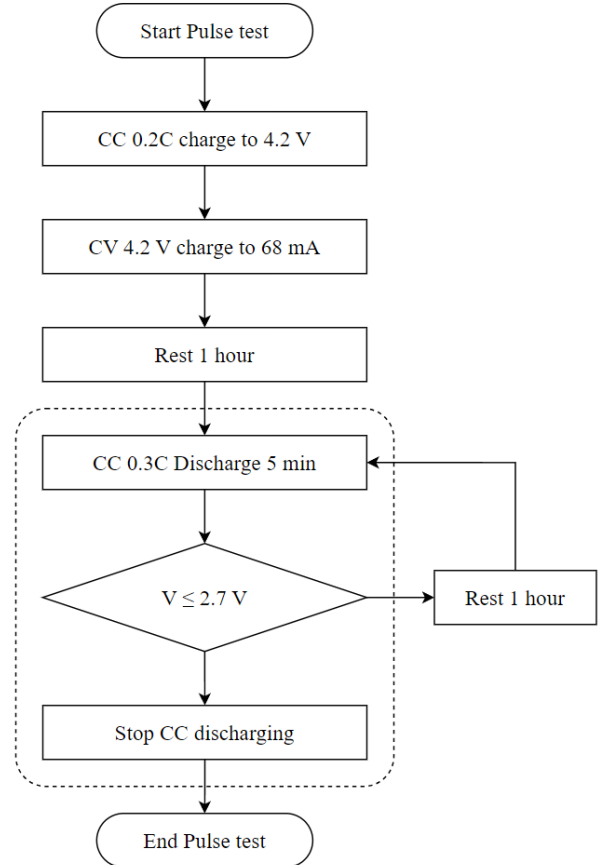

Fig. 1: GITT test protocol for Li-ion battery characterization.

A total of 38 pulses were recorded during the test. However, the final pulse was excluded from the analysis as the battery reached the cut-off voltage, rendering it invalid for accurate RC parameter extraction. The complete test duration, excluding the initial charging phase, was 41 hours.

B. Pulse detection

Pulse detection is a critical step in processing GITT measurement data, enabling the identification of voltage transients associated with charge transfer and diffusion processes. The detection algorithm extracts key points from the voltage response, specifically at the transition between load and

relaxation phases. These points are essential for parameter estimation in ECM modeling.

Fig. 2 illustrates the detected pulses throughout the experiment, where red markers indicate data points surrounding the load pulse, and green markers correspond to the relaxation phase. These selected pairs ensure that both the immediate voltage drop and subsequent relaxation dynamics are captured for further analysis.
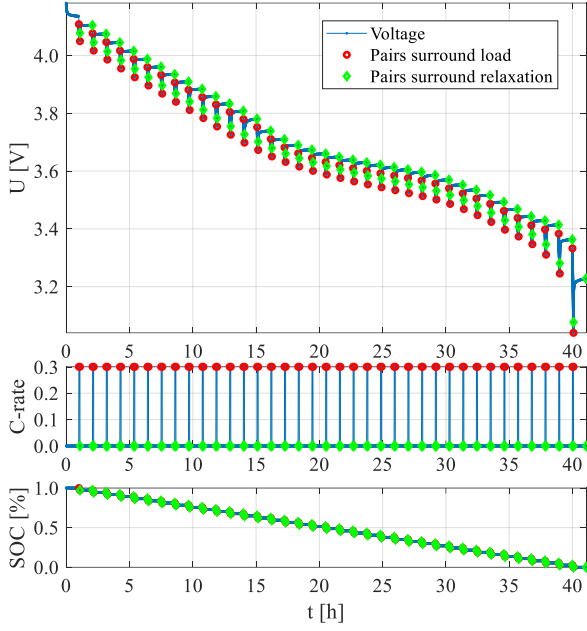

Fig. 2: Detection of pulse phases during GITT measurement.

To validate the detection accuracy, each cycle was individually examined. Fig. 3 provides a magnified view of a single pulse, showing the voltage drop upon current application and the subsequent recovery phase. This behavior directly reflects internal resistance, charge transfer effects, and diffusion processes, which are fundamental for extracting ECM parameters.

The detected pulse pairs serve as input for ECM parameterization, where the relaxation curve is fitted to a multi-time constant model to estimate resistance and capacitance values. This approach ensures a precise representation of battery dynamics, improving the fidelity of ECM-based simulations and predictions.

C. ECM parameters

Accurate parameter estimation is essential for developing an ECM that effectively represents the dynamic behavior of Li-ion batteries. The parameter identification process is based on analyzing the battery's voltage response to controlled current pulses using the GITT. The selected ECM structure consists of a series resistance R_s and three RC pairs, allowing for a refined

characterization of both fast and slow transient processes occurring within the cell [17, 18].

A critical component of the model is the series resistance R_s, which primarily accounts for ohmic losses, including electrolyte resistance, current collector resistance, and contact resistances at the electrode interfaces. The value of R_s is extracted from the immediate voltage drop observed at the onset of each current pulse, as shown in Fig. 3. This drop is attributed to the resistive elements in the battery and is computed as:

$$R_s = \frac{\Delta U_\Omega}{I} \tag{1}$$

where ΔU_Ω represents the instantaneous voltage drop upon current application and I is the applied pulse current. This resistance remains relatively stable across different SOC, assuming no significant degradation effects.
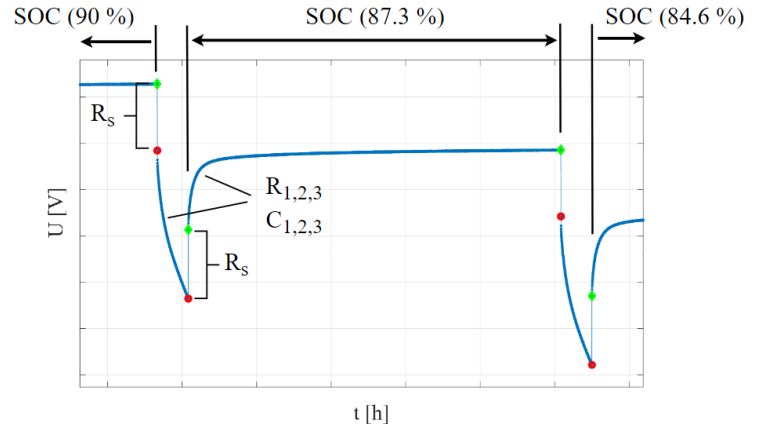

Fig. 3: Description of voltage response phases to a current pulse during GITT measurement.

Beyond the ohmic resistance, the battery exhibits a multi-exponential relaxation behavior following the current pulse, which is attributed to charge transfer and diffusion-related processes. To accurately capture these effects, a 3RC ECM configuration is employed, where each RC pair represents a distinct transient response. The first RC branch (R_1,C_1) corresponds to fast charge transfer dynamics occurring at the electrode-electrolyte interface, while the second (R_2,C_2) and third (R_3,C_3) branches describe slower diffusion and redistribution processes within the electrode material [18]. The circuit representation of the 3RC ECM model, including the series resistance and parallel RC elements, is shown in Fig. 4.

$$U(t) = U_{\text{OCV}} - R_s I - \sum_{i=1}^{3} R_i I \left(1 - e^{-\frac{t}{\tau_i}}\right) \tag{2}$$

where the time constant associated with each RC pair is defined as:

$$\tau_i = R_i C_i \qquad (3)$$

Fig. 3 illustrates the voltage response at different SOC levels, highlighting the identification of R_s from the instantaneous voltage drop and the role of each RC branch in shaping the transient behavior. The extracted parameters R_i and C_i are fitted by optimizing the ECM response to the measured voltage curve, ensuring that the model accurately reflects the observed relaxation dynamics.
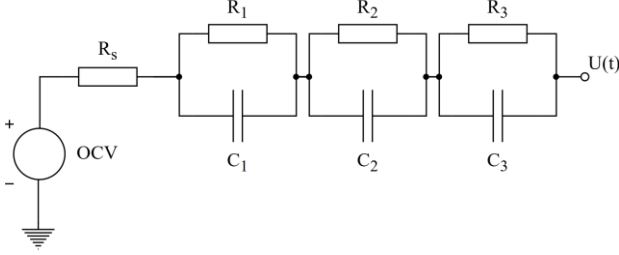

Fig. 4: 3RC ECM for Li-ion battery representation.

D. Parameters estimation and optimization

Although the general structure of the ECM and the fundamental relationships between its components are well-defined, directly computing the resistance-capacitance (R_i, C_i) pairs from the measured relaxation response is challenging due to the overlapping contributions of multiple transient processes. To obtain accurate parameter values, an iterative optimization procedure is employed, ensuring that the model-generated voltage response aligns with experimental data.

Since the relaxation process is governed by multiple time constants τ_i, an initial estimate of their values is first assigned based on empirical knowledge and constrained within predefined boundaries:

$$\tau_{min,i} \leq \tau_i \leq \tau_{max,i} \qquad (3)$$

These values serve as a starting point for an optimization algorithm that minimizes the error between the measured voltage and the modeled ECM response. The objective function follows a least-squares approach:

$$\min_{R_i, C_i} \sum_k \left(U_{measured}(t_k) - U_{model}(t_k) \right)^2 \qquad (3)$$

where $U_{measured}(t_k)$ represents the experimentally recorded voltage at discrete time sample t_k and $U_{model}(t_k)$ is the corresponding simulated voltage response from the ECM. The optimization iteratively adjusts R_i and C_i until the model accurately replicates the observed relaxation dynamics.

III. RESULTS

The results demonstrate the effectiveness of the proposed parameter estimation approach based on the GITT. Fig. 5 presents a comparison between the measured voltage response and the simulated output of the 3RC ECM. The close correspondence between experimental and simulated data confirms that the extracted parameters accurately capture the battery's transient behavior. The residual analysis further supports the validity of the parameterized model, showing that the error voltages remain within an acceptable range.
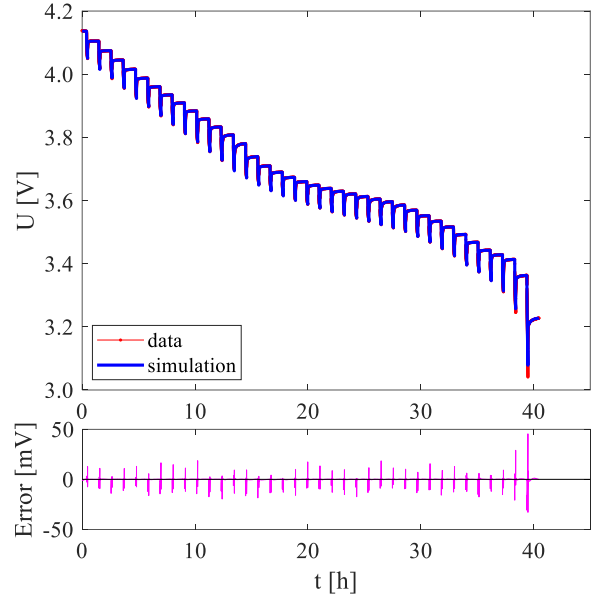

Fig. 5: Comparison of measured and simulated voltage during GITT measurement, with corresponding error analysis.

The estimated ECM parameters across different SOC are summarized in Table I, where the resistance and capacitance values of each RC branch are provided. These results highlight the ability of the proposed approach to extract key electrical characteristics of the battery while preserving physical plausibility. The variation of ECM parameters with SOC reflects the underlying electrochemical processes, ensuring that the model remains applicable over a wide range of operating conditions.

TABLE I: ECM PARAMETERS

Parameter	Mean value
R0	1.04 mΩ
R1	0.48 mΩ
C1	11.80 kF
R2	1.24 mΩ
C2	79.90 kF
R3	1.21 mΩ
C3	1.09 MF

IV. Conclusion

This study presents a robust methodology for parameterizing a 3RC ECM using the GITT. The experimental approach enables the precise identification of internal resistances and time constants, capturing both fast and slow relaxation effects. The optimization process ensures that the extracted parameters provide an accurate representation of Li-ion battery dynamics, as confirmed by the strong correspondence between simulated and measured voltage responses. The results, summarized in Table I, demonstrate the capability of the proposed approach to enhance the fidelity of ECM-based simulations, ultimately improving state estimation and predictive maintenance. Future research may focus on extending this methodology to different battery chemistries and operational conditions, further strengthening its applicability in advanced energy storage systems.

Acknowledgment

References

[1] C. R. Birkl, M. R. Roberts, E. McTurk, P. G. Bruce, and D. A. Howey, "Degradation diagnostics for lithium ion cells", *Journal of Power Sources*, vol. 341, pp. 373-386, 2017.

[2] Y. Li, W. Guo, D. -I. Stroe, H. Zhao, P. Kjær Kristensen, L. Rosgaard Jensen, K. Pedersen, and L. Gurevich, "Evolution of aging mechanisms and performance degradation of lithium-ion battery from moderate to severe capacity loss scenarios", *Chemical Engineering Journal*, vol. 498, 2024.

[3] M. Jiang, D. Li, Z. Li, Z. Chen, Q. Yan, F. Lin, C. Yu, B. Jiang, X. Wei, W. Yan, and Y. Yang, "Advances in battery state estimation of battery management system in electric vehicles", *Journal of Power Sources*, vol. 612, 2024.

[4] R. Mehta and A. Gupta, "Mathematical modelling of electrochemical, thermal and degradation processes in lithium-ion cells—A comprehensive review", *Renewable and Sustainable Energy Reviews*, vol. 192, 2024.

[5] P. Ramadass, B. Haran, R. White, and B. N. Popov, "Mathematical modeling of the capacity fade of Li-ion cells", *Journal of Power Sources*, vol. 123, no. 2, pp. 230-240, 2003.

[6] P. M. Gomadam, J. W. Weidner, R. A. Dougal, and R. E. White, "Mathematical modeling of lithium-ion and nickel battery systems", *Journal of Power Sources*, vol. 110, no. 2, pp. 267-284, 2002.

[7] J. M. Reniers, G. Mulder, S. Ober-Blöbaum, and D. A. Howey, "Improving optimal control of grid-connected lithium-ion batteries through more accurate battery and degradation modelling", *Journal of Power Sources*, vol. 379, pp. 91-102, 2018.

[8] M. -K. Tran, M. Mathew, S. Janhunen, S. Panchal, K. Raahemifar, R. Fraser, and M. Fowler, "A comprehensive equivalent circuit model for lithium-ion batteries, incorporating the effects of state of health, state of charge, and temperature on model parameters", *Journal of Energy Storage*, vol. 43, 2021.

[9] M. Lagnoni, C. Scarpelli, G. Lutzemberger, and A. Bertei, "Critical comparison of equivalent circuit and physics-based models for lithium-ion batteries: A graphite/lithium-iron-phosphate case study", *Journal of Energy Storage*, vol. 94, 2024.

[10] Q. Yang, J. Xu, B. Cao, X. Li, and J. Xu, "A simplified fractional order impedance model and parameter identification method for lithium-ion batteries", *PLOS ONE*, vol. 12, no. 2, Feb. 2017.

[11] H. Li, Z. Lyu, and M. Han, "Robust and fast estimation of equivalent circuit model from noisy electrochemical impedance spectra", *Electrochimica Acta*, vol. 422, 2022.

[12] J. Sun and J. Kainz, "Optimization of hybrid pulse power characterization profile for equivalent circuit model parameter identification of Li-ion battery based on Taguchi method", *Journal of Energy Storage*, vol. 70, 2023.

[13] B. Yao, Y. Cai, W. Liu, Y. Wang, X. Chen, Q. Liao, Z. Fu, and Z. Cheng, "State-of-charge estimation for lithium-ion batteries based on modified unscented Kalman filter using improved parameter identification", *International Journal of Electrochemical Science*, vol. 19, no. 5, 2024.

[14] B. Sungur and A. Kaleli, "State of Charge Estimation for Lithium-Ion Batteries Using Optimized Model Based on Optimal HPPC Conditions Created Using Taguchi Method and Multi-Objective Optimization", *Applied Sciences*, vol. 14, no. 20, 2024.

[15] F. -A. LeBel, P. Messier, A. Sari, and J. P. F. Trovão, "Lithium-ion cell equivalent circuit model identification by galvanostatic intermittent titration technique", *Journal of Energy Storage*, vol. 54, 2022.

[16] J. Naranjo-Balseca, C. Martínez-Cisneros, and A. Várez, "Modelling Li-V2O5 Batteries Using Galvanostatic Intermittent Titration Technique and Electrochemical Impedance Spectroscopy: Towards Final Applications", *Batteries*, vol. 10, no. 6, 2024.

[17] F. -A. LeBel, P. Messier, A. Sari, and J. P. F. Trovão, "Lithium-ion cell equivalent circuit model identification by galvanostatic intermittent titration technique", *Journal of Energy Storage*, vol. 54, 2022.

[18] M. A. A. Mohamed, T. F. Yu, G. Ramsden, J. Marco, and T. Grandjean, "Advancements in parameter estimation techniques for 1RC and 2RC equivalent circuit models of lithium-ion batteries: A comprehensive review", *Journal of Energy Storage*, vol. 113, 2025.

Optimized 3D Resin Printing for Microfluidic Chip Fabrication

Jaromír Jarušek
Department of Microelectronics, FEEC
Brno University of Technology
Jaromir.Jarusek@vutbr.cz

Imrich Gablech
Department of Microelectronics, FEEC
Brno University of Technology
Imrich.Gablech@vutbr.cz

Abstract— **This paper presents and evaluates printed microfluidic chips using a consumer-grade resin printer. Two fabrication approaches are explored, focusing on the detailed fabrication workflow of open-channel and embedded-channel-based Tesla mixers, followed by a chamber for electrochemistry. The structure of fabricated chips was evaluated using optical and scanning electron microscopy and consequently tested by dye channel visualization. Furthermore, the chips had bulk electrodes for three-electrode cyclic voltammetry measurements. The solution flow was controlled using an automated microfluidic workstation.**

Keywords— *Masked Stereolithography (MSLA), Optical transparency, Tesla micromixers, Electrochemical sensing, Scanning Electron Microscopy, Additive manufacturing*

I. INTRODUCTION

Microfluidics is a discipline that focuses on manipulating fluids on a microscopic scale with volumes in the picolitre to microliter range. That is achieved by utilizing channels with dimensions ranging from tens of micrometers up to several millimeters. This technology covers various applications, including chemical sensors, DNA analysis, Lab-on-Chip systems (LoC), and Organs-on-Chip, which mimic the functions of human organs, enabling realistic *in-vitro* drug testing and personalized medicine. [1][2]

Fabrication techniques may generally be divided according to the volume fabrication scale into low-volume and high-volume production. For low-volume production, techniques commonly used for microelectromechanical systems (MEMS) include microfabrication techniques, soft-lithography via PDMS casting on a mold, laser fabrication, and laminate manufacturing from individual layers of polycarbonate (PC) or polymethylmethacrylate (PMMA) sheets. On the other hand, hot-embossing and injection molding are typically used for high-volume production. [3]

Chips fabricated by most of the previously mentioned techniques require further enclosure. The simplest option is bonding PDMS chips to glass. For silicon chips, common methods include anodic bonding and adhesive bonding. Thermoplastic chips, aside from adhesive bonding, also allow for thermal fusion, solvent bonding, and chemical bonding. [4][5]

Stereolithography (SLA), also known as vat photopolymerization, is an additive manufacturing technique. The traditional method is based on curing photopolymer resin with an ultraviolet (UV) laser, forming 3D objects layer-by-layer. Another exposure method is digital light processing, which uses digital micro-mirror devices. The highest-quality photopolymerization method is two-photon polymerization, which uses near-infrared femtosecond pulses. [6]

An inexpensive method of vat photopolymerization is masked SLA (MSLA), which uses a liquid crystal display (LCD) panel as a mask for UV exposure. [7] Recent advances in LCD technology have provided small pixel sizes, which are also interesting for microfluidic fabrication. [8] Results of 3D-printed microfluidics using consumer-grade MSLA printing have already been presented together with the open-source online platform Flui3d for designing 3D microfluidics, including compensation techniques for consumer-grade printers and resins. [9] This shows that MSLA printers are suitable for broader adoption in fabricating microfluidic chips but require software tools to compensate for their limitations.

Other limitations in stereolithographic fabrication methods of microfluidics are the parameters of the resins, mainly viscosity and penetration depth (D_P). Both values are desirable to be low for printing microfluidics. [10] High D_P may lead to resin curing inside previously printed channels and cause permanent blockage, which is referenced in this paper as z-axis overcuring. This issue can be solved by tuning the chemical composition of the resin, printing parameters, or modifying traditional printing process workflow. Channel printing with a thickness as small as 10 μm was demonstrated using a custom-built system. The process involves two exposure steps: first, a thin ceiling layer is formed within the resin vat, which is then transferred in situ onto the chip to enclose the microchannel. [11]

This paper presents high-resolution, low-cost methods for fabricating microfluidic chips using an MSLA 3D printer, which is suitable for development and prototyping as an alternative to silicon-based lithography and soft-lithography techniques.

II. DESIGN AND FABRICATION OF MICROFLUIDIC CHIPS

A. Description of fabricated chips

A chip for electrochemical detection using cyclic voltammetry was designed and used to evaluate printer performance and its suitability for future research. The design consists of two sets of Tesla micromixers with three inlets, an electrochemical cell chamber, and one outlet. The first set of Tesla micromixers mixes the electrolyte with an electrochemical mediator, while the second set further mixes in the analyzed compound. The dimensions of the Tesla micromixer cell are

shown in Fig. 1. The smallest channel dimension is 110 μm. The chamber includes ports for three cylindrical electrodes.
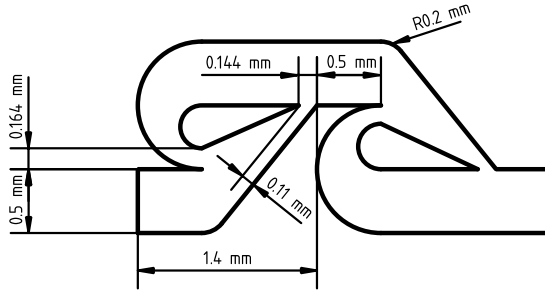

Fig. 1.   Designed geometry of Tesla micromixers.

Two versions of 3D models of the designed chips were created for open-channel and embedded-channel chip fabrication. For the open-channel design, the nominal depth of the pattern was 500 μm and holes for ports were cut through a 2 mm thick chip base. For the embedded-channel design, the nominal depth of the pattern was increased to 900 μm to account for tolerance and compensation for z-axis overcuring. The supporting base and cover ceiling thicknesses were 1 mm and 600 μm, respectively. For easier placement of port tubing and electrodes, simple tube connectors were added on top of the chip ceiling, and holes were cut through the ceiling and connectors. Additional supporting pillars with a diameter of 300 μm were added to the chamber to avoid its collapse.

To evaluate if entrapped resin inside the embedded channels, after the formation of the channel ceiling, has a negative impact on the quality of the resulting printed chip, a slightly modified version with an additional drain channel was also created. Dimensions of the drain channel were $(0.4 \times 0.6 \times 4.1)$ mm^3.

B. Parameters of printer, setting, and resin

The tested MSLA printer was the Elegoo® Mars 5 Ultra, featuring a tilting vat mechanism for printed layer release and LCD with a resolution of 8520×4320 pixels with dimensions (18×18) μm^2. The display is capable of pixel dimming and thus anti-aliasing. The printer uses a 405 nm UV source. The average value of UV light intensity of the used unit at the time of printing was (3.8 ± 0.3) mW·cm^{-2} and was measured using the ChituSystem® UV light meter.

The CHITUBOX® .ctb file format was used to print data. Files were generated using CHITUBOX® Pro V1.5.0 software. The values of the gray range for anti-aliasing settings in the slicer were 128 and 255. Additionally, the open-source software UVtools was used for advanced printing data corrections, such as pixel dimming for z-axis overcuring compensation.

Phrozen® Aqua Resin Clear Plus was used to print the transparent chips. Advertised viscosity is $(250 - 400)$ mPa·s, and density is $(1,05 - 1,25)$ g·cm^{-3}. Three values of normal layer exposure time were determined using calibration models. Note that all exposure values are for 50 μm layer thickness. For an accurate (x-y axis) embossed-like 2D pattern, an exposure time of 6.25 s was determined using standard Photonsters Validation Matrix v2 [12]. For 3D structures, standard AmeraLabs Town [13] model and custom design embedded channel models were used. Using the AmeraLabs Town model, an exposure time of

4 s was determined for precise z-axis exposure. The embedded channel required a further decrease of exposure as low as $(2.95 - 3.25)$ s, where 2.95 s is the borderline for printed layers delamination during printing. Bottom layer exposure was 12 s.

Jacobs' working curve describes the growth of the cured resin layer in relation to the absorbed UV energy dose and can be derived from the attenuation of light intensity in resin by Beer-Lambert law [14]. The working curve of the used resin was measured and approximated in two parts, as in Fig. 2. Part with $D_P = 225$ μm and critical exposure time $t_C = 4.63$ s approximates curing behavior during printing, but extrapolation below 100 μm can be considered less accurate when compared with results of calibration. The second part approximates post-curing and is expected to change D_P after a sufficient dose of UV energy.
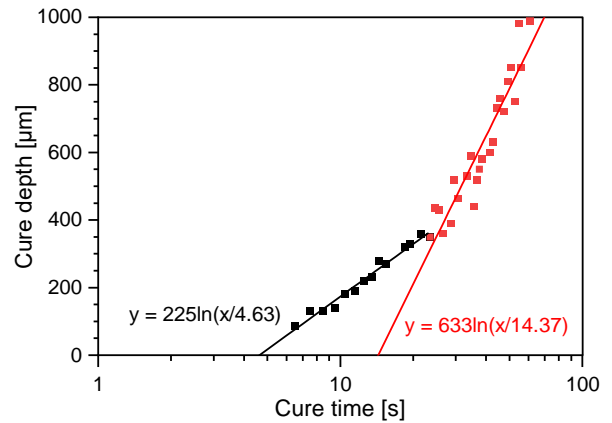

Fig. 2.   Jacobs working curve of Phrozen Aqua Resin Clear Plus.

Post-curing of chips was performed in the Elegoo® Mercury Plus 2.0 wash and cure station, which uses 405 nm UV LED sources with a total rated power of 48 W.

C. Fabrication workflow

1) Open-channel chips

The model of the open-channel chips was sliced using CHITUBOX® Pro slicer in multi-parameter mode to set separate exposure times for the chip base with holes and microfluidic pattern.

The printed chips were left on the build platform for cleaning. Liquid resin residues were repeatedly washed off with isopropyl alcohol (IPA) using a wash bottle and subsequently blow-dried with compressed air. Attention was paid to removing the resin from the port holes.

The cleaned chips were post-cured on the build platform for ≈ 10 minutes without rotation. Post-curing on the build platform was used to enhance the mechanical properties of the chips and minimize deformation during chip removal from the build platform using a spatula.

The removed chips were then inspected for the correct formation of smaller holes for the ports. Partially enclosed holes were then reworked by a combination of drilling and punching. To remove contaminants and formed debris, the chips were cleaned using IPA in an ultrasonic bath for ≈ 5 minutes.

In cases where the chips were slightly bent, chips were heated using a hotplate to 75 °C and flattened by manual pressing against a glass slide and then cooled down to ambient temperature.

To enhance the optical clarity of the chips, the imprinted pattern from the build platform was masked using resin overglaze. First, the port holes were covered using polypropylene (PP) single-sided tape; then, the chip base was manually coated with the same resin used for printing chips. The coating of the chips was performed to minimize the formation of bubbles in the next step. A drop of resin was sandwiched between the coated chip base and PP foil to form a glossy surface finish. The resin was then cured using the printer in fullscreen exposure mode for 60 s.

In the end, the PP foil and the PP tape were removed, and uncured resin residues were cleaned with IPA.

2) Monolithic 3D-like microfluidics embedded channels

This method represents a simple approach to 3D resin-printed microfluidics. Models of chips with embedded channels were sliced in single-parameter mode. Anti-aliasing wasn't applied because these values lay in the small to high underexposure range.

Printed chips were removed from the build platform using a spatula and then cleaned using IPA, first by dipping and agitating for 30 s and second by an ultrasonic bath with IPA for ≈ 3 minutes. Finally, chips were blow-dried using compressed air.

3) Advanced multiparametric slicing with z-axis overcuring compensation

This method combines the layer exposure settings used in methods 1) and 2). Chips were sliced in multiparameter mode with two printing profiles in two separate groups for a total of 4-layer groups. The chip base and lower part of the pattern were sliced with 6.25 s layer exposure and anti-aliasing. The upper part (150 μm below the ceiling) of the pattern and ceiling were sliced using 4 s layer exposure except for the last two upper layers of ceiling that were sliced using 6.25 s for better mechanical properties of the chip surface. Finally, the rest of the chip, which includes tube connectors, was sliced using 4 s layer exposure.

The printing data were further modified using UVtools with the "Light bleed compensation" function to dim pixels of 8 lower ceiling layers that form bridges over channels. Pixel dimming was set to change exposure time to a decreasing sequence, starting from 3.15 s to 2.85 s. At this exposure time, parts of layers won't form at full thickness but should still be mechanically reliable for short bridges. The remaining partially cured resin between layers will shield the channels from UV penetration. The printing and cleaning procedures were similar to method 2).

In the case of the model with the additional drain channel, a small amount of the resin was used to carefully fill the additional drain channel. The resin was then cured using the printer in full-screen exposure mode for 60 s.

D. Open channel chip enclosing

This section is focused on adhesive bonding. Tests of thermocompression bonding and solvent bonding using acetone and chlorinated hydrocarbons didn't result in successful results.

The same printing resin was used as an adhesive. Three types of covers were used for chip sealing: standard microscope glass slide, glass coverslip, and hard polyvinyl chloride (PVC) foil.

The resin was applied on cover materials using spin coating at a speed of 500 rpm for 60 seconds. The thickness of the coated layer was estimated gravimetrically to be 28 μm.

Chips were then lightly pressed against the coated layer to form a bond without pockets or bubbles. The resin was then cured using the printer in full-screen exposure mode for 60 s, and uncured residues were cleaned using IPA.

E. Chip assembly

For microfluidic testing and electrochemical measurement using embedded and enclosed channel chips, an interface between the chip and fluid sources was created, and three electrodes were installed. The interface consisted of metal tubing with an outer diameter of ≈ 0.8 mm and inner diameter of ≈ 0.55 mm, which was bent by ≈ 45°. Tubing was held by designed connectors in the case of embedded-channel chips. In contrast, additional cylindrical hollow beads were used to support the enclosed-channel chips. Polyether ether ketone capillaries with a nominal outer diameter of 360 μm were then inserted into the tubing.

The following materials were used for electrodes: for the counter electrode, a graphite rod with an outer diameter of 2 mm; for the working electrode, platinum with an outer diameter of 0.6 mm; and for the pseudoreference electrode, silver wire anodized in saturated potassium chloride solution.

All ports with inserted tubes and capillaries were sealed using 3M™ Scotch-Weld™ DP490 epoxy adhesive. An example of the assembled chip with embedded channels and tubing for the automated microfluidic workstation is in Fig. 3.
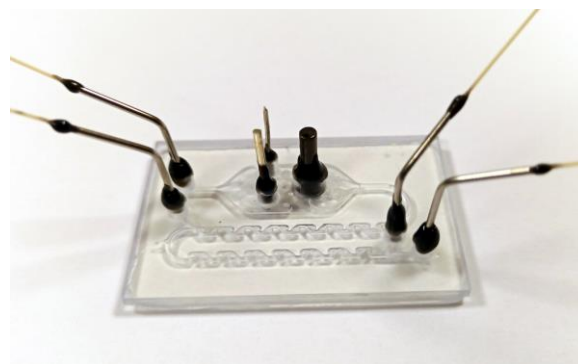

Fig. 3. Chip with embedded channels fabricated by advanced multiparametric slicing with z-axis overcuring compensation.

III. MICROFLUIDIC CHIPS EVALUATION

A. Scanning electron microscopy (SEM) of open channels

Chips were coated by a 150 nm thin film of copper using thermal evaporation to avoid sample charging and allow

conductive connection to the sample holder during SEM imaging, enhancing the sample contrast.

SEM imaging was performed using TESCAN FE MIRA II with an In-Beam detector at 3 kV electron beam voltage. Results are in Fig. 4.
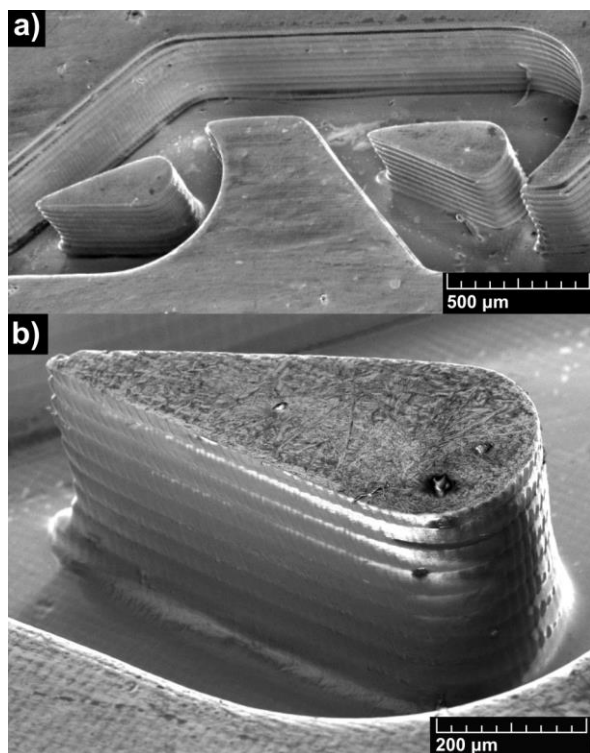

Fig. 4. SEM images of the open-channel chip. a) Tesla micromixer unit, b) detail of stream divider.

B. Dye channel visualization

Yellow and cyan dye inks for inkjet printers were used for color visualization. Inlet capillaries of the first set were connected to plastic syringes with a Luer-Lock connector using LabSmith CapTite™ C360 fitting and C360 to Luer-Lock adaptor. The inlet to the second set of micromixers was closed using C360 fitting, CapTite™ interconnect, and CapTite™ plug. Results are shown in Fig. 5
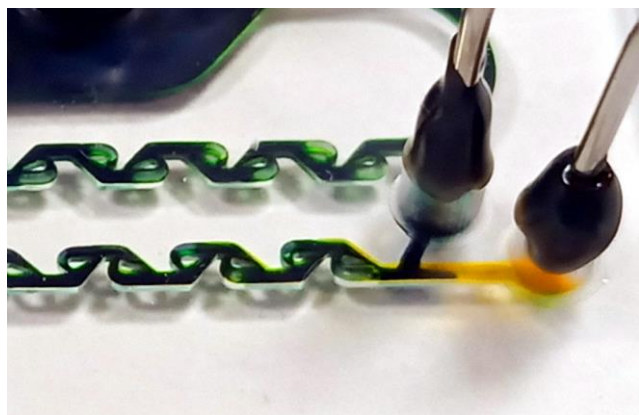
Fig. 5. Details of Tesla micromixers are highlighted using inkjet dyes.

Further, visualization with ≈ 10μM solution fluorescein in water was performed. Fluorescein solution was then introduced into micromixers by the first inlet, and IPA was introduced by the second and third inlets. Fluorescence in Fig. 6 was captured using a setup consisting of a 470 nm light source, single lens reflex camera, and optical filter.
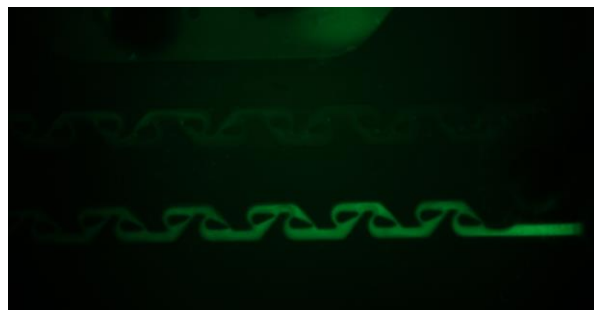

Fig. 6. Detail of mixing of fluorescein and IPA.

C. Optical microscopy

Initially, the stereomicroscopic inspection with an external light source using two gooseneck illuminators was used to evaluate the quality of embedded channels. This method was chosen instead of optical microscopes because the adjustable light direction allowed for better visualization. The result in Fig. 7. shows a comparison of quality for two printing settings for embedded channel chips.
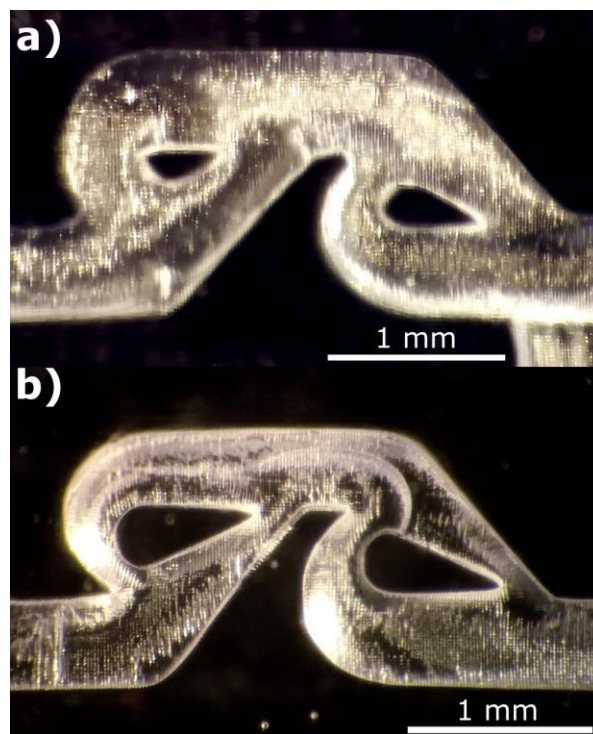

Fig. 7. Detail of Tesla micromixer unit in embedded-channels chip a) printed with single parameter slicing at layer exposure time 3.25 s, b) printed with multi-parameter slicing.

D. Electrochemical testing

The assembled chip was connected to the LabSmith uProcess™ breadboard microfluidic workstation composed of

an automation interface, valve manifold, analog sensor manifold, syringe pumps, selector valves, pressure sensors, and CapTite™ reservoirs. The workstation provided controlled flows for the preparation of analyzed solutions. For electrochemical testing, only inlets of the first set of the micromixers were used.

Cyclic voltammetry was then performed using Autolab III potentiostat. The Measurement process was semi-automated using Autolab Nova 2 and LabSmith uProcess™ software. Cyclic voltammograms of different $[Fe(CN)_6]^{3-}/[Fe(CN)_6]^{4-}$ concentrations. Different concentrations were achieved by tuning the relative flow rates. Results are in Fig. 8.
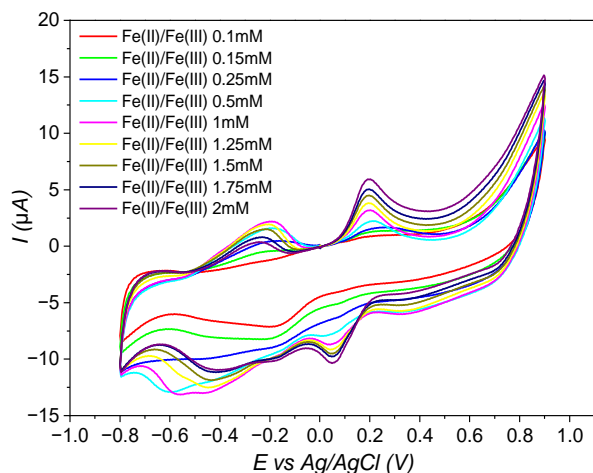
Fig. 8. Cyclic voltammograms of different concentrations of $[Fe(CN)_6]^{3-}/[Fe(CN)_6]^{4-}$.

IV. DISCUSSION

From Fig. 4a, it can be concluded that consumer-grade MSLA printers can produce small features with sufficient quality, as can be seen around the smallest channel width with the designed value of 110 µm. In this case, it should also be considered that this part of the channel has an aspect ratio of ≈ 4. Further, it can be observed in Fig. 4b that the printer can also produce sharp details, such as the tip of the Tesla micromixer. Sharpness could be further improved using software compensation that accounts for diffraction and adjusts the chip design geometry to better match the LCD raster. It was found that SLA resin can be used as an adhesive for bonding open-channel chips. However, the reliability of bonds differs for tested chip covers. Chips may detach from microscope glass slides due to slight deformations caused by temperature fluctuations, prolonged exposure to solutions, or residual stress. The effects of such deformation are mitigated by bonding to cover the clip or PVC foil because of the cover's flexibility. However, bonds to flexible covers are more prone to accidental peel-off. The overall process of bonding can be further optimized by ensuring controlled thickness of adhesive and elimination of squeezing out adhesive during assembly while ensuring bond without bubbles and pockets.

Inkjet dye color visualization in Fig. 5 shows that the embedded-channel Tesla micromixers were fabricated with good geometrical integrity. A minor defect is visible near the two adjacent inlets, where the ceiling above a stream divider

appears to be detached. This issue could likely be eliminated by adjustments to exposure parameters and pixel dimming of bridging layers.

Fig. 6 demonstrates that fabricated chip prototypes can be tested using fluorescein without significant loss of contrast caused by extensive autofluorescence.

The difference in print quality of encapsulated-channel chips is shown in Fig. 7. In Fig. 7a, there is a visible loss of detail, especially in stream dividers, caused by underexposure. Fig. 7b shows similar quality to open-channel chips.

Additionally, the drain channel was found to be an important part of embedded-channel chips. The version without a drain channel suffered from a clogged inlet channel in the second set of Tesla micromixers.

Finally, Fig. 8 shows sets of cyclic voltammograms with a clear trend in the increase of the current of redox peaks with increasing concentration. Since variation of concentration is achieved by changing relative flow rates, it can be concluded that the fabricated chip works properly in the intended case scenario.

V. CONCLUSION

It was demonstrated that consumer-grade MSLA printers could fabricate microfluidic chips with fine details, such as Tesla micromixers with minimal feature spacing of 110 µm. Fine details can be achieved both in open-channel and embedded-channel chips using multiparameter slicing. It can be concluded that MSLA printers can potentially be used to fabricate advanced microfluidic designs, such as Lab-on-chip or Organ-on-Chip, which require precise fluid control and insertion of electrodes.

REFERENCES

[1] T. Kurdadze, F. Lamadie, K. A. Nehme, S. Teychené, B. Biscans, and I. Rodriguez-Ruiz, "On-Chip Photonic Detection Techniques for Non-Invasive In Situ Characterizations at the Microfluidic Scale", *Sensors*, vol. 24, no. 5, 2024, doi: 10.3390/s24051529.

[2] N. Farhang Doost, S. K. Srivastava, X. Lin, Y. Zhu, and Y. Zhao, "A Comprehensive Review of Organ-on-a-Chip Technology and Its Applications", *Biosensors*, vol. 14, no. 5, 2024, doi: 10.3390/bios14050225.

[3] S. Scott and Z. Ali, "Fabrication Methods for Microfluidic Devices: An Overview", *Micromachines*, vol. 12, no. 3, 2021, doi: 10.3390/mi12030319.

[4] A. Shakeri, S. Khan, N. A. Jarad, and T. F. Didar, "The Fabrication and Bonding of Thermoplastic Microfluidics: A Review", *Materials*, vol. 15, no. 18, 2022, doi: 10.3390/ma15186478.

[5] C. Iliescu, H. Taylor, M. Avram, J. Miao, and S. Franssila, "A practical guide for the fabrication of microfluidic devices using glass and silicon", *Biomicrofluidics*, vol. 6, no. 1, Mar. 2012, doi: 10.1063/1.3689939.

[6] A. Al Rashid, W. Ahmed, M. Y. Khalid, and M. Koç, "Vat photopolymerization of polymers and polymer composites: Processes and applications", *Additive Manufacturing*, vol. 47, 2021, doi: 10.1016/j.addma.2021.102279.

[7] T. Siripongpreda, V. P. Hoven, B. Narupai, and N. Rodthongkum, "Emerging 3D printing based on polymers and nanomaterial additives: Enhancement of properties and potential applications", *European Polymer Journal*, vol. 184, 2023, doi: 10.1016/j.eurpolymj.2022.111806.

[8] K. M. Leong *et al.*, "Democratizing Access to Microfluidics: Rapid Prototyping of Open Microchannels with Low-Cost LCD 3D Printers", *ACS Omega*, vol. 9, no. 45, Nov. 2024, doi: 10.1021/acsomega.4c07776.

[9] Y. Zhang, M. Li, T. -M. Tseng, and U. Schlichtmann, "Open-source interactive design platform for 3D-printed microfluidic devices", *Communications Engineering*, vol. 3, no. 1, 2024, doi: 10.1038/s44172-024-00217-0.

[10] H. Shafique *et al.*, "High-resolution low-cost LCD 3D printing for microfluidics and organ-on-a-chip devices", *Lab on a Chip*, vol. 24, no. 10, May 2024, doi: 10.1039/D3LC01125A.

[11] Y. Xu *et al.*, "In-situ transfer vat photopolymerization for transparent microfluidic device fabrication", *Nature Communications*, vol. 13, no. 1, 2022, doi: 10.1038/s41467-022-28579-z.

[12] "Photonsters Validation Matrix v2", 2021. https://www.thingiverse.com/thing:4707289/files (accessed Apr. 05, 2025).

[13] "AmeraLabs Town v2", 2018. https://www.thingiverse.com/thing:2810666/files (accessed Mar. 16, 2025).

[14] P. F. Jacobs, "Fundamentals of Stereolithography", Accessed: Mar. 16, 2025. [Online]. Available: http://hdl.handle.net/2152/64400

Valeo

ŠKOLA DONE.
BUDOUCNOST
GREEN!

Zkušení kolegové, kteří vědí která bije.
Zajímavá technologická řešení a hlavně
jejich testování v praxi. Projekty, které vás
posunou na vyšší úroveň.
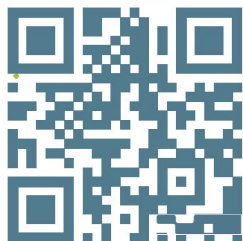
Pro lepší práci
jděte na:

VALEO.JOBS.CZ

Towards Early Rail Crack Detection: Characterizing Stress Wave Behavior through Experimentation and FE Modeling

Pavla Kočková
Department of Physics
Faculty of Electrical Engineering and Communication
Brno, Czech Republic
82059@vut.cz

Vladimír Holcman
Department of Physics
Faculty of Electrical Engineering and Communication
Brno, Czech Republic
holcman@vut.cz

Abstract—**This article was written as a part of project aimed at developing a measuring device for continuous monitoring and diagnostics of switch rails (also known as blades or tongues), which are key components of switches, sometimes referred to as turnouts. This part of the railway is subjected to significant dynamic loads, which often lead to failures resulting in serious traffic accidents. Current monitoring methods, based on the detection of incipient cracks using ultrasound, eddy currents, or visual inspection, are insufficient. This paper provides the first insight into the design of measuring equipment that uses the acoustic emission method to monitor processes within the material, predict the onset of crack formation, and prevent the occurrence of hazardous situations in a timely manner.**

Keywords—acoustic emission, switch rails, failure detection

I. INTRODUCTION

Acoustic emission is a physical phenomenon in which plastic deformation of solid materials is accompanied by acoustic cracking or noise generated within the material. A sudden redistribution of stress inside the material causes the formation of a stress wave, which propagates through the sample, and it is possible to measure the response of this stress wave on the surface of the solid using a special sensor. This measurement process is known as the acoustic emission method. Monitoring these effects can provide valuable information about their sources, which are mainly the formation and localization of cracks.

Acoustic emission is classified as a nondestructive diagnostic method. During the measurement, it is possible to choose between two different approaches. In the first method, the acoustic noise generated by loading the sample is measured. During the loading process, cracks form and create acoustic noise, which can be measured on the surface of the tested specimen. With the appropriate arrangement of sensors, the location and development of the cracks can be determined. This approach is suitable for long-term measurement, such as in the case of building structures, where it can be used to observe stress redistribution and, primarily, to predict structure failure. The structure is not influenced by the measurement in any way, and the process can be carried out during operation without restrictions.

In the second method, the acoustic emission signal is applied to the solid by an external transducer. This approach is suitable for comparing the loaded sample with unloaded reference sample.

II. MEASUREMENT SETUP

A. Project Introduction

In the case of our research, the second type of measurement setup was utilized. The subject of the examination is a part of the railway switch known as switch point or tongue. This part of the structure is significantly stressed by a dynamic and fatigue load, which can lead to crack formation and development. The aim of the entire project is to propose and design a measurement methodology using a non-destructive acoustic emission method that could provide continuous measured values. The first step in evaluating the results is to compare the measured values with baseline or reference values established during initial testing in the laboratory and using a mathematical model. This comparison helps to understand the progression or new formation of damage. Since the measurement is taken over time, the trend can be analyzed. In this initial research, the goal is to compare the results of mathematical simulation (regarding signal propagation along the tongue rail, whether or not a crack is present) with the experimental acoustic signal measurements performed in the laboratory.

B. Measurement Path of the Acoustic Signal

The block diagram of the measurement apparatus is shown in Fig. 1, with a general description provided below. A fully automated workplace for acoustic emission signal measurement and assessment was developed. The research laboratories of the Department of Physics at BUT have long been engaged in the theoretical and experimental study of noise in electronic materials, components, and devices. As a result, they are equipped with specialized instruments for studying fluctuation phenomena in solid materials. Among the available equipment in these laboratories, the low-noise preamplifiers PA15 (S3 Sedlak s.r.o.) were primarily used to amplify AE signals, along with the AM22 (S3 Sedlak s.r.o.) amplifiers, which feature a filter bank for additional amplification and filtering of the measured AE signals.

A piezoelectric transducer was used as the source of AE signal. This transducer excites a mechanical-train pulse that propagates along the rail and is detected by acoustic emission

sensors. The obtained AE signal is fed to the preamplifier, with the shortest possible transmission path chosen to minimize interference from surrounding influences. The preamplifier intensifies the strength of the measured acoustic signal. A 12V battery was used as the voltage source for the preamplifier, which also helps to suppress external interference of the acoustic signal. Next, the signal continues to the amplifier (if necessary), which contains a filter bank to remove the undesirable frequencies (for example, the sound of passing vehicles, maintenance work, etc.) that could influence the results. From the amplifier, the signal reaches the oscilloscope, where it is converted into digital form. Through the Ethernet switch, the laptop, oscilloscope, and generator communicate with each other using Ethernet cabling. The generator is connected to the transducer, thereby closing the signal path. Piezoelectric sensors from various manufacturers are used to detect the acoustic emission signals. The sensors meet the requirements for the frequency range of AE signals (at least up to 1 MHz) and are most commonly attached to the sample using beeswax. This method ensures good acoustic contact between the sample and the sensor, allowing for easy mechanical attachment and subsequent removal of the sensors. The AE signals are fed into the input of the low-noise amplifier PA15, which has a bandwidth of 3 Hz to 1 MHz, sufficient for the measured AE signals.
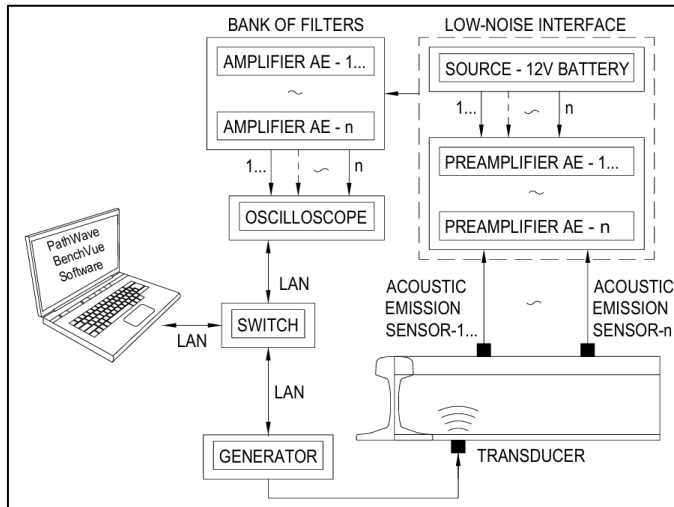

Fig. 1.   Experimental setup

In this particular case, we are using a four-channel oscilloscope. The Keysight InfiniiVision DSOX2024A is a high-performance digital storage oscilloscope designed for precise signal analysis. With a bandwidth of 200 MHz and a sampling rate of 2 GSa/s, this oscilloscope offers exceptional accuracy and high-resolution waveform capture. It is ideal for a wide range of applications, providing advanced triggering, deep memory, and an intuitive user interface. For each specified channel, the specified signal path was used – four amplifiers (if needed, depending on the measurement conditions), four preamplifiers, and four acoustic emission sensors were employed. With a convenient arrangement of sensors, it is also possible to evaluate the location of (potential) cracks. The oscilloscope and generator are remotely controlled from the lapto via a new application available for free from the

manufacturer Keysight. The application is called PathWave BenchVue Software and provides an easy way to evaluate the measured values without the need to program custom software. This program eliminates many of the issues associated with bench testing. It allows for a quicker transition past the test development phase and facilitates faster access to results by simplifying instrument connection, control, and test sequence automation. PathWave BenchVue Apps can be used to configure the most commonly used controls and measurements from instruments, visualize multiple measurements simultaneously, log and export data and images, create automated test sequences, and more.

III.   Mathematical Simulation Results

The first step in designing a solution to the aforementioned issue was to create a mathematical model of the rail segment, identical to the real element used for laboratory measurements. The aim of the mathematical simulations was to verify experimental data, help to understand how the signal propagates along the length of the rail, and predict areas where potential defects might arise. In the first model, an acoustic signal transducer was placed on the web of the unloaded rail, and the signal propagation is shown in the Fig. 2. The excitation signal in the mathematical simulations was a pulse with a rise and fall time of 10 µs and a pulse duration of 30 µs. In the next model, an elliptical crack was simulated at the center of the base of the rail. When the acoustic wave reached the crack, the walls of the crack began to vibrate due to the effect of the original signal, resulting in the appearance of a new vibration source. The evaluation and localization of these secondary signal sources should help in preventing defects at rail joints.
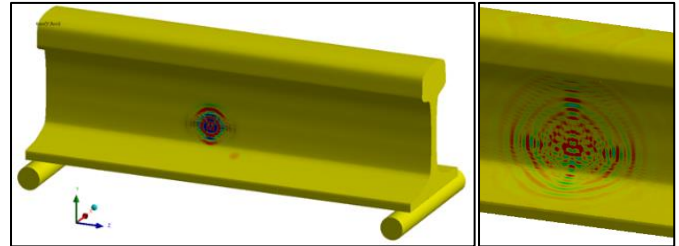

Fig. 2.   Mathematical simulation results

IV.   Measurement Path Functionality Verification

After assembling and creating the measurement path, it was necessary to verify the functionality of the individual components and the correctness of the entire setup. This verification was carried out using the aforementioned PathWave BenchVue application and through a method Hsu Nielsen source (ASTM E976) ČSN EN 1330-9, also known as the Pen-Test. It is commonly used for calibrating sensors in laboratory conditions due to its simplicity and speed. The essence of this method involves breaking a 3 mm long pencil lead, with a diameter of either 0.3 mm or 0.5 mm, against the surface of the material. The lead is placed in a special pencil that ensures the breakage is always consistent. When the lead presses against the material and then breaks, the surface is suddenly relieved, and a significant amount of energy is released in the form of acoustic emission. The Pen-Test is particularly suitable for calibrating sensors because it consistently generates essentially the same waves.

REFERENCES

[1] T. Trčka, Využití elektromagnetické a akustické emise pro diagnostiku moderních kompozitních materiálů, PhD thesis, Brno University of Technology, 2014.

[2] P. Koktavý, Nedestruktivní diagnostika a fyzika dielektrik, Brno University of Technology, 2006.

[3] C. B. Scruby, An introduction to acoustic emission. Journal of Physics E: Scientific Instruments, 20.8: 946, 1987.

[4] V. Barat et al., Investigation of Acoustic Emission of Cracks in Rails under Loading Close to Operational. Applied Sciences, 12: 11670, 2022.

Optimization of Fabrication Parameters for Atomic Force Microscopy Probes to Improve Image Resolution and Analysis

Denis Misiurev
Department of Physics
Brno University of Technology
Brno Czech Republic
xmisiu00@vutbr.cz

Holcman Vladimír
Department of Physics
Brno University of Technology
Brno Czech Republic
holcman@vut.cz

Abstract — **This study is part of a broader initiative to develop a comprehensive metric system for optimizing the fabrication of ultra-sharp Atomic Force Microscopy (AFM) probe tips. The system integrates data from multiple characterization techniques, including Focused Ion Beam (FIB) milling and Scanning Electron Microscopy (SEM) for morphological analysis, and Raman spectroscopy for assessing material composition. Detailed topographical and scanning data from AFM further inform the metric framework. Additionally, advanced simulations are conducted to model the distribution of the electric field between the sharp probe tip and the scanned surface. Electron behavior at the nanoscale interface is investigated using Monte Carlo and Molecular Dynamics simulations, providing insight into tip–surface interactions. Statistical and computational analyses are applied to identify correlations among fabrication parameters and performance indicators. This multifaceted approach aims to uncover the fundamental physical principles governing probe behavior, ultimately enhancing the precision, efficiency, and reproducibility of AFM probe fabrication for applications in nanotechnology and surface science.**

Keywords — *AFM, Sharp probe, Probe Fabrication, Metric System, Parameter Optimization, Microscopy, electrochemical etching, SEM, Tip convolution effect.*

I. Introduction

The application of scanning probe microscopy (SPM) techniques, such as Scanning Tunneling Microscopy (STM) and Atomic Force Microscopy (AFM), relies on the use of extremely sharp and mechanically robust probes to ensure minimal surface damage during scanning. In many cases, these probes must also be electrically conductive to enable localized current measurements, particularly when investigating electrical properties at the nanoscale. The surfaces examined with these techniques are typically very smooth—approaching atomic-level smoothness in STM, and under 100 nm surface roughness in standard AFM—meaning that the geometry of the probe within several hundred nanometers from the tip apex has limited influence on imaging quality.

Since its introduction by Murrel et al. in 1993, Conductive Atomic Force Microscopy (CAFM) has evolved significantly, combining the fundamental principles of both STM and AFM.

It enables simultaneous acquisition of topographical and electrical data, making it one of the most powerful tools for nanoscale electrical characterization [1]. CAFM employs ultra-sharp silicon tips, coated with a thin metallic film typically less than 20 nm thick, positioned at the end of a flexible cantilever. These conductive tips make direct contact with the sample surface, allowing precise measurement of current flow at localized points [2].

The radius at the tip apex (RTIP) of these probes generally ranges from 2 nm to 50 nm, enabling high-resolution electrical mapping over effective contact areas (Aeff) from 1 nm² to 800 nm² [3]. While topography is recorded via deflection measurements using a laser and photodiode system—similar to traditional AFM—the CAFM setup uniquely incorporates a current preamplifier connected to the tip to record electrical signals during scanning [4]. This dual-capability approach facilitates detailed exploration of material and device properties, especially in fields such as semiconductor analysis, resistive switching devices, and nanocomposites.

In this context, the fabrication and optimization of conductive, ultra-sharp AFM tips become critical. This research contributes to these efforts by developing a comprehensive metric system informed by both experimental characterization and computational simulations, ultimately aiming to improve tip performance, fabrication control, and reproducibility across applications in nanotechnology.

II. Sample preparation

Tungsten (W) was selected as the tip material owing to its exceptional physical and electrical properties, which render it highly suitable for scanning probe microscopy (SPM) applications. Its high melting point, substantial hardness, and excellent electrical conductivity make it particularly advantageous for the fabrication of robust, conductive, and ultra-sharp tips. Moreover, tungsten's resistance to mechanical deformation and chemical degradation under ambient and vacuum conditions ensures the long-term stability and reliability of the fabricated tips during operation. These attributes, combined with its compatibility with electrochemical processing, have established tungsten as a standard material in the production of high-aspect-ratio tips for techniques such as conductive atomic force microscopy (CAFM) and scanning tunneling microscopy (STM).

Electrochemical etching was employed as the fabrication method due to its capability to yield nanometer-scale apex radii

with high reproducibility and minimal equipment complexity. This method relies on the controlled anodic dissolution of a tungsten wire in an alkaline electrolyte, typically a sodium hydroxide (NaOH) solution. The wire, serving as the working electrode, is partially immersed in the electrolyte and subjected to a bias voltage relative to a counter electrode. Etching predominantly occurs at the meniscus formed at the liquid–air interface, where localized current density and ion exchange promote selective material removal. The geometric characteristics of the resulting tip—such as apex radius, taper angle, and surface smoothness—can be finely tuned by varying process parameters, including electrolyte concentration, submersion depth, applied voltage, and the diameter of the initial tungsten wire.

While electrochemical etching is widely regarded as a standard and scalable approach for tungsten tip fabrication, several technical challenges remain. These include precise control over the termination point of the etching process to avoid over-etching or tip blunting, maintaining tip symmetry, and achieving consistent tip sharpness across multiple fabrication cycles. Alternative methods, such as mechanical polishing and focused ion beam (FIB) milling, offer enhanced control at the expense of increased complexity, cost, and processing time.

In this study, systematic electrochemical etching experiments were conducted to investigate the influence of key process parameters on the morphological characteristics of tungsten tips. The method's inherent versatility and high degree of controllability facilitated the production of sharp and stable tips, laying the groundwork for subsequent characterization and optimization within the broader framework of AFM probe fabrication research.

Tungsten probes are known for their straightforward manufacturability, achieving extreme sharpness with tip diameters of less than 10 nm, and exhibiting considerable robustness due to the inherent stiffness of the metal. However, the issue of surface oxidation poses a challenge when electrical conductivity between the sample and the probe is necessary. In STM applications, the tip is typically cleaned in situ by applying a high voltage against a sacrificial area of the sample. However, this approach proves difficult for AFM applications involving nano–patterned surfaces and is entirely impractical for neural probe applications. As such, as–etched tungsten tips are frequently utilized as an initial step in the fabrication of more sophisticated probes.

The etching process of the tungsten tips involves immersing a tungsten wire, typically of 99.5% purity and 125 μm, 180 μm and 250 μm in diameter, into a solution of NaOH with a concentration ranging from 3 to 5 M with submerging depths 1,2 and 3mm (Figure 1). The etching process is initiated by applying an etching voltage U=9V, etching current I=100 mA.
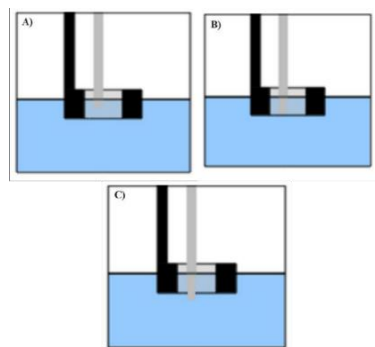

Fig. 1. Submerging depths 1 A), 2 B) and 3 C) mm

The chemical reaction of the tungsten electrode written in a more standard scientific notation:

$$W + 8(OH)^- \rightarrow WO_4^{-2} + 4H_2O + 6e^-$$

As the etching progresses, a narrow neck forms as a result of the most rapid removal of wire material occurring near the air–liquid interface, ultimately leading to the creation of a sharp tip once the submerged portion of the wire detaches. It is crucial to terminate the etching process promptly once the sharp tip is formed, as continued etching would result in the formation of a dull probe. Optimal etching conditions are determined by varying the solution concentration and submerged wire depth. The parameter curves around the optimal point are analyzed to identify the most favorable conditions.

III. SCANNING PROCEDURE.

In the proposed experimental setup, the NT–MDT AFM system (Figure 2), operating in semicontact mode with a resonance frequency approximately around 7–8 kHz, is selected as the primary tool for scanning. The system will employ custom-produced sharp probes to investigate their influence on the resulting images obtained by AFM. The chosen primary sample for evaluation is the TESCAN calibration mesh typically used for SEM.

The decision to utilize the NT–MDT AFM system in semicontact mode with specific probe characteristics ensures precise surface probing and data acquisition. Operating within the resonance frequency range of 7–8 kHz enhances the system's sensitivity to sur-face features, allowing for high–resolution imaging of the sample under investigation. Additionally, the scanning speed is set to 0.2 Hz, which balances the need for detailed resolution with the practicality of scan duration, ensuring comprehensive data capture without undue time consumption. To obtain a single image, the scanning procedure takes approximately 30 minutes.

To ensure accurate and consistent evaluation of the custom-produced probes, the scanning procedure must be carefully controlled to maintain the same scanning location for each probe. Given the necessity of comparing data across different probe s, meticulous attention will be paid to adjusting the scanning position to ensure it remains consistent for each probe. This involves precisely aligning the probe over the same area of the TESCAN calibration mesh for every scan.

A calibration mesh was applied to the entire image to prevent any mismatches and ensure a uniform average across the image. This process involved leveling the image to the substrate to maintain consistency and accuracy in the analysis.

Fig. 2. Solver Nano AFM STM system

By maintaining consistency in the scanning location and conditions, the resulting data will accurately reflect the performance of the custom-produced probes. This rigorous scanning protocol is crucial for correctly evaluating the probes and understanding their influence on the AFM images, ultimately contributing to the refinement and optimization of AFM imaging techniques.
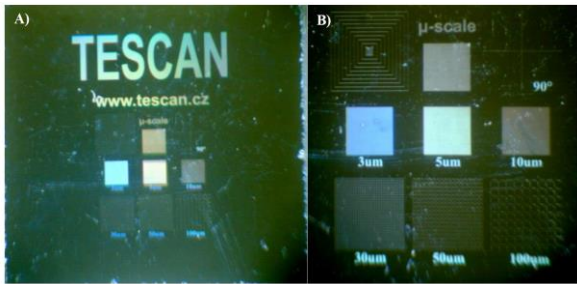

Fig. 3. Tescan calibration mesh

The calibration mesh (Figure 3) serves as an ideal test specimen due to its well-defined surface topography and known geometric features, enabling accurate assessment of the AFM system's performance. Moreover, maintaining consistency in the scanning location throughout the evaluation process ensures reproducibility and comparability of obtained data.

The AFM scanning procedure will involve systematic raster scanning of the calibration mesh surface, capturing topographical information at nanoscale resolution. Subsequent analysis of the acquired data will enable the assessment of probe-sample interactions and the impact of probe characteristics on image quality and surface topography representation.

Overall, the proposed AFM scanning procedure utilizing the NT–MDT AFM system offers a robust approach to evaluating probe performance and obtaining high–resolution topographical data of the calibration mesh sample. This contributes to the advancement of AFM imaging techniques and their applications in surface characterization.

IV. RESULTS AND DISCUSSIONS.

The resulting sharp probes have been systematically summarized in the tables (Tab 1-3), categorizing them based on single concentrations and varying wire thicknesses. A comprehensive summary of the optimal results is presented in Table 4.

In addition to the results, we have provided images depicting the tip diameter of the sharpest probe (Figure 4-6).

Tab 1. Resulting table of sharp probe of 125μm wire

NaOH Concentration (M)	Wire Thickness (μm)	Submergence Distance (mm)	Cone Thickness (nm)
3	125	1	280.36
3	125	2	349.57
3	125	3	390.55
4	125	1	358.27
4	125	2	477.35
4	125	3	318
5	125	1	311
5	125	2	227.36
5	125	3	221.55

Tab 2. Resulting table of sharp probe of 180 μm wire

NaOH Concentration (M)	Wire Thickness (μm)	Submergence Distance (mm)	Cone Thickness (nm)
3	180	1	309.26
3	180	2	329.6
3	180	3	554.37
4	180	1	360.25
4	180	2	288.52
4	180	3	314.18
5	180	1	517.25
5	180	2	334.9
5	180	3	421.96

Tab 3. Resulting table of sharp probe of 250 μm wire

NaOH Concentration (M)	Wire Thickness (μm)	Submergence Distance (mm)	Cone Thickness (nm)
3	250	1	302.98
3	250	2	334.52
3	250	3	231.58
4	250	1	672.69
4	250	2	559.47
4	250	3	206.06
5	250	1	337.54
5	250	2	535.87
5	250	3	1127

Tab 4. Resulting table of the sharpest probes

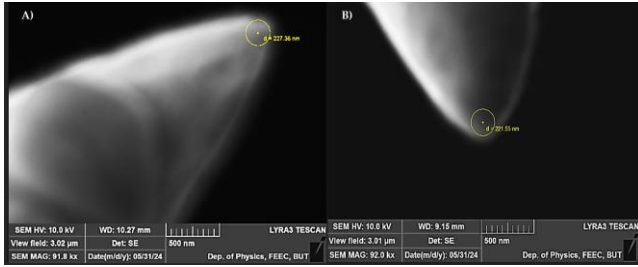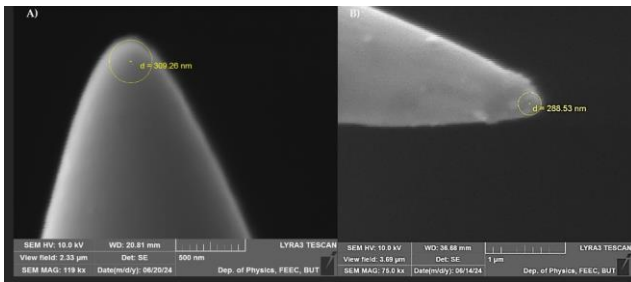| NaOH Concentration (M)	Wire Thickness (μm)	Submergence Distance (mm)	Cone Thickness (nm)
5	125	2	227.36
5	125	3	221.55
3	180	1	309.26
4	180	2	288.52
4	250	3	206.06

Fig. 4. Sharp probes 5M 125μm 2 A) and 3 B) mm

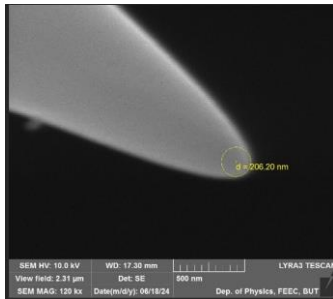
Fig. 5. Sharp probes 3M 180μm 1mm A) and 4M 180 μm 2 mm B)

Fig. 6. Sharp probes 4M 250 μm 3mm

From the resulting tables of produced sharp probes (Tab. 1-4), it becomes evident that for thicker wires, a lower concentration of NaOH solution is more beneficial, while for thinner wires, a higher concentration of NaOH solution is preferable. This can be explained by the differing etching durations required to create a more unified, cone-like tip on the sharp probes.

For thicker wires, the longer etching duration associated with lower NaOH concentrations facilitates a more controlled and gradual removal of material. This allows for the creation of a smoother and more tapered probe tip, reducing the likelihood of irregularities and defects. The slower etching process helps

ensure uniformity and precision, which is crucial for the performance of the probe in imaging applications.

Conversely, for thinner wires, a higher concentration of NaOH solution is beneficial as it provides a more rapid etching process. This faster etching is necessary to achieve the desired sharpness without over-etching or damaging the delicate structure of thinner wires. The quicker etching process helps to form the sharp probe tip more efficiently, optimizing the overall quality and performance of the probe.

The data on sharp probe production reveals that the optimal submergence distance for achieving high-quality probe tips is influenced by the specific application and wire thickness. Specifically, submergence distances of 2 mm and 3 mm have been identified as particularly favorable under different conditions.

The length of the submerged wire is identified as the most critical parameter. Wires that are deeply submerged are susceptible to premature detachment before proper neck formation, while those that are only shallowly submerged tend to show suboptimal etch-ing results. The surface tension of the NaOH solution and the submergence depth of the tungsten wire are interconnected factors that significantly influence the electrochemical etching process. When the tungsten wire is sub-merged deeper into the etchant solution, more of its surface area comes into contact with the solution. This increased surface ex-posure allows for a greater interaction between the metal surface and the etchant solution. As a result, there's a higher probability of metal ions being dissolved from the surface of the wire.

A solution with lower surface tension will wet the tungsten wire more effectively, ensuring uniform coverage and consistent etching, especially at greater depths. Converse-ly, high surface tension may result in poor wetting, with the solution forming beads or droplets on the surface, leading to non-uniform etching.

During electrochemical etching, hydrogen bubbles can form on the wire's surface. High surface tension can cause these bubbles to adhere to the wire, blocking the solution from reaching the surface and disrupting the etching process. Lower surface tension facilitates bubble detachment, maintaining continuous contact between the solution and the wire. Uniform distribution of the etchant solution due to low surface tension ensures even current density across the wire's surface. High surface tension can cause uneven distribution, leading to irregular etching.

Greater submergence depth increases the surface area exposed to the NaOH solution, enhancing the rate of electrochemical reactions. Proper control of surface tension ensures that this increased surface area is uniformly etched. However, high surface tension can hinder this process by causing uneven solution distribution. Temperature control is also essential. Higher temperatures decrease surface tension, enhancing wetting properties but also increasing the reaction rate. Thus, careful control of temperature is necessary to bal-ance these effects. Additionally, introducing surfactants can lower the surface tension, improving wetting and bubble detachment. The concentration and type of surfactant must be optimized to avoid unwanted side reactions.

Balancing the submergence depth and surface tension involves optimizing the exposure of the tungsten wire to ensure adequate etching without over-immersion. Experi-mental calibration is often necessary to achieve this balance. Testing different submergence depths can help determine the optimal level for uniform etching without excessive material removal. Adjusting solution properties, such as NaOH concentration, temperature, and additives, helps achieve the desired surface tension and etching characteristics.

Deeper submergence ensures that the etchant solution can access even the recessed or less accessible areas of the tungsten wire. In complex or intricate geometries, such as fine details or crevices, deeper immersion ensures that the etchant can penetrate effectively, reaching areas that may be shielded or less exposed with shallower submergence.

Greater immersion depth can also contribute to more uniform etching across the entire surface of the tungsten wire. With increased access to the surface, the etchant solution can act more evenly, dissolving metal ions from all regions of the wire. This helps prevent uneven etching and ensures consistent results, particularly in applications where uniformity is crucial.
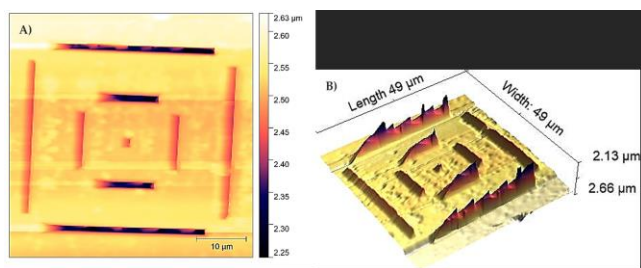

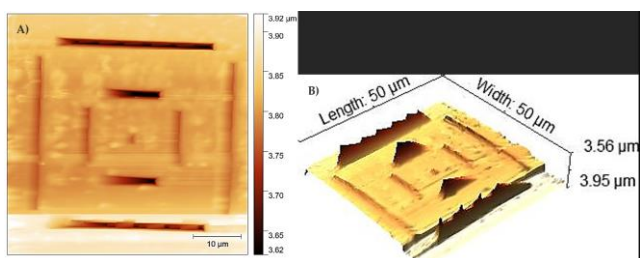Fig. 7. Topograthy A) and 3D B) images of 5M 125 µm 3mm sharp probe

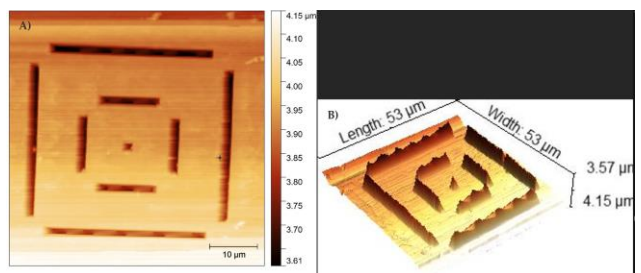Fig. 8. Topograthy A) and 3D B) images of 5M 125 µm 2mm sharp probe

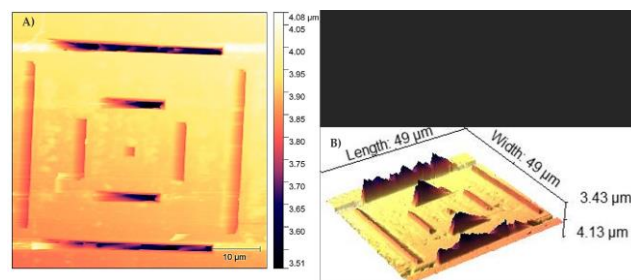Fig. 9. Topography A) and 3D B) images of 4M 180 µm 2mm sharp probe

Fig. 10. Topography A) and 3D B) images of 4M 180 µm 3mm sharp probe
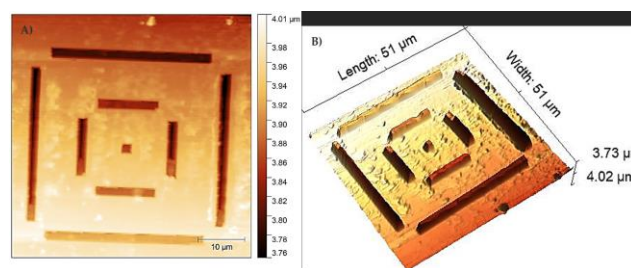

Fig. 11. Topography A) and 3D B) images of 3M 250 µm 3mm sharp probe

After careful evaluation of the obtained results from AFM images (Figure 7,8,9,10), it was found that the worst images in terms of contrast and average roughness across the surface were obtained from the 125 µm thickness wire (Figure 7,8). Even though this wire produced almost the sharpest probe, the results were unsatisfactory.

Considering the thickness of the wire, the potential flaw could be attributed to the signal-to-noise ratio. Thicker wires may introduce more noise during the imaging process, leading to poorer image quality despite achieving sharp probe tips. This increased noise can obscure fine details and contribute to higher surface roughness measurements, com-promising the overall effectiveness of the probe. Further investigations into optimizing the wire thickness and improving the signal-to-noise ratio are necessary to enhance the quality of AFM images and the performance of electrochemically etched probes.

In the realm of 3D imaging, the accurate recognition of indentations presents a significant challenge, particularly when these features are small and located centrally within the image. Current 3D imaging techniques often struggle to detect minute indentations due to several factors inherent in the imaging process and the subsequent data interpretation.

One primary issue is the resolution of the imaging system. Small indentations, especially those situated in the middle of the image, may fall below the resolution threshold of the imaging device, making them indistinguishable from the surrounding surface. Additionally, the central region of an image can suffer from focal inconsistencies or lens aberrations, further complicating the recognition of fine details.

On the other hand, the best results were obtained with the 3M 250 µm 3mm and 4M 180 µm 2mm sharp probes (Figure 9,11). These images, alongside the 3D images, demonstrated the best contrast among all scanned images. The 4M 180 µm 2mm probe, in particular, provided the sharpest results, which can be

attributed to its fine tip, allowing for high-precision scanning and better resolution of small indentations.

The 3M 250 µm 3mm probe also yielded excellent results, although its slightly larger tip size compared to the 4M probe might result in marginally less detail. However, both probes significantly outperformed others in terms of contrast and detail clarity, making them suitable for applications where accurate detection of minute features is critical.

The sharpness of a probe is a critical factor in 3D imaging, as it directly influences the ability to resolve fine details. The 4M 180 µm 2mm probe, being the sharpest among those tested, provided the highest resolution, enabling the most accurate identification of small indentations. This precision is essential for applications in fields such as materials science, where detecting small surface features can impact the assessment of material properties and quality.

It is important to mention that the 5M 125 µm 3mm and 5M 125 µm 2mm probes, due to their even finer sharpness, have the potential to offer even better contrast and detail resolution. The finer tip size of 125 µm allows for greater sensitivity in detecting surface variations, which could lead to more pronounced contrast and better overall image quality. These probes, therefore, hold promise for achieving superior imaging results, particularly in scenarios where the highest level of detail is required.

V. Conclusion

We produced a set of sharp probes under various conditions to evaluate their quality in terms of the contrast of scanning images. Each probe was manufactured with different parameters, including submergence distance, NaOH concentration, and etching duration, to assess how these factors influence the final image quality.

Once the probes were produced, they underwent a scanning procedure to assess their performance. The objective was to determine how well each probe performed in capturing detailed and high-contrast images. This evaluation involved analyzing the scanning images produced by each probe to measure their effectiveness in resolving fine details and producing clear, high-contrast results.

By comparing the scanning images from each probe, we aimed to identify the conditions that led to the best contrast and overall image quality. This assessment provides valuable insights into the optimal manufacturing conditions for sharp probes and helps guide future production efforts to achieve the highest possible quality in imaging applications.

The performance of these sharp probes highlights the importance of selecting the appropriate probe specifications based on the specific requirements of the imaging application. While the 3M and 4M probes have shown excellent results, the potential of the 5M probes suggests that further improvements in contrast and detail resolution are possible with the right choice of probe.

However, it is worth noting that even though the 5M 125 µm 3mm and 5M 125 µm 2mm probes are among the sharpest available, this does not necessarily guarantee the best scanning image quality in AFM. While the finer tip size of 125 µm allows for greater sensitivity in detecting surface variations, this increased sharpness does not always translate to superior contrast and detail resolution.

Various factors can influence the overall image quality, including the material properties of the sample, the specific scanning conditions, and the inherent noise in the imaging system. In some cases, the ultra-fine tip might lead to increased sensitivity to noise and surface roughness, potentially compromising the clarity of the scanned image.

Therefore, despite their potential for higher sensitivity, the 5M probes may not always provide the best imaging results in every scenario. Other probe characteristics and imaging parameters must be carefully considered to achieve optimal contrast and detail resolution in AFM imaging.

References

[1]   J L. Jiang *et al.*, "Understanding current instabilities in conductive atomic force microscopy," *Materials (Basel).*, vol. 12, no. 3, pp. 1–10, 2019, doi: 10.3390/ma12030459.

[2]   S. Peillon *et al.*, "Adhesion of tungsten particles on rough tungsten surfaces using Atomic Force Microscopy," *J. Aerosol Sci.*, vol. 137, no. July, p. 105431, 2019, doi: 10.1016/j.jaerosci.2019.105431.

[3]   P. McDonnell, T. Graveson, C. Rackson, and W. J. Kim, "A detailed study of scaling behavior in electrochemical etching of tungsten wires: Effects of non-uniform etching," *J. Phys. Chem. Solids*, vol. 74, no. 1, pp. 30–34, 2013, doi: 10.1016/j.jpcs.2012.07.014.

[4]   G. Han and H. S. Ahn, "Fabrication of tungsten probe for hard tapping operation in atomic force microscopy," *Ultramicroscopy*, vol. 161, pp. 66–73, 2016, doi: 10.1016/j.ultramic.2015.10.027.

Analysis of Retail Electricity Prices in the Czech Republic

1st Ing. Šimon Chmelař
BRNO UNIVERSITY OF TECHNOLOGY
Brno, Czech republic
xchmel31@vutbr.cz

2nd Ing. Lukáš Radil, Ph.D.
BRNO UNIVERSITY OF TECHNOLOGY
Brno, Czech republic
radil@vut.cz

Abstract—This paper presents an in-depth analysis of retail electricity prices in the Czech Republic, emphasizing their volatility and dependence on wholesale market mechanisms. The study develops a computational model to estimate the composition of wholesale electricity prices from the retail prices offered by suppliers. The research incorporates historical price trends, various trading strategies, and market structures to evaluate the stability and sustainability of retail pricing. The practical part of this study applies MATLAB-based calculations to assess whether electricity suppliers are sufficiently hedged against market fluctuations, ensuring their ability to meet customer demands. The findings contribute to the understanding of electricity pricing structures and highlight the importance of regulatory measures in mitigating price volatility.

Index Terms—bilateral trading, exchange trading, analysis of wholesale electricity prices, electricity, business strategy, price modeling, regression analysis, market dynamics, HPFC curve, LAD analysis, Monte Carlo method

I. Introduction

Electricity prices in the Czech Republic have seen extreme volatility in recent years due to market liberalization, geopolitical events, and supply chain shocks. Notable disruptions—such as post-pandemic demand, restricted gas flows from Russia, and the 2022 energy crisis—exposed vulnerabilities in supplier strategies, particularly among those relying on short-term market purchases. A striking example was the collapse of Bohemia Energy in 2021.

This paper, developed in cooperation with the Czech Energy Regulatory Office, investigates whether electricity suppliers base their retail prices on stable, long-term wholesale contracts or adopt speculative short-term procurement strategies. The analysis combines real-world price data with statistical modeling to estimate the composition of wholesale contracts underlying final tariffs.

After a brief overview of electricity trading mechanisms, the study presents the dataset structure and outlines the mathematical methods used to analyze procurement behavior. The core analysis focuses on two suppliers—E.ON Energie and CENTROPOL ENERGY—whose differing strategies illustrate the impact of market volatility and risk exposure.

The final sections interpret the results and highlight implications for consumers and regulators. The aim is to support a more transparent, data-driven understanding of how retail electricity prices are formed in liberalized market environments recommendations [1]–[4].

II. Types of Electricity Trading

Electricity trading is shaped by the non-storability of electricity—generation and consumption must be balanced in real-time. In the Czech Republic, trading occurs through both bilateral (OTC) agreements and regulated exchange markets.

A. Bilateral Trading (OTC)

OTC trading involves direct agreements between two parties, often without transparency. Key instruments include:

- **Forward Contracts:** Customized contracts for future delivery at fixed prices; commonly used for long-term hedging.
- **Futures:** Standardized exchange-traded contracts offering liquidity and reduced counterparty risk.
- **Swaps:** Enable price stability by exchanging fixed and floating price exposure.
- **Options:** Provide the right, not obligation, to trade electricity at a pre-defined price; useful for risk management.

B. Exchange Trading

Exchange-based trading, such as via PXE, is transparent and standardized. It includes:

- **Long-Term Markets:** Allow purchase of electricity months or years in advance through monthly, quarterly, or yearly contracts.
- **Short-Term Markets:** Include day-ahead and intra-day trading, offering real-time balancing and flexibility.
- **Merit Order Principle:** Dispatches electricity sources by marginal cost, favoring renewables; can lead to price volatility during tight supply [1]–[4].

III. Data Structure

The analysis in this study relies on multiple datasets representing various segments of the Czech electricity market. These include:

- **Wholesale market data** from PXE (Power Exchange Central Europe), including prices of forward contracts with different maturities.
- **Spot market and imbalance data** from the Czech market operator OTE, providing daily and hourly trading data.
- **Retail price data** from supplier price lists, covering multiple consumer categories and contractual types.

The data spans several years and is organized along two key dimensions:

- **Time structure:** Monthly and daily averages, seasonal patterns, and extreme price events (e.g., 2021–2022 spikes).
- **Contract types:** Long-term (yearly, quarterly), short-term (day-ahead), and spot transactions, categorized by pricing mechanism.

For modeling purposes, all prices are normalized to EUR/MWh and aligned on a consistent time axis. Contracts are mapped to retail tariffs based on their expected delivery periods and market context.

Special attention was paid to aligning supplier retail prices with the composition of wholesale contracts. This alignment enables comparative modeling and highlights whether retail offerings reflect underlying procurement strategies.

Despite occasional gaps and format inconsistencies, the data provides a robust basis for statistical modeling and scenario analysis in subsequent sections [4].

IV. Modeling Methods

This section introduces the mathematical and statistical methods used to analyze the composition of electricity prices and the likelihood of procurement on various contracts. Each method is explained with its purpose and suitability, followed by real data results using a reference price of 85 EUR/MWh.

A. Price Match Under Threshold Method

This method identifies the share of prices (for each contract type) that are lower than or equal to a supplier-defined fixed price P_z, here set at 85 EUR/MWh. The calculation is based on counting the percentage of prices meeting this condition:

$$R = \frac{\text{Number of prices } \leq P_z}{\text{Total number of prices}} \times 100 \qquad (1)$$

Where:

- P_z is the fixed price set by the supplier (85 EUR/MWh),
- R is the percentage of prices below or equal to P_z,
- The numerator represents the count of prices that meet the condition,
- The denominator is the total number of observed prices for the contract type.

This method serves as a basic eligibility check to determine whether a specific type of wholesale contract could realistically be used as the basis for a supplier's retail offer. It is not probabilistic in nature but provides a useful first-level filter.

Advantages:

- Easy to interpret,
- Requires minimal computational effort.

Disadvantages:

- Does not reflect the shape or variance of data,
- Result may be sensitive to the choice of threshold.

The high match rate for annual contracts suggests that they likely formed the basis of supplier pricing in 2022. In contrast, monthly and spot products show almost zero alignment with

TABLE I
SHARE OF PRICES ≤ 85 EUR/MWH (2022)

Contract Type	Percent Match (%)
Annual	87.60
Quarter 1	48.24
Quarter 2	44.40
Quarter 3	19.38
Quarter 4	0.00
Monthly (Jan–Dec)	0.00
Spot Prices	2.74

the target price, indicating that suppliers relying on such instruments would not have been able to offer competitive retail rates during the analyzed period.

This method does not differentiate between how often or how long the price was below the threshold. However, it gives a quick indication of which contract types are even remotely compatible with a given price level. As a result, it is particularly useful as a preliminary screening tool before applying more advanced modeling techniques [4].

B. Nearest Neighbour Method

This method evaluates how many market prices lie within a defined tolerance band around the supplier's fixed price P_z. If a given price C satisfies the following condition:

$$n = \sum (|C - P_z| \leq \delta) \qquad (2)$$

then it is considered a match.

Where:

- n is the number of matching prices,
- C represents the set of all contract prices for a given year and type,
- P_z is the supplier's fixed price (85 EUR/MWh),
- δ is the tolerance margin (±10% = 8.5 EUR).

The calculation proceeds through a `for` loop evaluating how many prices fall within the tolerance interval. The resulting data is printed in a format shown in Table **??**, where the number of matching prices is listed for each contract type.

Advantages:

- Simple to implement and visualize,
- Useful for preliminary match detection.

Disadvantages:

- Sensitive to the choice of margin,
- Ignores price distribution and contract duration.

TABLE II
MATCHES WITHIN TOLERANCE BAND (±8.5 EUR) BY CONTRACT TYPE.

Contract Type	Matches
Annual	29
Quarterly (Q1–Q4)	56 / 31 / 33 / 2
Monthly (Jan–Dec)	19 / 0 / 0 / 0 / 5 / 0 / 0 / 0 / 0 / 0 / 0 / 0
Spot Prices	8

As shown in the table, the method indicates a relatively high number of matches for quarterly contracts, particularly in Q1, Q2 and Q3, and a smaller number for annual and spot

products. Monthly contracts mostly fail to meet the tolerance, confirming that they are less aligned with the supplier's fixed price [4].

C. Difference Analysis Method

This method calculates the average absolute difference between the market price C and the supplier's price P_z:

$$R = |C - P_z| \tag{3}$$

Where:

- C is the average price of a given contract type,
- P_z is the supplier's fixed price (85 EUR/MWh),
- R is the calculated average absolute difference.

Advantages:

- Easy to interpret,
- Allows contract ranking by proximity to retail price.

Disadvantages:

- May be skewed by outliers,
- Does not take variance or shape of distribution into account.

TABLE III
AVERAGE PRICE DIFFERENCES BY CONTRACT TYPE (2020)

Contract Type	Average Difference (EUR)
Annual	43.62
Quarterly (Q1–Q4)	Q1: 31.55, Q2: 41.96, Q3: 42.13, Q4: 39.46
Monthly (Jan–Dec)	Jan: 33.09, Feb: 35.92, Mar: 43.73, Apr: 49.67, May: 53.19, Jun: 52.33, Jul: 49.97, Aug: 51.18, Sep: 46.77, Oct: 45.24, Nov: 41.64, Dec: 42.85
Spot Price	51.41

This method was used primarily for the 2020 dataset due to its lower volatility difference Analysis Method.

D. Mean Absolute Deviation (MAD)

The MAD method is used to assess price stability in volatile electricity markets. It builds on the previous difference analysis method but extends it by calculating the average of all absolute differences between observed market prices and the supplier's fixed price P_z (set here at 85 EUR/MWh).

A lower average deviation indicates higher price stability and suggests that a given contract type was likely used in the supplier's pricing. The method provides a useful indicator of how closely market prices align with a fixed target.

The calculation is defined as:

$$\alpha = \frac{\sum_{i=1}^{N} |C_i - P_z|}{N} \tag{4}$$

Where:

- α is the mean absolute deviation,
- C_i are observed market prices,
- P_z is the supplier's fixed price (85 EUR/MWh),
- N is the number of observations.

Each contract type's deviation is inverted and normalized into a probability distribution, where lower deviation means

higher procurement probability. The weights are scaled to sum up to 100 % [5].

The following table shows the procurement probabilities calculated for the year 2020:

TABLE IV
PROCUREMENT SHARE BY CONTRACT TYPE – MAD METHOD (2020, P_z = 85 EUR)

Contract Type	Procurement Probability (%)
Annual	30.97
Quarterly (Q1–Q4)	Q1: 5.35, Q2: 1.34, Q3: 4.01, Q4: 1.43
Monthly (Jan–Dec)	Jan: 5.10, Feb: 1.57, Mar: 3.86, Apr: 1.08, May: 3.18, Jun: 1.08, Jul: 3.38, Aug: 1.10, Sep: 1.24, Oct: 1.24, Nov: 0.46, Dec: 1.31
Spot Prices	26.28

E. Monte Carlo Simulation

Monte Carlo simulation uses random sampling to estimate the likelihood that a contract portfolio would result in the supplier's price. The method follows these steps:

1) Define a probability model for price behavior,
2) Generate random combinations of prices for each contract,
3) Calculate the average price for each combination,
4) Compare outcomes with the supplier's fixed price.

The method assumes that prices follow historical distributions and estimates how often different contract types result in plausible matches.

Advantages:

- Captures uncertainty and volatility,
- Highly flexible and extendable.

Disadvantages:

- Computationally intensive,
- Sensitive to input distribution and assumptions [6], [7].

TABLE V
PROCUREMENT SHARE BY CONTRACT TYPE – MONTE CARLO METHOD (FIXED PRICE = 85 EUR)

Contract Type	Procurement Probability (%)
Annual	6.56
Quarterly (Q1–Q4)	Q1: 4.27, Q2: 4.28, Q3: 3.05, Q4: 4.38
Monthly (Jan–Dec)	Jan: 1.14, Feb: 1.21, Mar: 1.29, Apr: 1.12, May: 1.11, Jun: 1.26, Jul: 1.20, Aug: 1.45, Sep: 1.14, Oct: 1.18, Nov: 1.00, Dec: 1.21
Spot Prices	63.09

F. Chi-Square Test (χ^2)

The chi-square test evaluates whether observed distributions of contract-based prices match expected distributions generated from model assumptions. The test statistic is:

$$\chi^2 = \sum \frac{(O_i - E_i)^2}{E_i} \tag{5}$$

Where:

- O_i is the observed frequency for price bin i,
- E_i is the expected frequency for price bin i.

This test helps validate the consistency of the observed supplier price structure with modeled procurement strategies.

Advantages:

- Statistically rigorous,
- Can highlight significant deviations.

Disadvantages:

- Sensitive to sample size and binning method,
- Limited to categorical data representation [8]–[10].

G. DBSCAN Clustering (Based on Chi-Square Test)

The DBSCAN (Density-Based Spatial Clustering of Applications with Noise) algorithm is used in this study as a follow-up analysis to the chi-square test. While the chi-square test identifies individual combinations of contracts that produce results statistically close to the supplier's price, DBSCAN is employed to discover structure and dominant patterns among these combinations.

By analyzing the high-dimensional output of the chi-square test, DBSCAN helps determine whether contract portfolios leading to successful price matches form natural groupings (clusters) in the data space. The method enables the identification of a dominant cluster of procurement strategies and calculates average contract shares within it—providing a representative estimate of likely supplier behavior.

Key parameters of the DBSCAN algorithm:

- ε (epsilon): neighborhood radius around each point,
- MinPts: minimum number of points required to form a cluster.

The algorithm classifies data points as:

- **Core points** – those with at least MinPts neighbors within radius ε,
- **Border points** – located near core points but lacking sufficient density,
- **Noise** – outliers that do not belong to any cluster.

This clustering approach allows further interpretation of the chi-square analysis results by filtering out noise and highlighting coherent procurement strategies.

Advantages:

- Detects complex, non-linear cluster shapes,
- No need to predefine the number of clusters,
- Robust to noise and outliers.

Disadvantages:

- Sensitive to parameter selection (ε, MinPts),
- May struggle with clusters of varying density.

The average contract shares calculated from the dominant DBSCAN cluster are used as a final estimate of the supplier's likely procurement strategy, grounded in real contract combinations that produce statistically plausible pricing outcomes [11], [12].

V. RESULTS AND INTERPRETATION

This section applies the previously described modeling methods to real electricity supplier data. The goal is to evaluate the effectiveness and consistency of each method and compare

how well they estimate the supplier's procurement structure based on their offered retail prices.

The analysis focuses on two suppliers — **E.ON Energie, a.s.** and **CENTROPOL ENERGY, a.s.** — selected for their contrasting procurement strategies. E.ON is generally considered a conservative supplier, favoring long-term contracts and higher hedging. In contrast, CENTROPOL is assumed to rely more heavily on short-term and spot market procurement.

The retail prices used for comparison were calculated as the average of all available tariffs, price lists, and distribution areas offered by each supplier. The test years were 2020 and 2022, as these represent periods with complete datasets for all contract types and differing market volatility.

TABLE VI
SUPPLIER AVERAGE RETAIL PRICES USED FOR MODELING

Supplier	2020 Price (EUR/MWh)	2022 Price (EUR/MWh)
E.ON Energie	85.00 EUR	85.00 EUR
CENTROPOL E.	72.00 EUR	103.00 EUR

The selected price for each supplier was used as the fixed reference point P_z in all models. This ensures consistency in interpreting outputs such as absolute deviations, matching ratios, and probabilistic estimates across the tested methods.

The following subsections present results for both suppliers, grouped by method and year.

A. Chi-Square Test

The Chi-Square test was used to evaluate the statistical consistency of observed contract prices with supplier retail prices. In 2020, both suppliers showed nearly identical results due to stable market conditions and similar pricing. However, in 2022, the test highlighted a significant divergence — E.ON retained a high match with annual contracts, while CENTROPOL was significantly weighted toward spot procurement.

TABLE VII
CHI-SQUARE TEST RESULTS – PROCUREMENT PROBABILITIES (%)

Contract Type	E.ON (2020 / 2022)	CENTROPOL (2020 / 2022)
Annual (%)	24.73 / 29.58	24.75 / 9.49
Quarterly (%)	24.75 / 9.63	24.75 / 9.48
Monthly (%)	24.95 / 8.69	24.95 / 9.34
Spot (%)	25.57 / 52.10	25.57 / 71.69

Comment: In 2022, CENTROPOL's procurement strategy appears highly unhedged, contrasting with E.ON's continued reliance on annual contracts.

B. Monte Carlo Simulation

Monte Carlo simulation modeled the probability that a supplier's price resulted from a given contract mix. While results were nearly identical in 2020, in 2022 the differences were striking — E.ON leaned heavily on long-term procurement, while CENTROPOL favored spot and monthly markets.

Comment: This method reinforces the contrast — CENTROPOL's procurement in 2022 shows a strong speculative profile.

TABLE VIII
MONTE CARLO SIMULATION – PROCUREMENT PROBABILITIES (%)

Contract Type	E.ON (2020 / 2022)	CENTROPOL (2020 / 2022)
Annual (%)	54.72 / 71.16	55.03 / 2.32
Quarterly (%)	9.31 / 6.23	9.26 / 24.98
Monthly (%)	8.68 / 8.93	8.56 / 27.97
Spot (%)	27.29 / 13.68	27.15 / 44.73

C. Mean Absolute Deviation (MAD)

The MAD method calculates average deviation from the supplier's price, inverts and normalizes the values into probability estimates. It is based on numerical stability rather than modeling volatility or distribution.

TABLE IX
MEAN ABSOLUTE DEVIATION – PROCUREMENT PROBABILITIES (%)

Contract Type	E.ON (2020 / 2022)	CENTROPOL (2020 / 2022)
Annual (%)	31.02 / 24.22	30.87 / 17.27
Quarterly (%)	13.04 / 11.46	14.27 / 9.32
Monthly (%)	30.90 / 37.66	31.27 / 40.66
Spot (%)	25.04 / 26.66	23.59 / 32.75

Comment: Though less dynamic, MAD remains consistent across years and suppliers. It confirms CENTROPOL's shift toward short-term contracts in 2022.

D. Summary of Results

The applied methods revealed distinct strengths in analyzing supplier procurement strategies.

Monte Carlo simulation and the **Chi-square test** offered deep insights into the probabilistic structure of pricing behavior, capturing contract variability across suppliers. Despite their complexity and computational demands, these methods provided the most accurate estimates and are best used in combination to mitigate bias.

The **Mean Absolute Deviation (MAD)** method, while simpler, proved to be a stable benchmark due to its consistency across scenarios. It complemented the probabilistic models and extended the **Difference Analysis** by offering normalized results.

In contrast, methods like the **Nearest Neighbour**, **Difference Analysis**, and the **Threshold Count** model contributed less to final interpretations. Although numerically informative, they lacked depth in explaining procurement dynamics and were not included in the main synthesis.

Overall, complex statistical models outperformed simpler tools in identifying contract structures behind retail pricing.

VI. CONCLUSION

This study analyzed how Czech electricity suppliers form their retail prices based on procurement strategies. Using multiple methods — including Monte Carlo simulation and chi-square testing — it assessed whether prices reflect stable, long-term contracts or riskier short-term purchases.

Results showed a clear contrast: E.ON Energie relies on long-term contracts, ensuring price stability, while CENTROPOL ENERGY's 2022 strategy was dominated by short-term and spot market purchases, leading to higher volatility.

Consumer impact: Suppliers with poor hedging may pass market risk to households, while stable procurement supports price predictability and supply security.

Regulatory recommendation:
- Require minimum hedging levels,
- Monitor procurement mix through regular reporting,
- Encourage transparency via benchmarking tools.

Future research: Broader datasets and real-time pricing (e.g., from smart meters) could enhance model accuracy and regulatory oversight.

In conclusion, data-driven procurement modeling can support supplier evaluation, risk management, and informed energy policy.

REFERENCES

[1] ed.). Historie českého elektrárenství a vznik ČEZ, a. s. Online. JANOUŠEK, Radek. Www.enviweb.cz. 2012. Dostupné z:<https://www.enviweb.cz/90953> [cit. 2025-01-03].

[2] JANÍČEK, Lukáš (ed.). Structure of the electricity market. Online. Https://cms.law. 2015. Dostupné z:<https://cms.law/en/int/expert-guides/cms-expert-guide-to-electricity/czech-republic.> [cit. 2025-01-03].

[3] HROZEK, Dian. Účastníci trhu s elektřinou. Online. Https://oenergetice.cz. 2016. Dostupné z: <https://oenergetice.cz/trh-s-elektrinou/draft-ucastnici-trhu-s-elektrinou.> [cit. 2025-01-03].

[4] CHMELAŘ, Šimon. Analýza maloobchodních cen elektrické energie. Brno: Vysoké učení technické v Brně, Fakulta elektrotechniky a komunikačních technologií, Ústav elektro- energetiky, 2024, 76 s. Diplomová práce. Vedoucí práce: Ing. Lukáš Radil, Ph.D.

[5] FROST, Jim. Mean Absolute Deviation: Definition, Finding & Formula. Online. Https://statisticsbyjim.com. 2021. Dostupné z: <https://statisticsbyjim.com/basics/mean-absolute-deviation/.> [cit. 2025-04-06].

[6] FABIAN, František; KLUIBER, Zdeněk. Praha: PROSPEKTRUM s.r.o., 1998. ISBN 80-7175-058-1. Kapitola 1.2, s. 14.

[7] TESAŘ, Jiří; BARTOŠ, Petr. České Budějovice: Pedagogická fakulta Jihočeské univerzity v Č. Budějovicích, Katedra fyziky Dostupné z: <https://dsp.vscht.cz/konference_matlab/MATLAB06/prispevky/tesar_bartos/tesar_bartos.pdf> [cit. 2025-04-06].

[8] ŘEHÁČKOVÁ, Adriana. CHÍ-KVADRÁT TEST NEZÁVISLOSTI. Online. Https://www.statistickyneklasicky.cz. 2024. Dostupné z: <https://www.statistickyneklasicky.cz/chi-kvadrat-test-nezavislosti/.> [cit. 2025-04-06].

[9] SCHUBERT, Erich; SANDER, Jörg a ESTER, Martin. SHARE ON DBSCAN Revisited, Revisited: Why and How You Should (Still) Use DBSCAN. In: SHARE ON DBSCAN Revisited, Revisited: Why and How You Should (Still) Use DBSCAN. Xiaowei, 2017. ISBN ISSN 0362-5915.

[10] BAGDONAVICIUS, V.; NIKULIN, M. S. Chi-squared goodness-of-fit test for right censored data. The International Journal of Applied Mathematics and Statistics. 2011, pp. 30–50.

[11] BALHAR, Lubomír. Shlukování (Clustering). Online. Https://naucse.python.cz. 2021. Dostupné z: <https://naucse.python.cz/2020/pydata-ostrava-jaro/pydata/clustering/.> [cit. 2025-04-06].

[12] ESTER, Martin; KRIEGEL, Hans-Peter; SANDER, Jörg; XU, Xiaowei. A density-based algorithm for discovering clusters in large spatial databases with noise. In: SIMOUDIS, Evangelos; HAN, Jiawei; FAYYAD, Usama M., eds. Proceedings of the Second International Conference on Knowledge Discovery and Data Mining (KDD-96). AAAI Press, 1996, pp. 226–231. ISBN 1-57735-004-9. CiteSeerX 10.1.1.121.9220.

Rapid Prototyping Platform for the Control and Testing of Electric Drives

Miroslav Kozumplík
Department of Control and Instrumentation
FEEC, Brno University of Technology
Brno, Czech Republic
Miroslav.Kozumplik@vut.cz

Abstract—**This paper presents a cost-effective rapid prototyping platform for the control and testing of electric drives. The proposed platform consists of a ZedBoard development board and a custom-designed printed circuit board featuring a two-level voltage source inverter for motor control. The implementation of control algorithms and peripherals management in FPGA on the ZedBoard is automated using the HDL Coder toolbox in MATLAB/Simulink, while real-time parameter tuning and data logging are enabled by Embedded Coder toolbox. The modularity of the platform allows for easy adaptation to different motor types and control strategies. The paper provides a description of the hardware architecture, the implementation of control algorithms on the rapid prototyping platform, and the capabilities of FPGA-based motor control. Experimental results demonstrate the platform's ability to perform real-time control with minimal latency, showcasing its suitability for research and development of advanced motor control strategies. These results highlight the potential of the proposed system as a versatile and efficient tool for both academic research and industrial applications.**

Keywords—*Rapid prototyping platform, Simulink, HDL Coder, FOC, ZedBoard, Two-level voltage source inverter, PMSM*

I. INTRODUCTION

The field of electric drive control is continuously evolving, requiring increasingly advanced control algorithms to ensure high efficiency, precision, and steady-state torque performance. Given the complexity and escalating demands of electric drive control, the use of efficient tools for developing and testing control algorithms is crucial. One of the most effective methodologies addressing this challenge is the concept of rapid prototyping.

Rapid prototyping platforms provide a modern approach to the designing and testing of control algorithms for electric drives. Their primary objective is to reduce the time and cost associated with the entire development process of control algorithms. By enabling an iterative design process, these platforms help minimize errors, accelerate the transition from development to deployment, and offer a consistent framework for analyzing motor behavior under various control strategies. A typical development cycle of control algorithms using a rapid prototyping platform, together with their validation on a Hardware-in-the-Loop (HIL) system, is illustrated in Fig. 1. [1][2]
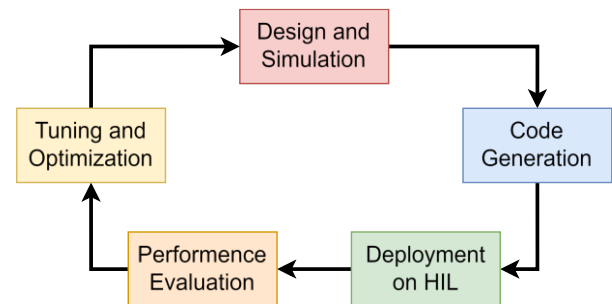

Fig. 1. Development cycle of control algorithms on the rapid prototyping platform

The goal of this paper is to introduce a newly developed and low-cost alternative to existing rapid prototyping platforms for electric drive control.

II. CONTROL STRATEGIES AND IMPLEMENTATION PLATFORMS

A. Field-Oriented Control

Permanent magnet synchronous motors (PMSMs) have gained popularity over traditional induction motors due to their higher efficiency and superior performance. As a result, they are widely used in industrial automation, robotics, and electric mobility.

Currently, the field-oriented control (FOC) algorithm is one of the most widely used control algorithms for these electric drives. This technique enables efficient regulation of both torque and magnetic flux by using Clarke and Park transformations to convert the three-phase system into the dq reference frame. Clarke transformation first converts the three-phase stator currents into an orthogonal αβ coordinate system, which represents a stationary reference frame. Subsequently, the Park transformation maps these αβ components into a rotating dq reference frame, which aligns with the rotor flux, effectively decoupling torque and flux control. By decoupling flux and torque control, FOC achieves precise and dynamic motor operation, mirroring the behavior of DC motors. FOC requires real-time measurement of phase currents and rotor position in electrical coordinates. The core of the algorithm consists of PI controllers that control dq currents. PWM signals are used for switching the transistors in a two-level voltage source inverter. A block diagram of the FOC method is shown in Fig. 2. [3]
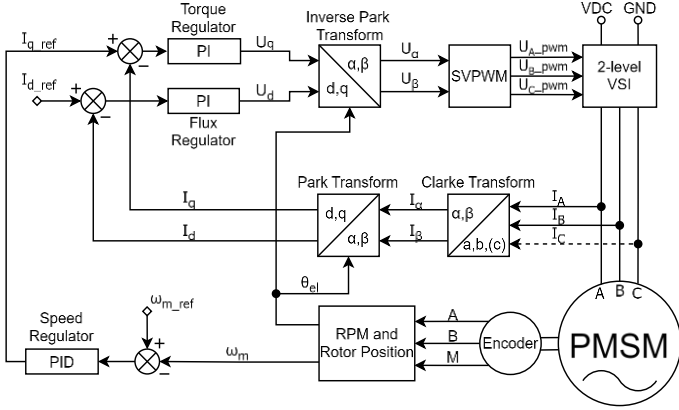
Fig. 2.   Block diagram of field-oriented control of a PMSM

B. Control Units

Motor control algorithms can be implemented on various computing platforms, each with its own balance of performance, latency, and cost.

One of the most common and cost-effective solutions is the use of general-purpose microcontrollers (MCUs). Modern MCUs offer sufficient computational power and dedicated hardware for numerical processing, making them functionally comparable to specialized digital signal processors (DSPs). The execution time of an FOC cycle typically ranges from a few to several tens of microseconds. [4] Commonly used MCU platforms for motor control include the Texas Instruments C2000 series [5] and STMicroelectronics STM32F4 series [6].

For high-performance applications like industrial servo drives or aerospace propulsion, field-programmable gate arrays (FPGAs) are widely used. Due to their parallel processing capabilities and flexibility, FPGAs enable extremely fast control, achieving FOC execution times ranging from tens to hundreds of nanoseconds. Notable FPGA platforms are the Zynq series from AMD Xilinx. [7]

Application-specific integrated circuits (ASICs) are custom hardware components designed for specific applications. They offer maximal performance and power efficiency but come with significantly higher development costs.

Rapid prototyping platforms allow fast development, testing, and optimization of motor control algorithms. These systems support real-time implementation and tuning, making them highly valuable for research and development in motor control. However, this advantage comes at a high cost, often exceeding tens of thousands of USD. Well-known solutions include Speedgoat platforms, which integrate with MATLAB/Simulink Real-Time [8], and dSPACE systems, featuring ControlDesk software for tuning and visualization [9].

III.   Rapid Prototyping Platform

The proposed rapid prototyping platform consists of a ZedBoard development board and a custom-designed printed circuit board featuring a two-level voltage source inverter.

Fig. 3 illustrates the complete setup of the ZedBoard, two-level voltage source inverter, and PMSM.

A. ZedBoard

The ZedBoard is an affordable development board incorporating the AMD Xilinx Zynq-7000 XC7Z020 system-on-chip (SoC) and multiple peripheral interfaces. The Zynq-7000 XC7Z020 integrates a fully programmable dual-core ARM Cortex-A9 processor (Processing System, PS) alongside a hardware-programmable Artix-7 FPGA (Programmable Logic, PL). Due to its FPGA part, the Zynq-7000 benefits from flexibility, reconfigurability, parallel processing, and real-time hardware modifications at the gate level without chip replacement. The complexity of HDL programming is mitigated by the MATLAB/Simulink HDL Coder add-on, which enables automatic generation of IP cores from Simulink models.

Additionally, the ZedBoard includes a low-pin-count FPGA Mezzanine Card (LPC-FMC) interface, offering 68 single-ended I/O pins. This expansion interface allows connection to external modules, such as the digital I/O for controlling the voltage source inverter (VSI).

B. Two-Level Voltage Source Inverter

To implement vector control in an electric drive system, a four-layer printed circuit board (PCB) was designed and manufactured. The PCB is capable of powering either two independent three-phase motors, a single six-phase motor, or a multiple three-phase motor configurations.

The power section of the PCB is electrically isolated from the control section using an isolation barrier composed of quad-channel digital isolators ADuM140/1 from Analog Devices. This isolation barrier provides galvanic isolation, ensuring the ZedBoard is protected from the high-power section of the PCB. The digital interface between the PCB and the ZedBoard platform is established via the FMC connector. Because directly soldering an FMC connector onto the PCB is complex and costly, the AD-DAC-FMC-ADP adapter from Analog Devices is used. This adapter converts signals from the LPC-FMC connector into two TE Connectivity 6469028-1 connectors on the PCB.
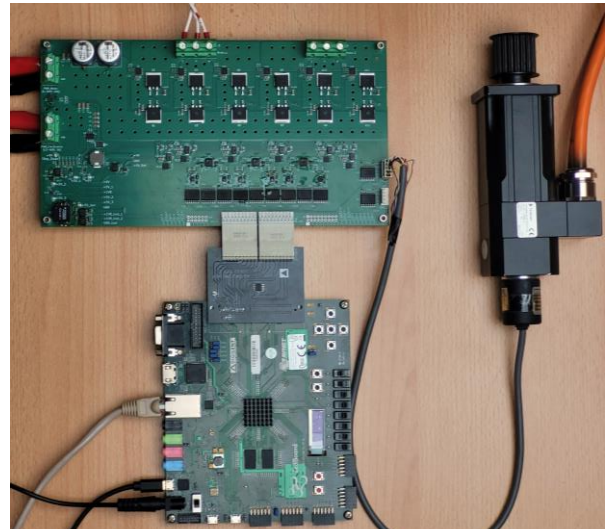

Fig. 3.   Complete setup of the proposed rapid prototyping platform

The power management system operates at a supply voltage of 15 to 60 V with a maximum current of 5 A. Meanwhile, the two-level voltage source inverter supports an output range of 0 to 60 V, drawing up to 20 A. The PCB integrates all key components needed for motor control using the ZedBoard. It includes two independent two-level voltage source inverters, each built with six Infineon IPB038N12N3G MOSFETs arranged in three legs. These transistors are controlled by Infineon 2EDL8024GXUMA1 dual-channel MOSFET drivers. A dead time of 200 ns prevents short circuits within an inverter leg, considering that the IPB038N12N3G MOSFETs exhibit a total turn-off delay and fall time of 91 ns.

Phase current measurement is handled by Allegro Microsystems ACS724LLCTR-10AB-T SMD Hall-effect current sensors, covering a -10 A to 10 A range. Their analog output is sent to Analog Devices AD4020 ADC, which offers 20-bit resolution and a 1.8 MSPS conversion rate. Measuring current multiple times per FOC cycle, combined with high resolution, enhances motor diagnostics, and expands testing possibilities. The ADC conversion result is transmitted to the ZedBoard platform via SPI communication. [10]

IV. SOFTWARE DEVELOPMENT APPROACH

A. Traditional Xilinx FPGA Programming Approach

Vivado Design Suite is a development environment by AMD Xilinx that provides tools for embedded system development using FPGAs, covering both hardware and software integration. The first step in the traditional workflow in Vivado is to create a project and specify the target FPGA device. Next, HDL files are linked with IP core blocks within the block design using the IP Integrator. Sampling periods of each IP core are configured and an XDC constraints file is prepared, specifying pin assignments.

Once these steps are completed, synthesis translates HDL code into a logical representation for the FPGA, resulting in a synthesized netlist. The next step is implementation, where logical blocks are mapped to specific FPGA LUT resources. The design components are then connected through signal routing, and a timing analysis is performed to verify that the system meets the required timing constraints. Finally, a bitstream is generated and uploaded to the FPGA using Vivado Hardware Manager via USB JTAG.

However, this traditional workflow described above is not well-suited to rapid development and testing of control algorithms, mainly due to the HDL programming effort and the time-consuming process. Therefore, this paper introduces an alternative, faster, and more efficient method.

B. Automated Code Generation Approach

To generate HDL code for the PL section, the MATLAB/Simulink HDL Coder add-on is used. The HDL Workflow Advisor guides the automatic code generation process. First, Xilinx Vivado is set as the synthesis tool, performing necessary tasks in the background. This step also defines the target processing unit, pin assignments, and the target frequency of the generated IP core. Second, the Simulink model is checked for sample-time conflicts or algebraic loops. Third, the actual IP core is generated for the PL section of the

Zynq XC7Z020 SoC. Designers can choose between VHDL or Verilog as the target programming language or generate a traceability report highlighting the timing-critical path.

The final stage is the Embedded System Integration process, performed in step 4 of the HDL Workflow Advisor. In step 4.1, a Vivado project is automatically created, including the necessary IP cores integrated into the block design, and an XDC constraints file. The next phase utilizes another MATLAB Simulink extension, Embedded Coder. In step 4.2, it automatically generates C code for the ARM Cortex-A9 processor from a designated portion of the Simulink model. Additionally, a Simulink Software Interface Model is generated, facilitating real-time communication between the ARM processor and MATLAB/Simulink on a PC via External Mode. In steps 4.3 and 4.4, FPGA bitstream generation and upload are completed.

Communication between the IP core in the PL section and the processor in the PS section can utilize AXI4-Lite for low-volume, register-based transfers or combine AXI4-Lite with AXI4-Stream for high-volume, high-speed data transfers. When data rates of approximately 2 MB/s or more are required, AXI4-Stream with a Direct Memory Access (DMA) controller is recommended, allowing efficient block transfers to DDR memory for offline retrieval or via specialized protocols. In this scenario, AXI4-Lite can be used concurrently for parameter tuning and control signal manipulation.

Alternatively, Simulink can perform real-time tuning and data exchange using External Mode over TCP/IP. However, this method is limited by its throughput, typically ranging from few hundreds of kB/s to a few MB/s, due to protocol overhead. Consequently, AXI4-Lite alone often suffices in scenarios requiring only moderate transfer rates of up to several MB/s. Fig. 4 illustrates a high-level architecture diagram showing streaming data transfers between the processor and FPGA fabric on the Zynq platform.
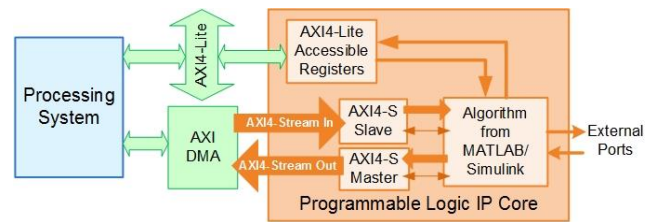

Fig. 4. High-level architecture of AXI4-Stream and AXI4-Lite interfaces (from automatically generated IP core documentation in HDL Coder)

V. FOC CONTROL EXPERIMENT

The FOC for the PMS motor TGT2-0032-30-24 has been implemented in Simulink. The algorithm is divided into six IP cores, which are interconnected in a single Vivado project.

The first IP core, running at 100 MHz, manages SPI communication with three 20-bit ADCs measuring the phase currents at a sampling rate of 1 MSPS. This data is then processed in the second IP core, where it is converted from 20-bit ADC values to a current range of -10 A to 10 A. Additionally, the average of 50 measured samples is computed. The resulting average is provided to the FOC algorithm at a frequency of 20 kHz, which is also the PWM frequency.

The next two IP cores handle signal processing from an incremental encoder ES 28-6-1024-05-D-R. They compute sine and cosine values of the rotor's electrical position for the Park transformation, detect the direction of rotation, and calculate the RPM. The FPGA executes the IP core handling encoder signals A, B, and M at 100 MHz. The high frequency allows the RPM calculation to be based on counting pulses: a counter resets at every rising edge of the A signal and measures the time between two consecutive A pulses. The RPM is then computed using the formula:

$$RPM = \frac{60}{C_A * 10e^{-9} * 1024} \tag{1}$$

where C_A is the counter value between A pulses, $10e^{-9}$ represents the counter clock period, 1024 is the encoder resolution, and 60 converts seconds to minutes.

Another IP core contains the FOC control algorithm, where phase currents are first transformed from abc to dq coordinates using Clarke and Park transformations. A PI controller controls I_d for flux control, while another PI controller regulates I_q for torque control. The time constants of the controllers match the RL circuit time constant of the PMSM motor. During the rotor alignment phase, a step change is applied to I_d while I_q remains at zero, and a current probe is used to fine-tune the PI gains. The algorithm then performs inverse Park and Clarke transformations, followed by space vector PWM (SVPWM) to generate gate drive signals for the MOSFETs. The VSI converts DC power into AC waveforms for motor operation.
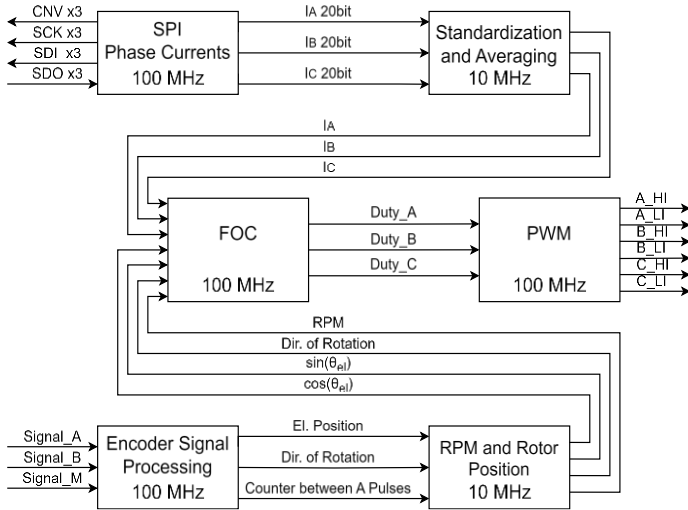
Fig. 5.   Connection diagram of the individual IP cores

The FOC IP core runs at 100 MHz. To ensure all calculations are completed on time, delay elements are introduced to synchronize operations. The execution time for one FOC cycle is 100 ns, corresponding to a 10 MHz computation rate. This high computational frequency of the FOC algorithm guarantees a fast response to load variations and minimizes control latency. Additionally, the high sampling rate enables oversampling of currents and position feedback within a single PWM period, thereby reducing measurement noise and enhancing estimation

accuracy. Furthermore, this rapid internal loop operation facilitates future upgrades, including higher switching frequencies, various PWM generation methods (e.g., half-reload PWM), or simultaneous multi-motor control, thus extending the platform's versatility and longevity.

The sixth and final IP core generates center-aligned PWM signals that drive the MOSFET switches of the two-level voltage inverter. The PWM switching frequency is set to 20 kHz. The connection diagram of the individual IP cores is shown in Fig. 5.

Additionally, a Simulink interface model has been developed using Embedded Coder. This interface enables real-time FOC control adjustments and allows logging of various internal signals via External Mode. The rapid prototyping platform thus provides an effective environment for testing and developing motor control strategies. A sample Simulink interface model is shown in Fig. 6.
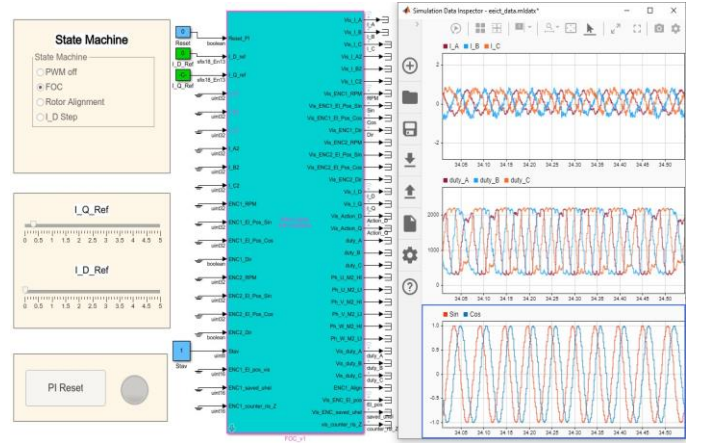

Fig. 6. Simulink interface model

Fig. 7 shows the measured phase current waveforms of the unloaded PMSM motor TGT2-0032-30-24, acquired at the maximum achievable sampling rate of 2 kHz (approximately 176 kB/s) using AXI4-Lite and External Mode, as experimentally determined in this study.
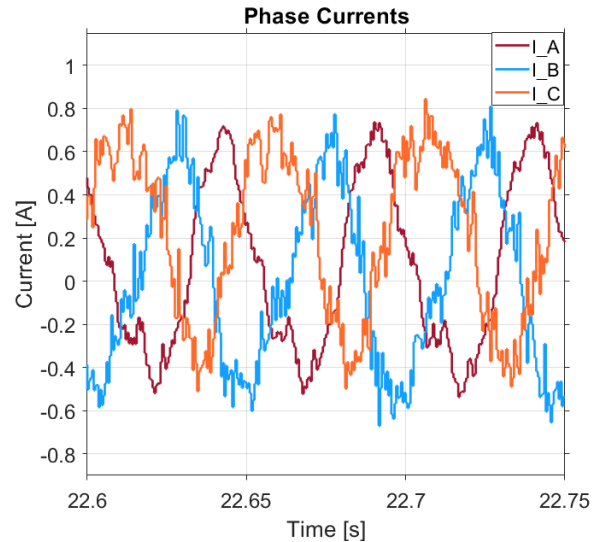

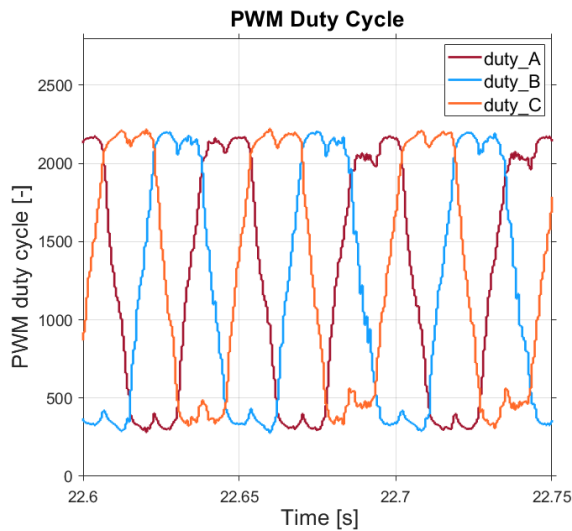Fig. 7.   Phase currents waveforms of the unloaded PMSM TGT2-0032-30-24

Fig. 8.   PWM duty cycle waveforms from the FOC in the range from 0 to 2500

The resulting duty cycle waveforms from the FOC algorithm for PWM generation in the range from 0 to 2500 are shown in Fig. 8.

VI. Conclusion

This paper presents a cost-effective alternative to existing rapid prototyping platforms for electric motor control. The proposed platform consists of a combination of a ZedBoard and a custom-designed two-level voltage source inverter. The ZedBoard platform includes the SoC Zynq 7000 XC7Z020 and peripherals. The SoC Zynq 7000 integrates an FPGA with an ARM processor, providing substantial computational power. Communication between the Artix-7 FPGA and the ARM Cortex-A9 processor is managed via the AXI4-Lite interface. Additionally, the real-time communication via External Mode between the ARM processor and Simulink allows for seamless monitoring and control of algorithm variables during operation, enabling efficient system tuning and debugging.

The designed and manufactured PCB includes phase current sensors, AD converters, connectors for signal transmission and encoder power supply, and the voltage inverter itself, capable of controlling either two three-phase or one six-phase electric motor. The inverter on the PCB is designed for a maximum DC output of 20 A and a DC bus voltage of 60 V. The board can accommodate more computationally powerful devices than the SoC Zynq 7000 XC7Z020 on the ZedBoard. The newly developed board could also support and test the upcoming AMD Versal Gen 2 SoC. The AMD Versal Gen 2 SoC combines high-performance integrated CPUs with programmable logic FPGA and AI engines and is set to be released in the second quarter of 2025.

A field-oriented control implementation for the PMSM motor TGT2-0032-30-24 was demonstrated at the end of the paper to validate the functionality of the developed rapid prototyping platform. All control algorithm components and peripheral handling mechanisms were implemented in six Simulink models. Using the MATLAB/Simulink HDL Coder

extension, IP cores were automatically generated for the FPGA from these models. A key advantage is the ability to modify any of these IP cores. This flexibility allows for changes in modulation type, real-time current signal processing, implementation of computationally demanding control algorithms, multi-motor control, adjustments of PWM frequency and type, and many more modifications.

These features make the developed rapid prototyping platform a suitable, cost-effective, and user-friendly tool for developing and testing control algorithms.

References

[1]   CARPIUC, S. and VILLEGAS, C. *FPGA-based rapid control prototyping of permanent magnet synchronous motor servo drives.* In: PCIM Europe 2019; International Exhibition and Conference for Power Electronics, Intelligent Motion, Renewable Energy and Energy Management. Nuremberg, Germany, 2019, pp. 1–6.

[2]   DUFOUR, C., LAPOINTE, V., BELANGER, J. and ABOURIDA, S. *Hardware-in-the-loop closed-loop experiments with an FPGA-based permanent magnet synchronous motor drive system and a rapidly prototyped controller.* In: 2008 IEEE International Symposium on Industrial Electronics. Cambridge, UK, 2008, pp. 2152–2158. DOI: 10.1109/ISIE.2008.4677105.

[3]   KRISHNAN, R. *Permanent Magnet Synchronous and Brushless DC Motor Drives.* Online. Boca Raton: CRC, c2010. ISBN 978-0-8247-5384-9.

[4]   HAVENS, Brian C. *Motor Control Microcontroller Performance Comparison.* Online. 2018. Available from: https://www.brianchavens.com/2018/09/20/motor-control-microcontroller-performance-comparison/. [Accessed 2025-03-16].

[5]   TEXAS INSTRUMENTS. *TMS320F2837xD Dual-Core Real-Time Microcontrollers Datasheet (Rev. P).* Online. 2013, 2024. Available from: https://www.ti.com/product/TMS320F28377D. [Accessed 2025-03-16].

[6]   STMICROELECTRONICS. *RM0090 Reference Manual (Rev. 21): STM32F405/415, STM32F407/417, STM32F427/437 and STM32F429/439 advanced Arm®-based 32-bit MCUs.* Online. 2024. Available from: https://www.st.com/en/microcontrollers-microprocessors/stm32f4-series/documentation.html#. [Accessed 2025-03-16].

[7]   AMD. *Zynq 7000 SoC Technical Reference Manual (v1.14).* Online. 2023. Available from: https://docs.amd.com/r/en-US/ug585-zynq-7000-SoC-TRM/Zynq-7000-SoC-Technical-Reference-Manual. [Accessed 2025-03-16].

[8]   SPEEDGOAT. *Real-Time Target Machines.* Online. Available from: https://www.speedgoat.com/products-services/real-time-target-machines. [Accessed 2025-03-16].

[9]   DSPACE. *Rapid Prototyping Systems.* Online. Available from: https://www.dspace.com/en/pub/home/applicationfields/foo/prototyping-systems.cfm. [Accessed 2025-03-16].

[10]   KOZUMPLÍK, Miroslav. *Řízení servopohonu pomocí platformy Zedboard (Servo-Drive Control by Zedboard Platform).* Online. Master's Thesis, supervised by Libor Veselý. Brno: Brno University of Technology, Faculty of Electrical Engineering and Communication, Department of Control and Instrumentation, 2024. Available from: https://hdl.handle.net/11012/245974. [Accessed 2025-03-15].

How to Measure Induction Machines: A Practical Methodology

1st Martin Světlík
Dep. of Power Electrical
and Electronic Engineering
Brno University of Technology, FEEC
Brno, Czech Republic
xsvetl06@vutbr.cz

2nd Jan Bárta
Dep. of Power Electrical
and Electronic Engineering
Brno University of Technology,FEEC
Brno, Czech Republic
bartaj@vutbr.cz

Abstract—The accurate measurement of induction machines is crucial for assessing their performance, efficiency, and reliability. This paper presents a practical methodology for measuring induction machines. The proposed method encompasses multiple test scenarios, including nominal load tests, load variation tests, and reduced voltage tests. Key parameters such as stator resistance, torque, power factor, and efficiency are systematically measured and analyzed. The measurement setup is designed to ensure precise data acquisition while minimizing errors due to thermal variations. The results provide valuable insights into machine losses and efficiency distribution, facilitating further optimization in industrial applications.

Index Terms—Induction machines, Industry standards, Measurement techniques

I. Introduction

Induction machines are extensively used in industrial applications due to their durability and cost-effectiveness. Precise performance evaluation is crucial for optimizing their operation, improving energy efficiency, and ensuring adherence to industry standards. Standardized testing procedures provide a comprehensive framework for assessing machine parameters [1]–[5]. Unlike studies that emphasize post-processing techniques, this research focuses on direct measurement methodologies, ensuring high accuracy and repeatability in real-time data acquisition.

The primary objective of this study is to present a structured methodology for measuring induction machines, focusing on real-time data acquisition and loss analysis. Unlike studies emphasizing post-processing techniques [6], [7], this work prioritizes direct measurement approaches to ensure high accuracy and repeatability. The methodology includes multiple test procedures, such as nominal load testing, load variation analysis, and reduced voltage testing. These procedures provide a holistic view of machine performance, aiding in loss identification and efficiency enhancement [8], [9].

Several studies have explored equivalent circuit parameter

estimation through finite element analysis [10]–[12]. However, practical measurements remain essential for validating simulation-based approaches and ensuring real-world accuracy. Empirical testing remains a cornerstone in induction machine research, as theoretical models often require experimental verification to account for real-world operating conditions [13]–[15]. This study contributes to the existing body of research by outlining a systematic measurement framework applicable to both laboratory and industrial environments. The approach aims to improve measurement accuracy while ensuring repeatability and reliability, ultimately contributing to better machine design and energy-efficient operation.

II. Measurement Methodology

This chapter describes the methodology used for measuring induction and synchronous machines. The flowchart illustrating this methodology is shown in Fig. 1. All measurements, except for the initial resistance measurement, must be performed on a thermally stabilized machine. As a thermally stabilized machine, consider a machine whose temperature change is below 1 K in half an hour. To guarantee this condition, the ambient temperature must be also stabilize.

Before starting the measurement, it is essential to determine the resistance of each stator winding at ambient temperature.

A. Nominal Load Test

The purpose of the nominal load test is, as its name suggests, to analyze the machine under rated operating conditions—i.e., at rated power, nominal torque, and rated speed. Since the test must be conducted on a warmed-up machine, it is necessary to increase its load to at least the nominal value. For the purpose of accelerate the heating process, significantly reducing the time required for thermal stabilization, it is even possible to overload a tested machine. However, if the warm-up is performed by overloading, the load must be reduced to the nominal value before the measurement to ensure steady-state temperature conditions. The measurement is repeated ten times within a ten-second interval, and the measured data are summarized in Table I. These values are then used for post-processing, including, for example, the calculation of nominal efficiency.
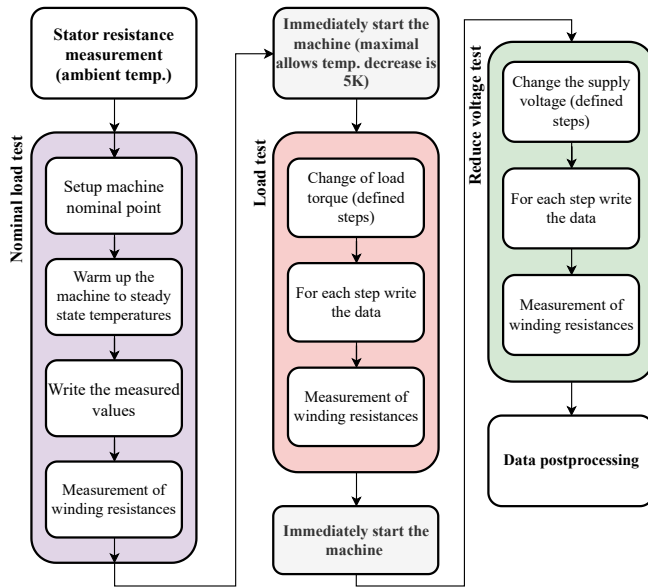
Fig. 1. Block diagram of the measurement setup.

TABLE I
TABLE OF MEASURED VALUES

Variable	Unit Mark
Torque	T_{mech}
Speed	s
Currents of all three phases	I_1, I_2, I_3
Voltage of all three phases	V_{12}, V_{23}, V_{31}
Input frequency	f
Output power	P_{mech}
Input power	P_{in}
Power factor	$\cos\varphi$
Winding temperature	T_{win}
Frame temperature	T_{Fr}
Ambient temperature	T_{amb}

Immediately after the measurement at the nominal operating point, it is essential to stop the machine and measure the resistance of each stator winding. This should be done three times: at 30 seconds, 60 seconds, and 90 seconds after stopping. The table used for this measurement is presented in Tab. II.

TABLE II
RESISTANCE VALUES OVER TIME

t (s)	R_{12} (Ω)	R_{21} (Ω)	R_{31} (Ω)
30			
60			
90			

The machine must be restarted and loaded immediately after the resistance measurement. Immediately start ensures, the maximum allowable temperature drop between this measurement and the next test, the load test, is 5K.

B. Load test

The second measurement is the load test, which consists of measuring the machine's performance under different load torques. The measurement points are summarized in Tab. III. All measurements are taken sequentially without waiting for the machine's temperatures to reach steady state. The recorded data are again summarized in Tab. I. For each measurement point, ten measurements are taken at one-second intervals and averaged during post-processing.

TABLE III
MEASUREMENT RESULTS

Num of measurement	Load	
1	1.25	
2	1.10	
3	1.00	T_{nom}
4	0.75	
5	0.50	
6	0.25	

As after the nominal load test, resistance must be measured immediately after measuring the last point. The procedure remains the same, so Tab. II can be used again for recording the measurements. These values also serve as the initial data for the reduced voltage test.

The machine must be restarted immediately after the resistance measurement to ensure all measurements are taken under warmed-up conditions.

C. Reduce voltage test

This final test is required for determining the machine's efficiency. During this test, the machine operates without load but remains coupled to the system. The coupling is maintained because it is necessary for speed measurement. Tab. IV summarizes the voltage levels applied during the test. The second measurement point in this table corresponds to the no-load test, as the machine is supplied with nominal voltage. For each point, ten measurements are taken at one-second intervals, similar to the previous cases.

The recorded data are again summarized in Tab. I, although torque and output power measurements are not necessary. However, since the measurement setup is fixed and the torque and power measurement is a default feature of the device used for speed measurement, they are recorded nonetheless. The final resistance measurement immediately after completing the reduced voltage test is essential to successfully conclude the testing procedure. The same measurement procedure is followed, and Tab. II can be used again for recording the values. After successfully completing all measurements, data post-processing can begin. However, this aspect is beyond the scope of this paper.

III. MEASUREMENT

This chapter describes the measured machine as well as the measurement setup, including a description of the devices

TABLE IV
MEASUREMENT RESULTS

Num of measurement	Voltage	
1	1.10	
2	1.00	
3	0.95	
4	0.90	U_n
5	0.60	
6	0.50	
7	0.40	
8	0.30	

Fig. 3. Block diagram of measurement setup.

used. Additionally, photographs of the machine and the test bench setup are presented.

A. Measured machine

The machine selected for measurement, based on the presented methodology, is shown in Fig. 2. It is a squirrel cage induction machine with a low rated output power of 35 W. Its nominal torque is 0.115 Nm at a rated speed of 2895 rpm. For a more detailed analysis and better control of machine boundary conditions, PT 1000 thermocouples have been placed in the stator slot of each phase.

Fig. 4. Detail photo of coupled machine

the primary measurement devices. The measurement setup includes the Yokogawa **WT 3000** power analyzer, the Magtrol unit type **6400**, a computer, and a three-phase sine wave generator. This setup enables the acquisition of all required data, particularly due to its connection to the computer, ensuring precise and efficient data collection.

Fig. 2. Manufactured machine

B. Measurement setup

The measurement setup is designed to capture all required values. A block diagram of this setup is shown in Fig. 3. As illustrated in the diagram, the power analyzer, temperature measurement unit, and torque sensor are all connected to a computer. This configuration allows for simultaneous data acquisition and direct storage into a single file, facilitating more efficient post-processing. Furthermore, detailed photographs of the test bench setup with the coupled machine are provided in Fig. 4. The image also shows the eddy current brake, the Torquemaster measurement shaft (tensometer) type **M 204**, and the National Instruments temperature sensing card type **NI-9219**. Additionally, Fig. 5 presents an image showcasing
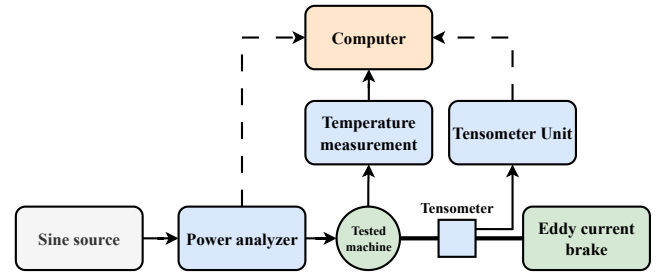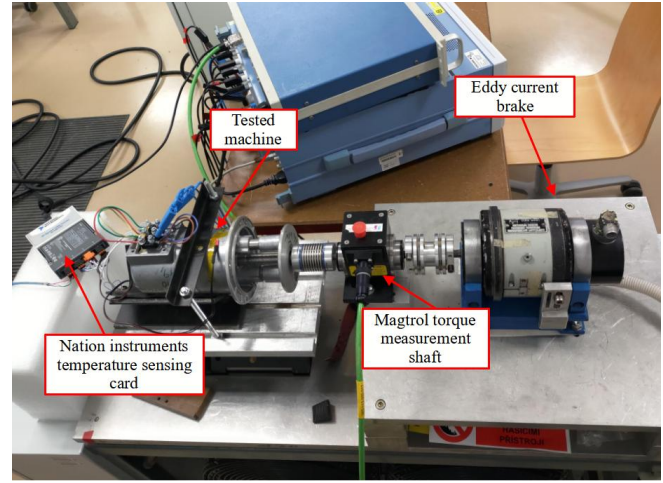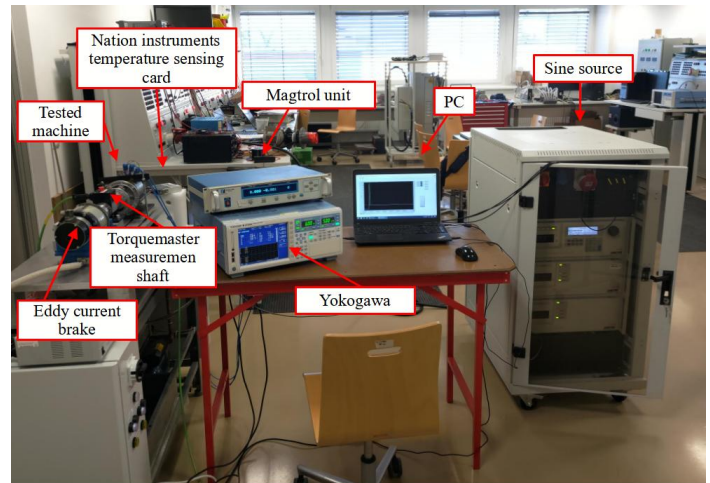

Fig. 5. Photo of measurement setup and used devices

IV. Results of measurement

Since the post-processing of the measured data is beyond the scope of this paper, only the raw, uncorrected data are presented in this chapter. The measurement results are summarized in Tab. V. In practice, the measured values need to be corrected for temperature variations based on the resistance of the winding. However, as stated earlier, post-processing is outside the scope of this work. In Table V, the values

TABLE V
TABLE OF POWER AND EFFICIENCY CORRECTIONS

Symbol	Unit	Percentages of Nominal Load					
		125%	115%	100%	75%	50%	25%
P_mech	W	43.75	40.25	35	26.25	17.5	8.75
s	%	4.20	3.93	3.53	2.8	2.07	1.43
P_1	W	85.1	81.17	74.48	63.43	52.67	43.56
P_Fe	W	8.69	8.75	9.14	9.03	9.21	9.35
$P_\text{f,a}$	W	12.36	12.39	12.41	10.79	10.89	10.18
P_Cu	W	17.03	16.66	16.18	15.55	15.40	15.11
P_r	W	2.49	2.19	1.75	1.09	0.58	0.27
$\cos\varphi$	-	0.55	0.53	0.49	0.43	0.36	0.30
η	%	51.41	49.59	46.99	41.38	33.22	20.08

for mechanical output power P_mech, slip s, input power P_1, core losses P_Fe, friction and additional losses $P_\text{f,a}$, stator Joule losses P_{Cu}, rotor losses P_r, power factor $\cos\varphi$, and efficiency η are presented for various load levels.

Based on the measured data, the efficiency at the nominal point is **46.99 %**, which is a reasonable value for small electric machines. Loss distribution analysis, as shown in Fig. 6, indicates that the dominant loss component is stator Joule losses, which arise due to high stator resistance caused by conductor size limitations. In small machines, high resistive losses in the stator are typical due to limited conductor cross-sections.
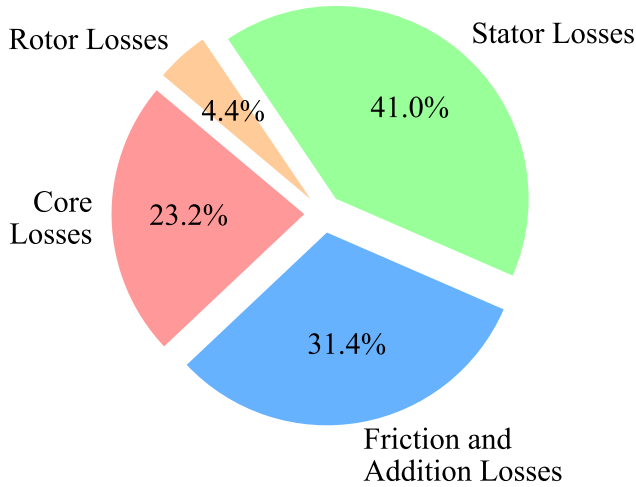

Fig. 6. Percentage distribution of losses at the rated point of machine

V. Conclusion

This paper has presented a structured methodology for measuring induction machines. The proposed approach ensures an accurate assessment of machine parameters while maintaining repeatability and minimizing measurement errors. The results emphasize the importance of thermal stability and precise resistance measurement in determining efficiency and power losses.

The findings demonstrate that the primary contributors to losses in small induction machines are stator Joule losses, which arise due to the limited cross-sectional area of the stator conductors. By implementing the precise measurement techniques outlined in this study, engineers can optimize machine performance and reduce energy consumption. The methodology provides a solid foundation for improving the design and operation of induction machines, contributing to enhanced energy efficiency.

Future work will focus on describing the corrections. These corrections are essential for refining the measurement process and ensuring that results accurately reflect real-world operating conditions. By addressing these corrections, the methodology can be further refined to improve the precision and reliability of measurements across a broader range of induction machine types.

References

[1] ČSN EN 60034-2-1 ed. 2, *Rotating Electrical Machines - Part 2-1: Standard Methods for Determining Losses and Efficiency from Tests.* Czech Standards Institute, 2007.

[2] J. Holtz, "Sensorless control of induction machines—with or without signal injection?" *IEEE Transactions on Industrial Electronics*, vol. 54, no. 1, pp. 7–30, 2008.

[3] P. Vas, *Sensorless Vector and Direct Torque Control.* Oxford University Press, 1998.

[4] A. Boglietti, A. Cavagnino, M. Lazzari, and F. Profumo, "The safety margins in the thermal analysis of induction motors," *IEEE Transactions on Industry Applications*, vol. 45, no. 2, pp. 712–718, 2009.

[5] W. Xu, Z. Zhang, and J. Zhu, "Loss evaluation and efficiency analysis of induction machines based on finite-element method," *IEEE Transactions on Magnetics*, vol. 49, no. 7, pp. 4029–4032, 2013.

[6] T. G. Habetler and R. G. Harley, "Complete characterization of induction machines: Identification, parameter estimation, and state estimation," *IEEE Transactions on Industrial Electronics*, vol. 39, no. 3, pp. 460–468, 1992.

[7] M. Villani, F. Bianchi, and M. Fabri, "A comprehensive loss model for high-speed induction machines including harmonic effects," *IEEE Transactions on Industrial Electronics*, vol. 63, no. 2, pp. 697–707, 2016.

[8] A. Persson, "Analysis of measurement methods for efficiency evaluation of induction motors," *IEEE Transactions on Industry Applications*, vol. 53, no. 4, pp. 3421–3430, 2017.

[9] G. Joksimović, "Condition monitoring of induction machines: A comprehensive review," *IEEE Transactions on Energy Conversion*, vol. 34, no. 2, pp. 624–634, 2019.

[10] Z. Ling, L. Zhou, S. Guo, and Y. Zhang, "Equivalent circuit parameters calculation of induction motor by finite element analysis," *IEEE Transactions on Magnetics*, vol. 50, pp. 833–836, Feb. 2014.

[11] A. Belahcen and L. A. Pellikka, "Computation of losses in electrical machines using finite element method," *IEEE Transactions on Magnetics*, vol. 47, no. 7, pp. 1796–1803, 2011.

[12] Z. Zhu, "Electrical machine analysis using finite element method," *IEEE Transactions on Magnetics*, vol. 46, no. 8, pp. 3315–3320, 2010.

[13] K. Shao, "Experimental verification of finite element models for induction motors," *IEEE Transactions on Magnetics*, vol. 48, no. 2, pp. 459–466, 2012.

[14] J. Faiz, "Comparison of analytical and numerical solutions for induction machine parameter determination," *IEEE Transactions on Energy Conversion*, vol. 18, no. 1, pp. 4–11, 2003.

[15] S. Chapman, *Electric Machinery Fundamentals*.   McGraw-Hill, 2011.

Design and Optimization Workflow for Industrial Induction Machines

1st Martin Světlík
Dep. of Power Electrical
and Electronic Engineering
Brno University of Technology, FEEC
Brno, Czech Republic
xsvetl06@vutbr.cz

2nd Jan Bárta
Dep. of Power Electrical
and Electronic Engineering
Brno University of Technology,FEEC
Brno, Czech Republic
bartaj@vutbr.cz

Abstract—The design and optimization of industrial induction machines require a systematic approach to meet performance, efficiency, and manufacturing constraints. This paper presents a structured workflow that integrates finite element methods, analytical modeling, and optimization techniques to enhance machine design. The methodology consists of defining manufacturer constraints, developing electromagnetic and thermal models, and optimizing machine parameters using the Non-Dominated Sorting Genetic Algorithm II. The proposed approach ensures high efficiency, minimal losses, and manufacturability while reducing computational time. A case study demonstrates the effectiveness of the workflow and highlights significant improvements in machine performance after optimization.

Index Terms—Cost-effectiveness, Induction machines, Industrial applications

I. Introduction

Induction machines, widely employed in industrial applications such as pumps, fans, compressors, and conveyor systems, are known mainly for their robustness and reliability. They are particularly favored for their durability and ease of maintenance, making them a key component in various sectors, including manufacturing, energy generation, and transportation [1]. Despite their widespread use, achieving an optimal balance between performance, cost, and manufacturability remains a significant challenge for engineers and designers. The complexity of these machines, coupled with the need to meet stringent performance criteria, poses difficulties in the design and manufacturing process [2].

Traditional design approaches often rely on empirical formulas and analytical calculations, which offer a quick estimation of key machine parameters, such as torque, efficiency, and power losses [3], [4]. While these methods have been successful for decades, they fail to provide the high level of precision required for modern, high-efficiency designs, especially as the demand for energy-efficient and cost-effective solutions grows [5], [6]. The limitations of empirical models arise from their inability to account for the complex, nonlinear behavior of

induction machines under various operating conditions [7].

To overcome these challenges, advanced computational techniques such as Finite Element Method (FEM) simulations have gained popularity for their ability to provide accurate, detailed electromagnetic performance evaluations [8], [9]. FEM allows for the modeling of complex geometries and the calculation of electromagnetic fields, enabling precise predictions of machine performance, including magnetic flux density distribution, torque generation, and power losses [10], [11]. However, the primary drawback of FEM is its computational expense, particularly when numerous design iterations are required [12], [13]. As such, FEM simulations are often reserved for the final design stages or used in conjunction with faster, less computationally intensive methods for earlier design phases [14], [15].

To mitigate the computational demands of FEM simulations, analytical models are commonly employed in the initial stages of machine design [16]. These models, based on simplified assumptions and approximations, provide a quicker way to estimate machine parameters such as the electrical and mechanical power outputs, torque characteristics, and efficiency levels. Analytical methods, when combined with FEM simulations, can significantly reduce the time spent on design iterations, allowing for faster optimization and prototyping [17].

Moreover, optimization techniques have emerged as a critical tool for refining induction machine designs. Among these, the Non-Dominated Sorting Genetic Algorithm II (NSGA-II) stands out for its ability to solve multi-objective optimization problems without requiring predefined weighting factors for the objectives. NSGA-II allows the simultaneous optimization of several design parameters, such as efficiency, cost, and thermal performance, by generating a set of optimal solutions, known as the Pareto front [6], [11]. This algorithm has been successfully applied to the optimization of induction machines, enabling designers to achieve the best trade-offs between competing objectives [16], [18].

II. Methodology

This chapter presents the whole process of designing an induction machine in the step. This process consists of four main steps, **Manufacturer's requirements and limitations**,

Designing itself, **Optimization** and **Manufacturing documentation**. These steps, enhanced by the machine's manufacturing process, are encapsulated in the methodology flow chart presented in Fig.,1. This paper does not primarily address the machine's manufacturing, so this aspect is not elaborated upon further. The rest of necessary steps are described in more detail in separate chapters. The proposed methodology integrates the
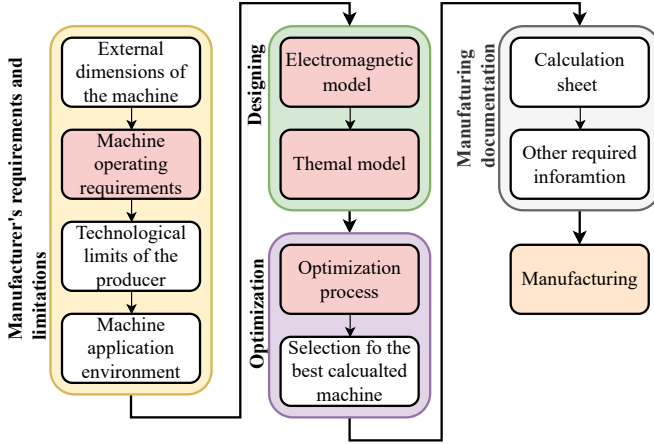

Fig. 1. Flow chart of proposed methodology

Finite Element Method (FEM) with analytical calculations and optimization algorithms, specifically the Genetic Algorithm (GA). However, in certain stages of the process, the application of empirical formulas proves beneficial. These formulas enhance result accuracy while also facilitating a more straightforward manufacturing process for machine components and the overall assembly. Simplified manufacturing and assembly procedures contribute to a reduction in the total cost of the machine.

The FEM is utilized for the analysis of the electromagnetic model. While FEM is generally regarded as a highly accurate method, this level of precision comes at the cost of significant computational time. Nevertheless, it enables the detailed evaluation of machine losses through advanced post-processing operations. These losses serve as critical input parameters for thermal analysis, making their precise computation essential.

In addition to FEM, analytical calculations are also employed in setting up the model. Specifically, analytical methods are used to determine the resistance of the stator winding and rotor bars. For calculating the stator winding fill factor, both analytically derived equations and empirical formulas can be utilized. The use of empirical calculations enhances the reliability of the model, as the winding design is one of the most critical aspects of the entire process. These formulas allow engineers to operate within safe design limits, ensuring the maximum achievable fill factor for the given machine specifications. The development of an accurate electromagnetic model requires extensive knowledge and expertise, as multiple factors must be carefully considered to obtain precise and reliable results.

The thermal model is analyzed exclusively using analytical

methods. Unlike FEM, these methods offer significantly faster computation times. However, they are often considered less accurate due to the simplifications inherent in the applied formulas and the difficulty in accounting for nonlinearities present in real machines. Despite these limitations, experienced designers can achieve high accuracy, with errors typically within a few percentage points, particularly in steady-state analyses. Furthermore, the substantial reduction in computation time outweighs the minor accuracy loss, making analytical methods a highly efficient approach for thermal modeling.

Both the electromagnetic and thermal models are combined and used in the optimization process. The optimization is carried out using the Non-Dominated Sorting Genetic Algorithm II (NSGA II), which searches for the model that provides the best efficiency while meeting the necessary parameters. This method is particularly useful when there are multiple objectives to consider and does not require assigning weights to those objectives. However, it can be computationally demanding, especially with large groups of solutions and many objectives. Additionally, the algorithm's performance depends heavily on how its parameters are set.

III. Manufacturer's requirements and limitations

The first stage involves defining the manufacturer's requirements and constraints. The manufacturer typically specifies the maximum outer diameter, axial height, and other dimensional limits of the machine. Additionally, the operational requirements, including rated speed and rated output power, are established. Based on these parameters, the nominal torque and overload capability are determined. The relationship between these parameters is illustrated in Fig. 2. A thorough
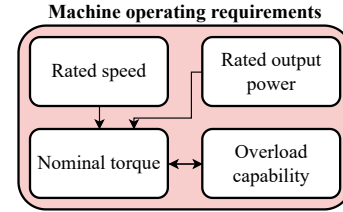

Fig. 2. Machine operating requirements flow chart

understanding of the manufacturer's technological limitations is crucial for the design process. The lack of this knowledge could result in a machine design that the manufacturer cannot produce, thus increasing the overall cost of the methodology. These limitations generally include the maximum feasible stator slot fill factor, the minimum allowable air gap length, and the degradation of the electromagnetic properties of materials used in the stator and rotor assembly.

Additionally, it is essential to consider the machine's operating environment. For instance, certain conditions may prohibit the use of a fan for frame cooling or expose the machine to high ambient temperatures, which must be accounted for during the design phase. All these factors serve as fundamental inputs for both the electromagnetic and thermal models.

For the purpose of the presented methodology, a machine

with a rated speed of **2930 rpm** and an output power of **40 W** has been selected. These specifications result in a nominal torque of **0.114 Nm**.

IV. DESIGNING

After gathering all the necessary inputs for the design process, the next step is to set up the electromagnetic and thermal models. This chapter will first describe the setup of the electromagnetic model, followed by the thermal model.

A. Electromagnetic model

The key inputs required for the electromagnetic model, along with the major outputs obtained from it, are summarized in Fig. 3. As illustrated in this block diagram, it is essential to define the stator winding, the geometry and number of rotor bars, the stator slot geometry, and the number of pole pairs (typically linked to the nominal speed). Additionally, the moment of inertia, which depends on the rotor and shaft geometry, must also be considered. The outputs of the electro-
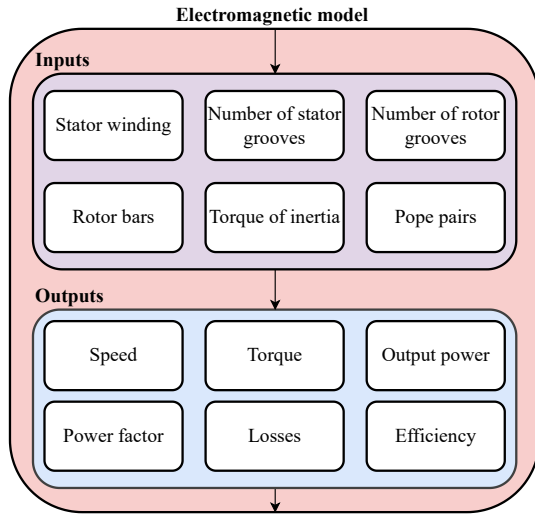
Fig. 3. Electromagnetic model flowchart

magnetic model play a crucial role in evaluating the machine's performance. It is essential to accurately assess stator winding losses, rotor bar losses, and core losses. These loss components serve as essential inputs for the thermal network, making precise loss estimation a key aspect of the modeling process.

By considering the manufacturer's requirements and technological constraints, the stator and rotor geometry has been defined, as shown in Fig. 4. This geometry represents the initial design, which will be subject to further optimization. The figure also includes details on the stator winding configuration, rotor bar arrangement, and the analyzed magnetic flux density distribution along with the corresponding flux lines. In this configuration, the initial number of stator copper conductors per phase Z_q is **600**, the fill factor k_{cu} is **0.36**, and the conductor diameter d_{Cu} is **0.28** mm^2. Additionally, the stator contains **12** slots Q_s, the rotor has **17** aluminum bars Q_r, the rotor moment of inertia J_{rot} is **0.322** g·m^2, and the active length
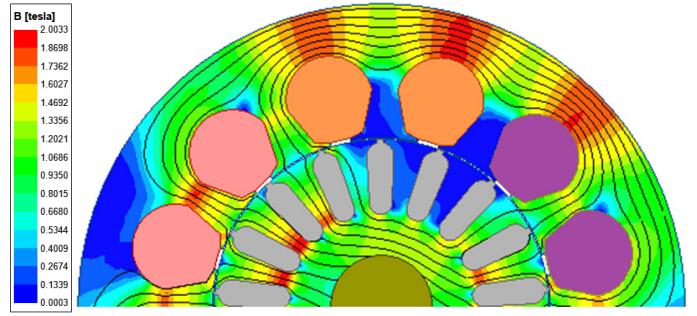

Fig. 4. Initial geometry used for electromagnetic model with plotted magnetic flux density and flux lines

L_{Fe} is **34** mm.

The machine configured in this manner achieved a torque of $T = $ **130.2** mNm, a speed of $n = $ **2943.73**, and efficiency of $\eta = $ **0.29**. The calculated loss components include core losses $\Delta P_c = $ **4.18** W, stator Joule losses $\Delta P_{Cu} = $ **89.23** W, and rotor Joule losses $\Delta P_r = $ **4.1** W. The results obtained for speed, losses, and geometric dimensions serve as essential inputs for the subsequent thermal calculations, representing the next step of the design process.

B. Thermal model

The next step in the design process is the creation and analysis of the thermal model, where the block diagram illustrating the required inputs and the resulting outputs can be observed in Fig. 5. In this type of model, there are typically
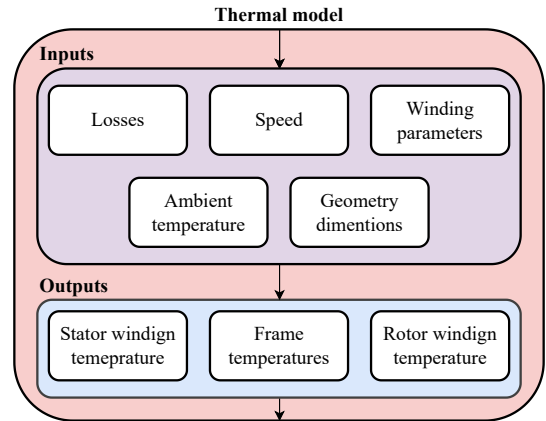

Fig. 5. Diagram presents inputs and outputs of thermal model

two kinds of inputs. The first category consists of inputs that are not dependent on the electromagnetic model. An example of this is the ambient temperature, which is influenced by the location where the machine is placed. The second category includes inputs that are typically connected to the electromagnetic model. These inputs include loss components, speed, winding parameters (such as the type of stator groove insulation or the geometrical dimensions of the end windings), and geometry dimensions, which are the same as those used

in the electromagnetic model.

The outputs of the thermal model are the temperatures of the individual machine components. Typically, the temperature model is created to analyze the temperatures of the stator winding T_{s}, the frame T_{fr}, and the rotor winding T_{r} or rotor bars (depending on the rotor type). Specifically, the temperatures T_{s} and T_{r} directly influence the resistances of the stator R_{s} and the rotor R_{r}. Variations in these resistances have a significant impact on the behavior and properties of the electromagnetic model.

The thermal model proposed for calculating the temperatures of the designed machine is illustrated in Fig. 5. This model consists of 29 distinct points where the temperatures are calculated and analyzed to understand the machine's thermal behavior under various operating conditions. These points are strategically positioned throughout the machine to capture the temperature distribution, offering detailed insights into heat flow, dissipation, and potential hotspots within the system. Based on the presented thermal model, the calculated
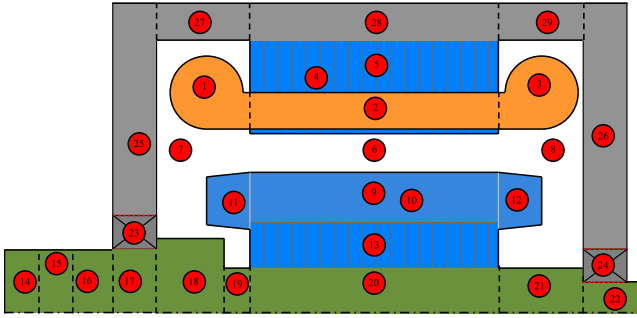

Fig. 6. Thermal model dedicated for optimization

temperatures are $T_{\mathrm{s}} = \mathbf{118}°C$, $T_{\mathrm{r}} = \mathbf{96.3}°\mathrm{C}$, and $T_{\mathrm{fr}} = \mathbf{75.87}°\mathrm{C}$. These temperature values are used in the optimization process to adjust the resistance of the stator winding and rotor bars, ensuring accurate evaluation of thermal and electromagnetic performance.

V. Optimization

This chapter focuses on the application of optimization techniques. The optimization aims to identify a machine model that meets the requirements for high efficiency, minimal torque ripple, and reduced active length. A shorter active length decreases material consumption and reduces manufacturing costs, making the design more economically viable.

A. Optimization process

During the optimization process, it is essential to establish a connection between the electromagnetic and thermal models to allow iterative refinement of the final results. This connection is graphically represented in Fig. 7. As shown, key input for optimization includes the definition of geometric constraints, winding boundary conditions, and additional parameters such as the maximum permissible operating temperature and the minimum acceptable efficiency. These constraints ensure that the optimized model remains feasible and valid. Defining valid
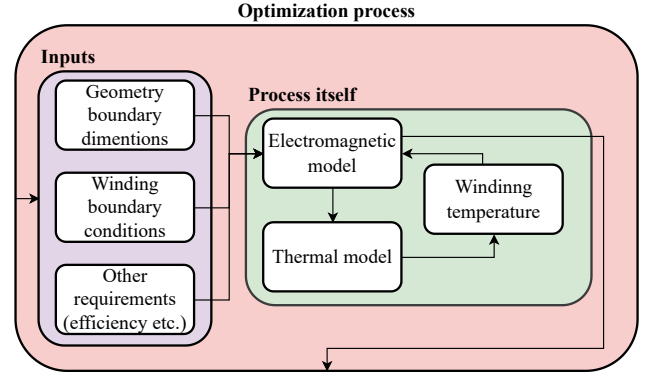

Fig. 7. Flow chart of optimization process

boundaries is a critical step in preparing the optimization process. These boundaries ensure that the final machine design remains manufacturable. Moreover, properly setting these boundaries can help reduce the overall computational time, which remains extremely high, ranging from days to months, even under optimal conditions.

B. Optimized machine

The final machine, selected based on the optimization results, is presented in Fig. 8. The optimized design features smaller stator slots and an enlarged stator yoke, which is advantageous for two-pole machines as they typically exhibit higher flux linkage in this region. Furthermore, the rotor bar shape has been modified, reducing the total cross-sectional area, which increases resistance and can enhance the machine's torque characteristics. Additionally, the figure illustrates the magnetic flux density distribution and flux lines, providing insight into the electromagnetic performance of the optimized design. The optimized model achieved the following param-
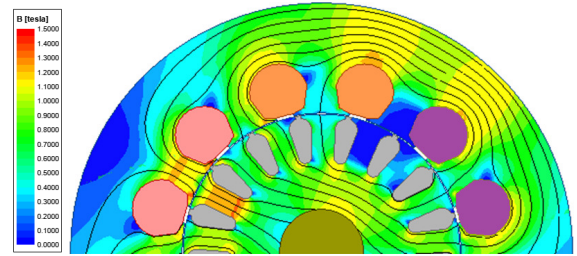

Fig. 8. Optimized geometry with ploted magnetic flux density and flux lines

eters: torque $T = \mathbf{129}\,\mathrm{mNm}$, speed $n = \mathbf{2936.3}\,\mathrm{rpm}$, and efficiency $\eta = \mathbf{0.73}$. The calculated loss components are: core losses $\Delta P_{\mathrm{c}} = \mathbf{5.75}\,\mathrm{W}$, stator copper losses $\Delta P_{\mathrm{Cu}} = \mathbf{7.96}\,\mathrm{W}$, and rotor copper losses $\Delta P_{\mathrm{r}} = \mathbf{0.94}\,\mathrm{W}$. In this configuration, the number of stator conductors per phase is $Z_{\mathrm{q}} = \mathbf{500}$, with a copper fill factor of $k_{\mathrm{Cu}} = \mathbf{0.348}$ and conductor diameter $d_{\mathrm{Cu}} = \mathbf{0.236}\,\mathrm{mm}^2$. The total moment of inertia is $J_{\mathrm{tot}} = \mathbf{0.330}\,\mathrm{g·m}^2$. The iron length L_{Fe}, as well as the stator and rotor slot numbers Q_{s} and Q_{r}, remain unchanged compared to the non-optimized machine. The temperatures

of the optimized machine are $T_s = \mathbf{76.1}°\text{C}$, $T_r = \mathbf{73.5}°\text{C}$, and $T_{\text{fr}} = \mathbf{60.1}°\text{C}$. The values of the original and optimized machines are compared in Tab. I.

Parameter	Original	Optimized
Efficiency, EF, %	29	79
Statot winding temperature, T_s, °C	118	76.1
Rotor temperature, T_r, °C	96.3	73.5
Frame temperature, T_{fr}, °C	75.87	60.1
Rotation speed, n, rpm	2943.73	2936.3
Nominal torque, T, mNm	130.2	129
Winding losses, P_{Cu},, W	89.23	7.96
Core losses, P_C,, W	4.18	5.75
Rotor losses, P_r,, W	4.1	0.94
Fill factor, k_{Cu}, (-)	0.36	0.348

TABLE I
TABLE OF VALUES AT NOMINAL POINT

VI. Manufacturing documentation

The manufacturing documentation is derived from the optimization results and must include fundamental details such as the active length, the length of the air gap, the outer and inner diameters of the stator and rotor, as well as the number of stator and rotor slots. Additionally, it should contain a detailed description and diagram of the winding type and connection, the surface area of the stator slot, and the precise specifications of the materials required for the manufacture of the machine.

From an electromagnetic perspective, the documentation must also specify the nominal current, operating frequency, and voltage. In addition, it should include the rated speed, the number of poles, and the power factor. Lastly, all this information must be supplemented by a calculation sheet, providing extensive details, including mass calculations for the stator and rotor slots.

VII. Conclusion

This study presents an integrated workflow for the design and optimization of induction machines, combining Finite Element Method (FEM) simulations, analytical modeling, and advanced optimization algorithms. The proposed approach ensures precise and accurate evaluation of electromagnetic performance while simultaneously adhering to manufacturability constraints, which are often a limiting factor in real-world applications. By utilizing the Non-Dominated Sorting Genetic Algorithm II (NSGA-II), the optimization process is able to effectively balance multiple, sometimes competing, design objectives such as efficiency, thermal stability, and cost. This multi-objective approach leads to optimized solutions that enhance the overall performance of the induction machine, ensuring it meets the desired specifications with minimal trade-offs.

The case study presented in this paper highlights the successful implementation of this workflow, where the optimized induction machine shows significant improvements in both efficiency and thermal stability compared to the initial design.

These improvements contribute to reduced power losses, extended operational lifetimes, and enhanced reliability, making the optimized design more suitable for industrial applications. The ability to achieve better performance metrics while keeping manufacturability in check underscores the potential of the proposed methodology for real-world engineering applications.

References

[1] B. K. Bose, "Modern power electronics and ac drives," *Prentice Hall*, 2014.

[2] L. Wang and X. Li, "A review on design of induction motors for industrial applications," *Electric Power Systems Research*, vol. 146, pp. 238–248, 2017.

[3] H. Tavakolizadeh, M. Karami, and F. Zare, "Design and optimization of an induction motor using an analytical method and fem," *IEEE Transactions on Industrial Applications*, vol. 52, no. 2, pp. 1320–1328, 2016.

[4] H. Cohen and D. Fenton, "The development of electric motor performance optimization using analytical techniques," *IEEE Transactions on Energy Conversion*, vol. 21, no. 3, pp. 486–493, 2006.

[5] N. Bianchi, S. Bolognani, and S. Mezzetti, "Design of induction motors: Optimization based on electromagnetic, thermal, and mechanical losses," *IEEE Transactions on Industrial Applications*, vol. 41, no. 4, pp. 1077–1083, 2005.

[6] C. Xu, X. Deng, and H. Chen, "Design and analysis of high-efficiency induction motors using multi-objective optimization," *Energy*, vol. 111, pp. 379–389, 2016.

[7] T. A. Lipo, "Induction motor analysis and design for efficiency optimization," *IEEE Transactions on Power Electronics*, vol. 27, no. 8, pp. 3579–3589, 2012.

[8] B. Venkatesh and R. Srinivas, "Finite element method (fem) for electromagnetic field analysis in induction motors," *IEEE Transactions on Magnetics*, vol. 47, no. 9, pp. 3486–3492, 2011.

[9] D. Tursini, A. Bellini, and F. Ferraris, "Design optimization of an induction motor using finite element analysis," *Energy*, vol. 55, pp. 758–765, 2013.

[10] Z. Jiang, X. Zhang, and X. Li, "Electromagnetic performance prediction of induction motors using fem-based simulation," *IEEE Transactions on Industrial Electronics*, vol. 66, no. 5, pp. 3974–3981, 2019.

[11] X. Shao, L. Liu, and Z. Li, "Application of finite element method for optimal design of electrical machines," *Energy Conversion and Management*, vol. 81, pp. 118–126, 2014.

[12] P. Rama, A. Gupta, and A. Zivkovic, "Challenges of fem in large-scale induction motor simulations," *IEEE Transactions on Industrial Applications*, vol. 54, no. 3, pp. 1478–1485, 2018.

[13] Z. Zhang, X. Guo, and Q. Li, "Simulation of electrical and mechanical performance of induction motors using fem," *Journal of Electrical Engineering & Technology*, vol. 12, no. 2, pp. 887–894, 2017.

[14] P. Shah and S. Rana, "Fem-based multi-objective optimization for induction motor design," *Journal of Magnetism and Magnetic Materials*, vol. 432, pp. 275–283, 2017.

[15] T. Kim, J. Lee, and B. Kim, "Fem-based induction motor design optimization for high efficiency and low losses," *IEEE Transactions on Power Electronics*, vol. 34, no. 6, pp. 5068–5076, 2019.

[16] M. Kaviani and S. Zeynali, "Optimization of induction motor design using analytical models and fem," *Energy*, vol. 75, pp. 674–682, 2014.

[17] J. Simão, A. Costa, and J. Rodrigues, "Induction motor optimization based on analytical and numerical methods," *IEEE Transactions on Energy Conversion*, vol. 31, no. 4, pp. 1725–1732, 2016.

[18] A. Panda, A. Soni, and D. Chatterjee, "Pareto optimization of induction motors using nsga-ii for multi-objective trade-off analysis," *IEEE Transactions on Industrial Electronics*, vol. 65, no. 5, pp. 3882–3892, 2018.

Advanced Transformer Design Optimization via Simulated Annealing

1st Miroslav Mrajca
Department of Power Electrical and Electronic Engineering
FEEC, Brno University of Technology
Brno, Czech Republic
Miroslav.Mrajca@vut.cz

2nd Petr Silling
Department of Computer Graphics and Multimedia
FIT, Brno University of Technology
Brno, Czech Republic
isilling@fit.vut.cz

Abstract—**This paper presents an innovative approach to the design of distribution oil transformers using the Simulated Annealing optimization algorithm. The proposed method can be implemented as software capable of fully replacing a human designer in the search for optimal transformer configurations, minimizing cost, weight, or other design criteria. The study provides an in-depth analysis of the algorithm's functionality and its suitability for transformer design. A significant portion is dedicated to explaining how the transformer calculation is integrated into the algorithm, detailing input parameters, design variables, output parameters, and optimization constraints that determine whether a design meets the required specifications. Finally, the effectiveness of the optimization algorithm is compared to human designers, focusing on the duration of the design process and the achieved cost minimization.**

Index Terms—**transformer design, Simulated Annealing, optimization, automatic process, cost minimization**

I. Introduction

A distribution transformer is one of the fundamental components required for electrical energy transmission. Although transformers achieve an efficiency well above 99%, their losses still account for approximately 5% of total global electricity consumption, as reported in [1]. For this reason, as stated in [2], the European Commission has introduced stricter limits on the losses of all power transformers installed within the European Union (EU) as part of the Ecodesign requirements. These limits have been further tightened, with the second stage of the Ecodesign regulation having come into effect on July 1, 2021. And according to [3], additional reductions in transformer losses are currently under discussion for future implementation.

According to [4] these regulations have significantly impacted transformer prices in the European market, as loss reduction can only be achieved by increasing the amount of aluminum, copper, and transformer steel—key materials that also heavily influence the final cost. In addition to higher prices, stricter efficiency requirements have led to a substantial increase in transformer size and weight, sometimes causing difficulties when replacing older transformers in existing installations designed for smaller units.

Furthermore, all transformer manufacturers supplying the EU were forced to recalculate their entire range of transformer designs, many of which had been verified through years of practical use. This requirement placed a significant burden on manufacturers, often necessitating hundreds of new calculations within a very short timeframe, made even more challenging by the shortage of specialized staff. This recalculation process has already been carried out twice, and at least one more round is expected in the near future.

Additionally, material prices have become highly volatile due to the rising demand for high-quality materials, such as electrical steel as stated in [5], as they are essential to minimize losses while meeting Ecodesign standards. As a result, periodic recalculations of transformer designs can be beneficial for optimizing costs based on current material prices.

A major challenge in this extensive recalculation process is that most manufacturers still rely on manual calculations or, at best, semi-automatic software, for example [6], where a human designer searches for the most efficient combination of variables representing the transformer design. The quality of the final design depends solely on the experience of the designer and the time available to explore different configurations.

Therefore, a fully automated calculation method that eliminates human intervention is needed. This paper presents an innovative approach to distribution transformer design using the Simulated Annealing algorithm presented in [7], which is particularly well-suited for solving the highly nonlinear and primarily discrete mathematical model that underlies transformer calculations with a focus on use in manufactory.

II. Transformer Design Process

The optimization algorithms considered in this paper are efficient only when applied to purely analytical calculation methods, which rely on mathematical equations, tables, and approximations. While finite element method (FEM) analysis is commonly incorporated in the transformer design process, analytical calculations are generally sufficient for the majority

of distribution transformers, as stated in [8]. FEM analysis is particularly useful for obtaining more precise calculations of specific parameters; however, due to its high computational cost, it is inappropriate for a large number of iterations in optimization processes. Consequently, FEM is more commonly required for high-voltage power transformers rather than medium-voltage distribution transformers.

The paper works with the calculation methodology for three-phase, oil-immersed, hermetically sealed distribution transformers, which typically convert medium to low voltage. The approach incorporates the most common modern technologies used in transformer manufacturing.

The active part consists of a core-type magnetic circuit with three limbs, constructed using Step-Lap technology. Each limb contains two concentric windings: the inner low-voltage winding, made of conductive foil, and the outer medium-voltage winding, which is of the multilayer type. The multilayer winding consists of round wire turns arranged in layers with inter-layer insulation made of resin-impregnated paper. The conductors of both windings can be made of copper, but aluminum is more frequently used due to cost considerations.

The transformer tank comprises a bottom tub and corrugated walls, which enhance cooling efficiency and compensate for oil expansion due to temperature changes, eliminating the need for a conservator. The tank is sealed with a cover that integrates bushings for both voltage sides, a filling pipe, a tap-changer, and other accessories.

These technological constraints define the transformer design variables, which must be selected either manually by a human or automatically by an algorithm. This selection enables the complete calculation of the output parameters based on the input specifications, as illustrated in Fig. 1. The figure outlines the entire transformer design procedure within the red rectangle labeled *Mathematical model of the transformer*. It also separates the design variables into distinct blocks for optimization (or manual selection), categorized into two groups: variables related to the active part and those associated with the tank design. At the beginning of the calculation process (and also during optimization), input parameters must be defined. Additionally, material properties and constants, provided in tabulated form, are required for all calculations necessary to achieve a complete transformer design.

The mathematical model of the transformer begins with the calculation of the inner foil low-voltage winding parameters, including its dimensions and electrical characteristics, which are derived from the selected design variables and required input specifications. Once the low-voltage winding parameters are established, the outer high-voltage winding is designed using a similar approach. The dimensions of both windings then enable the calculation of the magnetic core, followed by the estimation of no-load losses. Load losses and short-circuit impedance are determined based on the electrical properties and geometric dimensions of the windings.

Subsequently, the second group of design variables is used to determine the tank dimensions. By incorporating the known dimensions of the active part, the full dimensions of the tank, as well as the overall size of the transformer, can be computed. From the designed corrugated walls of the tank and the total transformer losses, the oil temperature rise at full load is calculated. The process concludes with an estimation of the winding temperature rise, which depends on the oil temperature rise, winding losses, and physical dimensions.

III. Optimization in Transformer Design

Optimization problems in the electrical engineering domain generally involve several constraints that must be satisfied while minimizing an objective function. For oil distribution transformers, design optimization presents a particular challenge, since the underlying mathematical model is highly nonlinear in nature and operates exclusively with discrete or discretized variables. Its constraints include electromagnetic properties, material availability, physical dimensions, thermal limits, and cost considerations. *Constrained optimization* (CO) provides a systematic approach to handling these constraints while searching for the most optimal solution.

Formally, a constrained optimization problem can be defined as the task of minimizing an *objective function* $f(\mathbf{x})$ of one or more variables $\mathbf{x} \in \mathbb{R}^n$:

$$\mathbf{x}^* = \operatorname*{argmin}_{\mathbf{x}} f(\mathbf{x}) \quad \text{subject to} \quad \mathbf{x} \in \mathcal{C}, \qquad (1)$$

where $\mathbf{x}^* \in \mathbb{R}^n$ is the *optimal solution* and $\mathcal{C}$ is the set of all feasible solutions defined by design *constraints*.

Methods for solving CO problems can typically be divided into exact and heuristic methods. Exact methods, such as Integer Nonlinear Programming (INLP), provide rigorous mathematical guarantees. However, their applicability to transformer design is limited by the problem's inherent nonlinearity, discontinuity, and complex interplay between individual constraints. Heuristic approaches, such as evolutionary algorithms and Tabu Search by [9], offer greater flexibility, but generally require extensive parameter tuning and significant computational resources. Given these limitations, more generalized heuristic techniques, such as Simulated Annealing introduced in [7], are better suited for transformer design optimization.

A. Simulated Annealing

Simulated Annealing (SA) presented in [7] is a probabilistic optimization algorithm inspired by the physical process of annealing in metallurgy. During annealing, a material is heated to a high temperature and then gradually cooled, allowing its atomic structure to settle into a stable, low-energy configuration. SA mimics physical annealing by introducing a temperature parameter, which allows the algorithm to accept changes that may temporarily increase the value of the optimized objective function $f(\mathbf{x})$ to escape local minima. The probability of accepting inferior states decreases with time alongside the temperature, essentially balancing exploration and exploitation. The stochastic nature of SA makes it particularly effective for nonlinear and discontinuous discrete optimization problems. As a result, it has been successfully
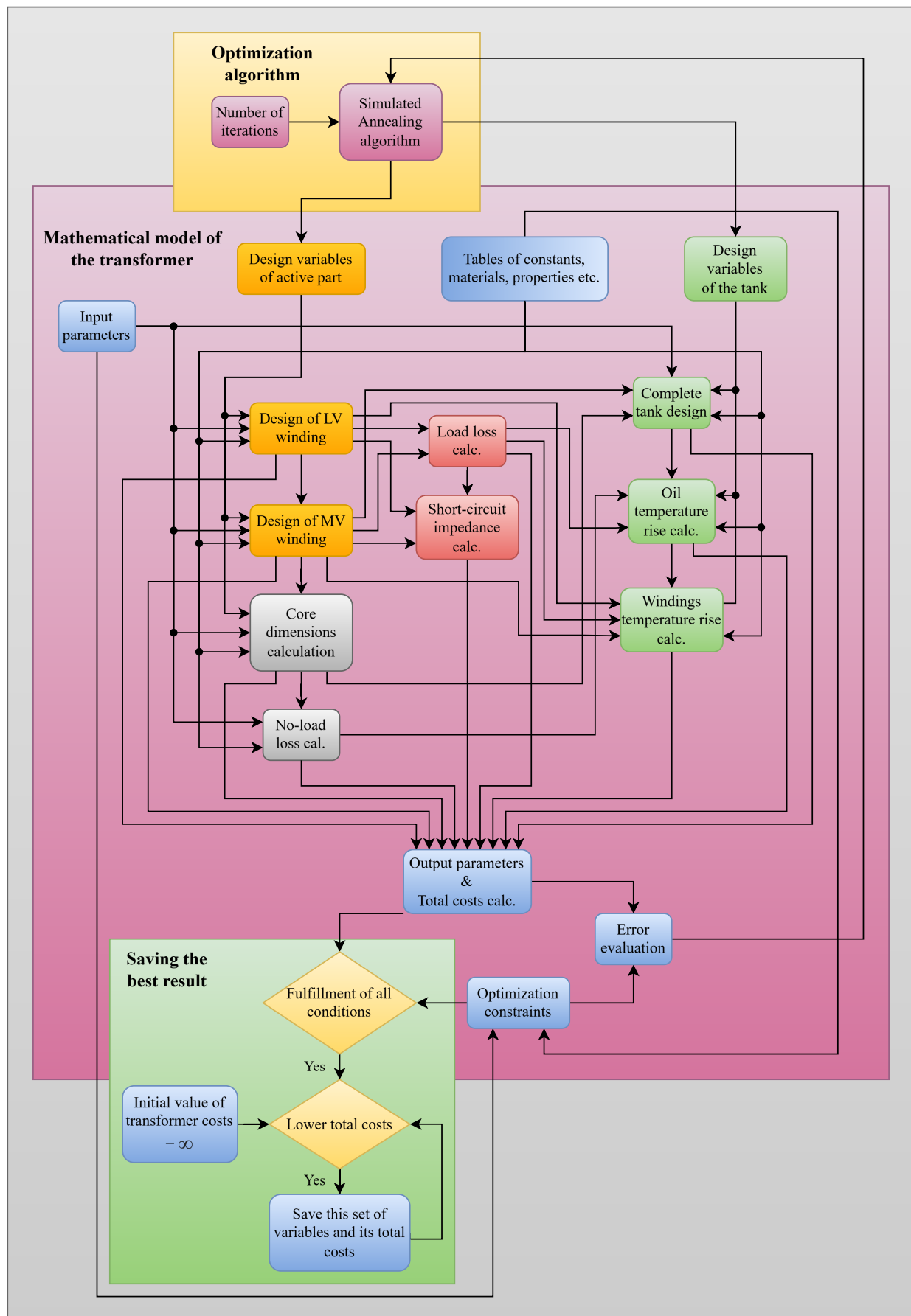
Fig. 1. Block diagram of the optimization algorithm Simulated Annealing for transformer design.

applied to many different engineering problems, including concrete beam and brushless motor design according to [10], [11]. To the best of our knowledge, this is the first work that applies SA to the design of transformers.

Formally, SA works iteratively in discrete time steps, accepting new candidate solutions $\mathbf{x}'$ with probability P_t:

$$P_t = \begin{cases} 1 & \text{if } f(\mathbf{x}') < f(\mathbf{x}_t) \\ e^{-\frac{f(\mathbf{x}')-f(\mathbf{x}_t)}{T_t}} & \text{otherwise} \end{cases}, \qquad (2)$$

where $\mathbf{x}_t$ and T_t represent the candidate solution and temperature from time t, respectively. The initial candidate solution $\mathbf{x}_0$ is chosen at random. The optimization ends once the specified number of steps completes or the temperature reaches zero.

For transformer design, constraint-related penalization is further incorporated into the optimization process. In particular, each constraint is assigned a weight and a nonnegative penalty function, which increases in value with the degree of constraint violation and is zero if and only if the constraint is fully satisfied by a given candidate solution. The weights are determined by the relative influence of the constraints on the design process and the value range of the corresponding penalty function. The penalization strategy effectively transforms design optimization from a constrained problem to an unconstrained one, enabling a more straightforward application of SA.

Specifically, the constrained penalization modifies the objective function as follows:

$$f'(\mathbf{x}) = f(\mathbf{x}) + \sum_k w_k \cdot c_k(\mathbf{x}), \qquad (3)$$

where $f'(\mathbf{x})$ is the penalized objective function and $c_k(\mathbf{x})$ and w_k are the penalty function and relative weight of the k-th constraint, respectively.

With the penalized objective function, SA can be directly applied to transformer design optimization, where it can replace traditional human-driven design optimization. Compared to manual design, it offers a more scalable and highly flexible optimization procedure that can be further adapted to the specific needs of transformer design. For example, it can be customized to prioritize the parameters of the core and windings before optimizing secondary components, such as the transformer tank. Furthermore, SA can be easily extended to parallel environments by executing multiple optimization runs in independent threads, increasing the probability of finding globally optimal designs when more computational resources are available.

B. Incorporating the algorithm into the design process

The replacement of the human designer in the transformer design process by the SA optimization algorithm is illustrated in Fig. 1 by the superior loop in the yellow rectangle with the label *Optimization algorithm*. The input parameters are extended by parameter representing the number of required iterations, which affects the duration and the final lowest price.

Rated power	kVA	50	630	1,600
Voltage ratio	kV	22,000 / 400		
Connection group	-	Dyn1		
Short-circuit impedance	%	4	4	6
Primary winding taps	%	$\pm 2 \times 2.5$		
Maximum no-load loss	W	81	540	1,080
Maximum load loss	W	750	4,600	12,000
Frequency	Hz	50		
Temperature rise (oil / windings)	K	60 / 65		

Once all relevant output data are obtained from the individual calculation steps, the total material cost of the transformer is quantified. The calculated output parameters are then evaluated against the optimization constraints. If all conditions are met and the cost of the obtained design is lower than the previous saved value, the solution, along with the optimized variables, is stored by another loop displayed in Fig. 1 in the green rectangle with label *Saving the best result*. A crucial aspect of the optimization process is error evaluation, wherein the total cost is increased by an error value that represents the deviation of the output parameters from the specified constraints. This evaluation is influenced by recalibration factors, which can be set to emphasize the importance of specific output parameters over others.

Regardless of the outcome, the final adjusted cost is fed back into the SA algorithm, which uses this information to guide subsequent iterations in optimizing variable selection. This iterative process continues until the predefined number of iterations is reached. At the end of the optimization, the combination of variables that yields the lowest material cost while satisfying all constraints is retained. If no feasible solution exists for the given input parameters, or if the algorithm fails to find one within the set iteration limit, the process terminates with an error declaration. Alternatively, an upper iteration limit can be defined so that if a valid solution is not found before reaching the limit, the process is stopped prematurely without completing all iterations.

IV. COMPARISON BETWEEN MANUAL AND ALGORITHMIC OPTIMIZATION

To evaluate the effectiveness, time savings, and potential cost reductions achieved by applying the SA algorithm, three different transformers were selected for comparison. These transformers are commonly used in the Czech 22 kV distribution network, and their main specifications are given in Table I.

The design process for these transformers was tracked over time, and the progression of the lowest transformer costs obtained through algorithmic optimization and conventional manual calculation is shown in Fig.2. The manual calculations were performed by a professional transformer designer with five years of experience at Elpro-Energo Transformers s.r.o. The calculations were performed using software that incorporates the same mathematical equations and tables described in Section II, but with manual selection of variables. In contrast,
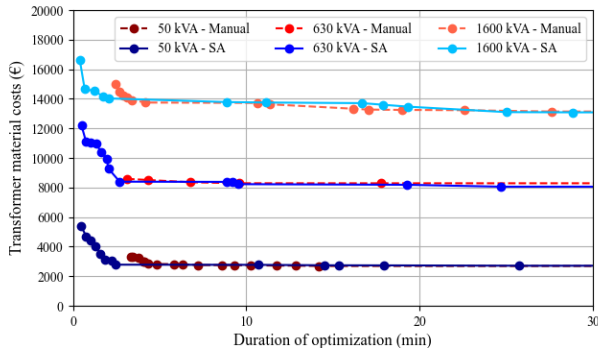
Fig. 2. Comparison of the lowest transformer costs over time between manual calculation and algorithm-based optimization for three designs.

the optimization algorithm was executed on a server equipped with a 32-core Intel(R) Xeon(R) E5-2650 v2 processor operating at 2.60 GHz.

The cost development trends indicate that the SA algorithm can obtain an initial valid design significantly faster than manual calculation. Moreover, the SA algorithm converges steeply, reaching cost values close to the minimal achievable value even before the first valid manual calculation is completed for all tracked designs. However, as the results approach the minimum cost, the rate of convergence slows. At a certain point, the manual calculation method reaches similar cost values, and in all examined cases, it eventually achieves slightly lower costs. However, around the 20-minute mark, manual calculations begin to stagnate, unable to further reduce transformer costs. In contrast, SA optimization continues to find new local minima beyond this point and could potentially identify even lower-cost solutions if the process were extended. However, any additional improvements are expected to be marginal.

After 30 minutes, the maximum observed cost difference between the final results was €56 for the 1600 kVA design and €231 for the 630 kVA design, both in favor of the SA optimization method. For the 50 kVA design, both methods ultimately produced the same result. This outcome suggests that for higher-rated transformers, where factors such as temperature rise and tank design add complexity, the number of variables and possible configurations increases, making optimization more beneficial. Consequently, it can be concluded that for high-rated power transformers and more complex designs, such as special types with multiple windings or different winding configurations, where manual calculations can take hours, the optimization algorithm proves to be significantly more effective than conventional methods.

V. Conclusion

The results demonstrate that incorporating the Simulated Annealing algorithm into the transformer design process is significantly more effective than conventional manual calculations. The algorithm not only produces valid results more quickly but also ultimately achieves better outcomes in terms of final material costs, as evidenced by three different typical

transformer designs. Additionally, the SA algorithm can be adapted to minimize transformer dimensions or losses if required. This highlights its immense potential in the future of electrical engineering, offering a powerful tool for designing electrical machines without the need for direct involvement of experienced professionals.

Although the methodology described in this paper is based on the most common type of distribution transformer, it can be easily extended to more specialized transformer designs that incorporate different technologies. In such cases, where additional design options and variables need to be optimized, the algorithm's efficiency is expected to surpass that of conventional manual calculations even further.

Furthermore, calculations using the SA can be enhanced through surrogate modeling techniques, such as Gaussian Process Regression, to improve parameter estimation beyond analytical equations. These models can effectively replace time-consuming FEM analyses or integrate insights from previously manufactured transformers while maintaining the efficiency of fast analytical evaluations, as described in [12].

References

[1] M. Cuesto, M. Oliva, and K. Pollari, "Driving down energy losses in transformers," *Transformers Magazine*, vol. 6, no. 4, pp. 67–71, 2019.

[2] "Commission regulation (EU) no 548/2014," Brussels, 2014. [Online]. Available: https://eur-lex.europa.eu/legal-content/EN/ALL/?uri=CELEX:32014R0548

[3] "Commission regulation (EU) no 2019/1783," Brussels, 2019. [Online]. Available: https://eur-lex.europa.eu/legal-content/EN/TXT/PDF/?uri=CELEX:32019R1783

[4] A. D. Almeida, B. Santos, and F. Martins, "Energy-efficient distribution transformers in europe," *Energy Efficiency*, vol. 9, no. 2, pp. 401–424, 2016. [Online]. Available: http://link.springer.com/10.1007/s12053-015-9365-z

[5] H. Mu, K. Shen, and C. Ma, "Introduction of thin gauge grain-oriented electrical steel products of baosteel and their application in power transformers," *Electrical Steel*, vol. 3., no. 4., pp. 7–11, 2021. [Online]. Available: http://www.bwjournal.com/dgg/EN/Y2021/V3/I4/7

[6] E. I. Amoiralis, P. S. Georgilakis, M. A. Tsili, A. G. Kladas, and A. T. Souflaris, "Complete software package for transformer design optimization and economic evaluation analysis," *Materials Science Forum*, vol. 670, pp. 535–546, 2010. [Online]. Available: https://www.scientific.net/MSF.670.535

[7] S. Kirkpatrick, C. D. Gelatt, and M. P. Vecchi, "Optimization by simulated annealing," *Science*, vol. 220, no. 4598, pp. 671–680, 1983. [Online]. Available: https://www.science.org/doi/abs/10.1126/science.220.4598.671

[8] S. Kulkarni and S. Khaparde, *Transformer Engineering: Design, Technology, and Diagnostics*, 2nd ed. Boca Raton, Florida, USA: CRC Press, 2013.

[9] F. Glover, "Tabu search—part i," *ORSA Journal on Computing 1*, vol. 3, pp. 190–206, 08 1989.

[10] D. Fodorean, L. Idoumghar, A. N'diaye, D. Bouquain, and A. Miraoui, "Simulated annealing algorithm for the optimisation of an electrical machine," *IET Electric Power Applications*, vol. 6, pp. 735–742, 2012. [Online]. Available: https://digital-library.theiet.org/doi/abs/10.1049/iet-epa.2011.0029

[11] S. O. A. Olawale, O. P. Akintunde, M. O. Afolabi, O. A. Agbede, O. Ozuor, and O. S. I. Fayomi, "Optimization of singly reinforced beam design using simulated annealing," *IOP Conference Series: Materials Science and Engineering*, vol. 1107, no. 1, p. 012118, apr 2021. [Online]. Available: https://dx.doi.org/10.1088/1757-899X/1107/1/012118

[12] M. Mrajca, V. Bilek, J. Barta, and R. Cipin, "Transformer no-load losses calculation using machine learning," in *2024 International Conference on Electrical Machines (ICEM)*. Torino, Italy: IEEE, 2024, pp. 1–7. [Online]. Available: https://ieeexplore.ieee.org/document/10700285/

ŠKODA Kariéra

Stáže a závěrečné práce

Studuješ vysokou školu a zároveň chceš získat pracovní zkušenosti? Zkus odbornou stáž ve ŠKODA AUTO. Pod vedením našich odborníků se zapojíš do inovativních projektů – třeba těch v oblasti elektromobility. Získané znalosti pak můžeš zúročit i ve své závěrečné práci.

Doktorandský program

Aplikuj výsledky svého výzkumu v reálném prostředí, využívej nejnovější technologie a dej své disertační práci nový rozměr. Poskytneme ti flexibilní pracovní dobu a možnost spolupracovat s profesionály ve svém oboru.

Trainee program

Dokončil jsi studia a přemýšlíš kam dál? Trainee program pro absolventy ti pomůže najít obor, který tě bude opravdu bavit a naplňovat. V průběhu jednoho roku budeš na plný úvazek pracovat v mezinárodním týmu, poznáš různá oddělení a vycestuješ na zahraniční stáž.

Volné pozice

Vyber si ze široké nabídky volných pozic, staň se součástí nejprogresivnější české firmy a tvoř s námi budoucnost automobilového průmyslu.

f Škoda Auto Kariéra | Instagram @WeAreSKODA | in Škoda Auto a.s. | YouTube Škoda Auto - Career
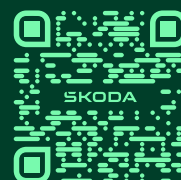
Image Reconstruction in Electrical Impedance Tomography through 1D-Convolutional Neural Network

Serge Ayme Kouakouo Nomvussi
Department of Theoretical and Experimental Electrical Engineering
Brno University of Technology
Brno, Czech Republic
244245@vut.cz

Jan Mikulka
Department of Theoretical and Experimental Electrical Engineering
Brno University of Technology
Brno, Czech Republic
mikulka@vut.cz

Abstract—**This paper presents a comparative analysis of image reconstruction performance using a 1D-Convolutional Neural Network (1D-CNN) against the Total Variation and the Gauss-Newton methods. The evaluation, conducted across multiple tests conditions, demonstrates that the 1D-CNN consistently outperforms both conventional methods in terms of correlation coefficient and structural similarity index (SSIM). In noise-free scenarios, the 1D-CNN achieves significantly higher correlation and SSIM values, indicating superior reconstruction accuracy. Furthermore, in the presence of noise (30 dB and 60 dB), the performance of the Total Variation and Gauss-Newton methods deteriorates considerably, whereas the 1D-CNN maintains high correlation and SSIM values, demonstrating strong robustness to noise. These findings highlight the effectiveness of deep learning-based approaches for image reconstruction, making the 1D-CNN a promising alternative to traditional reconstruction techniques.**

Keywords—1D- convolutional Neural Network, Total Variation, Newton-Gauss, EIT.

I. INTRODUCTION

Electrical Impedance Tomography (EIT) is widely used in biomedical imaging, geophysics, and industrial process monitoring to reconstruct an object's internal conductivity distribution [1-3] based on electrical measurements taken at its boundary. Despite its advantages, EIT is highly ill-posed and sensitive to measurement noise, posing challenges for accurate reconstruction [4]. Traditional reconstruction methods, such as the Gauss-Newton, Total Variation, and back-projection algorithms, require significant computational resources and often produce blurry reconstructions [5-10]. While the Gauss-Newton method performs well in noise-free conditions, its accuracy deteriorates significantly in the presence of noise, limiting its applicability in real-world scenarios [11].

Deep learning has emerged as a promising alternative for EIT image reconstruction, offering improvements in both speed and accuracy [4]. Convolutional Neural Networks (CNNs), in particular, have been extensively applied to image processing tasks. However, most existing deep learning-based EIT methods rely on 2D CNNs, which may not optimally process the inherently sequential 1D voltage measurements acquired in EIT [5]. Given this sequential nature, 1D CNNs provide a more suitable architecture for feature extraction and conductivity estimation [12].

In this work, we propose a 1D CNN-based approach for EIT image reconstruction that directly maps voltage measurements to conductivity distributions. By leveraging the efficiency of 1D convolutions, our method aims to enhance the performance of the reconstructed images.

II. METHODS

A synthetic dataset was generated using the EIDORS framework [13], a MATLAB-based tool for forward and inverse modeling in EIT. The dataset comprises circular and rectangular targets with varying conductivities (ranging from 0.01 S/m to 0.12 S/m) placed in a water-filled container (0.04 S/m). Electrodes surrounding the container facilitate current injection and voltage measurement, following predefined injection and measurement patterns. The dataset contains 17745 samples, including variations in noise levels introduced through white Gaussian noise. Each sample consists of:

- Train_voltage: [208 x 10647] matrix of voltage measurements.

- Train_conductivity: [1024 x 10647] matrix of conductivity distributions.

- Validation and test datasets: Similar structure with 3549 samples each.

To ensure numerical stability and improve the efficiency of the training process, the data is preprocessed through normalization of both voltage and conductivity values. This normalization mitigates the effects of varying scales and enhances the convergence of the learning algorithm. Each sample contains 208 voltage measurements as input features and 1024 conductivity values as output labels, as mathematically formulated in Equations (1) and (2).

$$U = (U_1, \quad U_2, \dots, U_i) \qquad with\ i = 1,2,\dots 208, \quad (1)$$
$$\sigma = (\sigma_1, \quad \sigma_2, \dots, \sigma_j) \qquad with\ j = 1,2,\dots 1024. \quad (2)$$

The proposed one-dimensional (1D) Convolutional Neural Network (CNN) architecture comprises four key components: an input layer, a hierarchical feature extraction mechanism utilizing convolutional layers, a flatten layer for dimensionality reduction, and a series of fully connected layers for conductivity estimation. A detailed structural representation of the network is shown in Fig. 1.
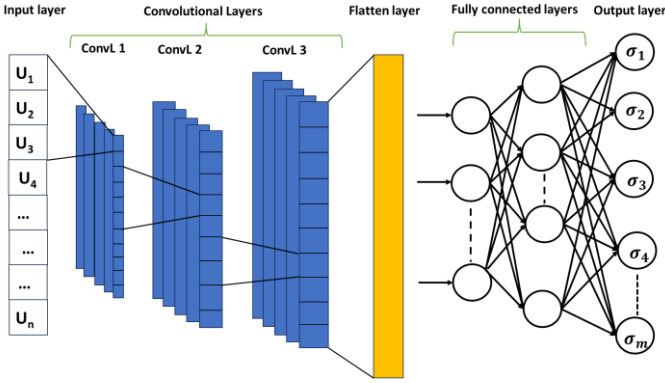

Fig. 1. Architecture of the new method

The network begins with a sequence input layer of size 208, corresponding to the number of voltage measurements per sample. This layer ensures that the spatial and temporal relationships among the voltage readings are preserved, allowing the model to effectively capture meaningful patterns.

Feature extraction in this model is accomplished through a series of three 1D convolutional layers (ConvL), each designed to progressively learn higher-level representations from the input data. These convolutional layers use a kernel size of 3, ensuring a localized receptive field that captures important patterns and dependencies. The first convolutional layer (ConvL 1) uses 128 filters, enabling the extraction of fundamental low-level features. As the network deepens, the second convolutional layer (ConvL 2) increases to 256 filters, enabling the model to learn more complex patterns. Finally, the third convolutional layer (ConvL 3) uses 1024 filters, significantly boosting the capacity of the network to capture intricate and abstract high-level representations.

To improve training stability and efficiency, each convolutional layer is followed by a Batch Normalization (BN) layer. Batch normalization normalizes activations, reducing internal covariate shifts to stabilize training and accelerate convergence. It also serves as a form of regularization, enhancing the model's generalization performance. After batch normalization, a Rectified Linear Unit (ReLU) activation function is applied to introduce non-linearity. The ReLU function, mathematically defined as:

$$f(U) = max(0, \ U). \qquad (3)$$

This ReLu function ensures that all negative values are set to zero, while positive values remain unchanged. This non-linear transformation helps the network learn complex representations and mitigates the vanishing gradient problem, which can hinder deep networks from learning effectively. By combining convolutional layers, batch normalization, and ReLU activation, the model effectively extracts hierarchical features, facilitating robust and efficient learning.

After the convolutional layers have extracted hierarchical features from the input data, a flatten layer is applied to transform the multi-dimensional feature maps into a one-dimensional vector. This transformation is essential, as it enables the transition from convolutional operations to fully connected layers, which operate on flattened representations. By preserving the extracted spatial features while restructuring them into a linear form, the flattening process ensures that the network can effectively process the learned patterns in subsequent layers.

After this, the extracted features are refined and interpreted through a series of fully connected layers (FCLs), which are essential for mapping the learned representations to the final output. The first fully connected layer (FCL 1) has 128 neurons, allowing the model to integrate low-level features into more meaningful representations. The second fully connected layer (FCL 2) follows, with 256 neurons, further increasing the network's capacity to model complex relationships. The third and final fully connected layer (FCL 3) has 1024 neurons, enabling a deep, highly expressive feature space that captures intricate dependencies. Each fully connected layer is followed by a ReLU activation function to enhance the model's learning capacity.

The final stage of the network predicts conductivity values, with the last fully connected layer containing 1024 neurons. Each neuron represents a predicted conductivity value, capturing the underlying spatial relationships learned from the input data. A regression layer is applied at the output to ensure the final prediction is suitable for regression tasks. This layer computes the final conductivity map, representing the model's estimated conductivity values across the input domain.

To optimize the learning process and improve the network's performance, we use the Adam optimizer, a popular choice for deep learning applications due to its ability to adapt the learning rate and incorporate momentum. This makes Adam particularly effective in navigating the complex loss landscapes of deep networks, ensuring efficient training. The training process uses several key hyperparameters: L2 regularization is set to 0.0002,

helping prevent overfitting by penalizing large weights and promoting generalization. The mini-batch size is set to 16, allowing the model to process data in manageable chunks while maintaining computational efficiency. Training is set to run for a maximum of 1000 epochs, providing ample time for the network to converge. The initial learning rate is set at 0.0005, providing a balance between making significant progress and allowing for fine-tuning over time. During training, the performance of the model is validated every 5 epochs, ensuring that progress is monitored, and adjustments can be made. To avoid overfitting and ensure generalization, early stopping is implemented: if validation loss does not improve for 10 consecutive steps, training halts to prevent unnecessary computation.

The performance of the model is evaluated using the Mean Squared Error (MSE) loss function, which measures the average squared differences between the predicted conductivity values T_i and the true values Y_i. The MSE is defined as:

$$MSE = \frac{1}{N} \sum_{i=1}^{M} (Y_i - T_i)^2). \qquad (4)$$

The correlation coefficient (Corr), as calculated in Equation (5), is a crucial metric for assessing the degree of correlation between the recovered image Y^*_{mn} and the original image Y_{mn}. This coefficient provides insights into the strength of the correlation, offering a quantitative measure of the quality of the reconstructed conductivity map. The correlation coefficient is instrumental in discerning how well the recovered image aligns with the original image. The parameters $\overline{Y^*_{mn}}$ and $\overline{Y_{mn}}$ represent the mean values of the recovered and original images, respectively.

$$corr = \frac{\sum_m \sum_n (Y^*_{mn} - \overline{Y^*_{mn}})(Y_{mn} - \overline{Y_{mn}})}{\sqrt{(\sum_m \sum_n (Y^*_{mn} - \overline{Y^*_{mn}})^2)(\sum_m \sum_n (Y_{mn} - \overline{Y_{mn}})^2)}}. \quad (5)$$

The structural similarity index (SSIM), formulated in Equation (5), is a perceptual metric that assesses the quality of the reconstructed image by considering luminance, contrast, and structural fidelity. Unlike traditional error-based metrics, SSIM evaluates image similarity based on structural content, making it more aligned with human visual perception. An SSIM value of 1 indicates perfect structural similarity between the original and reconstructed images, while values below 1 suggest variations in image quality.

$$ssim(x, y) = \frac{(2\mu_x \mu_y + C_1)(2\sigma_{xy} + C_2)}{(\mu_x^2 + \mu_y^2 + C_1)(\sigma_x^2 + \sigma_y^2 + C_2)}, \quad (6)$$

where $\mu_x, \mu_y, \sigma_x, \sigma_y$ and σ_{xy} are the local means, standard deviations, and cross-covariance for images x, y. C_1 and C_2 are small constant which prevent division by zero.

III. RESULTS

The training and validation loss values recorded over multiple epochs illustrate the model's learning progression and generalization capability, as shown in Fig. 2. Initially, both losses were high, starting at 56.9 (training) and 41.6 (validation) at epoch 1. A rapid decline is observed during the early stages, with losses significantly reducing by epoch 50 (training: 33.2, validation: 32.1), indicating effective learning. However, after approximately 100 epochs, the validation loss reduction slows and stabilizes around 25.15 from epoch 400 onward, while the training loss continues to decrease, reaching 5.34 at epoch 495. This growing discrepancy suggests potential overfitting, where the model continues to improve on the training data but no longer generalizes effectively to unseen data. These results highlight the importance of implementing early stopping or regularization techniques to balance training performance and generalization ability.
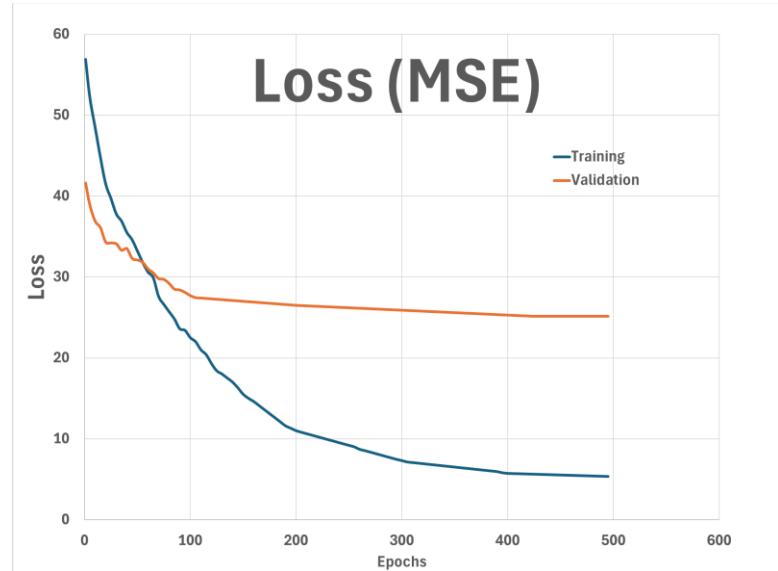

Fig. 2. Loss of the new 1D-CNN proposed method

TABLE I.   COMPARISON NEW METHOD AND TOTAL VARIATION

Position / Noise	Model	Reconstructed image Total Variation algorithm	Reconstructed image with 1D-CNN
1/No		corr = 0.627 ssim = 0.964	corr = 0.967 ssim = 0.989
2/No		corr = 0.795 ssim = 0.612	corr = 0.978 ssim = 0.631
3/No		corr = 0.608 ssim = 0.555	corr = 0.721 ssim = 0.591
4/Yes 60 dB		corr = 0.070 ssim = 0.542	corr = 0.927 ssim = 0.614
5/Yes 30 dB		corr = 0.046 ssim = 0.489	corr = 0.951 ssim = 0.617

dropping to 0.070 and 0.046, respectively, while the 1D-CNN maintains significantly higher correlation values of 0.927 and 0.951. Similarly, the SSIM values for the TV algorithm (0.542 and 0.489) remain lower than those of the 1D-CNN (0.614 and 0.617), underscoring the latter's robustness to noise. These findings highlight the superior performance of the 1D-CNN in reconstructing images with higher fidelity and resilience to noise, making it a more effective approach than the traditional TV algorithm.

TABLE II.   COMPARISON NEW METHOD AND GAUSS-NEWTON

Position / Noise	Model	Reconstructed image Gauss-Newton algorithm	Reconstructed image with 1D-CNN
1/No		corr = 0.703 ssim = 0.929	corr = 0.967 ssim = 0.989
2/No		corr = 0.455 ssim = 0.609	corr = 0.978 ssim = 0.631
3/No		corr = 0.38 ssim = 0.512	corr = 0.915 ssim = 0.591
4/yes 30 dB		corr = 0.071 ssim = 0.601	corr = 0.927 ssim = 0.614
5/Yes 60 dB		corr = 0.052 ssim = 0.561	corr = 0.951 ssim = 0.617

The results in Table I demonstrate that the proposed 1D-CNN consistently outperforms the Total Variation (TV) method across all tested conditions, both in noise-free and noisy scenarios. In the absence of noise (Positions 1–3), the 1D-CNN achieves higher correlation coefficients (0.967, 0.978, and 0.721) and SSIM values (0.989, 0.631, and 0.591) compared to the TV algorithm (correlation: 0.627, 0.795, 0.608; SSIM: 0.964, 0.612, 0.555), indicating superior reconstruction accuracy. The performance gap becomes more pronounced in the presence of noise at 60 dB and 30 dB (Positions 4–5), where the TV algorithm exhibits a substantial decline, with correlation

The results in Table II demonstrate that the proposed 1D-CNN consistently outperforms the Gauss-Newton algorithm across all tested conditions, including both noise-free and noisy scenarios. Under noise-free conditions (Positions 1–3), the 1D-CNN achieves significantly higher correlation coefficients (0.967, 0.978, and 0.915) and SSIM values (0.989, 0.631, and 0.591) compared to the Gauss-Newton algorithm (correlation: 0.703, 0.455, 0.38; SSIM: 0.929, 0.609, 0.512), highlighting its superior reconstruction accuracy. The disparity in performance becomes even more evident under noisy conditions at 30 dB and 60 dB (Positions 4–5), where the Gauss-Newton algorithm experiences a substantial degradation in correlation (0.071 and 0.052) and SSIM (0.601 and 0.561). In contrast, the 1D-CNN maintains significantly higher correlation values (0.927 and 0.951) and SSIM scores (0.614 and 0.617), demonstrating its robustness to noise. These results confirm that the 1D-CNN is more effective than the Gauss-Newton algorithm in preserving structural details and maintaining high-fidelity image reconstruction, particularly under noisy conditions.

IV. DISCUSSION

The results of this study confirm that the proposed 1D-CNN outperforms the Total Variation and the Gauss-Newton methods in all tested conditions. In noise-free scenarios, the 1D-CNN consistently achieves higher correlation coefficients and SSIM values, indicating superior image reconstruction quality. While both the TV and Gauss-Newton algorithms show moderate performance in the absence of noise, their effectiveness significantly declines in the presence of noise, particularly at 30 dB and 60 dB. The TV algorithm exhibits a drastic drop in correlation, reaching as low as 0.046 under 30 dB noise, while the Gauss-Newton algorithm performs similarly poorly, with a correlation of 0.052 under 60 dB noise. In contrast, the 1D-CNN maintains high correlation values (above 0.9) and relatively stable SSIM scores, demonstrating its strong resilience to noise. These findings suggest that deep learning-based methods, such as the 1D-CNN, provide significant advantages in image reconstruction, particularly in noisy environments where traditional techniques fail. The results highlight the potential of CNN-based approaches to improve reconstruction accuracy in practical applications, such as medical imaging, signal processing, and remote sensing, where robustness to noise is critical. Future work will explore the optimization of network architectures and the application of 1D-CNN models to more complex reconstruction tasks.

REFERENCES

[1] Harikumar, R. Prabu, and S. Raghavan, "Electrical impedance tomography (EIT) and its medical applications: a review," *Int. J. Soft Comput. Eng.*, vol. 3, no. 4, pp. 193–198, 2013.

[2] A. Adler and D. Holder, Eds., *Electrical Impedance Tomography: Methods, History and Applications*. Boca Raton, FL, USA: CRC Press, 2021.

[3] A. Adler and R. Guardo, "Electrical impedance tomography: regularized imaging and contrast detection," *IEEE Trans. Med. Imaging*, vol. 15, no. 2, pp. 170–179, 1996.

[4] T. Zhang, M. Hirano, K. Oka, and Y. Tagawa, "Advances of deep learning in electrical impedance tomography image reconstruction," *Front. Bioeng. Biotechnol.*, vol. 10, Art. no. 1019531, 2022.

[5] R. Hrabuska, P. Dostal, V. Vasicek, and P. Kromer, "Image reconstruction for electrical impedance tomography: Experimental comparison of radial basis neural network and Gauss–Newton method," *IFAC-PapersOnLine*, vol. 51, no. 6, pp. 438–443, 2018.

[6] T. Zhang, M. Hirano, K. Oka, and Y. Tagawa, "Advances of deep learning in electrical impedance tomography image reconstruction," *Front. Bioeng. Biotechnol.*, vol. 10, Art. no. 1019531, 2022.

[7] T. A. Khan, S. H. Ling, and A. A. Rizvi, "Optimisation of electrical impedance tomography image reconstruction error using heuristic algorithms," *Artif. Intell. Rev.*, vol. 56, no. 12, pp. 15079–15099, 2023.

[8] M. R. Islam and M. A. Kiber, "Electrical impedance tomography imaging using Gauss-Newton algorithm," in *Proc. Int. Conf. Informatics, Electron. Vis. (ICIEV)*, Dhaka, Bangladesh, 2014, pp. 1–5.

[9] M. Farha, "Combined algorithm of total variation and Gauss-Newton for image reconstruction in two-dimensional electrical impedance tomography (EIT)," in *Proc. Int. Sem. Sensors, Instrum., Meas. Metrol. (ISSIMM)*, Bandung, Indonesia, 2017, pp. 25–29.

[10] L. I. Rudin, S. Osher, and E. Fatemi, "Nonlinear total variation based noise removal algorithms," *Physica D: Nonlinear Phenom.*, vol. 60, no. 1–4, pp. 259–268, 1992.

[11] S. A. K. Nomvussi and J. Mikulka, "Enhanced image reconstruction in electrical impedance tomography using radial basis function neural networks," *Meas. Sci. Rev.*, vol. 24, no. 6, pp. 200–210, 2024.

[12] X. Li, X. Liu, B. Zhao, Y. Zhou, and G. Wang, "One-dimensional convolutional neural network (1D-CNN) image reconstruction for electrical impedance tomography," *Rev. Sci. Instrum.*, vol. 91, no. 12, pp. 1–7, 2020.

[13] A. Adler and W. R. B. Lionheart, "Uses and abuses of EIDORS: An extensible software base for EIT," *Physiol. Meas.*, vol. 27, no. 5, pp. S25–S42, 2006.

Driver inattention state: an overview of distraction, drowsiness, visual perception and infrared imaging

Sabrina Boujenfa, M. Sc.
*Faculty of Electrical Engineering
and Communication
Brno University of Technology*
Brno, Czech Republic
ORCID: 0000-0002-7078-183X

The identification of driver inattention is of critical importance in the context of road safety, given that inattention constitutes one of the primary causes of road traffic accidents. This paper examines several factors that contribute to driver inattention, with a particular focus on distraction, drowsiness, visual perception and infrared imaging. Distraction can be triggered by external (e.g. mobile phones) or internal (e.g. cognitive load) factors, while drowsiness significantly reduces responsiveness and attention. Visual perception is a key indicator of the driver's state of alertness. Modern driver monitoring systems increasingly use infrared imaging and eye-tracking technologies to analyse eye movements and detect signs of distraction or drowsiness at an early stage. This article provides a general overview of these aspects and shows how technological developments can help to improve the detection of inattention and increase driving safety.

Keywords — consciousness, distraction, drowsiness, monitoring, visual perception, infrared

I. INTRODUCTION

Monitoring of driver drowsiness and assessment of driver consciousness have been conducted for years to improve road safety, with a variety of methods being used to respond effectively to the constantly evolving conditions. The near-term outlook for vehicle development is the advancement of autonomous [1] driving technologies, which have the potential to free up the driver's attention for other tasks by providing assistance in certain driving functions. However, as these technologies become more prevalent, it becomes increasingly important to consider how drivers will respond to the reduced need to monitor the traffic around them. There exists a possibility that drivers may become distracted by other forms of stimuli as a result of relying on these assistance systems. Additionally, it is important to note that the Peltzman effect, a theory grounded in obligatory safety regulations, posits that the utilization of assistance systems may not necessarily diminish the number of accidents, but rather lead to a rise in careless driving behaviour [2].

II. DRIVER STATE INATTENTION WITH THE FOCUS ON DISTRACTION

Driver distraction is defined, „when a driver is delayed in the recognition of information needed to safely accomplish the driving task because some event, activity, object or person within or outside the vehicle compelled or tended to induce the driver's shifting attention away from the driving task" [3],[4], quoted from [5]. According to the National Highway Traffic Safety Administration (NHTSA), there are three types of driver distraction. The three types of distraction are presented below following [4], [6]. The first type of distraction is called "visual distraction" and can be understood as an obstruction that affects the field of vision [4] quoted from [6]. This includes any obstruction caused by a lack of visibility from the inside of the vehicle to the outside of the vehicle. A visual distraction can be an initiated distraction caused by the driver, such as looking or operating the navigation system [4] quoted from [6], [7], [8] [9]. Visual impairment can occur due to weather conditions such as rain or fog [10], [11]. This can make it difficult or impossible to detect traffic signs, other vehicles or road markings [10], [11], and visual clutter like advertising or changing traffic signs can also impair visual perception [11]. This increases the risk of an accident, and important visual information may not be recognised in a timely manner [10], [11], this is something common, for example, when someone gets lost in a thought or such as staring but not noticing [4] quoted from [6].

The second type of distraction can be described as biomechanical or manual distraction. This refers to physical distraction. It means the active removal of the hands from the steering wheel and a physical gesticulation [4] quoted from [12] and [13]. Furthermore, the same principles apply to the use of a smartphone while driving. A study conducted by the NHTSA [14], [15] indicates that composing a digital text message is a significant contributing factor to the risk of vehicular accidents. This phenomenon can be attributed to the fact that, in addition to other factors that may impede safe driving, such as visual and cognitive distraction, which will be discussed in greater detail below, operating a smartphone while driving necessitates the use of one hand for input, thereby reducing the number of hands available to control the vehicle. Furthermore, the study [14], [15], posits that operating a smartphone entails a convergence of visual, biomechanical, and cognitive distraction. As indicated by [16], [17], the typical driver will look away from the road for

approximately 23 seconds, a period that could result in a considerable increase in the risk of an accident. Furthermore, consuming food or beverages while operating a vehicle may also result in biomechanical distraction. As discussed in greater detail in the studies [16], [17], [18], the act of eating or drinking while operating a vehicle can significantly increase the risk of an accident. The act of holding objects or food in one's hands can impede the ability to control a vehicle, as visual and cognitive distractions are limited. As previously stated in the section on visual distraction, operating or adjusting air conditioning systems, radio stations, music playlists, or interior and exterior mirrors, etc., also results in increased accident risks [8], [14], [16], [17], [9].

The third type of distraction can be understood as cognitive or mental distraction. This distraction refers to any distraction related to perceiving, thinking, or remembering. Thus, any visual and biomechanical distraction is accompanied by cognitive distraction [13]. The following examples illustrate the phenomenon of cognitive or mental distraction. One of the most prevalent forms of cognitive distraction is the tendency for thoughts to become diffusely wandering, which can be attributed to a number of factors, including emotional impairment, stress, or worry. This phenomenon is exemplified by drivers who become mentally detached from the immediate driving situation. This results in a slower perception of situations and a slower reaction to dangerous situations [74], [15], [76], [77]. Other cognitive distractions include attempts to solve problems, thinking about professional or private situations, and emotionally aroused conversations with fellow drivers [75], [77], [78], [18], [9]. An interesting aspect of driver distraction is discussed in [19]. This states that there are tasks that do not require our full attention and that the remaining attentional capacity is then used for other activities [19]. This approach is noteworthy because it assumes that driving requires the driver's full attention.

III. Driver State Inattention with the focus on Drowsiness

As defined in [20], drowsiness refers to feeling sleepier than usual and having the potential to fall asleep at any moment, even if it is unwanted or prohibited. The term 'drowsy driving' refers to the act of driving while feeling sleepy, as stated in reference [21]. According to the National Highway Traffic Safety Administration (NHTSA), drowsy driving is one of the leading causes of car accidents. According to [21], these conditions can lead to a driver being less aware of their surroundings and becoming distracted from the task of driving According to reference [21], circumstances such as, lack of sleep, sleep disorders, alcohol consumption, medication, or the time of day can affect possible causes that can lead to drowsy driving. Previous research has shown that hybrid monitoring systems that utilise more than one measurement parameter provide a reliable system. According to [22], sensor systems, both invasive and non-invasive, are used for the detection of drowsiness, and measurements of both physiological and behavioural factors are used.

Extensive research has been carried out in the general area of distraction and drowsiness and vehicle-based measurements, behavioural measurements and physiological measurements are used [23]. The review paper [24] similarly presents various methods based on driver physiological signals (EEG, EMG, ECG, breathing frequency), driver facial features (percentage of eye closure, head position, gaze direction, etc.) and vehicle driving parameters (steering wheel position, vehicle position) are briefly reviewed for accuracy, sensitivity invasiveness's, anti-jamming and cost. The cited paper [24] outlines a range of techniques that utilize the driver's physiological indicators (such as EEG (electroencephalography), EMG (electromyography), ECG (electrocardiogram), respiratory rate, facial features (percentages of eye closure, head position, and gaze direction)) and driving automation parameters (steering wheel position and vehicle positioning.) It also briefly addresses metrics and considerations such as precision, sensitivity, invasiveness, immunity, and expense.

Invasive methods, that necessitate placing sensors on the driver's body to determine physiological signals, like the alpha band of the EEG, achieve desirable outcomes [25]. Nevertheless, non-invasive methods are commonly employed in practical applications because they do not cause stress or discomfort to the driver. Distraction and drowsiness have been extensively researched in general, using vehicle-based [23], [26], [27], behavioral [23], [28]–[30] and physiological measures [23], [31]–[35].

To improve the robustness of the detection sensor data fusion and a combination of multiple methods have been proposed where driver's' eye tracking is one of the most commonly used information for drowsiness detection [36]. Occupant monitoring through image acquisition in the combination of steering wheel position, steering angle and steering angle speed has been proposed [37].

The recognition of road events through the direction of gaze is also a large field of research [38]. In the field of drowsiness research, the movement of the eyes, blinking and the head position is recognized as significant for state of consciousness estimation and subsequent. The direction of gaze is also an indicator for assessing the driver's condition [39], [40]. Specific studies that categorise the direction of gaze in relation to pupil movement have recognized that methods based on single eye are vulnerable to eye localization errors, therefore evaluation based on both pupils is beneficial [40].

In addition to these parameters focusing on eyes, camera systems that monitor spatially large head/body movements also gain a high weight for observing the driver as evaluation of head dynamics [41] and detection of distractions [42] can contribute to the evaluation of consciousness. According to the current state of research, it can be defined that drowsiness behaviour can

be reliably detected by eye observation, by the support of camera systems and illuminators and by the head position [43].

IV. TECHNOLOGICAL APPROACH TO MONITOR DRIVER SATE OF CONSCIOUSNESS

A. Visual Perception

The process of visual perception enables the recognition, interpretation and classification of our surrounding environment [44]. The eye responds to changes in light by allowing light of a particular wavelength to pass through the pupil and lens onto the retina. This is where the photosensitive cell is stimulated. It provides proximal stimulation [45]. The visible spectrum ranges from 0.35 μm to 0.78 μm [46].

Perception with one eye is called monocular, perception with two eyes is called binocular [47], [48]. The field of vision is defined by either monocular or binocular vision. The binocular field of vision is not twice as large as the monocular field of vision, but is slightly larger; the fields of vision overlap at the point where the two fields of vision meet, usually at the centre [47]. With the head at rest, it is estimated that the visual field is expanded by 60° horizontally (left, right) and 40° vertically (up, down), taking into account eye motion [47], [48]. It allows the binocular field of view to expand into a single field of view through horizontal and vertical eye movement. Adjusting your field of vision requires moving your head or body [47], [48].

The eye movements as such can be described with the help of a gaze path (scan paths) and with the help of fixations and saccades (fast jumps of the gaze). When a person fixates on a point, your eye stays in one place for tenths of a millisecond to several seconds, but the eye does not remain still, there is a slight tremor in both eyes, this is called microtremor. Microtremor is characterised by an amplitude of 1 - 3 angular minutes and a frequency of 20 – 150 Hz. Microtremor is necessary for stable vision, otherwise the image on the retina disappears [47], [48], [49]. Change blindness occurs as soon as the change in an object, scene or image is overlooked because attention is not focused on the change. The interaction of saccades and fixations is described by a typical scan path. The movement of the eyes until the target object is reached is referred to as the gaze movement [47], [50], [51]. According to [50], eye movements include all movements that are detected and interpreted solely by observing the eye. These will be used in this research. According to [50], a change of gaze refers to micro-movements of the eye, so-called micro-saccades, in which the eye is re-positioned away from the previously fixated object [47].

B. Infrared Imaging

The technical terms "thermography" and "infrared thermography" [52] are used to describe night vision devices and thermal imaging technologies. A research report published by Spherical Insights & Consulting indicates that the demand for night vision devices will increase by 127.23% in 10 years (2032) [53]. Infrared thermography is a non-contact method for visualising thermal radiation that is invisible to the human eye using cameras [52], [54]. To gain a deeper understanding of infrared thermography, it is essential to consider the electromagnetic spectrum. The electromagnetic spectrum is the wavelength range of electromagnetic radiation. It is defined by frequency, wavelength and photon energy [55]. Frequencies in the electromagnetic spectrum range from 1Hz to 1025Hz [56]. Electromagnetic radiation is a form of energy with specific electrical and magnetic properties [55].

There are different types of radiation in the electromagnetic spectrum. These are characterised by the frequency they operate at and the wavelengths they cover. The following types are distinguished: gamma rays, X-rays, ultraviolet, visible light, infrared, microwaves and radiowaves [56]. This research concentrates on the infrared range. In the electromagnetic spectrum, the infrared (IR) is indicated in the same way as in Figure 1. Wavelengths (λ) are expressed in micrometre. The infrared range covers three different wavelengths (λ), from 0.78 μm to 1000 μm.

V. CONCLUSION

Distraction and fatigue represent a significant factor in the impairment of the driver's capacity to react and perceive, thereby markedly increasing the risk of accidents. In the context of the ongoing development of autonomous driving functions, it is imperative to closely monitor driving behaviour, with a view to detecting both distractions and drowsiness at an early stage. Infrared-based imaging can be used as a cost-effective non-intrusive tool to detect distraction and/or drowsiness; additional R&D in this field is of critical importance to further advance the transportation safety.

VI. ACKNOWLEDGMENTS

VII. REFERENCES

[1] © SAE International from SAE J3016™, 'SAE Levels of Driving Automation™ Refined for Clarity and International Audience', *SAE International*, 2021. https://www.sae.org/blog/sae-j3016-update (accessed Oct. 31, 2024).

[2] The Decision Lab, 'The Peltzman Effect'. https://thedecisionlab.com/reference-guide/psychology/the-peltzman-effect (accessed Oct. 25, 2023).

[3] M. A. Regan, C. Hallett, and C. P. Gordon, 'Driver distraction and driver inattention: Definition, relationship and taxonomy', *Accid. Anal. Prev.*, vol. 43, no. 5, pp. 1771–1781, 2011, doi: https://doi.org/10.1016/j.aap.2011.04.008.

[4] K. L. Young, M. A. Regan, and M. Hammer, 'Driver Distraction: A Review of the Literature', *Distracted Driv.*, no. November, p. 66, 2003, [Online]. Available:

https://www.monash.edu/__data/assets/pdf_file/0007/217177/Driver-distraction-a-review-of-the-literature.pdf.

[5] J. R. Treat, 'A study of precrash factors involved in traffic accidents', 1980, [Online]. Available: https://api.semanticscholar.org/CorpusID:112512111.

[6] H. ITO, B. ATSUMI, H. UNO, and M. AKAMATSU, 'Visual distraction while driving: trends in research and standardization', *IATSS Res.*, vol. 25, no. 2, pp. 20–28, Jan. 2001, doi: 10.1016/s0386-1112(14)60067-4.

[7] C. Chen, X. Zhao, H. Liu, G. Ren, and X. Liu, 'Influence of adverse weather on drivers' perceived risk during car following based on driving simulations', *J. Mod. Transp.*, vol. 27, no. 4, pp. 282–292, 2019, doi: 10.1007/s40534-019-00197-4.

[8] M. A. Regan and O. Oviedo-Trespalacios, 'Driver Distraction: Mechanisms, Evidence, Prevention, and Mitigation', in *The Vision Zero Handbook: Theory, Technology and Management for a Zero Casualty Policy*, K. Edvardsson Björnberg, M.-Å. Belin, S. O. Hansson, and C. Tingvall, Eds. Cham: Springer International Publishing, 2020, pp. 1–62.

[9] ChatGPT, 'OpenAI', *ChatGPT*, 2024. https://openai.com (accessed Sep. 19, 2024).

[10] United States Department of Transportation, '2. CURRENT RESEARCH AND PRACTICES | FHWA', *U.S. DEPARTMENT OF TRANSPORTATION*. https://highways.dot.gov/safety/other/visibility/roadway-visibility-research-needs-assessment/2-current-research-and (accessed Sep. 15, 2024).

[11] T. Cvahte Ojsteršek and D. Topolšek, 'Influence of drivers' visual and cognitive attention on their perception of changes in the traffic environment', *Eur. Transp. Res. Rev.*, vol. 11, no. 1, p. 45, 2019, doi: 10.1186/s12544-019-0384-2.

[12] the Royal Society for the Prevention of Accidents, 'Mobile Phones and Driving : a Literature Review', no. August, 1997, [Online]. Available: file:///Users/baumann/Documents/Mendeley Desktop/mobile_phone_litreview.pdf.

[13] B. Hamilton, J. Grabowski, and AAA Foundation for Traffic Safety, 'Cognitive Distraction: Something to Think About-Lessons Learned from Recent Studies About the Sponsor', *AAA Found. Traffic Saf.*, 2013, Accessed: Dec. 10, 2023. [Online]. Available: www.AAAFoundation.org.

[14] National Highway Traffic Safety Administration, 'Teen Safe Driving: How Teens Can Be Safer Drivers', *United States Department of Transportation*, 2024. https://www.nhtsa.gov/road-safety/teen-driving (accessed Sep. 19, 2024).

[15] National Highway Traffic Safety Administration, 'Distracted Driving Dangers and Statistics | NHTSA', *United States Department of Transportation*, 2024. https://www.nhtsa.gov/risky-driving/distracted-driving (accessed Sep. 19, 2024).

[16] G. M. Fitch *et al.*, 'The Impact of Hand-Held And Hands-Free Cell Phone Use on Driving Performance and Safety-Critical Event Risk Final Report', *Dep. Transp. Natl. Highw. Traffic Saf. Adm.*, no. April, pp. 1–273, 2013, [Online]. Available: https://www.nhtsa.gov/DOT/NHTSA/NVS/Crash Avoidance/Technical Publications/2013/811757.pdf.

[17] V. T. T. Institute, 'New VTTI study results continue to highlight the dangers of distracted driving | Virginia Tech Transportation Institute', *Virginia Tech Transportation Institute*, 2024. https://featured.vtti.vt.edu/2013/05/new-vtti-study-results-continue-to-highlight-the-dangers-of-distracted-driving/ (accessed Sep. 19, 2024).

[18] N. Becker, H. W. Rust, and U. Ulbrich, 'Weather impacts on various types of road crashes: a quantitative analysis using generalized additive models', *Eur. Transp. Res. Rev.*, vol. 14, no. 1,

p. 37, 2022, doi: 10.1186/s12544-022-00561-2.

[19] M. A. Reagan, J. D. Lee, and K. Young, *Driver distraction : theory, effects, and mitigation*. CRC Press Taylor & Francis Group, 2009.

[20] D. C. Dugdale, D. Zieve, and Department of Medicine University of Washington School of Medicine, 'Drowsiness', 2021. https://medlineplus.gov/ency/article/003208.htm (accessed Dec. 10, 2023).

[21] A. Rehman and E. Suni, 'Drowsy Driving: Dangers and How to Avoid it', 2022. Accessed: Dec. 10, 2023. [Online]. Available: https://www.sleepfoundation.org/drowsy-driving.

[22] A. Lemkaddem *et al.*, 'Multi-modal driver drowsiness detection: A feasibility study', in *2018 IEEE EMBS International Conference on Biomedical and Health Informatics, BHI 2018*, Apr. 2018, vol. 2018-Janua, pp. 9–12, doi: 10.1109/BHI.2018.8333357.

[23] A. Sahayadhas, K. Sundaraj, and M. Murugappan, 'Detecting driver drowsiness based on sensors: A review', *Sensors*, vol. 12, no. 12, pp. 16937–16953, Dec. 2012, doi: 10.3390/s121216937.

[24] S.-Y. Shi, W.-Z. Tang, and Y.-Y. Wang, 'A Review on Fatigue Driving Detection', *ITM Web Conf.*, vol. 12, p. 01019, Sep. 2017, doi: 10.1051/itmconf/20171201019.

[25] P. C. Nissimagoudar and A. V. Nandi, 'Precision Enhancement of Driver Assistant System Using EEG Based Driver Consciousness Analysis & Classification', in *Process Efficient Artificial Neural Network-Based Approach for Channel Selection and Classification of Seizures*, 2020, pp. 247–257.

[26] C. C. Liu, S. G. Hosking, and M. G. Lenné, 'Predicting driver drowsiness using vehicle measures: recent insights and future challenges.', *J. Safety Res.*, vol. 40, no. 4, pp. 239–245, 2009, doi: 10.1016/j.jsr.2009.04.005.

[27] P. M. Forsman, B. J. Vila, R. A. Short, C. G. Mott, and H. P. A. Van Dongen, 'Efficient driver drowsiness detection at moderate levels of drowsiness.', *Accid. Anal. Prev.*, vol. 50, Jan. 2013, doi: 10.1016/j.aap.2012.05.005.

[28] Y. Sun, 'Yawning Detection Based on Gabor Wavelets and LDA', *J. Beijing Univ. Technol.*, pp. 409–413, 2009, [Online]. Available: https://api.semanticscholar.org/CorpusID:203964783.

[29] Z. Zhang and J. Zhang, 'A new real-time eye tracking based on nonlinear unscented Kalman filter for monitoring driver fatigue', *J. Control Theory Appl.*, vol. 8, no. 2, pp. 181–188, 2010, doi: 10.1007/s11768-010-8043-0.

[30] B.-C. YIN, X. FAN, and Y.-F. SUN, 'MULTISCALE DYNAMIC FEATURES BASED DRIVER FATIGUE DETECTION', *Int. J. Pattern Recognit. Artif. Intell.*, vol. 23, no. 03, pp. 575–589, 2009, doi: 10.1142/S021800140900720X.

[31] M. Akin, M. B. Kurt, N. Sezgin, and M. Bayram, 'Estimating vigilance level by using EEG and EMG signals', *Neural Comput. Appl.*, vol. 17, pp. 227–236, 2008, [Online]. Available: https://api.semanticscholar.org/CorpusID:22487841.

[32] A. K. Kokonozi, E. M. Michail, I. C. Chouvarda, and N. M. Maglaveras, 'A study of heart rate and brain system complexity and their interaction in sleep-deprived subjects', in *2008 Computers in Cardiology*, 2008, pp. 969–971, doi: 10.1109/CIC.2008.4749205.

[33] R. N. Khushaba, S. Kodagoda, S. Lal, and G. Dissanayake, 'Driver drowsiness classification using fuzzy wavelet-packet-based feature-extraction algorithm.', *IEEE Trans. Biomed. Eng.*, vol. 58, no. 1, pp. 121–131, Jan. 2011, doi: 10.1109/TBME.2010.2077291.

[34] W. C. Liang, J. Yuan, D. C. Sun, and M. H. Lin, 'Changes in physiological parameters induced by indoor simulated driving: Effect of lower body exercise at mid-term break', *Sensors*, vol. 9, no. 9, pp. 6913–6933, 2009, doi: 10.3390/s90906913.

[35] G. Yang, Y. Lin, and P. Bhattacharya, 'A driver fatigue recognition

model based on information fusion and dynamic Bayesian network', *Inf. Sci. (Ny).*, vol. 180, no. 10, pp. 1942–1954, 2010, doi: 10.1016/j.ins.2010.01.011.

[36] S. Samiee, S. Azadi, R. Kazemi, A. Nahvi, and A. Eichberger, 'Data fusion to develop a driver drowsiness detection system with robustness to signal loss', *Sensors*, vol. 14, no. 9, pp. 17832–17847, 2014, doi: 10.3390/s140917832.

[37] J. C. Lisseman and L. Cech, 'Insassenüberwachungssysteme und -Verfahren [Occupant monitoring systems and procedures]. German patent DE112015005413T5.', 2015.

[38] L. Fletcher and A. Zelinsky, 'Driver inattention detection based on eye gaze - road event correlation. The International Journal of Robotics Research', *Int. J. Rob. Res.*, vol. 28, no. 6, pp. 774–801, 2009, doi: 10.1177/0278364908099459.

[39] W. Yafei, T. Zhao, D. Xueyan, J. Bian, and X. Fu, 'Head pose-free eye gaze prediction for driver attention study', *2017 IEEE Int. Conf. Big Data Smart Comput. (BigComp), Jeju, Korea (South),* pp. 42–46, 2017, doi: 10.1109/BIGCOMP.2017.7881713.

[40] J. Jo, S. J. Lee, K. R. Park, I. J. Kim, and J. Kim, 'Detecting driver drowsiness using feature-level fusion and user-specific classification', *Expert Syst. Appl.*, vol. 41, no. 4 PART 1, pp. 1139–1152, 2014, doi: 10.1016/j.eswa.2013.07.108.

[41] S. Martin, A. Tawari, and M. M. Trivedi, 'Monitoring head dynamics for driver assistance systems: A multi-perspective approach.', in *IEEE Conference on Intelligent Transportation Systems, Proceedings, (ITSC 2013), The Hague, Netherlands*, 2013, pp. 2286–2291, doi: 10.1109/ITSC.2013.6728568.

[42] D. Tran, H. M. Do, W. Sheng, H. Bai, and G. Chowdhary, 'Real-time detection of distracted driving based on deep learning', *IET Intell. Transp. Syst.*, vol. 12, no. 10, pp. 1210–1219, 2018, doi: 10.1049/iet-its.2018.5172.

[43] F. Friedrichs and B. Yang, 'Camera-based drowsiness reference for driver state classification under real driving conditions', *IEEE Intell. Veh. Symp. Proc.*, pp. 101–106, 2010, doi: 10.1109/IVS.2010.5548039.

[44] C. Bellebaum, P. Thoma, and I. Daum, 'Visuelle Wahrnehmung: Was, Wo und Wie', in *Neuropsychologie*, Wiesbaden: VS Verlag für Sozialwissenschaften, 2012, pp. 31–46.

[45] P. M. Bak, 'Visuelle Wahrnehmung', in *Wahrnehmung, Gedächtnis, Sprache, Denken Allgemeine Psychologie I – das Wichtigste, prägnant und anwendungsorientiert*, 2020, pp. 29–45.

[46] A. Luib, *Infrarot-Thermographie in der Bauforschung: Anwendungsmöglichkeiten und Grenzen*. University of Bamberg Press, 2022.

[47] P. Sprenger, 'Visuelle Wahrnehmung und visuelle Aufmerksamkeit', in *Prozesse bei der strukturierenden Mengenwahrnehmung und strukturnutzenden Anzahlbestimmung von Kindern im Elementarbereich*, 2021, pp. 51–83.

[48] N. Birbaumer and R. F. Schmidt, *Biologische Psychologie*. Springer Berlin, Heidelberg, 2006.

[49] K. Holmqvist, M. Nyström, R. Andersson, R. Dewhurst, H. Jarodzka, and J. van de Weijer, *Eye tracking: a comprehensive guide to methods and measures*, no. 1. OUP Oxford, 2011.

[50] M. Joos, M. Rötting, and B. M. Velichkovsky, 'Die Bewegungen des menschlichen Auges: Fakten, Methoden, innovative Anwendungen', in *Psycholinguistik/ Psycholinguistics. Ein internationales Handbuch/An International Handbook*, Berlin & NY: de Gruyter, 2003, pp. 142–168.

[51] G. Drusch and J. M. C. Bastien, 'Analyzing Web pages visual scanpaths: Between and within tasks variability', *Work*, vol. 41, no. SUPPL.1, pp. 1559–1566, 2012, doi: 10.3233/WOR-2012-0353-1559.

[52] LUMITOS AG, 'Thermografie'. https://www.chemie.de/lexikon/Thermografie.html (accessed Aug. 05, 2024).

[53] Spherical Insights, 'Globaler Markt für Nachtsichtgeräte Größe, Prognose 2022 - 2032'. https://www.sphericalinsights.com/de/reports/night-vision-device-market (accessed Aug. 05, 2024).

[54] Axis Communications AB, 'Wärmebildtechnologie | Axis Communications'. https://www.axis.com/de-de/solutions/thermal-imaging (accessed Aug. 05, 2024).

[55] A. Manickavasagan and H. Jayasuriya, *Imaging with electromagnetic spectrum: Applications in food and agriculture*, vol. 9783642548. Springer-Verlag Berlin Heidelberg, 2014.

[56] BYJU'S E-Learning Providers, 'Electromagnetic Spectrum - Definition, Characteristics, Range, Diagram', 2021. https://byjus.com/jee/electromagnetic-spectrum-and-electromagnetic-waves/ (accessed Nov. 30, 2023).

The Methods of Accurate Measurement of Tilt Azimuth within Small Angles of Tilt

Veronika Junasová
Department of Microelectronics
Faculty of Electrical Engineering and Communication, Brno
University of Technology
Brno, Czech Republic
xjunas00@vutbr.cz

Vladimír Levek
Department of Microelectronics
Faculty of Electrical Engineering and Communication, Brno
University of Technology
Brno, Czech Republic
levek@vut.cz

Abstract—**This article focusses on the determination of the tilt azimuth within the small angles of tilt using accelerometer. Azimuth is usually acquired using magnetometers and is then called the magnetic azimuth. In practice, magnetometers are commonly accompanied by other inertial sensors or filtering. The azimuth can be relatively easily acquired using a single magnetometer, which has to be properly calibrated against the magnetic materials in its surroundings. For further improvement in accuracy of measurement, a sensor fusion or filtering is necessary. The advantages and drawbacks of using magnetometer and filtering are discussed. In contrast to these more complex techniques, a different configuration of measurement is used further in the article. The main focus is to present a low-cost and easy-to-integrate method of measurement. It consists of the definition of the accelerometer position, which is rotated by 45°. In this configuration, the accelerometer alone can be used to determine the azimuth of the tilt and the tilt itself. That is given by the better distribution of gravitational force among accelerometer axes and their sensitivity. This is prooved by mathematically derived equations. In the final results, the measurement with the rotated accelerometer is shown, and the improvement in accuracy and statistics is determined.**

Keywords—accelerometer, tilt azimuth, heading, noise, coordinate system

I. INTRODUCTION

The azimuth is commonly understood as the tilt angle from the north. As such, it is often called magnetic azimuth and information about it is used in different fields of application, for example, mobile phones, navigation, space applications, aviation, geodetic applications, and many more [1]. The azimuth often accompanies other parameters that describe the position in a three-dimensional space. In this work, the focus is on tilt angle and its azimuth, which can be referred to as tilt heading or tilt direction.

The tilt angle can be defined as the deviation in degrees from a certain line or point, which is usually one of the referential axes x, y, or z in a three-dimensional space. It is possible to obtain the angle of tilt relatively accurately using only an accelerometer without the need for complex filtering or complicated mathematics and matrices. The measurement of tilt can be considered simple; however, the information about inclination from a predefined line is not entirely sufficient in some applications. Additional data about the direction of the tilt might

be desired. Therefore, the azimuth of the tilt must be defined and acquired along with the tilt angle. This paper is inspired by the measurement required in geodesy when a drilled hole needs to be measured and any tilt has to be spotted precisely. When the tilt from the vertical line occurs, it is necessary to also determine its direction in space; therefore, the tilt azimuth is desired. In such application, the tilt angle is up to a few degrees. Therefore, the precondition for this work is the need for accurate measurements of the tilt and tilt azimuth within small angles of tilt. Furthermore, the solution should be low-cost and relatively easy and quick to integrate into the system without the additional computational costs. Therefore, MEMS accelerometers are preferred due to their cost and accessibility.

The tilt azimuth can be obtained by various sensors and techniques, which deliver different accuracy of measurement and complexity of the used method. As such, these techniques have certain advantages and disadvantages associated with them. The most straightforward and commonly used method to measure the tilt azimuth is to use one magnetometer. This magnetometer has to be properly calibrated otherwise the estimation of azimuth would not bear any significance. However, the accuracy in this case might be insufficient and calibration may cause problems. Moreover, in the drilled hole, the calibration might prove even more challenging. To boost the accuracy, usually another sensor is used along with the magnetometer. To combine the output of the magnetometer and an additional sensor, the sensor fusion is used alongside filters. Although their performance is superior, they can be difficult and time consuming to implement.

Accurate measurement of tilt and tilt azimuth proves to be a challenging task for a person who needs a simple and quick solution. The accelerometer is an ideal sensor for this. It measures tilt angle directly, and there is a relatively simple equation for obtaining tilt azimuth with it. However, the tilt heading measurement using an accelerometer is vastly inaccurate within small angles of tilt. This paper presents the mathematical derivation of equations which theoretically justify the unreliable results of tilt azimuth measurement under the mentioned circumstances. From there it is derived why the accuracy of measurement would benefit from rotation of the accelerometer in a more convenient angle. At the end, the measurements are shown with statistical processing to prove the theoretical presumption to be correct.

A. Measurement of Tilt Using Accelerometer

The tilt can be defined as the inclination from a certain line, typically a horizontal or vertical line. According to this reference line, the equation for tilt quantification from the sensors output differs. In this work, the considered tilt will be given as the inclination angle from the vertical line parallel to the gravitational force, respectively gravitational acceleration. In other words, it is the deviation in degrees from the referential z_{ref} axis. Therefore, the equations stated or derived in this article are mostly in relation to the referential z_{ref} axis. The tilt angle associated with the z axis is commonly marked as ψ. Labels for the inclination from x axis is φ and from the y axis it is θ, as shown in the Fig. 1 [2]. The referential coordinate system with the rotation angles between the referential axes and actual axes of the tilted object is depicted.
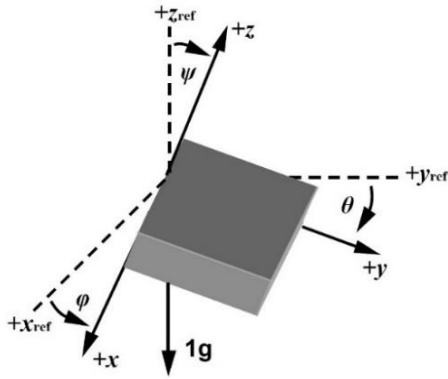

Fig. 1. The referential coordinate system with marked rotation angles between the tilted and referential axes [3].

To obtain the tilt angle, the accelerometer can be used. It is an inertial sensor that measures the static and dynamic acceleration applied to it. Especially useful for the determination of tilt is the ability to measure static acceleration. When the accelerometer is stationary, the only force applied to it is gravitational force, and therefore only acceleration it senses is gravitational acceleration equal to 1 g. This acceleration is considered constant, and it is at all times orientated to the Earth centre, as is illustrated in the Fig. 1.

The accelerometers can have one to three axes perpendicular to each other. When the accelerometer is tilted and motionless, the gravitational acceleration, the only present acceleration, splits among all accessible axes of the accelerometer in accordance with the angle of tilt. In order to obtain the most accurate measurement, three axes are necessary. Otherwise, in case of an accelerometer tilting in the direction of the missing axis, the part of the gravitational acceleration would not be captured, and the resultant quantification would not be as accurate as when three axes are present [3; 4]. This is part of the reason why three axis accelerometers are the most suitable for tilt quantification, and such sensor will be used in all following theoretical derivations of equations as well as experiments.

The equation for the tilt angle can be derived by applying basic trigonometry and the Pythagorean theorem. Let the output acceleration appearing on each axis of accelerometer be marked

as A_x, A_y and A_z. When the accelerometer is steady the vector sum of all three outputs A_x, A_y and A_z gives 1g. This is based on the Pythagorean theorem applied in three-dimensional space. The equation for angle of tilt ψ using only information of acceleration from the axis A_z of the accelerometer and the known value of 1 g is [3]:

$$\cos \psi = \frac{A_z}{1g}. \tag{1}$$

Similarly, the equation for the angle of tilt φ using only the acceleration A_x is given as [3]:

$$\sin \varphi = \frac{A_x}{1g}. \tag{2}$$

The same as (2) would apply to the angle θ using acceleration A_y [3]. Using only one axis for tilt determination is possible; however, it is not accurate [3,4]. As stated previously, the three-axis accelerometer is ideal for measuring tilt. Therefore, the following equation for tilt ψ obtaining is derived for accelerometer with all three axes available. When the accelerometer is still, the whole gravitational acceleration is divided among all three axes at all times. The only thing that changes is the portion of it on each axis based on the actual tilt angle. This is depicted in Fig. 2 from which the equation for tilt angle can be derived.
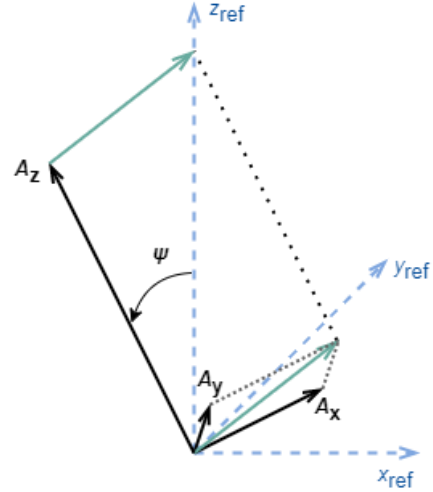
Fig. 2. The graphical representation of the tilt angle for the derivation of tilt angle equation [5].

The accelerometer in Fig. 2 is tilted by an angle ψ from the referential axis z_{ref} in such a way that all three accelerations are positive. Considering the proportions of accelerations A_x, A_y and A_z, the shown tilt is relatively small, since the acceleration A_z is significantly larger than A_x and A_y and obtains a major part of gravitational acceleration. The accelerations A_x and A_y create a plane on which the resultant of their vector sum, drawn as a green arrow, lays. It can be deduced, that the tangent of the angle ψ is a quotient of the vector sum resultant formed by accelerations A_x and A_y and the acceleration A_z [3,5]:

$$\tan \psi = \frac{\sqrt{A_x^2 + A_y^2}}{A_z}. \tag{3}$$

The result of (3) is the tilt angle in degrees and it obtains values from −90° to 90°. When tilt ψ would result in 0°, it means that there is no inclination from the vertical referential axis z_{ref}. The output angle of 90°, respectively −90°, indicates that the measuring device is perpendicular to the reference axis z_{ref}.

B. Magnetic Azimuth and Filtering

The information about tilt alone might not be sufficient, and the knowledge of its heading may be required to properly define the system. As mentioned in the introduction, in certain applications it is necessary to recognise the direction to which the device, or sensor, is tilted. This is usually referred to as azimuth. The magnetometers are used most often to acquire magnetic azimuth.

Equations for quantification of magnetic azimuth using magnetometers are relatively simple. The problem with magnetometers is their calibration. To obtain relevant data, all sensors must be calibrated [6]. This process is simple with accelerometers and gyroscopes compared to magnetometers. The calibration is a quite complex process, which is described in detail in [7] and [8]. However, it can be said that adding a magnetometer to the device in order to measure azimuth comes with the disadvantage of complex calibration, which has to be regularly repeated in order to get relevant data. Another disadvantage is the accuracy of magnetic azimuth measurement using magnetometer alone. The measured azimuth deviates significantly from the actual set angle, as presented in [8]. Moreover, the magnetometers measure magnetic north and not true north, as is desired in some applications.

To achieve more accurate measurements, sensor fusion or digital filters are widely used. These solutions require the usage of another sensor, which means that solely one magnetometer would not be sufficient and to the application another device has to be added. The incorporation of filter comes with the higher demands for processing and adds the computational time and costs. Another drawback of using filters is the fact that the filters can be time consuming to understand and implement into the system.

C. Azimuth Measurement Using Accelerometer

The azimuth of tilt can also be obtained from the outputs of the accelerometers alone. Though it is unusual to measure azimuth with an accelerometer, the equation is quite simple, and this method poses an advantage that there is no need to add different sensors to the system. The equation can be deduced from the configuration in Fig. 3. Referential axes are represented with the accelerations A_x, A_y, A_z on each axis of the tilted accelerometer. It is visible that the same angle of tilt can head in different directions. This tilt azimuth can obtain angle anywhere in the whole circle; hence, it can obtain values anywhere from 0° to 360°. To define the azimuth, there is a need to establish a reference line to which it will be determined. Let the reference line be axis y and let the azimuth be labelled α.

From Fig. 3 the tilt azimuth can be deduced with the established line y as a referential line. The equation would be given as [5]:

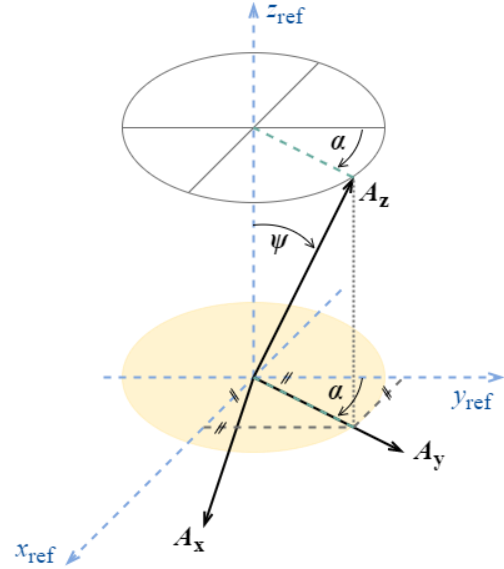$$\tan \alpha = \frac{A_x}{A_y}. \tag{4}$$

Fig. 3. The graphical representation of tilt ψ and the azimuth of tilt α [5].

The angle of tilt azimuth ψ determined using (4) gives the result in degrees in the range from −90° to 90°. However, the desired output should be a whole circle, that is, it should reach 360° instead of 180°. There are two options how to achieve this. The signs of output values of axes x and y can be used to determine the quadrant in which the result lays and to alter the azimuth angle accordingly. The second possibility is to use the function atan2 and to convert the result from radians to degrees, as shown in [5]:

$$\alpha = \frac{180}{\pi} \cdot \text{atan2} \left(\frac{A_x}{A_y} \right). \tag{5}$$

The advantage of this method of tilt azimuth determination is simplicity and the lack of the need for additional sensors. However, the azimuth obtained from the accelerometer alone may be inaccurate when the tilt angle is small. This will be discussed and derived further in the article and a solution will be presented.

III. MATHEMATICAL HYPOTHESIS AND EXPERIMENTS

In the previous theoretical chapter, it was established that it is possible to measure azimuth of tilt using only an accelerometer. The impact of the distribution of gravitational acceleration and the noise on the tilt and its azimuth measurement will be derived in this chapter. The focus here is on mathematical hypothesis why the impact of noise is more dominant on axes perpendicular to the gravitational acceleration compared to the parallel axis and how this theoretically affects the measurement of tilt azimuth. At the end, the measurement supporting the hypothesis is carried out.

A. Noise and Distribution of Gravitational Acceleration

Noise is present in any measurement and cannot be eliminated without the use of complex filters. However, it is possible to define the theoretical impact of noise on measurement and then propose the solution for optimization. For this, (1) and (2) will be used. The acceleration on each axis has
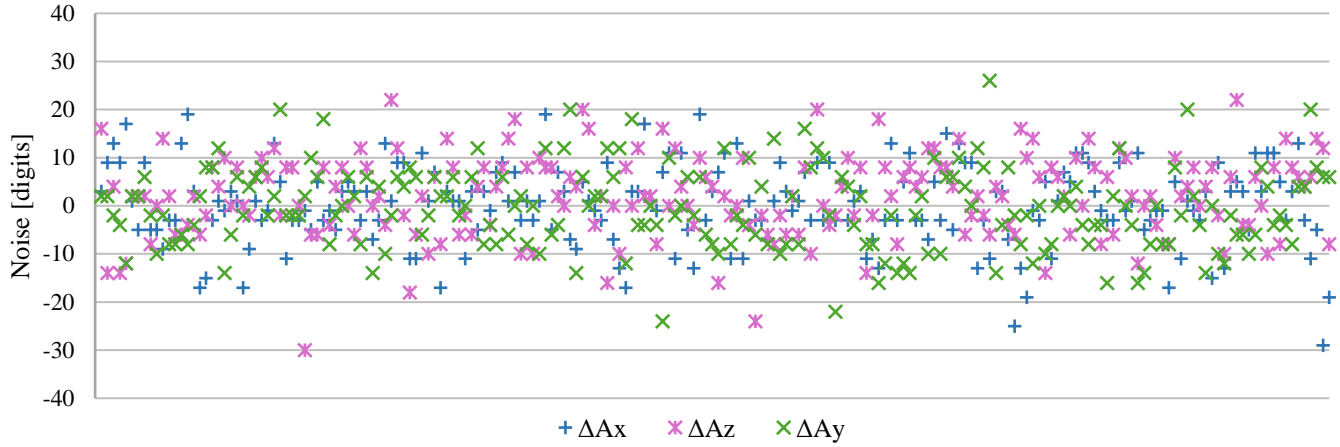
Fig. 4. The measured noise on axis x (blue colour), y (green colour) and z (purple colour) of the accelerometer without tilt.

superimposed noise. Let the axis z of an accelerometer measure $A_z + \Delta_{Az}$ where A_z is the actual acceleration and Δ_{Az} is the superimposed noise. Similarly for axis x and y, let the output be $A_x + \Delta_{Ax}$, respectively $A_y + \Delta_{Ay}$, where A_x, A_y is acceleration on given axis, and Δ_{Ax}, Δ_{Ay} is superimposed noise on them. Then the equations can be written as follows:

$$\cos\psi = \frac{A_z + \Delta_{Az}}{1g}, \tag{6}$$

$$\sin\varphi = \frac{A_x + \Delta_{Ax}}{1g}, \tag{7}$$

$$\sin\theta = \frac{A_y + \Delta_{Ay}}{1g}. \tag{8}$$

When the tilt angle is relatively small, the measurement is not accurate, as is proved in the previous work [5]. The gravitational acceleration is then distributed in such a way that dominant part of it is measured on axis z and minor portion is measured on axes x and y. Let the tilt angle be so small that the acceleration on the axis z of the accelerometer is:

$$A_z \approx 1g \tag{9}$$

and then the accelerations on the axes x and y are approximately:

$$A_x \approx A_y \approx 0g. \tag{10}$$

From this presumption, the angles ψ, φ and θ can be written as:

$$\cos\psi \approx \frac{1g + \Delta_{Az}}{1g} \approx 1 + \frac{\Delta_{Az}}{1g}, \tag{11}$$

$$\sin\varphi \approx \frac{0g + \Delta_{Ax}}{1g} \approx \frac{\Delta_{Ax}}{1g}, \tag{12}$$

$$\sin\theta \approx \frac{0g + \Delta_{Ay}}{1g} \approx \frac{\Delta_{Ay}}{1g}. \tag{13}$$

From equations (11), (12) and (13) it is theoretically possible to deduce that the noise on the axis z should have a lower impact on the calculation of angle ψ than the noises on the axes x and y on angles φ and θ. This is given by the mathematical behaviour of the used functions and derived equations. To prove this assumption and the correctness of the derived equations, the

experiment was carried out. In Fig. 4 the noise on all axes after calibration of the accelerometer is depicted.

From Fig. 4 it is visible that the noise taken on 200 samples is stochastic on all axes. The sensor used to measure it is the inertial measurement unit IIM-42652 which incorporates a three-axis accelerometer and a three-axis gyroscope in one measurement unit [9]. 1000 samples were taken in total from which the angles ψ, φ and θ were quantified using (1), (2) and statistically processed. The average value and standard deviation of each angle were calculated, and the results are summarised in Table I. From there it is proved that the noise on the axes x and y has a bigger impact on the accuracy of measurement compared to the noise on the axis z. Therefore, the measurement confirms the theoretical hypothesis.

TABLE I. THE AVERAGE VALUE AND STANDARD DEVIATION OF MEASURED ANGLES

	φ	θ	ψ
Average value [°]	-0,0005	-0,0008	0,03740
Standard deviation [°]	0,031	0,029	0,020

B. The Impact of Noise on Tilt Azimuth

Equation (4) to determine azimuth utilises only accelerations from axes x and y. When the angle of tilt ψ is small, most of the gravitational acceleration is measured on A_z. Therefore, equations (9) and (10) apply. From there, the equation (4) for azimuth obtaining can be altered as:

$$\tan\alpha = \frac{A_x}{A_y} \approx \frac{\frac{\Delta_{Ax}}{1g}}{\frac{\Delta_{Ay}}{1g}} \approx \frac{\Delta_{Ax}}{\Delta_{Ay}}. \tag{14}$$

It is clear that in the quantification of tilt azimuth only noise is involved and no or minimal portion of actual gravitational acceleration. Therefore, the measurement of the tilt azimuth is inaccurate and of no significance. To improve the measurement, the impact of noise needs to be eliminated. This can be done by definition of a new coordinate system, which would position the accelerometer in such an angle that the noise and its effect would be negligible to the eventual measurement. The proposition that should optimise the measurement consists of rotation of the accelerometer by 45°. In this position, the gravitational

acceleration would be distributed among axes more evenly, and noise would not have such influence on the measurement since it would be negligible compared to the actual value of acceleration on each axis.

C. Measurement of Azimuth of Tilt

To prove the proposition for optimisation of the measurement, the data were acquired with device laying horizontally, which is also shown in the Fig. 4. Then the device with accelerometer was rotated by 45° to achieve the proposed position of the sensor. 1000 samples were taken for both methods, and azimuth of tilt was calculated. In Fig. 5 the first 200 azimuth angles are shown. The azimuth measured without rotation is portrayed with blue colour and azimuth obtained after rotation is depicted by green colour. It is clear that the first azimuth is incoherent. On the other side, the azimuth utilising the proposed optimisation is stable, and noise does not affect it.
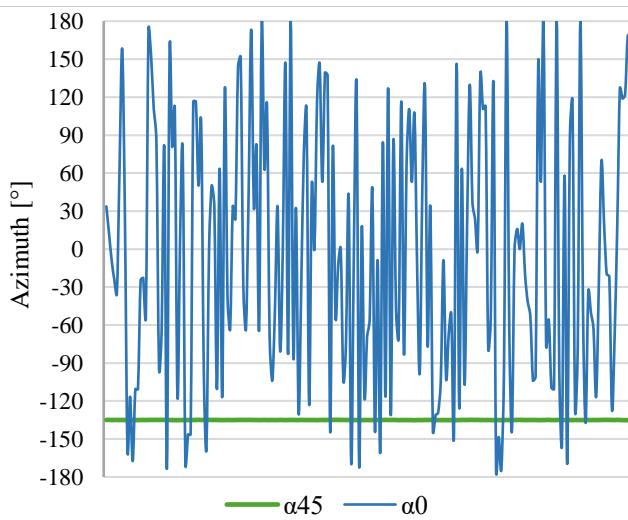

Fig. 5. The azimuth of tilt measured without rotation (blue colour) and in the new proposed position (green colour).

The obtained azimuth angles were statistically processed and are summarised in the Table II. The azimuth without rotation α_0 deviates significantly and the average value does not even make sense. The azimuth of the rotated configuration α_{45} has an average value -134,99 ° with a standard deviation 0,055°.

TABLE II.   THE AVERAGE VALUE AND STANDARD DEVIATION OF THE MEASURED AZIMUTH OF TILT

	α_0	α_{45}
Average value [°]	-3,70	-134,99
Standard deviation [°]	105,232	0,055

IV. Conslusion

This article describes several methods of acquiring azimuth of tilt using accelerometer, or magnetometer alone or with the use of sensor fusion, respectively digital filters. The focus is on the low-cost, quick, and easy to incorporate method of measurement of the tilt azimuth when the angle of tilt is small. The theoretical explanation and derivation of measurement and needed equations are included. The measurement of azimuth of tilt using an accelerometer, which is not a very common method, is included at the end of the theoretical part. The advantage of this method is that there is no need to add different sensors to the measuring system, which reduces the financial costs. However, the accuracy within small angles of tilt is inadequate. The problem was established with the derivation of equations concerning noise. It was deduced that the impact of noise demonstrates itself more on the axes perpendicular to the gravitational acceleration and less on the axis parallel to it. Since the tilt azimuth equation uses only axes perpendicular to the gravitational acceleration, the measurement would be inapplicable when the tilt angle is small. However, with rotation of the sensor, the noise would be less significant compared to actual measured acceleration and it would manifest itself less. This was experimentally proven with the measuring device rotated by 45°. The tilt azimuth was measured and statistically processed in this position and in the original position. The results show that the derived mathematical hypothesis was correct, and the measurement is more accurate with a rotated sensor. Therefore, this is an easy and fast to integrate method of measurement with the minimal time and financial costs. Further improvement in this field could be the analytical definition of the new coordinate system in which the position of the accelerometer would measure the tilt and azimuth of the tilt most accurately. Then compare the proposed orientation with the measurement from magnetometer with and without filters.

References

[1] J. FRADEN, Handbook of modern sensors: physics, designs, and applications, 5th ed, San Diego: Springer International Publishing, 2016. ISBN 978-3-319-19302-1.

[2] T. YOUNG, Performance of the jet transport airplane: analysis methods, flight operations, and regulations, 1st ed, Wiley, 2018. ISBN 978-1-119-68278-3.

[3] C. Fisher, "AN-1057: Using an accelerometer for inclination sensing", Analog Devices, rev. 0, 2010.

[4] S. Luczak, "Single-axis tilt measurement realized by means of MEMS accelerometers", Int. J. Mech. Eng. Educ., vol. 18, pp. 341–351, 2011.

[5] V. Junasová, V. Levek, and P. Šteffan, "The proposal for optimization of direction of tilt measurement in small angles", in 2023 46th International Spring Seminar on Elctronics Technology (ISSE), IEEE 2023. ISBN 979-8-3503-3484-5.

[6] Á. López Revuelta, "Orientation estimation and movement recognition using low cost sensors," Blekinge Institute of Technology, Karlskrona, Sweden, pp. 79, 2017.

[7] Ch. KONVALIN, "Compensating for Tilt, Hard-Iron, and Soft-Iron Effects," Questex, 2009.

[8] V. Junasová, V. Levek, and P. Šteffan, "The precise measurement of magnetic azimuth", in Proceedingd II of the 29th Student EEICT 2023, VUT, FEKT, 2023. ISBN 978-80-214-6154-3.

[9] TDK InvenSense, "IIM-42652 Datasheet: High-performance 6-Axis SmartIndustrial™ MotionTracking MEMS Device for Industrial Applications," 2021.

General Solution of Linear Planar Weakly Delayed Discrete Systems with Multiple Delays and with a Singular Matrix of Non-delayed Terms

1st Marie Hartmanová

Department of Mathematics
Brno University of Technology
Faculty of Electrical Engineering and Communication
and Central European Institute of Technology
Brno, Czech Republic
marie.hartmanova@vut.cz

2nd Josef Diblík

Department of Mathematics
Brno University of Technology
Faculty of Electrical Engineering and Communication
and Central European Institute of Technology
Brno, Czech Republic
diblik@vut.cz

Abstract—A planar weakly delayed linear discrete system with multiple delays is considered. Assuming that the conditions for weakly delayed systems are fulfilled, the general solution of the system is constructed in the previously not considered case of the matrix of nondelayed terms having a single nonzero eigenvalue with the second one being zero. Then, there exists a non-delayed planar discrete system that, for all sufficiently large values of the independent variable, has the same general solution. New findings are illustrated with an example and discussed in relation to the previously known investigations. The formulas derived can be useful in digital signal processing.

Index Terms—system of discrete equations, linear system, multiple delays, initial problem, single zero eigenvalue, formula for general solution

I. INTRODUCTION

We consider a planar linear discrete delayed system

$$y(n+1) = Cy(n) + \sum_{s=1}^{r} D_s y(n-k_s), \quad (1)$$

where n is an independent variable ranging over the set of integers $\mathbb{N}_0 := \mathbb{N} \cup \{0\}$, $\mathbb{N} := \{1, 2, \dots\}$, $r \in \mathbb{N}$ is fixed, $k_s \in \mathbb{N}$ are fixed numbers called delays such that $k_1 < k_2 < \cdots < k_r$, $y = (y_1, y_2)^T \colon \{-k_r, -k_r + 1, \dots\} \to \mathbb{R}^2$ is a two-dimensional column dependent vector, the symbol T denotes the transpose, and C and D_s are 2 by 2 real constant matrices with entries c_{ij} and d_{ij}^s, $i, j = 1, 2$, respectively. Throughout the paper, we assume the matrix C being singular and having a single nonzero eigenvalue with the second one being zero. We also assume $D_s \neq \Theta$, $s = 1, \dots, r$ where Θ is a 2 by 2 zero matrix. The symbol $\mathbb{Z}$ used in the paper denotes the set of all integers. A solution of the system (1) is defined as

a sequence $y \colon \{-k_r, -k_r + 1, \dots\} \to \mathbb{R}^2$ satisfying (1) for each $n \in \mathbb{N}$. The initial data

$$y(-k_r) := \varphi(-k_r), \dots, y(0) := \varphi(0), \quad (2)$$

with given fixed values $\varphi \colon \{-k_r, -k_r + 1, \dots, 0\} \to \mathbb{R}^2$, define a unique solution $y = y(n)$ of the system (1). We do not explicitly mention all the needed basic facts from the theory of discrete equations. Instead, we refer to [1], [7], [8], [10]–[13] for their rudiments.

Below, we investigate the system (1) assuming that the matrices C and D_s, $s = 1, \dots, r$ satisfy conditions that define so called weakly delayed systems. These conditions derived in [2] (we refer also to [3], [6]) state that system (1) is weakly delayed if and only if the following conditions hold simultaneously:

$$d_{11}^s + d_{22}^s = 0, \quad (3)$$

$$\begin{vmatrix} d_{11}^s & d_{12}^s \\ d_{21}^s & d_{22}^s \end{vmatrix} = 0, \quad (4)$$

$$\begin{vmatrix} c_{11} & c_{12} \\ d_{21}^s & d_{22}^s \end{vmatrix} + \begin{vmatrix} d_{11}^s & d_{12}^s \\ c_{21} & c_{22} \end{vmatrix} = 0, \quad (5)$$

$$\begin{vmatrix} d_{11}^s & d_{12}^s \\ d_{21}^t & d_{22}^t \end{vmatrix} + \begin{vmatrix} d_{11}^t & d_{12}^t \\ d_{21}^s & d_{22}^s \end{vmatrix} = 0 \quad (6)$$

where $s, t = 1, 2, \dots, r$ and $t > s$. Conditions (3)-(6) guarantee that the values of the determinants of the two matrices

$$C - \nu I \quad \text{and} \quad C + \sum_{s=1}^{r} \nu^{-k_s} D_s - \nu I,$$

where I is a 2 by 2 unit matrix, are identical for all values $\nu \in \mathbb{C}$ except for the value $\nu = 0$, which is excluded. This implies the nonexistence of zero eigenvalues of the matrix C. Conditions (3)-(6) can be simplified as indicated in the following lemma [3, Theorem 1].

Lemma 1: System of conditions (3)–(6) is equivalent with the following system of conditions (7)–(9):

$$d_{11}^s + d_{22}^s = 0, \tag{7}$$

$$\begin{vmatrix} d_{11}^s & d_{12}^s \\ d_{21}^t & d_{22}^t \end{vmatrix} = 0, \tag{8}$$

$$\begin{vmatrix} c_{11} & c_{12} \\ d_{21}^s & d_{22}^s \end{vmatrix} + \begin{vmatrix} d_{11}^s & d_{12}^s \\ c_{21} & c_{22} \end{vmatrix} = 0, \tag{9}$$

where $s, t = 1, 2, \ldots, r$.

The results of the paper generalize some of those, derived in [5], where weakly delayed planar linear discrete systems with single delay are considered.

II. PRELIMINARIES

In [3] it is shown that, if conditions (3)–(6) hold provided that eigenvalues of C are different from zero, then the behaviour of the solutions of system (1) eventually becomes (for $n \geq k_r$) the same as the behaviour of solutions of a planar linear discrete system without delays

$$u(n + 1) = \mathcal{C}u(n) \tag{10}$$

where $n \in \mathbb{N}_0$ $u = (u_1, u_2)^T \colon \mathbb{N}_0 \to \mathbb{R}^2$ is two-dimensional column dependent vector and $\mathcal{C}$ is a suitable 2 by 2 constant matrix having the same eigenvalues as the matrix C, and its entries are found.

The case of the matrix C having a single zero eigenvalue or two zero eigenvalues is not covered by the results in [2], [3] and the present paper aims to analyze the case of one eigenvalue being nonzero while the second one zero. Below we derive formulas for the general solution of the system (1) assuming "ad hoc" that the matrices C and D_s, $s = 1, \ldots, r$ satisfy conditions (7)–(9).

The property of the system being weakly delayed is invariant regardless of the type of regular transformation. It is proved in [2] that if

$$y(n) = Mw(n), \ n \geq -k_r, \tag{11}$$

where the matrix M is regular, then the system

$$w(n + 1) = C^* w(n) + \sum_{s=1}^r D_s^* w(n - k_s) \tag{12}$$

arising from (1), where

$$C^* = M^{-1}CM, \quad D_s^* = M^{-1}D_s M \tag{13}$$

is again weakly delayed, i.e., the entries of matrices $C^* = \{c_{ij}^*\}_{i,j=1}^2$ and $D_s^* = \{d_{sij}^*\}_{i,j=1}^2$ satisfy the same conditions as those formulated above for entries of the matrices C and D_s, $s = 1, \ldots, r$ by (7)–(9). The proof in [2, Lemma 2] in the case of singular matrix C cannot be applied. If conditions (7)–(9) hold for matrices C and D_s, where the matrix C is singular, they remain valid for matrices C^* and D_s^* in system (12) as well. Since, in the case considered, $\det C = 0$, conditions (7)–(9) can be written shortly as

$$\operatorname{tr} D_s = 0, \ \det D_{st} = 0, \ \det(C + D_s) = 0, \tag{14}$$

where $s, t = 1, \ldots, r$ and

$$D_{st} := \begin{pmatrix} d_{11}^s & d_{12}^s \\ d_{21}^t & d_{22}^t \end{pmatrix}.$$

The proof of following theorem is omitted.

Theorem 1: If, for matrices C, D_s and D_{st}, $s, t = 1, \ldots, r$ conditions (14) hold, then for matrices C^*, D_s^* and D_{st}^*, $s, t = 1, \ldots, r$, where

$$D_{st}^* := \begin{pmatrix} d_{11}^{s*} & d_{12}^{s*} \\ d_{21}^{t*} & d_{22}^{t*} \end{pmatrix},$$

conditions

$$\operatorname{tr} D_s^* = 0, \ \det D_{st}^* = 0, \ \det(C^* + D_s^*) = 0 \tag{15}$$

hold as well.

The notion of a solution to system (12) is a formal adaptation of the definition of solution to system (1). A solution to (12) is defined in a unique way through the initial data

$$w(-k_r) := \psi(-k_r), \ldots, w(0) := \psi(0),$$

connected with the initial data (2) by transformation (11), i.e.,

$$\varphi(n) = M\psi(n) \implies \psi(n) = M^{-1}\varphi(n), n = -k_r, \ldots, 0. \tag{16}$$

III. $\mathcal{Z}$-TRANSFORM AND ITS INVERSE

The $\mathcal{Z}$-transform will be used to find the general solution of the system (1). Therefore, some auxiliary formulas are needed. Let $p, q \in \mathbb{Z}$ and define

$$\binom{p}{q} := \frac{p!}{q! \cdot (p - q)!} \text{ if } p \geq q \geq 0 \text{ and } \binom{p}{q} := 0 \text{ otherwise.}$$

The symbol δ_{pq} will denote in the following the Kronecker delta defined by the formula

$$\delta_{pq} = \begin{cases} 1 & \text{if } p = q, \\ 0 & \text{if } p \neq q, \end{cases}$$

where p and q are integers.

Let $l(n) = (l_1(n), l_2(n))^T$, $n = -k_r, -k_r + 1, \ldots$ be a given two-dimensional sequence such that its $\mathcal{Z}$ transform, defined by the series

$$\mathcal{Z}l(n) = L(z) = (L_1(z), L_2(z))^T := \sum_{k=0}^{\infty} \frac{l(k)}{z^k} \tag{17}$$

exists, where z is a complex variable. The values of $l(n)$, where $n = -k_r, \ldots, -1$ are not used in the definition (17). These are not lost in the following because all of them will be used in the below formula for $\mathcal{Z}$-transform of the sequence $l(n - m)$. Formulas that we use for $\mathcal{Z}$-transform are the following:

$$\mathcal{Z}l(n + 1) = \sum_{k=0}^{\infty} \frac{l(k + 1)}{z^k} = zL(z) - zl(0), \tag{18}$$

and

$$\mathcal{Z}l(n - m) = \frac{1}{z^m} L(z) + \sum_{i=0}^{m-1} \frac{l(-m + i)}{z^i}, \tag{19}$$

where $m \in \mathbb{N}$. We will also need some formulas for the inverse $\mathcal{Z}^{-1}$-transform. Let $s \in \mathbb{Z}$ and $\lambda \in \mathbb{C} \setminus \{0\}$ be fixed. Then, the inverse $\mathcal{Z}^{-1}$-transform of the function

$$U_1(z) := \frac{1}{z^s(z - \lambda)}$$

is computed by the formula

$$\mathcal{Z}^{-1}U_1(z) = \{u_1(n)\}_{n=0}^\infty, \ u_1(n) = \binom{n-s-1}{0}\lambda^{n-s-1}. \tag{20}$$

If $U_2(z) := 1/z^s$ with fixed $s \in \mathbb{N}_0$, then

$$\mathcal{Z}^{-1}U_2(z) = \{u_2(n)\}_{n=0}^\infty, \ u_2(n) = \delta_{sn}. \tag{21}$$

IV. GENERAL SOLUTION IN THE CASE OF ONE ZERO AND ONE NONZERO EIGENVALUES

Consider system (1) and assume that the matrix C has eigenvalues $\lambda_1 = \lambda \neq 0$ and $\lambda_2 = 0$. Then, by a suitable regular transformation (11), we derive a system (12) where the matrix C^* has the Jordan form $J(C)$ of the matrix C, i.e.,

$$C^* = J(C) = \begin{pmatrix} \lambda & 0 \\ 0 & 0 \end{pmatrix} \tag{22}$$

and system (1) can be written as

$$w(n+1) = J(C)w(n) + \sum_{s=1}^r D_s^* w(n - k_s), \ n \geq 0 \tag{23}$$

with matrices D_s^* computed by formulas (13). If matrices C, D_s, $s = 1, \dots, r$ satisfy assumptions (14), then, by Theorem 1, matrices

$$C^* = J(C) = M^{-1}CM, \ D_s^* = M^{-1}D_sM, \ s = 1, \dots, r \tag{24}$$

satisfy conditions (15). These conditions, in the considered case, are the following

$$d_{11}^{s*} = d_{22}^{s*} = 0, \ s = 1, \dots, r \tag{25}$$

and

$$d_{12}^{s*}d_{21}^{t*} = 0, \ s, t = 1, \dots, r. \tag{26}$$

Below, we use (25) and (26) without any special comment. Recall that the initial data ψ, for system (23), derived from initial data (2) by transformation (11) are computed by (16). Let us find the $\mathcal{Z}$-transform of the sequence $w(n)$ defined by system (23). Denote $\mathcal{Z}w(n) = W(z) = (W_1(z), W_2(z))^T$. Then

$$\mathcal{Z}w(n+1) = J(C)\mathcal{Z}w(n) + \sum_{s=1}^r D_s^* \mathcal{Z}w(n - k_s).$$

Using formulas (18), (19), we derive

$$zW(z) - zw(0))$$

$$= J(C)W(z) + \sum_{s=1}^r D_s^* \left(\frac{1}{z^{k_s}}W(z) + \sum_{i=0}^{k_s-1} \frac{w(-k_s + i)}{z^i} \right)$$

which can be rewritten as

$$\mathcal{A}W(z) = \mathcal{B}, \tag{27}$$

where (property (25) is applied)

$$\mathcal{A} := zI - J(C) - \sum_{s=1}^r \frac{D_s^*}{z^{k_s}} = \begin{pmatrix} z - \lambda & -\sum_{s=1}^r \frac{d_{12}^{s*}}{z^{k_s}} \\ -\sum_{s=1}^r \frac{d_{21}^{s*}}{z^{k_s}} & z \end{pmatrix}$$

and

$$\mathcal{B} := \begin{pmatrix} zw_1(0) + \sum_{s=1}^r d_{12}^{s*} \sum_{i=0}^{k_s-1} \frac{w_2(-k_s + i)}{z^i} \\ zw_2(0) + \sum_{s=1}^r d_{21}^{s*} \sum_{i=0}^{k_s-1} \frac{w_1(-k_s + i)}{z^i} \end{pmatrix}.$$

To find the inverse $\mathcal{Z}^{-1}W(z)$ we rewrite (27) so that the formulas for the inverse $\mathcal{Z}$-transform are simply applicable. First compute, with the aid of (26), $\det \mathcal{A} = z(z - \lambda)$. Then

$$\mathcal{A}^{-1} = \begin{pmatrix} \frac{1}{z - \lambda} & \sum_{s=1}^r \frac{d_{12}^{s*}}{z^{k_s+1}(z - \lambda)} \\ \sum_{s=1}^r \frac{d_{21}^{s*}}{z^{k_s+1}(z - \lambda)} & \frac{1}{z} \end{pmatrix}.$$

Now we can find the function $W(z)$:

$$W(z) = \mathcal{A}^{-1}\mathcal{B}$$

$$= \begin{pmatrix} \frac{zw_1(0)}{z - \lambda} + \sum_{s=1}^r \frac{w_2(0)d_{12}^{s*}}{z^{k_s}(z - \lambda)} + \sum_{s=1}^r d_{12}^{s*} \sum_{i=0}^{k_s-1} \frac{w_2(-k_s + i)}{z^i(z - \lambda)} \\ w_2(0) + \sum_{s=1}^r \frac{w_1(0)d_{21}^{s*}}{z^{k_s}(z - \lambda)} + \sum_{s=1}^r d_{21}^{s*} \sum_{i=0}^{k_s-1} \frac{w_1(-k_s + i)}{z^{i+1}} \end{pmatrix}.$$

We are able to determine components $w_1(n)$, $w_2(n)$ of the vector $w(n)$ as the inverse $\mathcal{Z}$-transform of components $W_1(z)$, $W_2(z)$ of the vector $W(z)$. By formulas (20), (21), for $n \geq 0$, we obtain

$$w_1(n) = \binom{n}{0}\lambda^n w_1(0) + w_2(0) \sum_{s=1}^r d_{12}^{s*}\binom{n - k_s - 1}{0}\lambda^{n-k_s-1}$$

$$+ \sum_{s=1}^r d_{12}^{s*} \sum_{i=0}^{k_s-1} w_2(-k_s + i)\binom{n - i - 1}{0}\lambda^{n-i-1}$$

and

$$w_2(n) = \delta_{0n}w_2(0) + w_1(0) \sum_{s=1}^r d_{21}^{s*}\binom{n - k_s - 1}{0}\lambda^{n-k_s-1}$$

$$+ \sum_{s=1}^r d_{21}^{s*} \sum_{i=0}^{k_s-1} w_1(-k_s + i)\delta_{i+1,n}.$$

This result can be formulated in the following theorem.

Theorem 2: Let constant 2 by 2 real matrices C and D_s, $s = 1, \dots, r$ be given such that the matrix C has one eigenvalue $\lambda \neq 0$ and another equal to zero. Assume, moreover, that conditions (14) hold and that a regular transformation (11) transforms the system (1) into system (23) with matrices $J(C)$, D_s^*, $s = 1, \dots, r$ determined by formulas (24), where the matrix $J(C)$ of non-delayed terms has the form (22). Then,

the solution of the system (1) satisfying the initial data (2), i.e.,

$$y(n) = \varphi(n), \quad n = -k_r, -k_r + 1, \ldots, 0,$$

is given by formula

$$y(n) = Mw(n), \quad n \geq 1,$$

where $w(n) = (w_1(n), w_2(n))^T$,

$$w_1(n) = \lambda^n w_1(0) + w_2(0) \sum_{s=1}^{r} d_{12}^{s*} \binom{n - k_s - 1}{0} \lambda^{n - k_s - 1}$$

$$+ \sum_{s=1}^{r} d_{12}^{s*} \sum_{i=0}^{k_s - 1} w_2(-k_s + i) \binom{n - i - 1}{0} \lambda^{n - i - 1}, \quad (28)$$

$$w_2(n) = w_1(0) \sum_{s=1}^{r} d_{21}^{s*} \binom{n - k_s - 1}{0} \lambda^{n - k_s - 1}$$

$$+ \sum_{s=1}^{r} d_{21}^{s*} \sum_{i=0}^{k_s - 1} w_1(-k_s + i) \delta_{i+1, n}, \quad (29)$$

and the values $w(n) := \psi(n)$, $n = -k_r, \ldots, 0$ used in (28), (29) are defined by (16), i.e.,

$$\psi(n) = M^{-1}\varphi(n), \quad n = -k_r, -k_r + 1, \ldots, 0.$$

V. REDUCTION OF GENERAL SOLUTION

We will reduce formulas (28), (29) to show that they have a simple form. Let $n \geq k_r + 1$. Then

$$\binom{n - j - 1}{0} = 1 \quad \text{if} \quad j = 0, \ldots, k_r + 1$$

and

$$\delta_{0n}, \quad \delta_{j+1, n} = 0 \quad \text{if} \quad j = 0, \ldots, k_r - 1.$$

If $n \geq k_r + 1$, formulas (28), (29) reduce to

$$w_1(n) = \lambda^n w_1(0) + w_2(0) \sum_{s=1}^{r} d_{12}^{s*} \lambda^{n - k_s - 1}$$

$$+ \sum_{s=1}^{r} d_{12}^{s*} \sum_{i=0}^{k_s - 1} w_2(-k_s + i) \lambda^{n - i - 1}, \quad (30)$$

$$w_2(n) = w_1(0) \sum_{s=1}^{r} d_{21}^{s*} \lambda^{n - k_s - 1}. \quad (31)$$

VI. NON-DELAYED SYSTEMS

In this part, we will construct non-delayed two-dimensional discrete system (10) having, for $n \geq k_r + 1$, the same solutions as initial system (1).

Theorem 3: Assume that all the hypotheses of Theorem 2 hold and that $d_{12}^{1*} = 0$. Then, the set of all solutions of the system (1) generated by arbitrary initial data (2), i.e.,

$$y(n) = \varphi(n), \quad n = -k_r, -k_r + 1, \ldots, 0,$$

coincides for $n \geq k_r + 1$ with the set of all solutions of the system (10), i.e., with the system

$$u(n + 1) = \mathcal{C}u(n), \quad n \geq 0, \quad (32)$$

generated by all initial data $u(0)$, where the matrix $\mathcal{C}$ is defined by the formula

$$\mathcal{C} = M\mathcal{C}^* M^{-1}$$

and the matrix $\mathcal{C}^*$ is defined by the formula

$$\mathcal{C}^* = \begin{pmatrix} \lambda - d & d\left(\sum_{s=1}^{r} d_{21}^{s*} \lambda^{-k_s - 1}\right)^{-1} \\ (\lambda - d)\sum_{s=1}^{r} d_{21}^{s*} \lambda^{-k_s - 1} & d \end{pmatrix}, \quad (33)$$

where d is an arbitrary fixed constant. The solutions of the system (32) are defined by the formula

$$u(n) = MU(n), \quad n \geq 1$$

where $U(n) = (U_1(n), U_2(n))^T$,

$$U_1(n) = K\lambda^n, \quad U_2(n) = K\lambda^n \sum_{s=1}^{r} d_{21}^{s*} \lambda^{-k_s - 1}$$

and K is an arbitrary constant.

Theorem 4: Assume that all the hypotheses of Theorem 2 hold and that $d_{12}^{1*} \neq 0$. Then, the set of all solutions of the system (1) generated by arbitrary initial data (2), i.e.,

$$y(n) = \varphi(n), \quad n = -k_r, -k_r + 1, \ldots, 0,$$

coincides for $n \geq k_r + 1$ with the set of all solutions of the system (10), i.e. the system

$$u(n + 1) = \mathcal{C}u(n), \quad n \geq 0,$$

generated by all initial data $u(0)$, where the matrix $\mathcal{C}$ is defined by the formula

$$\mathcal{C} = M\mathcal{C}^* M^{-1}$$

and

$$\mathcal{C}^* = \begin{pmatrix} \lambda & b \\ 0 & 0 \end{pmatrix},$$

where b is an arbitrary fixed constant. The solutions of the system (32) are defined by the formula

$$u(n) = MU(n), \quad n \geq 1$$

where

$$U(n) = (U_1(n), U_2(n))^T, \quad U_1(n) = L\lambda^n, \quad U_2(n) = 0$$

and L is an arbitrary constant.

VII. EXAMPLE

Let $r = 2$, $k_1 = 1$, $k_2 = 2$, and let matrices C, D_1 and D_2 be specified as

$$C = \begin{pmatrix} 10 & -20 \\ 4 & -8 \end{pmatrix}, \quad D_1 = \begin{pmatrix} 2 & -4 \\ 1 & -2 \end{pmatrix}, \quad D_2 = \begin{pmatrix} 4 & -8 \\ 2 & -4 \end{pmatrix}.$$

The eigenvalues of the matrix C are $\lambda_1 = 2$, $\lambda_2 = 0$. For these matrices, (7)–(9) hold and the system

$$y(n + 1) = Cy(n) + D_1 y(n - 1) + D_2 y(n - 2) \quad (34)$$

is a particular case of the system (1). The change of the dependent variable $y(n) = Mw(n)$, where $n \geq -k_r = -2$ by formula (11) with the matrix

$$M = \begin{pmatrix} 5 & 2 \\ 2 & 1 \end{pmatrix}$$

transforms the system (34) into one of the type (23)

$$w(n+1) = C^* w(n) + D_1^* w(n-1) + D_2^* w(n-2),$$

where

$$C^* = \begin{pmatrix} 2 & 0 \\ 0 & 0 \end{pmatrix}, \; D_1^* = \begin{pmatrix} 0 & 0 \\ 1 & 0 \end{pmatrix}, \; D_2^* = \begin{pmatrix} 0 & 0 \\ 2 & 0 \end{pmatrix}.$$

Theorem 2 is applicable. Then, the solution of the system (34) is given by the formula $y(n) = Mw(n)$, $n \geq 1$, where

$$w_1(n) = 2^n w_1(0) \tag{35}$$

and

$$w_2(n) = w_1(0) \left(\binom{n-2}{0} \lambda^{n-2} + 2 \binom{n-3}{0} \lambda^{n-3} \right)$$
$$+ w_1(-1)\delta_{1,n} + 2(w_1(-2)\delta_{1,n} + w_1(-1)\delta_{2,n}). \tag{36}$$

Using formulas (30), (31) we derive, for $n \geq 3$,

$$w_1(n) = 2^n w_1(0) \tag{37}$$

and

$$w_2(n) = 2^n w_1(0)(2^{-2} + 2 \cdot 2^{-3}) = 2^{n-1} w_1(0). \tag{38}$$

Comparing formulas (35), (36) with (37), (38), we see that the formula (36) has been simplified and changes to formula (38).

Finally, let us construct a nondelayed system, which has the same solutions as the system (34) if $n \geq 3$. Theorem 3 is applicable Then, the set of all solutions of the system (34) generated by arbitrary initial data (2), i.e.,

$$y(n) = \varphi(n), \;\; n = -2, -1, 0,$$

coincides, for $n \geq 3$, with the set of all solutions of the system (32),

$$u(n+1) = \mathcal{C}u(n), \;\; n \geq 0,$$

generated by all initial data $u(0)$, where the matrix $\mathcal{C}$ is computed by the formula

$$\mathcal{C} = M\mathcal{C}^* M^{-1}$$

and the matrix $\mathcal{C}^*$ is defined by the formula (33), i.e.

$$\mathcal{C}^* = \begin{pmatrix} 2-d & 2d \\ (2-d)/2 & d \end{pmatrix}$$

and d is arbitrary constant.

VIII. Conclusions

The paper considers weakly delayed linear planar discrete system (1) with constant coefficients. The results obtained generalize some of those proved in [5], where planar weakly delayed discrete systems with single delay are considered. All the solutions of system (1) are found provided that the matrix of nondelayed terms has one nonzero eigenvalue with another one being zero. The formulas derived are simplified for $n \geq k_r + 1$ and it is shown that, for such values, the set of all solutions of the system (1) coincides with the set of all solutions of another linear planar discrete system that does not contain delays. Such formulas can be useful in digital signal processing. It is an open problem whether the results presented can be extended to some linear planar discrete systems with non-constant coefficients, such as

$$y(n+1) = Cy(n) + \sum_{s=1}^{r} \alpha_s(k) D_s y(n - k_s), \;\; n \geq 0,$$

where $\alpha_s(k)$ are discrete functions. For some more motivations to further research, we refer to [4], [5], [9].

References

[1] R.P. Agarwal, "Difference equations and inequalities: Theory, methods, and applications," 2000, CRC Press.

[2] J. Diblík and H. Halfarová, "General explicit solution of planar weakly delayed linear discrete systems and pasting its solutions," Abstr. Appl. Anal. 2014, doi:10.1155/2014/627295, 1–37.

[3] J. Diblík, H. Halfarová, and J. Šafařík, "Two-parameters formulas for general solution to planar weakly delayed linear discrete systems with multiple delays, equivalent non-delayed systems, and conditional stability," Appl. Math. Comput. 459 (2023), 128270, 14 pp.

[4] J. Diblík, and H. Halfarová, "Weakly delayed linear systems with variable coefficients," In Matematika, informační technologie a aplikované vě. Brno, Univerzita obrany, 2017. s. 1-16. ISBN: 978-80-7231-417-1.

[5] J. Diblík, and M. Hartmanová, "Non-delayed linear planar discrete systems with constant coefficients equivalent to linear planar discrete delayed systems with constant coefficients," Matematika, informační technologie a aplikované vědy, MITAV 2024. Brno: Univerzita Obrany, 2024. s. 1-9. ISBN: 978-80-7582-493-6.

[6] J. Diblík, D. Khusainov, and Z. Šmarda, "Construction of the general solution of planar linear discrete systems with constant coefficients and weak delay," Adv. Difference Equ. 2009, Art. ID 784935, 18 pages, doi:10.1155/2009/784935.

[7] S. N. Elaydi, "An Introduction to Difference Equations," Third Edition, Springer, 2005.

[8] M. Sami Fadali, and A. Visioli, "Digital Control Engineering, Analysis and Design," Third Edition, Academic Press in an imprint of Elsevier, Elsevier, 2019.

[9] M. Hartmanová, and J. Diblík, "General solution of a planar linear discrete system with a weak single delay in the case of single zero eigenvalue of the matrix of nondelayed terms," Proceedings I of the 30th Conference STUDENT EEICT 2024, Editor: Assoc. Prof. Vítězslav Novák, Publisher: Brno University of Technology, Faculty of Electrical Engineering and Communication, 2024, 1st Edition, 343–347. ISBN 978-80-214-6231-1.

[10] V. Lakshmikantham, and D. Trigiante, "Theory of Difference Equations," Second Edition, Marcel Dekker, Inc., 2002.

[11] A. V. Oppenheim, and Ronald W. Schafer, "Discrete-Time Signal Processing," Third Edition, Pearson, 2009.

[12] J. G. Proakis, and D. G. Manolakis, "Digital Signal Processing, Principles, Algorithms, and Applications," Fourth Edition, Pearson, 2006.

[13] M. A. Radin, "Difference Equations for Scientists and Engineering: Interdisciplinary Difference Equations," World Scientific, 2019.

Formal specification of control system design in industrial domain

1st Silvestr Vaculovič
Dept. of Control and Instrumentation
Brno University of Technology
Brno, Czech Republic
silvestr.vaculovic@vutbr.cz

2nd Jakub Arm
Dept. of Control and Instrumentation
Brno University of Technology
Brno, Czech Republic
jakub.arm@vut.cz

Abstract—When designing an industrial control system, multiple aspects need to be taken into account and it is often necessary to make some trade-offs in the choice of hardware resources, communication technologies and topologies of the system being built. Usually a balance is sought between the cost and functionality of the selected components and the overall system architecture. A formalised description of the architecture allows the standardisation of individual industrial control system design solutions, on the basis of which the optimal solution can be selected. Another use of the formalization of the control system architecture description is to automate the design or traceability of the implementation from design to implementation. A formal specification of the electrical part containing the control system was performed on a sample industrial machine, followed by an analysis of the suitability of the different architectures using Theory of Inventive Problem Solving (TRIZ).

Index Terms—Formal specification, industrial control system

I. INTRODUCTION

The single-purpose machine is designed for filling liquid products into more bottles simultaneously. The quantity of the filled product is measured by magnetic flow meters. Batch and other parameters are set directly from the machine control panel. Individual recipes can be saved for each product, which include settings such as filling volume, filling speed, filling style, filling nozzle movement and other parameters.

The single-purpose machine is controlled by an integrated Programmable Logic Controller (PLC) and Human-Machine Interface (HMI) system. This control system also serves as the operator panel. Through the panel, the operator can control and monitor machine conditions. Control buttons for Start, Stop, Safety Circuit Activation and Emergency Stop are located below the operator panel. The all-in-one unit with Input/Output (I/O) pins contains expansion modules located on the cabinet mounting plate. The power supply, circuit breaker and power section are integral parts, ensuring the operation of the device. The safety circuits of the machine meeting the requirements of Safety Category 0 are also implemented at this level.

The following chapter focuses on a literature search of available literature in the field of industrial control system design. It summarises approaches oriented towards automation, standardisation and formal verification.

The third chapter focuses on analyzing the control of the single-purpose machine, identifying Positive Effects (PEs) and Negative Effects (NEs) relationships, and formulating innovation questions. Furthermore, the roll-up method is applied to eliminate elements with low functional significance. The unfolding method is then used to expand the possibilities of utilizing diagnostic and condition data obtained from individual components.

The fourth chapter focuses on finding and solving technical and physical contradictions. The found technical contradiction is solved using the Altshuler matrix. The physical contradiction is solved using separation procedures.

The fifth chapter focuses on the practical applications of formal description in industrial control systems. It demonstrates how structured modeling can enhance design efficiency with industry standards. At the end of the chapter, improvement metrics are evaluated.

II. RELATED WORK

In [1], Reusable Automation Components (RACs) are introduced as a framework helping development of industrial control logic promising to shorten development and modification times, and to reduce programming errors. The formal specification uses temporal logic to describe time-related properties, therefore, a designed system can be verified. The idea helps practitionars to build an industrial control system, however, it lacks of standardization and focuses only on software blocks.

Authors in [2] present a framework for industrial component modelling incorporating hardware and software part in comply with IEC 61131-3 standard. Moreover, the framework enables the verification of a created functionality. An event logic is used for the behaviour description of a mechatronic component. This object-oriented approach enables modelling of the system behaviour and readability by a user. However, the contribution does not describe the mechanical system in more details.

In article [3], an approach of component modelling for industrial control system is introduced. It is based on multifaceted method that enables creating and upgrading a repository of reusable components. The component model inherits the composition pattern architecture. One of the model layer is based on discrete event system enabling formal synthesis of a system. The article, however, does not address the internal mechanic composition of a component.

The paper [4] presents an approach for using Semantic Web technology for access harmonization and utilization for industrial devices and control systems in distributed and dynamic environments. Standard IEC 62264 is adopted for plant model ontology allowing description of the structure of equipment and devices in e.g. a production facility. The paper exhibits more conceptual structures for component description, however, it does not present any further usage.

In [5], an architecture of a web service poviding ontology-based description of an industrial facility is demonstrated. The architecture uses Web Ontology Language (OWL) as a technology stemming ontology. The application enabling manufacturing reconfiguration according to its structure is exhibited. However, the proposed system addresses only an industrial system at machine level.

Paper [6] present an automatic technique to annotate an industrial schemas using Linked Open Data (LOD) and Fuzzy ontology. The result is a set of linked Extensible Markup Language (XML) elements. The described purpose is to be used later on by programs and systems while a heating process decomposed to its elements is only presented.

Authors in [7] presnets an automatic technique for the design and configuration of control applications. The purpose is to achieve more flexible and reconfigurable manufacturing systems. The approach employs automation agents to create an infrastructure for control software based on the standard IEC 61499. Although the paper presents the hardware-near control application for physical manufacturing components based on agent technology, it does not address the hardware component structure in more details.

The paper [8] presents a framework that utilizes a knowledge-based approach to automate the component mapping in the code generation process. As data mapping ontology, Semantic Web Rule Language (SWRL) is used to create a structure of mechanical components in the given Festo industrial line. Authors conducted a survey among programmers which results a reduction in mapping time of 75 % due to automatic selection of FB for mapping for a given component. The automatic component mapping for PLC variables is another usage of the formal specification of components forming an industrial control system.

In article [9] TRIZ is described as a methodology for the analysis and synthesis of innovative tasks. The aim of TRIZ is to support engineers in moving from the "what is" to the "what will be" state. The methodology focuses on identifying engineering contradictions and resolving them using the Altshuller matrix. The authors state that the original matrix was developed for mechanical systems and highlight its fragile applicability to software and data models. The paper therefore discusses its extension with new features that focus on previously unaddressed areas.

Based on the discussed approaches, this paper further focuses on the analysis and optimization of the control system design, which serves as a case study for the TRIZ implementation.

III. ANALYSIS

A. System Definition and Simplification

The technical system of the object of interest consists of a control system to which input and output components (functional elements) are connected via binary and analogue signals. The control unit, labeled as KE1, and the expansion cards of the control system KE2, KE3, and KE4 are defined as separate functional elements. Components such as contactors, frequency inverters, drives, sensors, flow meters, or terminal blocks have been grouped into higher functional units, as their detailed division would not add any value. Conversely, grouping was not appropriate for pneumatic terminals, as it allowed for better tracking of individual links.

In order to solve the problem effectively, it was necessary to focus only on the main aspects of the control system and its effects. Therefore, the technical system was simplified to include only the relevant components. Mechanical parts such as the cabinet, mounting plate, DIN rails or cable trays were therefore neglected in the model. All cables, wires and fasteners are also neglected.

B. Identification of effects

The analysis identified key system effects, which can be categorized as PEs and NEs. PEs represent desirable features that enhance system management and operational efficiency, while NEs may cause limitations, errors, or reduced performance. The identified effects are as follows:

Possitive Effects - analyze, protect, detect, diagnose, inform, secure, communicate, power, control, manage, switch, synchronize, connect.

Negative Effects - calibrate, wear out, overload, interfere, impose, distort, delay.

Although the cabling was not included in the model, the PEs and NEs related to their function were retained in the analysis and only transferred to other components. Conversely, the thermal couplings between components were neglected as they are assumed to be addressed by proper sizing of the fan. Also, potential couplings related to mechanical components that were not included in the model have been eliminated as their direct influence on the control system is negligible.

C. Innovation questions

Based on the analysis of PEs and NEs in the system, key problem areas were identified. These areas led to the formulation of innovative questions, which are summarized in the following:

- How to reduce energy intensity?
- How to provide better diagnostics of the whole system to make it more efficient?
- How to solve the problem of requiring a large number of High-Speed Counter (HSC) inputs for flowmeters without limiting functionality?
- How to adjust the allocation of outputs so that terminals are not controlled from multiple cards?
- How to solve the problem of wrong wiring of multi-core cable of terminals to terminals?
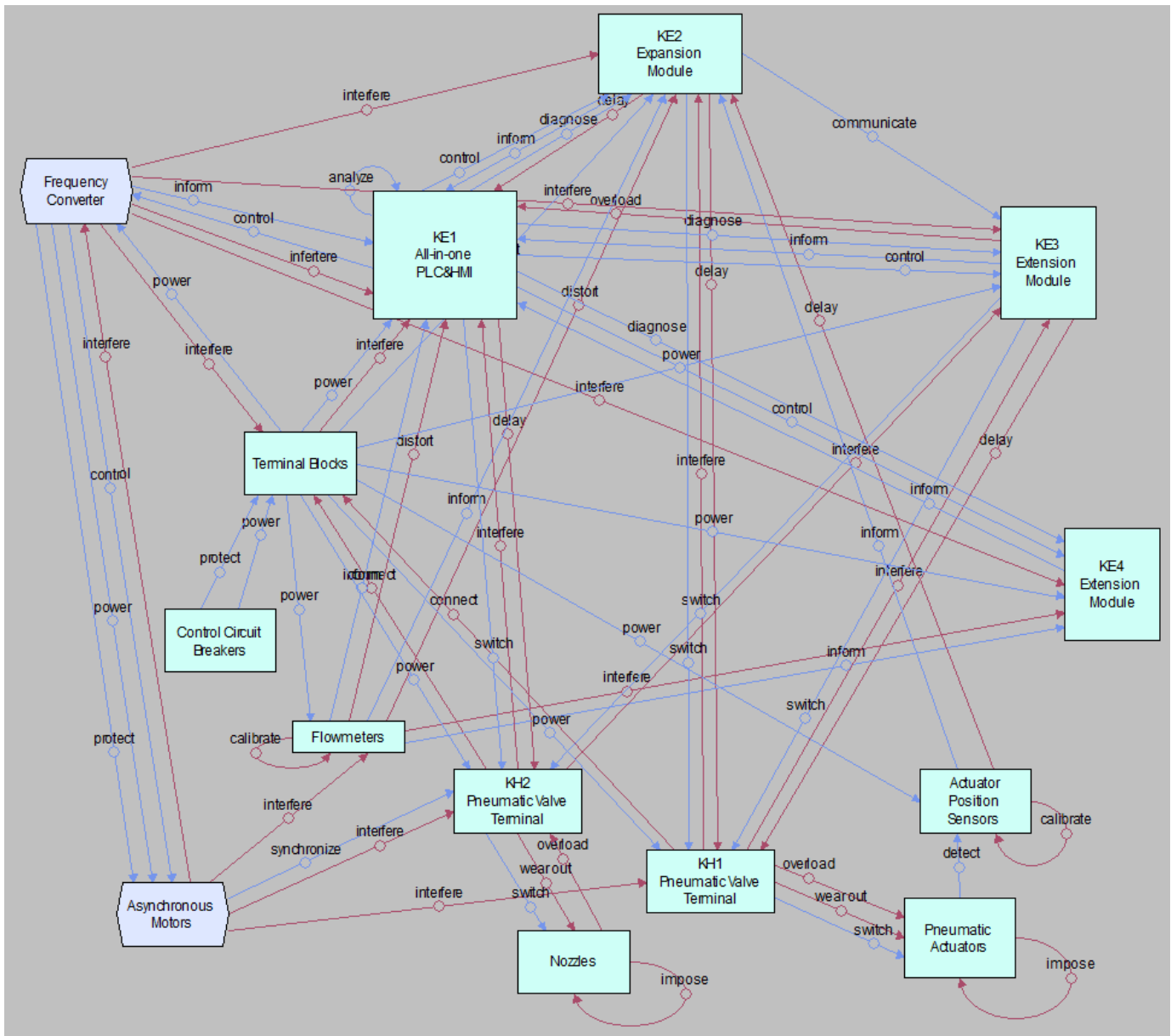
Fig. 1. Analysis performed in TechOptimizer

D. Trimming of the Technical System

The trimming method was used to remove the elements of the technical system that cause the most problems or have low functional significance. Expansion cards KE2, KE3, and KE4 were identified as elements with minimal added value. These cards could be removed from the project if another element providing equivalent functionality could be found

The flowmeters generate HSC signals on the amount of liquid flowed and, according to the available documentation, also have IO-Link communication. In a model scenario with six filling paths, their use would eliminate the need for 12 HSC inputs on the PLC, thus reducing hardware requirements. At the same time, 34 terminal blocks could be eliminated in the cabinet, which would simplify wiring. The IO-Link

implementation would require the system to be augmented with two IO-Link units (Port Class B), which would be connected to the flowmeters via cabling and located close to them. These units would provide power and data transfer to the cabinet via one power and one data cable. Communication with the control system would be via Modbus TCP or Profinet protocols.

In an analogous way, the control of the valve terminals labeled as KH1 and KH2 can be transferred directly to the terminals themselves. By implementing this solution, the terminals would take over the valve control function, with the PLC communicating with them via an industrial communication protocol instead of binary outputs. The Profinet and IO-Link protocols were considered as suitable options for this

application. Given that IO-Link is already integrated into the system, IO-Link was identified as the preferred solution due to the availability of free ports in the existing topology. However, Profinet remains a viable alternative, offering additional flexibility in communication architecture. Implementing this solution would eliminate 24 terminal blocks in the cabinet.

By applying the lead reduction method, dependencies on KE3 and KE4 are minimized. The IO-Link and Profinet technologies are also more resistant to electromagnetic interference, further mitigating negative effects. This approach additionally reduces cabling complexity, installation time, and overall design effort.

E. Unfolding of the Technical System

The unfolding method is directly related to the previous chapter trimming. Since the flow meters and valve terminals will function as separate units communicating with the control system, it is possible to use diagnostic and status information, transmitted via industrial communication protocols, in addition to control data.

However, the proposed solution is not compatible with the existing control system, which requires a switch to a more modern PLC control system supporting these technologies.

IV. Synthesis

A. Technical contradiction

The introduction of the IO-Link, Profinet communication protocol brings significant benefits such as simplified wiring, reduced wiring complexity, increased diagnostic efficiency and improved system scalability. However, these positive benefits are offset by negative impacts that include higher component acquisition costs, the need for staff training and development work associated with infrastructure reorganization.

To find the optimal trade-off between these conflicting requirements, an Altshuler Matrix was used to provide recommended strategies. The basic version of this table contains 39 parameters. It is first necessary to identify the characteristics that are relevant to the technical system. Subsequently, a so-called mismatch mapping is used to compare the selected parameter to be improved with a parameter whose value can be negatively affected by this improvement. The intersection of these two characteristics in the matrix provides a recommendation of one or more innovation principles that have been successfully applied in the past to solve similar engineering problems. The following principles were selected from this table.

- 27 - Reliability
- 31 - System cost (NE)
- 32 - Ease of production (PE)
- 35 - Customizability, versatility
- 36 - Complexity of design (PE)
- 38 - Degree of automation

In further consideration, less important parameters were omitted and the focus was on parameters 31, 32 and 36. No innovative principles were identified when comparing parameters 31 and 32, while principles 1 (Division) and 19

(Periodic Action) were obtained for parameters 31 and 36. The solution lies in the gradual introduction of communication protocols. It would be advisable to implement the S7-1200 control system first, then test Profinet communication on a less complex machine. Once the functionality has been verified, IO-Link technology could be introduced for pneumatic terminals, allowing experience to be gradually gained and effectively transferred to more complex systems. Each phase of implementation should be accompanied by thorough training of personnel.

B. Physical contradiction

A physical contradiction occurs when one element of a system has conflicting requirements for its parameter. As with technical contradictions, it is necessary to analyze the PEs and NEs and seek an effective solution. Physical contradictions can be overcome by separation procedures that allow the desired properties to be achieved without compromising functionality. The following key physical contradictions were identified in the analyzed system:

- Dimensions of the cabinet
- Cooling of the cabinet
- Accuracy and speed of flowmeter measurements
- Reliability vs. flexibility of the system
- Elimination of electromagnetic interference (EMI)

The solution could lead to the use of separation in the space, or the introduction of protective enclosures. The solution in this case could be to run the power and signal cables separately, but this would negate the desired effect. As a possible solution, a separating partition in the cable trays is offered. Another option is to use cables with shielding, which, however, increases the overall cost of the technology.

V. Usage

The previous analysis focused on improving the physical architecture of control systems using TRIZ methods. However, optimizing hardware alone is not sufficient. Automation of control system design and validation is also required. We identify and demonstrate possible applications of formal description in industrial control systems. Based on the literature, we have identified usage in:

- Verification of PLC-based applications for compliance with IEC 61131-3.
- Design and implementation of PLC program in compliance with IEC 61499.
- Creation of RACs for PLC-based control systems.
- Design of manufacturing system topologies enabling dynamic reconfiguration.
- Automated mapping of process variables to automation components.

Our proposal is based on a system that enables the structured design and automation of hardware components within an industrial control system through the incorporation of ontologies. The system can automatically generate schematic representations and functional configurations based on predefined

engineering parameters. Furthermore, it supports intelligent component selection by analyzing the system architecture and verifying its compliance with design constraints. The system also facilitates the validation of control system functionality, extending its application to functional safety verification.

To evaluate the benefits of the proposed approach, we define the following performance metrics:

- Reduction in hardware complexity
- Decrease in design and implementation time
- Error rate reduction
- System scalability

VI. Conclusion

This paper presents a method incorporating the formal description demonstrated for an industrial control system. Methods based on TRIZ and ontology automation were investigated and used. The analysis focused on hardware and software aspects, including PLC programs and the use of RACs. The proposed methodology aims to improve design efficiency, reduce error rates and ensure compliance with industry standards.

This approach has not yet been experimentally verified. The proposed methodology is expected to automate hardware design, leading to greater modularity and better scalability. Configuration automation and the use of RACs could shorten design and implementation time. These factors could also help reduce the error rate. Subsequent steps could lead to optimization at the PLC level, from variable mapping to automated programming.

Future work should focus on practical verification of these concepts in a real industrial environment. This includes experimental testing and quantification of the actual impact of the proposed methodology.

Acknowledgment

References

[1] O. Ljungkrantz, K. Akesson, M. Fabian, and C. Yuan, "Formal specification and verification of industrial control logic components," *IEEE Transactions on Automation Science and Engineering*, vol. 7, no. 3, pp. 538–548, 2010.

[2] M. Bonfe and C. Fantuzzi, "Design and verification of mechatronic object-oriented models for industrial control systems," in *EFTA 2003. 2003 IEEE Conference on Emerging Technologies and Factory Automation. Proceedings (Cat. No.03TH8696)*, vol. 2, 2003, pp. 253–260 vol.2.

[3] D. Côté and R. St-Denis, "Component-based method for the modeling and control of modular production systems," *IEEE Transactions on Control Systems Technology*, vol. 21, no. 5, pp. 1570–1585, 2013.

[4] D. Hästbacka and A. Zoitl, "Towards semantic self-description of industrial devices and control system interfaces," in *2016 IEEE International Conference on Industrial Technology (ICIT)*, 2016, pp. 879–884.

[5] B. Ramis, L. Gonzalez, S. Iarovyi, A. Lobov, J. L. Martinez Lastra, V. Vyatkin, and W. Dai, "Knowledge-based web service integration for industrial automation," in *2014 12th IEEE International Conference on Industrial Informatics (INDIN)*, 2014, pp. 733–739.

[6] A. Brek, O. Djama, and Z. Boufaida, "Using lod and fuzzy ontology to annotate industrial schemas," in *2018 International Conference on Smart Communications in Network Technologies (SaCoNeT)*, 2018, pp. 232–236.

[7] W. Lepuschitz, A. Zoitl, and M. Merdan, "Ontology-driven automated software configuration for manufacturing system components," in *2011 IEEE International Conference on Systems, Man, and Cybernetics*, 2011, pp. 427–433.

[8] B. R. Ferrer, B. Ahmad, A. Lobov, D. Vera, J. L. M. Lastra, and R. Harrison, "A knowledge-based solution for automatic mapping in component based automation systems," in *2015 IEEE 13th International Conference on Industrial Informatics (INDIN)*, 2015, pp. 262–268.

[9] K. Lippert and R. Cloutier, "Triz for digital systems engineering: New characteristics and principles redefined," *Systems*, vol. 7, no. 3, p. 39, 2019.

Review of Autonomous UAV Methods in GNSS-Challenging Environments

1ˢᵗ Šimon Prokop
Dept. of Theoretical and Experimental Electrical Eng.
Brno University of Technology
Brno, Czech Republic
221488@vut.cz

2ⁿᵈ Petr Marcoň
Dept. of Theoretical and Experimental Electrical Eng.
Brno University of Technology
Brno, Czech Republic
marcon@vut.cz

Abstract—**Interest in autonomous UAVs has been growing due to the need in many different industries to seek a robust and efficient system that can work even in remote areas without any other intervention. This paper provides a comprehensive review of recent advancements in autonomous UAV methodologies, with a particular focus on three key areas: planning, navigation, and AI-driven algorithms. The review examines the strengths and limitations of traditional approaches, such as Kalman filters and SLAM-based methods, while also exploring the potential of AI-driven techniques, particularly deep reinforcement learning (DRL), in enhancing UAV autonomy. Although recent developments show promising results, challenges remain in scalability, computational efficiency, and adaptability to complex environments. The findings suggest future research directions toward hybrid methodologies that integrate classical and AI-based techniques to improve UAV performance in real world scenarios.**

Index Terms—**GNSS-Challenging environments, Autonomous system, AI-driven, Antispoofing, Antijamming, Sensors, Navigation, Control, Planning, GNC.**

I. INTRODUCTION

Unmaned aerial vehicles (UAVs) play an important role in many real-life scenarios, e.g. agricultural fertilization, military missions, or wildfire location, where proper guidance, navigation and control (GNC) are critical aspects of the mission. However, many of these missions take place in remote areas, areas with GNSS-challenging environment, or even under conditions of active jamming. Therefore, UAVs must be capable of partial or full autonomy to secure a quality result.

This paper provides a review of the currently used methods deployed in autonomous UAV and multi-UAV (swarm UAV) systems, particularly those designed to function in GNSS-challenging environments. Key areas of focus include articles that delve into the development of fully or partly autonomous systems with use of traditional methods of navigation, planning or alternatives in form of AI. By examining these approaches, we will gain a fundamental understanding of the techniques currently shaping UAV autonomy. Furthermore, the aim of this article is to find gaps in these methods for further research.

Contribution

This study examines the current methodologies used in autonomous UAVs, with a particular focus on comparing

classical approaches—such as SLAM, Kalman filters, and direction-of-arrival (DOA) estimation—with emerging AI-driven solutions. The key contributions of this study are as follows.

- **Description of traditional and AI-based techniques** – We describe several traditional and AI-based approaches used in UAV. We examine widely used methods, highlighting their strengths, limitations in real-life UAV operations. Simultaneously, we analyze AI-driven methods, particularly deep reinforcement learning (DRL) and neural network-based solutions, which offers new possibilities in exchange for different drawbacks.
- **Evaluation of scalability, robustness and computational efficiency** – While classical methods often offer well-established foundations and lower computational costs, AI-based approaches provide enhanced adaptability and better robustness but at the expense of increased processing requirements. This review discusses the trade-offs associated with each approach and their feasibility.
- **Identification of research gaps** - Despite recent advances, both traditional and AI-driven methods face challenges in terms of robustness, real-time adaptability, and generalization to unseen environments. This paper outlines potential research directions, presenting hybrid methodologies that integrate the reliability of classical models with the learning capabilities of AI techniques to enhance UAV performance.

The rest of the paper is organized as follows. Section II. briefly describes frequently used techniques and their fundamental logic in UAVs from both AI and traditional methods. This is followed by a review of papers that incorporate these methods while integrating innovative approaches. Section III. presents a comparison of both approaches, followed by a discussion and conclusions in Section V.

II. METHODOLOGY

When it comes to methods in UAV we need to specify the target usage of these techniques. Typically, the usage categories are split into three main categories – Guidance, Navigation, and Control. However, these three parts often overlap. If we are talking about an autonomous system, its control unit will be purely dependent on internal navigation

and planning, i.e. no direct user intervention will be possible. Therefore, we can omit the Control category. The main purpose of the Guidance category is to lead the drone in its environment and ensure that the drones are on the correct path. There are numerous ways available to accomplish this.

- **Waypoints navigation** – The basic solution is to give a drone location or a sequence of locations in the form of waypoints which the drone follows. Consequently, the drone itself blindly follows linear trajectories from point A to point B.
- **Path planning** – A more sophisticated way to lead the drone is path planning. There are quite a few path planning algorithms, ranging from the state-of-the-art Dijkstra's algorithm [1], A* algorithm and their modifications to complex swarm path planning algorithms, for example Ant Colony Optimization (ACO) [2] or Particle Swarm Optimization (PSO) [3]. In general, the goal of path planning is to determine the most efficient and fastest route to a given destination. Initially, the path consists of scattered points that are later refined into a final trajectory. [4]
- **AI Path planning** – The significant increase in the use of AI-based path planning algorithms has been driven primarily by Deep Reinforcement Learning (DRL), Machine Learning (ML), or Partially Observable Markov Decision Process (POMDP). [4] Despite their long training time, these AI models perform great in complex environments and have a fast reaction time.

In the navigation part, the UAV receives information about its position and orientation relative to a specific reference point. With this information, the drone can be located while maintaining the necessary stabilization, which is a crucial attribute for the overall system. Various methods are used to obtain this information.

- **Dead reckoning (DR)** – Is probably the oldest technique in the book. DR is a navigation technique used to estimate a vehicle's current position based on previously known positions, velocity, heading, and time elapsed. Unlike absolute positioning methods such as Global Navigation Satellite Systems (GNSS), dead reckoning relies solely on internal motion sensors and does not require external references. [5]
- **Inertial Measurement Units (IMU)** – The unit combines an accelerometer and a gyroscope to measure acceleration and angular velocity. This information is integrated to provide the current position of the UAV. Additionally, the IMU may contain magnetometer or barometer for more accurate heading information or altitude estimation. [6]
- **Global Navigation System (GNSS)** – To understand, what we lost in GNNS-challenging situations, we need to understand it. The most common and well-known method in navigation is the GNSS using one or more constellations: the US Global Positioning Signal (GPS), the European GALILEO, the Chinese BEIDOU or the Russian GLONASS. GNSS uses trilateration to obtain

the correct position. To determine it, a GPS receiver calculates how long it takes for signals from multiple satellites to reach it. By multiplying this travel time by the speed of radio waves (approximately 300,000 km or 186,000 miles per second), the receiver estimates its distance from each satellite. Each measurement defines a sphere with the satellite at its center and the receiver somewhere on its surface. When signals from at least three (in reality four, due to an inaccuracy in the receiver's clock) satellites are processed in this way, the receiver's internal system pinpoints its exact location by finding the intersection of these spheres, providing precise latitude, longitude, and altitude. [7]

- **Visual Odometry (VO)** – VO refers to the process of estimating a UAV movement, including both translation and rotation relative to a reference frame, by analyzing a sequence of images captured from its surroundings. VO represents a specific application of the broader Structure-from-Motion (SFM) technique, which addresses the challenge of reconstructing a 3D representation of an environment while simultaneously determining camera poses from either ordered or unordered image sequences. Usually, the VO is split into Monocular and Stereo models where each may encounter different problems. In general, there are three estimation techniques: 3D to 3D, 3D to 2D, and 2D to 2D. [8]
- **Simultaneous Localization And Mapping (SLAM)** – As the name suggests, this techniques combine localization and mapping. Generally, SLAM algorithms work by building maps of an unknown environment from multiple sources while keeping track of their own position in it. [9] Due to many applications, the SLAM may be sorted into many categories. Yousif et al. [8] sorted the SLAM into filtering and smoothing categories with different versions of SLAM. The filtering methods focus on addressing the online SLAM problem, where only the UAV's current state and the map are continuously updated by integrating sensor data as it is received. In contrast, the smoothing approaches tackle the full SLAM problem by estimating the posterior (robot poses and map) over the entire trajectory alongside the map. The filtering category can include **Extended Kalman Filters (EKF)**, **Particle Filters (PF)**, or **FastSLAM**, which is SLAM with Rao-Blackwellized particle filter for large-scale environments. The smoothing category can include for example **Visual SLAM (V-SLAM)**, **RGB-D SLAM**, that is basically V-SLAM with RGB-D sensors, or **GraphSLAM**.
- **AI navigation** – AI-based navigation most often build on the shortcomings of classical methods. For example, ML methods can enhance navigation by improving the accuracy and robustness of the UAV's position and orientation estimation in filtering SLAM techniques (e.g. EKF-SLAM with ML model for better handle of non-linear filters, or enchancing V-SLAM technique with computer vision and ML for faster mapping). [4]

There are a large number of traditional methodologies, many of them are especially focused on estimation, detection, and relocation with help from visual odometry (VO), Kalman filters, DOA, or other techniques mentioned above. For active jamming situation, Zhou et al. [10] proposed a solution for communication and localization. The solution work on power frequency domain inversion, where GNSS information is sent through different RF frequency band based on the position and frequency of the jamming signal. However, this solution must meet the condition that the number of nodes in the swarm is larger than the number of jammers. This obstacle solved Zhou et al. [11] with the leverage of multi-source direct-of-arrival (DOA) estimation that applied space-time DOA matrix techniques against spoof attacks. Different antijamming solutions presented by Wang et al. [12] by power optimization and trajectory planning. In this case, the UAV managing situation through IRR characterization with a power control and transmit power based on the Stanckelberg equilibrium game framework.

An effective strategy for multi-UAV outdoor operations involves a hierarchical structure, often referred to as a father-son or leader-follower configuration. This approach presented Causa et al. [13] with a generalized dilution of precision (generalized DOP) and setting the optimal father position based on the needed position of the son. The generalized DOP performed well under difficult conditions and significantly improved the achieved accuracy. The idea of generalized DOP (geDOP) was extended in a follow-up paper [14] with added Extended Kalman Filter for estimation of son's navigation state and may perform well in almost real-time scenarios.

The previously mentioned article by Causa et al. [14] introduced the first of the partly autonomous system, which works independently. Minervini et al. [15] presented a different approach to altitude estimation using adaptive Kalman filters and the V-SLAM algorithm with Mahanalobis distance for the detection of inconsistencies. This system works well in restricted indoor areas with various obstacles in the way of the drone, but is not suitable for estimation in larger fields and longer mission duration. Mugnai et al. [16] applied a similar approach with vision-based framework which operates on the basis of finite-state machine planner. This solution was tested in an indoor real environment in the Leonardo Drone Contest.

Horyna et al. [17] proposed visual-based estimation for a decentralized multi-robot system. In this research, a group of UAVs perform a multi-robot state estimation with the use of a velocity estimator fused with the optical flow data. The velocity estimation contains fused data from IMU and UVDAR that enhances the estimation precision during dynamic maneuvers.

In a follow-up article for fast swarming UAVs Horyna et al. [18] presented a decentralized approach heavily based on the visual perception of individual UAVs on board without communication. The main contributions are the flocking controller, which represents the stabilization and collective velocity of the UAVs in the swarm, enhanced Multi-Robot State Estimation

(MRSE) for safe deployment in unknown environments, and overall swarming framework. The velocity estimation is proposed through the state feedback control rule, which causes some inaccuracies. Finally, this framework was compared with state-of-the-art solutions and achieves better results in terms of speed and reliability without explicit communication.

Mishra et al. [19] proposed a complex and highly scalable framework for full-autonomy UAVs. The framework contains four main blocks: sensing, perception, planning, and controls. These blocks are made up of various subtasks which are responsible for correct function in all essential aspects of GNC. The computer vision-based algorithm for autonomous flight was introduced by Kuroswiski et al. [20], using the Ardupilot suite for flight control and integrates a Raspberry Pi for processing. A computer vision algorithm identifies landmarks from preloaded geo-referenced images to correct errors accumulated by inertial systems.

B. AI-driven solutions

Similar approach applied to the UAV swarm position and formation control presented by Ma et al. [21]. The vision-based approach is enhanced with hierarchical architecture using the deep learning object detection algorithm YOLOv7 and advanced real-time tracking DeepSORT, which introduces the Mahalanobis distance and utilizes the cosine distance in the SORT algorithm. Subsequently, this system was simulated in Rflysim software. After simulation, the real flight test takes place with three position tasks. However, the paper does not consider the complicated outdoor task, but mentions their implementation in follow-up work with a proposal for more UAVs in the swarm.

The use of machine learning does not have to be limited to detection or distance estimation. In contrast, total autonomy can be built on machine learning or other AI algorithms. Imanberdiyev et al. [22] presented a high-level model-based reinforcement learning algorithm called TEXPLORE. TEXPLORE consists of three main parts, which are action selection, model learning and planning. While planning and model learning run in the background, the action selection part interacts with the environment by taking actions as fast as required. The model is learning based on trial-and-error interactions in 3-4 decision trees based on the C_{4-5} algorithm, which will eventually create the final model. To avoid misunderstanding of environmental conditions, the models of the environment are learned by forming a random forest, which naturally causes uncertainties in the models. This model significantly outperforms the previously used Q-learning method, with only a few iterations in the learning process and real-time operation.

However, this approach offers only partial autonomy. The fully autonomous system presented by Wang et al. [23] directly enables mapping of the measurements of the raw UAV sensor to the control signals for navigation, which enables full autonomy in more complex environments. The system uses a deep reinforcement learning framework to solve the partially observable Markov decision process (POMDP). The framework integrates the Fast-Recurrent Deterministic Policy

Gradient algorithm (Fast-RDPG) with hierarchical planning to provide UAVs with a dual-layer decision-making process. This combination allows for high-level strategic goal setting and low-level reactive behaviour to dynamically adapt to obstacles and environmental changes.

Lei et al. [24] proposed a different and very interesting framework based on digital twin intelligent cooperation for UAV swarm situations. This framework combines a high-fidelity digital twin model of the physical system with a machine learning-based decision-making model to enable optimal real-time decision-making. Despite the unique idea, the implementation suffers from a lack of speed in updating the digital model.

III. Comparison of the solutions

This section provides a comparative analysis of traditional and AI-driven UAV methodologies based on key performance criteria: implementation complexity, scalability, robustness, and computational efficiency.

A. Implementation Complexity

Traditional approaches, such as Kalman filters and SLAM-based methods, require significant domain expertise and precise sensor calibration. These methods rely on predefined models and accurate environmental information. In contrast, AI-driven solutions, such as deep reinforcement learning (DRL), reduce dependency on predefined models but require extensive training datasets and computational resources.

B. Scalability

Classical approaches often face scalability issues due to their reliance on fixed models and assumptions. Multi-UAV systems using methods like DOA estimation require centralized coordination, limiting their ability to scale in dynamic environments. AI-driven methods, particularly those that leverage deep learning frameworks, offer greater adaptability, making them more suitable for large-scale UAV swarms. However, their deployment is constrained by the need for extensive computational power and training.

C. Robustness

Traditional methods exhibit robustness in structured and predictable environments but struggle with complex and unpredictable conditions, such as GNSS spoofing or jamming. AI-based approaches demonstrate enhanced adaptability by learning from diverse datasets and dynamically adjusting to environmental changes. For example, DRL-based navigation techniques outperform classical methods in highly dynamic and partially observable conditions. However, AI-driven solutions may suffer from reliability issues when faced with completely new or adversarial scenarios.

D. Computational Efficiency

Kalman filters and SLAM-based techniques are computationally efficient and feasible for real-time applications. However, these methods lack the flexibility to handle complex real-time decision-making scenarios. AI-based approaches, such as

Fast-RDPG and model-based reinforcement learning, require significant processing power, which can be a limiting factor for real-time UAV operations, especially on resource-constrained platforms. Hybrid approaches that integrate classical methods with AI-driven enhancements present a promising direction to balance computational efficiency and adaptability.

In summary, while traditional methods remain valuable for specific applications that require efficiency and reliability, AI-driven techniques provide enhanced adaptability and decision-making capabilities. The optimal approach depends on the specific operational constraints and mission requirements of UAV systems in GNSS-challenging environments. Future research should focus on hybrid methodologies that integrate the efficiency of classical methods with the adaptability of AI-driven frameworks and their optimalization.

IV. Conclusion

This review highlights the advancements in methods for enabling UAV autonomy in GNSS-challenging environments. The surveyed methods span traditional GNC methods and upcoming AI-driven systems. Classical approaches such as Kalman filters, SLAM, V-SLAM and other estimations remain essential for tasks requiring localization and path planning in visually rich environments. However, these methods face limitations in scalability and adaptability to large-scale or dynamic conditions.

AI-driven methods, particularly those that leverage deep reinforcement learning (DRL), demonstrate significant potential to address these limitations. Fast-RDPG-based frameworks, which effectively manage the partially observable Markov decision process (POMDP), enable robust navigation and decision-making by integrating high-level strategic planning with low-level reactive capabilities. These advancements open the door for fully autonomous systems capable of operating in complex and unpredictable environments, outperforming traditional algorithms in terms of adaptability and scalability.

Despite these innovations, several challenges remain. Many state-of-the-art solutions lack robustness in extreme environmental conditions or require significant computational resources, limiting real-time applications. Additionally, collaborative multi-UAV operations with minimal communication overhead require further exploration to ensure efficiency in large-scale swarm deployments.

Future research should focus on the integration of computationally efficient algorithms with enhanced decision making capabilities. Expanding the robustness of vision-based and AI-driven frameworks to handle adverse conditions, such as severe weather or cluttered environments, is also crucial. Finally, a unified approach that combines the strengths of classical and AI-based methods could provide the adaptability, efficiency and reliability required for UAV operations in GNSS-challenging environments.

References

[1] DIJKSTRA, E. W. A note on two problems in connexion with graphs. Online. Numerische Mathematik. 1959, roč. 1, č. 1, s. 269-271.

ISSN 0029-599X. Available at: https://doi.org/10.1007/BF01386390. [accessed 2025-03-15].

[2] BRAND, Michael; MASUDA, Michael; WEHNER, Nicole and XIAO-HUA YU. Ant Colony Optimization algorithm for robot path planning. Online. In: 2010 International Conference On Computer Design and Applications. IEEE, 2010, V3-436-V3-440. ISBN 978-1-4244-7164-5. Available at: https://doi.org/10.1109/ICCDA.2010.5541300. [accessed 2025-03-15].

[3] KENNEDY, J. and EBERHART, R. Particle swarm optimization. Online. In: Proceedings of ICNN'95 - International Conference on Neural Networks. IEEE, 1995, p. 1942-1948. ISBN 0-7803-2768-3. Available at: https://doi.org/10.1109/ICNN.1995.488968. [accessed 2025-03-15].

[4] REZWAN, Sifat and CHOI, Wooyeol. Artificial Intelligence Approaches for UAV Navigation: Recent Advances and Future Challenges. Online. IEEE Access. 2022, roč. 10, s. 26320-26339. ISSN 2169-3536. Available at: https://doi.org/10.1109/ACCESS.2022.3157626. [accessed 2025-01-09].

[5] Dead Reckoning for GNSS Denied Scenarios – An Introduction. Online. Advanced Navigation. Available at: https://www.advancednavigation.com/tech-articles/an-introduction-to-dead-reckoning/. [accessed 2025-03-16].

[6] Understanding Inertial Measurement Unit (IMU): Basics, Applications, and Future Trends. Online. GuideNav: The Global Standard in Inertial Navigation Excellence. Available at: https://guidenav.com/understanding-inertial-measurement-unit-imu-basics-applications-and-future-trends/. [accessed 2025-03-16].

[7] LOGSDON, Tom S. GPS. Online. Encyclopedia Britannica. Available at: https://www.britannica.com/technology/GPS. [accessed 2025-03-14].

[8] YOUSIF, Khalid; BAB-HADIASHAR, Alireza and HOSEIN-NEZHAD, Reza. An Overview to Visual Odometry and Visual SLAM: Applications to Mobile Robotics. Online. Intelligent Industrial Systems. 2015, roč. 1, č. 4, s. 289-311. ISSN 2363-6912. Available at: https://doi.org/10.1007/s40903-015-0032-7. [accessed 2025-03-16].

[9] DURRANT-WHYTE, H. and BAILEY, T. Simultaneous localization and mapping: part I. Online. IEEE Robotics & Automation Magazine. 2006, roč. 13, č. 2, s. 99-110. ISSN 1070-9932. Available at: https://doi.org/10.1109/MRA.2006.1638022. [accessed 2025-03-16].

[10] ZHOU, Jianwei; WANG, Wenjie; HONG, Xi a ZHANG, Chenhao. Multi-UAV Cooperative Anti-Jamming For GNSS Signals Based on Frequency-Domain Power Inversion. Online. IEEE Sensors Journal. 2024, s. 13. Available at: https://ieeexplore.ieee.org/document/10632041. [accessed 2024-09-10].

[11] ZHOU, Jianwei; WANG, Wenjie a ZHANG, Chenhao. Multi-source DOA estimation based on multi-UAV collaboration in complex GNSS spoofing environments. Online. IET Radar, Sonar & Navigation. 2024, roč. 18, č. 10, s. 1837-1847. ISSN 1751-8784. Available at: https://doi.org/10.1049/rsn2.12620. [accessed 2024-11-18].

[12] WANG, Haichao; DING, Guoru; CHEN, Jin; ZOU, Yulong a GAO, Feifei. UAV Anti-Jamming Communications With Power and Mobility Control. Online. IEEE Transactions on Wireless Communications. 2023, roč. 22, č. 7, s. 4729-4744. ISSN 1536-1276. Available at: https://doi.org/10.1109/TWC.2022.3228265. [accessed 2024-12-30].

[13] CAUSA, Flavia; VETRELLA, Amedeo Rodi; FASANO, Giancarmine a ACCARDO, Domenico. Multi-UAV formation geometries for cooperative navigation in GNSS-challenging environments. Online. In: 2018 IEEE/ION Position, Location and Navigation Symposium (PLANS). IEEE, 2018, s. 775-785. ISBN 978-1-5386-1647-5. Available at: https://doi.org/10.1109/PLANS.2018.8373453. [accessed 2025-01-06].

[14] CAUSA, Flavia a FASANO, Giancarmine. Improving Navigation in GNSS-Challenging Environments: Multi-UAS Cooperation and Generalized Dilution of Precision. Online. IEEE Transactions on Aerospace and Electronic Systems. 2021, roč. 57, č. 3, s. 1462-1479. ISSN 0018-9251. Available at: https://doi.org/10.1109/TAES.2020.3043543. [accessed 2025-01-06].

[15] MINERVINI, Alessandro; PRIMATESTA, Stefano a GUGLIERI, Giorgio. Enhanced Altitude Estimation for Unmanned Aerial Vehicles in a GNSS-denied Environment. Online. International Conference on Unmanned Aircraft Systems (ICUAS). 2024, roč. 2024, č. -, s. 7. Available at: https://ieeexplore.ieee.org/abstract/document/10556904. [accessed 2025-03-15].

[16] MUGNAI, Michael; TEPPATI LOSÉ, Massimo; HERRERA-ALARCÓN, Edwin; BARIS, Gabriele; SATLER, Massimo et al. An Efficient Framework for Autonomous UAV Missions in Partially-Unknown GNSS-Denied Environments. Online. Drones. 2023, roč. 7, č. 7. ISSN 2504-446X. Available at: https://doi.org/10.3390/drones7070471. [accessed 2024-11-18].

[17] HORYNA, Jiri; KRATKY, Vit; FERRANTE, Eliseo a SASKA, Martin. Decentralized Multi-robot Velocity Estimation for UAVs Enhancing Onboard Camera-based Velocity Measurements. Online. In: 2022 IEEE/RSJ International Conference on Intelligent Robots and Systems (IROS). IEEE, 2022, s. 11570-11577. ISBN 978-1-6654-7927-1. Available at: https://doi.org/10.1109/IROS47612.2022.9981894. [accessed 2024-11-25].

[18] HORYNA, Jiří; KRÁTKÝ, Vít; PRITZL, Václav; BÁČA, Tomáš; FERRANTE, Eliseo et al. Fast Swarming of UAVs in GNSS-Denied Feature-Poor Environments Without Explicit Communication. Online. IEEE Robotics and Automation Letters. 2024, roč. 9, č. 6, s. 5284-5291. ISSN 2377-3766. Available at: https://doi.org/10.1109/LRA.2024.3390596. [accessed 2024-11-19].

[19] MISHRA, Sakshi a PALANISAMY, Praveen. Autonomous Advanced Aerial Mobility—An End-to-End Autonomy Framework for UAVs and Beyond. Online. IEEE Access. 2023, roč. 11, s. 136318-136349. ISSN 2169-3536. Available at: https://doi.org/10.1109/ACCESS.2023.3339631. [accessed 2025-01-09].

[20] KUROSWISKI, Andre Rossi; DE OLIVEIRA, Neusa Maria Franco a SHIGUEMORI, Elcio Hideiti. Autonomous long-range navigation in GNSS-denied environment with low-cost UAV platform. Online. In: 2018 Annual IEEE International Systems Conference (SysCon). IEEE, 2018, s. 1-6. ISBN 978-1-5386-3664-0. Available at: https://doi.org/10.1109/SYSCON.2018.8369592. [accessed 2024-11-25].

[21] MA, Liqun; MENG, Dongyuan; HUANG, Xu a ZHAO, Shuaihe. Vision-Based Formation Control for an Outdoor UAV Swarm With Hierarchical Architecture. Online. IEEE Access. 2023, roč. 11, s. 75134-75151. ISSN 2169-3536. Available at: https://doi.org/10.1109/ACCESS.2023.3296603. [accessed 2025-03-15].

[22] IMANBERDIYEV, Nursultan; FU, Changhong; KAYACAN, Erdal a CHEN, I-Ming. Autonomous navigation of UAV by using real-time model-based reinforcement learning. Online. In: 2016 14th International Conference on Control, Automation, Robotics and Vision (ICARCV). IEEE, 2016, s. 1-6. ISBN 978-1-5090-3549-6. Available at: https://doi.org/10.1109/ICARCV.2016.7838739. [accessed 2025-01-13].

[23] WANG, Chao; WANG, Jian; SHEN, Yuan a ZHANG, Xudong. Autonomous Navigation of UAVs in Large-Scale Complex Environments: A Deep Reinforcement Learning Approach. Online. IEEE Transactions on Vehicular Technology. 2019, roč. 68, č. 3, s. 2124-2136. ISSN 0018-9545. Available at: https://doi.org/10.1109/TVT.2018.2890773. [accessed 2025-01-13].

[24] LEI, Lei; SHEN, Gaoqing; ZHANG, Lijuan a LI, Zhilin. Toward Intelligent Cooperation of UAV Swarms: When Machine Learning Meets Digital Twin. Online. IEEE Network. 2021, roč. 35, č. 1, s. 386-392. ISSN 0890-8044. Available at: https://doi.org/10.1109/MNET.011.2000388. [accessed 2024-11-27].

Multifunctional 3D Printed Unmanned Aireal Vehicle

Matěj Mlynář
Gymnázium Žamberk
Žamberk, Czech Republic
matej.mlynar.005@gmail.com

Supervised by:
Mgr. Kateřina Jirešová
Gymnázium Žamberk
Žamberk, Czech Republic
katerina.jiresova@gyz.cz

Supervised by:
Ing. Tomáš Jukl
OEZ Letohrad
Letohrad, Czech Republic
tomas.jukl@oez.com

Abstract—**This paper is focused on explaining the design process and functionality of multifunctional, long range, unmanned aerial vehicle, with the intention to be printed, repaired or modified with use of any common 3D printer. This paper also focuses on a few possible future uses and improvements for said unmanned aerial vehicle.**

Keywords—unmanned aerial vehicle, 3D printing, drone, multifunctional

I. INTRODUCTION

Ever since the dawn of mankind, we always looked up to the sky and were amazed by birds with their ability to fly. Nowadays we have means to produce our own flying machines. We even started to make them remotely controlled, and with that the Unmanned Aireal Vehicles (afterwards referred to as UAV) were born. With the popularity of UAVs rising in the last few years, especially quadcopters, they are being implemented into many different fields of work [1]. So, when I was looking for an idea on the topic of my work, these facts convinced me to choose making of the UAV, as it provided some freedom of design and also many different possible uses. This paper mainly focused on explaining my design process of making my UAV, with some possible uses and later improvements.

As I had little prior experience with making or flying a UAV, I started this project with a lot of research around the topic. Another reason why I chose this project is that I have a lot of experience with 3D printing, that is why I decided to use a 3D printer as a main form of construction for the UAV. I also had quite a lot of experience with 3D modeling and designing in SolidWorks [2], from when I gained my CSWA (Certified SolidWorks Associate) certification, so using SolidWorks as my primary modeling tool for this was probably the best choice for me.

Because there are many different ways to make a UAV, with equally as many different uses for it, so I decided on a few main goals for my UAV, which are:

- Simple manufacture, in my project, I strongly relied on 3D printing
- Long range flight, because I wanted this UAV to cover as much area per flight as possible
- Multifunctionality and future modifiability, as I wanted this UAV to be versatile and also so I could later develop modifications (see more in section V. and VI.).

With the start of this project, I also got an opportunity to attend internship in a local company OEZ Letohrad, which helped development of this UAV with consultations, advice and partial founding of this project.

II. CONSTUCTION

As long-range flight was one of my main goals, I settled on design with fixed wings and one push motor with a 10-inch, two leaf, foldable propeller. I designed this UAV into smaller segments, so they can fit on to most of the common 3D printers and can be easily modified or replaced if needed. The design of the UAV is my own work, and it is a result of my different early sketches and 3D models. The only thing I took some inspiration in from different models was the way to attach the back wing to the body, using two thin tubes. Which I found quite common in the UAV community, at least for UAVs with motor in the back. The 3D printer used for this project was my modified Ender 3 V2. Because weight is one of the major factors in long-range flights. I decided to use Light Weight PLA (or LW-PLA) as a main type of filament, specifically Black eSun LW-PLA [3], as it was the easiest one for me to obtain. I chose LW-PLA because it offered good weight properties, as it can be up to 21% lighter than normal PLA, even if it is at cost of some strength [4], but that does not really affect me, as I have installed PVC tubes as reinforcement in the wings. Lighter body meant that I had more freedom choosing electronics and also for the future modifications.

The UAV consists of 3 main parts (Fig. 1):

A. Fuselage has shape of a tube, as it offers good aerodynamics with decent amount of space, and it is also easy to print.

B. Front wings are separated into 4 segments, with one long aileron on each side. I used Clark-Y Airfoil, because of its good performance at low speeds with ailerons down, and low drag with ailerons in normal position [10].

C. Back wing has teardrop airfoil, so the airflow is approximately the same on top and bottom sides of the wing, for the best elevator performance. There are two separate elevators on the back wing with one vertical stabilizer on each side.
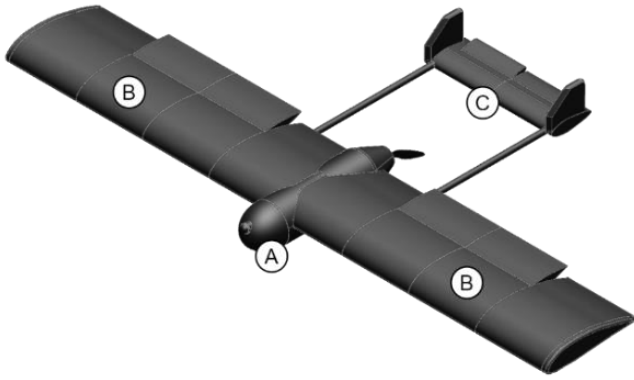
Fig. 1 – Picture of the UAV with highlighted parts

The change of direction is achieved by a combination of aileron and elevator input, as I decided to not use rudder for less complicated construction, even at cost of some agility, which should not be crucial for most of my UAV flights, I might add rudder in later iteration if there will be need for better agility.

Take-off with this UAV is achieved by a help of custom cart which is used as wheels, until the UAV leaves the ground, leaving the cart on ground. As of now, this UAV needs fairly long space for reaching its take off speed (see section IV.).

The actual process of assembling the UAV was more or less simple, as I have spent long time designing the parts to easily fit together. But even after all the preparation, I still had to modify some of the parts by hand, as I have made some changes of electronics between printing some of the parts and putting the UAV together, however after the final assembly I have updated all the part files, so they are ready to use.

III. ELECTRONICS

Electronics in this UAV have 6 main components (Fig. 2):

1. Two 2200 milliampere hour, six cell batteries connected in parallel for a total of 4400 milliampere hours. The batteries are mounted in the fuselage under the wings, because they are the heaviest component, and I do not want them to offset the center of mass too much. There is the possibility for future use of bigger batteries, up to 17000 milliampere hours of total battery.
2. EM3110[9] Motor mounted in the back of the fuselage
3. Matek F405-Wing-V2 [5] flight controller mounted in the nose section of UAV. This controller, with an integrated gyroscope, accelerometer and barometer, is used for communication between all the different modules, stabilization and maintaining flight. I am also using this controller to convert 22 volts from batteries to 5 volts used in the rest of the UAV. With this controller there is a possibility for later partial automation of the UAV.
4. Six MG90D servos that are used for movement of flaps. There are two servos for each of the ailerons, so they are moved evenly because of their length. There is also one servo for each of the elevators, so they can be controlled separately.

5. 2.4 gigahertz receiver with double antenna, for better connection, mounted in the back of the UAV. For control of the UAV, I am using ExpressLRS [6] which is an open-source radio control link.
6. An additional feature of my UAV is the Universal Mounting Spot (UMS) on the bottom of the middle section of the fuselage. This is a custom-made mounting spot which can be used to mount and connect different instruments such as:
   - Infrared camera
   - Thermal camera
   - High quality camera
   - Lidar module
   - Ground penetrating radar
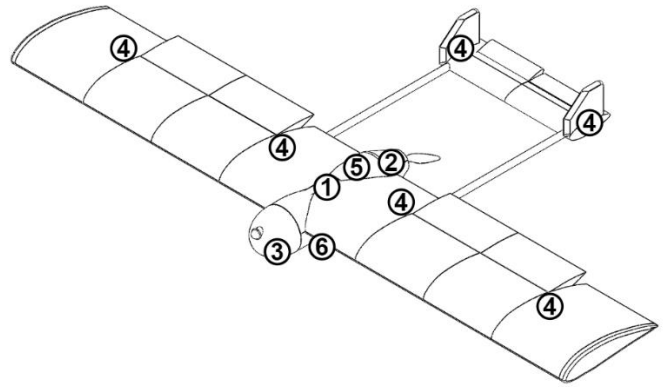   - Possible other instruments

Fig. 2 – Picture of UAV with highlighted components

In the Fig. 3 we can see the simplified wiring diagram of my UAV, we can also see connections for future components (see dashed line borders)
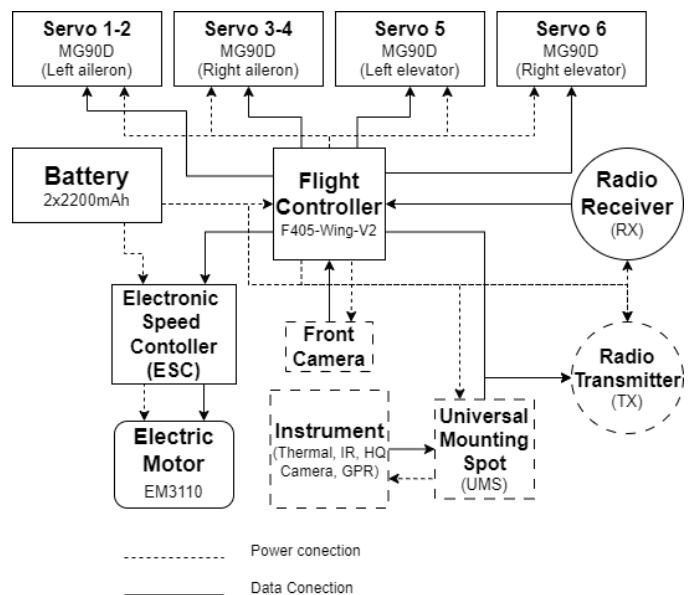

Fig. 3 – Simplified wiring diagram

IV. PARAMETERS

Here we can see in Tab. 1. with some basic parameters, which we can use to calculate some theoretical properties flight properties of the UAV:

Weight of the body	3412.5 g
Weight of the components	840.5 g
Total weight	4253 g
Wingspan	1625 mm
Wing area	47200 mm²
Length of the body	844 mm
Diameter of fuselage	100 mm
Operational motor power (50%)	276.7 W
Maximal motor power (100%)	1248.6 W
Optimal take-off weight	5000 g

Tab. 1 – Table of basic parameters

To determine the speed needed for take-off with optimal take-off weight, we can use the lift formula:

$$L = \frac{1}{2}\rho v^2 S C_L \qquad (1)$$

Where L stands for lift, ρ stands for density of air, v is for the velocity of the UAV, S is for surface area of the wings and C_L stands for lift coefficient which for Clark-Y is approximately $C_L = 1.3$ for angle of attack of 15 degrees [10]. The result is that we need at least $v = 43.2$ km/h to achieve flight, but this value does not consider in the position of ailerons on the wings, because with them facing downwards, the speed needed is likely to decrease, as the lift coefficient should be higher [10].

V. POSSIBLE USE

Because this UAV can be modified and it is meant to be multifunctional, I cannot really specify all the possible uses for it, but I can at least specify a few of them, which were on my mind in the process of making this UAV.

When an avalanche happens, and there is possibility of people being buried under snow, their survival chances depend on how quickly they can be dug up [7]. And for those situations I think using a UAV could potentially help save those victims using ground penetrating radar (GPR), which could be used to locate people under snow [8], as UAV can cover large and hard to reach areas in short amount of time, even at the cost of some accuracy of the GPR due to data noise caused by the UAV being off ground. This application would need more testing in the field and more development, to surely determine if it is feasible, so I am planning to continue working on this option to see its future development. Also, another use could be during search and rescue using thermal camera, because deploying UAV is fast and easy, and it would potentially save the time needed to call a helicopter equipped with thermal camera, and also the UAV could be easily stored in any emergency service vehicle or building.

Another possible use for my UAV could be terrain scanning, which could be used in many different fields of work [1], like construction, farming, or nature protection or with a mounted thermal camera, the UAV could be used for wildlife monitoring.

I also want this UAV to be relatively easy to 3D print and assemble, so it could be in the printed, modified or repaired anywhere, as the only thing needed for its manufacture is some common 3D printer and few other previously specified parts, and could be used widely across different work fields.

VI. FUTURE IMPROVEMENTS

There is a limit of what I can do on my own, so there are a few things I would like to add or focus on in future iterations of this UAV, such as:

a. Easily accessible battery assembly, so both batteries can be taken out at once from outside and replaced. This would improve the effectiveness of my UAV, because it would not need any charging between flights.

b. Simplified construction, which would lead to some weight loss, thus better flight efficiency, saving material and easier 3D printability.

c. Making my own PCBs with modules, so I could possibly make the UAV easier to assemble and maybe little lighter.

d. Contra-rotating propellers, which could improve efficiency and stability of UAV by canceling the centrifugal force of the airflow caused by single propeller and therefore focusing more direct airstream on the back wing. The UAV with this feature would need some kind of gearbox, which would increase its complexity, but could lead to better flight performance.

e. Develop simple and safe way to launch the UAV from ground. Maybe like a ramp, catapult or maybe develop a way to launch the UAV from moving car to help achieve take-off speed in much shorter distance.

f. Make my drone partially autonomous, so it can do basic actions, like flying to a point, over some area or following some object or path on its own.

VII. TEST FLIGHT

In Tab. 2. below we can see theoretical flight data, for the UAV, in current configuration, with perfect conditions:

Flight duration	24 min
Distance flown	20160 m
Weight of the UAV	5000 g
Speed	50 km/h

Tab. 2 – Flight parameters

These values should be used as a benchmark for future modifications and will be tested as soon as possible to see if they are right.

VIII. CONCLUSION

In this paper, I have focused on an explanation of my journey with designing and building my own 3D printed UAV. I have also explained some possible uses for it. Even though I have finished this UAV, there are always things to improve, and I plan to continue developing said UAV, with more modifications and improvements in the future.

ACKNOWLEDGMENT

REFERENCES

[1] Mohsan SAH, Khan MA, Noor F, Ullah I, Alsharif MH. Towards the Unmanned Aerial Vehicles (UAVs): A Comprehensive Review. *Drones*. 2022; 6(6):147.

[2] "SolidWorks", Mar. 05, 2025. https://www.solidworks.com/

[3] "eSun PLA-LW" Mar. 5, 2025. *https://www.esun3d.com/*.

[4] C. A. Griffiths, A. Rees, A. Morgan, and F. Korkees, "Optimisation of 3D printing for microcellular polymers," *Polymers*, vol. 15, no. 19, p. 3910, Sep. 2023

[5] "F405-WING-V2" Mar. 05, 2025. https://www.mateksys.com/?portfolio=f405-wing-v2

[6] ExpressLRS, "High performance Open source Radio Control link," Mar. 05, 2025 . https://www.expresslrs.org/

[7] S. Rauch *et al.*, "Avalanche survival rates in Switzerland, 1981-2020," *JAMA Network Open*, vol. 7, no. 9, p. e2435253, Sep. 2024

[8] Mongelos, Pedro, et al. "Using a Drone-based Ground Penetrating Radar for Avalanche Victim Search: A Case Study from Northern Spain." (2021).

[9] "GEPRC EM3110" Mar. 05, 2025. https://geprc.com/product/geprc-em3110-900kv-motor/

[10] A. Zhao, Z. Hui, H. Jin, and D. Wen, "Analysis on the aerodynamic characteristics of a continuous whole variable camber airfoil," *Journal of Physics Conference Series*, vol. 1215, no. 1, p. 012005, May 2019

Electroactivity of Polyvinylidene Fluoride Fibers Probed by SPM

Jan Buchta

Gymnázium Matyáše Lercha

Brno, Czech Republic

xbuchta@gml.cz

Supervised by doc. Mgr. Dinara Sobola Ph.D.

Faculty of Electrical Engineering and communication

Brno, Czech Republic

sobola@vut.cz

Abstract — **In this study, the piezoelectric response of the polyvinylidene fluoride (PVDF) polymer was investigated using piezoresponse force microscopy (PFM), a mode of scanning probe microscopy (SPM). Atomic force microscopy (AFM) was employed to characterize the surface morphology of the PVDF fibers in detail. The signals acquired from the cantilever tip were processed using Nova software, enabling the analysis and comparison of phase and amplitude responses of the probe under varying applied voltages.**

Keywords — PVDF, AFM, Piezoelectricity, Topography, Fiber

I. Atomic force microscopy

Atomic Force Microscopy (AFM) is a high-resolution, non-optical microscopy technique capable of three-dimensional imaging of a wide range of surfaces. It enables non-destructive characterization of surface topography at the nanoscale, with resolution primarily determined by the radius of the probe tip. AFM was invented in 1986 by Gerd Binnig, Calvin Quate, and Christoph Gerber, building upon the principles of scanning tunneling microscopy [1].

A. Advantages

One of the main advantages of this method is that it does not require sample pre-treatment or operation in a vacuum environment, unlike scanning electron microscopy (SEM). Additionally, AFM offers exceptionally high spatial resolution, making it suitable for detailed surface characterization at the nanoscale.

B. Disadvantages

The limitations of AFM include relatively slow scanning speed, as the acquisition of a single high-resolution image can take over twenty minutes. Additionally, the scanning area is typically confined to small surface regions. The vertical (Z-axis) scanning range is also limited in range of micrometers. Furthermore, the finite width of the AFM tip can lead to convolution effects, potentially distorting the representation of fine surface features.

C. AFM Principals

AFM utilizes a sharp probe (tip) to scan the sample surface. A laser beam is focused on the back side of the cantilever holding the tip, and the reflected light is detected by a position-sensitive photodiode. As the tip interacts with the surface and moves across its features, the deflection of the cantilever alters the angle of the reflected laser beam, causing it to shift across the photodiode. The Nova software processes these positional changes to reconstruct a detailed three-dimensional model of the surface from numerous data points. AFM can operate in three primary modes: contact, semi-contact (tapping), and non-contact, each offering different interaction mechanisms between the tip and the sample.

D. Construction

The AFM is mounted on an anti-vibration table to minimize external mechanical interference during measurement (Figure 1). The AFM is equipped by optical camera with integrated illumination for precise sample visualization and tip alignment. The sample is placed on adjustable sample stage (scanner), allowing accurate positioning relative to the scanning probe.

Above the sample, the set-up (head) containing the laser and photodetector (photodiode) is located. Two adjustment screws are used to align the laser beam precisely onto the back of the cantilever tip, while another pair of screws allows fine-tuning of the photodiode position to ensure the reflected beam
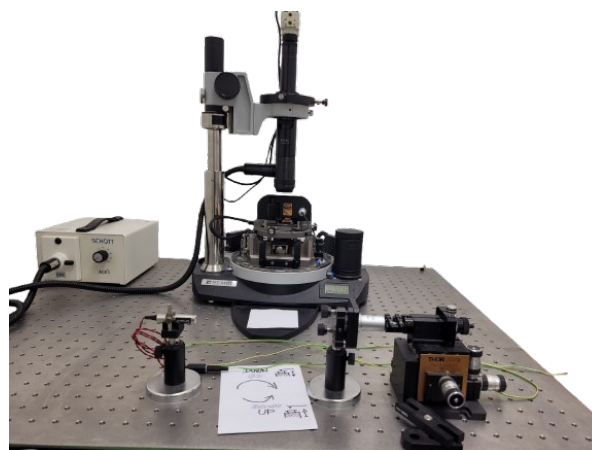

Figure 1: AFM

strikes its center. All components are interconnected through a control unit, which manages the positioning system.

E. Scanning

The measurement procedure begins with activating the anti-vibration table to ensure a stable environment. Subsequently, the Nova software is launched, followed by powering on the SPM controller. The software performs an initial system check to verify operational readiness. Once confirmed, the sample is placed onto the adjustable stage, and the laser beam is carefully aligned with the cantilever tip, ensuring accurate reflection onto the center of the photodiode using the alignment screws. The appropriate imaging mode (contact, semi-contact, or non-contact), scanning frequency, and scan direction should be defined. The scanner then moved up until the tip is brought into proximity with the sample surface. Scanning is initiated through the software interface. In some cases, tip instability or sample displacement may occur during scanning. To resolve such issues, it is often effective to reduce the scan frequency or adjust the scan direction to stabilize the interaction. Figure 2 presents a 3D surface scan obtained using this procedure.
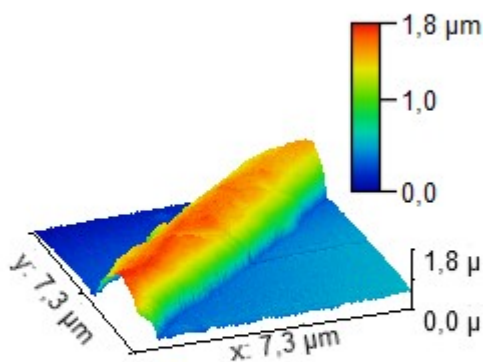

Figure 2: PVDF Fiber

F. Working modes

There are two primary operational modes in Atomic Force Microscopy (AFM):

Contact Mode (Static Mode): In contact mode, the AFM tip maintains continuous physical contact with the sample surface throughout the scan. This mode allows for direct interaction between the tip and the sample, providing high-resolution topographical information. However, this constant contact can lead to lateral forces that may deform the sample or affect delicate features.

Dynamic Mode, which is further subdivided into Semi-contact Mode and Non-contact Mode

Semi-contact Mode (Tapping Mode): In this mode, the AFM tip oscillates at or near its resonant frequency, driven by a piezoelectric element. During each oscillation cycle, the tip makes intermittent contact (or "taps") with the sample surface. This reduces the lateral forces acting on the sample compared to contact mode, minimizing potential damage while still providing detailed surface topography.

Non-contact Mode: In non-contact mode, the AFM tip oscillates above the sample surface without making direct contact. The tip interacts with the sample primarily through long-range forces, such as Van der Waals forces, that occur as

the tip and sample come into close proximity. This mode is particularly useful for imaging soft or delicate samples, as it minimizes the risk of surface damage.

II. PVDF

Polyvinylidene fluoride is a highly non-reactive, biocompatible thermoplastic polymer. Its chemical formula is $C_2H_2F_2$. PVDF is used for its high purity and resistance to temperature, UV light and nuclear radiation and chemicals like acids, organic solvents and alcohols. In 1969 strong piezoelectricity in PVDF, which is used in tension sensors, was observed [2].

G. Applications

In electronics PVDF is used as insulation on electrical wires because of its low weight, flexibility and resistance. PVDF is also material used in the production of composite electrodes for lithium-ion batteries. The electrodes get soaked in the solution of 1-2% PVDF and some active lithium storage material. When the dissolvent evaporates the electrode becomes covered by PVDF.

PVDF is used in piezoelectric sensors in airplanes, satellites, robots and also biomedicine. These sensors are very important for modern medicine, because they are monitoring vital functions such as heart rate, EKG, glucose level, brain activity, blood pressure, oxygen level, sleep quality, pH, hormones level, blood flow and much more. They are used to stimulate the nerves [3].

Another use of PVDF is as an additive to paints to preserve from corrosion, to handle nuclear waste or to protect surfaces. PVDF pipes are used for transportation of ultra-pure water or aggressive chemicals.

H. Conformations

PVDF consists primarily of single bonds, which allow rotation around these bonds, leading to the formation of various conformations. The most commonly observed phases are α, β, and γ. While these phases share the same basic chemical composition, the different arrangements of bonds between the fluorine-carbon and carbon-hydrogen atoms result in distinct piezoelectric properties (see Figure 3).

- α Phase: The α phase features a non-linear chain, where the fluorine and hydrogen atoms are in a gauche conformation. This phase is not piezoelectric due to the antiparallel alignment of dipoles within its unit cell. The lack of a net dipole moment renders this phase suitable for applications where piezoelectric properties are not required, such as in pipes, valves, and cable insulation.

- β Phase: The β phase is the most piezoelectric phase of PVDF. In this phase, the polymer chain is linear, and the bonds between the fluorine-carbon and carbon-hydrogen atoms adopt a trans conformation. The arrangement of atoms creates a polarized structure with a non-zero dipole moment, enabling piezoelectric behavior. This phase is widely used in applications such as acoustic sensors, biomedical devices, microphones, and filtration system membranes.

- γ Phase: The γ phase is a mixed configuration, combining both gauche and trans conformations within the polymer chain. As a result, it exhibits weak

piezoelectric properties compared to the β phase. Despite its lower piezoelectric activity, the γ phase can be utilized in applications where moderate piezoelectric response is sufficient or where the material's mechanical properties are prioritized.
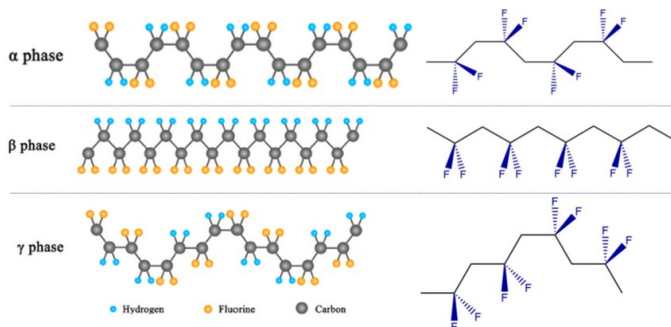

Figure 3: PVDF Conformations

I. Production of β phase

PVDF is synthesized through the polymerization of vinylidene fluoride (VDF) monomers, which is typically initiated by a reaction between chloroform or acetylene and hydrogen fluoride. During the polymerization process, long chains of PVDF are formed, predominantly in the α conformation. To create PVDF fibers, the polymer is dissolved in a polar solvent, such as acetone, dimethylformamide (DMF), or dimethylacetamide (DMAc), at a concentration of 5–10%. The solution is then subjected to electrospinning, where the solvent is evaporated, resulting in the formation of PVDF fibers.

III. Experimental part

J. Material and method

1) Microscope probes

The measurements were conducted using the NTEGRA Prima SPM microscope from Spectrum Instruments, which is capable of characterizing a wide range of material properties, including electrical resistance, magnetic and electrostatic forces, flexibility, and piezoelectricity. For measuring the piezoelectric properties, a gold-coated contact-mode tip was used to ensure proper conductivity. The semi-contact mode tip was employed for high-precision surface topography scanning, allowing detailed imaging of the sample surface.

2) PVDF

The PVDF fibers measured in this study predominantly contained the β phase. The PVDF was crystallized from a 20% solution, using dimethyl sulfoxide (DMSO) and acetone as solvents. For fiber stretching, a rotating electrically charged cylinder was employed. The winding process was carried out at a higher rotational speed of 2000 RPM, as increased RPM promotes the formation of finer fibers.

3) Measurement

The measurement process began by placing the sample, mounted on a gold-coated substrate, onto the scanner. To establish an electrical connection between the substrate and the SPM tip, the gold substrate was connected to the controller via a thin wire and mechanical contact. After powering on the anti-vibration table, the Nova software, and the microscope, I configured the laser and selected the contact piezoresponse force mode. The feedback value was adjusted to minimize background noise.

Using the microscope's camera, I selected a region of the fiber for scanning. For optimal results, the scanning speed was set to 0.2–0.3 Hz. The microscope scanned 256 lines per image, with each scan taking approximately twenty minutes to complete. Throughout the scanning process, I continuously monitored the progress.

For subsequent scans, I varied the voltage between the tip and the substrate. The voltages applied were: -10V, -5V, -2V, -1V, 0V, 1V, 2V, 5V, and 10V. The scanning area was 50x50 microns. Occasionally, the tip would move with the fiber, requiring me to stop the scan and adjust the scanning direction. The acquired images were then processed using Gwyddion software, where I adjusted the color schemes and reduced the background noise.

K. Results

The piezoelectric properties of PVDF provide valuable insights into the material's behavior under applied voltage. By examining these properties, one can observe how the deformation of the material correlates with the magnitude of the applied voltage. The polarization of PVDF is evident, as the dipoles orient differently under positive and negative voltages. Additionally, the piezoelectric response can reveal potential damage to the fiber, allowing for an assessment of its quality. In some cases, the intensity of the piezoelectric effect is voltage-dependent, with higher voltages potentially enhancing the piezoelectric response.

1) Polarization

Polarization refers to the alignment of dipoles within a material in response to an applied electric field. This effect can be observed in scans taken at different voltages, although in my measurements, only weak polarization was observed. In some of my scans, a noticeable difference was found between the results obtained at negative and positive voltages. Additionally, the region of highest current was consistently slightly shifted in each scan (see Figures 4 and 5).
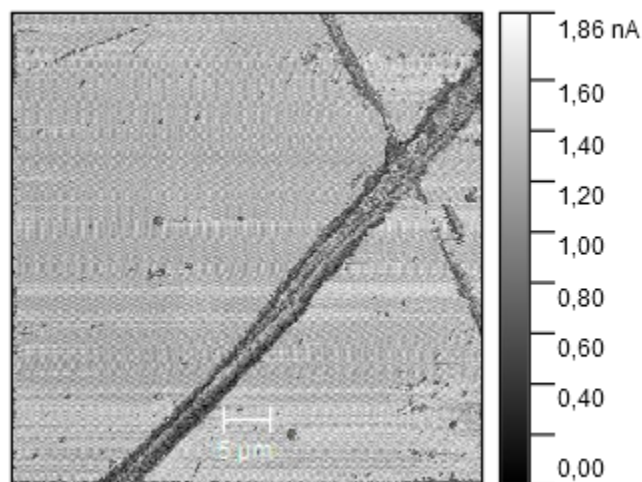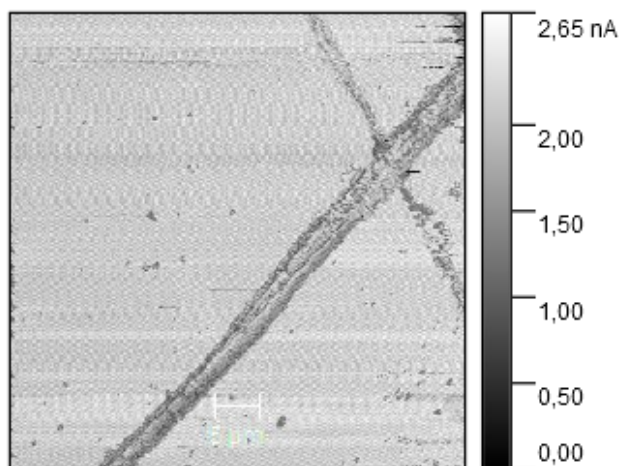

Figure 4: PVDF Fiber at -2V

Figure 5: PVDF Fiber at -10V

2)   Fiber quality

The quality of the fibers can be assessed through the scans. Areas with higher current, indicating a stronger piezoelectric response, are associated with a greater content of the β phase. In Figures 6 and 7, it can be observed that the current is stronger at the edges of the fiber, while the center exhibits much weaker current. To enhance the piezoelectric properties and overall quality of these fibers, they should be subjected to greater stretching, as the current configuration suggests an excess of the α phase. Increased mechanical strain would likely promote a higher β phase content. Interestingly, some fibers exhibited stronger piezoelectricity in the center than at the edges. Smaller areas with weaker current may indicate damage or cracks in the fiber, potentially caused by thermal shocks during production or the presence of impurities in the material.
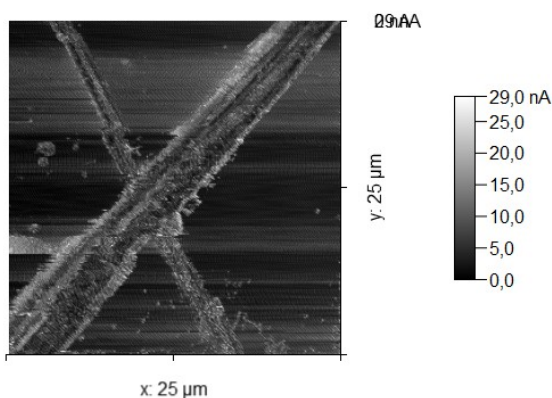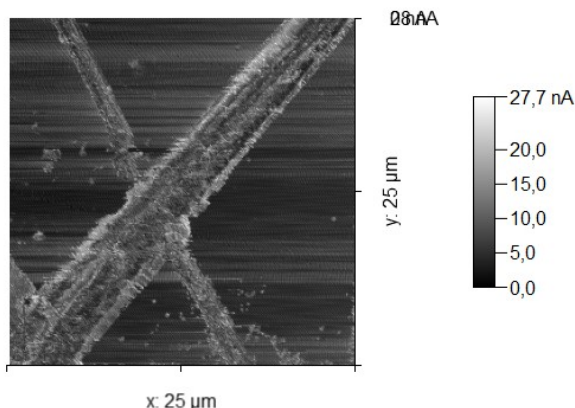

Figure 6: PVDF Fiber at 5V

Figure 7: PVDF Fiber at -5V

3)   Stimulation of the fibers

At zero voltage, the piezoelectric effect is weak at certain locations. However, upon applying a voltage, the fibers become more stimulated, resulting in an increased piezoelectric response. Higher voltages may also help repair small cracks and induce polarization within the fibers, further enhancing their piezoelectric properties (see Figures 8 and 9).
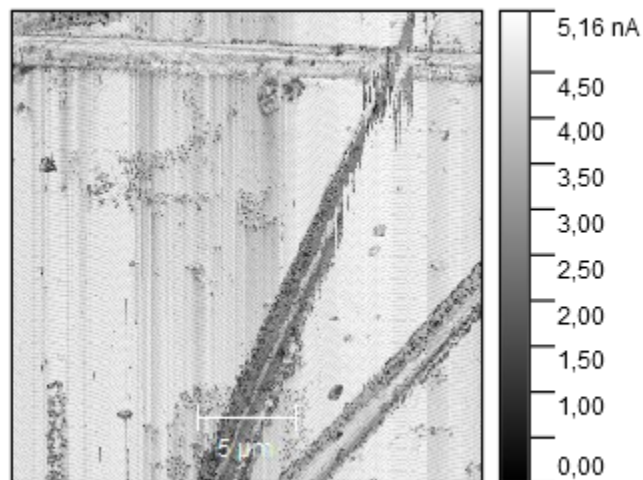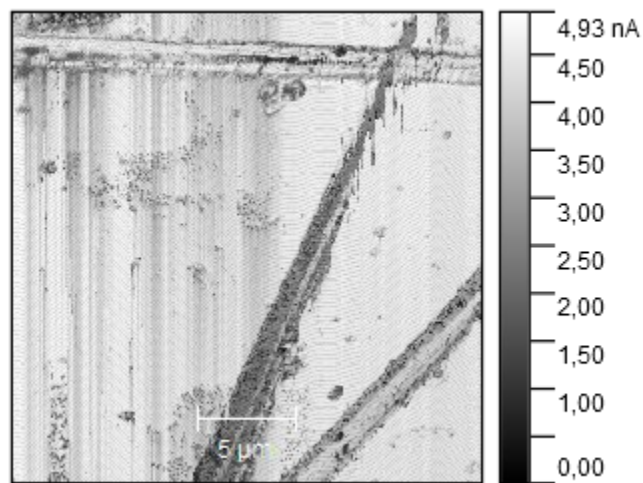

Figure 8: PVDF Fiber at -10V

Figure 9: PVDF Fiber at 0V

L. Conclusion and relevance

In this work, the piezoelectric properties of the β phase of PVDF were measured using Piezoresponse Force Microscopy mode. PVDF is considered a material of the future due to its piezoelectricity, resistance and stability. The findings from this study suggest that SPM modes can be instrumental in improving the quality of PVDF production. Additionally, the results indicate that applying higher voltages can enhance the material's piezoelectric responce.

REFERENCES

[1]   https://www.nanoscience.com/techniques/atomic-force-microscopy/

[2]   https://cs.wikipedia.org/wiki/Polyvinylidenfluorid

[3]   https://pubmed.ncbi.nlm.nih.gov/35994930/

[4]   https://matca.cz/technologie/analyticke-metody/afm/

[5]   *https://www.nanoandmore.com/what-is-atomic-force-microscopy?*
       gad_source=1&gclid=Cj0KCQiA_Yq-
       BhC9ARIsAA6fbAgXq6gv5K3mp7rzMrP1M_rf7l4ZV4I4DJ88lfBB0q0e1
       Kg_3x_dpMwaAvnhEALw_wcB

[6]   https://cs.wikipedia.org/wiki/Mikroskopie_atom%C3%A1rn
       %C3%ADch_sil

[7]   https://www.mff.cuni.cz/cs/kfm/experimentalni-vybaveni/mikroskopie-
       atomarnich-sil-afm

[8]   https://www.prf.upol.cz/files/PrF/katedry/kbf/materialy/MRSA_-_09-
       AFM-priprava_a_analyza_vzorku_.pdf

[9]   https://www.anamet.cz/mikroskopy-atomarnich-sil-afm/

[10]   https://www.researchgate.net/figure/a-b-and-g-PVDF-conformations-
       The-a-and-g-forms-contain-both-trans-and-gauche_fig5_382738176

[11]   https://dspace.vut.cz/server/api/core/bitstreams/20e1cbf5-0c8d-4c4f-
       bb89-cf2928b5c29c/content

STUDENT
EEICT

BRNO UNIVERSITY OF TECHNOLOGY
FACULTY OF ELECTRICAL ENGINEERING AND COMMUNICATION
TECHNICKÁ 3058/10, 616 00 BRNO, CZECH REPUBLIC

BRNO
UNIVERSITY
OF TECHNOLOGY

FACULTY OF ELECTRICAL
ENGINEERING
AND COMMUNICATION

www.eeict.cz

www.fekt.vut.cz